Proceedings

The 2nd ISIJ-VDEh-Jernkontoret Joint Symposium

(The 15th ISIJ-VDEh Seminar, The 9th Japan-Nordic Countries Joint Symposium on Science and Technology of Process Metallurgy)

12–13 June, 2017
Stockholm, Sweden

Organised by Jernkontoret
The Swedish Steel Producers' Association

Contents

POSTERS

Recent Research＆Development topics of Iron-making Technologies in NSSMC

Koji Saito

Nippon Steel & Sumitomo Metal Corporation, R&D

Abstract: The last decade was a turbulent for the steel industry. The reorganization of steel industry across borders has progressed and the increased demand for steel products has made the price of raw materials such as iron ore and metallurgical coal more volatile than ever. Ironmaking technology division in NSSMC has been exposed to global competition and has tried to cope with these changes and to increase its international competitiveness by developing such technologies as utilization of lower grade raw materials, productivity enhancement, measures for energy conservation and reduction of CO2 and NOx emission and so on. This paper describes the recent progress in ironmaking technologies in NSSMC.

1.Introduction

The circumstances surrounding the iron and steel industry have changed greatly. While the increased demand for steel products has caused a rise in the price of raw materials such as iron ore and metallurgical coal and the quality of raw material has been deteriorating, there is a growing need for developing technology to give solutions for various environmental problems such as energy shortage, increase in CO_2 and NO_x emission and so on. This plenary lecture provides a summary of the developments of ironmaking technologies in Japan for environmental solution, along with some examples of the development result and practical application such as RCA (Reactive Coke Agglomerate), LCC (Lime Coating Coke), SCOPE21 (Super Coke Oven for Productivity and Environment Enhancement toward the 21st century), COURSE50 (CO_2 Ultimate Reduction in Steelmaking Process by Innovative Technology for Cool Earth 50) project and so on.

2.Current Status of Japanese Steel Industry

2-1.Production and Raw Materials

In 2013, Japan's crude steel output increased for the first time in three years, climbing up 3.1% to 110.59 million tons (Figure 1)[0]. The Japanese steel industry depends entirely on imports for the two primary raw materials used to produce steel; iron ore and coal. In 2013, Japan's imports of iron ore increased for the second consecutive year. Among major suppliers to Japan, imports from Australia and Brazil accounted for 61.8% and 26.8% respectively (Figure 2) [0]. These two countries supplied about 90% of Japan's steelmaking iron ore imports. Metallurgical coal imports in 2013 also increased. Imports from Australia, which accounts for about 70% of all coal imports, increased 6.6% and those from Russia and Indonesia rose 7.3% and 14.1% respectively (Figure 2). But coal imports from Canada and the USA were down 6.3% and 14.3% respectively. The unit price of imported iron ore and coal was down in 2013, however, the cost of iron ore and coal is still high (Figure 3) [0].
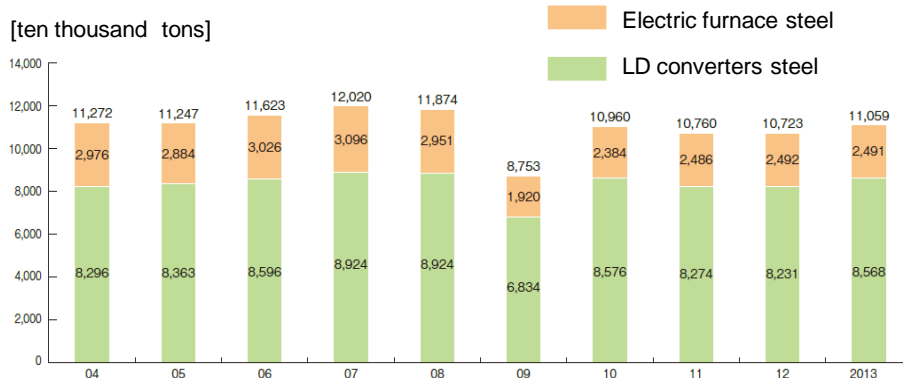
Figure 1. Changes in crude steel production in Japan.
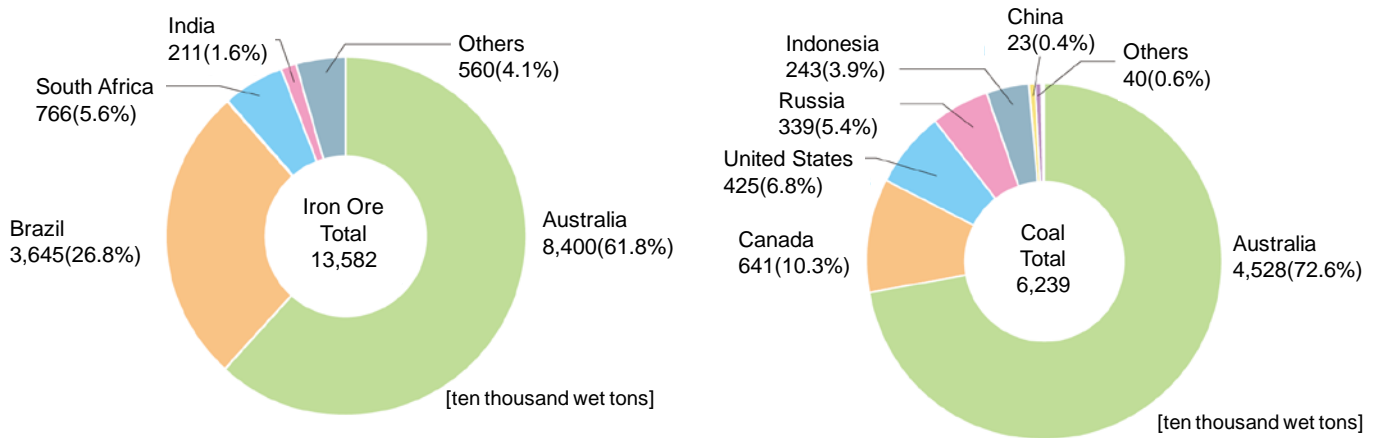
Figure 2. Iron ore and coal imported in 2013, by supplier country.
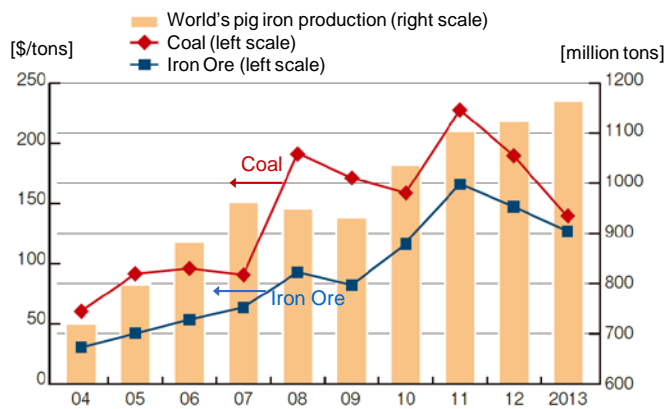
Figure 3. Price of imported iron ore and coal.

2.2 Energy and Environment

The Japanese steel industry has established a voluntary action plan for environmental protection. The plan includes the goal of achieving a 10% reduction on energy used in production processes (about 9% cut in CO_2 emissions) compared with the fiscal 1990 level based on average annual emissions between fiscal 2008 and 2012. Under the voluntary action plan, there have been many progresses in energy-conservation measures and improving operations. As a result, average annual energy consumption between fiscal 2008 and 2012 reached the target by falling 10.7% below the fiscal 1990 level as shown in Figure 4 because of a 2.7% decrease in crude steel production and an 8.0% improvement in unit energy consumption (Figure 5)[0]. In addition, CO_2 emissions were 10.5% below the fiscal 1990 level. The Japanese steel industry aims to achieve more emission reductions by utilizing state-of-the-art technologies to the greatest possible extent and by developing a revolutionary ironmaking process called COURSE50 and other innovative technologies.

In addition to energy conservation, reduction of NO_x emission from ironmaking process has been an important subject from the viewpoint of environment. Among all, decreasing NO_x emission in sintering process is a key issue in steel industry.

This plenary lecture provides a summary of the developments of ironmaking technologies in Japan for environmental solution, along with some examples of the development result and practical application.
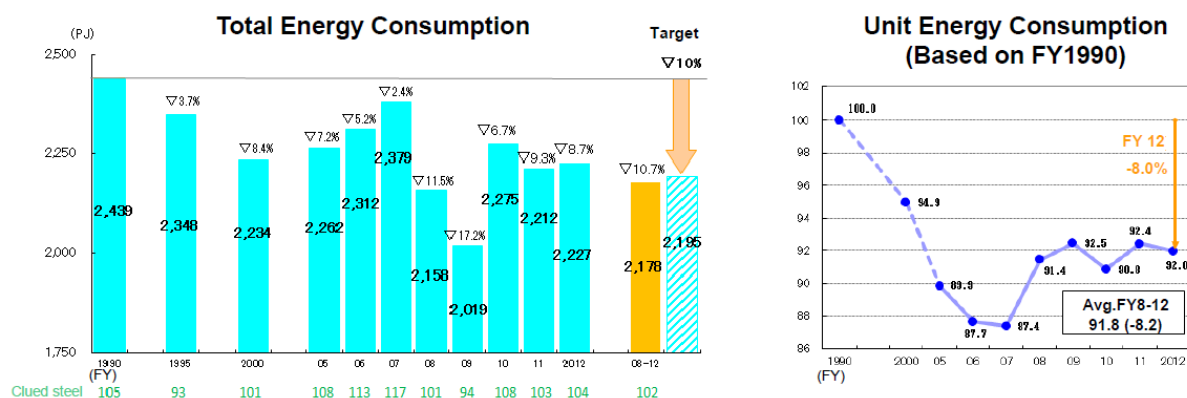
Figure 4. Changes in total energy consumption and unit energy consumption.
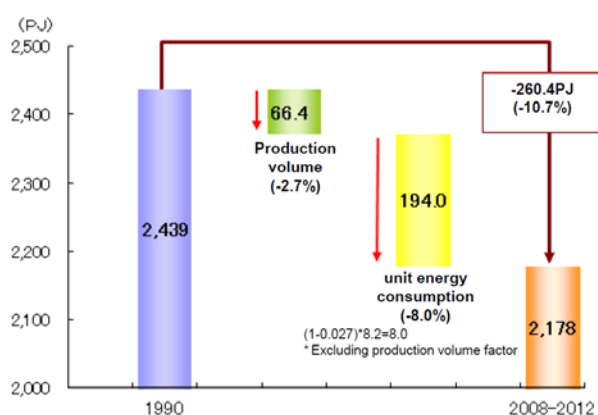
Figure 5. Causes of change in FY08-FY12 energy consumption.

3.Development of Sintering Technology

3-1 LCC (Lime Coating Coke)

Decreasing NO_x emission in sintering process is a key issue in steel industry. NSSMC (Nippon Steel & Sumitomo Metal Corporation) developed a new technology of decreasing NO_x emission in sintering process by using LCC (Lime Coating Coke)[0,0]. In this process, as shown in Figure 6, coke breeze is mixed with lime (CaO) and pelletized. As a result, coke is coated with CaO. LCC is mixed with iron ore and iron oxide is also coated on LCC (Figure 7). The mixture of CaO and iron oxide forms $CaO \cdot Fe_2O_3$ melt on coke surface when it is heated. $CaO \cdot Fe_2O_3$ coating layer promotes high temperature combustion and functions as catalyst for reducing NO_x. NSSMC introduced LCC in Oita works and started the commercial operation in 2013. By LCC process, NO_x emission in sintering process decreased and sinter productivity increased.
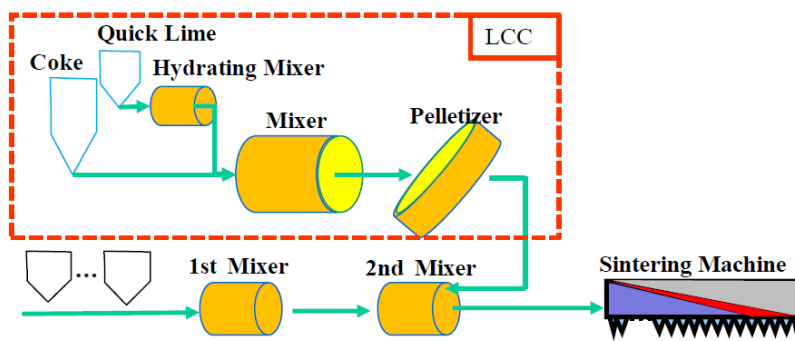
Figure 6. Process flow of LCC.
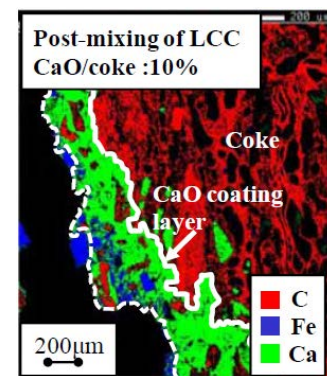
Figure 7. CaO coating layer on coke.

4.Development of Cokemaking Technology

4-1 DAPS

In coke oven, heat supplied by conduction is used for evaporating water, which is not energy efficient. In Japan, where energy cost is expensive, coal pre-treatment technology has been studied and developed to improve energy efficiency. The basic concept is to dry coal before it is charged into coke oven chamber. Two typical examples are CMC and DAPS[5]. CMC stands for coal moisture control. In CMC, coal is dried in steam tube dryer and the moisture decreases from 10% to 5-6%. The lower limit of the moisture in CMC process is determined by the emission level of coal fine dust. DAPS process has solved this problem by separating fine coals with fluidized bed dryer and agglomerating coal fines. DAPS stands for dry-cleaned and agglomerated precompaction system. The moisture is down to 2% and this process is more energy-efficient. NSSMC introduce CMC and DAPS in Oita works in 1983 and 1992 respectively. Furthermore, these processes have another advantage, which is to increase the blending ratio of low quality and cheap coal; slightly caking coal. Decrease in coal moisture results in the increase in the coal bulk density in coke oven chamber; which leads to the improvement of coke strength. Based on the same coke strength, the blending ratio of slightly-caking coal can be increased in coal drying process.

4-2 SCOPE21 (Super Coke Oven for Productivity and Environment Enhancement toward the 21st century)

The average working life of coke ovens in Japan is now about 40 years and the supply of coke is foreseen to decrease because of the deterioration of the coke ovens. Furthermore, the existing cokemaking process faces a lot of challenges such as depletion of metallurgical coal, environment and cost reduction. The Japan Iron and Steel Federation and the Center for Coal

Utilization, Japan had made an effort to develop the SCOPE21 process, Super Coke Oven for Productivity and Environmental enhancement toward the 21st century, which was a ten-year (1994-2003) national project[6]. The target of SCOPE21 was: 1) increasing the ratio of non- or slightly caking coal (poor coking coal) from 20% to 50%; 2) higher productivity for reducing the construction cost; 3) reducing NO_x by 30% and no smoke/no dust operation; 4) energy saving by 20% for reducing CO_2. The main characteristics of the SCOPE21 process are the rapid preheating of the coal charge and the rapid carbonization. The quality of coke can be improved by upgrading the coal coking quality with rapid preheating and by increasing the coal bulk density. The coking time and the coking energy can be reduced by preheating the charging coal. Coal is heated up to 350 ºC in the coal pretreatment facility. NO_x (nitrogen oxides) content in the exhaust gas can be reduced by improving the heating system of the coke oven.

After the national project finished, the feasibility of the commercial scale plant was studied in NSSMC, and the 1st SCOPE21-type new coke oven battery was constructed at Oita works and the operation of new coke plant was started in 2008 (Figure 8). The second SOPE21 type new coke oven started operation in 2013 at NSSMC Nagoya works (Figure 9). The coke production capacity is 1 million ton per year. The coal is dried in a fluidized bed dryer and fine coal is separated from coarse coal. The fine coal is agglomerated by an agglomerater, while the coarse coal is pre-heated rapidly to 350 ºC in a pneumatic pre-heater. Then the agglomerated fine coal is added to the coarse coal, and 250 ºC coal is charged into coke oven. The new coke oven adapted multiple stage burner and circulation exhaust gas system. Consequently, the NO_x concentration of combustion exhaust gas was below 170ppm at flue temperature of 1270 ºC in the COG (Coke Oven Gas) burning coke oven. Since the start-up of the new oven, the operation has been good and stable. This technology contributes to increasing Japan's world leading energy efficiency.

Oven type	SCOPE21-type
Number of ovens	64
Dimension of ovens H×L×W (m)	6.30×15.40×0.45
Coke production (t/d)	2730
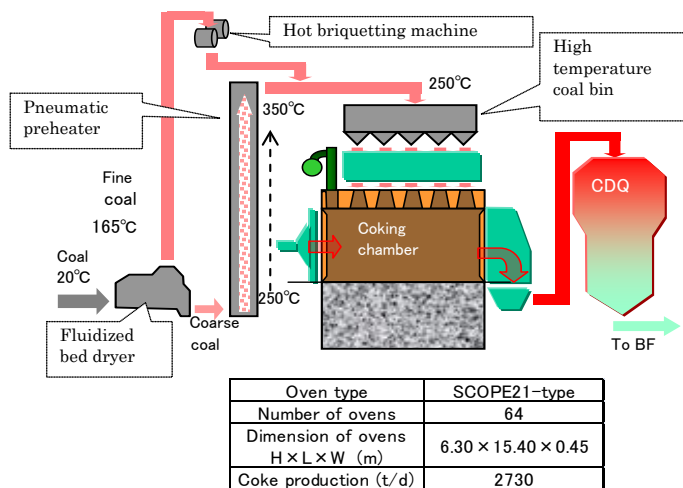
Figure 8. Process flow of Oita SCOPE21.

Figure 9. Overview of Nagoya SCOPE21.

5.Development of Blast Furnace Technology

5.1 RCA (Reactive Coke Agglomerate)

In this process, carbon and iron composite, RCA, is produced according to the process flow (Figure 10)[8]. Carbon and Iron oxide compound such as dust are mixed and pelletized in a disc pelletizer. After cured, the no-fired pellet product is charged into blast furnace. The carbon gasification starts at lower temperature due to the closely-positioned carbon and iron

oxide, which enhances the blast furnace reaction efficiency by decreasing the thermal reserve zone temperature. This technology was put to practical use at NSSMC Oita works in 2012. The use of RCA containing 20% carbon lowered the reduction equilibrium temperature, increased the gas utilization ratio and reduced the carbon consumption. The carbon consumption decreased 0.36 kg C/tHM per 1 kg C/tHM of input carbon derived from RCA.

Raw Material Hopper → Mixer → Disc Pelletizer → Sieve → Curing Yard → Sieve → Curing Yard

Disc Pelletizer   RCA
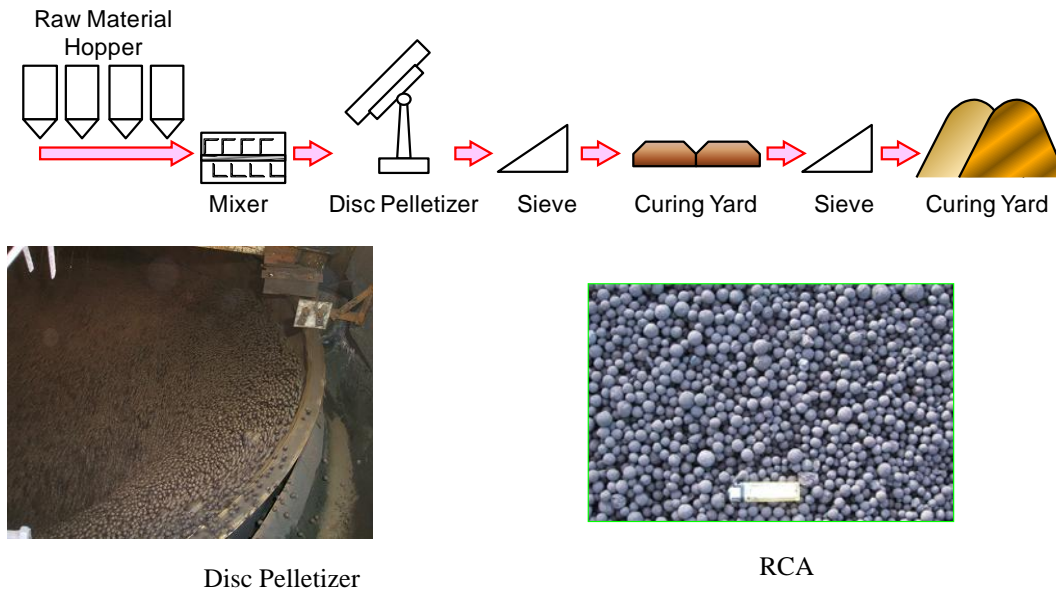
Figure 10. Process flow of RCA.

5.2 3D-Venus

It is indispensable to stabilize the blast furnace operation in order to increase productivity, decrease the reduction agent ratio and reduce CO_2 emissions from blast furnaces. In order to stabilize the blast furnace operation, it is important to know the phenomena in the blast furnace which changes with time and to take a proper action, however, it is very difficult to actually see the inside of the blast furnace. Therefore, to support the stability of blast furnace operations, we developed methods for collecting temperature and pressure data using about 500 thermocouples located in the stave coolers and 20 shaft pressure sensors. This is an online system called 3D Venus[9], which stands for three dimensional visual evaluation and numerical analysis system of blast furnace operation and visualizes the state of operations by using the large amount of data of the stave temperature and the shaft pressure of the blast furnace. These data are shown three dimensionally, second by second as shown in Figure 11. This system was first introduced to NSSMC Nagoya works in 2007 and to other works. This system enables a clear and objective understanding of the spatial and time series of the fluctuation of the shaft pressure and the packing structure of the charging material. Quick and quantitative assessment of the fluctuation in the state of the blast furnace has contributed to the stable blast furnace operation and decrease in the reduction agent ratio.
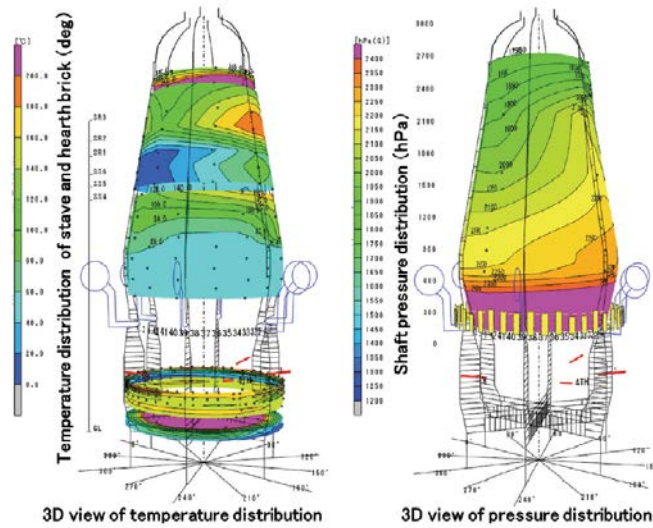
Figure 11. 3D Venus.

6.COURSE50 (CO₂ Ultimate Reduction in Steelmaking Process by Innovative Technology for Cool Earth 50)

6.-1 Outline of COURSE50

Since FY2008, Japanese four blast furnace steelmakers and one engineering company have been working on the "CO₂ Ultimate Reduction in Steelmaking Process by Innovative Technology for Cool Earth 50 (COURSE50) Project"[10] which is one of national projects commissioned from NEDO aimed at developing drastic new CO_2 emissions mitigation technologies from steelworks. Work is under way on developing a technology for using hydrogen for the reduction of iron ore (method for lowering blast furnace CO_2 emissions) (Figure 12). Hydrogen in the very hot coke oven gas (COG) generated during coke production is amplified and then used to replace some of the coke. Furthermore, for the separation of CO_2 from blast furnace gas (BFG), a revolutionary CO_2 separation and collection technology (technology for separating and collecting CO_2 from blast furnaces) will be developed that utilizes unused heat at steel mills. The goal is to use these technologies for low-carbon steelmaking that cuts CO_2 emissions by about 30%.
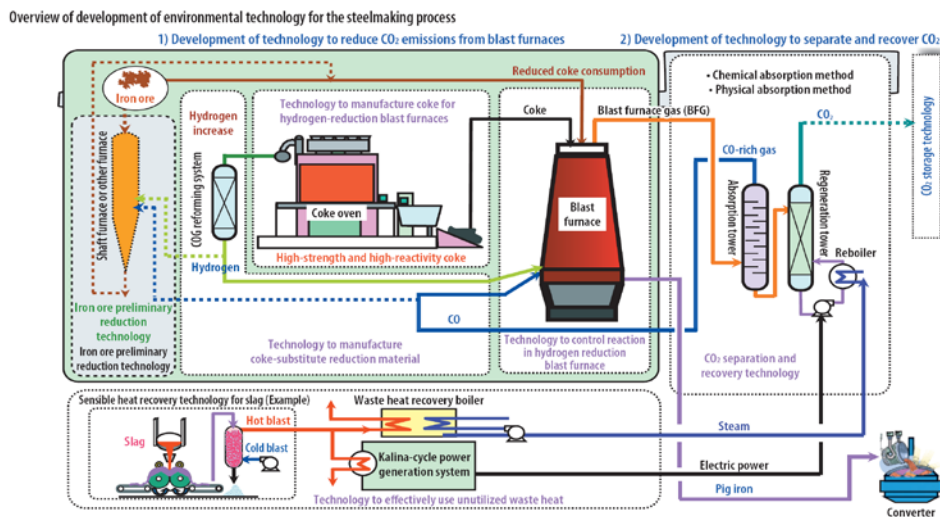
Figure 12. Outline of COURSE50.

6-2 Technology to reduce CO_2 from Blast furnace

Figure 13 shows the concept of iron ore hydrogen reduction. Coke oven gas (COG) or reformed COG called RCOG is used as reducing agents rich in hydrogen. RCOG is produced by amplifying its hydrogen content in COG by utilizing newly developed catalyst and unused waste heat of COG (800 °C). To investigate and evaluate the potential in replacing coke and coal as reducing agents in the blast furnace with COG or RCOG, a trial was carried out using LKAB Experimental Blast Furnace. As shown in Figure 14, hydrogen reduction was increased in both COG injection from blast tuyere and reformed COG injection from shaft tuyere because of the fast reaction rate of hydrogen reduction. Along with the experiment, a mathematical simulation model considering mass and heat transfer, reactions, and gas, solid and liquid flows inside the furnace was developed. As shown in Figure 15, both experiment and simulation confirmed that CO_2 reduction of about 3% is possible at blast furnace input.
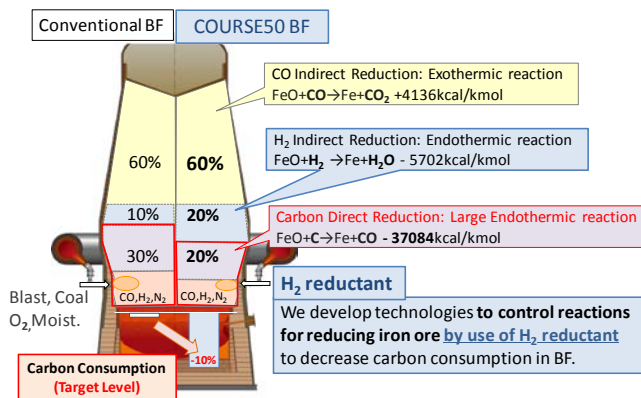
Figure 13. Concept of iron ore hydrogen
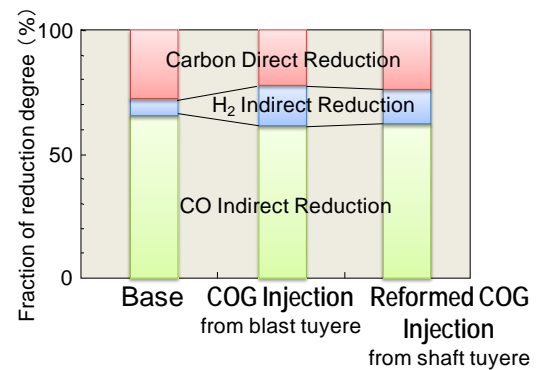
Figure 14. Comparison of fraction of reduction degree in the experimental blast furnace trial.
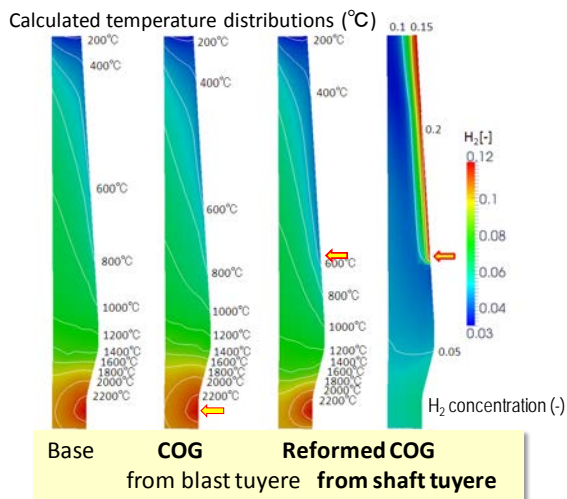
(a) Temperature profiles calculated by a mathematical simulation model.
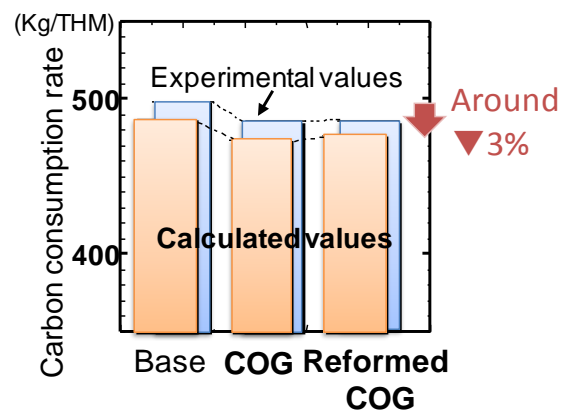
(b) Comparison of carbon consumption rate between observed and calculated ones.

Figure 15. Calculated temperature profile and carbon consumption rate in the experimental blast furnace trial.

6-3 Technology to reduce CO_2 from Blast furnace

The project is also developing technology to capture CO_2 from blast furnace gas (BFG) through chemical absorption and physical adsorption methods using unused waste heat in steelworks. Figure 16 shows the typical process flow of chemical absorption. (1) The absorbent comes in contact with the feed gas in the absorber counter-currently, and absorbs CO_2 selectively. (2) CO_2 rich absorbent is sent to the stripper, and releases CO_2 by heating at about $120℃$. (3) The regenerated absorbent is cooled and sent to the absorber to repeat the cycle. A high performance absorbent was developed to reduce the thermal energy consumption for the CO_2 separation from 4GJ/t-CO_2 to 2GJ/t-CO_2. In addition to the low energy consumption, the new absorbent easily releases CO_2 at a lower temperature than that of normal conventional process for regeneration. It means that there is the possibility to utilize the unused waste low temperature heat at low cost.

 6-4 Future plan

In Step 1 (2008-2012), the basic technology was developed and confirmed as planned. The main objective of Step 2 (2013-2017) is the integrated development of hydrogen reduction and CO_2 separation and recovery. A 10 m^3 scale trial blast furnace is constructed at Kimitsu Works to increase efficiency by optimizing conditions for gas input and used with the 30 ton-CO_2/day chemical absorption test plant (CAT30) (Figure 17). The goal of the project is to commercialize the first unit by around 2030 and to generalize the technologies by 2050 considering the timing of the replacement of blast furnace equipment under the precondition of economic potential and available CCS technology.
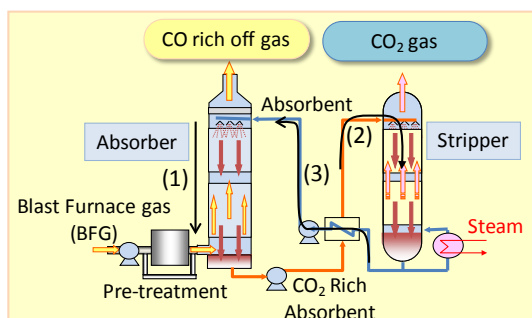
Figure 16. Chemical absorption process.
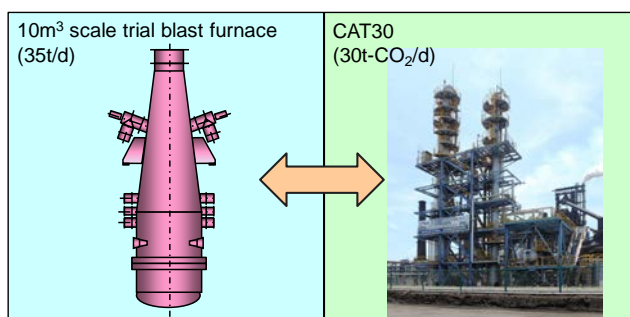
Figure 17. A trial blast furnace and CO_2 chemical

7.**Conclusion**

Looking ahead to 2020, the Japanese steel industry will be first in the world to begin using relatively new advanced energy-conservation technologies. The Japanese steel industry will continue to focus on development of revolutionary ironmaking technology for environmental solution and energy conservation to contribute to conserve energy with more efficient steel production processes and to achieve a low-carbon society. We will tackle various problems surrounding ironmaking through the maximum use of the most advanced technologies and will increase Japan's world-leading energy efficiency.

References:

1)The Japan Iron and Steel Federation, *The Steel Industry of Japan 2014*.

2)The Japan Iron and Steel Federation, *Steel Industry Measures to Combat Global Warming, Voluntary Action Plan Performance Report*. (December 2013).

3)K.Katayama et al., CAMP-ISIJ, 26(2014), 712.

4)K.Matsui et al., CAMP-ISIJ, 27(2014), 234.

5)K.Katayama et al., to be presented at AISTech 2015.

6)S.Nomura, Innovation of Ironmaking Technologies and Future International Collaboration, the 54th Committee on Ironmaking of Japan Society for Promotion of Science, Tokyo, 2014, pp 157.

7)K.Higuchi, H.Yokoyama, S.Kogure, T.Bito, A.Oshio, CAMP-ISIJ, 26(2013),17. (RCA)

8)K.Takeda, JRCM NEWS, No.323 (2013), 2.

9)S.Matsuzaki et al., to be presented at AISTech 2015.

10)M.Ujisawa et al., Innovation of Ironmaking Technologies and Future International Collaboration, the 54th Committee on Ironmaking of Japan Society for Promotion of Science, Tokyo, 2014, pp 47.

Steel Production in EUROPE and Germany 2017

P. Dahlmann, R. Fandrich, H. B. Lüngen,
Steel Institute VDEh

Abstract: After the decline in 2008/09, the European steel industry is still struggling to reach the pre-crisis production level. A report on current steel production in Europe with special focus on Germany is given. The paper provides figures on development of the steel industry, raw materials supply, continuous casting and ingot casting production. During the past 30 years, the German steel industry has made remarkable progress in terms of process efficiency. Therefore, key indicators like total output, energy consumption and emissions were compiled.

1. Steel Production in Europe

Germany is located in the geographic centre of the European Union's 28 member states. Basically for its 508 million inhabitants with an apparent steel use of 331.6 kg steel per-capita [1] the EU 28 produced 162.0 million tons crude steel in 2016.

The share of oxygen-steel making within the European production mix was 60.3 % in 2016, while electric steel production amounted to 39.7 %. The enterprises in the EU-28 countries focus on different strategies for steel production: Italy and Spain are dedicated to electric steel production to more than 65 %, Luxembourg even to 100 %, while Austria, the Netherlands, the Czech Republic, Slovakia and Hungary produce more than 90 % of their steel by oxygen steelmaking. Open hearth steel production has vanished completely in EU-28.
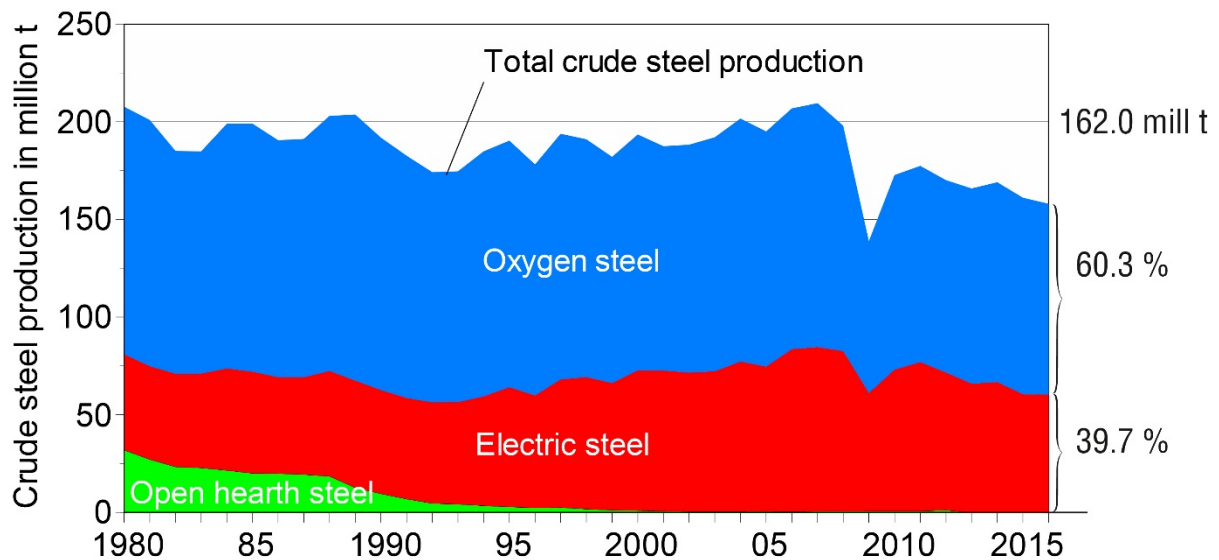
Figure 1. Crude steel in the EU-28 by process [1].

Due to the global financial crisis, the steel production worldwide dropped tremendously in 2009. In EU 28 the steel production dropped to 139 million tons which was a slump of 33 % compared to the production level of 210 million tons in 2007. During the following years 2010 and 2011, the production recovered to 177.7 million tons but decreased since that time to 162.0 million tons in 2016.

Since 2008, 9 oxygen steel works were closed down all over EU-28 with about 20 million tons crude steel nominal production capacity with individual capacities between 0.7 and 3.5 million tons per year. During the same period 22 electric steel mills shut down their electric arc furnaces with a nominal capacity of in total 14.2 million tons per year. Most important shut downs were realized in Spain, Italy, Germany, and France with in total more than 60 % of the shutdown EAF capacities in EU 28.

City	Country	Capacity in million tons
Duisburg	Germany	19.5
Taranto	Italy	8.0
IJmuiden	The Netherlands	7.5
Dunkerque	France	6,8
Dillingen + Völklingen	Germany	6.2
Linz	Austria	6.0
Gijon + Aviles	Spain	5.4
Salzgitter	Germany	5.2
Fos-sur-Mer	France	5.1
Dabrowa Gornicza	Poland	5.0
Gent	Belgium	5.0
Port Talbot	United Kingdom	4.5
Kosice	Slovakia	4.5
Cremona	Italy	3.8
Bremen	Germany	3.7
Esch, Differdange	Luxembourg	3.5
Scuntthorpe	United Kingdom	3.2
Bilbao	Spain	3.1

Table 1. Crude steel production sites of EU-28 with capacity > 3 million tons per year in 2017 [2].

However, the most productive plants in EU-28 are still on the market, **Table 1**. There are 18 sites with a crude steel production capacity of more than 3 million tons per year.

2. Steel Production in Germany

With 42.1 million tons, the total crude steel output in Germany amounted to 26 % of EU-28 crude steel production in 2016. **Figure 1** shows the location of the steelworks in Germany. 29.5 million tons or some 70.1 % of the total production were produced by oxygen steelmaking, 12.6 million tons or 29.9 % by electric steel making. The oxygen steel production was achieved in 9 steel plants operating 18 converters out of 21 with heat sizes between 150 and 380 tons. The electric steel production was achieved in 20 steelworks operating 25 EAF´s with heat sizes up to 150 tons, among them 3 DC furnaces with 125 tons to 140 tons [2].

Raw material input of German electric arc furnaces is nearly 95.7 % scrap. Only one electric steelwork has its own DRI base. With a raw materials input of in total 89.1 million tons, the German steel industry produced with 86,000 employees in 56 companies 40.4 million tons of finished steel products in 2015 [2].

	crude steel production 2016 in mill.t
(1) ArcelorMittal Hamburg	1.0
(2) ArcelorMittal Bremen	3.6
(3) Benteler	0.6
(4) Georgsmarienhütte Holding	1.3
(5) Salzgitter	5.7
(6) Brandenburger Elektrostahlw.	1.1
(7) Hennigsdorfer Elektrostahlw.	0.7
(8) ArcelorMittal Eisenhüttenstadt	1.9
(9) thyssenkrupp Steel Europe	9.7
(10) HKM	3.8
(11) ArcelorMittal Ruhrort	1.3
(12) Deutsche Edelstahlwerke	0.8
(13) Buderus Edelstahl	0.3
(14) Stahlwerk Thüringen	0.8
(15) ESF Elbe-Stahlwerke Feralpi	1.0
(16) BGH Edelstahl	0.2
(17) Dillinger Hüttenwerke	2.2
(18) Saarstahl	2.5
(19) Badische Stahlwerke	2.4
(20) Lech-Stahlwerke	1.2

Figure 2. Most important sites of German steel production [4].

Five coke oven plants are operated in Germany, today. In 2014, the coke oven plant HKM in Duisburg Huckingen was enlarged and received a second coke oven battery. With this increased capacity, the 5 German coke oven plants produced 9.22 million tons dry coke in 2016, and the 15 German blast furnaces produced in total 27.1 million tons hot metal.

During the 2008/09 crisis, the German crude steel production dropped down from 45.8 million tons in 2008 to 32.7 million tons in 2009, which was a decrease of 28.6 %. Since 2010, the steel production in Germany is recovering. However, since 2012, three electric steel mills were shut down, in addition, one ingot casting shop was closed. Since that time the crude steel production is stabilizing on a level between 42 and 43 million tons.

After comparable production drops in 2009 as in the core steel industry, the ingot production in Germany amounted to 1.7 million tons in 2011 and nearly reached again the all-time high of 2.0 million tons from 2008. Since 2012 the ingot production has reduced to 1.3 million tons in 2016. While at the beginning of the millennium, there was more bloom produced for rolling than for forging, the market demand has shifted. Since 2012 there have been more bloom for forging produced than for rolling

Production records can still be observed in remelting since 2014. The tonnage of steel produced by Electro Slag Remelting (ESR) or Pressurized Electro Slag Remelting (PESR) in Germany was 89060 tons in 2016, about 4.400 t were treated by Vacuum Arc Remelting (VAR). Today there are 20 ingot casting and 10 remelting shops operated in Germany.

3. Raw materials provisioning for Germany

40 million tons of iron ore was imported predominately from Brazil (50.6 %), Canada (17.1 %), Sweden (13.7 %) and South Africa (7.0 %). The steel works in Germany consumed 18.0 million tons of scrap basically produced in the country in 2016. The scrap imports comprised 4.3 million tons, while the exports added up to 8.6 million tons. Therefore Germany is a scrap exporting country. While foreign steel scrap supply comes in increasingly from Eastern Europe, scrap is exported from Germany via Benelux primarily.

The coking coal supplies comprised 11.52 million tons in 2016. This coking coal was supplied from Australia (46.3 %), USA (31.5 %), Canada (12.5 %) and Germany (4.5 %) and some other countries (5.2 %). Imported Coke and coke breeze supply comprised 0.62 million tons, coming basically from Poland (44.2%), Russia (23.8 %) and China (16.5 %). Injection coal supply for blast furnaces comprised 4.55 million tons in 2015. Main supplying countries were Russia (74.0 %), USA (14.6 %) and Germany (16.6 %). However, coal mining will be stopped in Germany by 2018.

4. Metallurgical main developments

Already in December 2012, Salzgitter AG and SMS Siemag AG started up its worldwide first BCT® plant (Belt Casting Technology) at Peiner Träger GmbH. By common development of both companies assisted by TU Clausthal University a promising step into direct strip casting has been made. This process could enable energy and resource saving production of new high performance steels with extremely high energy absorption capacity, so called HSD® steels (High Strength and Ductility) with manganese contents above 15 %. During the ongoing levelling phases the technical feasability could be proved in industrial scale, first HSD® melts could be cast savely. However, the continuous improvement process is going on both in Germanies integrated steelworks and in its electric steel mills as can been seen from tables 2 an 3.

ArcelorMittal Bremen	12/14 13	Slab Caster Twin-LF (300 t)	Revamping (Moulds) New installation
AM Ruhrort	13	RH	New installation
DH	11/16 10/15 3/13	BF 4 Thick slab caster CC 6 VD	New relining New installation: 500 mm thickness, replaces CC 3 Revamping
HKM	11/16 5/15	Blast Furnace B Slab Caster No. 3	New relining
tk-SE, DU Beeckerwerth	10/14	Slab caster 1	Revamping
tk-SE, DU Bruckhausen	10/14 9/13	BOF 2 (380 t) BOF 1 (380 t)	Revamping: +24 % Volume
tk-SE, DU Schwelgern	11/14	BF 2	New relining
Saarstahl	1/13	RH (200 t)	New installation
Salzgitter Flachstahl	11/15 10/15 15 9/14 10/13	Blast Furnace B BOF C Salb caster 2 BOF A (330 t) Blast Furnace A	New relining Revamping Revamping: +28% Volume Revamping New relining

Table 2. Metallurgical installations and revampings in German integrated steelworks [2].

Buderus Edelstahl GmbH	2/15	New secondary dedusting system
	10/14	New automatic teeming system (ingot casting)
DEW Witten	6/14	New secondary metallurgy (LF, 2x VD/VOD, alloying bunker system)

Table 3. New metallurgical installations and revampings in German electric steelworks [2].

5. Environment

While in 1948 the consumption of reducing agents in Germany's blast furnaces comprised 1100 kg/tons hot metal, it could be cut by 54 % to today 500 kg coke per ton hot metal by a number of technical innovations. These are a. o.: Ore beneficiation, use of overseas rich iron ores, blast furnace hot blast temperatures above 1200°C, O_2-enrichment, top pressure, burden distribution, gas flow control, improvement of Fe burden, improvement of coke and small coke in Fe burden.

Also the average slag volume of blast furnaces in Germany is on a very low level. It decreased from 980 kg/tons hot metal in 1947 to 280 kg/tons hot metal in 2016. About 95% of the slag produced during iron and steelmaking in Germany is circulated or exploited for production of fertilizers, building materials or cement. Just about 5 % have to be landfilled. The crude steel specific scrap consumption since 1982 has increased from 38 % to a level of 44 %, today [4].
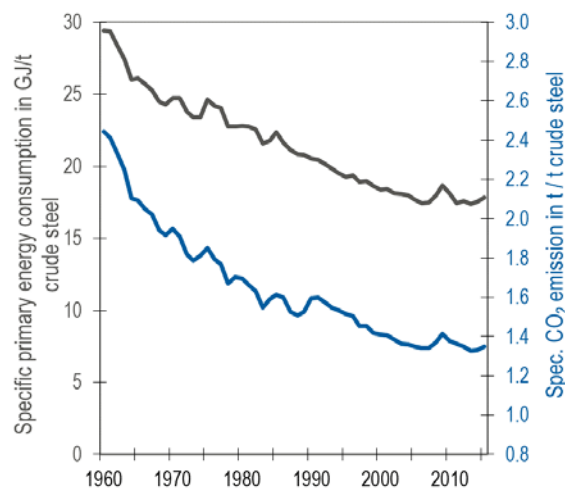
Figure 3: Energy efficiency and CO_2 emission of the steel industry in Germany.

The specific energy consumption for the total steel production via the blast furnace/converter and the EAF route decreased from almost 30 GJ/tonne crude steel in 1960, through 23 GJ in 1980, to the current 17.9 GJ/ton crude steel (-40 %), **Figure 3**. During the same period, specific CO_2 emissions declined about 42% from 2.4 ton CO_2/ton crude steel to 1.35 ton CO_2/ton crude steel.

Just a few of the many measures taken by plant operators and constructors that have led to this success, particularly regarding CO_2 reductions, are listed below, e.g.: the decrease in reducing

agent consumption for hot metal production in blast furnaces, the increased proportion of electric steel production and process innovations and the constant optimisation of processes regarding energy input, through the recovery of energy and improved coupling energy management.

References:

1) World Steel Association: World Steel in Figures 2017
2) VDEh database PLANTFACTS (5/2017)
3) Jahrbuch Stahl 2017. Eds.: Stahlinstitut VDEh, Wirtschaftsvereinigung Stahl. Verlag Stahleisen GmbH, 2013
4) Brochure „Fakten zur Stahlindustrie 2016". Eds.: Stahlinstitut VDEh, Wirtschaftsvereinigung Stahl, November 2016. (www.stahl-online.de)

HYBRIT – A Swedish National Development Project for CO2-free Ironmaking

Martin Pei, Executive Vice President & Chief Technical Officier, SSAB AB, Box 70, SE-101 21 Stockholm, Sweden

Åsa Sundqvist, Senior Vice President Operational Support & Business Development, LKAB, SE-983 81 Malmberget, Sweden

Andreas Regnell, Senior Vice President Strategic Development, Vattenfall AB, Evenemangsgatan 13, SE-162 92 Solna, Sweden

Abstract

The Swedish steel industry has a strong position in terms of efficient blast furnace operation and CO2 emission. This is result of a successful development work carried out in the 1980's at LKAB and SSAB followed by closing of sinter plants and transition to 100% pellet operation at all SSAB's five blast furnaces. SSAB is today the steel company with lowest carbon dioxide emission per ton hot metal produced by the blast furnace process. Pilot plant trials within the ULCOS project carried out at LKAB's experimental blast furnace at Swerea Mefos in Luleå Sweden showed that modifying the blast furnace with top gas recirculation combined with CCS, a reduction of approximately 50% CO2 emission is achievable. To drastically reduce CO2 emission further breakthrough technology is necessary to replace the blast furnace process for ironmaking. On April 4th 2016, SSAB together with LKAB and Vattenfall launched a project aimed at investigating the feasibility of a hydrogen based sponge iron production process, with CO2 emission free electricity as the primary energy source – HYBRIT (Hydrogen Breakthrough Ironmaking Technology). Currently a prefeasibility study project is ongoing which will be finalized at end of 2017. In the meantime a four year research program is in starting up phase. Both are supported by the Swedish Energy Agency.

Sweden has a unique opportunity for research and development for the HYBRIT project:
- A long tradition of developing iron ore reduction technologies
- A steel industry specialized in high end products requiring clean raw material
- A leading iron ore mining industry delivering advanced BF- and DR-pellets
- A fossil-free electricity system with excess capacity
- A suitable R&D environment with universities, research institutes and efficient coordination through branch organizations
- A nation with high ambition to drastically reduce CO2-emissions

Selected research focus areas for energy and material improvements in reduction and refining metallurgy

Eetu-Pekka Heikkinen, Ville-Valtteri Visuri, Hannu Suopajärvi, Antti Kemppainen,
Matti Aula, Petri Sulasalmi & Timo Fabritius
Process Metallurgy Research Unit, University of Oulu, Finland.

Abstract

Improvement of material and energy efficiencies of metallurgical processes affords large potential benefits from both economic and environmental perspectives. This paper aims to illustrate case studies in which efficiency of iron and steelmaking processes has been improved using different tools such as advanced experimental simulations, novel measuring and analyzing methods as well as mathematical process modelling. The case studies cover various process stages from raw material pretreatment and reduction to refining.

1. Introduction

Production of iron and steel is very material and energy intensive. Hence, the development of ironmaking and steelmaking processes by improving their material and energy efficiencies affords large potential benefits from both economic as well as environmental perspectives. Systematic improvement of iron and steelmaking processes requires understanding of the chemical and physical phenomena taking place in these processes. Metallurgical research and development aims to increase this understanding using various methods to obtain more information about the studied phenomena.

The aim of this paper is to briefly illustrate selected case studies in which material and energy efficiencies of iron and steelmaking processes can be improved using different experimental, analytical and modelling tools such as advanced experimental simulations, novel measuring and analyzing methods as well as modelling of unit operations based on the fundamental phenomena occuring in the processes (*cf.* Table 1). Recent research at the process metallurgy research unit at the University of Oulu, Finland, is used as an example. This paper focuses on the methods, whereas the results are available in the references.

Table 1. Case studies presented in this paper.

R&D method	Raw material pretreatment and Reduction metallurgy	Refining metallurgy
Experiments	Improved BF operation by simulating conditions (*Chapter 2*).	
	Reducing agent development with novel exp. techniques (*Chapter 3*).	
Modelling	Reducing agent development with carbon footprint model (*Chapter 3*).	Phenomenon-originated modelling of AOD & CAS-OB (*Chapter 4*).
Measurements		Use of OES in EAF (*Chapter 5*).

2. Improved blast furnace operation by industrial and laboratory scale testing

Raw materials and their performance in the blast furnace (BF) process provide a significant opportunity for cost savings related to energy and material consumption. Comprehensive testing is needed to improve the metallurgical properties of BF iron burden materials including iron ore pellets (*cf.* Figure 1a), coke and cold-bonded side product agglomerates. Many of the benefits are seen in material testing. Basically, burden material tests are used to select and develop materials as well as to understand material behaviour in the process. Different physical and metallurgical properties (such as strength and high temperature properties) as well as structure of burden materials (*cf.* Figure 1b) need to be investigated. For ferrous burden (*i.e.* iron ore pellets and ferrous by-products) cold crushing strength, low-temperature disintegration, reducibility, reduction-swelling behavior and softening behavior are of high importance (*cf.* Figure 2), whereas reactivity and hot strength are seen as important factors related to coke.

Extensive research work on the high temperature properties of iron burden has been carried out at the process metallurgy research unit at the University of Oulu in close collaboration with SSAB Europe Raahe steelworks and the Kyushu University. New methods were developed to evaluate the high temperature properties of the BF burden materials more accurately in comparison to standardized tests which are mostly carried out under constant temperature and atmosphere conditions. The new laboratory scale tests for burden high temperature behavior as well as the industrial Advanced Reduction under Load (ARUL) test are fine-tuned experiments with gas and temperature controls in order to simulate the actual BF conditions. Research work related to indirect reduction zone of BF was carried out with custom-made laboratory scale thermogravimetric furnaces which simulate BF conditions under various mixtures of CO, CO_2, H_2, H_2O and N_2 gases.

ARUL test has been used to study the softening behavior of ferrous burden materials. The formation of the cohesive zone has a significant effect on the efficiency of gaseous reduction in the BF shaft which in turn affects the efficiency of the entire BF process. There are various ferrous BF burden materials with different chemical compositions and softening properties which need to be tested. A thermodynamic-based tool has also been developed to estimate the BF burden softening and to calculate the solidus and liquidus temperatures. Formation of molten phases can be estimated using the original chemical composition of the iron burden material. Components of SiO_2, MgO, CaO, Al_2O_3 and Fe_{tot} are considered in the calculations. With the Phase Diagram module in FactSage phase diagrams for the 5-component FeO-SiO_2-CaO-MgO-Al_2O_3 systems with constant CaO, MgO and Al_2O_3 contents can be calculated. Reduction conditions can be taken into account by taking the partial pressure of oxygen into account as a variable the calculations. The tool can be used to estimate the softening and melting temperatures of ferrous burden materials in the BF.

The above mentioned methods have been used to study the behavior of pellets [1-6], sinter [6], briquettes [7] as well as reducing agents [8]. The results of the research work show the importance of correctly chosen experimental conditions and their effect on the burden high temperature properties. Based on the results of carried out research work, modified test methods are suggested to be used to evaluate iron pellet high temperature properties instead of standard tests.
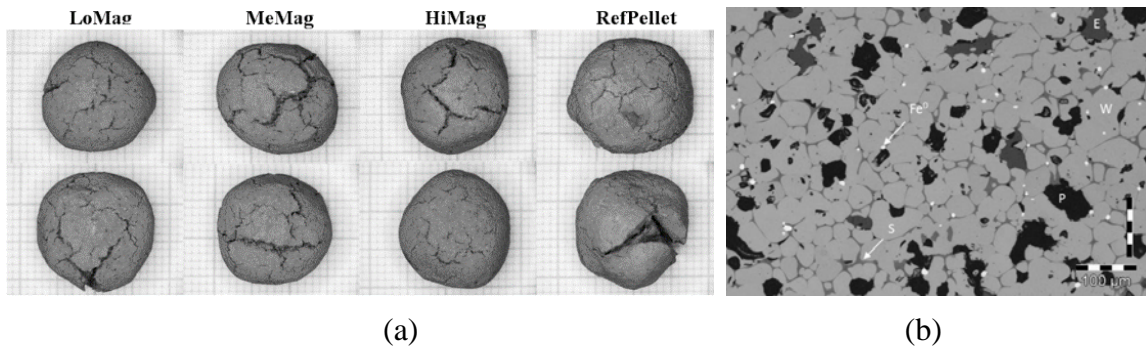
Figure 1. a) Reduced iron ore pellets. b) Optical microscope image from microstructure of partly reduced iron ore pellet.
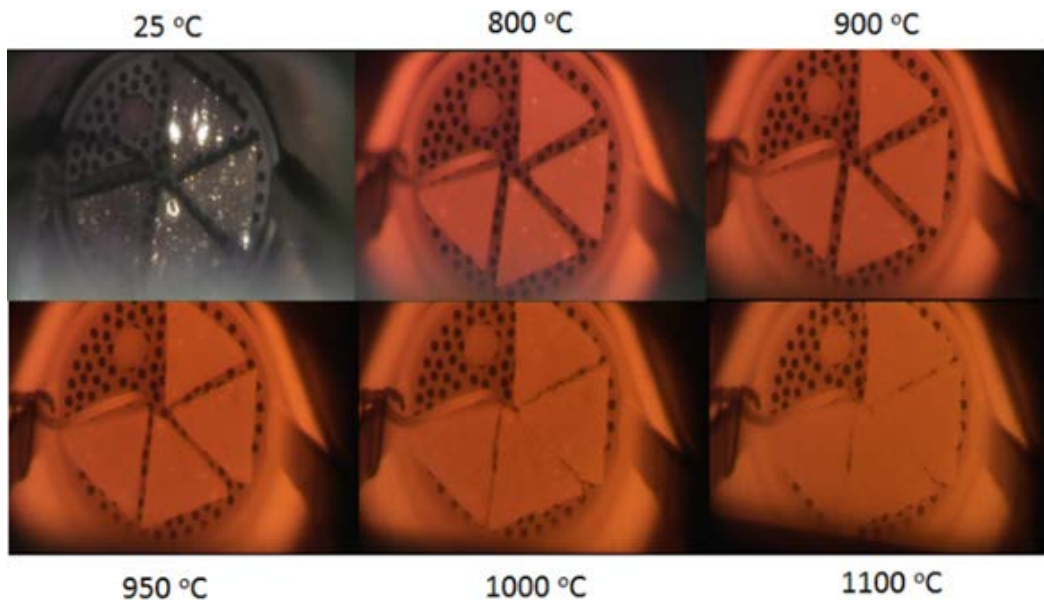
Figure 2. Reduction behavior of cold-bonded briquettes at 25-1100 °C temperature.

3. Reducing agent development for blast furnace iron making

Carbon-based reducing agents are utilized in blast furnace iron making in large quantities. The BF process is likely to remain the main technology for producing hot metal for steel making purposes for decades. Because of the varying and deteriorating coal qualities, and increasing environmental consciousness, there is a need to develop methods and tools that assist in reducing agent development and selection [9].

A new method has been developed to measure the hot strength of coke using a Gleeble 3800 thermomechanical simulator (*cf.* Figure 3a) [10,11]. The hot strengths of industrial cokes were determined at various temperatures, up to 1750 °C (*cf.* Figure 3b). Another method, the improved coke reactivity test was developed to measure the chemical reactivity of blast furnace coke in conditions simulating the actual blast furnace shaft gas [8]. Compared to the standard Coke Reactivity Index (CRI) test, the developed test takes into account the influence of the other main gas components in addition to CO_2, most importantly the influence of H_2 and H_2O, which leads to more accurate results (*cf.* Figure 3c-d). More accurate assessment of coke hot strength and reactivity in the BF simulating conditions facilitate technical and economic benefits in suitable coke and coal grade selection.
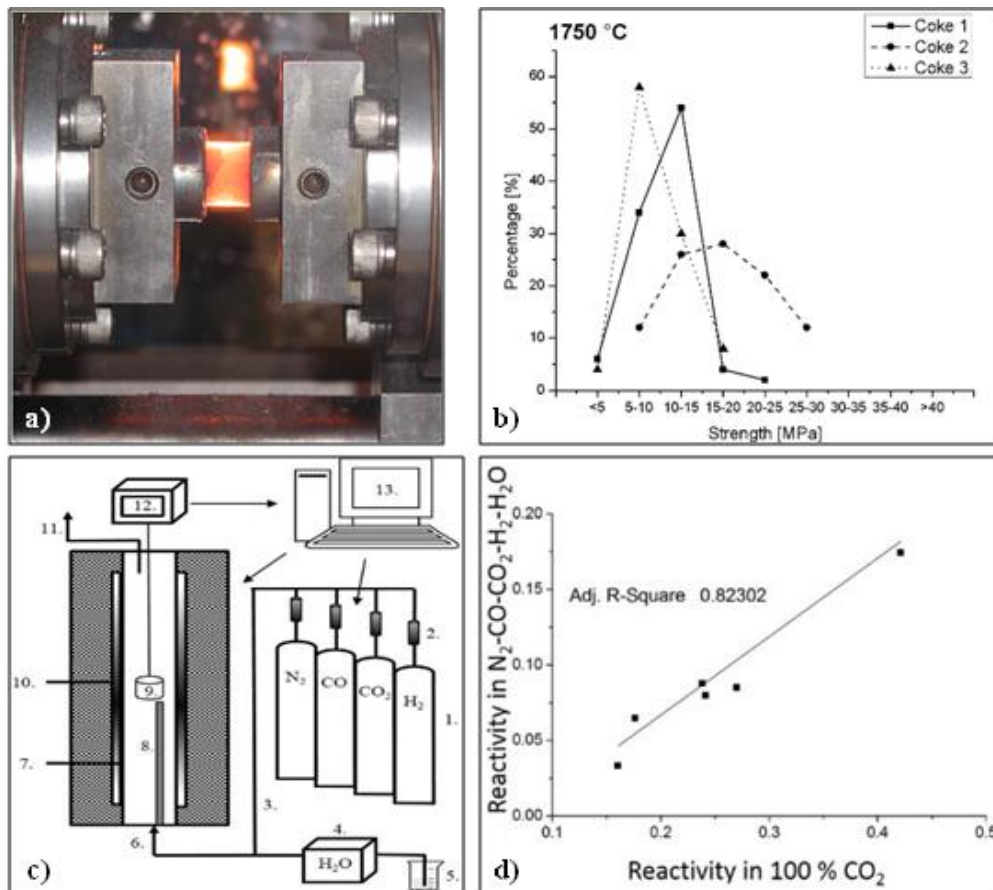
Figure 3. a) Coke sample in Gleeble 3800 thermomechanical simulator, b) Coke strength measurements conducted at 1750 °C, c) Layout of the TGA furnace used in improved coke reactivity test, d) Correlation between reactivity of coke at 1100 °C in high hydrogen gas and 100% CO_2 atmospheres.

Biomass-based reducing agents have gained considerable interest as a partial solution to CO_2 mitigation in the steelmaking industry. A carbon footprint (CFP) model has been developed for evaluating the CO_2 emissions resulting from biomass-based reducing agent production and the achievable CO_2 reduction in integrated steelmaking (*cf.* Figure 4a) [12]. According to the calculated scenarios, the carbon footprint of biomass-based reducing agents is considerably lower than the carbon footprint of fossil-based reducing agents (*cf.* Figure 4b).
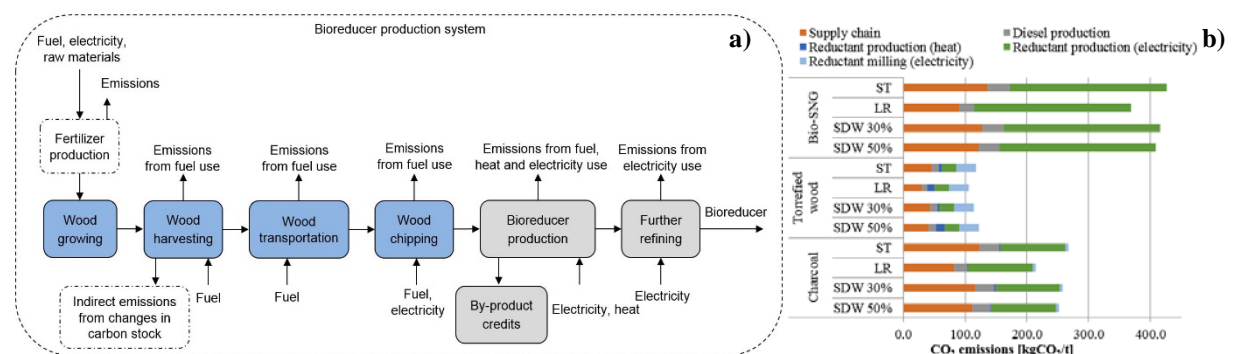
Figure 4. a) System boundary of the carbon footprint model, b) carbon footprint of biomass-based reducing agents produced from different wood-based raw materials.

4. Mathematical modelling of AOD and CAS-OB processes

Process simulators enable testing of new steelmaking practices with less time and costs. In order to study the influence of various process parameters on the process outcome, thermodynamic-kinetic simulators were developed for the Argon-Oxygen Decarburization (AOD) and Composition Adjustment by Sealed argon blowing – Oxygen Bubbling (CAS-OB) processes.

The simulators employ a modular structure and are designed around sub-models for the main phenomena in the process in question. The main sub-models of the simulators are shown in Table 2. Despite the many differences between the AOD and CAS-OB processes, they share many similar reaction mechanisms. More specifically, the sub-models employ a Law of Mass Action based kinetic approach for the treatment of the parallel mass transfer limited reactions [13]. Using this method, it is possible to introduce various kinetic constraints that affect the overall rates.

Table 2. Structure of the AOD and CAS-OB simulators.

Process/stage	Main assumptions	References
AOD		
Side-blowing	Reactions take place in the gas plume, which is treated as a three-phase plug flow reactor.	[14,15]
Top-blowing	Reactions take place simultaneously on the cavity and on the surface of the splashed metal droplets.	[16, 17]
Reduction	Reactions take place between steel bath and slag droplets.	[18,19]
CAS-OB		
Heat-up	Reactions take place simultaneously on the cavity and on the surface of the splashed metal droplets.	[20]
Reduction	Reactions take place between steel bath and slag droplets.	[21]

The results obtained indicate that the models yield reliable predictions for the composition and temperature of the metal bath [15,17,19,20,21]. For example, Figure 5a shows the predicted change in the composition of the metal bath during top blowing. Furthermore, they can be employed for optimizing several process parameters including the composition and temperature of the material inputs, composition and injection rate of gas, and the types of material additions and their feed rates.

So far, the AOD simulator has been used for sensitivity studies regarding the effects of the following parameters: a) the top lance position [17], b) composition of the top-blowing gas [17], c) feed rate of the reductants [19], and d) particle size of the reductants [19]. The simulator has been used alongside the automation system for studying optimal production practices. With the help of these simulations, significant improvements have been achieved regarding the top-blowing practice employed at Outokumpu Stainless Oy.

Because one of the main applications of the CAS-OB process is to heat up the metal bath, the CAS-OB simulator has a detailed description for the heat losses in the process. The results obtained in [20,21] suggest that the main source of heat losses during the heat-up and reduction stages is the heat radiation from the surface of the bath. Figure 5b illustrates the calculated heat losses during the reduction stage.
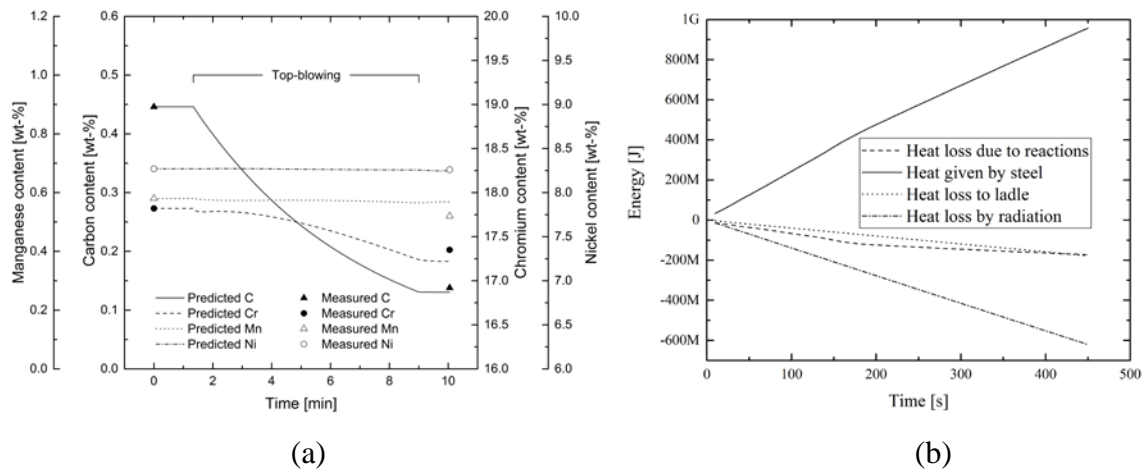
Figure 5. a) Changes in bath composition during top-blowing in the AOD process (reproduced from Visuri *et al.* [17]). b) Heat consumption from the steel phase in an example heat (reproduced from Sulasalmi *et al.* [21]).

In conclusion, it can be stated the simulators are powerful support tools for decision making and process optimization. In further work, the simulators will be put to industrial use.

5. OES in EAF steelmaking

Composition of the slag is an important factor when producing stainless steel grades with EAF. A too high chromium content of the slag in EAF causes a high chromium content in the tapped slag which in turn increases the amount of chromium losses thus decreasing the material efficiency of the stainless steel production. The chromium content in electric arc furnace slag has been measured on-line using a measurement based on the optical emission spectrum (OES) of the electric arc plasma. The high temperature of the plasma causes the slag to vaporize, and to excite. The light emitted from these excitations can be used to measure the plasma composition. There are also other possible methods for the use of on-line OES. [22-25]

The measurement system consists of an optical fiber, spectrometer and analysis computer. The light emitted from the furnace is gathered with optical fiber and transmitted to a spectrometer. Spectrometer breaks the light to wavelengths and measures the intensities of different wavelengths. The optical emission spectrum data is analysed with an analysis software specifically created for on-line spectrum analysis.
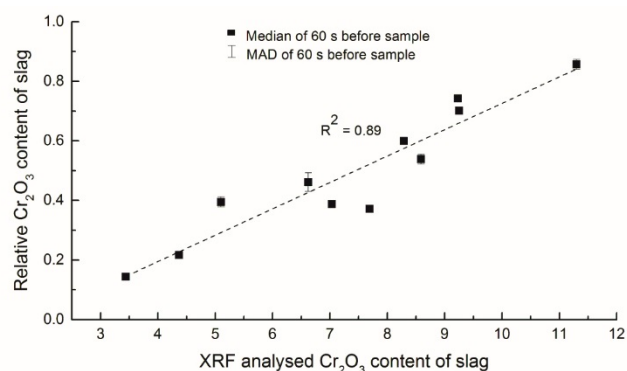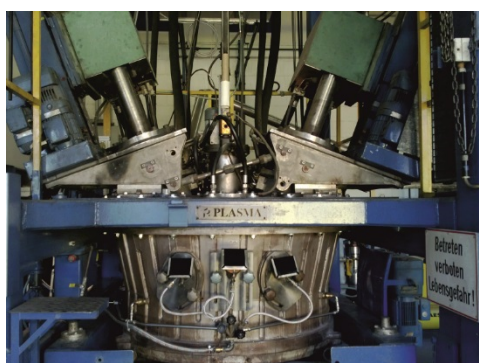
Figure 6. Pilot scale EAF and analysis of slag Cr_2O_3 content (Modified from [26]).

The measurement concept was originally tested in laboratory EAF at the University of Oulu. Further tests were conducted with pilot scale AC EAF at the RWTH Aachen University, Department of Industrial Furnaces and Heat Engineering (*cf.* Figure 6). In these measurements chromium powder was periodically added to the slag and changes in the optical emission spectra were observed. Slag samples were taken and analysed with XRF to provide a reference for the OES measurements. The comparison between OES and XRF analysis shows that the slag chromium content can be measured with an average absolute error of 0.64 wt-%-points and a standard deviation of 0.49 wt-%-points.

On-line optical emission spectroscopy is a promising tool for on-line slag composition analysis. Currently, it is possible to analyze the slag chromium content with sufficient accuracy in laboratory and pilot scale. The focus of the future development is the broadening of the slag composition analysis to other slag components and applying the methods in industrial scale. The work will be continued in the project OSCANEAF funded by the European Commission.

6. Summary and conclusions

Improvements in material and energy efficiency obtained using the methods presented in previous chapters are compiled in Table 3.

Table 3. Improvements in material and energy efficiency of iron and steelmaking processes obtained with different methods.

Method	Improved material and energy efficiency	Potential
Reducing agent development		
- with novel exp. techniques	Less reductants needed in the BF.	Use of low-grade raw materials and recycled materials.
- with carbon footprint model		Change from fossil to non-fossil reductants.
Improved BF operation by simulating conditions	Use of low-grade raw materials in the BF. Better yield by recycling dusts and other fine residues.	Use of low-grade raw materials with lower iron and higher sulphur content. Use of organic binders in BF burden materials.
Use of OES (EAF)	Decreased energy consumption. Higher productivity.	Decreased Cr-losses. Decreased wear of refractories.
Phenomenon-originated modelling of AOD & CAS-OB processes	Optimized use of process gases (*e.g.* Ar). Shortened tap-to-tap times and higher productivity.	Optimized use of reductants, slag formers and fluxes.

Concerning the material efficiency of the ironmaking processes, better understanding on the properties and behavior of BF burden materials (*i.e.* pellets, briquettes and coke) has made it possible to use recycled and lower grade materials in the burden materials thus increasing the yield in the production of hot metal. For example, use of briquettes as an additional burden material enables not only recycling of dusts and other fine iron-containing residues back to the process, but also the utilization of BF slag as a binding material [7]. Additional studies are needed in order to further broaden the raw material mix and to fully utilize currently unutilized residue materials. On the other hand, the increased understanding on the properties and behavior of coke [8,10,11] makes it possible to optimize the use of reductants and decrease the specific consumption of reductants in the BF. This, together with the use of carbon footprint model, gives tools to estimate the possibilities to replace fossil reductants with non-fossil materials [9,12].

Mathematical models of the steelmaking processes (such as AOD and CAS-OB) based on the fundamental phenomena taking place in these processes [13-21] have helped to optimize the process parameters (*e.g.* durations of different blowing stages and gas flow rates during these stages in the AOD process), which has enabled shorter tap-to-tap times, lower specific consumption of gases and eventually, higher productivity. The future potential lies in the use of these models to optimize to use of other raw materials such as reductants, slag forming agents and fluxes.

The measurements of optical emission spectra from electric arc furnaces [22-26] have provided information about local scrap melting which has allowed better control of arc voltage leading to increased productivity and decreased energy consumption in the steel scrap melting in the production of stainless steels. The results of the OES measurements indicate that the method could also be used to optimize EAF process control in order to decrease the oxidation of chromium and to decrease the refractory wear. The focus of the future development is in broadening the slag composition analysis to other slag components besides chromium oxide and applying the methods in industrial scale.

References

1) Iljana M, Mattila O, Alatarvas T, Visuri V-V, Kurikkala J, Paananen T & Fabritius T, Dynamic and Isothermal Reduction Swelling Behaviour of Olivine and Acid Iron Ore Pellets under Simulated Blast Furnace Shaft Conditions, *ISIJ International*, 52(2012)7, 1257-1265.

2) Kemppainen A, Mattila O, Heikkinen E-P, Paananen T & Fabritius T, Effect of H_2-H_2O on the reduction of olivine pellets in CO-CO_2 gas, *ISIJ International*, 52(2012)11, 1973-1978.

3) Iljana M, Mattila O, Alatarvas T, Kurikkala J, Paananen T & Fabritius T, Effect of Circulating Elements on the Dynamic Reduction Swelling Behaviour of Olivine and Acid Iron Ore Pellets under Simulated Blast Furnace Shaft Conditions, *ISIJ International*, 53(2013)3, 419-426.

4) Kemppainen A, Ohno K, Iljana M, Mattila O, Paananen T, Heikkinen E-P, Maeda T, Kunitomo K & Fabritius T, Softening behaviors of acid and olivine fluxed iron ore pellets in the cohesive zone of a blast furnace, *ISIJ International*, 55(2015)10, 2039-2046.

5) Iljana M, Kemppainen A, Paananen T, Mattila O, Pisilä E, Kondrakov M & Fabritius T, Effect of adding limestone on the metallurgical properties of iron ore pellets, *International Journal of Mineral Processing*, 141(2015), 34-43.

6) Iljana M, Kemppainen A, Paananen T, Mattila O, Heikkinen E-P & Fabritius T, Evaluating the Reduction-Softening Behaviour of Blast Furnace Burden with an Advanced Test, *ISIJ International*, 56(2016)10, 1705-1714.

7) Kemppainen A, Iljana M, Heikkinen E-P, Paananen T, Mattila O & Fabritius T, Reduction behavior of cold-bonded blast furnace briquettes under simulated blast furnace conditions, *ISIJ International*, 54(2014)7, 1539-1545.

8) Haapakangas J, Suopajärvi H, Iljana M, Kemppainen A, Mattila O, Heikkinen E-P, Samuelsson C & Fabritius T, Coke Reactivity in Simulated Blast Furnace Shaft Conditions, *Metallurgical and Materials Transactions B*, 47(2016)4, 2357-2370.

9) Suopajärvi H, Kemppainen A, Haapakangas J & Fabritius T, Extensive review of the possibilities to use biomass-based fuels in iron and steelmaking processes, *Journal of Cleaner Production*, 148(2017), 709–734.

10) Haapakangas J, Uusitalo J, Mattila O, Kokkonen T, Porter D & Fabritius T, A method for evaluating coke hot strength, *Steel Research International*, 84(2013), 65–71.

11) Haapakangas J, Uusitalo J, Mattila O, Gornostayev S, Porter D & Fabritius T, The hot strength of industrial cokes – Evaluation of coke properties that affect its high temperature strength, *Steel Research International*, 85(2014), 1608–1619.

12) Suopajärvi H, Pongrácz E & Fabritius T, Bioreducer use in Finnish blast furnace ironmaking – Analysis of CO_2 emission reduction potential and mitigation cost, *Applied Energy*, 124(2014), 82–93.

13) Järvinen M, Visuri V-V, Heikkinen E-P, Kärnä A, Sulasalmi P, De Blasio C & Fabritius T, Law of Mass Action Based Kinetic Approach for the Modelling of Parallel Mass Transfer Limited Reactions: Application to Metallurgical Systems, *ISIJ International*, 56(2016), 1543–1552.

14) Järvinen M, Pisilä S, Kärnä A, Ikäheimonen T, Kupari P & Fabritius T, Fundamental Mathematical Model for AOD Process. Part I. Derivation of the model, *Steel Research International*, 82(2011), 638–649.

15) Pisilä S, Järvinen M, Kärnä A, Ikäheimonen T, Fabritius T & Kupari P, Fundamental Mathematical Model for AOD Process. Part II: Model validation, *Steel Research International*, 82(2011), 650–657.

16) Visuri V-V, Järvinen M, Kärnä A, Sulasalmi P, Heikkinen E-P, Kupari P & Fabritius T, A Mathematical Model for Reactions during Top-Blowing in the AOD Process: Derivation of the Model, *Metallurgical and Materials Transactions B*, in press. DOI: 10.1007/s11663-017-0960-6.

17) Visuri V-V, Järvinen M, Kärnä A, Sulasalmi P, Heikkinen E-P, Kupari P & Fabritius T, A Mathematical Model for Reactions during Top-Blowing in the AOD Process: Validation and Results, *Metallurgical and Materials Transactions B*, in press. DOI: 10.1007/s11663-017-0961-5.

18) Visuri V-V, Järvinen M, Sulasalmi P, Heikkinen E-P, Savolainen J & Fabritius T, A Mathematical Model for the Reduction Stage of the AOD Process. Part I: Derivation of the Model, *ISIJ International*, 53(2013), 603–612.

19) Visuri V-V, Järvinen M, Savolainen J, Sulasalmi P, Heikkinen E-P & Fabritius T, A Mathematical Model for the Reduction Stage of the AOD Process. Part II: Model validation and Results, *ISIJ International*, 53(2013), 613–621.

20) Järvinen M, Kärnä A, Visuri V-V, Sulasalmi P, Heikkinen E-P, Pääskylä K, De Blasio C, Ollila S & Fabritius T, A Novel Approach for Numerical Modeling of the CAS-OB Process: Process Model for the Heat-Up Stage, *ISIJ International*, 54(2014), 2263–2272.

21) Sulasalmi P, Visuri V-V, Kärnä A, Järvinen M, Ollila S & Fabritius T, A Mathematical Model for the Reduction Stage of the CAS-OB Process, *Metallurgical and Materials Transactions B*, 47(2016), 3544–3556.

22) Aula M, Demus T, Echterhoff T, Huttula M, Pfeifer H & Fabritius T, On-line analysis of Cr_2O_3 content for the slag in pilot scale EAF by measuring optical emission spectrum of electric arc, *ISIJ International*, 57(2017)3, 478-486.

23) Aula M, Mäkinen A, Leppänen A, Huttula M & Fabritius T, Optical emission analysis of slag surface conditions and furnace atmosphere during different process stages in electric arc furnace (EAF), *ISIJ International*, 55(2015)8, 1702-170.

24) Aula M, Mäkinen A & Fabritius T, Analysis of arc emission spectra of stainless steel electric arc furnace slag affected by fluctuating arc voltage, *Applied Spectroscopy*, 68(2014)1, 26-32.

25) Aula M, Leppänen A, Roininen J, Heikkinen E-P, Vallo K, Fabritius T & Huttula M, Characterization of Process Conditions in Industrial Stainless Steelmaking Electric Arc Furnace Using Optical Emission Spectrum Measurements, *Metallurgical and Materials Transactions B*, 45(2014)3, 839-849.

26) Aula M, Demus T, Echterhoff T, Huttula M, Pfeifer H & Fabritius T, On-line Analysis of Cr_2O_3 Content of the Slag in Pilot Scale EAF by Measuring the Optical Emission spectrum of Electric Arc, *ISIJ International*, 57(2017)3, 478-486.

Development of Environmental-friendly Technology for Chromium Ore Smelting Reduction Converter

Nobuhiko ODA,[1] Goro OKUYAMA,[2] Futoshi OGASAWARA,[1] Yuichi UCHIDA,[3] Yuji MIKI,[1] Yasuo KISHIMOTO,[1] Hisashi OGAWA,[4] Yuta HINO,[1] and Naoki KIKUCHI[5]

1) Steel Research Laboratory, JFE Steel Corporation, Chiba, Japan
2) Head Office, JFE Steel Corporation, Tokyo, Japan
3) Formerly Steel Research Laboratory, JFE Steel Corporation. Now Nippon Institute of Technology, Saitama Japan
4) West Japan Works (Fukuyama), JFE Steel Corporation, Fukuyama, Japan
5) Steel Research Laboratory, JFE Steel Corporation, Fukuyama, Japan

Abstract: In order to increase the amount of chromium ore in the smelting reduction furnace, it is important to increase the amount of the heat supply to the furnace. Although various technologies have been developed with the aim of increasing post-combustion, the heat transfer efficiency of post-combustion to the molten metal is low. Furthermore, the post-combustion technologies could cause a risk of reducing refractory life. In this study, a technology using burner combustion which is substituted for the heat decarburization and post-combustion was developed. Experiments with 4 tons furnace and numerical calculations were carried out to consider a method of promoting heat transfer from the burner combustion heat to the metal. The behavior of heat transfer from the burner to the metal by particles heated through the flame was investigated. The following results were obtained;

The temperature increment of the metal increased by feeding heated particles of raw materials through the burner flame.

The quantity of heat transferred from the flame to the metal increases as the feeding rate of the heated particles increased.

From the results of the numerical simulation, both the particles temperature and the flame temperature decreased as the particle feeding rate increased. However, the total sensible heat of all particle raw materials increased.

As the feeding rate of the particles increased, heat transfer from the flame by radiation and convection decreased, and heat transfer by the sensible heat of the heated particles increased.

Based on these results, the developed technology was applied to the actual process. As a result, the energy supplied to the furnace per unit of chromium ore decreased by 17%.

1. Introduction

The chromium ore smelting reduction method has been introduced in the stainless steelmaking process in JFE Steel Corp.[1, 2] In this process, inexpensive chromium ore can be used as the chromium source for stainless steel which is substituted for chromium alloys. The chromium oxide in the ore is reduced by carbonaceous materials which are added in the furnace. As this reaction is endothermic, it is necessary to increase the amount of heat supply to the furnace in order to increase the feeding rate of the chromium ore.[3] Various technologies have been developed with the aim of increasing post-combustion.[4-8] However, the heat transfer efficiency to the molten metal and slag is low because post-combustion

occurs in the furnace space above the hot metal. Furthermore, the post-combustion technologies could cause a risk of reducing refractory life.

Burner combustion heat was considered as an alternative technology replaced for the heat of decarburization heat and post-combustion heat. However, if the hot metal is simply heated by the burner flame, combustion occurs in the space above the melt in the same way as in post-combustion. Therefore, the efficiency of heat transfer to the hot metal by simple burner combustion is also considered to be low. To solve this problem, we investigated a method for transferring the combustion heat of the burner to the hot metal efficiently by using chromium ore through the burner flame as a medium.

In this study, experiments with a 4 ton scale furnace and numerical calculations were carried out in order to investigate the relationship between the feeding conditions of the chromium ore and the heat transfer behavior from burner combustion to the hot metal. Based on the results, this technology was applied to the actual process.

2. Experiments with 4 ton melting furnace

2.1 Experimental procedure

Figure 1 shows a schematic diagram of the 4 ton scale low frequency induction melting furnace and a burner lance used in the experiment. The ore was supplied through the center hole of burner lance and propane gas as a fuel and oxygen gas as a combustion improver were blown through the outer nozzles.

The height of the burner lance was 1.5 m from the surface of molten metal. The experimental conditions are shown in Table 1. The flow rate of propane gas changed from 0.35 to 0.50 Nm^3/min, and the flow rate of oxygen gas was 6 times that of propane gas. The feeding rate of chromium ore was 0-9.6 kg/min. At this time, the average diameter of the chromium ore was approximately 200 μm.

In order to investigate the heat transfer behavior of burner combustion to the molten metal and slag, experiments were conducted under the three conditions shown below.

1) Burner only ("without addition of ore"),

2) Addition of chromium ore through the burner flame ("with addition of heated ore"), and

3) Addition of ore from outside the flame ("with addition of non-heated ore").

In the method "with addition of heated ore," the feeding rate of the chromium ore was varied in order to investigate the relationship between the heat transfer behavior of burner combustion and the feeding rate.

The initial temperature of the molten metal was 1380-1430°C. Prior to the experiments, the power supply condition in which the temperature of the metal did not change was investigated. We performed the burner heating experiments under that condition of electric power supply.

Figure 1. Experimental apparatus

Table 1. Experimental conditions

No.	propane Nm³/min	oxygen Nm³/min	Cr-ore kg/min	addition method of Cr-ore
1	0.50	3.0	0	without addition of ore
2	0.50	3.0	3.9	with addition of heated ore
3	0.50	3.0	8.1	with addition of heated ore
4	0.50	3.0	4.5	with addition of non heated ore

2.2 Experimental results

Figure 2 shows the change in the temperature of the hot metal when the propane flow rate of the burner was 0.5 Nm^3/min. Under this conditions, the hot metal temperature increased in an approximately linearly with time. The elevating temperature rate of hot metal, $\Delta T/\Delta t$, was calculated from the slopes shown in the figure. In the case "without addition of ore", the temperature increase rate of the hot metal $\Delta T/\Delta t$ was 3.0°C/min. In the case "with addition of non-heated ore," i.e., when the chromium ore was added from outside the flame, the elevation temperature rate was smaller, due to the sensible heat of the ore. In other words, addition of unheated chromium ore suppresses the temperature elevation of the hot metal. However, in the case of "with addition of heated ore," which the chromium ore was added through the burner flame in, $\Delta T/\Delta t$ of the hot metal was 2.5-2.7°C/min. The temperature increase rate was larger compared with the case "with addition of non-heated ore", even though the feeding rate of the chromium ore was the same. Moreover, in the case "with addition of heated ore,", the elevating temperature rate of the hot metal increased with the feeding rate under these experimental conditions.
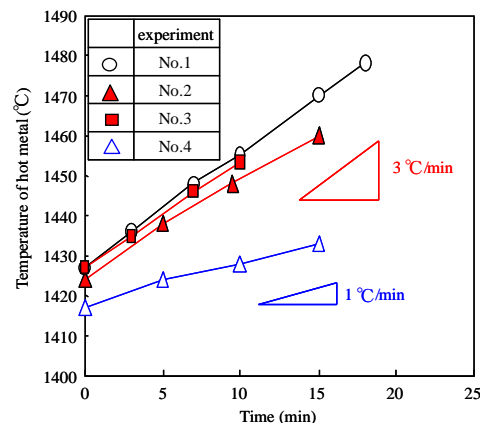
Figure 2. Change of hot metal temperature during burner blowing

Figure 3 shows the relationship between the Cr-ore feeding rate under the respective conditions and the sensible heat increment of the hot metal and slag. The sensible heat

increment of the hot metal and slag increased as the amount of Cr-ore increased in the case of "with addition of heated ore." In the case of "with addition of non-heated ore", the sensible heat increment of the hot metal and slag did not increase.
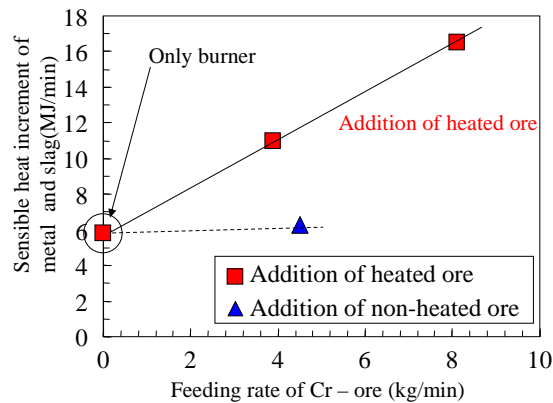
Figure 3. Relationship between feeding rate of Cr – ore and sensible heat increment of metal and slag

Figure 4 shows the relationship between the feeding rate of Cr-ore and the temperature of the atmospheric gas. Under the conditions "without addition of ore" and "with addition of non-heated ore", the temperature of the atmospheric gas was 1700 °C regardless of the feeding rate of Cr-ore, while under the condition "with addition of heated ore," the temperature decreased with the feeding rate. This result indicates that the radiation from the flame decreased due to the decrease of the flame temperature when chromium ore was added through the flame.

Figure 5 shows the heat balances at the propane flow rate of 0.50 Nm^3/min. "Unknown heat" was determined from the difference between the combustion heat of propane and the sum of the sensible heats of the hot metal, slag, and off gas. The unknown heat can be considered as the radiant heat transfer to the refractories. The unknown heat decreased with increasing the feeding rate of chromium ore. It was also indicated that the radiant heat transfer from the flame to the refractories decreased due to the decrease of the flame temperature. In the case of "with addition of non-heated ore", as mentioned previously, the sensible heat increments of the hot metal and slag did not increase. Based on these results, it was found that transfer of burner combustion heat to the hot metal increased by adding heated chromium ore through the burner flame.
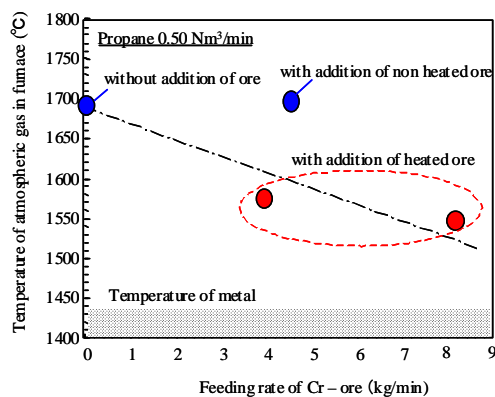
Figure 4. Relationship between feeding rate of Cr-ore and temperature of atmospheric gas
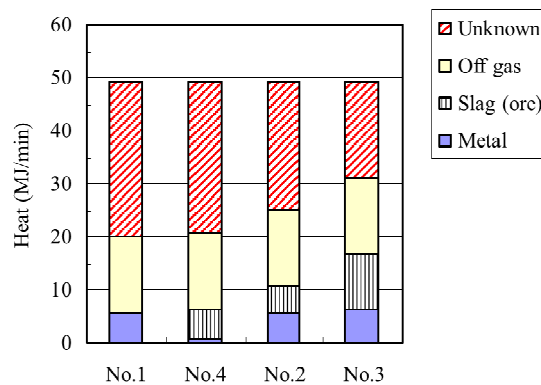
Figure 5. Comparison of heat balance

3. Numerical analysis of heat transfer behavior from combustion gas to particles

In order to discuss the experimental results presented in the previous section, the behavior of heat transfer from high temperature combustion gas to an ore particle was analyzed by numerical calculations.

The temperatures of the combustion gas and particles were calculated by combining the following calculations.

1) Calculation of combustion gas temperature by equilibrium calculation

2) Calculation of particle temperature due to heat transfer between combustion gas and particles

3) Calculation of particle heating time by equation of motion for particles

As for the flame temperature of the combustion gas, we considered the equilibrium of the 8 components (CO, CO_2, O_2, H_2, H_2O, OH, H, O) formed by the reaction of the combustion gas C_3H_8 with oxygen. The combustion gas temperature under the adiabatic condition was calculated by a trial-and-error method by using the equilibrium equations shown in Eq. (1) to (5) and the enthalpy balance equation of gas in Eq. (7) which was based on the condition shown by Eq. (6). [10]

In this equations, which are shown below, P_i is the partial pressure of component i, K_n is the equilibrium constant of equation (n), H^0 is the enthalpy of gas, and ΔH^0_{298} is the formation energy of propane. The subscript r means a reaction product, and p means a product. The equilibrium constants of each reaction and the enthalpy of each gas were obtained from JANAF Thermochemical Tables.[11]

Heat transfer from the high temperature gas to a particle was calculated from the heat balance expressed as Eq. (8), assuming that the particle will be a single particle and considering radiation heat transfer and convection heat transfer from the gas. Equation (9) shows the convection heat transfer term, and Eq. (10) shows the radiation heat transfer term, respectively. Assuming that the particle is spherical in shape, the Nusselt number "Nu" of the convection heat transfer was calculated by using the Ranz-Marshall's formula[12] shown in Eq. (11). Here, since the particle diameter was small in this study, the internal temperature in the particle was assumed to be the same, and it was also assumed that the surface area of the single particle is extremely small in comparison with the radiation area of the high temperature gas. The particle diameter used in the calculation was 200 μm, and the density, specific heat, emissivity, and thermal conductivity of the particle were assumed to be constant. The physical properties used in the calculation are shown in Table 2.

In the above-mentioned equations, m is the mass of a particle, d is the particle diameter, T_P is the temperature of the particle, T_g is the temperature of the combustion gas, $A_{S,P}$ is the surface area of the particle, c_P is the specific heat of the particle, ε_P is the emissivity of the particle, λ is the thermal conductivity of the gas, q_P is the convective heat transfer between the combustion gas and particles, q_R is the radiant heat transfer between the combustion gas and particles, Nu is the Nusselt number, Re is the Reynolds number, and Pr is the Prandtl number of the gas.

In order to estimate the residence time of a particle in the flame, the residence time was calculated from the equations of motion for the particle shown in Eq. (12) to (15).

Here, u is the gas velocity, u_P is the particle velocity, ρ_P is the density of the particle, ρ is the density of the gas, g is the acceleration of gravity, and μ is the viscosity of the gas. Also, C_d is the drag coefficient of the particle, which can be calculated from Eq. (15). [14]

Table 2. Parameters used for estimation of burner and particle temperatures

c_p	920	J/kg °C
ρ	4800	kg/m³
e_p	0.8	(-)
λ	0.03	W/mK
d	200	μm

$$CO_2 \Leftrightarrow CO + \frac{1}{2}O_2 \qquad (K_1 = \frac{P_{CO} \cdot P_{O_2}^{1/2}}{P_{CO_2}}) \qquad (1)$$

$$H_2O \Leftrightarrow H_2 + \frac{1}{2}O_2 \qquad (K_2 = \frac{P_{H_2} \cdot P_{O_2}^{1/2}}{P_{H_2O}}) \qquad (2)$$

$$H_2O \Leftrightarrow \frac{1}{2}H_2 + OH \qquad (K_3 = \frac{P_{OH} \cdot P_{H_2}^{1/2}}{P_{H_2O}}) \qquad (3)$$

$$\frac{1}{2}H_2 \Leftrightarrow H \qquad (K_4 = \frac{P_H}{P_{H_2}^{1/2}}) \qquad (4)$$

$$\frac{1}{2}O_2 \Leftrightarrow O \qquad (K_5 = \frac{P_O}{P_{O_2}^{1/2}}) \qquad (5)$$
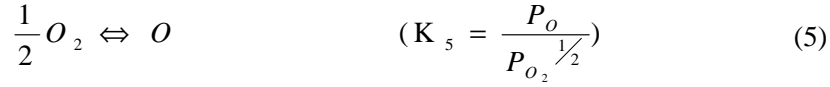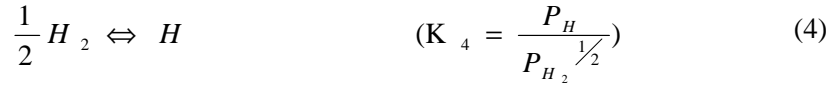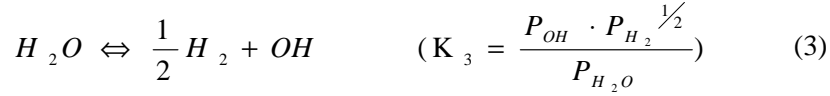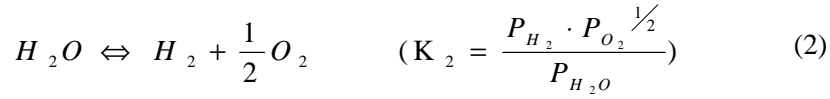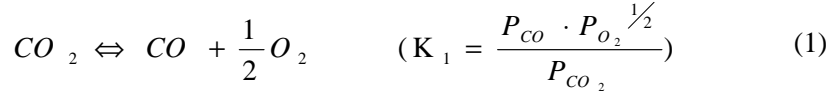
$$P \equiv P_{CO} + P_{CO_2} + P_{O_2} + P_{H_2}$$
$$+ P_{H_2O} + P_{OH} + P_H + P_O = 1\,atm \qquad (6)$$

$$(H^0 - H_{298}^0)_p = (H^0 - H_{298}^0)_r - \Delta H_{298}^0 \qquad (7)$$

$$\frac{du_P}{dt} = F_D \cdot (u - u_P) + \frac{g(\rho_P - \rho)}{\rho_P} \qquad (8)$$

$$F_D = \frac{18\mu}{\rho_P d_P^2} \cdot \frac{C_d \, Re}{24} \qquad (9)$$

$$Re = \frac{\rho d_P |u_P - u|}{\mu} \qquad (10)$$

$$C_d = \frac{24}{Re}(1 + 0.15\,Re^{0.687}) \qquad (11)$$

$$mc_{p,P} \frac{d(T_P)}{dt} = A_{S,P} \cdot q_P + A_{S,P} \cdot q_R \qquad (12)$$

$$q_P = \frac{Nu \, \lambda}{d}(T_g - T_P) \qquad (13)$$

$$q_R = \varepsilon_P \cdot \sigma(T_g^4 - T_P^4) \qquad (14)$$

$$Nu = 2 + 0.6\,Re_P^{1/2}\,Pr^{1/3} \qquad (15)$$

Figure 6 shows the relationship between the feeding rate of the particles and the temperatures of the particles and combustion gas. In addition, the relationship between the

feeding rate of chromium ore and the calculated values of the sensible heat of the heated chromium ore was also shown in this figure. The temperatures of particle and gas used here were calculated assuming that the residence time of particles through the flame was 0.10 sec. The temperatures of both the heated particles and the combustion gas decreased as the particle feeding rate increased. The particle temperature increased by the transfer of heat from the flame to the particles. As the increment of the sensible heat of the particles increased, the temperature of the combustion gas (i.e., the flame) dropped. Although the temperature of the chromium ore decreased as the Cr-ore feeding rate increased, the total sensible heat of the chromium ore increased due to the increase of the ore feeding rate.

Figure 7 shows a breakdown of the amount of heat transfer from the combustion gas to the hot metal and slag by radiation, convection and the amount of heat transfer by the sensible heat from the particles. The amount of heat transfer from the combustion gas by radiation and convection was assumed to be the difference between the experimental values of the sensible heat increments of the hot metal and slag and the calculated values of the sensible heat of the chromium ore in Fig. 6. In the case that the heated ore feeding rate is 0 kg/min (i.e., heat transfer occurs only by the flame), the amount of heat transfer to the metal by radiation and convection was small. In contrast, if the feeding rate of the heated ore increased, heat transfer to the metal and slag by radiation and convection decreased, and the heat transfer by the heated ore became dominant. The decrease of the amount of heat transfer by radiation and convection also indicates a decrease of the heat transfer to the refractories by radiation and convection.

From the above results, it was found that the ore particles heated through the flame acted as a medium of heat transfer from the flame to the molten metal and slag, and it was possible to transfer the heat of the burner combustion to the molten metal by the heated ore more efficiently than by post-combustion. This method made it possible not only to increase the heat supply to the molten metal and slag, but also to decrease the thermal load on the refractory by optimizing the feeding condition of the heated ore.
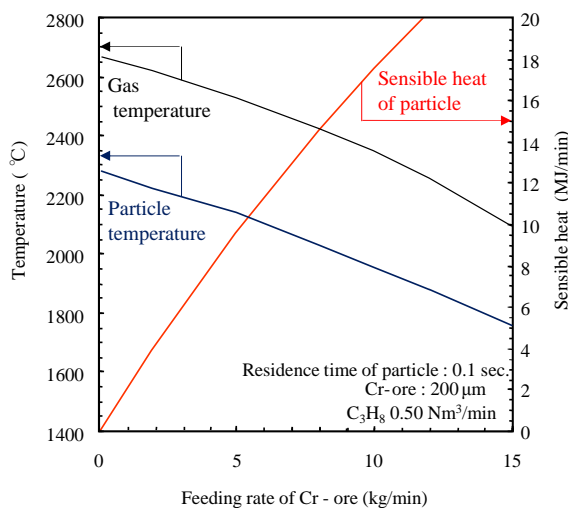
Figure 6. Relationship feeding rate of Cr–ore and temperature of particle and gas and sensible heat of particle
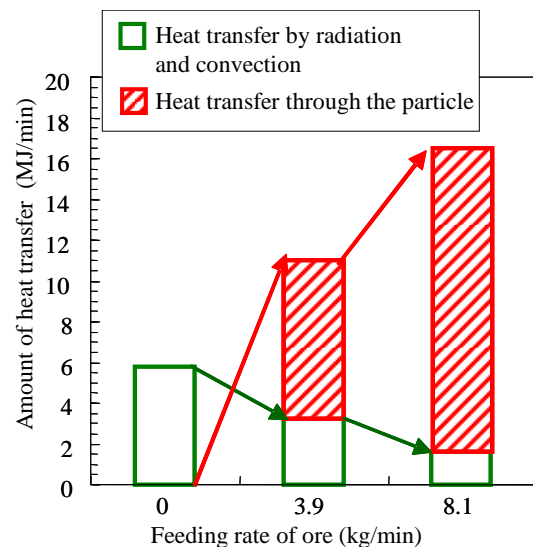
Figure 7. Comparison of heat transfer balance to metal and slag

4. Application of heated ore addition using burner lance to actual 185ton smelting reduction furnace

Based on the above results, the heated ore addition lance using the burner was applied to the actual smelting reduction furnace, which was a top and bottom blown converter in JFE Steel's East Japan Works (Chiba).

Figure 8 shows a schematic diagram of the actual converter with the burner lance for heated ore addition. The total flow rate of oxygen gas, which composed the top blown gas and the combustion improver of the burner, was equal to the flow rate under the condition without the burner. The flow rate of the bottom blown oxygen was the same as that in conventional operation. The amount of carbonaceous material was also reduced according to the decrease of top blown oxygen during the smelting reduction period. The lance height of the burner lance was the same as that of the main lance. All chromium ore was added to the molten metal through the burner lance.

Figure 9 shows the relationship between the amount of the chromium ore and the energy consumption. The energy consumption was defined as the sum of the heat generated by the decarburization reaction, post-combustion and burner combustion. The energy consumption per unit consumption of chromium ore added to the molten metal decreased by 17% at the same total flow rate of oxygen gas. From this, more efficient heat transfer can be achieved by the heated ore addition using the burner lance in the actual converter.
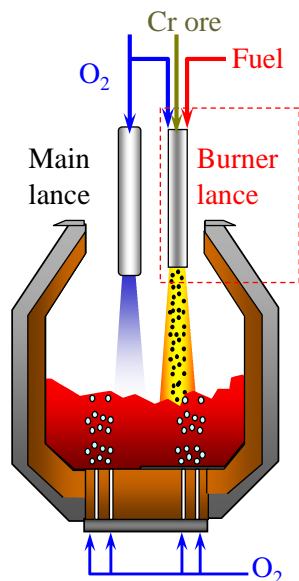
Figure 8. Schematic diagram of actual converter with burner lance for heated ore addition
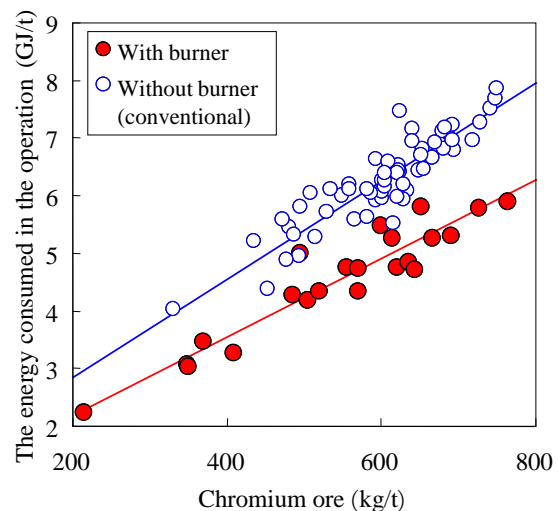
Figure 9. Relationship between amount of chromium ore and energy consumption

5. Conclusions

In order to improve the thermal efficiency in the chromium ore smelting reduction furnace, a technology of the feeding heated ore by using a burner lance was developed. This technique was applied to the actual process. The results are summarized as follows:

1) At the same feeding rate, the elevating temperature rate of the hot metal was increased by the method with addition of heated chromium ore through the burner flame.

2) In the method with addition of heated ore, heat transfer to the hot metal and slag increased with the ore feeding rate. Therefore, the atmospheric gas temperature in the furnace decreased, and the superheat calculated from the heat balance also decreased.

3) Changes in the particle temperature and combustion gas temperature were analyzed by numerical calculations. In the method "with addition of heated ore," the particle temperature and combustion gas temperature decreased as the ore feeding rate increased. Although a single particle temperature decreased at the higher feeding rate, the sensible heat of all particles increased.

4) When the heated particle feeding rate increased, heat transfer from the flame to the metal by radiation and convection decreased, and heat transfer through the particle increased.

5) The particles of chromium ore heated through the burner flame acted as a heat transfer medium. It made it possible to improve the efficiency of heat transfer from burner combustion to the hot metal and to decrease the thermal load on the refractory.

6) Based on the above-mentioned results, this technology was applied to the actual smelting reduction furnace in JFE Steel's East Japan Works (Chiba). In the actual plant test, the energy consumption per unit of chromium ore added to the molten metal decreased by 17% at the same total flow rate of oxygen gas.

References:

1) K.Taoka, C.Tada, S.Yamada, H.Nomura, M.Ohnishi and H.Bada, Production of Stainless Steel with Smelting Reduction of Chromium Ore by Combined Blowing Converter, *Tetsu-to-Hagané*, 76 (1990), 1863.

2) Y.Kishimoto, K.Taoka and S.Takeuchi: Development of Highly Efficient Stainless Steelmaking by Cr Ore Smelting Reduction Method, *Kawasaki Steel Giho*, 28 (1996), 213.

3) M.Matsuo, C.Saito, H.Katayama, H.Hirata and Y.Ogawa, Relation between Post-combustion, Heat Efficiency and Coal Consumption in Smelting Reduction of Iron Ore with Top-and-Bottom Blowing Converter, *Tetsu-to-Hagané*, 76 (1990), 1879.

4) M.Hirai, R.Tsujino, T.Mukai, T.Harada and M.Oomori, The Mechanism of Post Combustion in Converter, *Tetsu-to- Hagané*, 73 (1987), 1117.

5) N.Takashiba, M.Nira, S.Kojima, H.Take and F.Yoshikawa, Development of the Post Combustion Technique in Combined Blowing Converter, Tetsu-to- Hagané, 75 (1989), 89.

6) A.Shinotake and Y.Takamoto: Combustion and heat transfer mechanism in iron bath smelting reduction furnace, La Revue Metallurgie, 24 (1993), 965.

7) K.Takahashi, Y.Tanabe, K.Iwasaki, M.Muroya, I.Kikuchi and M.Kawakami, Key Factors to Improve Post-combustion in Pressurized Converter Type Smelting Reduction Vessel, *Tetsu-to-Hagané*, 76 (1990), 1887.

8) Y.Kato, J.Grosjean and J.Reboul, Theoretical Study on Gas Flow and Heat and Mass Transfer in a Converter, *Tetsu-to-Hagané*, 75 (1989), 478.

9) Y. Mizutani: *Combustion Engineering, 3rd Ed.*, Morikita Publishing Co., Ltd., Tokyo (2006), 71.

10) D. R. Stull and H. Prophet: JANAF Thermochemical Tables 2nd Ed.,National Standard Reference Data System, Washington, DC, (1971).

11) W.E.Ranz and W.R.Marshall, *Evaporation from drops*, Chem. Eng. Prog., 48 (1952), 141.

12) Z.Tanaka: New Approximate Equation of Drag Coefficient For Spherical Particles, *J. Chem. Eng. Jpn.*, 3 (1970), 261.

OPPORTUNITIES OF THE STEEL INDUSTRY TO CREATE SOLUTIONS FOR THE CIRCULAR ECONOMY

David ALGERMISSEN[1], Marija CANCAREVIC[2], Tim REKERSDREES[2], Henning SCHLIEPHAKE[2], Tobias ZEHN[2]

[1]FEhS - Building Materials Institute, 47229 Duisburg, Germany
[2]Georgsmarienhütte GmbH, 49124 Georgsmarienhütte, Germany

1. Abstract

Future changes in legislative regulations in Germany jeopardise the common use of slags in applications like road construction without further changes of the material. Improvements to modify the slags especially the EAF-slag will have to be performed. Georgsmarienhütte GmbH developed relevant transformation processes for the ladle furnace slag (LFS) as well as for the EAF slag.

Steel men operate maximum temperature processes. This creates chances to offer services for other cycles of materials, to generate additional sources of income thus significantly enhancing the standing of the steel industry in the eyes of the public. Replacing carbon containing materials such as charge coal and foaming coke by recycled polymer material could be a good opportunity for the steel industry to adapt itself to external recycling circles.

2. Introduction

During the steel production with electric arc furnaces (EAF) and the following secondary metallurgy, two types of slags are produced with very different properties. The black EAF slag contains metallic and oxide metals and has good physical properties for further use. In Germany, EAF slag is mainly used in road construction and earthworks. The white ladle furnace slag (LFS) is nearly metal free and typically disintegrates during cooling. It is often used for landfill construction, but also as liming fertilizer.

Future changes in legislative regulations in Germany [1] jeopardise the common use of slags in applications like road construction without further changes of the material. Improvements to modify the slags will have to be performed. The most effective way to do this is to treat the slags in liquid state, e.g. by adding conditioning materials, or to recycle them internally. Replacing carbon containing materials such as charge coal and foaming coke by recycled polymer material could be a good opportunity for the steel industry to adapt itself to external recycling circles.

As one of the bigger electric steel works, Georgsmarienhütte GmbH works on several research & development projects, in particular on the environmental safety of the utilised slags. Together with the FEhS – Institute, GMH has been involved in several public research projects and at the same time in internal projects to identify new ways

of recycling their own by-products and unused waste materials. For this work, the four Rs "ReThink – ReDuce – ReCycle – ReUse" are used as an orientation.

We are more than Steel men do not only produce steel meeting the highest requirements of their customers but also by-products with an intrinsic value they are often aware of. They specifically arrange the process chains in such a way that the intrinsic value is increased; for this purpose they fully develop new approaches to these solutions which have been regarded extraordinary so far.

Steel men operate maximum temperature processes; no one else controls facilities with an arc temperature exceeding 5000° C, molten materials with temperatures up to 1700° C and man-made lava in routine business; this creates chances to offer services for other cycles of materials, to generate additional sources of income thus significantly enhancing the standing of the steel industry in the eyes of the public.

3. Steel Plant Tomorrow

The processes described as follows are just three examples of the NoWASTE strategy of Georgsmarienhütte which comprise several new ideas, improvements and changes in the processes. Beside these by-products, several other materials are emitted, e.g. filter dust and scale. The aim of Georgsmarienhütte is to achieve a NoWASTE steel works in the following years. The steel works GMH of tomorrow can look like **Figure 1**.
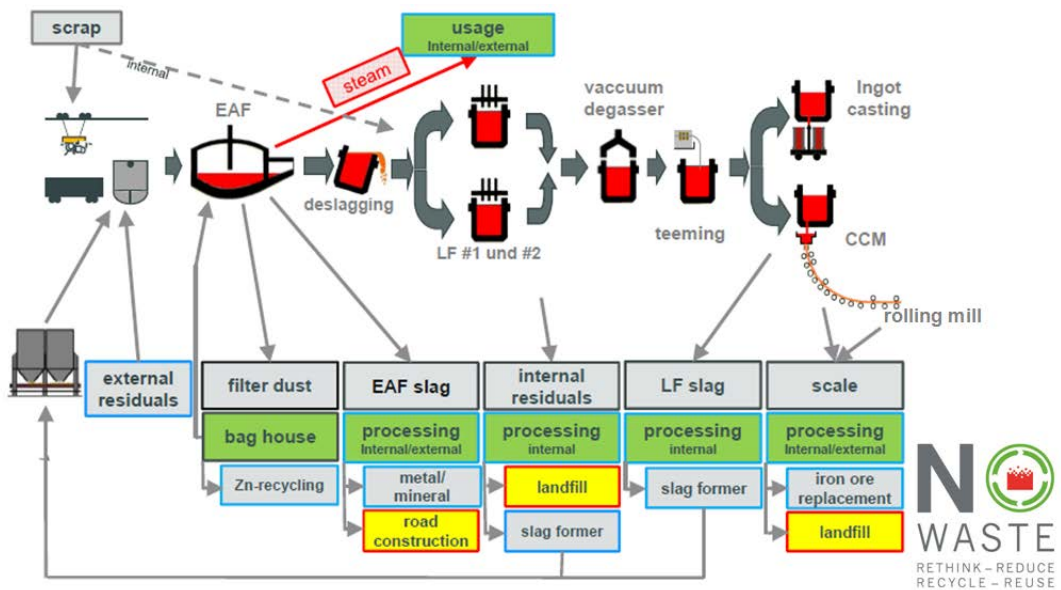
Figure 1: Our vision of a green steel works GMH

4. ReThink – ReDuce – ReCycle – ReUse

By analysing the process steps and the material flows of the steel works, GMH took into consideration all incoming raw materials and beside the main product steel all outgoing materials. In the first step we focused on the largest material flows. One of

the bigger mass flows, the ladle furnace slag (LFS), was identified as a potential material for internal recycling. This slag contains up to 60 wt.-% of lime, 14 wt.-% of dolomite and appreciable amounts of silica and alumina. Typically, primary raw materials like lime and dolomite are employed as a slag former in the EAF. Through internal recycling, LFS is a potential metallurgical substitute for lime and dolomite. The biggest challenge of using LFS as slag former is the internal logistics associated with transport and charge of the material into the EAF. While cooling down the slag in a slag pit, a mineral phase transition occurs that results in volume expansion. Due to this expansion, the slag disintegrates into fine particles, causing dust emissions during transport and charging [2].

The largest mass flow at all is the one of EAF slag. Today, this slag contains metallic and oxide metals and has good physical properties for further use in road construction. The environmental legislation, however, will become in future more and more restrictive. So it might be that this type of slag has to be taken to landfills. In Germany, the remaining capacities in the deposit areas are very low and it is nearly impossible to open new areas. Additionally landfill is counterproductive to the idea of a circular economy. So you have to re-think especially when you do not have a company owned land fill area. If you watch EAF slag running out of the furnace, could you accept it as already molten iron ore with an iron oxide content close to those ores our ancestors used in the 1940ies?

In the electric steel process there is a reasonable amount of carbon to be used either as charge carbon or to foam the slag in the EAF. Instead of using these "primary" raw material it is from an economic point of view very interesting to use recycled polymer materials available in huge quantities on the market.

5. Preventing disintegration of Ladle Furnace Slag

During solidification of LFS, several calcium silicate phases are formed from the melt. Further cooling results in a continuous conversion of these phases to their modifications. At approximately 500 °C the monoclinic β_H-C_2S (larnite) converts to rhombical γ-C_2S (calcio-olivine). The different densities of these phases (**Table 1**) result in a volume expansion of almost twelve percent.

	density [g/cm³]	crystal structure
β_H-C_2S (larnite)	3.31	monoclinic
γ-C_2S (calcio-olivine)	2.97	rhombical

Table 1: Density of β- and γ-modification of dicalcium silicate [6]

As described in literature, the decomposition of dicalcium silicate can be prevented by adding chemical substances that will make the β_H-C_2S-phase thermodynamically more favourable than γ-C_2S at 500 °C [3]. The addition of 1 wt.-% of B_2O_3 or P_2O_5 is sufficient to stabilize the slag. The compounds are integrated into the crystal structure of C_2S and inhibit the effective lattice energy.

Several barriers, however, exist to implement the recycling of LFS to the EAF in operational practice. On the one hand, the addition of boron or phosphorous to the EAF will have a negative influence on the produced crude steel, because these elements are steel polluters. On the other hand, a homogenous distribution of B or P in the LFS is a big challenge due to varying viscosity from tap to tap.

Another way of stabilising the dicalcium silicate in LFS is to change the cooling rate; this would not depend on any addition of conditioning substances. With faster cooling rates the crystal growth is inhibited and decomposition is avoided[2]. The very low thermal conductivity of the slag [4] makes it necessary to have a large surface area on the cooling device to ensure sufficiently fast cooling of the slag for finely crystalline microstructures to form.

Based on several laboratory experiments at FEhS, a pilot scale test plate, shown in **Figure 2**, was built at the melting shop where the LFS was solidified rapidly. Several trial campaigns were made to optimise the device and to define the basic conditions necessary to repeatedly achieve high stabilisation rates under industrial conditions, e.g. the required temperature of the LFS as well as the maximum thickness of the slag layer on the cooling device. From these trials, nearly totally stabilised LFS with a high lime content was produced with the possibility to charge it to the EAF without inhibiting dust emissions.

Figure 2: Cooling plate with LFS at the melting shop

The LFS was used to substitute the primary lime and no negative effects on the EAF process, e.g. higher energy consumption, were determined. However, it has to be taken into account that in an industrial practice the costs for material handling in the melting shop cannot be neglected and additional process steps are required which result in economic disadvantages.

6. Metallurgical treatment of EAF slags

Due to oxidizing conditions in the EAF, these slags can contain more than 40 wt.-% of iron oxide. While the metallic iron pieces are separated during the processing of the slag, the iron oxide cannot be recycled. A metallurgical step is necessary to reduce the Fe oxide, which requires a lot of energy and currently outweighs the advantages of the recycling.

Figure 3: Slag pot foam over   **Figure 4:** Segregated slag/metal

The innovative idea is to use the energy content of the slag for the reduction and to create a special mixture of reducing agents (Al, C, Si) to have a self-sufficient energy reducing process. The reduction rate of the EAF slag must not be 100 %, which would lead to a high viscosity with several disadvantages. Beside this, a complete reduction of the EAF slag would result in a phosphorous rich metal which cannot be recycled internally, so a happy medium has to be found.

First operational trials show good results of the metal quality and the environmental properties of the EAF slag. Accompanied by thermodynamic calculations, operational trials will be performed in the future to optimize the mixture of reducing agents, the process technology (e.g. foam over of slag pot, **Figure 2**) and the properties of EAF slag and reduced hot metal.

7. Polymer replaces carbon containing raw materials

By recycling containments for beverages in the paper industry a lot of polymer foils are generated also containing smaller amounts of metallic aluminium. This materials is not usable to recover pure PE or aluminium for high grade purposes. So the idea came up to agglomerate this mixture in a very simple way into a chargeable geometry and to use it as foam slag agent. Trials will be done in the near future.

References

1) Federal Ministry for the Environment, Nature Conservation, Building and Nuclear Safety, *"Draft of Substitute construction materials regulation"*, Germany, 2017
2) P. Drissen, D. Mudersbach, K. Schulbert, T. Zehn, "Stabilisierung sekundärmetallurgischer Schlacken aus der Qualitätsstahlerzeugung", *Report ofFEhS-Institute*, 19, No. 1, p. 10-14 (2012)
3) H. Lehmann, K. Niesel, P. Thormann: "Die Stabilitätsbereiche der Modifikation des C2S", *Tonidustrie Zeitung 93*, No. 6, p. 197-209 (1969)
4) K. Goto, H. Gudenau, K. Nagata, K.-H. Lindner,"Wärmeleitfähigkeiten von Hochofenschlacken und Stranggießpulvern im Temperaturbereich von 100-1550 °C", *Stahl und Eisen 105*, p. 1387-94 (1985)

Reducing environmental impact with clean steel produced with a clean process

Patrik Ölund
Ovako Group R&D

Keywords: clean steel, environment, power density, quantification

Abstract:

The advances of ladle metallurgy have led to very significant improvement in the internal cleanliness of low alloy steel products. This development, which started with the design of the first functioning ladle furnaces with effective stirring facilities, has now reached a level where steel produced in air-melting processes could compete with complex and costly re-melting processes. Consequently, the producers of high volume product now have a possibility to utilize the improved performance through increase the allowed loading or reduced component size, i.e. increase the power density. This may lead to significant increase in efficiency and/or weight savings that will have a positive environmental impact.

Moreover, the scrap-based process used to produce these steels will give very low carbondioxide emissions that will bring further positive contributions to the environment compared to many alternative processes.

New developments in testing procedures, particularly the control of the non-metallic inclusion content in steel to ensure that the correct quality is obtained.

The developments in steel processing are reviewed and recent progress in the rating of non-metallic inclusions is detailed, in particular as regards test methods encompassing ultrasonic techniques. The development of the high frequency ultrasonic technique has made it possible to assess micro inclusion populations more relevant to the product performance. Further, recent advances in structural fatigue initiation are discussed and related to content and morphology of micro-inclusions

INNOVATIVE MEASURES TO PREVENT DUST EMISSIONS

Kersten Marx

VDEh-Betriebsforschungsinstitut GmbH, Düsseldorf, Germany

Abstract

Secondary off-gas cleaning systems for BOF-dedusting are normally installed to evacuate the hot fumes produced especially during the converter operation steps scrap charging, hot metal charging, steel tapping and slag dump. Environmental issues and economic conditions are requiring efficient dedusting systems. The aim is therefore the effective control of dust emission to improve occupational health and environmental protection, as well as to de-crease maintenance costs and increase availability and productivity of the plant. Since the capital costs as well as the operation costs for dedusting systems in steel industry are high, an optimum design with regard to an economical operation is very important. Additionally dust suppression techniques were studied to reduce dust and flames to ease fume capture.

To fulfil these requirements VDEh-Betriebsforschungsinstitut (BFI) further developed meas-uring methods and simulation approaches to investigate actual or planned systems in order to improve their performance. Gas composition, dust concentration, temperature and flow velocity were continuously measured for different process phases to acquire boundary condi-tions for the model trials and the numerical simulation. The fume flow rate was determined with a new method (Structural PIV). The relevant dedusting facilities are studied with three-dimensional isothermal physical models. Additionally flow and temperature conditions as well as the fume propagation were simulated using a Computational Fluid Dynamics (CFD) pro-gramme. Necessary suction flow rates can be reduced by fume suppression techniques. A possible technique is the addition of inert gases in the region of the melt surface.

As a result of this investigation measures are provided enabling improved fume capture effi-ciency with minimized suction flow rate, leading to improved working conditions in the plant, prevention of fugitive emissions from roof vents and compliance with environmental stand-ards. These measures were successfully implemented in several steel plants.

Introduction

The filling of hot metal in converters is accompanied by the emission of large quantities of hot gases and dust. Installing auxiliary hoods requires special adaptation of the design and pre-cise positioning. Large amounts of energy are wasted, if hood geometry and the fume evac-uation volume do not fit properly to the different operating conditions. Studies in two steel plants were performed to compare and optimize different types of suction hoods (with and without vortex) and to develop effective techniques for fume and flame suppression.

1. Study at Steel Plant A

1.1 Measurements in the plant

In Steel Plant A no extraction hoods for secondary dedusting were installed in the direct vi-cinity of the two converters before the study. In contrast to nearly all other steel plants the normal practice in Steel Plant A at the time of the study was to charge scrap after hot metal in order to decrease the wear of the converter lining. When hot metal is charged into the empty converter vessel the fume emissions are moderate. But if scrap is charged after hot metal a flash develops, which is substantially loaded with dust. The chute works like a chim-ney, so that in the worst case the flames can penetrate deep into the bay.

The conditions in the flame during scrap and hot metal charging are quite unknown, because measurements directly in the flare are very difficult. Especially no data were available for the reversed charging sequence ("first hot metal, then scrap") In order to acquire boundary con-ditions for the model trials and the numerical simulation the gas concentration (O_2, H_2, CO_2 and CO), the temperature with/without radiation and the flow velocity were continuously measured with probes on a movable support (trolley) in a distance of 750 mm of the trolley wall. Additionally the dust concentration was measured for different process phases.

The temperature including the influence of radiation has been measured with a thermocou-ple, which was directly exposed to the flame. For the determination of the temperature with-out radiation a thermocouple was installed in a water-cooled probe. The ceramic tip of the probe, which shields the thermocouple, has not been cooled. With the help of a vacuum pump the flue gas from the flare is sucked off by the probe and thus its temperature was measured and its composition was analysed in the subsequent measurement equipment simultaneously. For the determination of the flow velocity a water-cooled cylinder probe was used. For the dust measurement a separate probe was used, which was not cooled. With the help of a vacuum pump the flue gas from the converter has been sucked off by the probe during the studied process phase and the dust was separated on a filter paper, which has been changed after every trial.

When hot metal is charged after scrap, only one peak in the measured temperature curve occurred, see **Figure 1**. The maximum temperature during hot metal charging was about 1100°C.
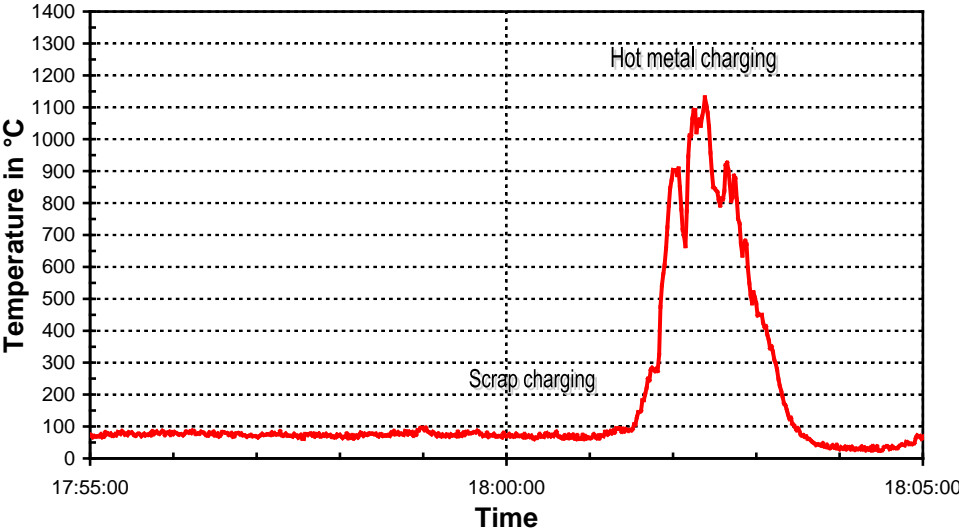
Figure 1: Measured temperature for charging sequence: 1. Scrap, 2. Hot metal

When hot metal was charged before scrap, only a small peak in the measured temperature curve occurred during hot metal charging. An additional higher peak occurred during the subsequent scrap charging. The maximum temperature during scrap charging was about 1300°C, see **Figure 2**.
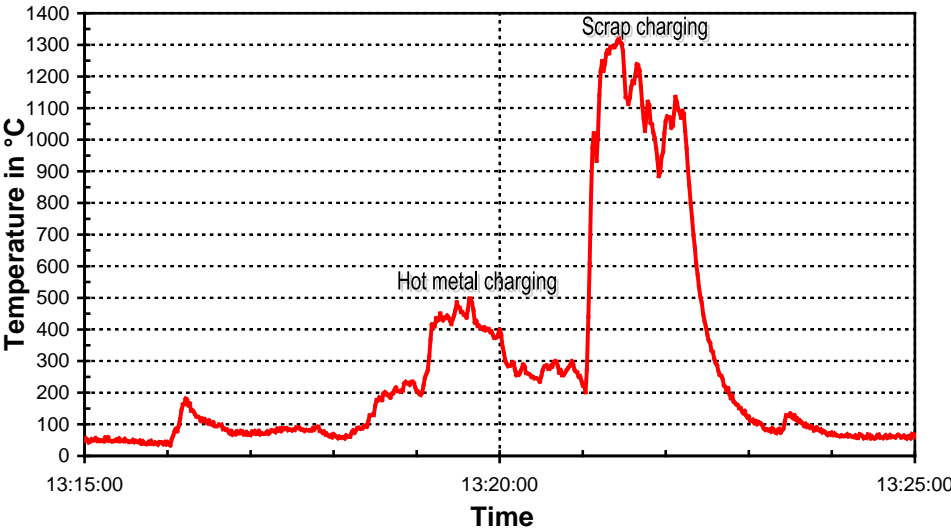
Figure 2: Measured temperature for charging sequence: 1. Hot metal, 2. Scrap

When hot metal was charged after scrap, only one peak in the measured curves for combus-tible gases occurred. The maximum concentration of CO and H_2 was lower than 3 Vol.-%, see **Figure 3**.
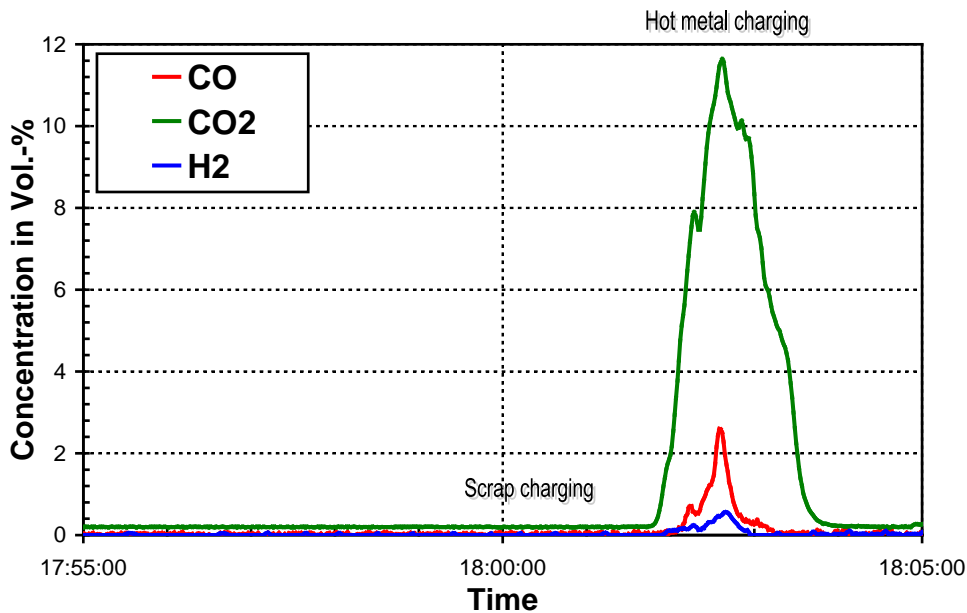
Figure 3:   Measured gas composition for charging sequence: 1. Scrap, 2. Hot metal

When hot metal was charged before scrap, only a small peak in the measured curve for CO_2-concentration occurred during hot metal charging. The concentration of combustible gases was not significant during hot metal charging. But additional higher peaks occurred during subsequent scrap charging. The maximum concentration of CO exceeded 10 Vol.-% and the maximum concentration of H_2 was about 7 Vol.-%, see **Figure 4**.
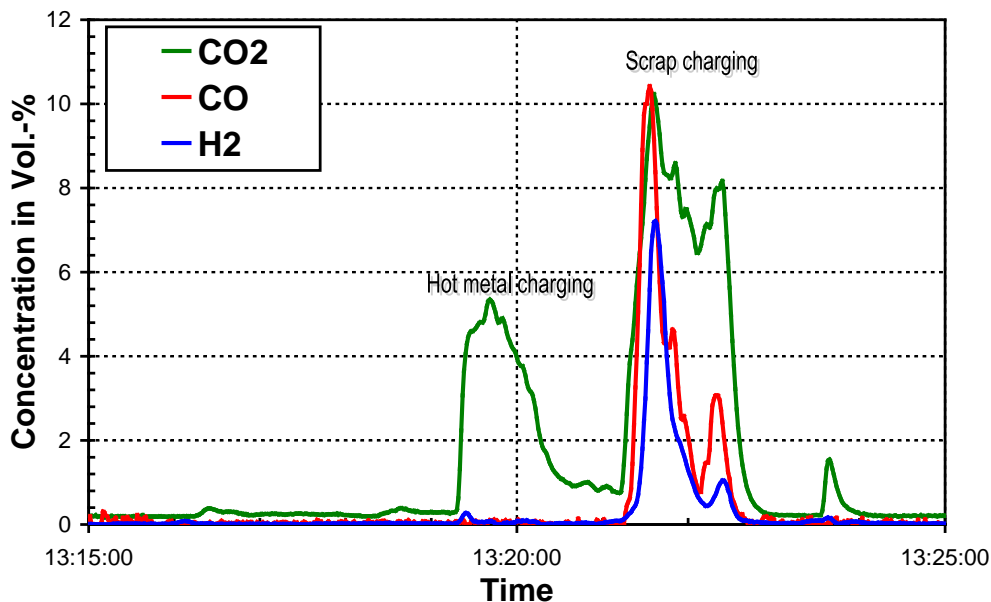
Figure 4:   Measured gas composition for charging sequence: 1. Hot metal, 2. Scrap

1.2 Development of improvements

The flow, temperature and concentration field in a representative part of the steelwork for the process phases "hot metal charging", was simulated using a CFD-programme. Additionally the influence of a cover on the scrap chute on the efficiency of the suction hood was deter-mined. Without cover on the chute the flames originating from scrap charging penetrate deep

into the charging bay. The corresponding calculated temperature field for this case is given in **Figure 5a**.
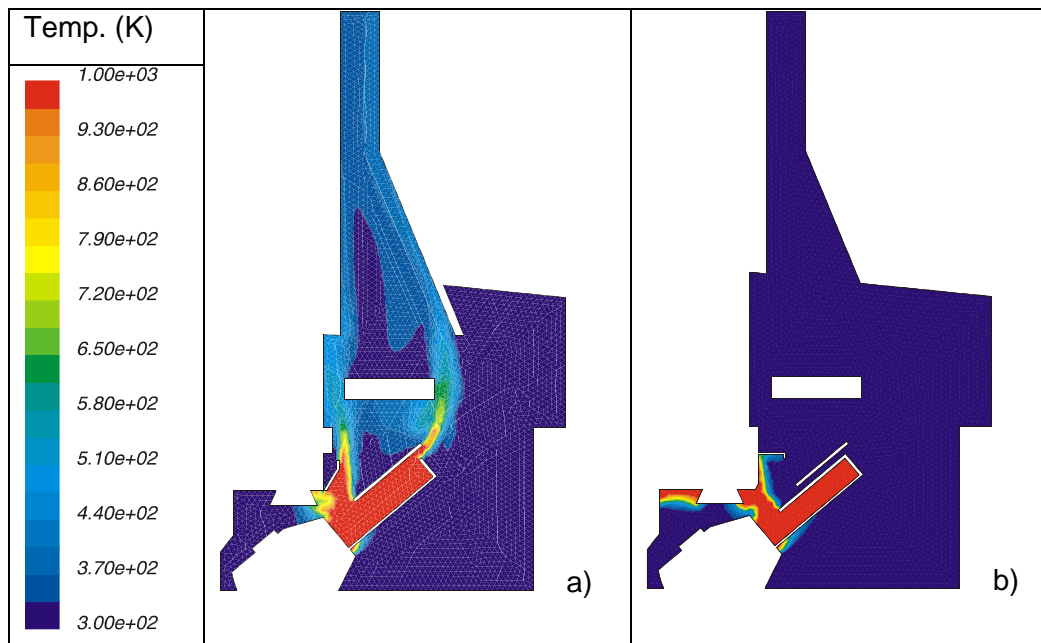
Figure 5: Calculated temperature field during scrap charging,
a) before optimization
b) with secondary dedusting and cover on scrap chute (b)

For this case the flow velocity out of the converter vessel is so high, that the flames hardly can be captured by a charging hood. But if the scrap chute is covered, the flames are di-rected to the enclosure and the greatest part of the fume can be captured by the hoods, see **Figure 5b**.

It is indispensable to provide the scrap chute with a cover, if an almost complete capture of the fumes during scrap charging should be achieved without changing the charging se-quence. Therefore additional operational trials were performed, in which the scrap chutes were equipped with a provisory cover, see **Figure 6**. For the observed charges the emissions were very low during scrap charging with covered chutes. Obviously a great part of the rising combustibles is sucked into the primary dedusting hood before they can react with the ambi-ent air. The preliminary trials with the covered chutes were very promising concerning opti-mized fume capture efficiency.

Figure 6: Scrap charging in hot metal, scrap chute without (left) and with cover (right)

2. Study at Steel Plant B

2.1 Documentation of the present practice

At Steel Plant B the primary off-gas system accomplished the secondary ventilation during charging via a by-pass function. However, the fume capture performance of the charging hood was very poor during converter charging and was not carried out at all during the blow-ing phase. During blowing and tapping a third off-gas system on the tapping side was acti-vated. The emissions captured by the charging hood and the primary off-gas system were cleaned by a venturi scrubber. The tapping hood was connected with a fabric filter. BFI has carried out a plant observation in order to acquire boundary conditions for the numerical and physical modelling.

In order to document the conditions at the converter video photographs were taken from dif-ferent views. Plume photography has proven an effective method of estimating buoyant plume volumes for hot emissions sources. BFI uses advanced image analysis software called Structural PIV for the quantification of fume flow rates. This methodology differs in several points from the classical PIV (**P**article **I**mage **V**elocimetry) technique. Instead of using a laser for creating a light sheet, white light or even day light is sufficient. The second differ-ence is the seeding method used. PIV is working with tracer particles. Structural PIV on the other hand works with small structures for example in fume clouds. The image analysis of of fume clouds is done by ensemble correlation averaging, which makes it possible to receive a mean flow field with a sufficient high signal-to–noise ratio. The advantages of Structural PIV are that it can be used on full-scale objects in the plant, less safety precautions are neces-sary and the equipment is cheaper. **Figure 7** shows as an example a determined flow field for the process phase "blowing".
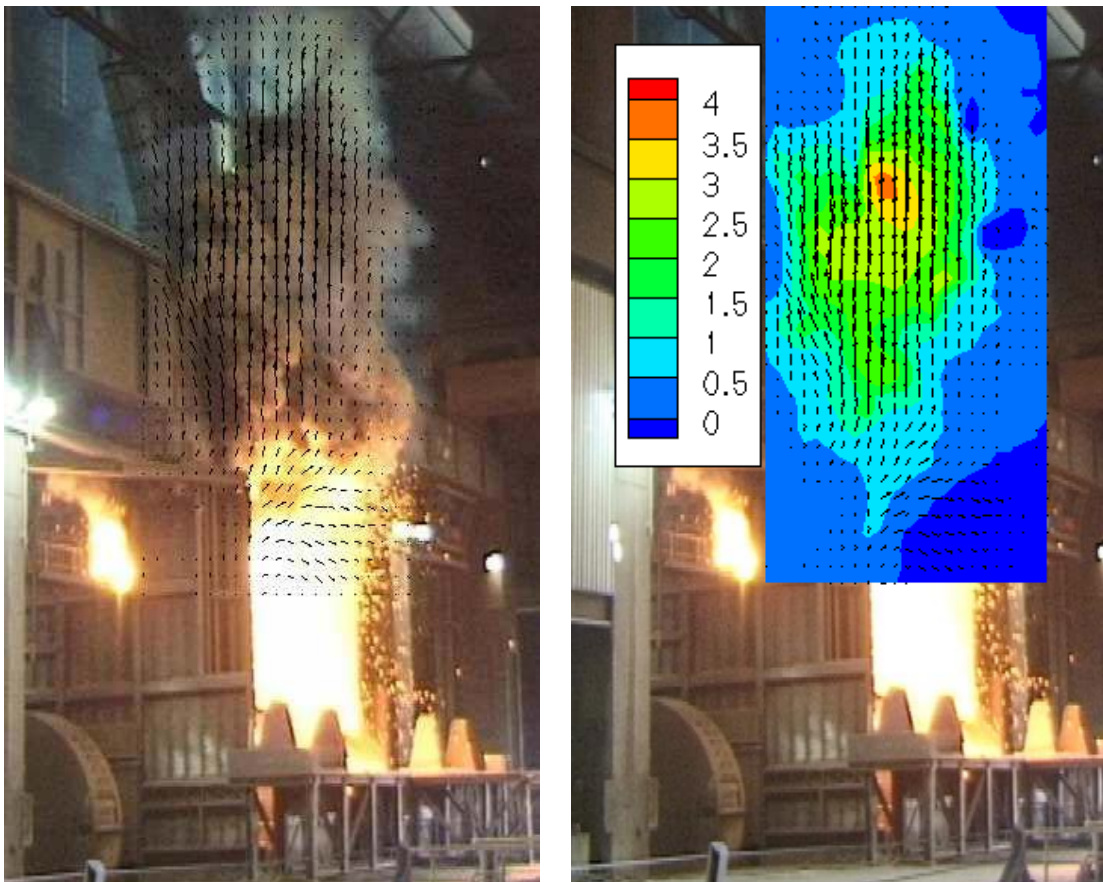
Figure 7:   Flow field determined with Structural PIV (velocity vectors and magnitude of ver-tical component in m/s) in fume emitted during blowing phase of the converter

2.2 Comparison of different charging hood types

Several hood types for the secondary off-gas system were studied. **Figure 8** shows a sketch of the old charging hood at Steel Plant B. In this hood a vortex is generated.
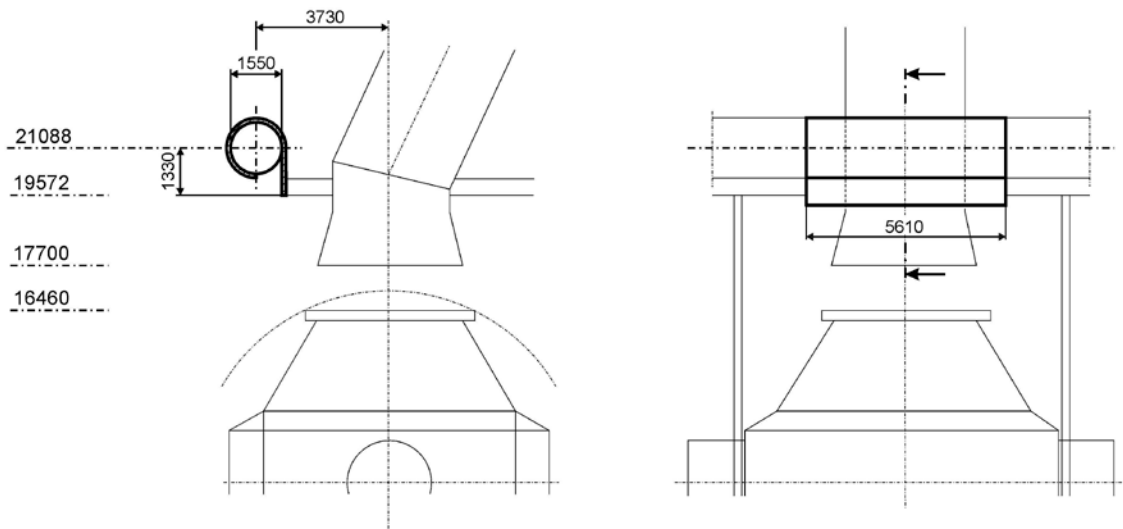
Figure 8: Geometry of the old charging hood (vortex hood)

Figure 9 shows the geometry of an optimized hood.
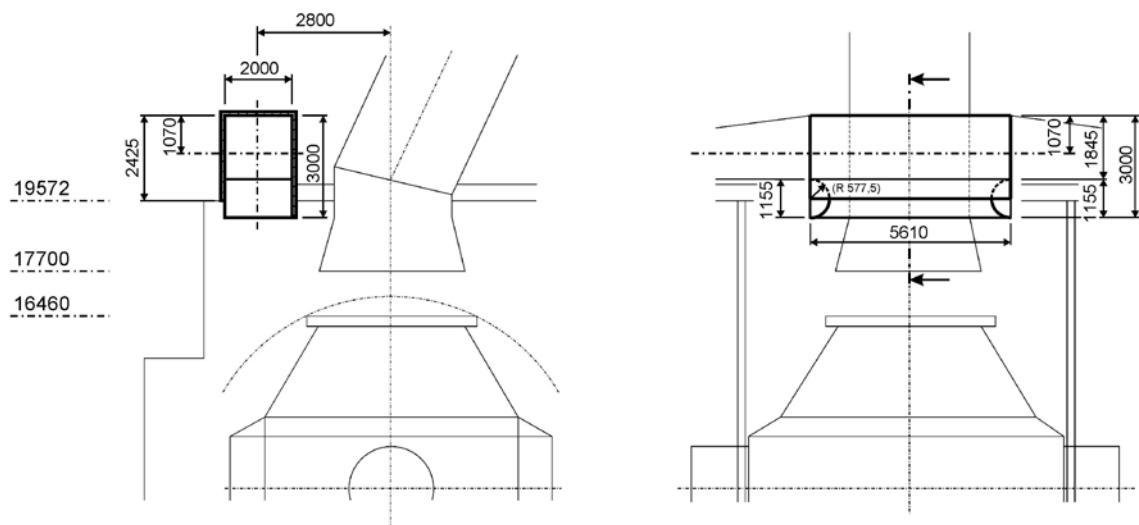
Figure 9: Geometry of the optimized charging hood

The process phase "hot metal charging" was calculated for the old hood with the planned flow rate of at least 750 000 m³/h (S.T.P.) through the charging hood. In order to take into account also extreme reactions during hot metal charging and to have a better comparison of the efficiency of the different hood types, it was assumed that fume leaves the converter ves-sel with a velocity of 32 m/s. In **Figure 10** the calculated velocity field in the central plane of hoods are plotted. The flow velocities are very high for the vortex type hood because the swirl in the hood produces an additional circumferential velocity component in the hood. This leads to a high pressure loss. In the optimized hood the velocity values are moderate, no detachment and recirculation of the flow can be observed.
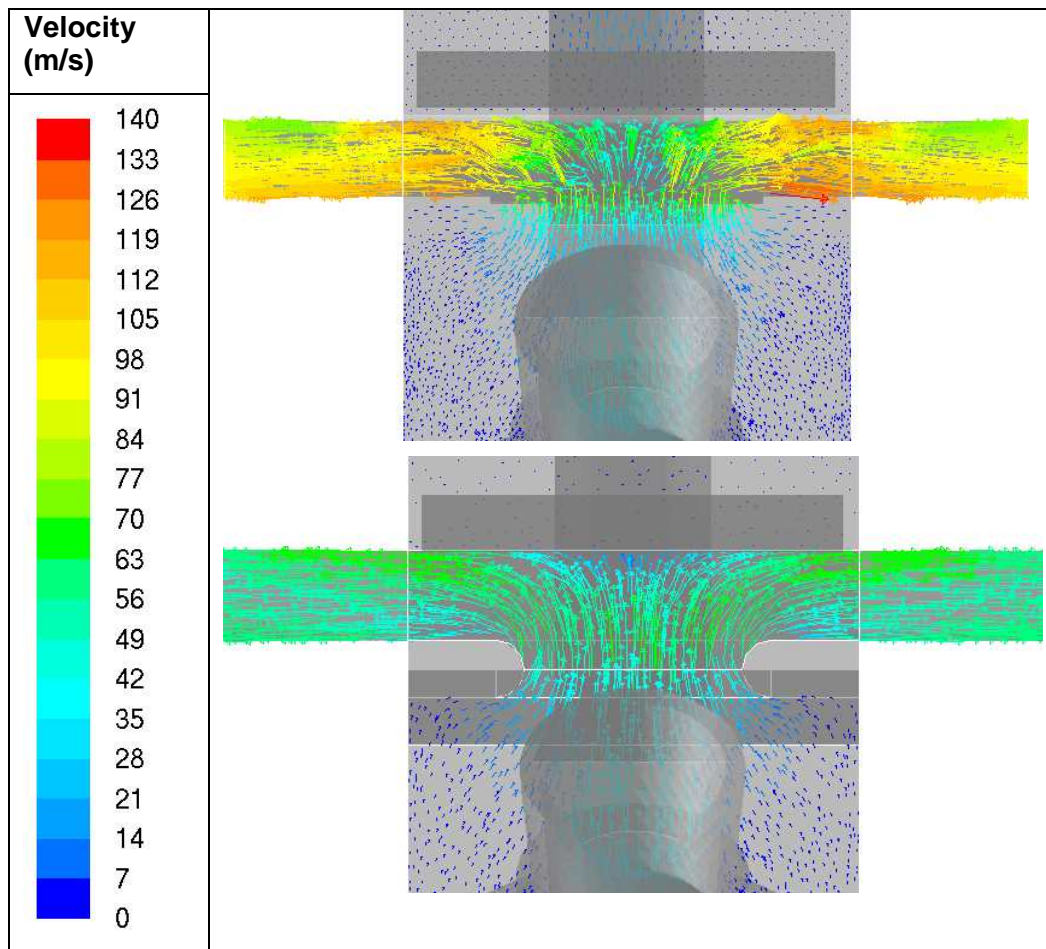
Figure 10: Calculated velocity field during hot metal charging, vortex hood (top) and optimized hood (bottom)
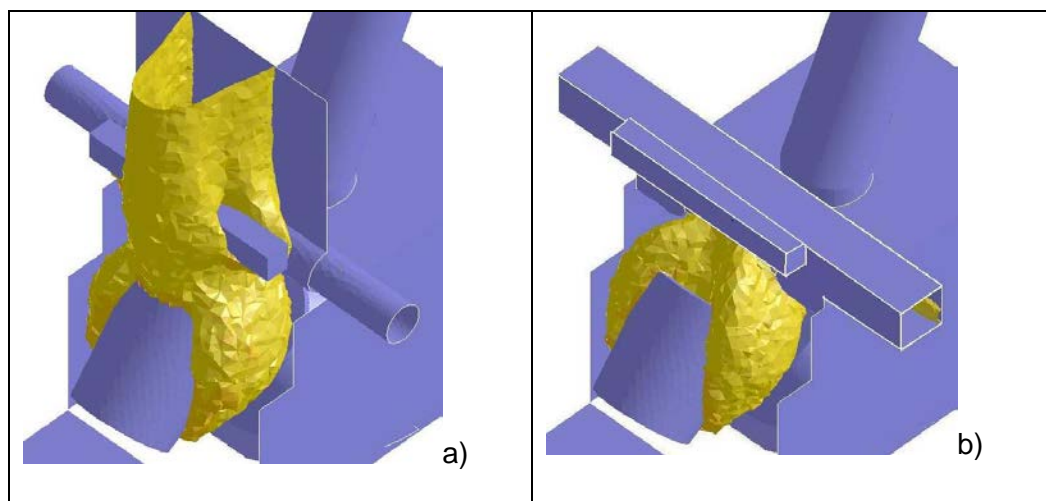
Figure 11: Calculated fume propagation, hot metal charging
a) old hood   b) optimized hood

In spite of the high velocity values in the vortex hood, complete fume capture is not achieved, see **Figure 11a**. So this hood geometry could not be recommended for the planned flow rates. The fume capture efficiency rises significantly with the optimized hood. **Figure 11b** shows the corresponding calculated fume propagation for a flow rate of 750 000 m³/h (S.T.P.) through the charging hood. Now the fume can be captured completely during hot metal charging.

2.3 Fume suppression

The basic idea of fume suppression is to eliminate contact of the liquid metal and atmospher-ic oxygen. Fume suppression with injection of CO_2 during hot metal charging was tested in further trials. Liquid CO_2 was stored in an insulated pressurized tank (20 bar, -20°C) on a road tanker. Lances (snow tubes) were constructed and built, in which the liquid CO_2 was expanded through a nozzle and a jet of gas and CO_2-crystals (snow) was discharged into the converter vessel. The CO_2-snow sublimates to CO_2-gas, when it is heated up. Outside the dog house a scaffold was put up on the 10 m-level. A lance was inserted through a hole in the dog house wall and was moved with a special developed manipulator. The road tanker was placed in a save place between the converters on 0 m-level. **Figure 12** shows the instal-lation of equipment for fume suppression.

Figure 12   Installation of equipment for fume suppression

Normally brown smoke is produced during hot metal charging. During injection of CO_2 with a lance of 80 mm diameter in the flames a white fog (water vapour) was rising instead of brown smoke. **Figure 13** shows the conditions without and with inertization in comparison.
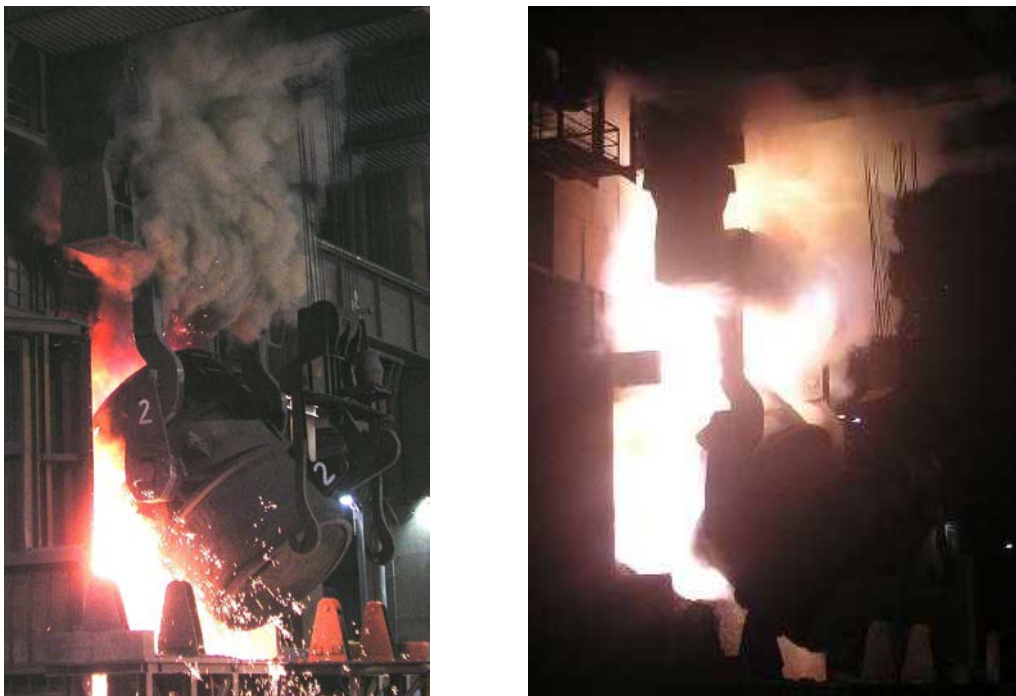
Figure 13 Fume and flame formation without (left) and with (right) CO_2-injection
          (360 kg/min)

In spite of the strongly restricted available space for a charging hood at Steel Plant B it was foreseen to realize a suction flow rate of up to 1 000 000 m³/h (STP). Therefore a hood ge-ometry had to be developed exclusively for these geometrical boundary conditions.

In **Figure 14** the calculated temperature field in the symmetry plane of the converter is plot-ted for the process phase hot metal charging for a suction flow rate of 1 000 000 m³/h (STP). It can be seen, that cold false air is entering the hood from the enclosure, but the fume is captured completely. **Figure 15** shows the calculated fume propagation for 1 000 000 m³/h (STP) suction flow rate.
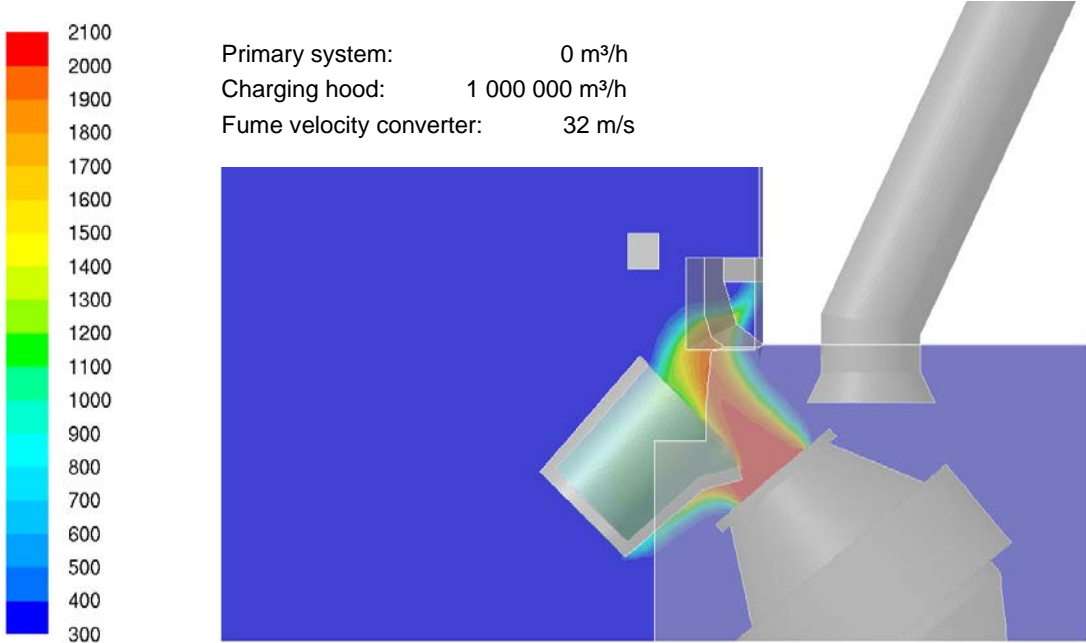
Figure 14 Calculated temperature field (K), hot metal charging, optimized hood, max. suc-
tion flow rate
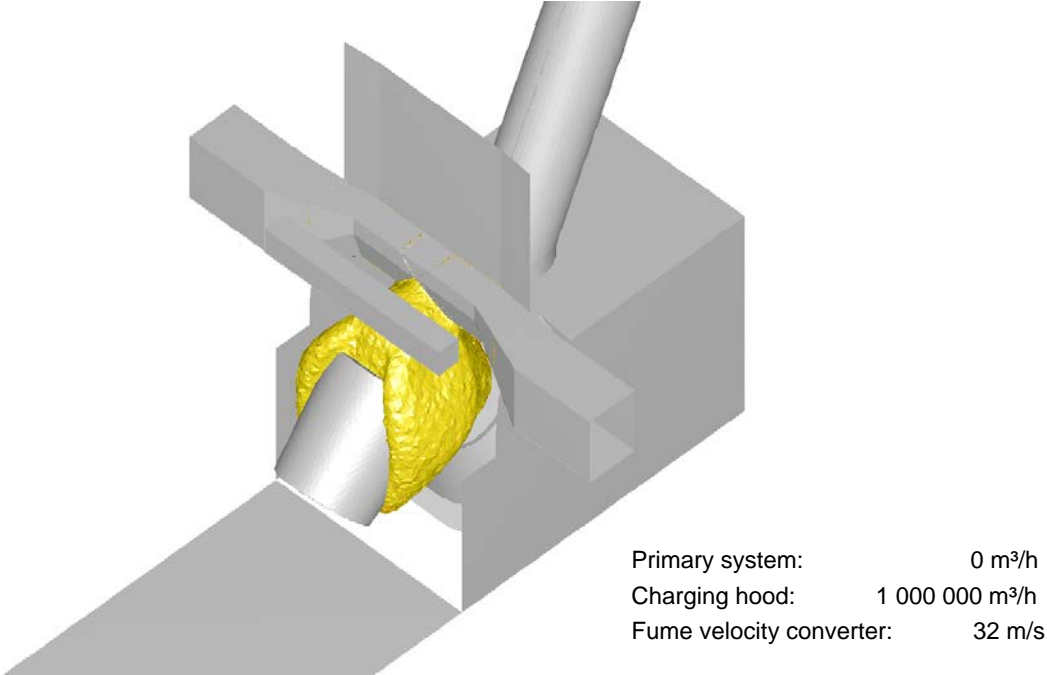
Figure 15 Calculated fume propagation, hot metal charging, optimized hood, max. suction
flow rate

Figure 16 shows the installed new charging hood above the converter during blowing.
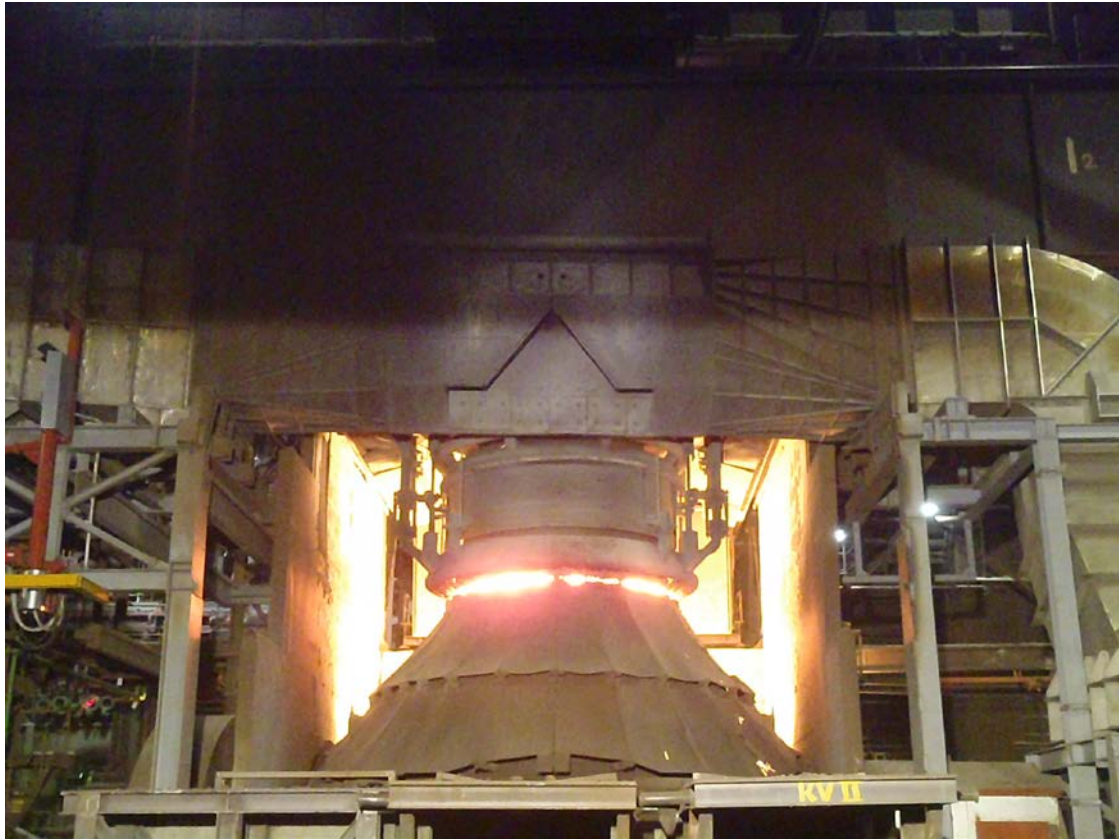
Figure 16 Converter with new charging hood during blowing

The performance of the hoods verified the results of the numerical simulation. The new hoods allow nearly complete fume capture during all process phases. **Figure 17** shows the fume capture during scrap and hot metal charging for a suction flow rate of about 750 000 m³/h STP.
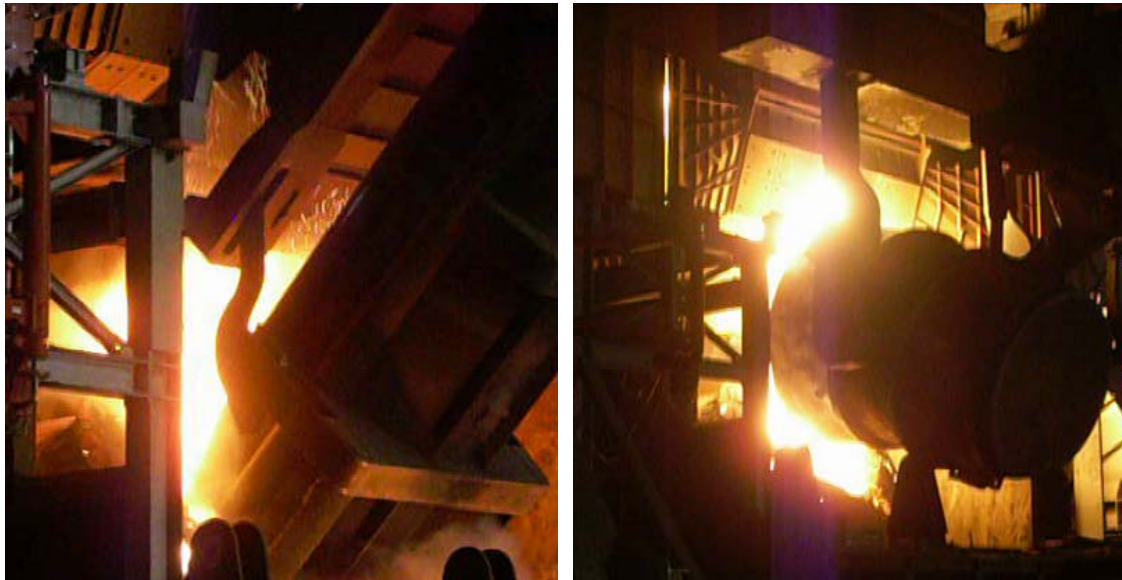
Figure 17   Fume and flame capture with the new charging hood during scrap charging (left)
and hot metal charging (right)

The new secondary dedusting system at Steel Plant B is now independent from the primary system and the charging hoods were constructed based on the findings of the project. A moveable skirt is used to close the gap between primary hood and converter mouth during blowing. The new charging hoods allow nearly complete fume capture during all process phases. From preliminary results can be estimated that it captures about 720 t of dust per year. So a significant improvement of the working conditions and environment can be ex-pected.

3. Conclusions

Measurements, observations and operational trials in the plant and calculations with a com-putational fluid dynamics programme were performed to provide the necessary basic infor-mation for planned and existing secondary dedusting systems. It can be concluded that nu-merical simulation is an important powerful tools for the optimization of dedusting systems if they are used with the necessary expert knowledge. Possible optimizing measures can be evaluated already in the design stage and the results can be transferred to the plant with good success. The technical risk can be greatly reduced and expensive remediation of de-fects can be avoided. With these tools BFI developed effective solutions to optimize dedust-ing systems for a great number of BOF shops.

A capable hood is a critical part to any dedusting system, because if the hood does not cap-ture the dust, the rest of the exhaust system is meaningless. Effective hoods for small avail-able space were developed and optimized by numerical simulation. The simulation tools are adequate to study and compare different types of suction hoods. The boundary conditions for the simulation can be gained by video documentation (plume photography and image analy-sis with Structural PIV) as well as measurements in the plant. A flare during scrap charging can be suppressed by a cover on the scrap chute. The method for fume suppression during hot metal charging with inert gases is expensive but probably applicable especially for small or medium sized converters with weak exhaust systems. The new secondary dedusting sys-tem at Steel Plant B is now independent from the primary system. The hoods, which were constructed based on the findings of the project, have a very good performance.

The knowledge gained can be used within the steel industry to provide cost-effective emis-sions reductions on the majority of BOF shops [1-5].

4. Acknowledgement

Referencies

[1]   Marx, K.: Efficient optimization of dedusting systems. 27es Journées Sidérurgique Inter-nationales 2006, December 14-15, 2006, Paris, France, pp. 154/155

[2]   Marx, K.; Rödl, S.: Efficient optimization of steelplant dedusting. The 6th European Ox-ygen Steelmaking Conference - Stockholm 2011, Programme No. 7-1

[3]   Marx, K.; Rödl, S.: Efficient optimization of steelplant dedusting. Stahl und Eisen 132 (2012) No. 6, pp. 61-71

[4]   Marx, K.; Rödl, S.: New approaches for efficient dedusting of basic oxygen furnaces. Journées Siderurgiques Internationales - Paris 2012, Session 2

[5]   Marx, K.; Wollenberg, M.: Development of effective dedusting of converters by innova-tive concepts and constructive optimisation (Bofdedust) **in:** Report of the Commission of the European Communities - EUR, Research Fund for Coal and Steel series, Lux-embourg/Office for Official Publications of the EC (http://bookshop.europa.eu), Report EUR 25907 EN 2013

A general Approach to the Reduction of CO_2 Emissions from the Steel Industry

Lauri Holappa

Aalto University School of Chemical Engineering

Department of Chemical and Metallurgical Engineering

Abstract: Iron and steel making is an energy-intensive branch of industry. Consequently, it is playing a significant role in global energy consumption and carbon dioxide emissions. The jointly approved target of limiting the global warming by 2050 is extremely challenging. In order to actualize its own share in cutting CO_2 emissions, great advancements must be done.

The present situation and feasible scenarios for the future are described. Potential methods to decrease CO_2 emissions in current processes via improved energy efficiency, increasing recycling and alternative energy sources are considered. Development programs for current and novel innovative processes as well as trends of energy usage in the future are surveyed. Finally, a simplified holistic model is represented demonstrating different actions for global solution of the steel industries´ CO_2 emissions problem.

1. Introduction

Today sustainability is a common worldwide concept involving all fields of human activity. Applied to industry it means economically and socially sound course of actions, which are environmentally protective and sustainable in the long term. From the environmental point of view, energy consumption has a central role. The global energy usage was estimated as 13.7 Btoe (billion tons oil equivalent) in 2014 [1]. Respectively, the anthropogenic carbon emissions including fuel combustion and cement production were 9.795 Gt C in 2014 (35.9 Gt CO_2) [2].

The overall progress of the world steel production during the last 150 years is shown in Fig. 1 [3]. In the early 19th century, the world annual steel production was only a few million tons. After the breakthrough of new technologies, converter and open hearth processes, it exceeded 30 Mt in 1900. In 1927, the steel production reached 100 Mt and 200 Mt in 1951. Then a "new industrial revolution" took place with innovative novel processes, and extensive investments in steel industry were performed in Japan, Soviet Union, United States and South Korea in the vanguard and the annual steel production attained the level of 700 Mt in the 1970s (the record 749 Mt in 1979). Then the growth stagnated due to economic crises and political changes until the turn of the millennium, when it attained 850 Mt in 2000. That was the overture to the "boom", in which China was the motor. The world production record so far is 1,670 Mt attained in 2014 [3]. China´s share is about 50 %.

Today China´s production seems to have reached an "established level", whereas other developing countries (India, Brazil and Russia in the forefront) are increasing steel production remarkably. In the near future, even the consumption will grow in developing countries. Still ten years ago scenarios predicted continuous growth up to 3000 Mt/year in 2050. Today, after the recession period and stabilization in China, the scenarios are more conservative and the estimate by World Steel Association is around 2,500 Mt in 2050 [3]. The future scenario until the year 2050 is sketched in Figure 2.
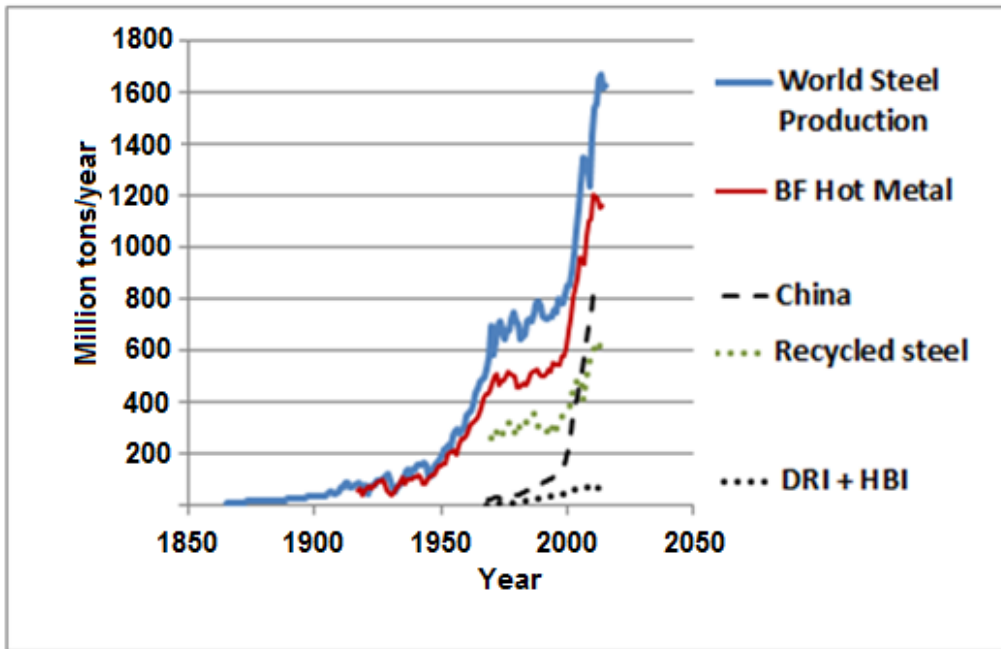
Figure 1. World production of steel, blast furnace hot metal and direct reduced iron from 1860 to 2016. The steel production in China and estimated fraction of recycled steel are shown as well [3].
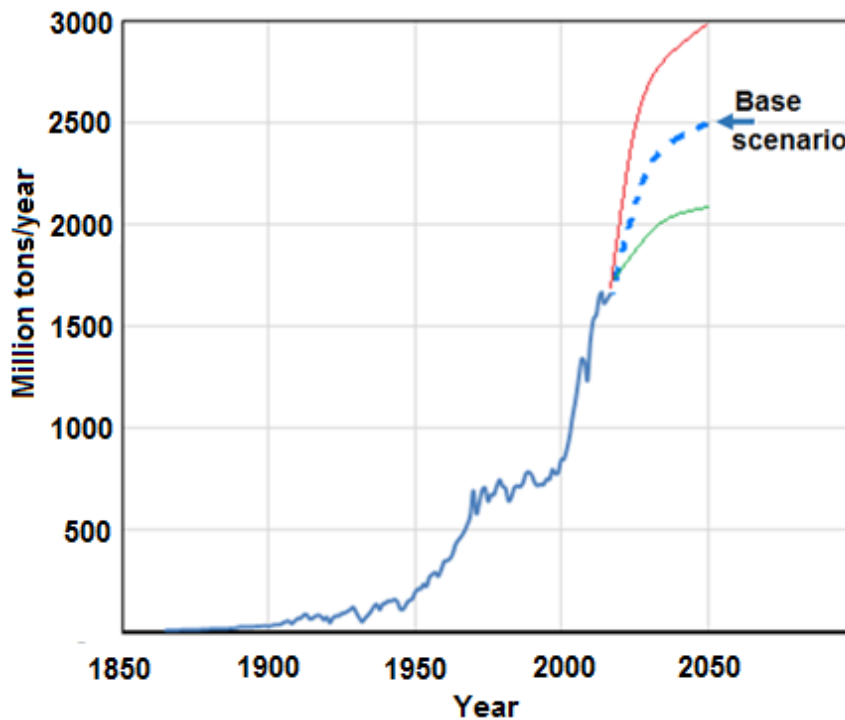
Figure 2. World production of steel from 1860 to 2016 and future scenarios until 2050 [3].

Figure 1 also shows the amounts of main raw materials of steel, namely blast furnace hot metal (BF HM), recycled steel (RS) and direct reduced iron (DRI). Of these, HM is mainly charged into converters to make steel, whereas RS and DRI go into electric furnaces. At present, over 73 % of crude steel comes from converter processes based on BF hot metal. Electric furnaces produce about 26 % utilizing recycled steel scrap as the main iron source, with small share of direct reduced iron. The open-hearth process is today a disappearing curiosity producing less than 0.5 % of the world steel.

2. Carbon dioxide emissions from fossil fuels combustion and steel production

Anthropogenic greenhouse gas (GHG) emissions have doubled since 1970 due to the rapid growth of population, expanded industrialization and rise of the standard of living. The observed growth can be seen in Figure 3. The scale in the figure is in Gt C/year (gigaton carbon). The conversion to CO_2 takes place by multiplying by 3.667, thus the current emission per year is about 36 Gt CO_2. Carbon dioxide is the most important GHG and its content in the atmosphere has increased from the level 300 ppm in 1950 to the current 400 ppm. The relation of GHG to global climate warming is indisputable. The red line in Figure 3 represents the growth of CO_2 emissions until the year 2050, if no radical changes in the climate policy were done [4,5]. This would also mean rapid climate warming which could carry catastrophic consequences. The United Nations´ Intergovernmental Panel on Climate Change (IPCC) has stated that CO_2 concentration must be stabilized at 450 ppm to have a fair chance of avoiding global warming above 2ºC, which was set as a limit at the COP 21/CMP 11 Conference in Paris Dec. 2015 [6]. The target of "stop the climate change" would require a 40 -70% cut of emissions by 2050, compared to 2010 level, and zero emissions by the end of the century. The green line in Figure 3 marks a 50 % reduction by 2050.
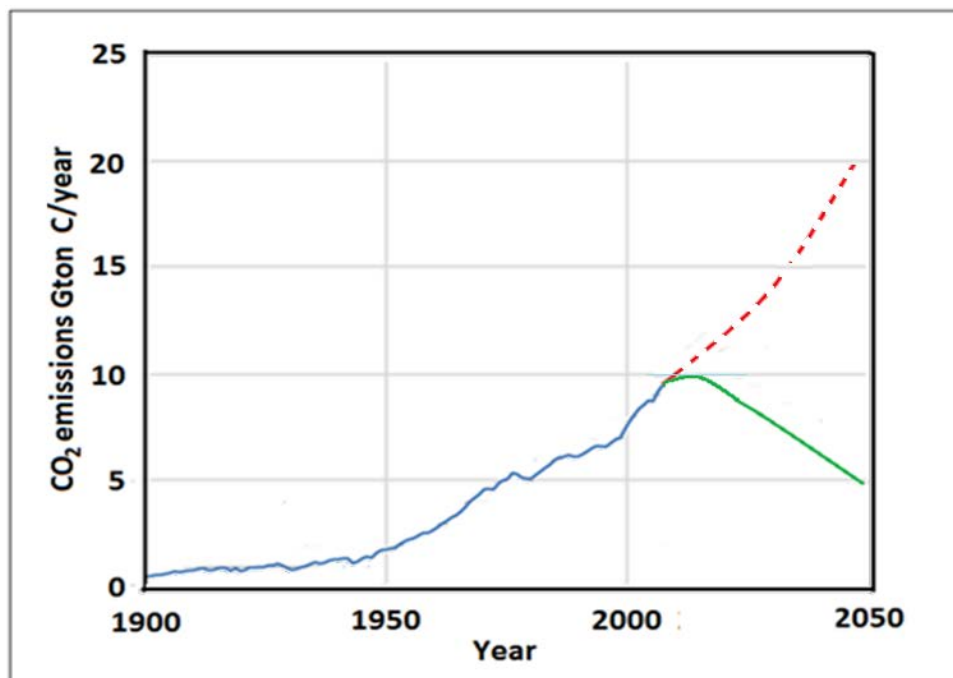
Figure 3. Global carbon dioxide emissions from fossil fuels 1900-2015 and a scenario to 2050 (RCP8.5; dash line) [5,6]. Green line is a target scenario for 50 % reduction in CO_2 emissions by 2050 (RCP3-PD [6]).

Iron making is an extremely energy-intensive process utilizing coal as the main primary energy source. The steel production was responsible for about 6.6 % of all anthropogenic CO_2 emissions corresponding to 2.4 Gt CO_2/year [2, 3]. These are, however, only the direct emissions from iron and steel making. If also indirect emissions including energy generation e.g. electricity is included, the number is around 3 Gt/year [6]. The specific emission is around 1.8 t CO_2/t steel, respectively. The overall global demands for elimination of CO_2 emissions set big challenges to the steel industry. Halving the emissions would mean total emissions 1.2 – 1.5 Gt CO_2/year depending on the calculation way. A simple estimate for the targets of the steel industry to the year 2050 was put forward here. By choosing the scenario with 2.5 Gt steel/year and a target for CO_2 emissions 1.25 Gt CO_2/year, we get a specific CO_2 emission of 0.5 t CO_2/t steel. The change from 1.8 to 0.5 t CO_2/t steel is dramatic, indeed. How could we attain this

level by 2050? The author considered the problem in 2011 by analyzing the steel production practices in different countries, by comparing with BAT values (Best Available Technology), by estimating emissions from different energy sources including electricity as well as the role of energy saving, low-carbon and carbon-free new innovative technologies [7,8]. The present contribution bases on the previous studies but is an up-dated, generalized version. Five key factors are discussed, which enable to solve the problem of drastic reduction of CO_2 from steel production [9].

3. Analysis of means to radically cut CO_2 emissions from steel industry

We can identify five key factors, which enable drastically reduce CO_2 from steel production. *The first key factor* is improved energy efficiency. A comprehensive study by IEA/OECD analyzed steel industries in different countries and showed improvement potential for each country, respectively [10]. The study was based on data of 2006, and showed the worldwide average of 4.1 GJ/t steel corresponding to 20 %.energy saving. The saving potential varied from 1.4 to 8.7 GJ/t in different countries the greatest potentials being in China, Ukraine, Russia, India and Brazil. In spite of great advancements done in ten years, the World Steel Association has still the target of energy saving with 15-20% [11]. Transfer of BAT technology worldwide in steel production facilities is an efficient and necessary way to save energy and cut CO_2 emissions.

The second key factor is recycling. Steel recycling was extremely valued throughout the Iron Age before industrialization. Because steel was a rare and expensive material, even reuse by remanufacturing second-hand products from "scrap" was most common. When steel became mass product, its price fell, reuse almost disappeared and interest to return scrap to steel producers weakened. However, collection of scrap and delivery to steel plants has been for long duly organized in industrialized countries, and recycling rate is moderate. Most of purchased scrap is used in electric arc furnaces, and smaller share in converters in which it is used as a coolant, typically 15-25 % of the iron charge. Until the turn of the century the share of EAF increased being about 34 % in 2001 but then the rapid growth in China, which based on BF + BOF route, changed the ratio and now the EAF´s share is only 26 % whereas BOF has 73 %, respectively [3]. The EAF share varies in different countries (100 % in some small countries, 60 % in United States, 40 % in EU, 6 % in China). The recent amounts of scrap in steel making are shown in Fig. 4. Purchased scrap means external "obsolete" scrap. Another group of scrap is internal "own" scrap which can be counted as the Remainder of Scrap use minus Purchased scrap. The numbers are somewhat smaller, probably due to missing data, compared with Figure 1, which data was calculated based on the balance of Fe metallics including BF hot metal, DRI+HBI and scrap.

Recently, the principle of "Circular economy" has gained ground. Intensified use of scrap is a self-evident goal. Newest scenarios assume significant growth in availability and use of steel scrap. A simple explanation is that the sudden growth of steel production in the early 2000 raised also the use of steel to a new level. In different applications, the steel components have varying lifetimes. Anyway, the rise in production should reflect in scrap availability a few decades later. Consequently, amount of scrap should strongly increase after the 2020s [13, 14, 15]. The estimated scrap ratio rises up to 50 % level by 2050. This means a substantial growth in EAF steel making whereas BOF production would stay approximately on its present level on the global scale [3, 15]. However, regionally e.g. in China availability of scrap will increase and the EAF route will grow remarkably from the current 6 % by partial transition from BF + BOF route. A general increasing demand will incite recycling and raise collection rates. Scenarios for scrap use in steel making are in Figure 5. The notation *Scrap* refers to usual recycling practice and *Scrap+* to boosted recycling rate including strong parallel actions in China too.

Figure 4. Scrap use for steel production and amount of purchased scrap as well as the total world steel production 2010 – 2015 [12].
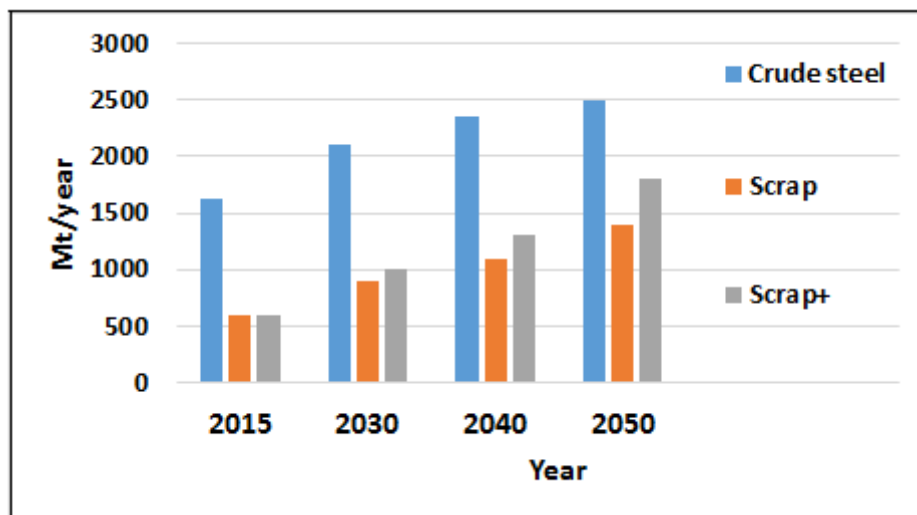
Figure 5. Scenarios for scrap use in steel production until 2050 related to steel production. Redrawn based on scenarios in the literature [3, 14, 15].

Comparison of energy efficiency in different countries or even steel plants is impossible if the boundary conditions (raw materials, energy sources, processes, products etc.) are different. However, even the efficiency of different process routes (e.g. ore-based and scrap-based steel production) can be compared by examining the specific energy consumption (GJ/t steel) against the recycling ratio, defined as percentage of scrap from the total Fe input [7, 8]. Correspondingly, the specific CO_2 emissions, ton CO_2/ton steel, can be presented like in Figure 6. The y-axis shows the specific CO_2 emission as a function of % REC (percentage of recycled steel) on the x-axis. The case x = % REC = 0 corresponds to 100 % ore based BF – BOF route steel making, whereas x = % REC = 100 means 100 % scrap based steel production i.e. EAF route. The full BAT line was drawn based on the rather conservative data by Worrell et al [16]. The BAT Line Range was estimated based on different CO_2 emissions from electricity generation, the low line referring to low emission electricity (hydro/nuclear power) and the high line to coal power stations, respectively. In this scale, the current position of "world steel" is at 1.8

t CO_2/t steel vs 34% REC [3]. Future BAT Lines were sketched based on potential progresses toward low-carbon energy sources in iron making as well as in energy generation.
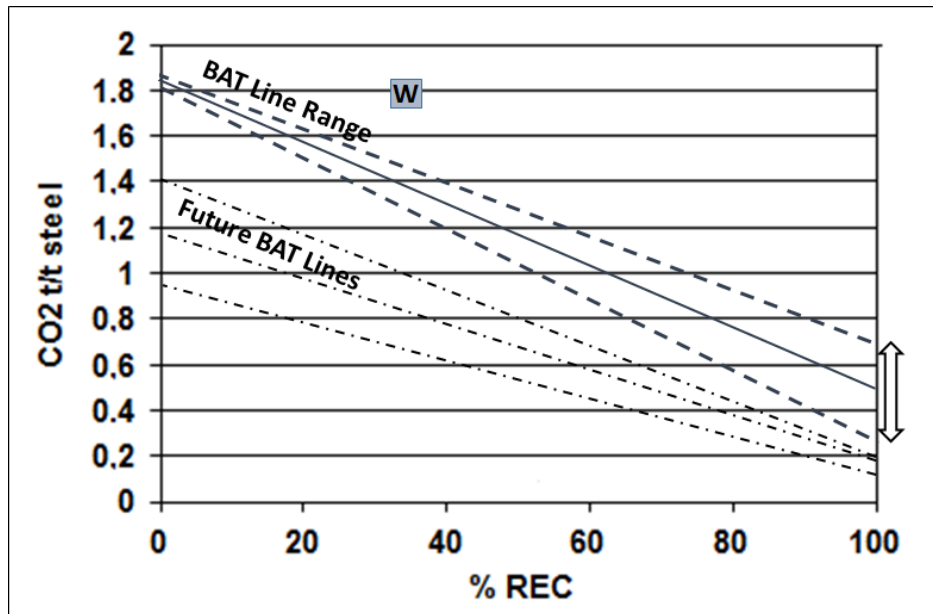
Figure 6. Specific CO_2 emissions from fossil fuels and electricity in iron and steel production as a function of Recycled steel ratio. BAT Line Range shows the best current practices and Future BAT Lines potential boundary conditions when new innovative technologies come into use. W = Current World position. Calculated based on literature data [3, 16-19].

In Figure 7, a possible route and actions were sketched showing how the specific CO_2 emissions from iron and steel production can be decreased from the current 1.8 t CO_2/t steel to the target value 0.5 t CO_2/t steel by the year 2050. The more detailed review is given below.
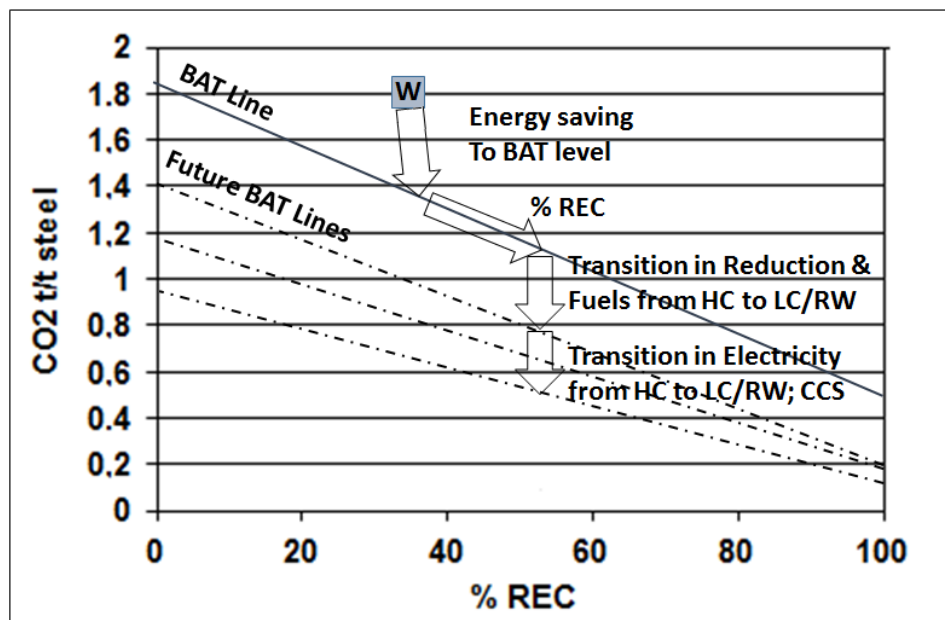
Figure 7. Prospective scenario to decrease the specific CO_2 emissions from iron and steel production from the current level (W) to the target value by 2050 (1.8 → 0.5 t CO_2/t steel). % REC = Recycled steel ratio, solid BAT line = present BAT function. Dotted lines show possible future BAT relations. CCS = CO_2 Capture and Storage.

Improving energy efficiency by 15-20 %, which was calculated as a potential leads to corresponding reduction in emissions, and the BAT line is attained (the first arrow downward from "W" in Figure 7) [3]. The second arrow along the BAT line shows the influence of the predicted growth in scrap ratio from 34 to 50 %. We notice that when these two actions come true in the next few decades, the specific emissions will come down below the level 1.2 t CO_2/t steel.

The third key factor focuses on the sources of CO_2 emissions. Direct emissions in iron and steel production come from fossil energy sources (coal, oil, natural gas) and their derivatives (coke, coke oven gas, off-gas from BF, BOF, EAF, etc.). Decrease of emissions by energy saving actions was already discussed. Further possibility is to transfer from high-carbon fuels, coal/coke to medium/low-C fuels like natural gas. Injection of hydrogen rich LC fuels in blast furnaces is one possible way to reduce CO_2. A short survey of new technologies follows later. Transition from HC reductants and fuels to LC and renewable energy sources turn the BAT line downward anticlockwise.

Except for direct emissions, even indirect emissions should be considered. The most important is electricity, *the fourth key factor* in this examination. "Electrification" is a growing trend in all sectors of the society. As well known, electricity is not a "clean" emission-free commodity. Depending on the type of power station i.e. primary energy source, the specific CO_2 emissions can be over 1000 g CO_2/kWh in a coal power station whereas in a gas power station the corresponding figure is around 500 g CO_2/kWh. Concerning non-fossil technologies, solar, wind, nuclear and hydro power stations the emissions are from 50 to 20 g CO_2/kWh, respectively [18,19] as presented in Table 1 below. As stated, the role of electric energy in steel production is remarkably growing, and thus its specific CO_2 emissions will have a very significant role when calculating the total emissions from steel industry. The world average from overall electricity generation was 519 g CO_2/kWh in 2014 [17]. China is the biggest steel producer and used to have quite high emissions from coal power stations, but by technology modernization the figure has fallen down to 681 g CO_2/kWh in 2014 [17]. By adopting such technologies, which utilize non-fossil or renewable (RW) primary energy the emission coefficients become an order of magnitude lower and the BAT line comes downward, respectively.

Table 1. CO_2 emissions from electricity supplied by different commercial technologies. The values are mean life-time emissions and were collected from IPCC Technical Summary Report, 2014 [18].

Primary energy Fossil	Coal	Gas	Biomass cofiring	Biogas; corn and manure	Biomass dedicated	Coal + CCS®
g CO_2/kWh	820	490	745	300	230	120-220
Non-fossil/RW	Solar	Wave	Geothermal	Hydro	Nuclear	Wind
g CO_2/kWh	40-50	20-40	40-50	20-30	20	20

®Pre-commercial technology with CO_2 capture and storage.

The fifth key factor is allocated for innovative new technologies, which will facilitate in achieving the low emission target. There are several national or international research programs worldwide acting in this field. Naturally, they have connections to the other key factors too.

• ULCOS program (Ultra Low Carbon Dioxide Steelmaking) by a European consortium with several projects. Top Gas Recycling Blast Furnace (TGR-BF) can save coke and reduce CO_2 emissions by 50% when CCS is applied. Technologies for CO_2 capture and Storage (CCS) were developed initially for coal power stations to decrease emissions by removing CO_2 from off-gases and then by depositing it into geological formations [20]. It could suit for process

industries as well. Another project, HIsarna is a new smelting reduction technology with reduced CO_2 emissions by 20%, compared to average blast furnace and by 80% with CCS. ULCORED is a direct reduction process utilizing reducing gas produced from natural gas. Even iron production by electrolysis of iron ore is under investigation. Of these projects Top Gas Recycling and HIsarna have proceeded to scaling up stage at the moment. [21, 22, 23].

• COURSE50 project (CO_2 Ultimate Reduction in Steelmaking process by innovative technology for cool Earth 50) in Japan [24, 25, 26]. The goal is to establish technologies, which contribute to mitigation of approximately 30 % in CO_2 emissions at integrated steel plants by 2050. Two technologies are under the scope: 1) Intensified hydrogen reduction of iron ore using coke oven gas to restrain carbon input in blast furnaces, and 2) Sequestration of CO_2 in the BF gas through the chemical absorption method and physical adsorption method by the effective utilization of unused waste heat in the integrated steel plants.

• POSCO project in Korea is investigating adaptation of CCS to the FINEX smelting reduction process. Also CO_2 capture from a blast furnace is under development [27, 28].

• The American Iron and Steel Institute (AISI) and the US Department of Energy (DOE) are managing a CO_2 breakthrough program to develop a flash ironmaking process utilizing iron ore fines and low-carbon gas for reduction. The process could bypass ore agglomeration and coke making which belong to the traditional iron making. Removal of CO_2 from off-gas or primary reducing gas are options, which could decrease emissions to a low level [29, 30].

• Renewable energy is a topic of the day but not at all any new item. Until 18th century, iron was produced in charcoal blast furnaces or bloomeries. Then mineral coal and its derivative coke overtook charcoal´s position. There was a great necessity for this innovation namely wide-ranging deforestation on British Islands. Today we have a new necessity, to stop the global warming in which biomass has a possible lot in the total solution. However, it is unrealistic to load too big expectations on bio energy (charcoal, biogas) in metallurgy. The role will be additional. The topic has been actively investigated worldwide. In Brazil charcoal is used in ferroalloys industry and in pilot iron BFs. In Australia comprehensive studies have been done to evaluate biomass resources, production technologies for charcoal, bio-oil and biogas and their usage in iron and steel making [31, 32]. A life cycle assessment of charcoal substitution for coal/coke showed 25 % reduction in GWP (Global Warming Potential) compared to conventional integrated BF-BOF route [32]. Present experiences and extensive studies have shown that utilization of biomass in iron and steel making is technically possible. However, the costs are relatively high and wide-ranging applications wait for higher CO_2 emission allowance prices.

• China produces today roughly half of the world steel. Most plants are new, erected after the year 2000. A big problem is to fit the excessive capacity into the stagnated markets [33]. On the other hand serious environmental problems force to improve energy systems, coal power stations are modernized to eliminate particle emissions and to improve efficiency. Corresponding requirements are set to steel industry as well. Positive progresses have been attained e.g. in energy consumption on BF-BOF route. Ongoing and future actions aim at new types of fuel, energy conservation and use of waste heat from slag [33],

• Recently, it was released that in Nordic countries a consortium of three companies representing steel producers, mining and energy (SSAB, LKAB and Vattenfall) has launched a project to develop a CO_2 emission free iron production [34, 35]. The project was named HYBRIT

(Hydrogen Breakthrough Ironmaking Technology). Hydropower, wind energy and bio mass were mentioned as potential energy sources.

4. Concluding remarks

The present global target to stop the climate warming by cutting CO_2 emissions has set great challenges to all sectors of the society. Steel industry as an energy-intensive branch has been ahead of really demanding tasks to readjust to the future goals. Great progresses have occurred in cutting specific energy consumption per ton steel and specific CO_2 emissions, respectively. However, the rapid growth of production since the year 2000 has increased the total emission.

By 2050, the world steel production is forecast to grow by about 50 % to the level 2.5 billion tons/year. At the same time, the CO_2 emissions should decrease by 60 % to the level 1.25 billion tons CO_2/year in order to be consistent with the global emission targets. This means that specific emissions should fall from 1.8 t CO_2/t steel (the current world average) to the level 0.5 t CO_2/t steel,. The prime means to attain this target are the following.

The first task is to raise the energy efficiency of the all steel industry to the current BAT level, which means, in average, 15-20 decrease in specific energy consumption. In many countries and steel plants, the deviation is much wider and the problems and necessary improving operations are readily identifiable.

The foreseeable substantial increase of scrap availability is a central positive factor to reduce specific energy consumption and CO_2 emissions. According to scenario evaluations, the mean scrap ratio will increase from 34 to 50 % on the increasing steel production level. This will mean remarkable growth in electric steel making. Certain transfer from BF – BOF into EAF will happen at least in China.

Decarbonization of energy is a further great potential, which can be utilized in two ways in steel production. Firstly, a partial transition from high carbon fuels and reductants to medium and low carbon or even renewable energy sources in the reduction process and throughout the whole route is happening. Secondly, electrification is a growing trend in steelmaking. Hence, the breakthrough of low emission technologies in electricity generation means great reduction in indirect CO_2 emissions in steel making.

Finally, new innovative processes, which aim at low carbon footprint by combining aforementioned means and utilizing renewable energy sources, are under development and some of them will attain industrial stage in the next few decades and thus influence for the common goal.

References:

1) IEA, *Key world energy statistics. Energy and Climate Change*. https://www.iea.org/publications/freepublications/publication/KeyWorld2016.pdf

2) *CO2-Earth 2016*. In: https://www.co2.earth/daily-co2

3) *World Steel Association 2016*; http://www.worldsteel.org/statistics/ statistics-archive.html

4) M. Meinshausen, S. J. Smith, K. Calvin, J. S. Daniel, M. L. T. Kainuma, J-F. Lamarque,,K. Matsumoto, S. A. Montzka, S. C. B. Raper, K. Riahi, A. Thomson, G. J. M. Velders, D.P. P. van Vuuren. *The RCP greenhouse gas concentrations and their extensions from 1765 to 2300*. (2011) 109: 213. doi:10.1007/s10584-011-0156-z

5) *The global carbon budget 2012*. In: http://www.globalcarbonproject.org/carbonbudget/ archive/2012/CarbonBudget_2012.pdf pp. 41

6) *2015 United Nations Climate Change Conference* in: https://en.wikipedia.org/wiki/2015_ United_Nations_Climate_Change_Conference

7) L. Holappa, *Toward Low Carbon Metallurgy in Iron and Steel Making*. Proceedings of the Guthrie Honorary Symposium, June 6-9, 2011. Montreal, pp. 248-254.

8) L. Holappa, *Toward Sustainability in Ferroalloys and Steel Production*. Fray International Symposium on Metals and Materials Processing in a Clean Environment; Cancun Mexico, Nov 27-Dec 1, 2011. Volume 5: Environmental, Health, Policy, Legal, Management and Social Issues. pp. 203-220

9) L. Holappa, *Energy efficiency and sustainability in steel production*. Proceedings of TMS Symposium on Applications of Process Engineering Principles in Materials Processing, Energy and Environmental Technologies. S. Wang, M. L. Free, S. Alam, M. Zhang, P. R. Taylor (Editors). An EPD Symposium in Honor of Professor Ramana G. Reddy. San Diego. February 26 –March 2, 2017. 401-410

10) IEA/OECD 2009. *Energy Technology Transitions for Industry, Strategies for the Next Industrial Revolution;* in: http:// www.oecd-ilibrary.org/energy/energy-technology-transitions-for-industry_9789264068612-en

11) World Steel Association. *Steel´s Contribution to a Low Carbon Future and Climate Resilient Societies* In: https://www.worldsteel.org/en/dam/jcr:66fed386-fd0b-485e-aa23-b8a5e7533435/Position_paper_climate_2017.pdf

12) BIR Bureau of International Recycling. *World Steel Recycling in Figures 2011 - 2015*. In: http://www.indicaa.com/site/uploads/pdf/WRF_BIR.PDF. 12

13) J. Morfeldt, W. Nijs, S. Silveira. *The impact of climate targets on future steel production - an analysis based on a global energy system model.* Journal of Cleaner Production 103 (2015) 469-482

14) R. Haslehner, B. Stelter, N. Osio; *Steel as a Model for a Sustainable Metal Industry in 2050.* October 07, 2015. Categories: Industrial Products & Processes, Sustainability. In: https://www.bcgperspectives.com/content/articles/metals-mining-sustainability-steel-as-model-for-sustainable-metal-industry-2050/

15) World Economic Forum; *Mining & Metals in a Sustainable World 2050*. In: http:// bwww3.weforum.org/docs/WEF_MM_Sustainable_World_2050_report_2015.pdf

16) E. Worrell, L. Price, M. Neelis, C. Galitsky, N. Zhou, (2008) *World best practice energy intensity values for selected industrial sectors*. Ernest Orlando Lawrence Berkeley National Laboratory, LBNL-62806 REV. 2.pp. 51

17) IEA, *CO_2 emissions from fuel combustions – Highlights.* In: https://www.iea.org/publications/freepublications/publication/CO2EmissionsfromFuelCombustion_Highlights_2016.pdf

18) T. Bruckner et al (19), 2014: Energy Systems. In: *Climate Change 2014: Mitigation of Climate Change. Contribution of Working Group III to the Fifth Assessment Report of the Intergovernmental Panel on Climate Change* [Edenhofer et al (15) (eds.)]. Cambridge University Press, Cambridge, United Kingdom and New York, NY, USA.

19) O. Edenhofer et al (62), 2014: Technical Summary. In: *Climate Change 2014: Mitigation of Climate Change. Contribution of Working Group III to the Fifth Assessment Report of the Intergovernmental Panel on Climate Change.* [O. Edenhofer et al (15) (eds.)]. Cambridge University Press, Cambridge, United Kingdom and New York, NY, USA.

20) Global CCS Institute, *The global status of CCS* 2016, Summary report. In: http://hub.globalccsinstitute.com/sites/default/files/publications/201158/global-status-ccs-2016-summary-report.pdf

21) J-P. Birat, *Steel and CO_2 – the ULCOS Program, CCS and Mineral Carbonation using Steelmaking Slag.* In: http://www.ulcos.org/en/docs/Ref01__Birat_slag_finaal.pdf

22) Y. Yang, K. Raipala, L. Holappa, Ironmaking: in S. Seetharaman, (Ed.), *Treatise on Process Metallurgy*, Vol.3: Industrial Processes, Part 1 Ferrous Process Metallurgy; L. Holappa, (Ed.), 2-88.

23) M. Abdul Quader, A. Shamsuddin, S.Z Dawal, Y. Nukman. *Present needs, recent progress and future trends of energy-efficient Ultra-Low Carbon Dioxide (CO2) Steelmaking* (ULCOS) program. Renewable and Sustainable Energy Reviews 55 (2016) 537–549

24) S. Tonomura, N. Kikuchi, N. Ishiwata, S. Tomisaki, Y. Tomita. *Concept and Current State of CO_2 Ultimate Reduction in the Steelmaking Process* (COURSE50) Aimed at Sustainability in the Japanese Steel Industry. J. Sustain. Metall. (2016) 2:191–199

25) K. Nishioka, Y. Ujisawa, S. Tonomura, N. Ishiwata, P. Sikstrom. *Sustainable Aspects of CO_2 Ultimate Reduction in the Steelmaking Process* (COURSE50 Project), Part 1: Hydrogen Reduction in the Blast Furnace. J. Sustain. Metall. (2016) 2:200–208

26) M. Onoda, Y. Matsuzaki, F.A. Chowdhury, H. Yamada, K. Goto, S. Tonomura. *Sustainable Aspects of Ultimate Reduction of CO_2 in the Steelmaking Process* (COURSE50 Project), Part 2: CO_2 Capture. J. Sustain. Metall. (2016) 2:209–215

27) POSCO; Carbon Report 2011, *Toward a Sustainable Society* In: https://www.iea.org/ media/ weowebsite/ ebc/POSCOCarbonReport2011.pdf ; pp .53

28) World Steel Association. *Taking carbon capture and storage a step further* In: https:// www.worldsteel.org/media-centre/Steel-news/Taking-carbon-capture-and-storage-a-step-further-.html

29) The American Iron and Steel Institute. *Technology Roadmap Research Program for the Steel Industry*. Final Report 31 Dec. 2010. In: https://www.steel.org/~/media/Files/AISI/ Making%20Steel/TechReportResearchProgramFINAL.pdf ; pp .36

30) H.Y. Sohn, Y.Mohassab. *Development of a Novel Flash Ironmaking Technology with Greatly Reduced Energy Consumption and CO_2 Emissions*. J. Sustain. Metall. (2016) 2:216–227

31) T. Norgate, N. Haque, M. Somerville, S. Jahanshahi. *Biomass as a Source of Renewable Carbon for Iron and Steelmaking.* ISIJ International, Vol. 52 (2012), No. 8, pp. 1472–1481

32) S. Jahanshahi, J. G. Mathieson, M. A. Somerville, N. Haque, T. E. Norgate, A. Deev, Y. Pan, D. Xie, P. Ridgeway, P. Zulli. *Development of Low-Emission Integrated Steelmaking Process.* J. Sustain. Metall. (2015) 1:94–114

33) J. Zhang, Z. Liu, K. Li, G. Wang, K. Jiao, T. Yang; *Current Status and Prospects of Chinese Steel Industry.* Scanmet V Conference. 12-15 June 2016, Luleå, Sweden. pp 15.

34) SSAB, LKAB, Vattenfall; *CO_2-emission free ironmaking.* Press conference. April 4, 2016 In: http://materialsbusinesscenter.se/wp-content/uploads/2016/09/160404-SSAB-CO2-emission-free-ironmaking-Short-version.pdf pp.17

35) M. Brolin, J. Fahnestock, J. Rootzén; *Industry´s electrification and role in the future electricity systems.* A strategic Innovation Agenda. 2017. In: ttps://www.diva-portal.org/smash/get/diva2:1073841/FULLTEXT01.pdf pp.74

Behavior of Spitting and Dust Generation in Converter

Yu Miyamoto[*1], Takashi Tsushima[*2], Yoji Takubo[*3], Takamitsu Nakasuga[*1], Sei Kimura[*1]
and Koichiro Semura[*1]

1:R&D Laboratory, Iron & Steel Business, KOBE STEEL, LTD.

2: Refining & Solidification Research Section, Materials Research Laboratory, KOBE STEEL, LTD.

3: Fluid & Thermal Engineering Research Section, Mechanical Engineering Research Laboratory, Technical Development Group, KOBE STEEL, LTD.

Keywords: BOF steelmaking, spitting, dust, nozzle, expansion, incurvation, axial velocity

Abstract : Some experiments were conducted with the aim of decreasing spitting and dust generation during blowing. The jet velocity can be decreased in the same flow rate with use of the nozzle which makes the jet flow over-expansion. It was confirmed that the breadth of jet flow is decided independently of the nozzle shape. The jet flow discharged from the nozzle was incurved. The behavior of the jet flow can be largely described by CFD analysis. It is recognized that spitting and dust generation decrease with a decrease in the axial top-blown jet velocity in 0.5 ton converter experiment.

1. Introduction

We have taken an approach to increase the production capacity of a converter and decrease steel loss during blowing. As a way of increasing production capacity, we investigated reducing the converter's cycle time by increasing oxygen flow rate during blowing. One problem is that when oxygen flow rate is increased, the dispersal of molten iron and slag, which is called spitting, increases. If spitting is allowed to continue, it leads to a reduction in crude steel production capacity due to the increase in time it takes to remove scull at the oxygen lance or refractory inside the furnace. Droplets generated by spitting and dust during blowing is responsible for a decrease in tapping yield.

Top-blow oxygen is typically supplied by a Laval nozzle[1]. It is important to understand the behavior of the top-blow oxygen jet blown from the Laval nozzle to resolve the problems mentioned above. The inherent features of a jet may include expansion and incurvation. To achieve soft blowing at the same flow rate, it is necessary to consider these phenomena. Computational Fluid Dynamics (CFD) analysis is applied for a variety of simulations. There are a lot of models, so calculation results can be different depending on selected turbulence model even though they are under the same conditions. In this study, the behavior of the jet flow discharged from Laval nozzle was investigated by comparison between experimental result and CDF analysis. An experiment to identify the cause of spitting and dust generation in 0.5 ton converter was carried out.

2. Analysis of jet flow

2-1. Experiment and analysis method

When the nozzle outlet pressure is equal to atmospheric pressure, the nozzle inlet pressure(P) is called the optimum pressure. The optimum pressure(P_{op}) is determined by the throat diameter and the outlet diameter. The expansion of jet flow is determined based on the state of the nozzle inlet pressure as follows.

$$P = P_{op} : \text{correct expansion}, \quad P < P_{op} : \text{over-expansion}, \quad P > P_{op} : \text{under-expansion}$$

Bidirectional jet velocity discharged from mono-hole nozzle was measured using the Laser

Doppler Velocimetry (LDV) system to investigate the behavior of jet flow at each expansion state. Velocity was also measured by pitot tube in some experiments. Figure 1 and Figure 2 show the experimental equipment. The incurvation of jet flow was measured using a multi-hole nozzle and compared with the results from the CFD analysis. Commercially available code ANSYS FLUENT 14.5 was used for the CDF analysis. The k-ε Realizable model and the k-ε model modified by Alam et al.[2] were used as a turbulence model which predicts attenuation and breadth.
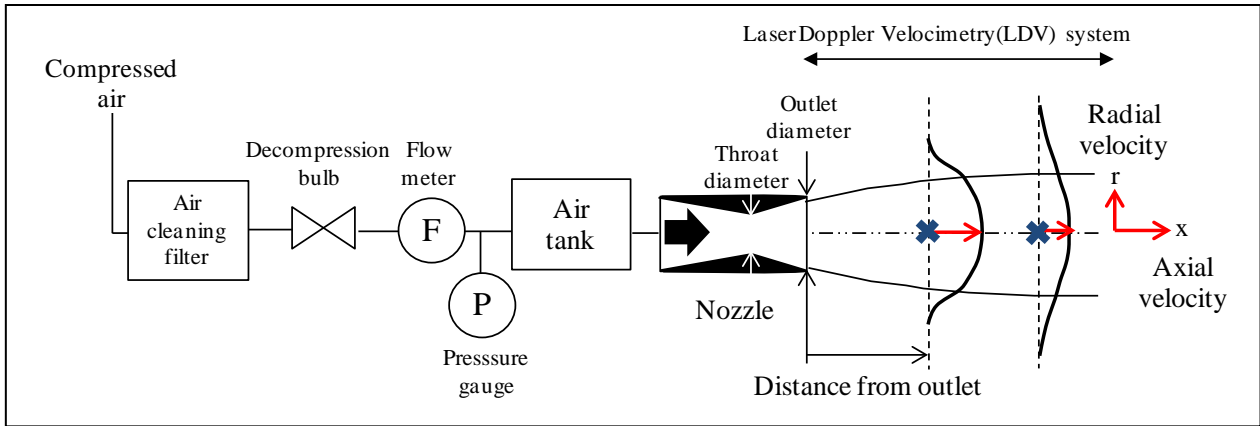
Figure 1 Schematic view of the equipment for the measurement of jet flow
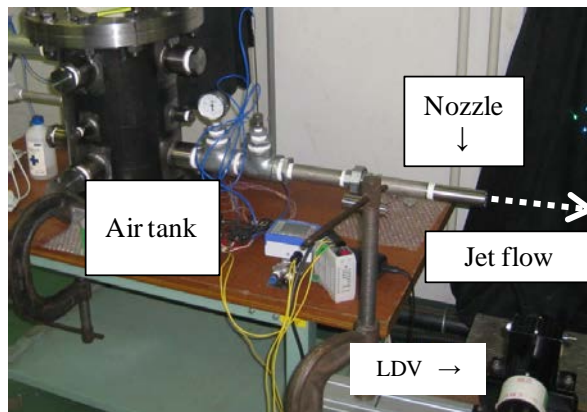
Figure 2 Picture of the equipment

2-2. Results and discussion

2-2-1. Behavior of jet expansion

Table 1 shows the shapes of nozzles used in the experiment. Figure 3 shows the plots of velocity using Pitot tube and LDV. The x-axis shows the axial distance from the nozzle tip (x), and the y-axis represents axial velocity (u). There was no difference between the Pitot tube and LDV. For this reason, only LDV was used in subsequent experiments. A fixed velocity region called the jet core exists in the jet flow discharged from the nozzle. Jet core length is expressed in equations (1) and (2) by Naito et al.[3].

$$M = H_c/x \qquad\qquad (1)$$

$$H_{cp} = M_{op} \times \left(5.88 + 1.54 \times M_{op}^2\right) \times d_t \qquad (2)$$

M : Much number [-], H_c : jet core length [mm]

H_{cp} : Jet core length in a state of correct expansion [mm]

x : Distance from nozzle outlet [mm]

M_{op} : Mach number at discharging from the nozzle in a state of correct expansion [-]

d_t : Nozzle throat diameter [mm]

Figure 4 shows the relationship between P/P_{op} and H_c/H_{cp} obtained from this study. This figure shows that H_c/H_{cp} increases monotonically with an increase in P/P_{op}. It was found that the axial velocity can be decreased by using over–expansion nozzle, which means making the outlet diameter much larger than the throat diameter.

Table 1 Shapes of mono-hole nozzle

Nozzle	Throat diameter d_t [mm]	Outlet diameter d_e [mm]	Number of holes [−]	Optimum pressure P_{op} [MPaG]
1	2.30	2.78	1	0.50
2	2.30	2.52	1	0.29
3	2.30	3.10	1	0.81
4	2.30	2.40	1	0.20
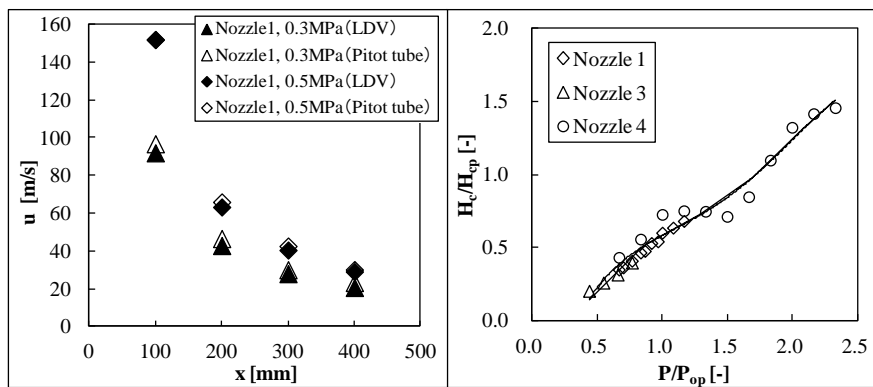
Figure 3 Relation between x and u   Figure 4 Relation between P/P_{op} and H_c/H_{cp}

Figure 5 shows the relationship between the radial distance from the center of jet flow (r) and the radial velocity (u_r). This represents the breadth of jet flow. Figure 6 shows the relationship between the proportion of r to x and the proportion of u_r to the central jet velocity (u_m). It was confirmed that the breadth of jet flow is determined independently of the nozzle shape.
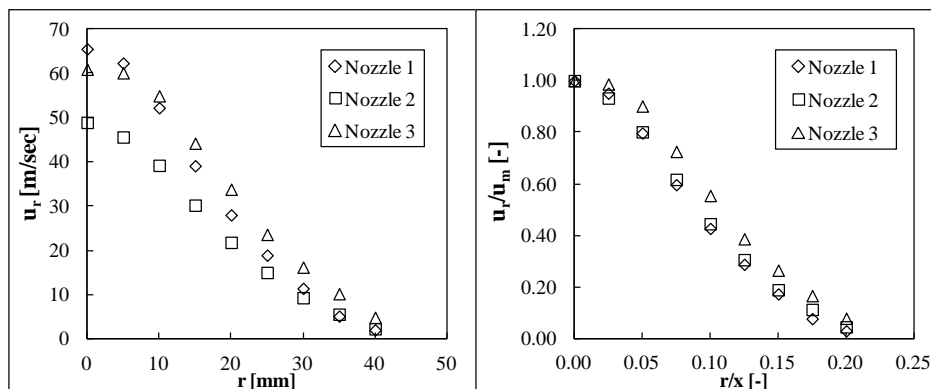
Figure 5 Relation between r and u_r Figure 6 Relation between r/x and u_r/u_m

2-2. Incurvation of the jet flow

Table 2 shows the shapes of nozzles used in the experiment. Nozzle 5 is the basic shape. Nozzle 6,

7, 8 were selected for comparison of the difference in outlet diameter inclined angle and number of holes. The deviation from the center line at the distance from the nozzle center was measured as shown in Figure 7. Figure 8 shows an example of the results. The x-axis is l/d_e, the y-axis is D/d_e. Figure 9 shows the comparison between measured value and the CFD simulation. It was confirmed that the jet flow incurves. In this experimental condition, the results can be described with the k-ε Realizable model. It was found that the CFD analysis can simulate the behavior of the jet flow, so the experimental condition in the 0.5 ton converter as described below was set up based on these results.

Table 2 Shapes of multi-hole nozzle

Nozzle	Throat diameter d_t [mm]	Outlet diameter d_e [mm]	Number of holes [-]	Inclined angle θ [deg]	Optimum pressure P_{op} [MPaG]	P/P_{op} [-]
5	2.30	2.52	2	15	0.29	
6	2.10	2.30	2	15	0.29	0.7～1.3
7	2.30	2.52	2	13	0.29	
8	1.63	1.78	4	15	0.29	
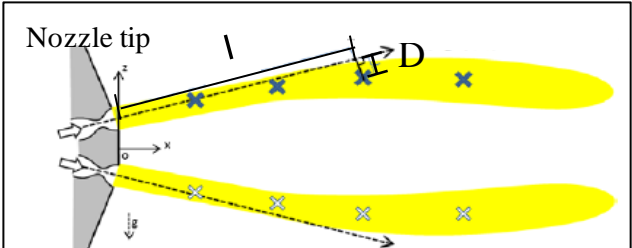
Figure 7 Schematic view of the measurement for the incurvation
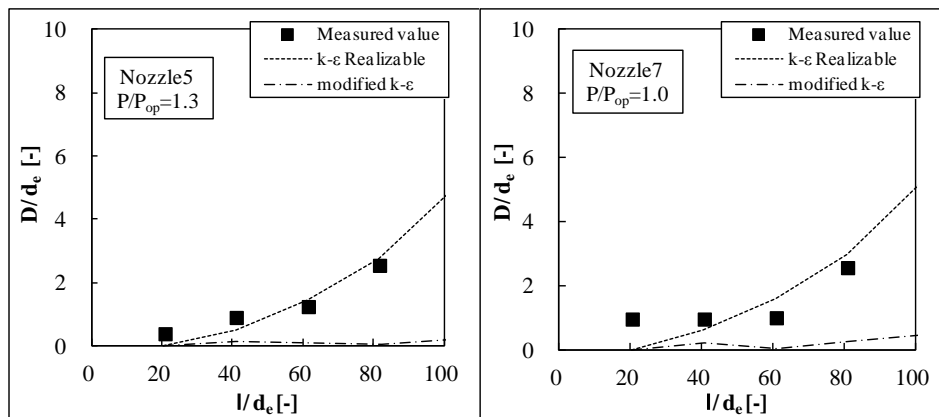
Figure 8 Examples of relation between l/d_e and D/d_e
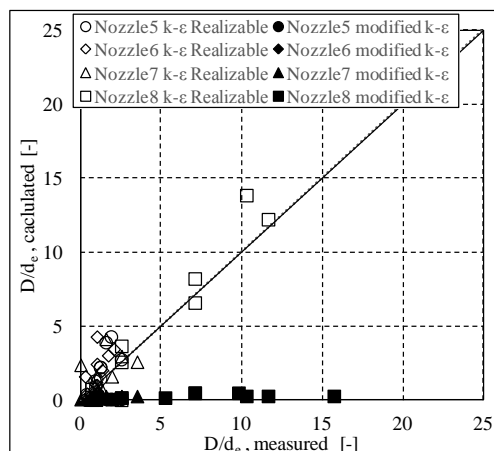
Figure 9 Comparison of measured D/d_e and calculated D/d_e

3. Blowing experiment in 0.5 ton converter

3-1. Selection of nozzle

It has been reported that the dispersal of molten iron and slag is correlated to the velocity of oxygen fluid[4]. There has been considerable research on spitting and dust generation and the site of CO gas occurrence associated with the decarburization reaction[5]. It is thought the dispersal of molten iron and slag is correlated with the oxygen feed rate and the area of fire point of oxygen fluid on the hot metal surface. We investigated the effect of axial velocity and fire point area on spitting and dust generation. To measure the impact of the velocity and the fire point area independently, two nozzles were selected as shown in Table 3. Figure 10 shows the relationship between the lance height and the jet velocity. Figure 11 shows the relationship between the lance height and the fire point area. These are calculated based on the results obtained from section 2. The fire point area was defined as the region where velocity is greater than 10 meter per second on the surface. Blowing experiment was carried out by using these nozzles.

Table 3 Shapes of nozzle

	Number of holes [-]	Inclined angle [deg.]	Throat diameter [mm]	Outlet diameter [mm]
A	6	15	2.5	3.4
B	5	13	3.5	5.3
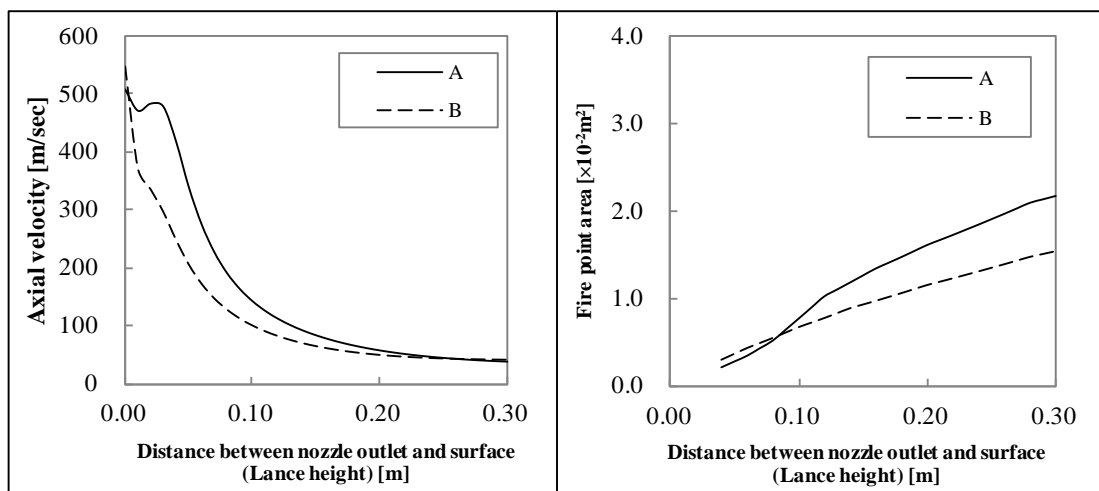
Figure 10 Relation between lance height and axial velocity

Figure 11 Relation between lance height and fire point area

3-2. Experimental method

Figure 12 shows a schematic diagram of the 0.5 ton converter. A blowing experiment was carried out by using two nozzles as above. Table 4 shows the experimental conditions. 500 kilograms of pig iron was dissolved in a high-frequency furnace and loaded into the 0.5 ton converter. Dephosphorized and desulfurized cold pig iron was used as raw material. The temperature of the metal and slag was measured before blowing, during blowing and after turndown using a sub lance. Argon gas was used as the bottom blowing gas. After every experiment, coarse droplets were collected from the gas cooler and fine droplets were collected from the bug filter. The collected droplets were evaluated in terms of the amount of spitting and dust.

Hirai et al.[6] calculated bubble burst ratio and fume ratio using equations (3), (4) and (5) derived from molybdenum or platinum concentration in droplets. Ferro molybdenum was added to the hot

metal as a tracer to calculate these ratios. The bubble burst ratio and fume ratio were calculated from the concentration of molybdenum in the collected droplets.

$$R_f \times (Mo/Fe)_f + R_b \times (Mo/Fe)_b = (Mo/Fe)_D \qquad (3)$$

$$R_f + R_b = 1 \qquad (4)$$

$$(Mo/Fe)_b \approx (Mo/Fe)_m \qquad (5)$$

R_f : Fume ratio in droplet, R_b : Bubble burst ratio in droplet

$(Mo/Fe)_f$, $(Mo/Fe)_b$, $(Mo/Fe)_D$, $(Mo/Fe)_m$: Proportion of Mo concentration to Fe concentration

subscript f : Fume, b : Bubble burst, D : Droplets, m : molten steel

where $(Mo/Fe)_f \approx 0$

Capacity	0.5ton
Blowing type	Oxygen top blowing and inert gas bottom blowing
Shell volume	$0.9 m^3$
After lining	$0.4 m^3$
Top blowing capacity	$\sim 4.0 Nm^3/min/ton$
Bottom blowing — Kinds of gas	N_2, Ar
Bottom blowing — Control range	$\sim 0.16 Nm^3/min/ton$
Bottom blowing — Number of tuyeres	4
Bottom blowing — Tuyere type	Single tube
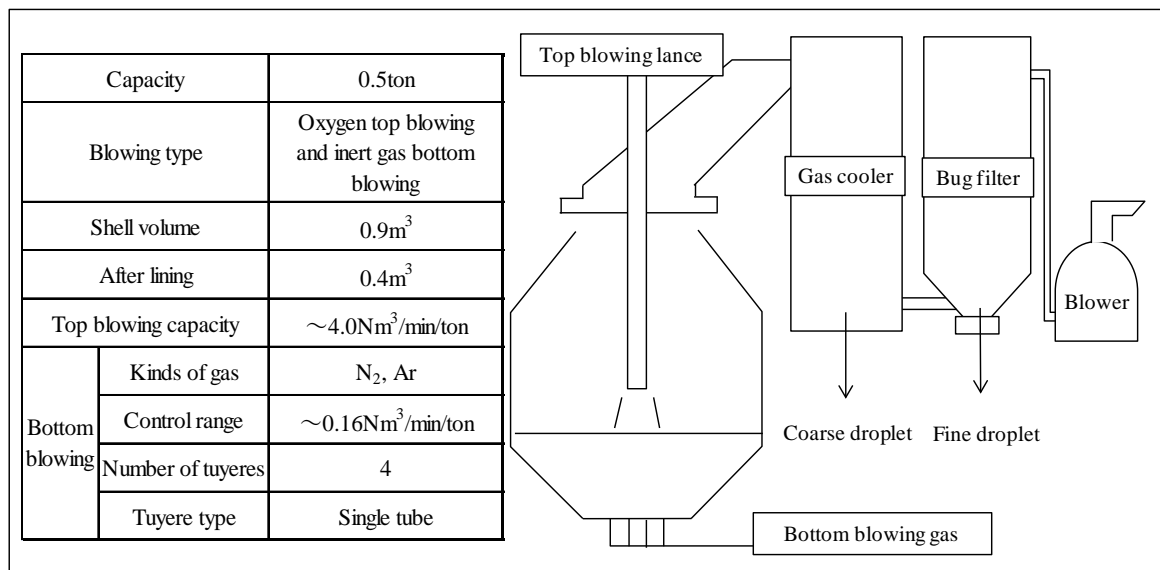
Figure 12 Specifications and schematic view of 0.5 ton converter.

Table 4 Experimental conditions

No.	Nozzle	Axial velocity [m/sec]	Fire point area [m²]	Top blowing gas flow rate [Nm³/min/ton]	Bottom blowing gas flow rate [Nm³/min/t]	Burnt lime [kg/ton]	Light-burnt dolomite [kg/ton]	Ferro molybdenum [kg/ton]
1	A	100	1.1×10^{-2}					1.6
2	A	80	1.1×10^{-2}					0
3	A	50	1.7×10^{-2}	4.0	0.08	16.0	8.0	1.6
4	B	100	0.7×10^{-2}					0
5	B	50	1.1×10^{-2}					1.6

3-3. Results and discussion

Table 5 shows the experimental results. It was confirmed that carbon concentration at turndown has decreased to the low-carbon region in each experiment. Figure 13 shows the grain size distribution of collected droplets. Figure 14 and Figure 15 show the relationship between axial

velocity and the amount of droplets. The amount of coarse droplets was independent of the axial velocity and the fire point area. It remained constant. The amount of fine droplets increased with the axial velocity. The amount of fine droplets increased as the fire point area decreased, in case of the same jet velocity. It was confirmed that droplets were inhibited by gently running a jet of oxygen onto the surface. At the same flow rate, decreasing the axial velocity or increasing the fire point area is effective to decrease droplet generation. If we apply this provision, it can be thought the modification of lance height. But it is difficult to change the fire point area significantly in real operation. On the basis of these results, we have taken the approach of decreasing droplet generation during blowing by examining the optimum nozzle shapes which can decrease the axial velocity under our operating conditions.

Table 5 Experimental results

No.	Axial velocity [m/sec]	Fire point area [m^2]	Coarse droplet [kg/ton]	Fine droplet [kg/ton]	Bubble burst ratio -	Fume ratio -
1	100	1.1×10^{-2}	0.4	10.7	0.39	0.61
2	80	1.1×10^{-2}	0.4	8.2	-	-
3	50	1.7×10^{-2}	0.6	3.0	0.31	0.69
4	100	0.7×10^{-2}	0.8	16.5	-	-
5	50	1.1×10^{-2}	0.6	7.5	0.30	0.70
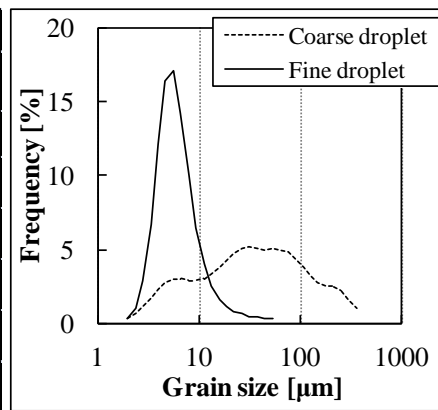
Figure 13 Droplet grain size dispersion
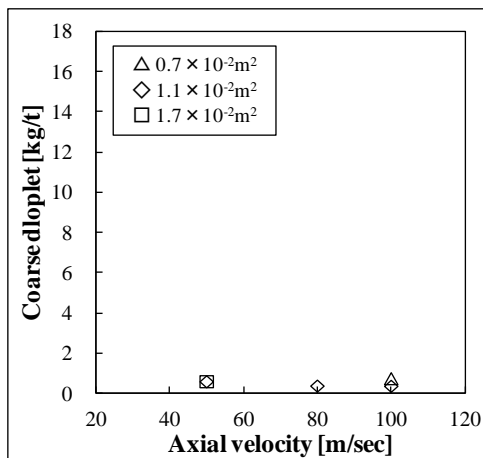
Figure 14 Relation between the axial

velocity and coarse droplet
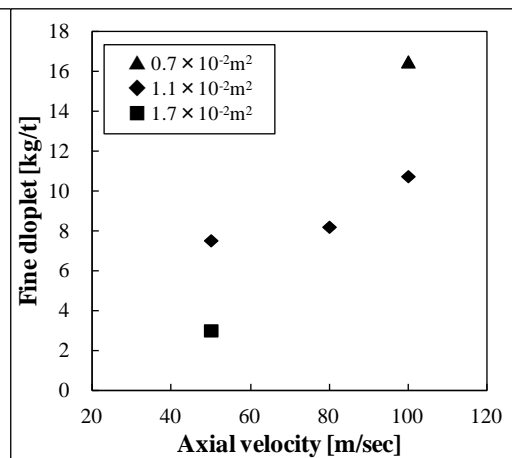
Figure 15 Relation between the axial

velocity and fine droplet

Figure 16 shows the bubble burst ratio and fume ratio calculated from equations (3), (4) and (5). The bubble burst ratio went up at high axial velocity. The change in fire point area had little or no effect on the ratio. It is also clear that bubble-burst-induced droplets increased with an increase in the axial velocity which promotes physical dispersion from increasing kinetic momentum on the surface. Neither bubble burst nor fume was the dominant factor for dust generation.
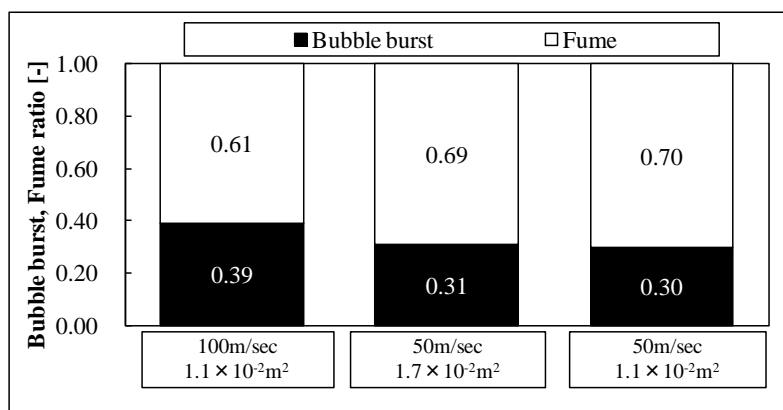
Figure 16 Comparison of bubble burst and fume ratio in droplets

In the present equipment configuration, droplet generation is measured only at one heat. We have a plan to enable the existing dust collector to measure the temporal change of dust generation during an experiment.

4. Conclusions

The behavior of top-blown jet flow was observed. The jet velocity can be decreased at the same flow rate as that of the nozzle which causes jet flow over-expansion.

The behavior of the jet flow can largely be described by CFD analysis by selection of appropriate turbulence model.

It was confirmed that decreasing the axial velocity is effective in reducing the amount of droplets at the same flow rate.

References:

1) Segawa, *Tetsu Yakin Han-nou Kougaku*, – Tokyo, 1977(Revised edition), 96.

2) Alam et al., The Minerals, Metals & Materials Society and ASM International 2010, *Computational Fluid Dynamics Simulation of Supersonic Oxygen Jet Behavior at Steelmaking Temperature*, Volume 41B(2010), 636-645.

3) Naito et al, Nippon Steel Technical Report, *Behavior of Jet from Top-Lance in BOF,* No.394(2012), 33-41.

4) Tanaka et al., Testu-to-Hagane, *Interaction between Gas and Liquid Caused by Jet Streams Blown to a Liquid Surface*, Volume 74(1988), No.8 1593-1600.

5) e.g., Ishikawa et al., Testu-to-Hagane, *Effect of bubble bursting on the decarburization of Fe-C melt : Study on fume formation in oxygen steelmaking III*, Volume 71(1985), S1043.

6) Hirai et al., Testu-to-Hagane, *The Mechanism of Dust Generation in Converter*, Volume 74(1988), No.10 1954-1961.

Investigating the Use of Biomass and Oxygen in Electric Steelmaking by Simulations Based on a Dynamic Process Model

Thomas Meier, Thomas Echterhof, Herbert Pfeifer
Department of Industrial Furnaces and Heat Engineering, RWTH Aachen University

Abstract:

The optimization of the electric arc furnace (EAF) is driven by increasing demands on sustainability and efficiency of the melting process. Therefore, alternative input materials as well as comprehensive process monitoring and control are aiming to minimize the ecological footprint of the electric steelmaking. Here, dynamic process models and simulations are able to contribute to those objectives through on- and offline application for investigations on alternative operation strategies.

Within this paper, a comprehensive dynamic process simulation model of the EAF is further developed to analyse industrial long-term trials with palm kernel shells (PKS) and to investigate different control strategies for modified oxygen usage in the EAF. The PKS were used as a substitute for fossil coal to reduce the carbon footprint of the steel production in EAFs and showed no negative impact during the tests. To simulate the different carbon carrier, the process model considers different coal compositions for charged and lanced carbon, which can be defined prior to the simulation via parameters. The results of the trials in industrial scale in comparison to the simulation results are used to prove the models parametrization and its capability of extrapolation for different input materials and control strategies. Those are afterwards applied to research varied modes of operation for an alternative oxygen input with adapted O_2-purities according to the production methods cryogenic, pressure swing adsorption (PSA) and membrane technology. The results from this application example are analysable in terms of productivity, tap-to-tap times, energy input and profit. In the future, the process model will be applicable for on- and offline utilization such as control and operation optimization and analysis of alternative input materials and EAF designs.

1. Introduction

In recent years, the optimization of the melting process is increasingly based on the use of computers and specialized software. Therefore, the evaluation of process data through algorithms and the application of dynamic process models are getting more and more into focus. The later are able to contribute to a more detailed understanding of energy and mass transfer in the EAF and thus to improved operation with better energy and resource efficiency. Especially the continuous increase in computational capacity during the last decades led to high complexity simulation models with enhanced calculation of thermochemistry, scrap melting, slag, radiation and other phenomena.[1-7]

The application of process simulations in the field of offline investigations of different modes of operation requires a comprehensive process model with a wide range of extrapolation capability. Here, deterministic models that are based on fundamental physical and mathematical equations are advantageous over statistical models.[8] For this reason, the re-

implemented and further developed dynamic EAF process model from Logar et al.[9, 10] is enhanced and applied for this study.

The following paper describes the consideration of alternative input materials and alternative modes of operation by self-controlled simulations in a dynamic process model of an EAF. Several results from trials and simulations for the usage of PKS are compared to results for conventional anthracite usage in an industrial EAF to prove the models extrapolation capability. After that, the model is used to study and assess different modes of operation in case of alternative oxygen usage in the EAF. The model enhancements and the simulations are performed in MATLAB 2016a.

Characterized as CO_2 neutral, PKS have proven their potential to substitute fossil carbon usage in the EAF by lab scale and industrial scale trial campaigns. According to the productivity and the energy consumption, no negative influence was observed. However, in case of the off-gas data, a different reaction behaviour was noticeable.[11, 12] The higher volatile matter (VM) of the PKS leads to increased CO contents in the off-gas during the early stage of the melting process.[13] Consequently, the mode of operation can be adapted to improve the CO post-combustion for an accelerated scrap melting.

One of the most important factors for optimized CO post-combustion is the injection of oxygen into the EAF via burners and injectors. In addition, oxygen is also important for an efficient conversion of chemical energy inside the EAF and the foamy slag practice. Different input strategies with adapted mass flows, modified injection times or the change of the oxygen purity in the input streams due to a different oxygen production are influencing the melting process significantly.

The applied process model is parameterized according to the usage of fossil coal in form of anthracite and delivers sufficient results as shown in former publications.[14, 15] In the first step, different types of coals are implemented to consider their composition specialties. After that, the data from the industrial trial campaigns for PKS are used to prove the models capability to provide accurate data in case of extrapolation. Hereafter, the EAF model is equipped with the possibility to change operation parameters for mass flows and power of the operation pattern and their periods of injection. As a first case of application, the change of operation parameters is analysed in combination with different oxygen usage. According to the three oxygen production processes, the purity of the oxygen in the input streams is changed from 99 % for cryogenic to 95 % for PSA and 40 % for the membrane technology. The results for the different oxygen injection and the changed operation pattern are evaluated in terms of productivity, profit and costs.

2. Process model description

The EAF process simulation model described within this paper is based on fundamental physical and thermodynamic equations. It was developed by Logar, Dovžan and Škrjanc on a holistic approach through consideration of main thermal, chemical and mass transfer phenomena in the EAF.[9, 10] This includes chemical reactions, melting rates, energy distribution and heat transfer through conduction, convection and radiation, which are implemented via first order ordinary differential equations (ODE). All these processes are integrated in a modular structure with sub-modules and interactions as shown in **Figure 1**.

Within the data module, basic information about the EAF, the input masses and the operation pattern is stored and transferred to the simulation. During the simulation, the operation pattern is evaluated and the input masses and powers transferred to the thermal, mass and energy calculation module to calculate heat and mass transfers. In parallel, the melting geometry is calculated according to the remaining mass of scrap inside the EAF. This

influences the energy distribution due to view factor and radiation calculation. The chemical reaction module is finally relevant for chemical energy conversion and mass transfers between different zones. Each of those zones or phases are defined for simplification with an assumed homogeneous temperature and homogeneous physical properties. The nine zones are shown in **Figure 2**. Logar et al. tested and validated the model with operational data and measurement from an industrial scale EAF.[9, 10]
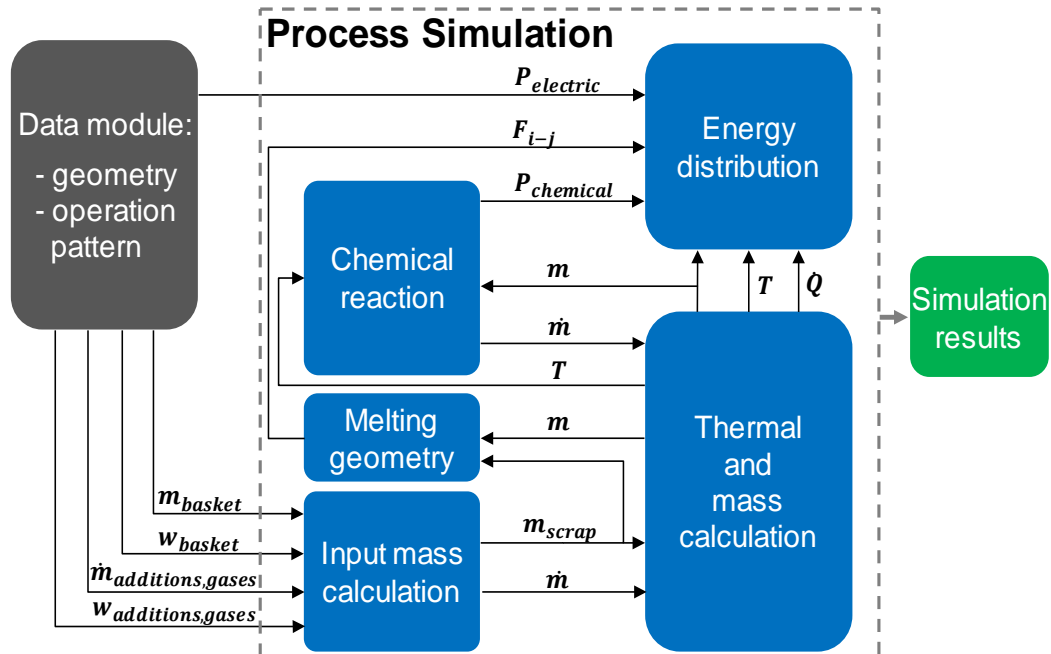
Figure 1. Overview about the EAF process model structure with sub-modules and interactions.
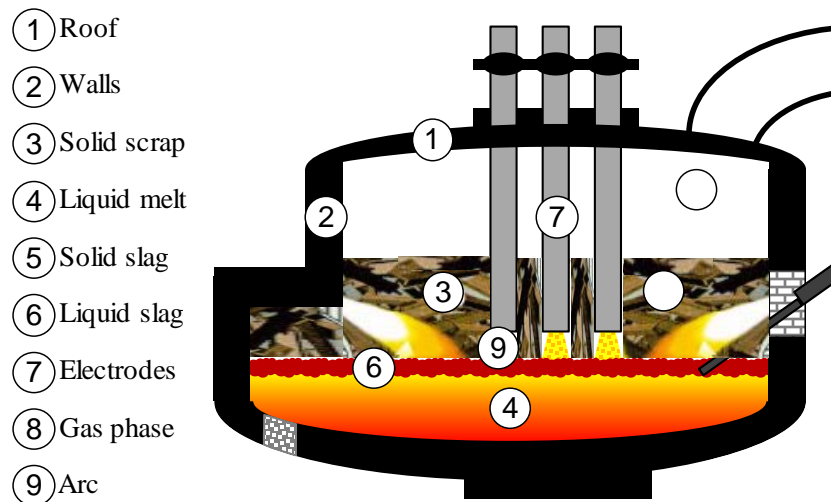
Figure 2. The homogeneous phases and zones of the EAF model.

To ensure best performance in case of accuracy and speed, the model was re-implemented at the Department of Industrial Furnaces to use the MATLAB internal numerical solver for ODEs and the opportunity, to perform simulations in parallel computing.[16] In addition, the model was further enhanced with a detailed gas phase simulation. Compared to Logar, the components H_2, H_2O and CH_4 were included in the gas phase modelling. Hence, additional reaction mechanisms like equilibrium reactions of Boudouard and water gas shift reaction are considered besides post combustion. The development of the gas-phase was validated with data from an industrial scale EAF.[15]

The improvement of the usability is achieved through a graphical user interface (GUI). This allows non-programmers an easy operability of the simulation model, either to recalculate already performed heats for further investigation or to carry out studies on the mode of operation. The GUI is given in **Figure 3**.
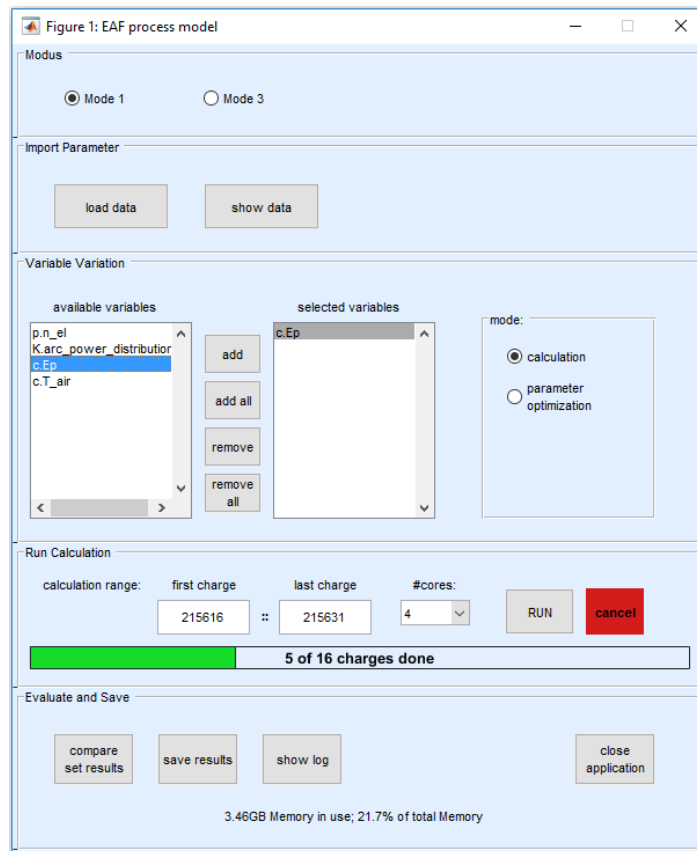
Figure 3. Graphical user interface of the process simulation model

3. Modelling of PKS usage and self-controlled simulations

3.1 Modelling different carbon carriers

The usage of different types of coal in the model as charge coal and injection coal is enabled through specification of three different coal compositions. One coal type for injection coal and two different types for charge coal, so that also coal mixtures are possible for charge coal. For the composition, the mass fractions of C, H_2, N_2, H_2O, O_2 and ash have to be defined. For the anthracite and PKS investigations, the compositions are given in **Table 1**. The model divides the coals into total carbon (C), gaseous components plus water and ash. The mass of ash is neglected in the simulation as it is small compared to the total mass of slag inside the EAF.

For the injection coal, the mass flow into the furnace is directly separated according to the three masses and added to the corresponding differential variables of the model. In detail, the mass flow of C is transferred to the mass of C present in the furnace while the mass flow of the gaseous components O_2, H_2, N_2 und H_2O, which are part of the injected coal, are transferred to the gas phase.

Table 1. Composition of anthracite, PKS and injection coal in mass-% (an)

	C_{total} [%]	C_{fix} [%]	VM [%]	N_2 [%]	H_2 [%]	O_2 [%]	H_2O [%]	Ash [%]	Lower heating value [MJ kg^{-1}]
Anthracite	81	80	9	5	3	0	6	5	33.5
PKS	53	25	64	1	6	29	8	3	19.5
Lance coal	93	83	11	0	1	0	2	4	31.8

For the charge coal, the total mass of coal is divided into the total mass of C, including the amount of C from volatile matters, the mass of ash and the remaining mass, consisting of N_2, H_2, O_2 and H_2O. Again, the mass of ash is neglected while the other two masses are separated into two different differential variables: the mass of pure C (m_{coal_C}) and the mass of gaseous components (m_{coal_vol}) according to **Equation (1)** and **(2)**. Due to that, two different rates of change for these two masses are defined, to represent different reaction behaviour.

$$m_{coal\_C} = m_{coal} \cdot \left(x_{coal\_C} - x_{coal\_O2} \cdot \frac{2M_C}{M_{O2}} \right) \qquad (1)$$

$$m_{coal\_vol} = m_{coal} \cdot \left[x_{coal\_N2} + x_{coal\_H2} + x_{coal\_H2O} + x_{coal\_O2} \cdot \left(1 + \frac{2M_C}{M_{O2}} \right) \right] \qquad (2)$$

The gaseous components, which are almost the volatiles, are transferred to the gas phase for further reactions. The oxygen content is thereby assumed to react directly with C to form CO, which is then released to the gas phase. The empirical **Equation (3)** is chosen to calculate the change of the mass of volatiles.

$$\dot{m}_{coal\_vol} = -kd_{vol} m_{coal\_vol}^{0.7} \left[1 - \left(\frac{V_{sSc}}{V_{sSc}(t=0)} \right)^2 \right] \qquad (3)$$

Here, kd_{vol} represents the change rate coefficient. The 0.7th power for the mass of volatiles limits the change rate at the beginning of the melting process for high amounts of volatiles while the bracket term accelerates the rate of change during the advance of the process. In contrast to that, the rate of change of C consists of three mass changes according to **Equation (4)**.

$$\dot{m}_{coal\_C} = -\dot{m}_{coal\_C-L} - \dot{m}_{coal\_C-CO} - \dot{m}_{coal\_C-Boudouard} \qquad (4)$$

Here, $\dot{m}_{coal\_C-L}$ represents the mass transfer to the mass of carbon available for decarburization and dissolving, $\dot{m}_{coal\_C-CO}$ represents the combustion of C to CO and $\dot{m}_{coal\_C-Boudouard}$ is the reaction rate according to the Boudouard reaction to form CO.

3.2 Modelling the simulations self-control algorithm

When it comes to research on alternative input materials and modes of operation, the model performs the simulation of the melting process without a pre-definition of a time fixed mode of operation. Therefore, the model is equipped with a self-control algorithm. This enables the simulation to adjust the input values for power and mass flows into the EAF according to current process variables during the simulation. For example, the input of natural gas through burners is decreased when the mass of scrap falls below a certain level. Furthermore, the simulation ends automatically when all scrap is melted, a minimum pre-defined temperature of the melt is reached and the carbon in the melt undercuts a maximum permissible fraction.

The mode of operation is definable by help of 13 parameters via GUI input. Those parameters are related to the melting process to calculate the set points or to switch the control variables. For example the maximum filling level of the EAF for charging further scrap baskets, when to start carbon injection according to the free bath surface and when to start and stop burners and oxygen injection have to be defined. In addition, the minimum and maximum mass flows and electrical power are definable according to the installed or planned periphery of the EAF.

The determination of the set points of the mass flows and electrical power are calculated through a multiplication of the corresponding values with several adjusting factors Φ. On example of the mass flow of post combustion oxygen, the calculation is given by **Equation (5)**. The factors Φ are determined by modified hyperbolic tangent functions and are multiplied according to **Equation (6)**. Φ_{O2_post} thereby consists of several factors $\Phi_{O2\_post,i}$ and a delay factor for closing the roof and moving the electrodes into the EAF.

$$\dot{m}_{O2\_post,set} = \dot{m}_{O2\_post,min} + \left(\dot{m}_{O2\_post,max} - \dot{m}_{O2\_post,min} \right) \cdot \Phi_{O2\_post} \tag{5}$$

$$\Phi_{O2\_post} = \Phi_{startdelay} \cdot \prod_i \Phi_{O2\_post,i} \tag{6}$$

Besides the parameters of the operation pattern, it is also possible to simulate heats with free definable scrap baskets. Here, the number of baskets, the amount of scrap and its composition, slag formers and the mass of coal can be defined via the GUI. Furthermore, for the mass of coal, the mass flows for the periphery and the parameters for the operation pattern the definition of variations is possible. All values are varied by the model according to the input from the operator, to build a set of several hundred different variances of EAF furnace operation. The variances of EAF operation are afterwards simulated and evaluated in parallel to find out optimal operation in terms of productivity, profit or costs under consideration of quality demands.

To test the self-control algorithm, the content of pure oxygen in the mass flows of oxygen input into the furnace is adjusted according to the methods of cryogenic, PSA and membrane production via GUI input. The corresponding values are 99 % for cryogenic, 95 % for PSA and 40 % for membrane production. It is assumed, that the remaining fraction to 100 % is nitrogen, which is added to the gas phase when oxygen is injected. For an oxygen equal input, the maximum mass flows for each oxygen input j are increased for the cases i (PSA and membrane) according to **Equation (7)**.

$$\dot{m}_{O2\_max,j,i} = \frac{\dot{m}_{O2\_max,j,kryogen}}{w_{O2\_max,j,i}} \cdot w_{O2\_max,j,kryogen} \tag{7}$$

4. Results and discussion

In this section, the results from the simulation of different carbon carriers and the investigation of different oxygen usage in the EAF are presented. For the simulations, a commercial PC with 3.40 GHz, 32 GB RAM and Windows 7 64-Bit version was used. Within MATLAB 2016a, a maximum initial step size of 10^{-15} s and a relative deviation tolerance of 10^{-9} is allowed. The maximum numerical solution step size is not restricted. The simulations are performed in parallel with four physical CPUs.

4.1 Results from PKS simulation

The simulation of different carbon carriers aims to validate the process models extrapolation capability by using the same parametrization for anthracite and PKS. As the off-gas composition is one of the main continuously measurable process values and the industrial trials have shown that the influence of PKS usage is visible in the CO content in the off-gas, these results are taken for evaluation.[13] Thereby, the simulation of the melting process for PKS and anthracite was performed completely offline.

The results are compared with measured data from an industrial scale EAF. To perform the simulation, the measured operation data from the furnace for the input masses, electrical and chemical energy input as well as the cooling of the roof and the wall and the off-gas mass flow are considered. For the hot heel, a constant mass of 60 t was assumed for all simulations and scrap is charged via two scrap baskets.

The industrial testing of PKS in the EAF included reference heats with anthracite as charge coal input. For the total amount of PKS, the mass was increased to achieve an equal input of the absolute heating value. This means in total, that an average mass of 1.4 t of PKS were charged into the EAF while 1.1 t of anthracite were charged for the reference process. Regarding the reference heats, 149 heats are simulated and evaluated in comparison to measured data within a simulation time of one hour for all heats. In case of the PKS trials, 364 heats are simulated with an approximate simulation time of two and a half hours.

For the comparison of the off-gas data, the measured (meas) and simulated (sim) data for PKS and anthracite (anthr) are averaged over their dataset of heats and the process time is normalized by help of the tap-to-tap time. Hence, the unsteady behavior of single heats is smoothed and the results are better comparable.

In **Figure 4**, the averaged simulated and measured off-gas mass fraction of CO and CO_2 are compared. The red lines are representing the results of the reference process with anthracite usage while the green lines are showing the results for PKS usage.
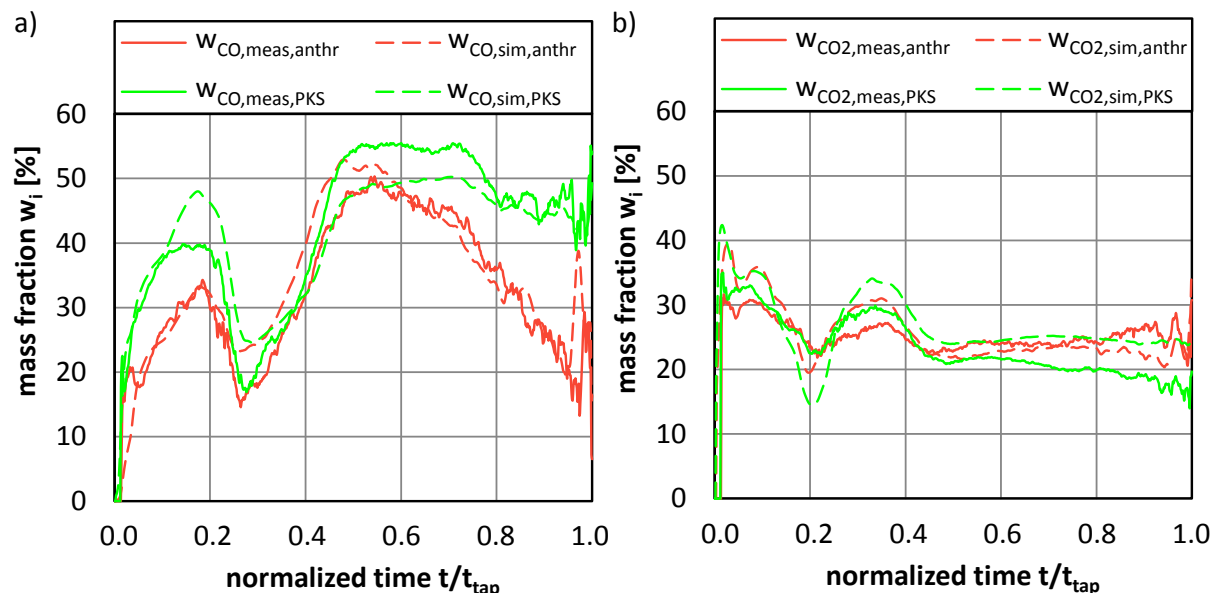

Figure 4. Off-gas mass fractions of a) CO and b) CO_2

In Figure 4 a), the red solid line shows no significant difference compared to the red dashed line for the corresponding simulation results. In comparison to anthracite, the mass fraction of CO in the off-gas is higher during the melting of the first scrap basket in case of PKS. This

aligns with theoretical expectations, which are based on the higher volatile content for PKS and their assumed higher reactivity. The simulation results for PKS, shown by the green dashed line, are significantly higher than the measured data reaching almost 48 %. In contrast to that, the simulation results are below the measurements during the second scrap basket melting. The rates of reaction have to be further adjusted so that the production of CO is shifted further to the second basket.

In Figure 4 b), the averaged off-gas mass fraction of CO_2 is presented with the same colour allocation like before. The courses of the anthracite and PKS cases are in the same range of magnitude with an increased difference at the end of the process of almost 5 %. However, significant differences are not clearly visible over the process time.

Figure 5 compares the specific off-gas energy output per ton of liquid steel (lSc) via boxplots. For the enthalpy, which is often named as sensible heat, the simulation reproduces the amounts determined from measured data for anthracite and PKS. The median values are almost in the same range of magnitude. However, the simulation results are leading to higher chemical energy output, which is caused by the increased CO output as shown in Figure 4. In addition, higher variances are obvious for the upper and lower quartiles for anthracite in comparison to PKS. This cannot be reproduced by the simulation and it is assumed, that these variances are caused by transient behaviour like accumulation of carbon in the EAF.
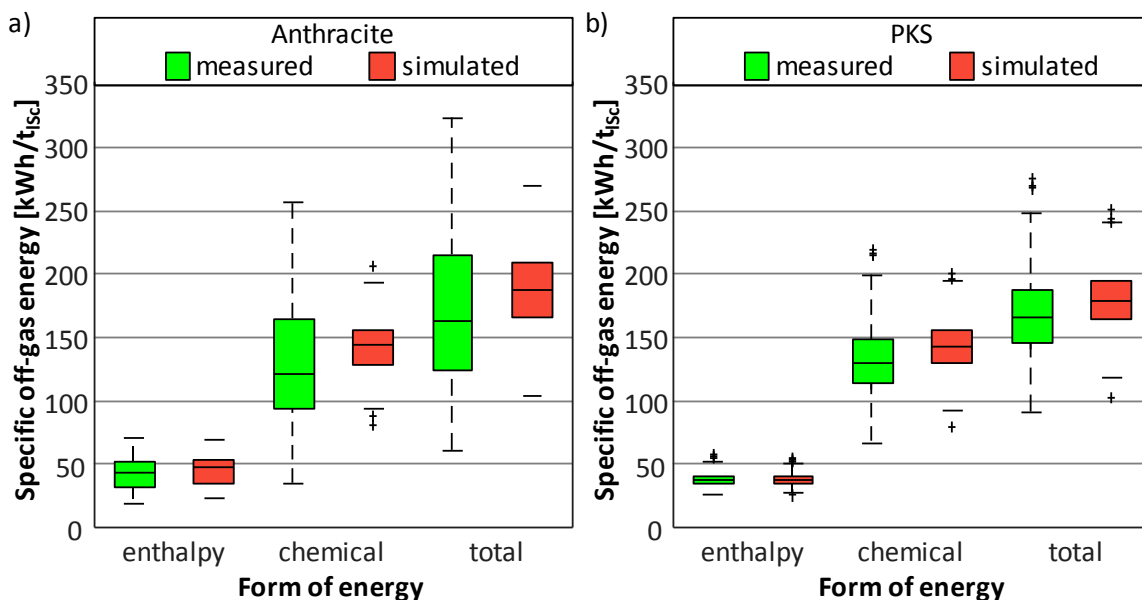
Figure 5. Measured and simulated off-gas energies for a) anthracite and b) PKS

4.2   Results from oxygen investigation with operation chart variation

The investigation of oxygen usage with different purities in the EAF aims to demonstrate the models capability of analysing different modes of operation through self-control and variation strategies. For the input, two scrap baskets with 90 t and 65 t scrap are charged into the EAF. The first basket includes 2 t of slag formers and 900 kg of anthracite. The tapping is achieved when the temperature reaches 1577 °C (1850 K) and the carbon content is lower than 0.1 %. The hot heel is defined to have 30 t. Five parameters are changed in two or three steps so that 108 different modes are simulated. The changed parameters are related to the increase of oxygen lancing, the decrease of oxygen injection for post combustion, the power decrease of the natural gas burners and the starting point for carbon injection.

An overview about the results obtained from the simulation is given by **Figure 6**. Here, the total power, used masses, energies and productivity is evaluated for a certain period. In total, 324 different results are given in the table, which are resulting from three different oxygen cases and 108 different modes of operation for each case. The results can be filtered and sorted. In Figure 6, this is done for the best result for productivity (batch number 174) and the worst result (batch number 117) for the different sets (1: cryogenic; 2: PSA; 3: membrane).

Set No	Charge No	Power On (s)	t_(Tap To Tap) (s)	CH4_burner (m3)	O2_burner (m3)	O2_lance (m3)	O2_post (m3)	O2_total (m3)	C_inj (kg)	T_tap (K)	m_tap (t)	w_C (%)
1	117	1998	2175	131,1	576,6	2846,8	189,4	3612,7	1236,2	1851	138,8	0,08
1	174	1863	2041	196,6	875,2	2820,8	381,2	4077,2	956,1	1851	137,7	0,07
2	117	2003	2181	131,3	588,8	2972,8	197,5	3759,1	1240,5	1851	138,8	0,08
2	174	1869	2047	196,9	904,9	2947,7	397,7	4250,4	960,9	1851	137,7	0,07
3	117	2137	2314	138,7	1012,6	7489,0	489,3	8990,9	1345,1	1851	138,3	0,08
3	174	2028	2206	207,4	1929,7	7609,5	982,8	10522,0	1090,5	1851	137,5	0,07

Set No	Charge No	e_electr (kWh/t)	e_coal (kWh/t)	e_C consumpt (kWh/t)	e_CH4 (kWh/t)	e_chem.rct. (kWh/t)	e_electrode_cons. (kWh/t)	e_oils, greases (kWh/t)	e_total_e_input (kWh/t)
1	117	382,7	133,6	7,2	7,1	77,7	5,2	39,0	652,4
1	174	360,4	116,7	9,1	10,7	93,4	6,6	39,4	636,0
2	117	383,7	133,8	7,2	7,1	77,7	5,2	39,0	653,7
2	174	361,5	117,0	9,1	10,7	93,1	6,6	39,4	637,3
3	117	408,4	141,0	7,9	7,5	81,3	5,6	39,2	690,9
3	174	391,8	125,5	9,2	11,3	95,2	6,3	39,4	678,6

Set No	Charge No	e_steel (kWh/t)	e_slag (kWh/t)	e_cooling (kWh/t)	e_off-gas (kWh/t)	e_electrode (kWh/t)	e_uncombusted_C (kWh/t)	e_total_e_output (kWh/t)	e_balance_diff (kWh/t)
1	117	379,6	30,4	97,6	135,0	0,7	2,7	646,1	6,4
1	174	379,6	33,7	91,7	123,9	0,7	1,1	630,8	5,2
2	117	379,6	30,4	97,9	136,0	0,7	2,7	647,3	6,4
2	174	379,6	33,7	92,1	124,9	0,7	1,1	632,1	5,2
3	117	379,6	31,1	105,9	166,3	0,7	1,5	685,1	5,8
3	174	379,6	34,1	101,7	156,2	0,7	1,0	673,4	5,2

Set No	Charge No	anual heats (n/a)	anual prod. (Mio. t/a)	worth of steel (Mio. EUR/a)	electricity (EUR/heat)	coal (EUR/heat)	natural gas (EUR/heat)	oxygen (EUR/heat)	electrodes (EUR/heat)	heat costs (EUR/heat)	anual costs (Mio. EUR)	anual profit (Mio. EUR)
1	117	8737	1,213									
1	174	9312	1,282									
2	117	8716	1,210									
2	174	9286	1,278									
3	117	8213	1,136									
3	174	8618	1,185									

Figure 6. Overview about the simulation results evaluation with filter and sorting options

The simulation results from the different oxygen input investigations were evaluated according to several different criteria like tap-to-tap time, productivity, energy consumption as well as costs and profit. The best results from the variation of the mode of operation are given in **Figure 7** as bar charts. It is obvious, that the results from the heats with oxygen with membrane technology are performing worst in comparison to cryogenic and PSA oxygen. Higher tap-to-tap times are decreasing the productivity and finally the profit, which is shown in relativity to the cryogenic result. The results between cryogenic and PSA are almost negligible, as the oxygen purity is 99 % and 95 %, respectively.

For a deeper insight how the results are changing due to the variation of the mode of operation, the energy balance of the best (174) and worst (117) heat for cryogenic is compared in **Figure 8**. The biggest differences are obvious in the electrical energy input and the total energy input. Due to an increased usage of oxygen in heat 174 compared to the heat 117, more chemical energy was released through oxidation of Fe so that less electrical energy is needed to achieve the melting goals. As a result, the slag contains higher energy for heat 174 due to an increased mass of FeO. Another effect is visible in the off-gas energy. Because of the shorter tap-to-tap time for heat 174, less energy is transported out of the EAF through the off-gas.

The main difference between the two heats 174 and 117 is the different starting point of increasing the lanced oxygen and the injection of coal for decarburization and slag foaming. The differences of these mass flows is shown in **Figure 9**. During the melting process of heat 174, the lanced oxygen is increased earlier, which leads to increased chemical reactions. In contrast to that, the injection of carbon starts later.
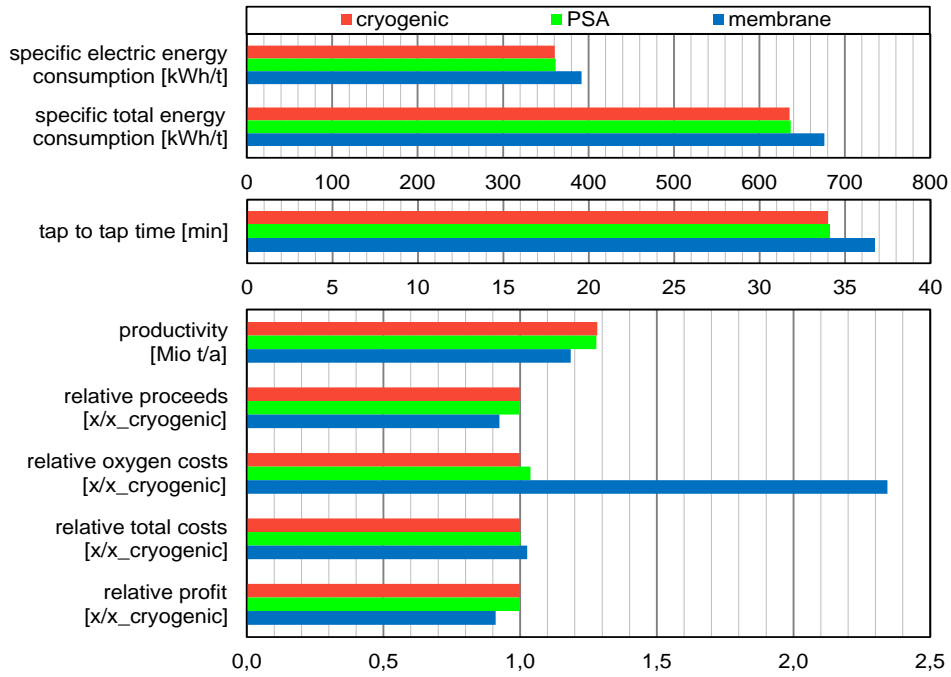
Figure 7. Comparison of the heats with the best results for different oxygen input
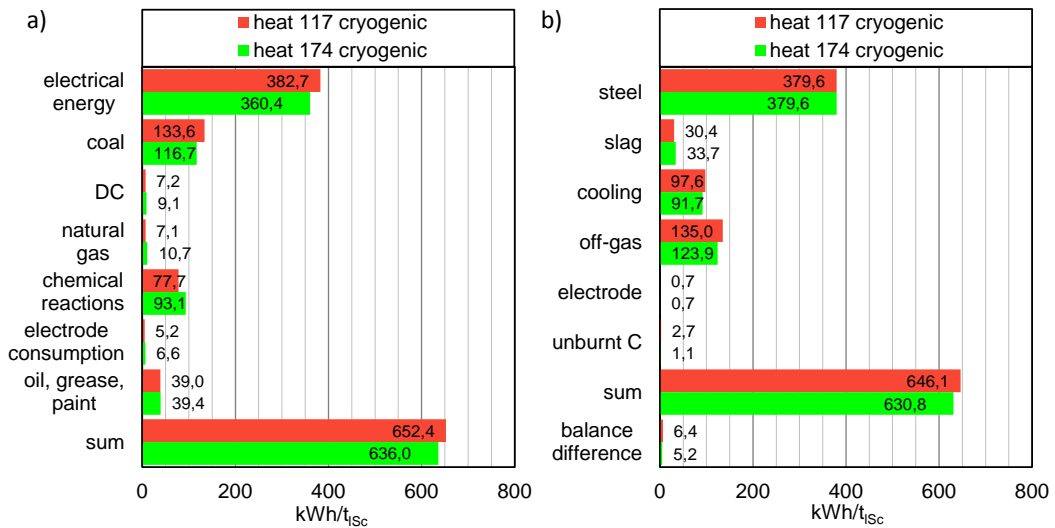

Figure 8. Energy balance a) input and b) output of batch 117 and batch 174 for cryogenic oxygen usage
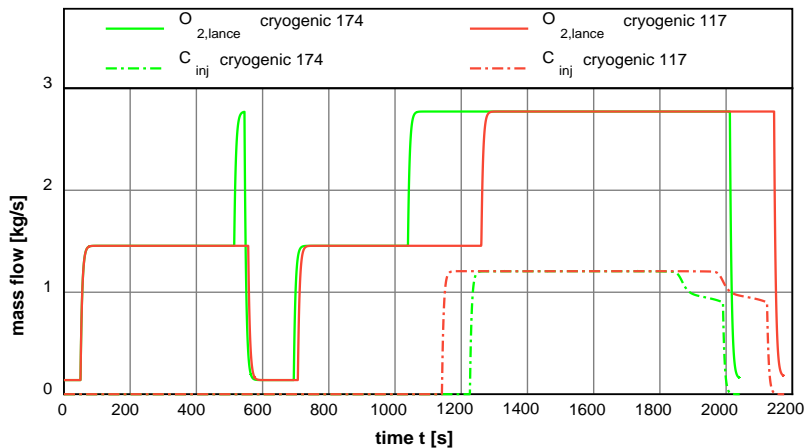

Figure 9. Mass flows of lanced oxygen and injected carbon for batch 174 and 117 for cryogenic oxygen

The influence of oxygen input from cryogenic and membrane production influences also the gas phase. Therefore, **Figure 10** shows the CO mole fraction in the off-gas- Due to an increased input of nitrogen together with the oxygen mass flow from membrane production, the CO fraction is lower than for cryogenic production. Also visible is the different starting point of carbon injection for the heats 174 and 117 (green and red dashed) before and after 1200 s, where the CO fraction suddenly increases.
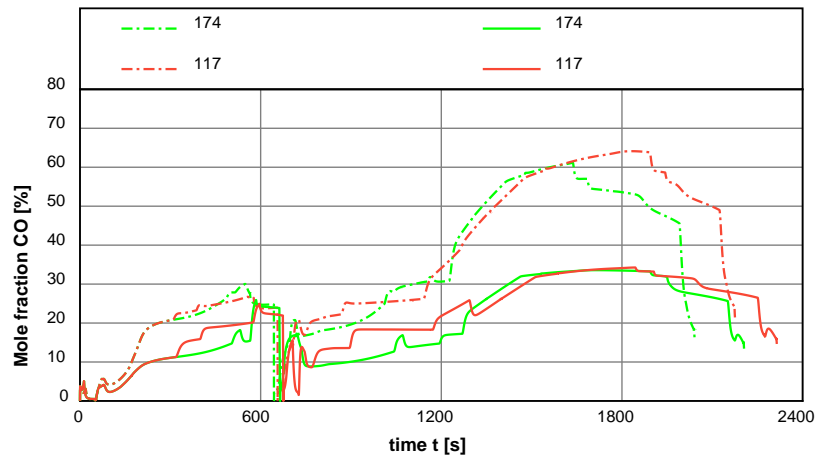
Figure 10. Molar fraction of CO in the off-gas for cryogenic and membrane oxygen

Further results that can be extracted from the simulation are given in **Figure 11**. Here, the net heat transfer into the scrap phase is compared in Figure 11 a) for the heats 174 and 117 for oxygen from cryogenic and membrane production. Especially during the melting of the second scrap basket, a significant higher energy transfer to the scrap is obvious, leading to an increased melting rate, thus accelerating the process.

As already mentioned, heat 174 leads to an increased slagging of Fe, due to a higher oxygen lancing compared to heat number 117. The oxidation can be followed up in Figure 11 b). Here, the FeO mass fraction in the slag is depicted over the process time.

Figure 11. Results for heat 117 and 174 for cryogenic (cryo) and membrane (mem) oxygen for a) heat flow into scrap phase and b) mass fraction of FeO in the scrap

5. Conclusion

The consideration of different carbon carriers in a dynamic process simulation of the EAF enables the investigation of different input materials. The presented model was further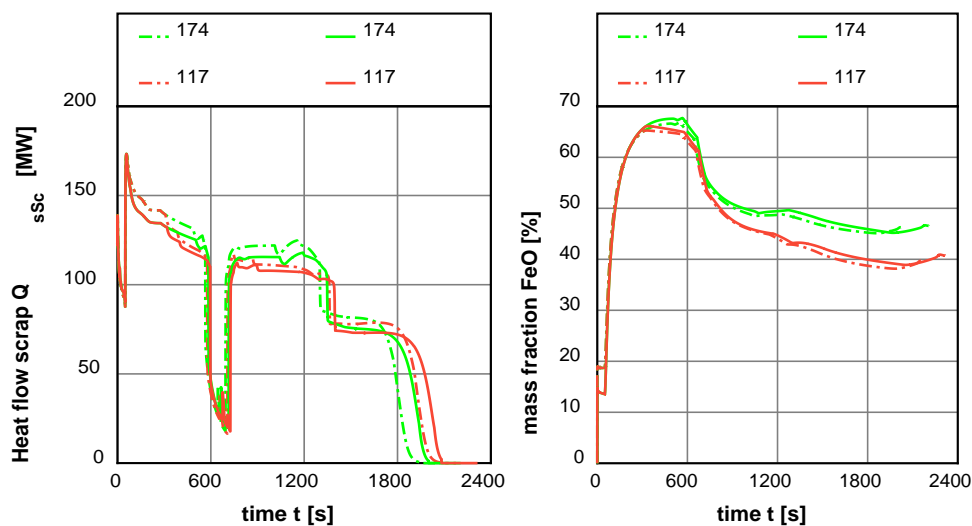 developed to enable the definition of different coals types for charging and lancing into the EAF to prove the extrapolation capabilities of the model. Therefore, the simulation of PKS was performed with the same model parametrization as used for the validation for anthracite usage.

The results of the PKS simulations reproduced the increased CO fraction in the off-gas due to the higher volatile matter in the PKS and the increased reactivity compared to anthracite. Despite the off-gas, other simulation results remained as they were in case of anthracite usage and are in line with industrial trial campaigns. Because of these results, higher post combustion oxygen injection could improve the energy conversion in the EAF, thus leading to higher melting ratios.

For future investigations on different modes of operation, the model was further developed and equipped with a self-control algorithm. Based on pre-definable parameters, the simulation changes the input values of power and mass flows according to the process behaviour. The variation of these parameters for different oxygen usage in the EAF delivered an optimized operation strategy in terms of productivity, energy consumption, profit and costs. However, further investigations under consideration of more parameter changes are intended and necessary.

In the future, the dynamic process simulation model will be further enhanced with automatic optimization strategies to research the energy and resource efficiency of the steel recycling process in the EAF.

6. References

1) P. Frittella, A. Lucarelli, L. Angelini, E. Filippini, B. Poizot, M. Legrand, iCSMelt applications to EAF operating practice optimization, *Iron and Steel Technology Conference and Exhibition, AISTech,* 2011.
2) Y. E. M. Ghobara, Modeling, optimization and estimation in electric arc furnace (EAF) operation, *M. App. Sc.-Arbeit*, 2013.
3) V. Logar, I. Škrjanc, Development of an electric arc furnace simulator considering thermal, chemical and electrical aspects, *ISIJ International,* Vol. 52 (2012), 1924-1926.
4) R. D. M. MacRosty, C. L. E. Swartz, Dynamic optimization of electric arc furnace operation, *AIChE Journal,* Vol. 53 (2007), 640-653.
5) P. Nyssen, G. Monfort, J. L. Junque, M. Brimmeyer, P. Hubsch, J. C. Baumert, Use of a dynamic metallurgical model for the on-line control and optimization of the electric arc furnace, *International Conference Simulation and Modelling of Metallurgical Processes in Steelmaking (SteelSim), 2,* 2007.
6) C. Ojeda, O. Ansseau, P. Nyssen, J. C. Baumert, J. C. Thibaut, M. Lowry, EAF process optimization tool using CRM dynamic model, *International Metallurgical Trade Fair with Congresses (METEC InSteelCon), European Steel Technology and Application Days (ESTAD), 2,* 2015.
7) J. Wendelstorf, K.-H. Spitzer, A process model for EAF steelmaking, *Iron and Steel Technology Conference, AISTech,* 2006.
8) G. E. P. Box, J. S. Hunter, W. G. Hunter, *Statistics for experimenters: design, innovation, and discovery*, Hoboken (NJ, USA), 2005.
9) V. Logar, D. Dovžan, I. Škrjanc, Modeling and validation of an electric arc furnace: part 1 - heat and mass transfer, *ISIJ International,* Vol. 52 (2012), 402-412.

10) V. Logar, D. Dovžan, I. Škrjanc, Modeling and validation of an electric arc furnace: part 2 - thermo-chemistry, *ISIJ International,* Vol. 52 (2012), 413-423.

11) T. Demus, T. Reichel, M. Schulten, T. Echterhof, H. Pfeifer, Increasing the sustainability of steel production in the electric arc furnace by substituting fossil coal with biochar agglomerates, *Ironmaking & Steelmaking,* Vol. 43 (2016), 564-570.

12) T. Echterhof, H. Pfeifer, Potential of biomass usage in electric steelmaking, EECRsteel 2011, *1st International Conference on Energy Efficiency and CO2 Reduction in the Steel Industry, 27th of June–1st of July,* 2011.

13) T. Echterhof, T. Demus, H. Pfeifer, L. Schlinge, H. Schliephake, Investigation of palm kernel shells as a substitute for fossil carbons in a 140 t DC Electric Arc Furnace, *European Electric Steelmaking Conference & EXPO (EEC), 11,* 2016.

14) T. Meier, *Modellierung und Simulation des Elektrolichtbogenofens (Dissertation)*, Aachen, 2016.

15) T. Meier, A. Hassannia Kolagar, T. Echterhof, H. Pfeifer, Process modeling and simulation of an electric arc furnace for comprehensive calculation of energy and mass transfer in combination with a model of the dedusting system, *European Electric Steelmaking Conference & EXPO (EEC), 11,* 2016.

16) T. Meier, V. Logar, T. Echterhof, I. Škrjanc, H. Pfeifer, Modelling and simulation of the melting process in electric arc furnaces - influence of numerical solution methods, *Steel Research International,* Vol. 87 (2015), 581–588.

Hydrogen Utilization on the Ironmaking Field

for the Reduction of CO₂ Emission

Yoshiaki Kashiwaya,

Graduate School of Energy Science, Kyoto University, Kyoto, Japan

Corresponding author: kashiwaya@energy.kyoto-u.ac.jp

Abstract: Hydrogen itself is not a primary energy and needs energy for its production, which means that CO_2 will be exhausted during the production process, more or less. However, when a Green Hydrogen can be produced, it is a best way to use the hydrogen instead of carbon.

In this paper, two kinds of iron ore were reduced and melted both under hydrogen and carbon atmosphere. The obtained iron metal under hydrogen atmosphere was quite pure one. The impurities in the metal were chemically and thermodynamically analyzed. The characteristics and benefits of hydrogen reduction were discussed in comparison with the carbon reduction.

The image of hydrogen furnace not depending on the fossil fuels was presented.

Keywords: hydrogen reduction, clean steel, inclusion, direct steelmaking

1. Introduction

Hydrogen itself is not a primary energy and needs an energy to produce, which means that CO_2 will be exhausted during the production process, more or less. However, the circumstance related to energy supply is going to change, because the use of fossil fuels is limited which is not eternal one. Moreover, the countries having large population are arising economically and need an energy for developing their countries. CO_2 content in the atmosphere is increasing and the environment of earth is changing quickly. We should cease to use the fossil fuel sooner or later, however, the time for ceasing is not clear and affected by an economic situation significantly. At the present time, Japan has a Fukushima's disaster of nuclear plants and Europe suffers for a financial crisis. The reduction of CO_2 emission seems to be tone down. Although such tide for CO_2 reduction affected to the research situation, we should prepare for the situations with the best way or possible ways.
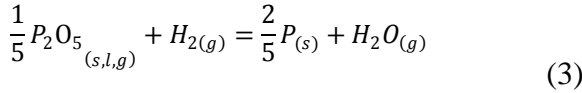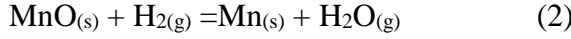
Although the hydrogen reduction has a high reaction rate in comparison with the CO reduction, the production of the hydrogen itself needs a cost and energy. The actual process of hydrogen reduction did not developed except the direct reduction process using the natural gas (CH_4 mainly). However, recently, the hydrogen reduction is focused on, because the problem of CO_2 emission is the most important problem for the people living on the earth.

When the Green Hydrogen, which does not accompany with the CO_2 emission, can be produced, the hydrogen reduction process can be an alternative process of the present ironmaking and steelmaking. In addition, when the residual fossil fuels are decreasing and the cost of fossil base energies are increasing drastically, the hydrogen process could be comparative with the present system.

Furthermore, the metallic iron obtained by hydrogen reduction is close to a pure iron without carbon. In addition, the tramp elements (Si, Mn and P) cannot be reduced thermodynamically

under hydrogen atmosphere (Eqs.(1), (2) and (3))[1]. On the other hand, most of inclusions such as Si, Mn, P are reduced by carbon and enter in the metallic iron in the lower part of BF (blast furnace) (Eqs.(1), (3) and (5)) [1].

(a) Hydrogen reduction

$$\frac{1}{2}SiO_{2\,(s)} + H_{2(g)} = \frac{1}{2}Si_{(s)} + H_2O_{(g)} \tag{1}$$

$$MnO_{(s)} + H_{2(g)} = Mn_{(s)} + H_2O_{(g)} \tag{2}$$

$$\frac{1}{5}P_2O_{5\,(s,l,g)} + H_{2(g)} = \frac{2}{5}P_{(s)} + H_2O_{(g)} \tag{3}$$

(b) Carbon reduction

$$\frac{1}{2}SiO_{2\,(s)} + C_{(s)} = \frac{1}{2}Si_{(s)} + CO_{(g)} \tag{4}$$

$$MnO_{(s)} + C_{(s)} = Mn_{(s)} + CO_{(g)} \tag{5}$$

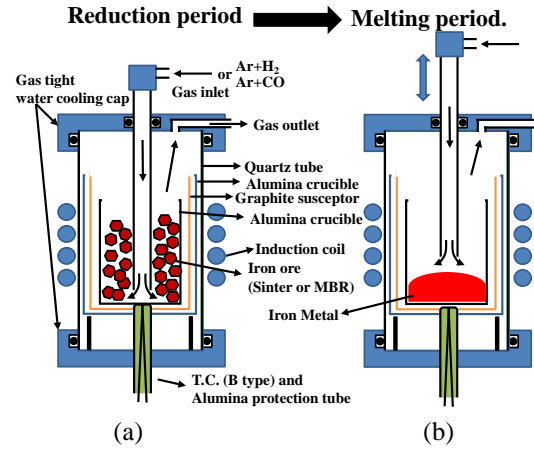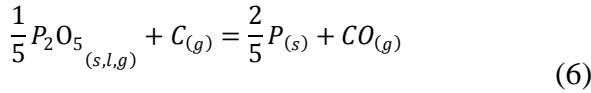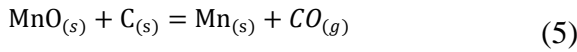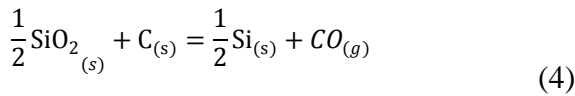$$\frac{1}{5}P_2O_{5\,(s,l,g)} + C_{(g)} = \frac{2}{5}P_{(s)} + CO_{(g)} \tag{6}$$
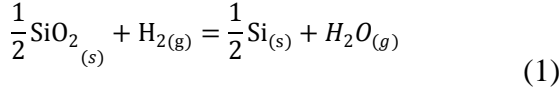
Fig.1 Schematics of experimental apparatus.

These features of hydrogen reduction should be especially focused on in this paper. This process leads to a 'Direct Steelmaking' in which just the addition processes of carbon and alloying elements are involved. If this direct steelmaking process was established, many processes such as the decarburization, desulfurization, dephosphorization and desiliconization were omissible in the entire conventional process.

In this study, two kinds of iron ore were reduced completely and then melted under hydrogen atmosphere, continuously. CO reduction was performed for the comparison with the results of hydrogen reduction. To clarify the reactions occurring in the systems, the thermodynamic study on the reduction reaction of impurities such as Si, Mn, P and S were performed.

Finally, an image of hydrogen iron- and steelmaking (Direct steelmaking) was proposed.

2. Experimental
2.1 Apparatus and procedure

Figure 1 shows the experimental apparatus for reduction and melting of iron ore. The furnace is an induction furnace and the reaction tube is a transparent quartz tube with 65 mmϕ O.D., 60 mmϕ I.D. and 500mmL. The quartz reaction tube was sealed with a water cooled aluminum cap at the both end and the gas sealing was achieved by O-ring set to the aluminum cap.

The iron ore samples were reduced and melted in a porous alumina crucible. The sample crucible was set in a graphite crucible which worked as a susceptor for heating. Finally, the graphite

Fig.2 Temperature profile of the reduction and melting experiment.

susceptor was set in a larger and porous alumina crucible for insulation. The reaction gas was blew into the crucible by a dense alumna lance (6 mmϕ O.D., 4 mmϕ I.D. and 600 mmL) and the end of lance was set about 5 mm from the bottom of crucible in order to flow the reaction gas throughout the sample bed (Fig.1(a)). As the total flow rate of reaction gas (Ar+24%H$_2$,
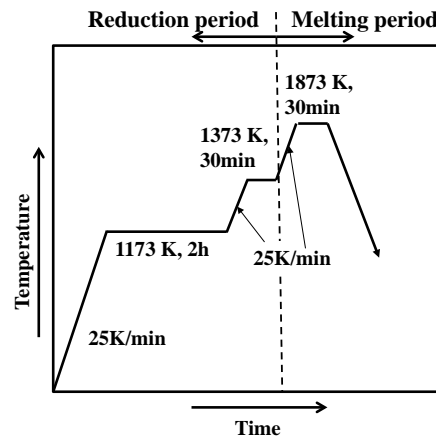
Ar+24%CO) was 500cm³/min (STP), the linear velocity of the gas was 66 cm/s which was high enough for eliminating the mass transfer control.

After the samples were reduced completely in a lower temperature (1173K-1373K), the alumina lance was pulled up to the top of sample bed as shown in Fig.1(b), and the reduced samples were heated to a higher temperature (1873K) for melting.

Figure 2 shows the heat pattern adopting in this experiment. The heating pattern consists of two periods. One is a reduction period and the other is a melting period. In this study, it is important that the reduction and melting operation were performed continuously without a taking out the sample from the crucible. This continuous reduction and melting process will give the thermodynamic advantage of hydrogen reduction as mentioned above.

In the reduction period, the sample was reduced at 1173K for 2 hours, and then, the sample was reduced completely at 1373K for 30 min. These procedures were important to prevent the crucible erosion from the residual FeO in the melting period. The heating-up rate was 25 K/min in the all steps and the cooling rate was about 50 K/min for high temperature range above 1473K and about 40 K/min to 20 K/min in the lower temperature range. The completely reduced sample was melted at 1873K and hold about 30 min. After that, the power of induction furnace was turned off and cooled down to the ambient temperature.

2.2 samples served

In this study, two kinds of sample were used. One was a sinter which was used for the actual blast furnace operation. The other was MBR (Minerações Brasileiras Reunidas) iron ore. The chemical compositions of the sinter and MBR ore are shown in Table 1. Total Fe (T.Fe) in the MBR ore is higher than that of sinter. The contents of FeO for sinter and MBR are 8.68% and 0.08%, which means the MBR used in this experiment is a pure hematite iron ore.

Table 1 Chemical composition of iron ore used   (mass%).

	T.Fe	FeO	Fe₂O₃	CaO	SiO₂	Al₂O₃	MgO	MnO	S	P
Sinter	60.57	8.68	76.82	8.42	4.92	1.76	0.99	0.22	<0.01	0.06
MBR	67.66	0.08	96.66	0.28	1.36	0.62	0.06	0.13	0.004	0.03

The sinter was crushed and sieved into coarse particles from 2 mmφ to 5 mmφ. As the MBR ore was a fine powder originally, it was once sintered at 1273K under air atmosphere. Then, the obtained block type MBR ore was crushed and sieved to the same size of the sinter.

Table 2 Weight of samples used and metal obtained.

Sample Name	Weight of sample (g)	Metal obtained (g)	$[\%C]_{Fe}$	Yield of metal
Sinter-H	61.63	35.45	0.004	95.0%
MBR-H	42.93	28.39	0.002	97.7%
Sinter-C	61.16	38.10	5.15	97.6%
MBR-C	48.67	34.52	4.68	99.9%

Table 2 shows the weights of samples used and the weight of metal button obtained after experiments. The notations '-H' and '-C' mean the hydrogen reduction and the CO reduction, respectively. The yields of metal for hydrogen reduction were 95 % to 97.6 % and those for CO reduction were 97.7 % to 99.9 %. In the case of sinter, as the content of FeO in slag will be high and remain until the melting period, the molten FeO slag will react with alumina crucible. It is the reason why the yield of metal for sinter was slightly lower than that of MBR. The contents

of carbon for Sinter-C and MBR-C are 5.15 % and 4.68%, respectively. The contents of carbon are close to the saturation in the metal iron (5.4% at 1873K). In the case of CO reduction, a graphite flake about 2 g was put in the bottom of crucible in order to reach the carbon saturation. However, as the carbon contents were lower than the saturation point, the reaction time (holding time of 30 min for melting at 1873K in Fig.2) might be short for reaching the complete saturation. From the result that the surface of solidified metal had an undissolved graphite pieces after experiment, it was considered that the effect of reaction time was relatively large.

3. Results and discussions

3.1 Analyses of obtained metals

Figure 3 shows the appearances of metallic iron obtained. Sinter-H and MBR-H show a clear metallic color, although the top view of sinter-H shows a thin rust film which might come from an exposure to air before the complete cooling down. Sinter-C and MBR-C show an appearance of cast iron. As indicating by arrows, some of graphite flake undissolved

Fig.3 Outlooks of iron buttons obtained

are attached on the surface of button. These buttons are cut and polished for the observation of microstructure.

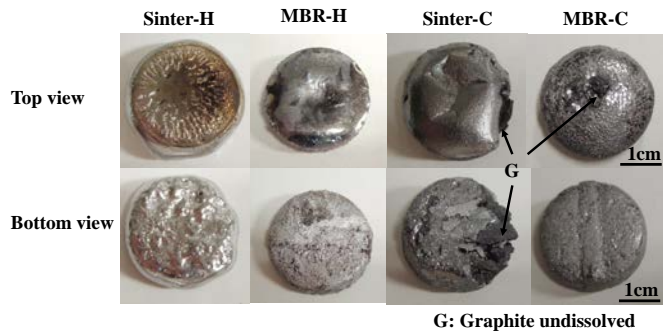The chemical composition of metals obtained in this experiment are compared in Figures 4 and 5. Fig. 4 shows the comparison of the contents of C, Si, Mn P, Al and O. Each column corresponds to the respective elements, the left hand side pair of bar in a column corresponds to the sinter-H and MBR-H, and the right hand side pair corresponds to the sinter-C and MBR-C.

Carbon contents of sinter-H and MBR-H are 40 ppm and 20 ppm, respectively. These carbons might come from the graphite susceptor. If other heating system without carbon material was used in the reaction system, the carbon content would be under the limit of analysis. Actually, since the pure iron needs a carbon addition together with the alloying elements for the production of steel, the small content of carbon in iron obtained by hydrogen reduction is not so important problem. Silicon contents of sinter-H and MBR-H are significantly lower than that of carbon reduction, that is excellent agree with the thermodynamic consideration mentioned above. Manganese contents of sinter-H and MBR-H are also low and about one third to one tenth for the carbon

Fig.4 Comparison of contents of impurities between hydrogen reduction and carbon reduction (C, Si, Mn, P, Al and O).

reduction. The manganese content also coincides with the thermodynamic prediction.

On the other hand, phosphorus contents of sinter-H and MBR-H are almost the same level with the carbon reduction. In this experiment, slag was not used and the equilibrium would establish in the contact between the alumina crucible and metal reduced. It is considered that the most of oxide impurities in the iron ore will react with the crucible. In addition, some of FeO remained will also react with the crucible. The detailed thermodynamic consideration were performed in the later section.
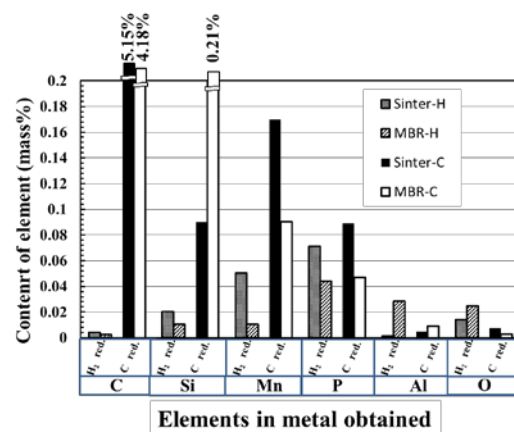
It is considered that the aluminum contents of sinter-H and MBR-H are to be a same level with the carbon reduction. However, Al in MBR-H is relatively high and Al in Sinter-H is under the limit of analysis. Although the meaning of these results is not known in this stage, the content of Al is not decided by the results of hydrogen and carbon reduction.

The oxygen level is high in the hydrogen reduction, which is characteristics in the hydrogen system, and the content of oxygen is from 140 ppm to 245 ppm, while the one in carbon reduction is from 29 ppm to 75 ppm.

Fig.5 shows the comparison of the contents of S, Ca, Mg and H in the metal obtained. The contents of S of sinter-H and MBR-H are less than half of the ones of sinter-C and MBR-C. The contents of Ca and Mg are difficult to understand, so that the level of these elements are very low. On the other hand, it is interesting to know the hydrogen content of sinter-H and MBR-H. Even in a melting and solidifying the iron under hydrogen atmosphere, the hydrogen content was very low and the same level with carbon reduction without hydrogen in the atmosphere. It could be concluded that the hydrogen absorbed in the iron melt was quickly evolved to the atmosphere during solidification. Since the hydrogen brittleness occurs in the welding, heating and plating process mainly, hydrogen
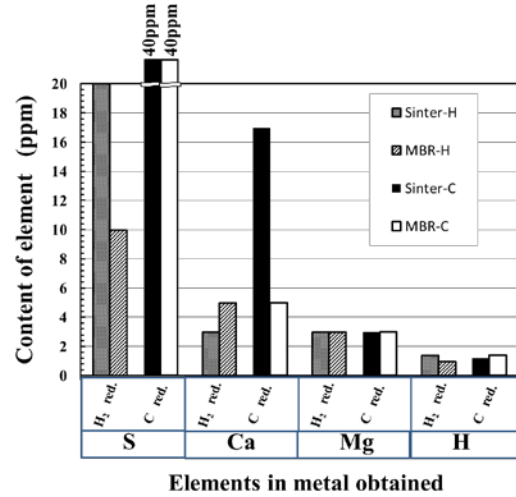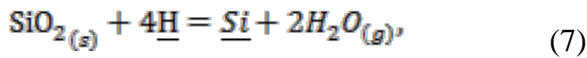

Fig.5 Comparison of contents of impurities between hydrogen reduction and carbon reduction (S, Ca, Mg, H).

reduction process is not necessary to take into account the hydrogen content in the solidified iron.

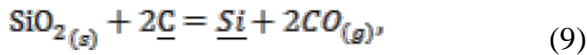3.2 Thermodynamic consideration of impurities.

The activity coefficients for the respective elements were calculated using the interaction parameters published by JSPS[2].

(1) SiO₂

The change of Gibb's energy for the reduction of SiO_2 by dissolved hydrogen ($\underline{H}$) in the molten iron (Eqs.(7) and (8)) is estimated using data book of JSPS[2]. Also, the SiO_2 reduction by dissolved carbon ($\underline{C}$) in molten iron (Eq.(9)) can be expressed as Eq.(10).

$$SiO_{2(s)} + 4\underline{H} = \underline{Si} + 2H_2O_{(g)}, \tag{7}$$

$$\Delta G°/cal = 38478 - 51.82 \cdot T \tag{8}$$

$$SiO_{2(s)} + 2\underline{C} = \underline{Si} + 2CO_{(g)}, \tag{9}$$

$$\Delta G°/cal = 127158 - 70.52 \cdot T \tag{10}$$

Fig.6 Variations of silicon activity for SiO_2 reductions by hydrogen and carbon.

Using Eqs.(7) and (9), the variations of activities of silicon (a_{Si}) were calculated and plotted in the Figure 6. In the case of hydrogen reduction (Eq.(8)), the activity of $\underline{H}$ was assumed to be 1×10^{-4}, because the $\log a_H$ obtained by the experiment was -3.997 and -3.851. The activity of SiO_2 (a_{SiO2}) was assumed to be 1.0. The $\log a_{Si}$ was -1.692 for sinter-H (■) and -1.996 for MBR-H (□). In order to fit these values, the partial pressure of H_2O (P_{H2O}) was 1.9×10^{-4} for sinter-H and 2.7×10^{-4} for MBR-H.

On the other hand, the silicon activities in carbon reduction (a_{Si} , Eq.(9)) were estimated using a_C=38 and P_{CO}=0.24 both for sinter-C and MBR-C. The Henrian activity of carbon (a_C=38) was estimated from Eqs.(11) and (12) at 1873 K.

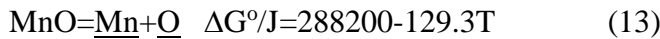$$C_{(gr)} = \underline{C} , \qquad \Delta G^o/J = 23484.8 - 43.51 \cdot T \qquad (11)$$
$$a_C(Henry) = \exp\left(\frac{-\Delta G^o}{RT}\right) \qquad (12)$$

While the experimental carbon activities (a_C) for sinter-C and MBR-C are 93.6 and 66.9, respectively, which are agree with the value obtained by Eqs.(11) and (12).

The activities of silicon ($\log a_{Si}$) for Sinter-C and MBR-C were -0.104 (●) and +0.19 (○), respectively, when the activities of SiO₂ (a_{SiO2}) were assumed to be 8×10^{-6} and 1.6×10^{-5} (Fig.6), respectively. The temperature dependence of a_{Si} of carbon reduction is larger than that of hydrogen reduction. In addition, the activity of SiO₂, a_{SiO2} of carbon reduction is significantly lower than that of hydrogen reduction.

Fig.7 Relationship of activity between Mn and O in the molten iron (Hydrogen reduction: a_{MnO}=0.01, Carbon reduction: a_{MnO}=0.0005)..

(2) MnO

The activity of MnO was estimated by Eq.(13) using the activities of oxygen ($\underline{O}$) and manganese ($\underline{Mn}$) obtained by the experiment.

$$MnO = \underline{Mn} + \underline{O} \quad \Delta G^o/J = 288200 - 129.3T \qquad (13)$$

The activities of Mn ($\log a_{Mn}$) for Sinter-H and MBR-H are -1.307 and -2.005, respectively. Since the oxygen activity (a_O) of hydrogen reduction is higher than that of carbon reduction, it is considered that the activity of MnO (a_{MnO}) will be higher than that of carbon reaction. Using Eq.(13), the relationship between $\log a_O$ and $\log a_{Mn}$ was calculated and plotted in Figure 7 with the assumption of the activity of MnO (a_{MnO}). As a result, the activity of MnO (a_{MnO}) for the hydrogen reduction was about 0.01 (0.01 for sinter-H and 0.005 for MBR-H), and the one for the carbon reduction was about 0.0005 (0.002 for sinter-C and 0.0005 for MBR-C).

4. Image of Hydrogen Furnace for Direct Steelmaking.

When H₂O gas is introduced into a carbon existing system in high temperature more than 1000°C, water gas reaction (Eq.(14)) will occur.
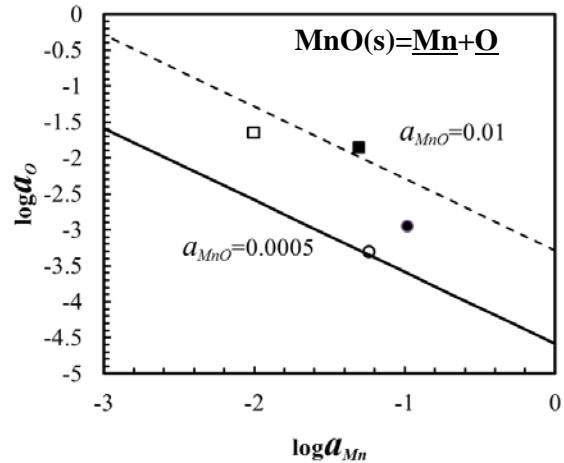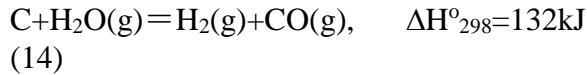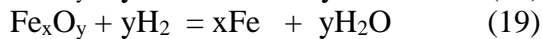
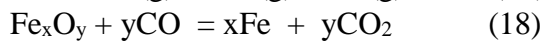$$C+H_2O(g)＝H_2(g)+CO(g), \qquad \Delta H^o_{298}=132kJ \quad (14)$$

The water gas reaction (14) is relatively large endothermic reaction. It is suspicious about the temperature decrease of the lower part of blast furnace (BF) through the increase of water gas reaction, when the hydrogen content increases.

The reactions are quite complicated in the coexisting system of hydrogen and carbon. In addition to Eq.(14), Boudouard reaction (15), Water gas shift reaction (16) and Water gas reaction II (17) will occur simultaneously.

Fig.8 Comparison between BF (Blast furnace) and HF (Hydrogen furnace)

$$C+CO_2(g) = 2CO(g) \qquad\qquad (15)$$
$$CO(g)+H_2O(g)＝H_2(g)+CO_2(g) \qquad (16)$$
$$C+2H_2O(g)＝2H_2(g)+CO_2(g) \qquad (17)$$
$$Fe_xO_y + yCO = xFe + yCO_2 \qquad (18)$$
$$Fe_xO_y + yH_2 = xFe + yH_2O \qquad (19)$$
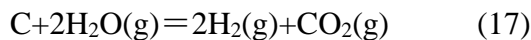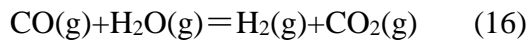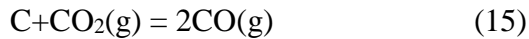
Furthermore, the reduction reactions of iron ore with CO gas and H_2 gas (Eqs.(18) and (19)) are added. The hydrogen reduction is also endothermic reaction and it has a disadvantage in view point of heat balance. However, in such a complicated reaction system, single endothermic reaction never proceeds alone. When the temperature decreases, the rate of endothermic reaction also decreases. There should be some kind of balance with input heat. Moreover, water gas shift reaction (16), which proceeds to the both sides in accordance with the condition, will be a key reaction.

Nogami, et al. demonstrated the possibility of high hydrogen content operation in BF using multi-phase BF simulator[3]. They concluded that the hydrogen can be added until 43% in bosh gas without the decrease of top gas temperature below 100ºC.

The question about the maximum hydrogen content in BF should be solved experimentally. However, as the BF needed a coke (fossil fuel), more or less, even if it was a very good reactor having high efficiency, we should prepare the time when fossil fuels vanish or cannot be used.

The image of iron- and steelmaking in such a circumstance will be a hydrogen furnace (HF) without any coke.

Fig.8 shows the comparison between BF and HF. The coke is a must material in BF and plays important roles which are a medium for gas and liquid permeation, a source of heat and CO gas through the combustion in the raceway and a carbon source for the carburization of metal. The cohesive zone, which will be constructed by the existence of coke layer and the carburization reaction in addition to the softening and melting reaction, also plays an important role for gas distribution throughout the BF. The thinning of cohesive zone through the increase of PCI results in a many difficulties for a BF operation. If we could not use the coke for BF, the BF operation would be impossible and the ironmaking might not exist. As mentioned above, we should prepare the situation when the coke or fossil fuel cannot use. The concept of hydrogen iron- and steelmaking is shown in Fig.8 and explained as follows;

(1) The reduction of iron ore finished around 900ºC by the high reaction rate of hydrogen.
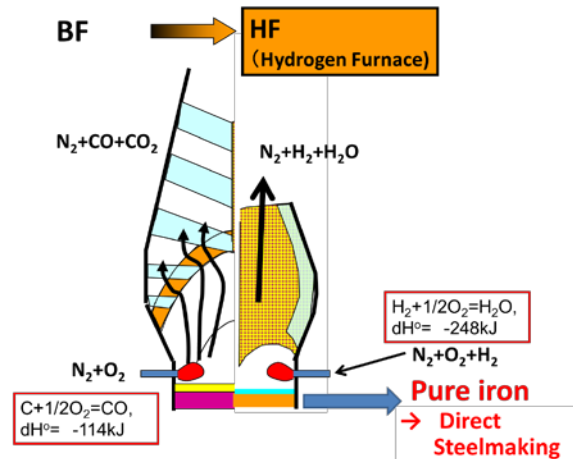
Here, how to prevent the sticking of iron is important research topic not only for the hydrogen ironmaking but also the BF under coke saving operation.

(2) The burden is melted fast by the hydrogen and oxygen combustion which is higher reaction enthalpy than the carbon combustion.

The enthalpy of hydrogen combustion (-284kJ) is twice than the carbon combustion (-114kJ). The theoretical combustion temperature of raceway in modern BF is around 2100°C, on the other hand, the maximum temperature of hydrogen combustion will be around 3800°C to 4000°C. It is desirable condition for increasing the productivity with higher melting ability by hydrogen, however, the extremely high temperature of the hydrogen combustion must be managed not to damage the furnace body and tuyere. The fast melting ability in hydrogen combustion can make the softening and melting zone thinner, which is desirable feature of HF.

(3) Since the productivity increases through a high melting ability of the hydrogen combustion, the height of BF can be lower.

When the height of furnace become lower, the strength of burden can be lower. This is quite important feature under the decrease of resources with high quality.

(4) The obtained metal is a high purity iron without carbon and the inclusions such Si, Mn, S and P.

In this paper, the pure iron obtained by hydrogen reduction was examined. Fig.9 shows the image of hydrogen iron- and steelmaking. It is so called a direct steelmaking. As the iron obtained by hydrogen furnace is quite high purity, the process will only be constructed by deoxidation, carbon addition (or only carbon addition process including deoxidation) and addition of alloying elements, which can be negligible the most of process in the present iron- and steelmaking process.

5. Conclusions

Two kinds of iron ore were reduced and melted both under hydrogen and carbon atmosphere. The obtained iron metal under hydrogen atmosphere was quite pure one. The impurities in the metal were chemically analyzed and thermodynamically examined. The characteristics and benefits of hydrogen reduction were discussed in comparison with the carbon reduction. The obtained results are summarized as follows:

(1) The iron metal obtained by the hydrogen reduction had high purity. The content of silicon was one tenth to the iron obtained by carbon reduction. Manganese was about one third to one tenth for the carbon reduction. However, phosphorus in the hydrogen reduction was almost the same level to the carbon reduction.

(2) The activities of elements (C, Si, Mn, P, S, Al, O, Ca, Mg, H) in iron metal were calculated based on the thermochemical data, and the relationships among those elements were elucidated.

(3) The image of hydrogen furnace was proposed and the possibility of direct steelmaking with hydrogen reduction was suggested under no fossil fuel circumstances.
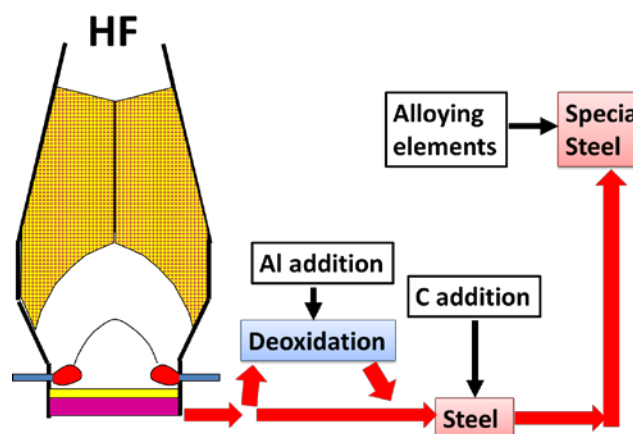
Fig.9 Image of hydrogen iron- and steelmaking (Direct steelmaking).

References:

1. Outokumpu HSC Chemistry for windows, ver.5.1, ISBN 952-9507-08-9, 2002
2. M. Hino and K. Ito: Thermodynamic Data for Steelmaking, The 19th Committee in Steelmaking, The Japan Society for Promotion of Science, 2009, Tohoku University Press, Sendai, 2009.
3. H.Nogami, Y.kashiwaya and D.Yamada: ISIJ International, 52, No.8.
4. Y.kashiwaya and M. Hasegawa: ISIJ International, 52, No.8.

A holistic approach of coke characterization aiming for optimized usage in the blast furnace process

Anrin Bhattacharyya, Johannes Schenk
Montanuniversität Leoben, Austria

Keywords: Coke, Blast Furnace, Characterization, Wetting, Alkali Elements

Abstract: Coke is not only the major source of energy, but also the most cost-intensive raw material for the blast furnace (BF) process. Slight variation in coke properties can cause significant changes in process efficiency and economics. In recent years, the Chair of Ferrous Metallurgy of the Montanuniversität Leoben has tried to develop a holistic approach for coke characterization using traditional as well as novel home-grown testing methods including sophisticated characterization techniques. This work will provide an overview of these testing methods focusing on the behavior of cokes during the process (from shaft to bosh) and also the effect of alkaline elements on coke properties.

1. Introduction

Coke is the major fuel as well as the costliest raw material of the Blast Furnace (BF) ironmaking process. It is not only the major reductant of the process, but it also provides strength to the burden under BF conditions. Total cost of coke is around 60% of the hot metal production and $1/3^{rd}$ of the steelmaking production cost in whole. As the world reserve of coking coal is gradually decreasing and the price of coke increasing steadily, coking coal has been attributed as a 'critical' raw material for ironmaking with high economic importance by European Commission (Figure 1) [1]. Therefore coke, a direct product from coking coals, requires careful investigation of its physical, chemical and mechanical properties for determining its suitability under operational requirements. Minimizing the specific coke consumption per ton of hot metal and maximizing the furnace efficiency are two big challenges for the BF operator.
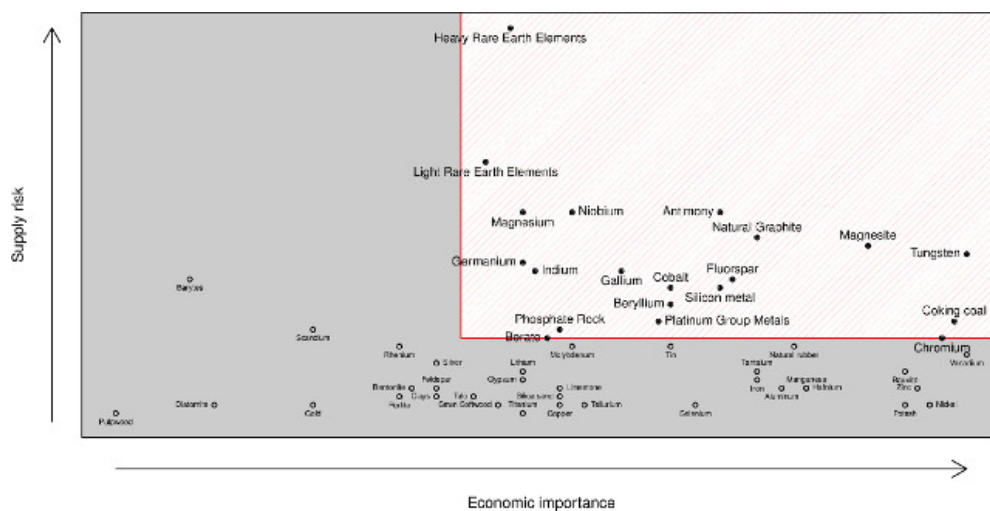

Figure 1: Critical Raw Materials for the EU [1]

In the past few years, the Chair of Ferrous Metallurgy at the Montanuniversität Leoben has tried to demonstrate how it is possible to characterize cokes aiming for a holistic forecast of their behaviors under actual process condition, using a combination of conventional and novel techniques. Apart from the chemical and mechanical properties of coke, its behavior at the simulated conditions of the bosh region of the furnace and the effects of alkaline elements on coke properties have also been investigated. The current work provides a concise overview on this novel holistic approach.

2. Overview of Different Experimental and Characterization Techniques

Coke Reactivity Index (CRI) and Coke Strength after Reaction (CSR) are considered as very important quality parameters for cokes to evaluate their suitability under industrial conditions. The method described in ISO 18894 [2] is used to determine these parameters. For most of the characterization methods, ISO 18894 treatment has been taken as reference. The test parameters such as temperature, gas composition and particle size have also been varied to investigate their effects. Alkaline elements have also been artificially introduced in coke to evaluate their influences. Brief descriptions of all characterization methods applied in this work are described below.

2. 1 Characterization methods

1) Raman Spectrometry – Spectrographic results obtained from various treated and untreated coke were correlated to their CRI/CSR values. It was observed that this method can be a promising tool to forecast on the quality and behavior of cokes under process conditions.

2) Morphological Characterization – Methods such as optical microscopy and petrography provide important information on the morphological properties of coke such as maceral analysis and vitrinite reflectance of coke.

3) Confocal Microscopy – This method has been applied as a novel method for the characterization of surface parameters (e.g. roughness) of coke. This is a powerful tool for 3D visualization of the surface topography.

4) BET Specific Surface Area – This is a completely novel approach to find out the specific surface area of the coke specimens, which has been achieved successfully. The heterogeneity of coke and absence of specific standards in this domain was the main motivation to develop a home-grown standard testing method for coke samples.

5) XRD Analysis – X-Ray diffractometry provides information of the crystallinity and amorphicity of the carbon structure. A turbostratic structure leads to more reactivity of coke by making it more vulnerable to reactive gases during its decent through the shaft. XRD is also useful to determine several crystallographic parameters, such as the domain size (Lc).

6) TEM Analysis – Transmission electron microscopy is a powerful tool to visualize the lattice orientation and crystallinity of graphite in the coke structure.

Methods 5 and 6 have been used for alkali treated samples exclusively.

2.2 Alkali treatment

Alkaline elements such as sodium (Na) and potassium (K) are known to have adverse effects on the blast furnace ironmaking process by catalyzing the Boudouard reaction and reducing the strength of coke in the lower zone of the furnace. In order to achieve a deeper insight on the effects of alkaline elements on coke reactivity and strength, some industrial coke samples impregnated with different alkaline species (Na & K) in various amounts have been tested under standard conditions to find out their CRI and CSR values. A home-grown controlled method is developed to induce external alkali in coke structure. Scanning electron microscopy, petrographic and Raman Spectrometric investigations demonstrate the change of structural properties. The mechanism of catalysis has been postulated in terms of atomic radii [3].

A breakthrough was achieved by TEM analysis of alkali treated and reacted samples. Na and K species have been found to infiltrate in the graphitic structure creating enormous lattice distortion, which is the most probable reason of drastic deterioration of coke properties under the influence of alkaline elements [4].

2.3 Wetting behavior at the bosh region

The physico-chemical phenomena happening in the bosh region of a blast furnace are highly significant in terms of efficient process control. After passing through the stack region, the burden materials reach the bosh zone where softening and melting are initiated. The major exception is coke, as it still remains in its solid state. The viscosity of slags and their tendency for static holdup in the coke bed of the bosh region in a blast furnace plays an important role on the process efficiency by directly influencing the free movement of the burden and furnace gas and thereby affecting the fuel consumption.

The major aim of this method is to find an effective way of using industrial coke specimens directly in the experiments instead of using synthetic graphite, coke analogues or special substrate preparations methods in order to remain as close as possible to actual process conditions. As a further step, to simulate the comparable porous coke structure at the bosh zone (after solution loss reaction), the coke pieces to be used as substrates have been treated under standard CRI conditions .

3. Results and Discussions

Some representative results are discussed in the current chapter.

3.1 Coke reactivity and strength

3 types of industrial cokes supplied by 3 different industries have been used in this work. The proximate results of the cokes are tabulated below (Table 1).

Table 1: Proximate analysis of coke samples (all values are in %)

	C1	C2	C3
Ash	10.70	10.10	9.35
Volatile Matter	0.19	0.37	0.65
Moisture	3.4	3.15	2.04
Fixed Carbon	85.71	86.38	87.96

Strength and reactivity tests of cokes in standard conditions are shown in Table 2.

Table 2: Standard CRI/CSR test results

	C1	C2	C3
CRI (Coke Reactivity Index)	26.65	28.2	30.2
CSR (Coke Strength after Reaction)	58.3	61.0	64.05

3.1.1 Variation of gas composition

Changing the gas composition from the standard condition shows significant changes on the reactivity and strength of coke. Cutting down the CO_2 (Case CO2N2) to half of its amount and introduction of N_2 in the system decreases reactivity. The possible reason is the lowering of the partial pressure of CO_2 (p_{co2}) in the system. Correspondingly, the CRI increases. In the condition CO2H2O, presence of H_2O in the system (20% by volume) increases the reactivity of coke by heterogeneous water gas reaction ($C + H_2O = CO + H_2$), and thus imparting significant increase of the CRI. The changes of CRI and CSR under variable gas compositions are compared in Figure 2 and Figure 3.
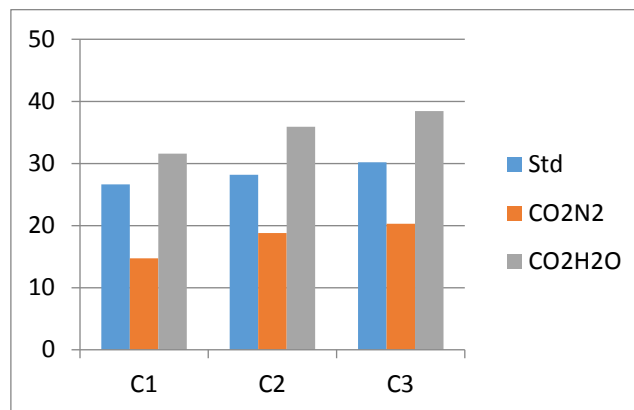

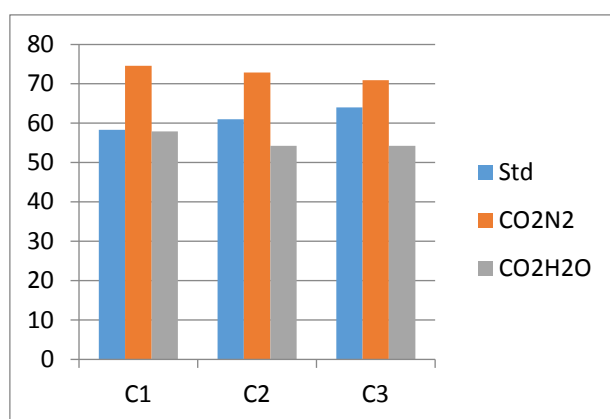**Figure 2**: CRI tests at different gas compositions

Figure 3: CSR tests at different gas compositions

3.2 Raman spectrometry

Raman spectroscopy is a promising method to characterize the microstructure of coke. It extracts a specific signature of a coke lump, which varies in a bulk sample used to estimate coke quality. Carbonacious material (CM) with a poor degree of structural organization characterizes a low-reactive and therefore high-quality coke, whereas better-organized CM is found in a lower-quality coke with a higher reactivity. This finding can be used to predict coke quality by Raman Spectrometry of CM as an alternative to the conventional ISO 18894 (2006) test.

Experiments in a test reactor, simulating the process conditions of iron making, explore the fate of metallurgical coke within a blast furnace by observing the microstructural evolution of the involved organic constituents. In the iron reduction zone of a blast furnace, the poorly ordered organic microstructure is transformed progressively towards a higher structural order. The complete details could be found from Rantitsch et. al [5].

3.3 Confocal microscopy

3D profilometry using confocal microscopy is a common tool for surface and corrosion engineers. In this method, a 3D profile of the surface could be constructed using reflected light. But, no available literature was found till date on the characterization of coke using this technique in the best of author's knowledge. It will be indicated later that the surface roughness and porosity of reacted coke greatly affect its wetting behavior and slag hold up in the bosh zone of the blast furnace. The important surface parameters have been measured and compared for both untreated and CRI tests treated samples. All the samples exhibit strong changes of their surface properties after treatment under CRI. It is observed that the surface roughness and valley depth increases significantly after reaction. This phenomenon in turn should give rise to higher specific surface area and pore volume of the coke sample. A new parameter called RMS Roughness Multiplicator (RRM) has been defined to indicate the proportional change of RMS roughess caused by the reaction. RRM is proportional to CRI (Figure 4).
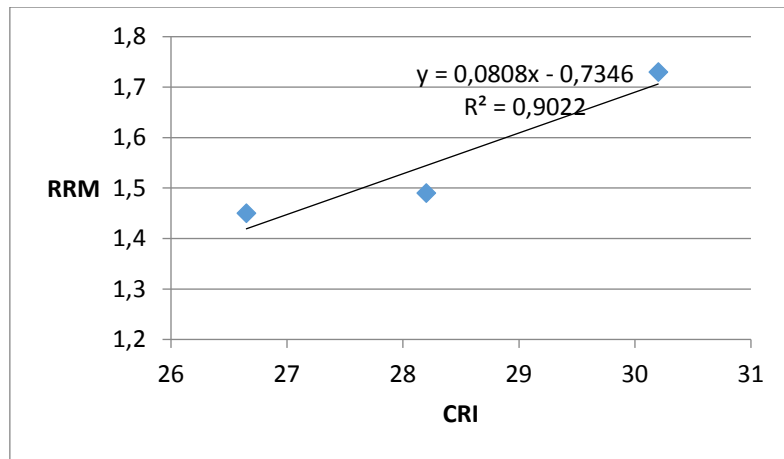
Figure 4: RRM against CRI

The 3D surface topographies of C1 for parent sample and standard treatment are shown in the following figures (5 and 6).
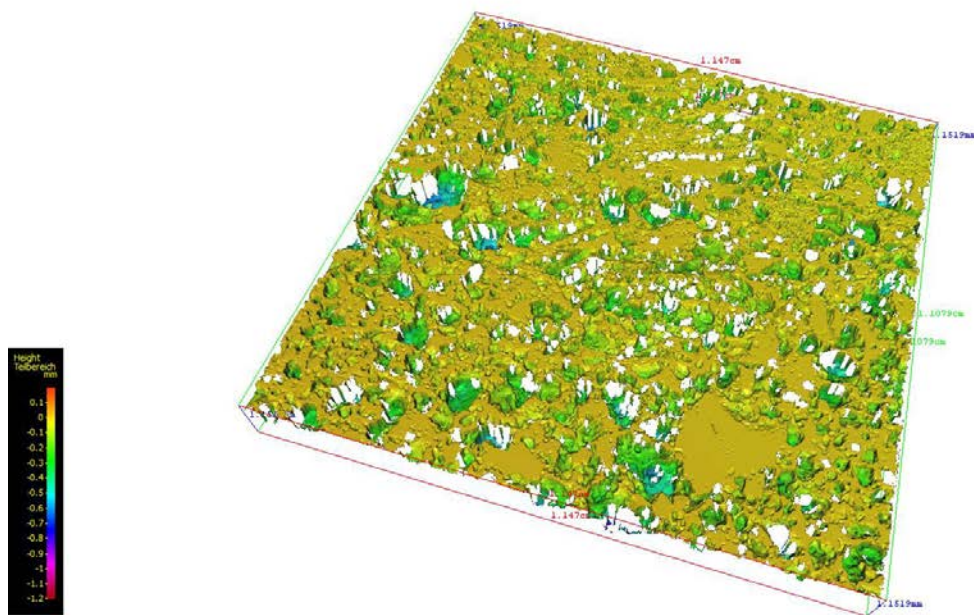
Figure 5: C1 - Untreated
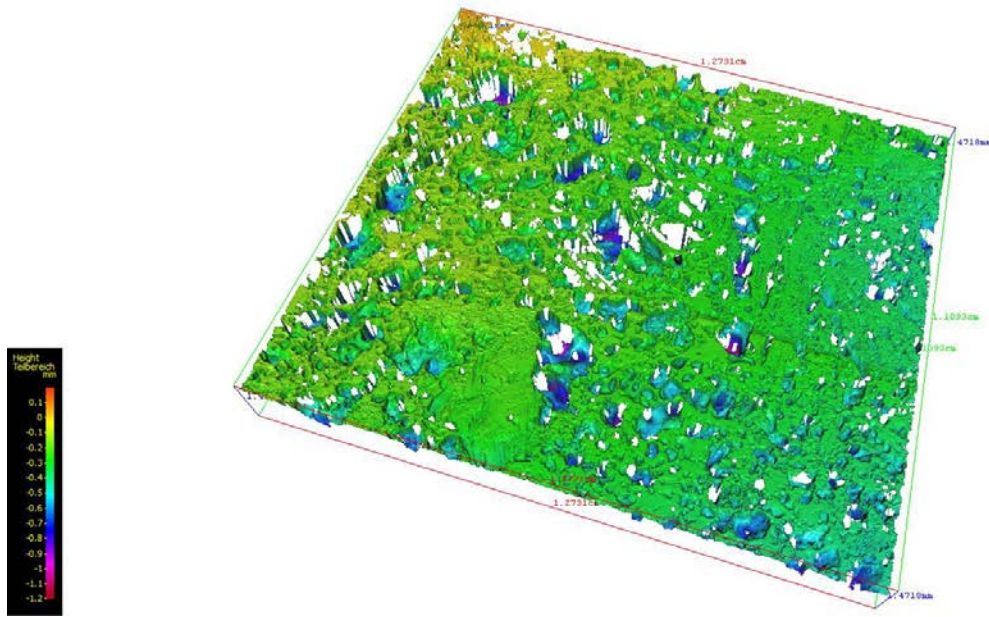
Figure 6: C1 - Standard CRI treatment

The topographic images are quite self-explanatory in nature. The change of the pore structure caused by Boudouard reaction could be evidently observed. The profile pictures obtained from the confocal microscopy also show the pore deepening phenomenon caused by CRI test.

3.4 BET and BJH method

3.4.1 Defining the appropriate particle size

Four particle size ranges from C1 were selected for testing to determine the variation of specific surface area with particle size. The result is shown in Figure 7. The BET surface area varies inversely to particle size. Also, interestingly, the standard deviation of BET values is much higher in the bigger particle size range (indicated by the small bars at every point). The reason behind this could possibly be the higher inhomogeneity in bigger particles corresponding to the smaller particle size. For this reason, particles having size range less than 0.25 mm have been selected for further tests.
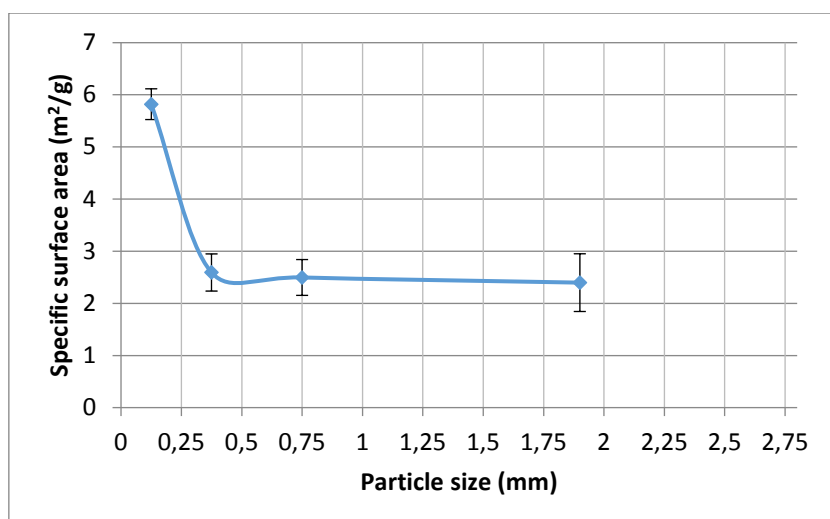
Figure 7: Particle size vs. specific surface area (sample C1)

3.4.2 BET results

The BET surface areas of all samples (before and after CRI tests) were measured using the method described by Bhattacharyya et al [6] using particles less than 0.25 mm in size. The BET surface area increases around 3 times after reaction for all cases (Table 3).

Table 3: BET results

Sample	BET Surface Area in m^2/g (Untreated) (A)	BET Surface Area in m^2/g (Treated) (B)	Surface Area Multiplicator (=B/A)	Corresponding CRI (or ChRI)
C1	5.82	18.35	3.15	26.65
C2	4.01	11.75	2.93	28.20
C3	3.51	11.53	3.28	30.20

3.4.3 BJH Tests

The analysis of cumulative pore area and volume by BJH method is much more complicated compared to BET and the tests are highly time consuming. The isotherm shapes confirm that coke and char consist of mainly meso and macropores and therefore, BJH method could be applied to them. BJH tests of selected samples have been performed. Figure 8 shows a typical isotherm for the adsorption and desorption curve of C2 (untreated).
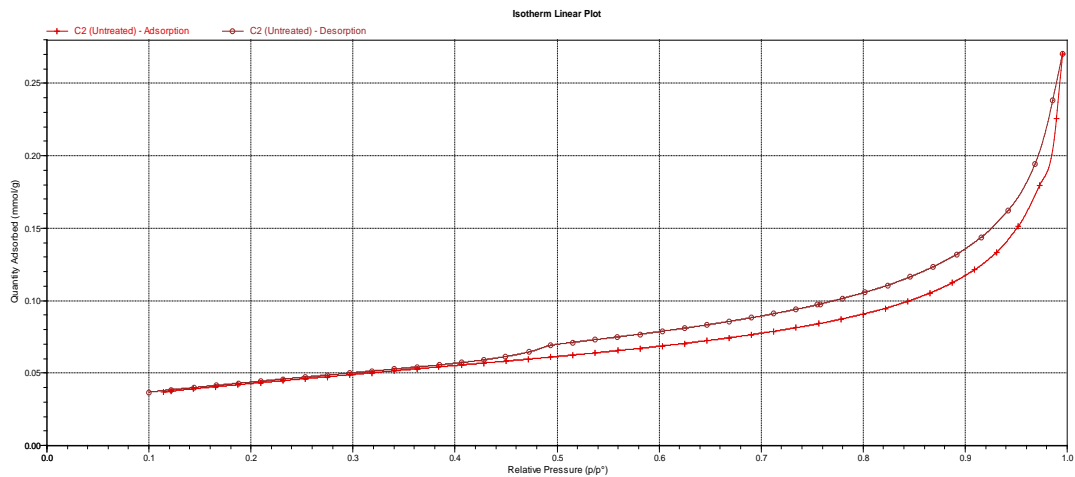
Figure 8: Adsorption and desorption isotherm of C2 (untreated)

The plot shows very less hysteresis during desorption, which indicates that the structure consists of very large pores. For most of the tests, the desorption-curve will be used for evaluation, as desorption process is considered to be an equilibrium process in terms of gas-solid interactions. The pore width or size, when plotted against pore volume or pore area both ordinarily and differentially, provides the value of the pore diameter which consists of the largest pore volume or area in the sample. From Figure 9 and Figure 10, it is observed that the largest part of the pore volume and area consists of 39 Å diameter pores.
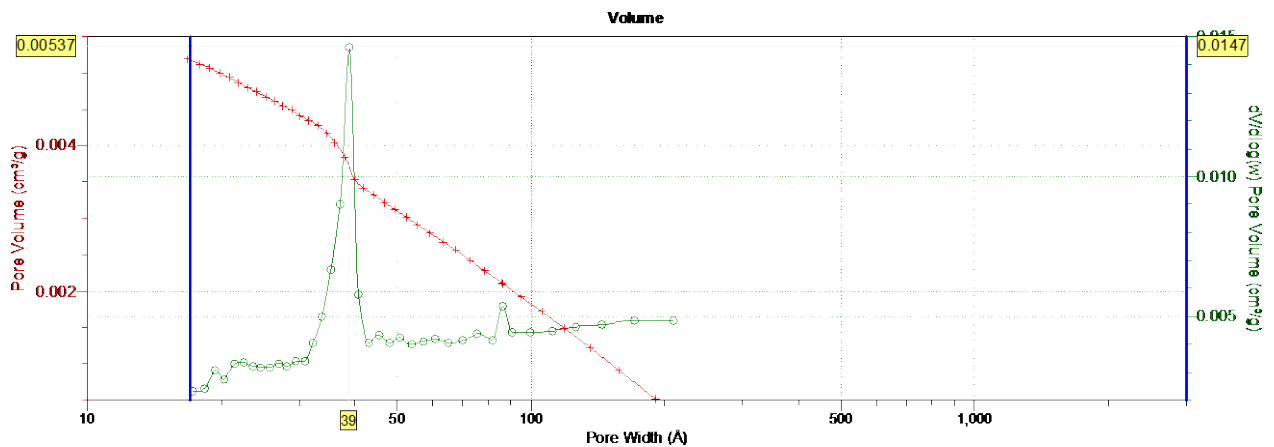
Figure 9: Pore width vs. pore volume (C2, untreated)
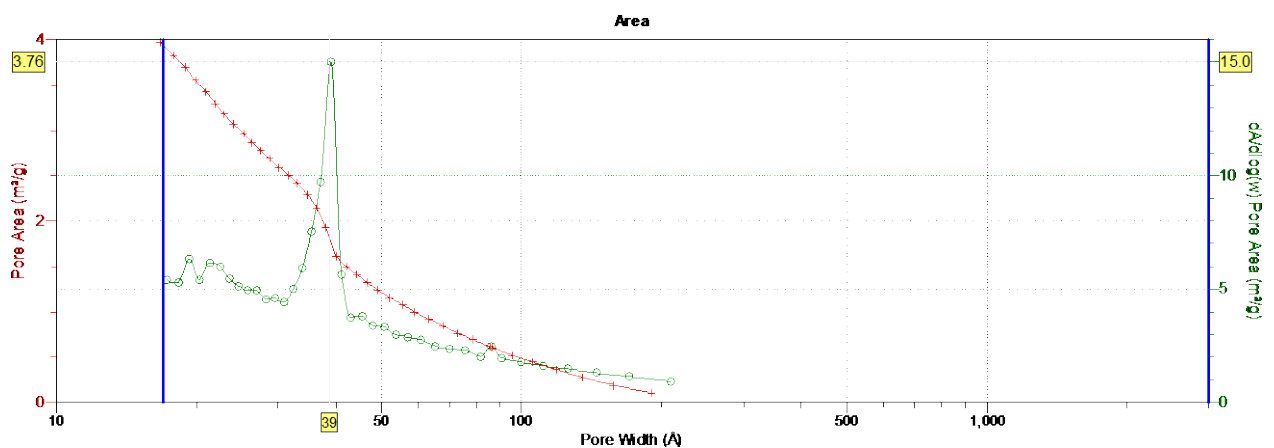
Figure 10: Pore width vs. pore area (C2, treated)

Table 4 shows some typical values obtained from BJH analysis of C2 and C3.

Table 4: BJH test results

Sample		Total Pore Volume (cm^3/g) at 0.995 relative pressure	Average Pore Width (Å)	Cumulative Surface Area of pores between 17 Å and 3000 Å (m^2/g)	Pore width consisting largest part of pore volume and area (Å)
C2	Untreated	0.00932	56.619	3.4802	39
	Treated	0.01634	44.537	8.6136	36
C3	Untreated	0.00902	58.422	3.9833	40
	Treated	0.01461	43.817	7.5902	36

The above results exhibit an interesting trend in surface properties due to CRI treatment. The total pore volume and cumulative surface area are increased. The average pore width has decreased, which may happen due to the higher ash content after reaction. However, more experiments will be done in future to find out the correlation between BET and BJH properties and their relation to reactivity.

3.5 Effect of alkaline elements

The presence of even a very little amount of alkaline elements in coke increases the CRI and decrease CSR enormously. Different characterization techniques were used to find out the effect of alkali elements on the structure.

3.5.1 SEM/EDX

SEM/EDX analyses of various alkali treated samples (after reaction) show fused aggregates (complex oxides) of alumina and silica containing Na and K, frequently scattered over the coke matrix. This type of structure is not observed in reacted samples without additionally added alkali. These aggregates have been generated by local fusion of the ash (which consists of basically alumina and silica) caused by alkaline oxides (by lowering the melting point). The phases ($NaAlSiO_4$ and $KAlSiO_4$) have been confirmed by X-Ray Diffractometry (XRD) of reacted alkali treated samples. Figure 11 shows a microscopic image of reacted and potassium treated coke sample.
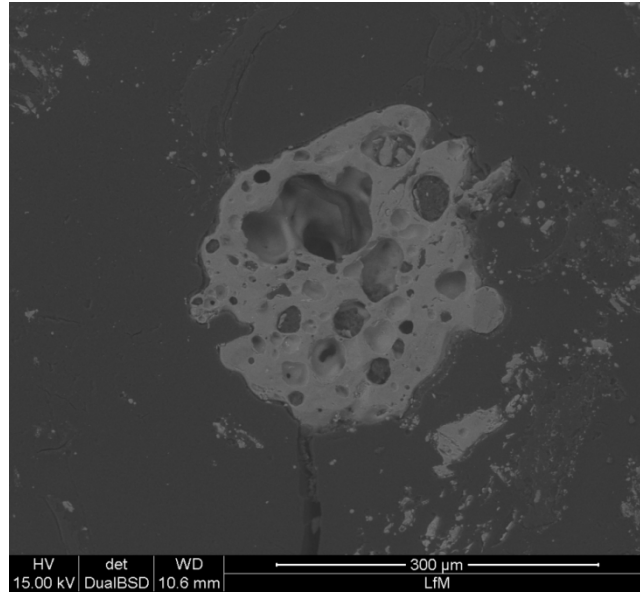
Figure 11: SEM image showing fused aggregate on the dark coke matrix (potassium treated and after reaction)

Apart from mechanical weakening, alkali treated and reacted coke samples generate a lot of fines during tumbling. All of these phenomena can be explained as a result of local fusion caused by lowering of the melting temperature of the ash phase by alkaline elements which may generate internal stress in the structure and subsequently make the structure weak.

3.5.2 X-Ray Diffractometry

The X-Ray diffractograms of the treated samples do not show any stable or metastable intermediate catalytic phases. Instead, the results indicate intensity peaks corresponding to complex oxides in the form of $KAlSiO_4$ and $NaAlSiO_4$ (respectively for K and Na treated samples), which might have resulted by the interaction between the ash phases in coke and alkaline oxides at high temperature. The hump around 25° is very characteristic of distorted graphite (high amorphicity). A diffractogram of C3 treated with K is shown in Figure 12.
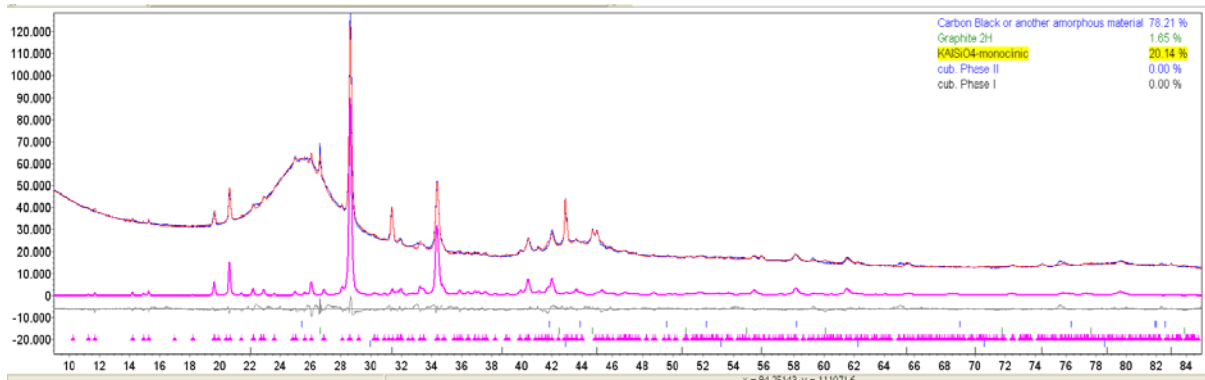
Figure 12: Diffractogram showing matching peaks of KAlSiO4

3.5.3 TEM Analysis

TEM analysis was also performed to investigate the effect on alkaline elements on the lattice structure of coke. The untreated coke structure consists of misaligned and crystalline graphite (Figure 13) which is comparatively disorientated by normal CRI treatment (without added alkali, not shown in figure). However the reacted and alkaline treated samples show a significantly distorted turbostratic graphitic structure surrounding alkali bearing particles (Figure 14). The EDX data confirm the presence of alkaline particles in the structure.
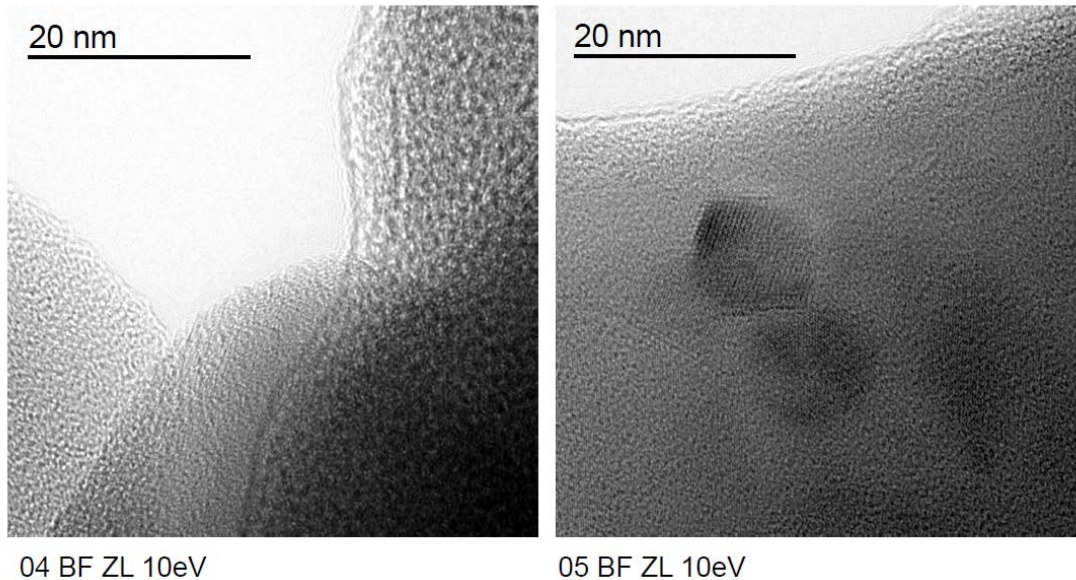
Figure 13: Left - turbostratic graphite lattice in parent coke, Right - presence of crystalline hexagonal graphitic lattice in the parent coke structure
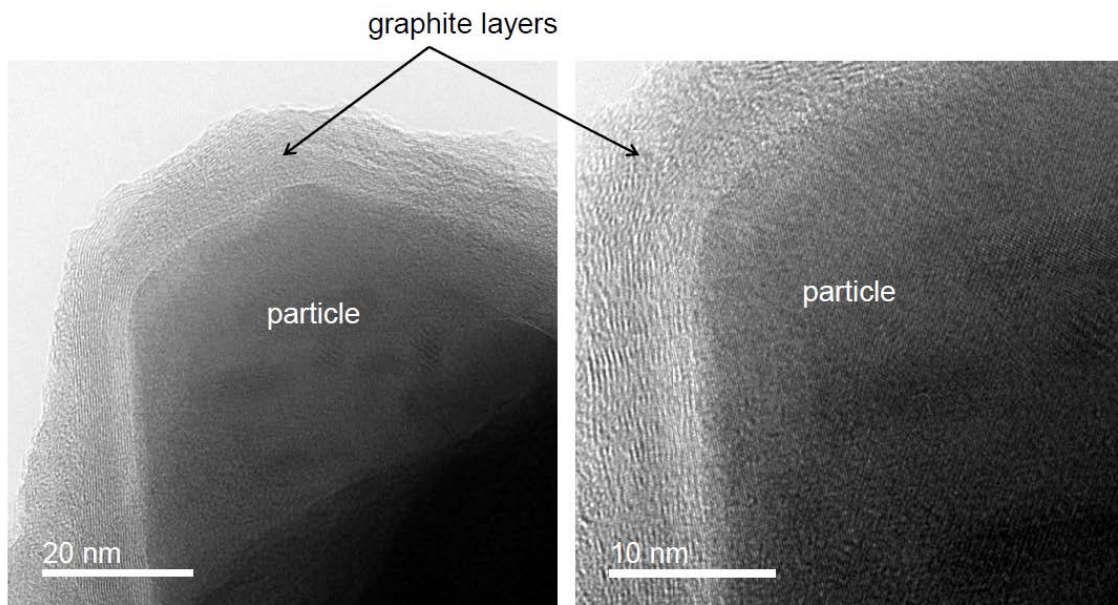
Figure 14: TEM images of C3 treated with K showing misaligned graphite layers oriented around an alkali bearing particulate component in the structure in two different magnifications. Note the turbostratic nature of the graphite lattice.

The possible mechanism of the catalysis of Boudouard reaction can be explained by the theory of ionic radii. The ionic radius of carbon is much smaller than that of sodium or potassium (Table 5).

Table 5: Effective ionic radii [7]

	Effective Ionic Radii (in Å)		
Elements	**Na^+**	**K^+**	**C^{4+}**
Ionic Radii	**1.02**	**1.38**	**0.16**

The TEM analysis depicted significant structural distortion of graphite layers under the influence of alkaline elements. It can be explained in terms of pronounced lattice disturbance at higher temperatures (1100^oC and above), which is possibly caused by the rapid diffusion of Na or K in the graphite crystal system (which has much lower atomic radius) followed by consequent expansion and distortion of the unit cells. This process of distortion caused by rapid diffusion of alkali atoms is likely to cause the higher reactivity and weakening of the carbon structure. This work is an important step to establish the theory of ionic radii as the reason behind the deterioration of coke properties under the influence of alkaline elements. Further research should be performed in future with a much broader scope for the advancement of understanding in this domain.

3.6 Wetting behavior analysis

Bhattacharyya et al [8,9] described an experimental method of simulating the wetting behavior between coke and slag/hot metal under the conditions of the bosh region of a blast furnace. More details could be obtained from the aforementioned publication. From these experiments, it can be inferred that cokes with lower reactivity values show more wettability at higher temperature than cokes with higher CRI values. In parallel, it can be also concluded that slags with low viscosity (i.e. high fluidity) show complete wetting at lower temperature. So, given a combination of a high CRI coke along with a low viscosity slag, it will show full wetting at a much lower temperature and vice-versa. It can also be noted that although apparently C2 and C3 exhibit the same behaviour, but the spreading of the slag drop on the coke surface and sinking temperature are different in all cases.

Many pores in a coke structure are long and interconnected. In one experiment, pictures acquired from the DST instrument show a slag droplet sinks inside the coke substrate in one area and little later oozes out from another part of the coke sample (Figure 15). Long interconnected pores inherent to the coke structure are broadened after CRI treatment and can hold some slag in the lumps.

(a)

(b)
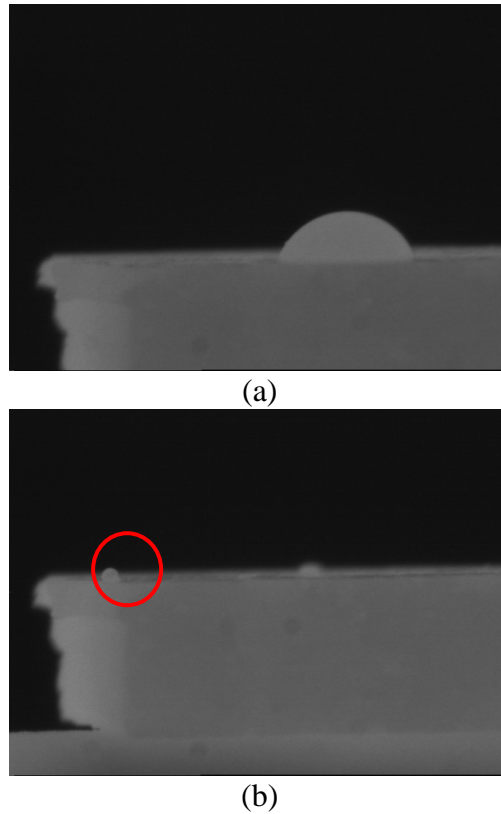
Figure 15: C2/Slag II combination, Temperature - approx. 1570ºC, (a) The slag droplet just before sinking, (b) After ca. one minute, tiny droplet oozing out from surface (marked with red)

4. Conclusion and Outlook

The foremost aim of this work would be to characterize coke from its parent form (as it is charged in the BF) tracing onwards all the to the bosh region. In the beginning, the reader might be prone to think about the defined experiments to be quite divergent. Apparently, they do not correspond immediately to the reader's mind. However, a closer observation will prove that the experiments are highly interconnected and they complement each other. Actually, they encompass the whole flow of material of carbon carriers right from the parent state to the end of the bosh region in blast furnace or melter-gasifier. Figure 16 (basic figure courtesy Zukor and Jastrzebski) depicts schematically the coverage area of all work packages for cokes.
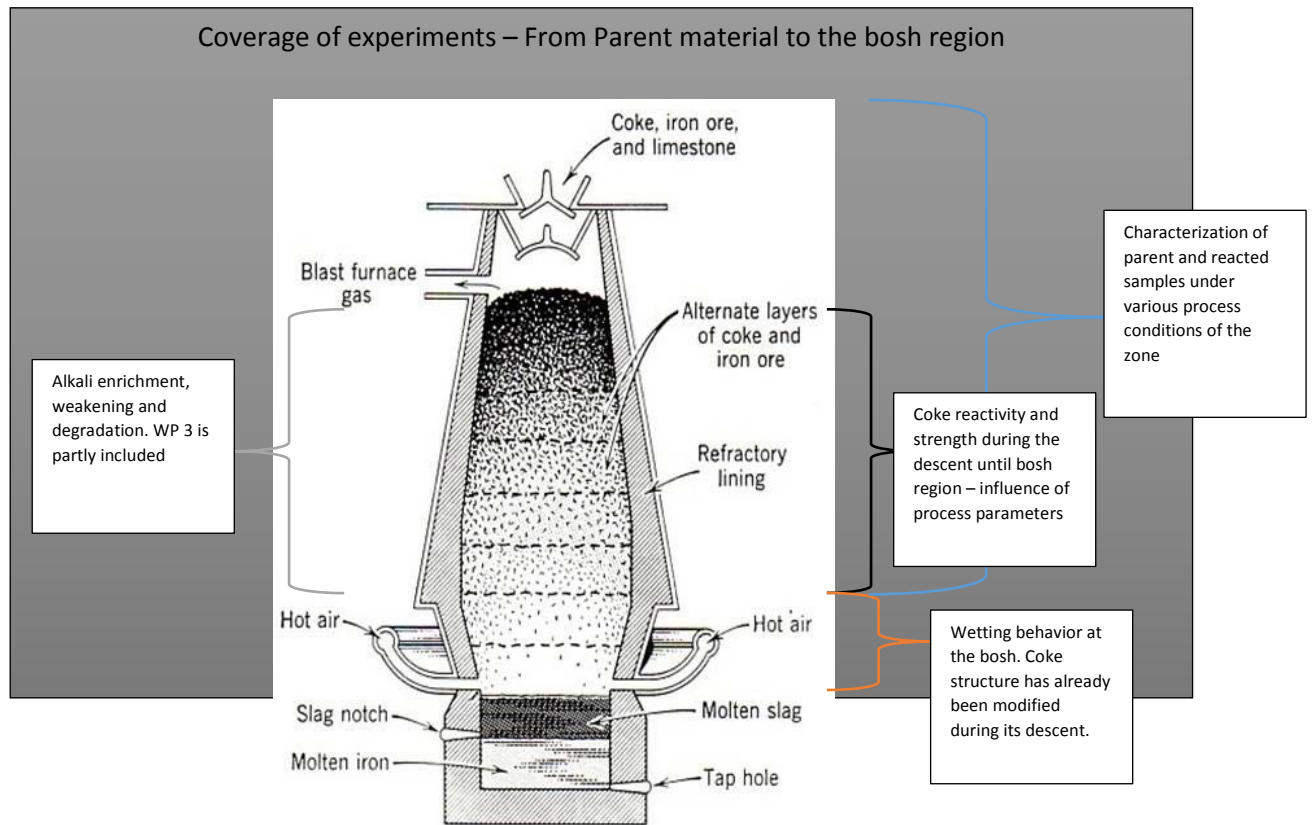
Figure 16: Scope of the experiments

This holistic approach of coke characterization throws a new light on the structure-property relationship of coke under blast furnace conditions. This approach does not only provide a comprehensive technique of coke characterization, but also leads to a quality forecast under operative conditions. However, knowledge never stops and there are always possibilities of exploring deeper and deeper into the concerned domain. In future, this work will be carried forward with a larger sample set and actual tuyere coke samples. A mathematical modelling of the wetting behavior will also be attempted for better understanding.

References:

1) http://ec.europa.eu/enterprise/policies/raw-materials/critical/index_en.htm (acquired on Oct. 2016)

2) ISO 18894: Coke -- Determination of coke reactivity index (CRI) and coke strength after reaction (CSR)

3) Bhattacharyya, A., Schenk, J., Rantitsch, G., Thaler, C. & Stocker, H., *Effect of alkaline elements on the reactivity, strength and structural properties of blast furnace cokes*, 2015, Metalurgija 54(3), p. 503-506

4) Bhattacharyya, A., Schenk, J., Letofsky-Papst, I. & Albering, J., *Effect of Alkaline Elements on Coke Structure under Blast Furnace Process Conditions,* May 2016, Metal 2016, Brno

5) Rantitsch, G., Bhattacharyya, A., Schenk, J. & Lünsdorf, K., *Assessing the quality of metallurgical coke by Raman Spectroscopy*, 2014 In : International journal of coal geology. 130, p. 1-7

6) Bhattacharyya, A., Schenk, J., Thaler, C. & Stocker, H., *Determination of the specific surface area of cokes and chars for simulated process conditions of blast furnace and smelting reduction routes,* Jun 2016 SCANMET V Proceedings, Lulea

7) Shannon, R. D.: *Revised effective ionic radii and systematic studies of interatomic distances in halides and chalcogenides*, Acta Crystallographica Section A 32 (1976), Nr. 5, S. 751–767

8) Bhattacharyya, A., Schenk, J., Arth, G., Stocker, H. & Thaler, C., *Experimental Analysis of the Interfacial Wetting Phenomena Between Slag and Coke Surface Under Simulated Conditions of the Bosh Region of Blast Furnace*, 4 May 2015, AISTech 2015 & ICSTI Proceedings, Cleveland

9) Bhattacharyya, A., Schenk, J., Jäger, M., Stocker, H. & Thaler, C., *Experimental Simulation of the Interaction of Slag and Hot Metal with Coke at the Bosh Region of Blast Furnace*, Dec 2016 In : Berg- und hüttenmännische Monatshefte : BHM. p. 1-6

Halogen Chemistry in Coal Utilization

Naoto Tsubouchi

Center for Advanced Research of Energy and Materials, Faculty of Engineering, Hokkaido University

Abstract: Pyrolysis of five types of coal with carbon contents of 73–92 wt%-daf has been performed via a temperature-programmed process by heating to 800 °C at 10 °C/min in a flow-type fixed bed quartz reactor to investigate the factors that control HCl formation. The profiles for the HCl formation rate depend strongly on the coal type, giving at least 4 distinct peaks at 280, 330, 470, and 580 °C, with the last one being common to all coal types studied. The yields of HCl at 800 °C for all the coals examined reach 60–90%, whereas the char-Cl yield is < 35% in every case. The HF yield is only < 5%, irrespective of the type of coal. These results indicate that coal-Cl is predominantly converted to HCl at temperatures up to 800 °C, and that coal-F is more stable thermally than coal-Cl. Notably, the HCl yield has no distinct relationship with the C, Cl, Na, or Ca content of the coal. When $CaCl_2 \cdot 6H_2O$ and $NaCl \cdot nH_2O$ impregnated on activated carbon or organic hydrochloride mixed physically with the carbon are pyrolyzed in the same manner as described above, the main HCl formation peak appears at 300 °C for the $CaCl_2$, 350 °C for the NaCl, and 270 °C for the hydrochloride. Washing Australian bituminous coal with water eliminates the observed HCl peak almost completely at 280 °C and lowers its formation at 280–370 °C, though the rate at $\geq$ 450 °C remains essentially unchanged. These observations indicate that the HCl formed at $\leq$ 370 °C originates from water-soluble inorganic chlorides and/or organic hydrochlorides; thus, the chlorine functionality in coal is one of the key factors that determine the temperature dependency of HCl formation. A method to quantitatively evaluate the functional forms of Cl using model chlorine compounds is proposed. HF formation from char occurs significantly during combustion, and the concentration increases considerably after the carbon in the char is apparently burned out.

1. Introduction

The chlorine present in coal (coal-Cl), which usually ranges from 100 to 3000 μg/g-dry[1], is released as hydrogen chloride (HCl) during pyrolysis, combustion, and gasification. As well-known, HCl formation is closely connected with the emissions of alkali metals and mercury. In an integrated gasification combined cycle that is expected to achieve high power generation efficiency, the evolved HCl causes corrosion problems on gas turbine materials and deteriorates the fuel cell's performance[2]. It is therefore important to examine the key factors controlling the formation of HCl. However, few papers on this topic have been reported[3-5].

In this work, I have focused on studying the dynamic behavior of HCl evolved during coal pyrolysis that inevitably occurs before char gasification. For this purpose, the HCl is monitored online. The relationship between the rate profile and the chlorine functionality in the coal is the primary purpose of this investigation.

2. Experimental

Five coals with different ranks from selected countries were examined in this work. All of the samples were air-dried at room temperature, ground, and sieved to coal particles with size fractions of 40–60 or 150–250 μm. Elemental and proximate analyses of all the coals are shown in Table 1.

Pyrolysis runs were performed in a temperature-programmed mode within a fixed-bed quartz reactor. The details of the apparatus have been described elsewhere[6]. Approximately 2.5 g of the dried sample

was first charged in a quartz-made cell in the reactor. The air in the entire system was then replaced completely with high-purity N_2 (> 99.9995%). Finally, the reactor was heated at 10 °C/min up to 800 °C in the N_2 flow (500 cm^3 (STP)/min). HCl and HF in the effluent were measured online with an IR analyzer and with a fluoride ion selective electrode, respectively. The chlorine in the char, denoted as char-Cl, was determined by absorption spectrophotometry using an aqueous solution of Cl-containing gas obtained by burning the char at 1350 °C. The yields of HCl and char-Cl were expressed in percent of the total chlorine in the feed coal. When the pyrolysis was repeated for a given coal sample, the reproducibility was within $\pm$ 5% for HCl and $\pm$ 4% for char-Cl.

To analyze the mineral compositions of the coal types, the samples were first burned at 815 °C to form an ash, which was then completely dissolved in an aqueous solution of aqua regia and HF at 115 °C. Eight cations (i.e., Na, Mg, Al, Si, K, Ca, Fe, and Ti) in the solution were determined by inductively coupled plasma emission spectrometry.

Table 1. Elemental and proximate analyses of five types of coal

Coal	Country[a]	Elemental analysis (wt%-daf)						Proximate analysis (wt%-dry)		
		C	H	N	S	Cl	O[b]	Ash	VM	FC[b]
HGI	VIE	91.5	3.4	1.3	0.55	0.021	3.2	10.2	4.7	85.1
YRB	AUS	89.5	3.7	2.0	0.78	0.14	3.9	9.8	7.3	82.9
CNZ	CHI	88.4	4.1	1.7	0.44	0.044	5.3	15.0	9.4	75.6
DRT	AUS	79.7	5.3	1.9	1.3	0.029	11.8	12.4	32.8	54.8
MBW	USA	73.4	5.2	1.6	0.43	0.044	19.3	4.3	38.0	57.7

[a]USA, United States of America; AUS, Australia; CHI, China; VIE, Vietnam. [b]Estimated by difference.

3. Results and discussion

Figure 1 shows the rate profiles of HCl formation during the temperature-programmed pyrolysis of the YRB, DRT, and CNZ coals. With the YRB coal, HCl started to evolve at 210 °C, and the profile gave a large, asymmetrical peak at 210–450 °C and a smaller one at 580 °C. By comparison, the formation of HCl from the DRT coal started at approximately 350 °C and showed the main and shoulder peaks at 470 and 580 °C, respectively. The CNZ coal had a small, broad peak at 450–750 °C, whereas the MBW and HGI coals gave maximal rate values at 470 and 580 °C, respectively. In other words, HCl formation depended strongly on the coal type, though the peak at 580 °C was present for all of the samples examined.
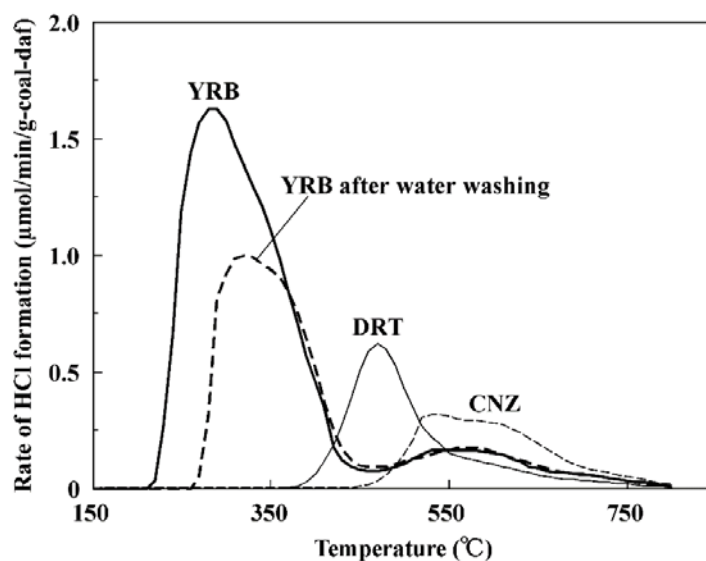

Figure 1. HCl formation in the temperature-programmed pyrolysis of selected coal types.

The evolution of HF started at around 300°C in every case, and the profile exhibited a small peak at 400°C and a large peak at about 680°C. HF yield was as small as < 5%, irrespective of the kind of coal. These results point out that coal-F is not readily released as HF during pyrolysis but rather retained in the char.

As estimated by integrating each profile depicted in Figure 1, the yield of HCl at 800 °C is summarized in Table 2, where the sodium (Na%) and calcium (Ca%) contents, expressed in wt% on a dry coal basis, are also provided. The yields were 86, 80, 61, 89, and 69% for the MBW, DRT, CNZ, YRB, and HGI coals, respectively, and the yield of char-Cl was < 35% in every case. No appreciable amount of Cl_2 was detectable, irrespective of type of coal. Thus, the chlorine mass balances fell within the reasonable range of 95–103%. This means that coal-Cl is converted predominantly to HCl at ≤ 800 °C. As shown in Table 2, there is no clear relationship between the Na% or Ca% in the coal and the HCl yield.

Table 2. Na and Ca contents in coal and the corresponding HCl yields at 800 °C

Coal	Content (wt%-dry)		HCl yield[a] (%)
	Sodium	Calcium	
HGI	0.043	0.03	69
YRB	0.10	0.26	89
CNZ	0.001	0.18	61
DRT	0.014	0.54	80
MBW	0.012	0.41	86

[a]Average value of the repeated experiments.

Figure 2 illustrates the HCl yield as a function of the coal carbon (C%) and chlorine (Cl%) content. No distinct correlation between the yield and C% or Cl% was observed. These observations indicate that the C%, Cl%, Na%, or Ca% contents in the coals do not greatly influence the HCl yield.
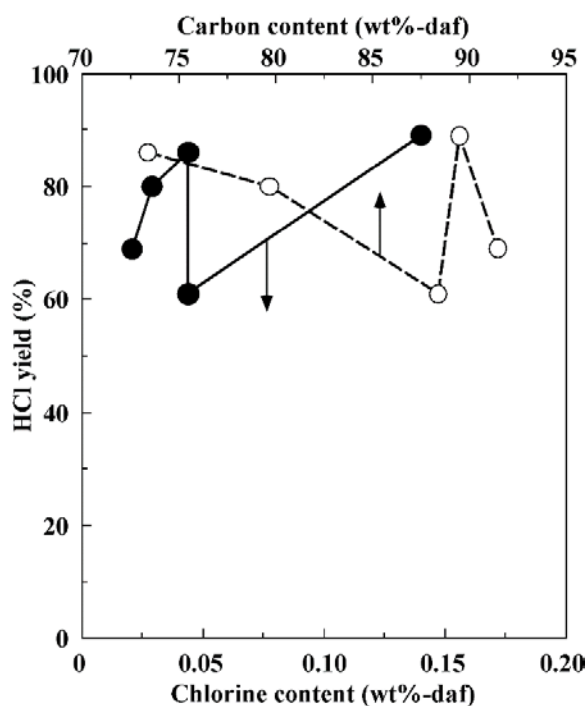

Figure 2. Influence of the carbon and chlorine contents in coal on the HCl yield at 800 °C.

The results noted above strongly suggest that the behavior of HCl formation during pyrolysis is closely connected with the distribution of chlorine functional groups in the coal. It has been reported that the

chlorine in American bituminous coal is present mainly as water-soluble inorganic chlorides such as $CaCl_2 \cdot 6H_2O$, $NaCl \cdot nH_2O$, and organic hydrochlorides[7]. In order to clarify the chlorine release from these compounds, they were first mixed with activated carbon to provide the samples with 0.2 wt% of Cl and then pyrolyzed in the same manner as described above. The results are summarized in Table 3. The $CaCl_2 \cdot 6H_2O$- and $NaCl \cdot nH_2O$-impregnated carbon provided the main peaks of HCl formation at 300 and 350 °C, respectively, whereas the physically mixed organic hydrochloride (tetracycline hydrochloride) gave a maximal rate value at 270 °C. As shown in Figure 1, these peak temperatures correspond to the large, asymmetrical peak observed for the YRB coal.

Table 3. HCl formation from the chlorine compounds added to activated carbon

Model compound	Chemical composition	Loading method	Peak temperature[a] (°C)
Tetracycline hydrochloride	$C_{22}H_{24}N_2O_8 \cdot HCl$	Physical mixing	270
NaCl hydrate	$NaCl \cdot nH_2O$	Impregnation[b]	350
CaCl2 hydrate	$CaCl_2 \cdot 6H_2O$	Impregnation[b]	300

[a]Average value of the repeated experiments.
[b]Followed by water removal at room temperature.

To examine whether or not these water-soluble chlorine compounds are actually present in the YRB coal, the coal was first soaked overnight in high purity water and then dried under vacuum at room temperature. The chlorine content after water washing decreased from the original value of 0.14 wt%-daf to 0.11 wt%-daf, and the extent of chlorine removal was approximately 20%. As shown in Figure 1, when the washed YRB coal was pyrolyzed, the HCl peaks at 210–280 °C almost disappeared, whereas those at 280–370 °C diminished; however, the rate at ≥ 450 °C was not changed significantly. A comparison of the profiles before and after washing the YRB coal with water suggests that the HCl peak observed at ≤ 450 °C for the original coal consists of at least two different peaks at approximately 280 and 330 °C. It is likely that the HCl formed at ≤ 370 °C arises from water-soluble inorganic chlorides and/or organic hydrochlorides.

In order to quantitatively evaluate the chlorine functionality in the original YRB coal, the rate profile for HCl formation was deconvoluted into $CaCl_2 \cdot 6H_2O$, $NaCl \cdot nH_2O$, and organic hydrochloride by a curve-fitting method using Gaussian peak shapes. The results are provided in Figure 3. The proportion of each chlorine type was estimated to be 35% for the CaCl2, 31% for the NaCl, 25% for the hydrochloride, and 9% for other compounds. At present, the sources for the HCl peaks observed at ≥ 450 °C are unknown, but chlorine species other than those mentioned may be present.
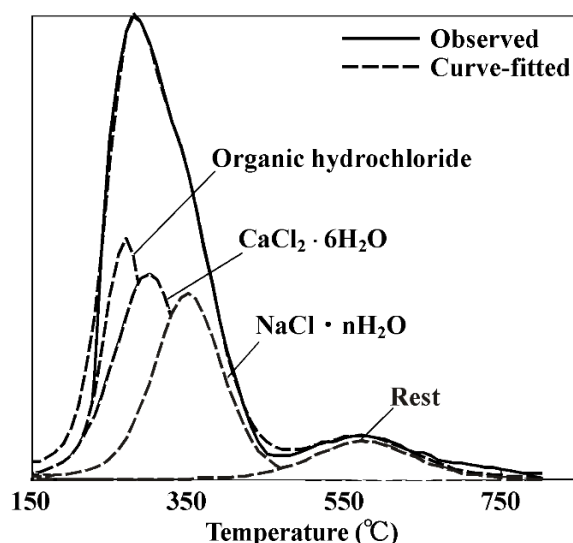

Figure 3. Deconvolution of the profile for HCl formation from the original YRB coal.

The concentration of HF or CO_2 evolved in the combustion process of YRB char after pyrolysis has been investigated. CO_2 formation started around 350 °C, and the concentration increased with increasing temperature, but it decreased during holding the sample at 1000 °C. Total amount of the CO_2 released corresponded to about 95% of the carbon present in the char. On the other hand, HF formation occurred predominantly after apparently complete release of CO_2, and the yield after 8 h soaking at 1000 °C was approximately 50%. On the basis of the above results, it can be speculated that coal-F exist mainly as mineral matters, and most of the F is retained at the carbon in ash after combustion. The accumulation of coal-F in fly ash during pulverized coal combustion has been suggested[8].

4. Conclusions

The formation of HCl during the temperature-programmed pyrolysis of five types of coal depends on the type of coal studied; at least four distinct peaks were observed at 280, 330, 470, and 580 °C. 60–90% of coal-Cl was released as HCl up to 800 °C, whereas HF yield was only < 5%, irrespective of the type of coal. No significant relationship was observed between the HCl yield and the C%, Cl%, Na%, or Ca% in the coals. It is likely that the formation of HCl observed at 210–370 °C arises from water-soluble inorganic chlorides and/or organic hydrochlorides. A curve-fitting method using model chlorine compounds was proposed to quantitatively describe the chlorine present in the coal. HF formation from char proceeded significantly during combustion, and the concentration increased considerably after the carbon in the char was apparently burned out.

References:
1) Davidson R. M. *Chlorine and Other Halogens in Coal.* IEAPER/28, IEA Coal Research, London, 1996.
2) Mitchell S. C. *Hot Gas Cleanup of Sulfur, Nitrogen, Minor and Trace Elements.* IEACCC, IEA Coal Research, London, 1998.
3) Herod A. A., Hodges N. J., Pritchard E., Smith C. A. Mass spectrometric study of the release of HCl and other volatiles from coals during mild heat treatment, *Fuel*, 62 (1983), 1331-1336.
4) Shao D., Hutchinson E. J., Cao H., Pan W-P. Behavior of chlorine during coal pyrolysis, *Energy Fuels*, 8 (1994), 399-401.
5) Quyn D. M., Wu H., Li C-Z. Volatilization and catalytic effects of alkali and alkaline earth metallic species during the pyrolysis and gasification of Victorian brown coal. Part I. Volatilization of Na and Cl from a set of NaCl-loaded sample, *Fuel*, 81 (2002), 143-149.
6) Wu Z., Ohtsuka Y. Nitrogen distribution in a fixed bed pyrolysis of coals with different ranks: formation and source of N_2, *Energy Fuels*, 11 (1997), 477-482.
7) Huggins F. E., Huffman G. P. *Chlorine in Coal.* Coal science and Technology Vol. 17, Elsevier, Amsterdam, 1991, 43-61.
8) Tsubouchi N., Hayashi H., Kawashima A., Sato M., Suzuki N., Ohtsuka Y. Chemical forms of the fluorine and carbon in fly ashes recovered from electrostatic precipitators of pulverized coal-fired plants, *Fuel*, 90 (2011), 376-383.

Effect of Scrap Composition on the Thermodynamics and Kinetic Modelling of BOF Converter

Florian Markus Penz[1], K1-MET GmbH, Linz, Austria;
Philip Bundschuh, Chair of Iron and Steel Metallurgy Montanuniversitaet Leoben, Austria;
Johannes Schenk, K1-MET GmbH, Linz & Chair of Iron and Steel Metallurgy Montanuniversitaet Leoben, Austria;
Harald Panhofer, voestalpine Stahl GmbH, Linz, Austria;
Krzysztof Pastucha, Primetals Technologies Austria GmbH, Linz, Austria;
Alexander Paul, voestalpine Stahl Donawitz GmbH, Donawitz, Austria;

Abstract:

Scrap is one of the main charging materials in the basic oxygen furnace process (BOF). It acts as a coolant for the exothermic reactions inside the BOF and as an iron source beside hot metal.

A dynamic simulation of the dissolution and melting behaviour of scraps deals with complex physical and chemical phenomena. Due to exact modelling of the BOF process, an optimization of tap-to-tap time followed by reduced operation costs might be possible. Based on a model for a BOF converter, coded in MatLab®, several scrap types were investigated. A thermodynamic and kinetic background describes the behaviour of the metal and slag phases during the blowing period of the BOF. This paper should show the effect of varying scrap compositions on the final crude steel composition after a defined blowing period. Furthermore, the influence on the final temperature and slag composition will be shown.

1. Brief background of the dynamic BOF model

Oxygen steelmaking in an LD converter was developed in the early 1950s in Linz and Donawitz. Since this time, the BOF process has gradually become the most dominant method of crude steel production. The main charging material in the BOF is hot metal, which accounts for 75 % to 95 % of the metallic charge; the remaining metallic charge is steel scrap. It is mainly used as a coolant for the process due to heat generation from the oxidation reactions of carbon, silicon, manganese and phosphorus. Decarburization is done with technically pure oxygen, which is blown onto the liquid metal surface at supersonic velocity. This ejects metal droplets that increase the reaction surface and the oxidation of impurities. [1, 2]

The BOF model used, coded in MatLab®, can be classified as a single-zone model based on thermodynamic and kinetic calculations. The single reaction zone in this model describes the converter steelmaking process as a heterogeneous thermodynamic system. Nearly all components can be conveyed between the metal and slag phases due to simultaneous chemical oxidation reactions on the interfacial surface. An exception is carbon, which is oxidized to become gaseous carbon monoxide and instantly removed from the reaction surface. Non-reversible oxidation process let the equilibrium thermodynamics of post combustion be

---

[1] Corresponding author; Email: Florian-Markus.Penz@k1-met.com

neglected. Post combustion itself is influenced by blown oxygen and sucked oxygen from atmosphere, wherein lance height and blowing rate have the highest impact. [3-5]

The theory of blowing oxygen consumption by V.E. Grum-Grzhimaylo for Bessemer converters is used for metal burning instead of the chain reaction theory. [6] Corresponding to this assumption, only iron is oxidized by blown oxygen. The remaining elements of the metal phase react with the iron oxide. In the thermodynamic system, the chemical composition of the metal and slag phases changes during the entire blowing period due to the blown oxygen. The simultaneous chemical reactions on the interfacial surface as well as the dissolution and melting behaviour of charged materials influence the melt and slag composition, as well. [3]

What is commonly used in Japan for investigations of the influence of kinetic parameters on chemical reaction rates as well as dephosphorization and desulfurization processes is the coupled reaction model developed by Ohguchi et al. [7-14] This model describes the concurrent oxidation-reduction reactions between metal and slag phases. [7] A chemical system for simultaneous chemical reactions between slag and metal phases based on thermodynamic data takes place on the interfacial surface. The reactions considered are listed in Equation **1.** All simultaneous oxidation-reduction reactions are calculated using Hess´ Law. [3]

$$\begin{cases} [Si] + 2[O] \leftrightarrow (SiO_2) \\ [Mn] + [O] \leftrightarrow (MnO) \\ [P] + 2.5[O] \leftrightarrow (PO_{2.5}) \\ [Ti] + 2[O] \leftrightarrow (TiO_2) \\ [V] + 1.5[O] \leftrightarrow (VO_{1.5}) \\ [Fe] + [O] \leftrightarrow (FeO) \\ [C] + [O] \leftrightarrow \{CO\} \end{cases} \qquad \textbf{(Eq. 1)}$$
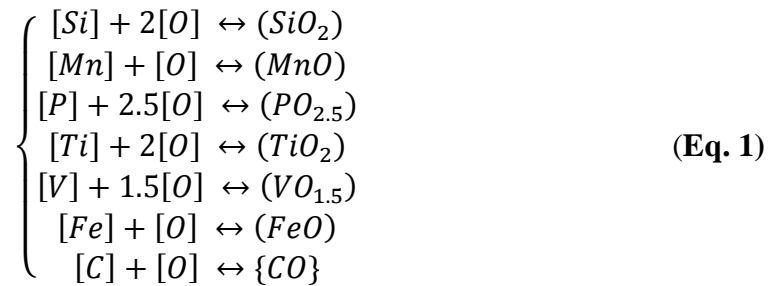
Almost the entire system is influenced by the alteration of one component parameter of the oxidation-reduction reactions, for example concentration or activity coefficients, making investigations of different parameters in the BOF process like process time or amounts of charged materials possible. Thermodynamic and kinetic equations together with the oxygen balance form the basis for the whole system. The following assumptions are made for the aforementioned equations:

- Chemical reactions at the interface between slag and metal are expeditious and equilibrated in each time step
- Fluctuations in iron concentration as well as lime concentrations are neglected
- Reaction rates are limited by mass transfer kinetics in metal and slag phases. [3]

More explanations of kinetic and thermodynamic calculations as well as the flow sheet of the model and the description of the melting and dissolution behaviour of slag formers, FeSi and pellets, are published by Y. Lytvynyuk et al. [3, 15]

Two mechanisms have to be considered for the melting and dissolution of scrap in the BOF model. [16, 17] For simplification, in the BOF model used, it is assumed that the surface temperature of the scrap is equal to the hot metal temperature without any temperature gradient.

a. Diffusive scrap melting: If the actual metal phase temperature is below the melting point of scrap, the melting and diffusion process of scrap depends on the carbon concentration difference between the charged scrap and the liquid hot metal. The melting point of scrap is assumed to be the temperature on the liquidus line of the

Fe-Fe$_3$C-Si-Mn diagram with the appropriate chemical composition of scrap. The mass transfer coefficient is a decisive factor in this case. According to the Fe-Fe$_3$C-Si-Mn diagram, low carbon scrap has a higher melting point than hot metal, with around 4.5 % carbon. For diffusive scrap melting, the model described employs **Equation 2** from Zhang L. and F. Oeters [18].

$$-\frac{\partial r}{\partial t} = k_{met} * \ln\left(\frac{\%C_{Scrap} - \%C_{HM}}{\%C_{Scrap} - \%C_{liq}}\right) \qquad \textbf{(Eq.2)}$$

The radius of the scrap particle is r in unit [m], and k_{met} is the mass transfer coefficient in the metal phase in [m s^{-1}]. C_{scrap} and C_{HM} are the carbon concentrations in the scrap and hot metal in [wt.-%]. C_{liq} describes the carbon concentration on the liquidus line. It is equal to the concentration of carbon on the liquid side at the concertation interface in each time step. [18] From a database of Fe-Fe$_3$C diagrams the values for the liquidus line are selected. The Phase diagrams including also a dependency of the actual Si and Mn content of the scrap phase. The phase diagrams are generated by the FactSage ® FSstel database. [3, 19]

b. Forced scrap melting: If the hot metal temperature exceeds the scrap melting point forced or convective scrap begins. In this case, the mass transfer could be neglected because the heat transfer is much higher. [17, 18] The driving force behind the convective scrap melting is the temperature difference between scrap and hot metal. The following equation (**Eq.3**) describes the forced scrap melting:

$$-\frac{\partial r}{\partial t} = h_{met} * \frac{T_{HM} - T_{liq}}{(L + (H(T_{scrap}) - H(T_{liq}))) * \rho_{scrap}} \qquad \textbf{(Eq.3)}$$

The heat transfer coefficient in the metal phase is h_{met} in [W m^{-2}K^{-1}]. The density of the scrap is ρ_{scrap} in [kg m^{-3}] and the latent heat of scrap melting is L in [J kg^{-1}]. T_{HM} and T_{liq} are the temperature of the metal phase and the liquidus temperature of the scrap in [K]. [3, 15] $H(T_{scrap})$ is the specific enthalpy of scrap at the actual temperature of the scrap surface and $H(T_{liq})$ is the specific enthalpy of the scrap melting point, respectively, in [J kg^{-1}]. [20]

The specific mixing power, which is created through bottom stirring and oxygen blowing, provides the basis for the mass transfer coefficient in the metal phase. The equation is a function of the total mixing power combined with the bath depth and the vessel geometry. [15] The heat transfer coefficient of the metal phase is approximated solely by a function of specific mixing power. [3, 17]

2. Description of input parameters

The following chapter gives an overview of the input parameters for the simulation with the BOF model. They are based on industrial materials and their chemical compositions. Several scrap types are used for investigation on the melting behaviour of scrap, the final temperature as well as the final slag and liquid metal compositions. Hot metal, scrap, solid BOF slag and sand are charged at the start of the process. During the entire process time, only lime is charged

as a simplification of the simulation. For each calculation, the amount of blown oxygen is equal and the blowing time is fixed at 12.6 min.

The initial chemical composition, mass and temperature of the hot metal are shown in **Table 1.**

Table 1: Hot metal specification

	Parameters of hot metal
Carbon content [wt.-%]	4.536
Silicon content [wt.-%]	0.410
Manganese content [wt.-%]	1.171
Phosphorus content [wt.-%]	0.100
Mass of hot metal [t]	53.60
Temperature [°C]	1318

Selected parameters of the initial slag as well as their compositions and the amounts of the charged solid converter slag, sand and the added lime are shown in **Table 2**.

Table 2: Selected chemistry of added slag, sand and lime

	Initial slag	Solid BOF slag 1	Sand	Lime
SiO_2 content [wt.-%]	11.32		92.79	0.980
MnO content [wt.-%]	11.93	2.960		
P_2O_5 content [wt.-%]	1.330			
FeO content [wt.-%]	29.66			
CaO content [wt.-%]	40.08	7.320		92.37
MgO content [wt.-%]	4.380	4.580		3.080
CO_2 content [wt.-%]				2.400
H_2O content [wt.-%]				0.170
Fe_2O_3 content [wt.-%]		67.88		
Fe content [wt.-%]		11.09		
Amount of charged material [t]	0.001	1.000	0.172	2.800

3. Investigated scrap compositions

In this paper, six different scrap types are analysed according to their melting and dissolution behaviour during the BOF process. The modelled chemical scrap compositions, weights, sizes and charging temperatures are displayed in **Table 3.** For the investigations, the charged mass, charging temperature and size are constant. The six scrap types vary considerably in carbon, silicon and manganese composition. Scrap 1 has high silicon content and low carbon content. Scrap 2 has medium carbon content and high manganese content. Scraps 3 and 4 have the same manganese content but scrap 3 is twice as high in carbon and silicon. Scrap 4 has a classic composition comparable to deep drawing steels. Scraps 3, 4 and 5 are peritectic steel grades. Scrap 6 has high carbon and manganese contents comparable to nearly perlitic steels.

Table 3: Scrap parameters

	Scrap 1	Scrap 2	Scrap 3	Scrap 4	Scrap 5	Scrap 6
Carbon content [wt.-%]	0.106	0.316	0.100	0.050	0.100	0.737
Silicon content [wt.-%]	1.488	0.211	0.100	0.051	0.200	0.349
Manganese content [wt.-%]	0.266	0.869	0.550	0.510	0.850	1.060
Phosphorus content [wt.-%]	0.014	0.016	0.015	0.015	0.015	0.013
Vanadium content [wt.-%]	0	0	0	0.002	0	0.001
Titanium content [wt.-%]	0	0.005	0	0.040	0.005	0.001
Iron content [wt.-%]	Rest	Rest	Rest	Rest	Rest	Rest
Mass of hot metal [t]	15	15	15	15	15	15
Size [m]	0.1	0.1	0.1	0.1	0.1	0.1
Temperature [°C]	20	20	20	20	20	20

4. Results and discussion

Applying the aforementioned parameters, the scrap melting was modelled. The following illustrations display the calculated influence of the different scrap compositions on the dissolution and melting behaviour of scrap as well as the final bath temperature. Furthermore the changes in the liquid metal and slag phase compositions will be described. For better understanding, the different types of scraps have the same coloration in each diagram.

4.1 Melting behaviour of scrap

Figure 1 illustrates the dissolution and melting behaviour of scrap. Around minute 10, a kink occurs, resulting from the change between diffusive and forced scrap melting. At this point, the melt temperature exceeds the melting temperature of the scrap. Under real process conditions, a smooth transition between the two melting mechanisms will take place. In the model, it is assumed that the melting point of scrap is specific on the liquidus line, while under real conditions the melting takes place in the two-phase area between the solidus and liquidus lines.

The graphs of scraps 1 and 6 show a rapid diffusive scrap melting. This happens according to a high value of the logarithmic term of **Equation 2**, which is a result of a low liquidus interface concentration of carbon. This effect is brought about due to the lowering and moving of the liquidus line in the Fe-Fe$_3$C-Si-Mn diagram containing higher manganese and silicon contents. Due to the low melting point of those two scrap types, the melting point of scrap is reached faster, whereby forced scrap melting starts earlier. Attributable to this fact, scrap melting is finished before the blowing process stops, compared to the other simulations. Low carbon steels which also have low silicon contents, like scraps 3, 4 and 5, tend to exhibit a slower diffusive scrap melting behaviour. In this case, the logarithmic term of **Equation 2** gets close to zero and at least zero in the case of scrap 5, which means scrap melting stops until the logarithmic term gets a positive value. Due to high oxygen activity, silicon is usually oxidized first beside iron in the converter process.
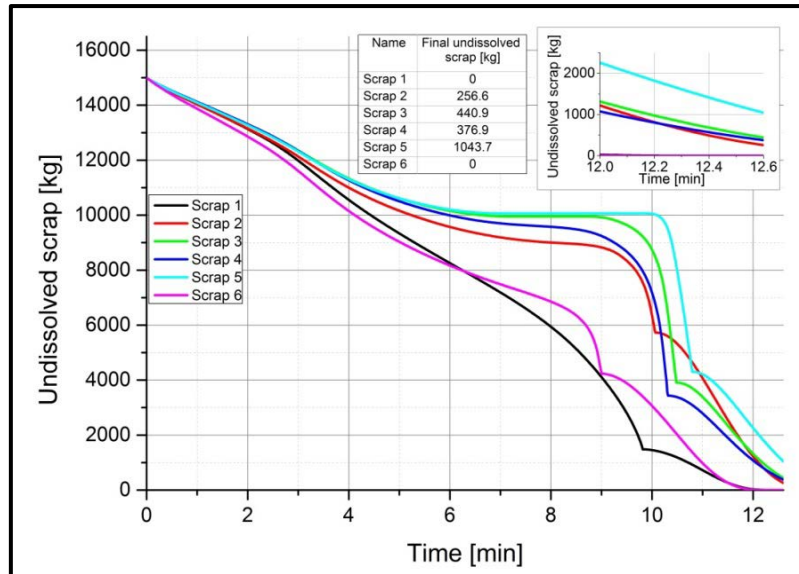
Figure 1: Illustration of undissolved scrap

The stagnation of the melting of scrap 5 between 7 and 9.9 minutes is explainable with **Figure 2**. At a blowing time of 10.8 minutes forced scrap melting starts with the aforementioned conditions of scrap 5. With **Equation 2** diffusive scrap melting is well describable if the carbon content of the melt is in the liquid area of the Fe-Fe$_3$C-Si-Mn diagram. The phase diagram in **Figure 2** includes 0.2 wt.-% Si and 0.8 wt.-% Mn. During the dynamical calculation of scrap 5, the carbon content of the hot metal drops below the liquidus line at t = 7 min. This leads to the case that the logarithmic term of **Equation 2** is zero and continues to be negative until the carbon content of the hot metal crosses the liquidus line again (t = 9.9 min). From a numerical point of view, there might be a growing of the scrap particle, which might not be possible in reality. According to the two-phase area, where austenite and liquid melt exist concurrently, and the lever arm rule a substantial portion of the area is liquid. Therefore, at least **Equation 2** is not reliable for all scrap types during diffusive melting.
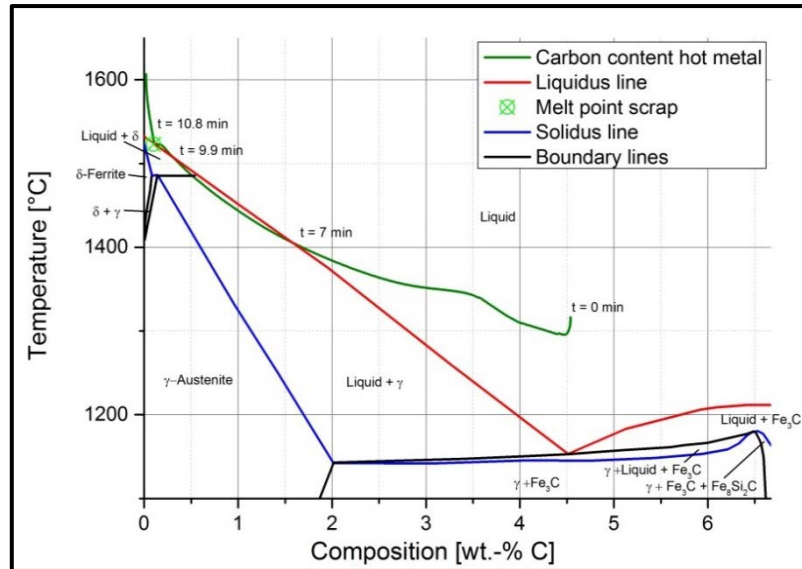
Figure 2: Fe-Fe₃C diagram including 0.2 wt.-% Si and 0.8 wt.-% Mn

4.2   Influence of scrap on the melt temperature

The melting of high carbon and silicon-containing scraps results in an increase in chemical heat which is generated through the oxidation of those elements. Due to the energy balance, an increasing energy input will conclude in a higher final temperature. In **Figure 3** the temperature of the hot metal is illustrated. Close to the end of the blowing period, a flattening of the temperature could be seen in the graphs of scraps 3, 4 and 5. According to their low carbon contents, less carbon will be delivered in addition; consequently, nearly all carbon from the liquid melt is oxidized earlier (**Figure 4**) and less heat can be gained due to oxidation. The flattening of the temperature also rests on the huge amount of undissolved scrap until the end of blowing which still consumes energy.
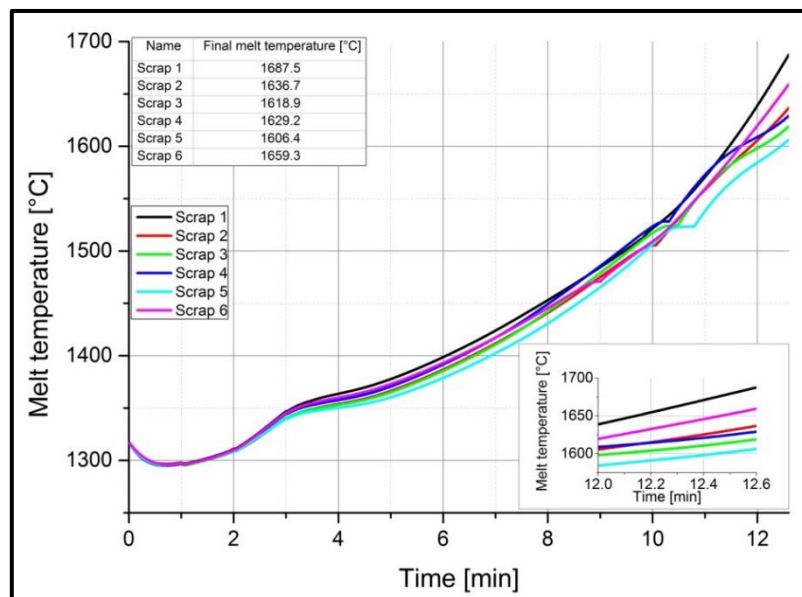

Figure 3: Influence of scrap on the melt temperature

130

4.3 Influence of scrap on decarburization behaviour

As already stated, scraps containing less carbon will not deliver additional carbon to the liquid metal. This effect leads to a faster decarburization of the hot metal during the blowing period, as presented in **Figure 4**. **Tables 1** and **2** shows that the amounts of charged material and the amount of blown oxygen as well as the blowing time are constant in all simulations. Because of the varied chemical compositions of elements in the different scrap types, the final carbon content of the liquid metal is also influenced. Especially scrap 1 has low carbon contents but high silicon content, which has a higher oxygen affinity than carbon. This results in a higher final carbon content.
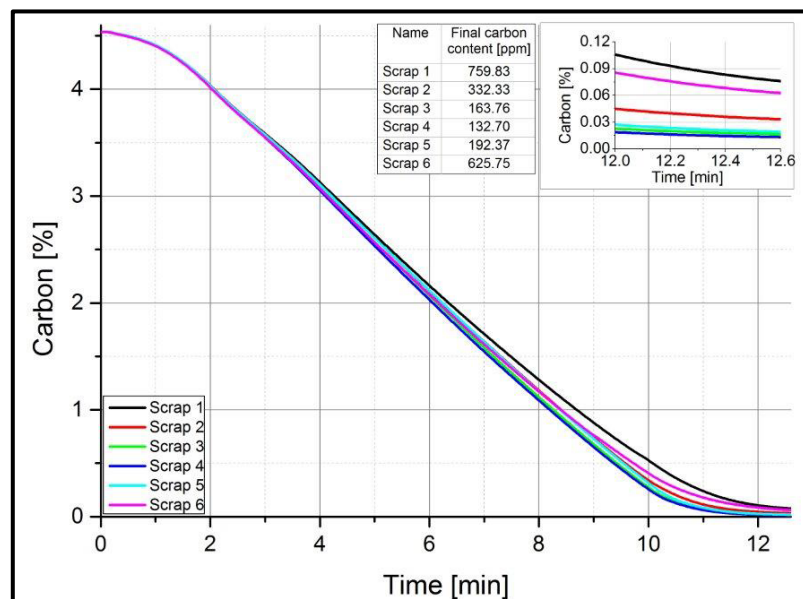

Figure 4: Carbon content of the liquid hot metal during blowing time

4.4 Influence of scrap on dephosphorization behaviour and manganese content

Dephosphorization of the hot metal is one of the main tasks of the BOF process. According to **Table 3**, the phosphorus concentration of scrap is nearly equal. At the beginning of the process, an oxidation of manganese and phosphorus occurs. After silicon is nearly oxidized and due to increasing bath temperatures as well as the still relatively high carbon activity, the stable oxides of manganese and phosphorus will be reduced. Low carbon contents will lead to an early decrease in carbon activity, which is why the oxidation of manganese and phosphorus starts earlier in the final stages (**Figure 5** and **Figure 6**).
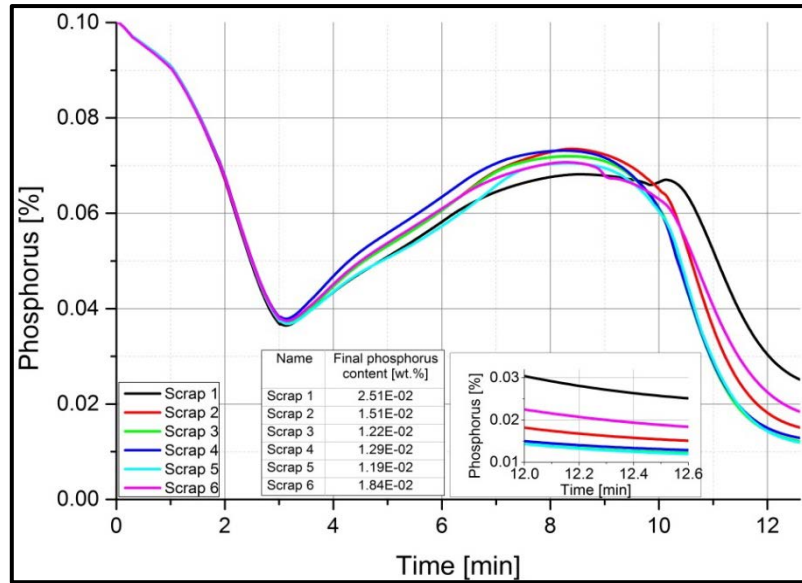
Figure 5: Phosphorus content of the liquid hot metal during blowing time

The manganese behaviour is similar to that of phosphorus. Scraps with high carbon and manganese contents tend to have higher final manganese contents, like scrap 6 in **Figure 6**.
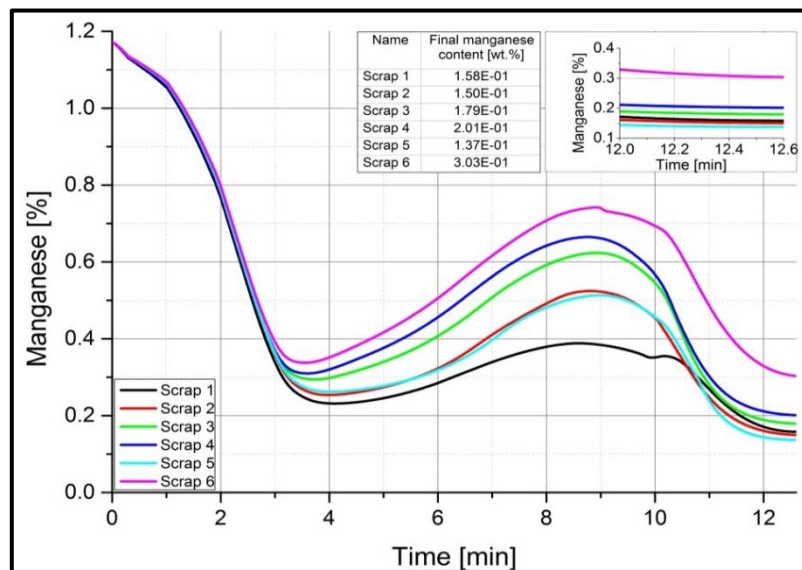

Figure 6: Manganese content of the liquid hot metal during blowing time

4.5 Alteration of the slag composition

The slag composition is inversely proportional regarding the mass balance of silicon, manganese and phosphorus. According to the contents of these elements in scrap, higher or lower amounts of the oxides are found in the slag. As an example, the silicon oxide content of the slag during the blowing time is illustrated in **Figure 7**. During the first three minutes, oxidation of silicon occurs. The smooth decrease is premised on the oxidation of other elements in the hot metal. In the final stages of the blowing period, an accelerated decrease in the silicon

oxide content occurs, which is a result of the strong iron oxidation due to the low carbon activity at the end of the process.
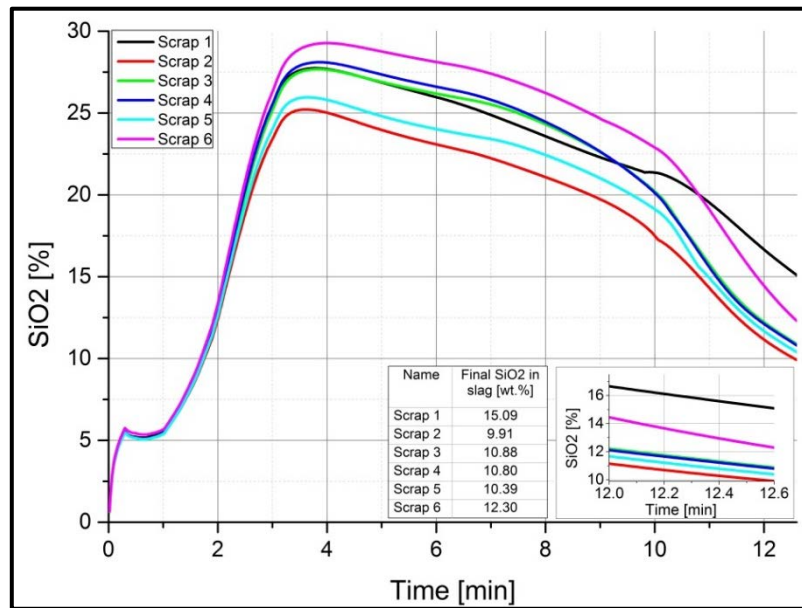

Figure 7: Trajectories of the silicon oxide during BOF process

As illustrated in **Figure 7**, the greater the value of the silicon content of the scrap, the higher is the final silicon oxide content of the slag, which further results in lower slag basicity. As noted in **Table 2**, the amount of charged lime is the same in all simulations. During the blowing process, lime dissolves in the liquid slag phase. The chemical composition of scrap has an impact such that elements like silicon, manganese and phosphorus get oxidized. For that reason, high amounts of those elements in the scrap lead to an increase in the related oxide phase. In the end the oxidation of iron also influences the final lime content in the slag phase (**Figure 8**).
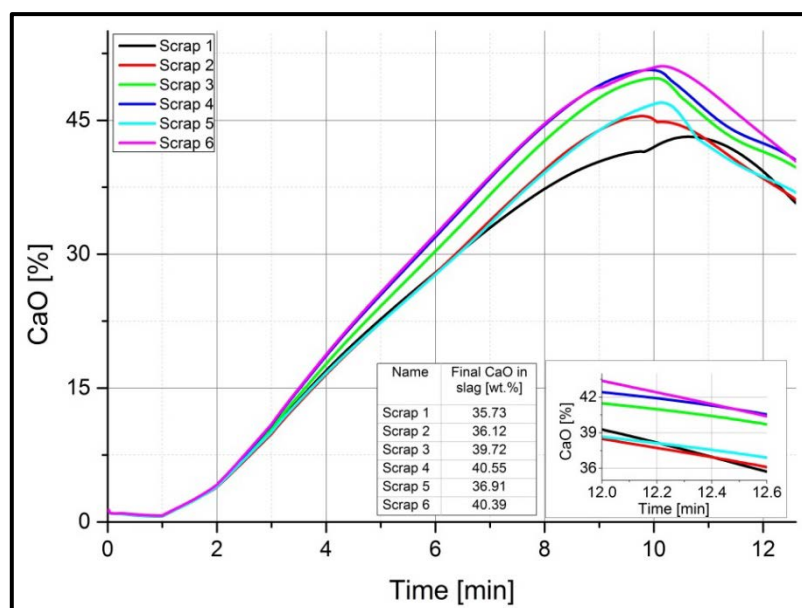

Figure 8: Lime content of the slag phase

5. Conclusion

This publication points out the dissolution and melting behaviour of scrap using a dynamic BOF simulation based on complex physical and chemical phenomena. Coded in MatLab®, this BOF model describes the behaviour of the metal and slag phases during the blowing period of the BOF, as well.

For the investigation, six scrap types with various chemical compositions were simulated as the charge material. For diffusive scrap melting, a literature-based equation was used, which highlighted the fact that the equation is not reliable for all scrap types, the reason is that it is just a simplification for describing the complex melting process, especially if the carbon content of the liquid hot metal crosses the liquidus line and reaches the two-phase area of the Fe-Fe$_3$C-Si-Mn diagram. According to the model calculations, faster melting of scrap could be indicated if both the carbon and the silicon content in the scrap are high. The background is the lowering of the melting point of scrap due to the higher content of these elements. Decarburization of low-alloyed scraps is faster if less carbon is delivered in addition. The faster decarburization also results in a prior decrease of carbon activity, which is why the oxidation of manganese and phosphorus starts earlier in the last quarter of the blowing period. The slag composition is influenced by the chemical scrap composition, especially the silicon, manganese and phosphorus content, as those elements will be oxidized and picked up in the slag phase.

In summary, the outcomes of this work clearly indicate that the chemical scrap composition has a strong impact in all fields of the BOF modelling and should be described as thoroughly and precisely as possible. Furthermore it shows that literature-based equations for scrap melting will are not always suitable for all scrap types. More work has to be done to describe the extraordinary field of the melting and dissolution of scraps and other charge materials in the BOF process.

References:

1) E.T. Turkdogan, *Fundamentals of Steelmaking*, The institute of materials, London, 1996.

2) A. Ghosh and A. Chatterjee, Ironmaking and Steelmaking theory and practice, PHI Learning Private Limited, Delhi, 2015.

3) Y. Lytvynyuk, J. Schenk, M. Hiebler and S. Sormann, Thermodynamic and Kinetic Model of the Converter Steelmaking Process. Part 1: The Description of the BOF Model, *Steel Research int.*, Vol. 85, No. 4 (2014), p. 537 – 543.

4) M. Hirai, R. Tsujino, T. Mukai, T. Harada and O. Masanao, Mechanism of Post Combustion in the Converter, *Transactions ISIJ*, Vol. 27 (1987), p. 805 – 813.

5) P. Bundschuh, J. Schenk, M. Hiebler, H. Panhofer and S. Sormann, Influence of CaO Dissolution on the Kinetics of Metallurgical Reactions in BOF-process, *Proceedings of the 7th European Oxygen Steelmaking Conference,* Trinec, 2014.

6) B. Boychenko, V. Okhotskiy and P. Kharlashin, *The converter Steelmaking*, Dnipro-VAL, Dnipropetrovsk, 2006.

7) S. Ohguchi, D. Robertson, B. Deo, P. Grieveson and J. Jeffes, Simultaneous dephosphorization and desulphurization of molten pig iron, *Iron and Steelmaking*, Vol.11, No. 4 (1984), p. 202 – 213.

8) S. Kitamura, T. Kitamura, K. Shibata, Y. Mizukami, S. Mukawa and J. Nakagawa, Effect of stirring energy, temperature and flux composition on hot metal dephosphorization kinetics, *ISIJ International*, Vol. 31, No. 11 (1991), p 1322 – 1328.

9) S. Kitamura, T. Kitamura, T. Aida, E. Sakomura, R. Koneko and T. Nuibe, Development of analyses and control method for hot metal dephosphorization process by computer simulation, *ISIJ International*, Vol. 31, No. 11 (1991), p 1329 – 1335.

10) S. Kitamura, H. Shibata and N. Maruoka, Kinetic Model of Hot Metal Dephosphorization by Liquid and Solid coexisting slags, *Steel Research int.*, Vol. 79, No. 9 (2008), p. 586 – 590.

11) F. Pahlevani S. Kitamura, H. Shibata and N. Maruoka, Kinetic Model Dephosphorization in Converter, *Proceedings of SteelSim*, Leoben, 2009.

12) S. Mukawa and Y. Mizukami, Effect of stirring energy and rate of Oxygen supply on the rate of hot metal dephosphorization, *ISIJ International*, Vol. 35, No.11 (1995), p 1374 – 1380.

13) M. Ishikawa, Analysis of hot metal desiliconization behaviour in converter experiments by coupled reaction model, *ISIJ International*, Vol. 44, No.2 (2004), p 316 – 325.

14) Y. Higuchi, Y. Tago, K. Takatani and S. Fukagawa, Effect of stirring and slag condition on reoxidation on molten steel, *ISIJ*, Vol. 84, No.5 (1998), p 13 – 18.

15) Y. Lytvynyuk, J. Schenk, M. Hiebler and H. Mizelli, Thermodynamic and kinetic modelling of the devanadization process in the steelmaking converter, *Proceedings of 6th European Oxygen Steelmaking Conference*, Stockholm, 2011.

16) M. Medhibozhskiy, *Thermodynamic and Kinetic Fundamentals of Steelmaking*, Vischashkola, Kyiv, 1979.

17) K. Isobe, H. Maede, K. Ozawa, K. Umezawa and C. Saito, Analysis of the Scrap Melting Rate in High Carbon Molten Iron, *ISIJ*, Vol. 76, No.11 (1990), p 2033 – 2040.

18) L. Zhang and F. Oeters, *Schmelzen und Mischen von Legierungsstoffen in Stahlschmelzen*, Verlag Stahleisen GmbH, Düsseldorf, 2012.

19) M. Zarl, *Development and evaluation of a BOF pre-processor model*, Master Thesis, Montanuniversität Leoben, 2017 (in press).

20) P. Bundschuh, *Thermodynamische und kinetische Modellierung von LD-Konvertern*, Dissertation, Montanuniversität Leoben, 2017 (in press).

Quantifying Crystallinity of Oxide Melts
by Electrical Capacitance Measurements

Noritaka Saito*, Yusuke Harada, and Kunihiko Nakashima
Department of Materials Science and Engineering, Kyushu University

Abstract: A theoretical model for predicting electrical capacitance of various materials was developed by taking into account geometrical configurations of crucible and rod electrodes. The calculated results were in good agreement with the corresponding measurement data obtained at room temperature (20°C) for liquid materials with known relative permittivity. The measured capacitances of aqueous suspensions containing oxide powders with various grain sizes and relative permittivity values systematically decreased at room temperature with increases in their volume fractions regardless of the sizes of the dispersed solid phases and matched the results obtained from the proposed capacitance prediction model combined with Lichtenecker's equation for calculating relative permittivity of dual-phases mixtures. In addition, the validity of the proposed model for predicting capacitances of supercooled oxide melt suspensions was tested at elevated temperatures (above 1300 °C). The observed decrease in capacitance for silicate melts with known crystallinities estimated from the corresponding phase diagrams was consistent with the data predicted by the proposed capacitance model combined with Nielsen's equation instead of Lichtenecker's equation due to the large differences in relative permittivity between the utilized oxide melts and the solid phases.

1. Introduction

Metal refining[1)-2)] as well as manufacturing of glass and ceramic materials require using chemical reagents in the molten state, and the functionality and quality of the resulting products are directly affected by the oxide melt treatment conditions. Various physical properties of single-phase oxide melts such as viscosity[3)-6)], density[7)-9)], surface tension[10)-12)], and thermal conductivity[13)-15)] have been evaluated at high temperatures (500~1600°C); however, these melts are often utilized in wide temperature ranges between the uniformly molten state and the supercooled one accompanied by consequent crystallization. In general, the crystallization of a supercooled oxide melt significantly affects its macroscopic and physical properties, such as viscosity and thermal conductivity of the produced solid phase. For example, the degrees of lubrication and insulation between an oscillating mold and molten steel during continuous casting[16)] significantly depend on the viscosity and crystallinity of the molten phase[6),17),18)] due to the rapid increase in the amount of dispersed solids. Consequently, the viscosity properties of a melt depend on its share rate, which can dramatically turn a Newtonian fluid into a non-Newtonian one[6),19)]. Some authors reported that the viscosity of CaO–SiO$_2$–R$_2$O (R=Li, Na, or K) melts
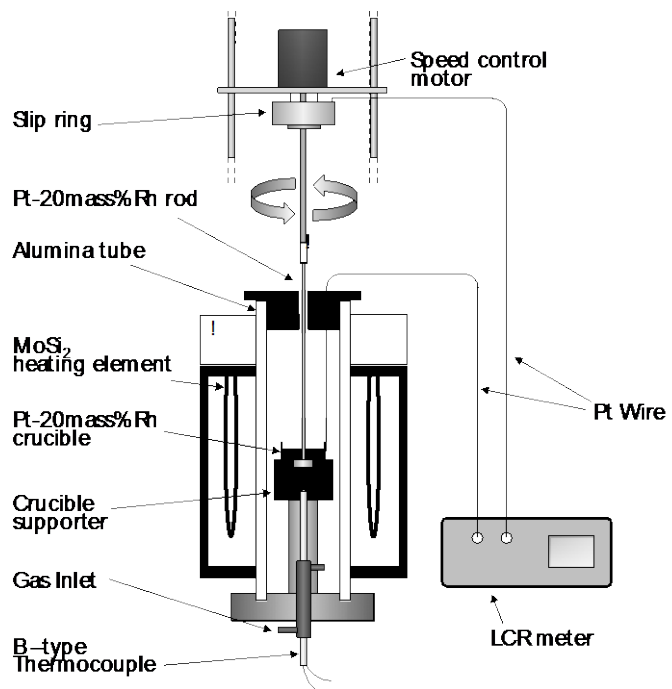

Fig.1 A schematic diagram of the electrical capacitance measuring system utilized in the present study.

exponentially increased with increasing crystallinity, and their flow behavior exhibited a transition from the Newtonian to the non-Newtonian one at a certain content of the produced crystalline phase[6)]. The latter also increased the

electromagnetic wave absorption rate, inhibited the radiation heat transfer process, and deteriorated melt thermal conductivity properties. Susa et al.[20] prepared $CaO–SiO_2–Al_2O_3–Na_2O–MgO–CaF_2–Fe_2O_3$ samples with different crystallinity values ranging between 0% and 60% by changing the duration of heat treatment and studied their reflectivity and transmissivity characteristics in a wavelength range of 300−2600 nm by using a spectrophotometer; as a result, the dispersed crystalline phases blocked the radiation heat transfer and decreased the material thermal conductivity. Therefore, the crystallinity degree of the supercooled oxide melts is essential for controlling the related physical and chemical processes.

Numerous studies on the crystallization behavior of oxide melts conducted by various methods including differential thermal analysis[21], scanning electron microscopy, and X-ray diffraction (XRD)[22)-23)] have been reported. Crystallinity of the prepared samples is usually quantified by either quenching them at particular temperatures followed by polishing with epoxy resins and subsequent microscopic observations or by utilizing internal standards during XRD measurements[6]. However, the above-mentioned methods were found to be very time consuming. In recent years, Ohta et al.[24] have introduced a new technique for evaluating the degree of crystallinity for supercooled Na silicate melts by measuring the electrical capacitance decrease resulting from the difference in electrical permittivity between the molten oxide and the solid phase, which was successfully utilized for detecting nano-sized crystals in a glass matrix during "nanoglass" production. Several groups used this method to investigate the effect of agitation on the crystallization behavior of continuously supercooled $CaO–SiO_2–R_2O$ (R=Li, Na, or K)[17] and $CaO–SiO_2–CaF_2$ melts[18] and found that the application of an agitation field increased their degree of crystallinity and changed the morphology of primal crystals.

Although the previous findings revealed that measuring the electrical capacitance of oxide melts could be a powerful tool for evaluating their crystallization behavior, no studies on the effect of the crystallinity degree on the flow and heat transfer properties of supercooled oxide melts have been reported yet. In the present work, we quantified in-situ the crystallinity of oxide melts at high temperatures by measuring their capacitances and compared the obtained data with the results of proposed time-efficient theoretical modeling.

2. Experimental

2.1 Electrical Capacitance Measurement Procedures and Related Theoretical Modeling

Fig. 1 contains a schematic of the capacitance measurement system. Pt−20 mass% Rh alloy was used for contact materials, while the values of measurement frequency and applied potential were equal to 10 kHz and 1.0 V, respectively. The detailed description of the utilized experimental setup can be found elsewhere[17].

A theoretical model for evaluating the electrical capacitance of a material with known relative permittivity was developed by taking into account the shapes and dimensions of the utilized crucible and rod electrodes. First, the internal space of the cylindrical electrode was divided into three sections, which were treated as three different capacitors with parallel-plate electrodes (see Figs. 2 and 3 describing various cylindrical electrode dimensions).

Thus, C_1 is the electrical capacitance between the lower rod surface (with diameter r_i) and the bottom of the crucible (with diameter r_0), which can be estimated by using the following calculated equation for a parallel-plate capacitor with electrodes of different sizes:

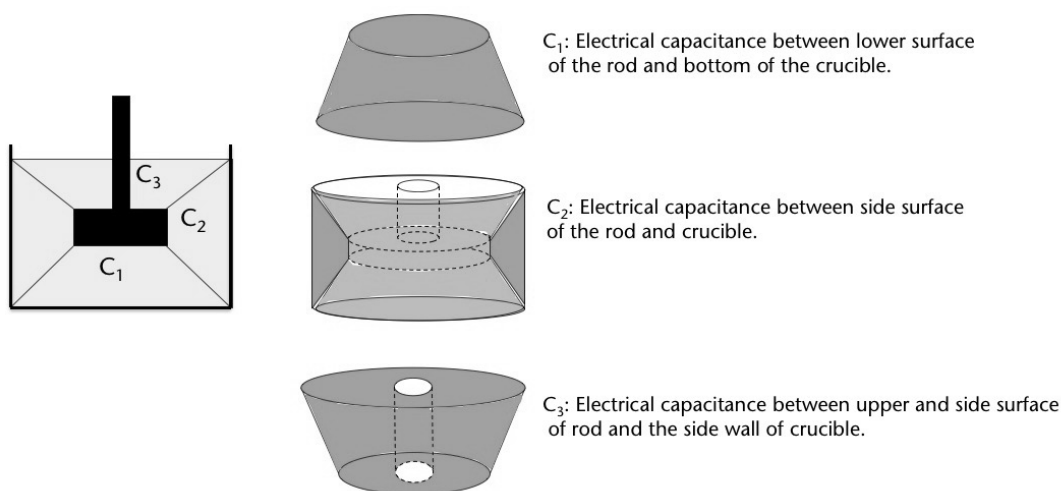$$C_1 = \frac{\varepsilon(S_1 - S_2)}{d \times \ln(S_1/S_2)} \cdots (1)$$

C_1: Electrical capacitance between lower surface of the rod and bottom of the crucible.

C_2: Electrical capacitance between side surface of the rod and crucible.

C_3: Electrical capacitance between upper and side surface of rod and the side wall of crucible.

Fig.2 A schematic diagram of the three capacitance components for the rod and crucible electrodes.

Here ε is the relative permittivity of the material between the plates, d is the distance between electrodes, and S_1 and S_2 are surface areas of the larger and smaller electrodes, respectively. C_2 is the capacitance between the side surfaces of the rod and the crucible and thus can also be treated as a capacitor with two dissimilar electrodes. Equation (2) was obtained from the formula for the parallel-plate capacitor with the side surfaces of the rod and the crucible rotated by a small angle $\Delta\theta$:
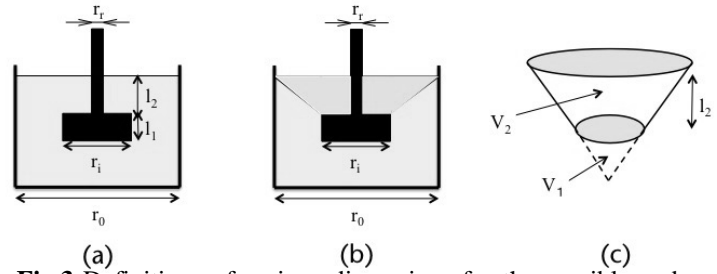

Fig.3 Definitions of various dimensions for the crucible and rod electrodes.

$$C_{2'} = \frac{\varepsilon l_1 (r_i - r_o)}{d \times \ln(r_i / r_o)} \Delta\theta \cdots (2)$$

Equation (3) can be derived by integrating equation (2) with respect to $\Delta\theta$ from 0 to 2π:

$$C_2 = \frac{2\pi\varepsilon l_1 (r_i - r_o)}{d \times \ln(r_i / r_o)} \cdots (3)$$

In order to evaluate the capacitance between the upper and side surfaces of the rod and the crucible side wall (C_3), it is necessary to eliminate its overlap area with capacitance C_2. For this purpose, a capacitance of a cylindrical part with diameter r_0 and height l_2 determined from the corresponding cylinder volume fraction was calculated. First, the volume $V_2 - V_1$ (see. Figs. 3 (b) and (c)) without the rod was divided into two cones. Equations (4) and (5) were obtained from the calculated values of cone volumes V_1 and V_2 with diameters r_i and r_0, respectively:

$$V_1 = \frac{1}{3} \times \frac{1}{4} \pi r_i^2 l_2 \times \frac{r_i}{r_o - r_i} \cdots (4)$$

$$V_2 = \frac{1}{3} \times \frac{1}{4} \pi r_o^2 l_2 \times \frac{r_o}{r_o - r_i} \cdots (5)$$

Therefore, equation (6) can be derived by calculating the excluded volume of the rod $V_2 - V_1$:

$$V_2 - V_1 = \frac{1}{12} \pi l_2 \times \frac{r_o^3 - r_i^3}{r_o - r_i} \cdots (6)$$

Equation (7) describes the ratio between volume V of a cylinder with diameter r_0 and height l_2 corrected for the rod volume V_r and the volume of a cylindrical part with diameter r_0 and height l_2 corresponding to capacitance C_3:

$$\frac{(V_2 - V_1) - V_r}{V - V_r} = \frac{\frac{r_o^3 - r_i^3}{r_o - r_i} - 3r_r^2}{3r_0^2 - 3r_r^2} = \frac{r_0^3 - 3r_r^2 r_0 + 3r_r^2 r_i - r_i^3}{3(r_o^2 - r_r^2)(r_0 - r_i)} \cdots (7)$$

As a result, the following formula for capacitance C_3 can be derived from equation (8):

$$C_3 = \frac{2\pi\varepsilon l_2}{\ln(r_o / r_i)} \times \frac{r_0^3 - 3r_r^2 r_0 + 3r_r^2 r_i - r_i^3}{3(r_o^2 - r_r^2)(r_0 - r_i)} = \cdots (8)$$

Table 1 Relative permittivity values for the liquid and solid phases utilized in this study.

liquid phase		

The sum of C_1, C_2, and C_3 defined above represents the theoretical capacitance calculated by taking into account the geometrical configurations of the crucible and rod electrodes.

To verify the feasibility of the theoretical model proposed above, capacitances of liquid phases with known relative permittivity (ultrapure water, methanol, and 2-

propanol) were systematically measured at room temperature and rod immersion depths between 4 and 16 mm varied at 2-mm intervals (the relative permittivity values for the liquids utilized in this study are listed in Table 1).

2.2 Capacitance Measurements for Aqueous Suspensions at Room Temperature

The applicability of the proposed theoretical model to dual-phase fluids was investigated by measuring the capacitance of aqueous suspensions at room temperature. Ultrapure water (with a specific resistance of 18.0 MΩ·cm) was used as a dispersion medium, while SiO_2 and Al_2O_3 powders with different relative permittivity values were employed as dispersed solid phases. The powder specifications were as follows: (a) ultrafine SiO_2 powder (99.9% purity, 1.42 μm mean diameter), (b) fine SiO_2 powder (99.9% purity, >63 μm mean diameter), (c) SiO_2 powder (99.9% purity, 105–420 μm mean diameter), and (d) ultrafine Al_2O_3 powder (99.99% purity, 0.1 μm mean diameter). The relative permittivity values for the SiO_2 and Al_2O_3 powders are listed in Table 1[25)-28)].

Ultrapure water and solid phases described above were weighed to obtain specified value of the solid volume fractions. The oxide powders were uniformly dispersed in ultrapure water by ultrasonic stirring, after which a crucible with the sample was placed into the capacitance-measuring device depicted in Fig. 1. Finally, a rod electrode was slowly immersed into the sample at a specified position, and the capacitance of the obtained suspension was evaluated.

2.3 Capacitance Measurements for Oxide Melt Suspensions at High Temperatures

The applicability of the model proposed in section 2.1 to oxide melt suspensions at high temperatures was investigated by measuring the capacitance of oxide suspensions with known volume fractions of the crystalline phases. Table 2 lists the chemical compositions of the oxide samples prepared in the present study from $CaCO_3$, SiO_2, Al_2O_3, and MgO reagent powders (99.9%, Sigma-Aldrich Japan Inc.,

Table 2 Chemical compositions (mol%) of the oxide samples utilized in this study.

CaO	

Tokyo, Japan). The initial powders were thoroughly mixed to produce the required compositions followed by premelting in a Pt crucible at 1600 °C in air and then quenching on a Cu plate. The obtained sample batch was placed in a Pt−20 mass% Rh crucible and annealed at 1600 °C for a specified period to produce a bubble-free and uniform melt, after which a Pt−20 mass% Rh rod was immersed into the sample melt to a depth of exactly 10 mm, and the same crucible and rod were used in section 2.2.

As mentioned above, two chemical compositions were used for the capacitance measurements (their corresponding phase diagrams are shown in Figs. 4 and 5). According to the phase diagram for the CaO−SiO$_2$−Al$_2$O$_3$−MgO system, the 45.0CaO−45.5SiO$_2$−2.3Al$_2$O$_3$−7.2MgO (mol%) composition is characterized by the liquidus temperature of 1400 °C, while the temperatures corresponding to the solid volume fractions of 10%, 20%, and 40% are equal to 1387 °C, 1370 °C, and 1320 °C, respectively. According to the phase diagram for the CaO−SiO$_2$−Al$_2$O$_3$ system, the 57.1CaO−3.5SiO$_2$−39.4Al$_2$O$_3$ (mol%) composition is characterized by the liquidus temperature of 1500 °C, while the temperatures corresponding to the solid fractions of 10%, 20%, 30%, and 40% are equal to 1484 °C, 1463 °C, 1437 °C, and 1403 °C, respectively.
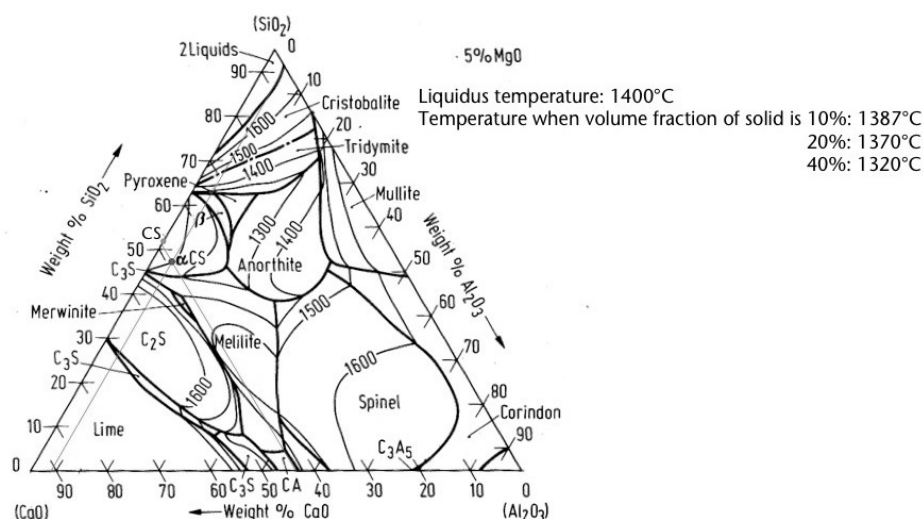
Fig.4 A phase diagram for the CaO−SiO$_2$−Al$_2$O$_3$−MgO system containing 5 mass% of MgO.
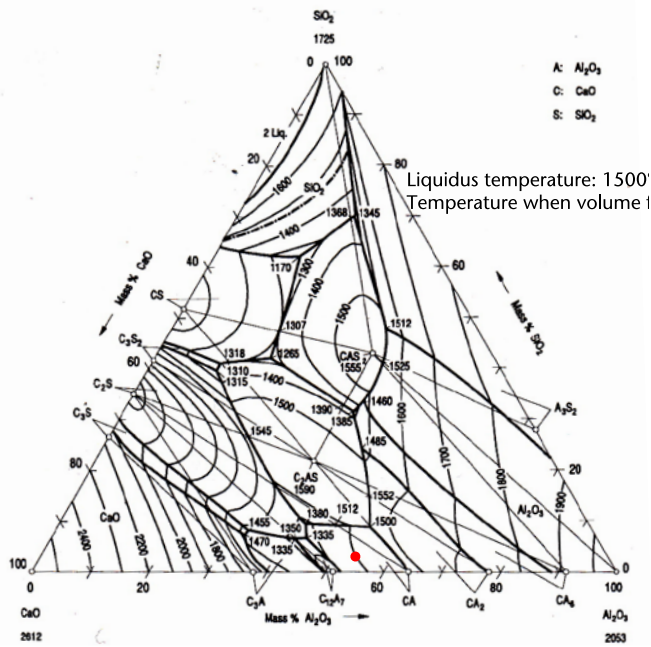
Fig.5 A phase diagram for the CaO−SiO$_2$−Al$_2$O$_3$ system.

3. Results and Discussion

3.1 Capacitance Theoretical Prediction at Room Temperature

Fig. 6 describes the results of the capacitance measurements for the liquids with known relative permittivity (ultrapure water, methanol, and 2-propanol) at various rod immersion depths (here the vertical and horizontal axes represent the experimentally measured capacitance values and the capacitance calculated by the proposed theoretical model, respectively). The graph depicted in Fig. 6(a) shows a linear relationship between the experimental capacitance values and the calculated ones with the observed y-axis intercept of around 104 pF corresponding to a stray capacitance (resulting from the internal electrical capacitance of the device circuit elements and impedance analyzer). Therefore, the measured capacitance values had to be corrected for the stray capacitance error (see Fig. 6(b)); the resulting plot passed through the origin and was characterized by a slope of 1.0066 indicating that the suggested theoretical model could reasonably reproduce the experimental capacitances of the liquid phase measured at room temperature.

The applicability of the proposed capacitance prediction model to the dual-phase fluids was investigated by measuring the capacitance of the aqueous oxide suspensions at room temperature. In general, when the electrode geometrical configuration and sample relative permittivity are known, it is possible to calculate the electrical capacitance for an alternating current circuit. In the present study, a crucible and a rod with identical dimensions were utilized (see Figs. 1 and 2) throughout the entire experimental procedure, which indicated the absence of electrical capacitance variations caused by the differences in electrode geometrical configurations. Thus, the measured electrical capacitance depended only on the sample relative permittivity and could be easily calculated in accordance with the proposed theoretical model. If a relationship between the relative permittivity of a dual-phase mixture and the volume fraction of each component exists, it is possible to quantify the mixture's crystallinity (corresponding to the volume fraction of the solid phase) by measuring its capacitance value. Equations (9)-(11) presented below describe a typical relative permittivity model for the dual-phase mixtures:
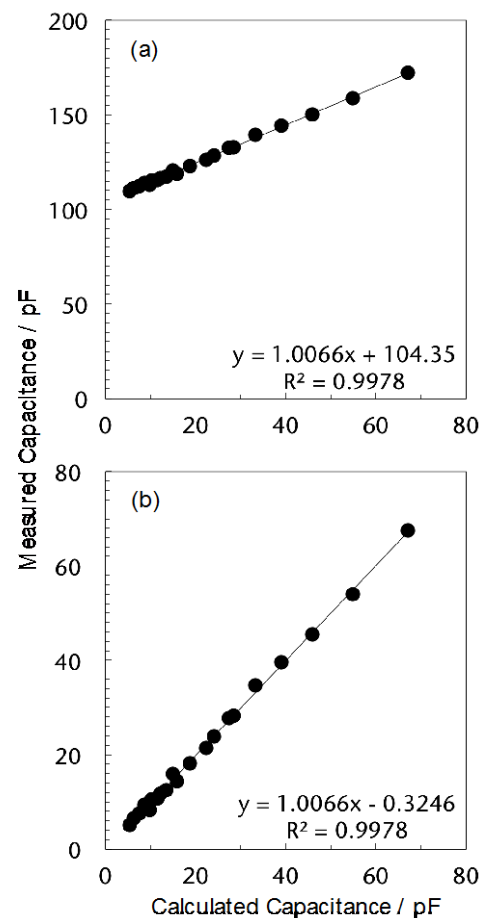

Fig.6 A comparison between the measured and calculated capacitance values for ultrapure water, methanol, and 2-propanol: (a) the raw data and (b) the data corrected for the stray capacity of the measuring system.

$$\log \varepsilon = V_1 \log \varepsilon_1 + V_2 \log \varepsilon_2 \cdots (9)$$

$$\varepsilon = \varepsilon_1 \frac{2\varepsilon_1 + \varepsilon_2 - 2(\varepsilon_1 - \varepsilon_2)V_2}{2\varepsilon_1 + \varepsilon_2 + (\varepsilon_1 - \varepsilon_2)V_2} \cdots (10)$$

$$\varepsilon = V_1\varepsilon_1 + V_2\varepsilon_2 \cdots (11)$$

Here equation (9) represents Lichtenecker's equation[29], and equation (10) corresponds to Maxwell-Wagner's equation[30]. ε, ε_1, and ε_2, are the relative permittivity values for the dual-phase mixture, the first phase, and the second phase; while V_1 and V_2 values correspond to the volume fractions of the first and the second phases, respectively. If the relative permittivity values for the liquid and solid phases are known, the relative permittivity of the dual-phase mixture
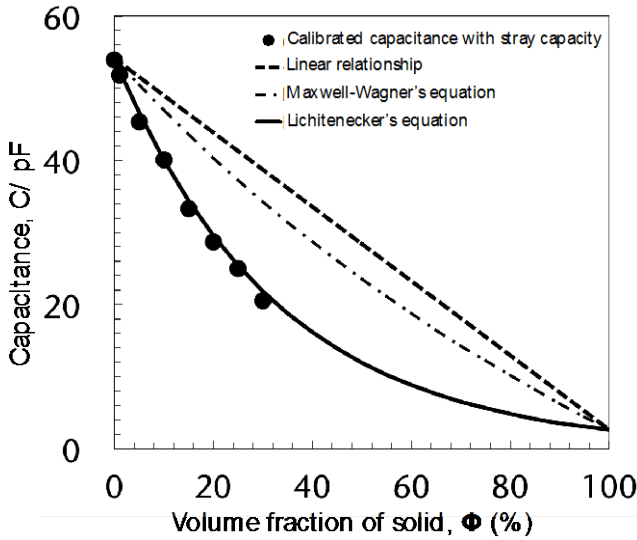

Fig.7 Experimental and theoretical capacitances of the aqueous SiO_2 suspensions containing different volume fractions of the SiO_2 powder with a mean particle diameter of 1.42 μm.

Fig.8 Experimental and theoretical capacitances of the aqueous SiO_2 suspensions containing different volume fractions of the SiO_2 powder with a mean particle diameter of 63 μm.

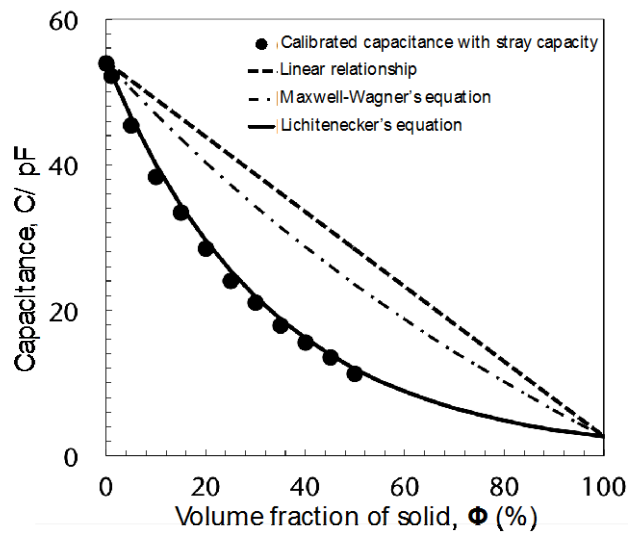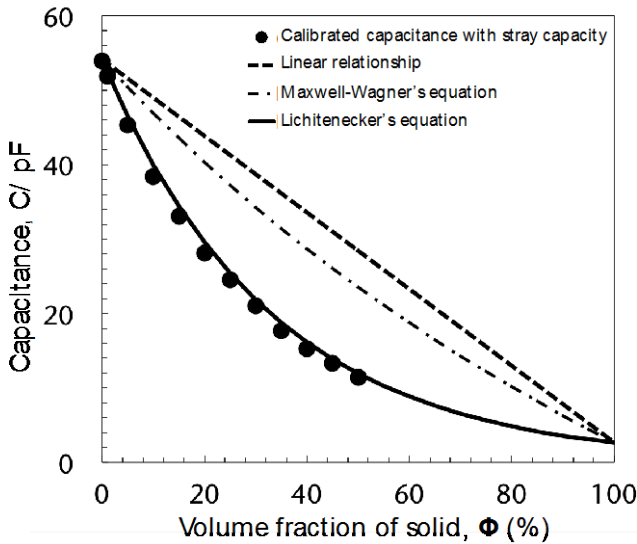**Fig.9** Experimental and theoretical capacitances of the aqueous SiO_2 suspensions containing different volume fractions of the SiO_2 powder with mean particle diameters of 105–420 μm.
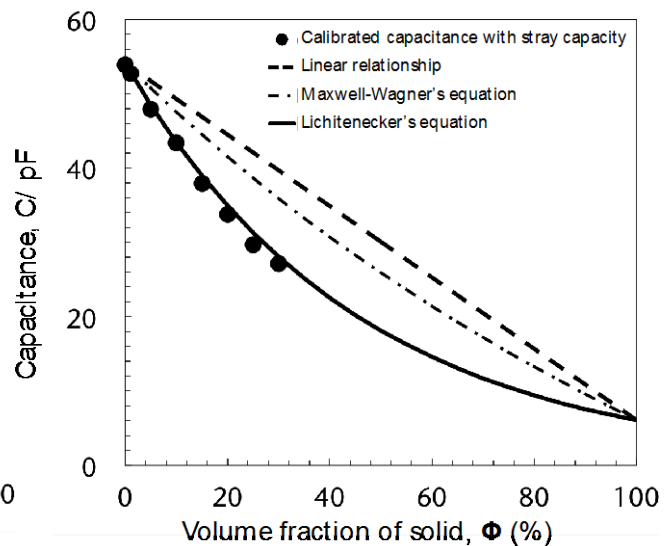

Fig.10 Experimental and theoretical capacitances of the aqueous Al_2O_3 suspensions containing different volume fractions of the Al_2O_3 powder with a mean particle diameter of 0.1 μm.

can be estimated by measuring its electrical capacitance.

Figs. 7−10 show the results of the electrical capacitance measurements as functions of the solid volume fractions for the following aqueous oxide suspensions: (a) ultrafine SiO_2 powder, (b) fine SiO_2 powder, (c) SiO_2 powder, and (d) ultrafine Al_2O_3 powder (the plotted solid lines were calculated by using equations (9)−(11) described above). The obtained results revealed that the electrical capacitances drastically decreased with increasing volume fractions of the dispersed oxides, and the resulting relationships could be successfully reproduced by using a combination of the proposed capacitance model with Lichtenecker's equation. When the same powders with different particle sizes were used, the observed decreases in electrical capacitance (corresponding to decreases in suspension relative permittivity) could be similarly reproduced by Lichtenecker's equation. Furthermore, the drastic capacitance decrease detected for the aqueous suspension containing ultrafine Al_2O_3 powder (characterized by a different relative permittivity value as compared to that of SiO_2) also obeyed Lichtenecker's equation. Therefore, the electrical capacitances of the aqueous oxide suspensions measured at room temperature were not affected by the relative permittivity of the dispersed solid phase or particle sizes and depended only on their volume fractions.

3.2 Capacitance Theoretical Prediction at High Temperatures

To verify the applicability of the proposed capacitance model at high temperatures, the capacitance variations for the molten oxide suspensions were systematically measured and then compared with the theoretical modeling results combined with the relative permittivity equations. In particular, capacitances of the oxide melt suspensions with specified compositions were measured between the liquidus and glass-transition temperatures, while the corresponding volume fractions of the solid phases were determined from the related phase diagram by using a lever rule.

As a typical example of the capacitance measurements, Fig. 11 shows the capacitance evolution for the 45.0CaO−45.5SiO$_2$−2.3Al$_2$O$_3$−7.2MgO (mol%) slag with a solid volume fraction of 10% obtained during isothermal annealing at 1387 °C. The measured electrical capacitance values initially decreased during the first 3 h of heating due to the expected increase in crystallinity. However, little capacitance changes were observed beyond this region owing to the absence of further crystallization in the supercooled oxide melt. Therefore, the crystallization process was found to be equilibrated after 6 h of heating at the specified experimental conditions.

Fig. 12 shows the capacitance variations for the 45.0CaO−45.5SiO$_2$−2.3Al$_2$O$_3$−7.2MgO (mol%) slag measured as functions of the solid phase volume fraction obtained from the corresponding phase diagram. The observed decrease in electrical capacitance corresponded to an increase in the volume fraction of the solid phase, similar to the aqueous suspensions. In order to predict the related capacitance values theoretically, the relative permittivity of the matrix melt was calculated backwards from the electrical capacitance of the 45.0CaO−45.5SiO$_2$−2.3Al$_2$O$_3$−7.2MgO (mol%) slag annealed at 1450 °C for 6 h (which corresponded to a uniform liquid region on the phase diagram) using the model described in Section 2.1. In addition, the relative permittivity of the primary CaO·SiO$_2$ crystalline phase was equal to 8.6[31]. However, the results presented in Fig. 12 indicate that Lichtenecker's equation could not be used to reproduce the measured slag experimental capacitances at high temperatures, although the same equation combined with the proposed capacitance model could successfully predict the
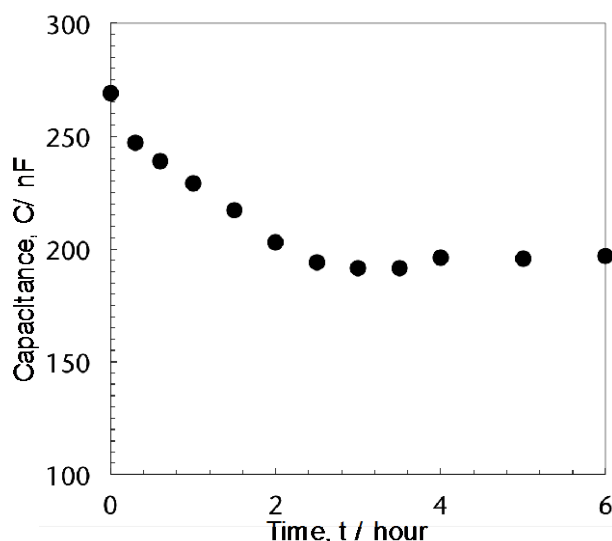
Fig.11 Capacitance change with time monitored for the 45CaO−45.5SiO$_2$−2.3Al$_2$O$_3$−7.2MgO(mol%) supercooled oxide melt at 1387 °C.
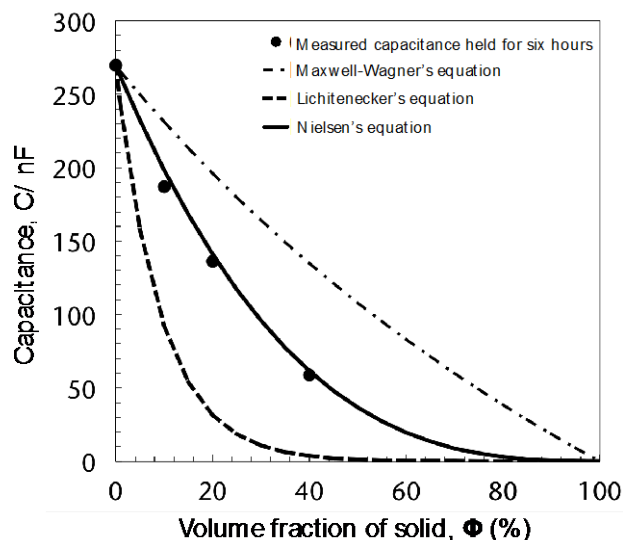
Fig.12 Experimental and theoretical capacitances of the 45CaO−45.5SiO$_2$−2.3Al$_2$O$_3$−7.2MgO (mol%) suspensions with different solid volume fractions.

capacitance decrease for the aqueous suspensions. The observed discrepancy could po ssibly be attributed to the large difference in relative permittivity between the melted and the crystalline phases. However, the obtained capacitance values for the 45.0CaO–45.5SiO$_2$–2.3Al$_2$O$_3$–7.2MgO (mol%) slag were successfully reproduced by using Nielsen's equation for estimating relative permittivity of binary mixtures[32]:

$$\varepsilon^n = V_1(\varepsilon_1)^n + V_2(\varepsilon_2)^n \cdots (12)$$

Here n is the dimensionless number depending on the mechanism of current propagation through the sample melt, which was equal to 1/3 in the present work. When the second phase is vertically distributed against the current propagation direction, n equals to 1; and when it is parallel to the direction of current propagation, n is -1[33]. The n value of 1/3 utilized in this study was previously suggested by Looenga[34] and corresponded to the random distribution of the second phase in a melt matrix.

Furthermore, in order to test the model applicability to different oxide systems, the electrical capacitance of the 57.1CaO–3.5SiO$_2$–39.4Al$_2$O$_3$ (mol%) slag was evaluated at different values of the solid volume fraction. Fig. 13 shows the capacitance evolution for the 57.1CaO–3.5SiO$_2$–39.4Al$_2$O$_3$ (mol%) slag with a solid volume fraction of 10% measured during isothermal annealing at 1484 °C. The obtained capacitance values decreased during the first 40 min of heating due to crystallinity increase, after which little changes in the measured capacitance were observed. Therefore, it can be concluded that the crystallization process was equilibrated after 1 h of annealing at the specified experimental conditions, which represented a shorter sample crystallization time due to the faster diffusion in a less viscous melt.

Fig. 14 shows the experimental electrical capacitance values for the 57.1CaO–3.5SiO$_2$–39.4Al$_2$O$_3$ (mol%) slag plotted as functions of the solid volume fraction and compared with the corresponding calculation results (the relative permittivity of the oxide melt was similarly back-calculated from the melt capacitance via the model described in Section 2.1). As expected, the obtained capacitances decreased with increasing solid volume fraction and could be fit by a combination of Nielsen's equation at n=1/3 with the proposed capacitance prediction model.

The obtained results indicate that the volume fraction of dispersed solids in supercooled oxide melts can be successfully quantified in-situ at high temperatures by using a relatively simple electrical capacitance model and suspension relative permittivity values calculated by using Nielsen's equation. However, the effects of the double-layer capacitance and internal impedance on the measured capacitance values have not been considered in the present work and thus can be investigated in future studies.

Fig.13 Capacitance change with time monitored for the 57.1CaO–3.5SiO$_2$–39.4Al$_2$O$_3$ (mol%) supercooled oxide melt at 1484 °C.
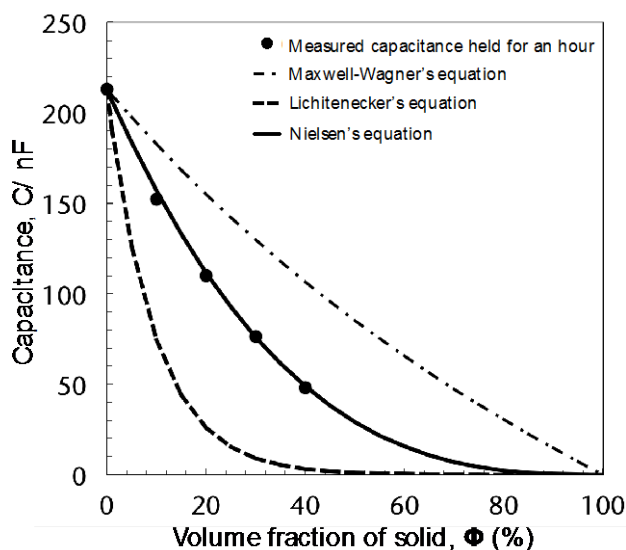
Fig.14 Experimental and theoretical capacitances of the 57.1CaO–3.5SiO$_2$–39.4Al$_2$O$_3$ (mol%) suspensions with different solid volume fractions.

4. Conclusions

A new in situ method for quantifying crystallinity of supercooled oxide melts was developed by measuring electrical capacitances of the aqueous suspensions at room temperature and oxide melt suspensions at high temperatures. In addition, a theoretical capacitance prediction model based on the geometrical configuration of the measurement electrodes was proposed.
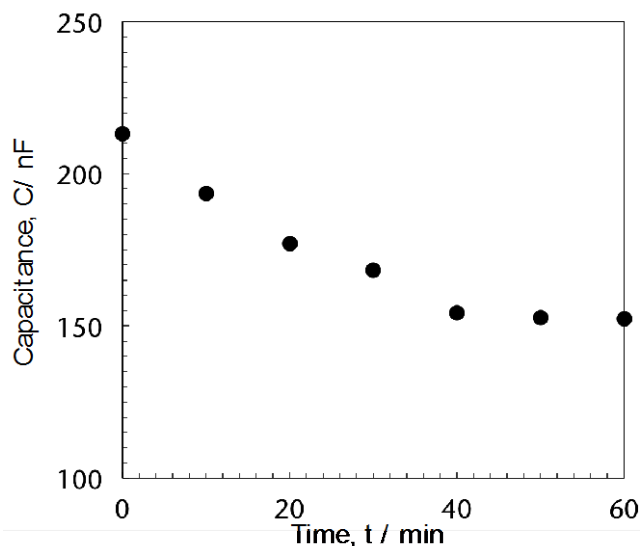
The results of the capacitance measurements conducted for several liquids with known relative permittivity at various rod immersion depths were consistent with the data obtained from the proposed capacitance prediction model. For the dual-phase fluids with various solid volume fractions, the measured values of electrical capacitance at room temperature could be described by Lichtenecker's equation and were independent of the solid phase relative permittivity or dispersed particle sizes.

The results of the capacitance measurements obtained for the oxide melts with various solid volume fractions at high temperatures revealed that the observed changes in electrical capacitance depended both on the relative permittivity and the volume fractions of the dispersed solid phases and could be described by Nielsen's equation.

In this study, the influence of the electric double layer near the electrodes on the electrical capacitance was not investigated. Furthermore, the capacitance of high-temperature uniform oxide melts was affected by their compositions; thus, it could be assumed that its magnitude likely depended on the melt manufacturing procedure. After the above-mentioned issues are resolved, the proposed theoretical capacitance prediction model may have broad applications in various fields.

References

1) R. Yamanaka, K. Ogawa, H. Iritani and S. Koyama: ISIJ Int., 32 (1992), 136.
2) E. Andersson and D. Sichen: Steel Res. Int., 80 (2009), 544.
3) D. Elwell, P. Capper and C.M. Lawrence: J. Cryst. Growth, 24/25 (1974), 651.
4) H.Y. Chang, T.F. Lee and T. Ejima: Trans. ISIJ, 27 (1987), 797.
5) K.C. Mills: ISIJ Int., 33 (1993), 148.
6) N. Saito, S. Yoshimura, S. Haruki, Y. Yamaoka, S. Sukenaga and K. Nakashima: Tetsu-to-Hagane., 95 (2009), 282 (in Japanese).
7) L.W. Coughanour, L. Shartsis and H.F. Shermer: J. Am. Ceram. Soc., 41 (1958), 324.
8) S. Hara and K. Ogino: Can. Metal. Quart., 20 (1981), 113.
9) H. Kania, K. Nowacki and T. Lis: Metalurgija, 52 (2013), 204.
10) M. Askari and A.M. Cameron: Can. Metal. Quart., 30 (1991), 207.
11) P. Vadasz, M. Havlik and V. Danek: Can. Metal. Quart., 39 (2000), 143.
12) E.J. Jung and D.J. Min: Steel Res. Int., 83 (2012), 705.
13) A. Nagashima: Int. J. Thermophys., 11 (1990), 417.
14) M. Hayashi, H. Ishii, M. Susa, H. Fukuyama and K. Nagata: Phys. Chem. Glasses, 42 (2001), 6.
15) Y. Kang, J. Lee and K. Morita: Metall. Mater. Trans. B, 44 (2013), 1321.
16) M. Suzuki, H. Mizukami, T. Kitagawa, K. Kawakami, S. Uchida and Y. Komatsu: ISIJ Int., 31 (1991), 254.
17) N. Saito, K. Kusada, S. Sukenaga, Y. Ohta and K. Nakashima: ISIJ Int., 52 (2012), 2123.
18) Y. Harada, K. Kusada, S. Sukenaga, H. Yamamura, Y. Ueshima, T. Mizoguchi, N. Saito and K. Nakashima: ISIJ Int., 54 (2014), 2071.
19) S. Haruki, S. Sukenaga, N. Saito and K. Nakashima: High Temp. Mater. Process, 30 (2011), 405.
20) M. Susa, A. Kushimoto, H. Toyota, M. Hayashi, R. Endo and Y. Kobayashi: ISIJ Int., 49 (2009), 1722.
21) T. Ootsuka, K. Hamano, K. Tsutsumi and M. Kurano: JCS−Japan, 104 (1996), 301.
22) G.H. Wen, X.B. Zhu, P. Tang, B. Yang and X. Yu: ISIJ Int., 51 (2011), 1028.
23) L. Zhou, W. Wang and K. Zhou: ISIJ Int., 55 (2015), 1916.
24) Y. Ohta, M. Kitayama, K. Kaneko, S. Toh, F. Shimizu and K. Morinaga: J. Am. Ceram. Soc., 88 (2005), 1634.
25) F.E. Critchfield, J.A. Gibson Jr. and J.L. Hall: J. Am. Ceram. Soc., 75 (1953), 1991.
26) R.M. Shirke, A. Chaudhari, N.M. More and P.B. Patil: J. Chem. Eng. Data, 45 (2000), 917.
27) G. Akerlof: J. Am. Chem. Soc., 54 (1932), 4125.
28) J. Robertson: Eur. Phys. J. Appl. Phys., 28 (2004), 265.
29) K. Lichtenecker: Phys. Z., 27 (1926), 115.
30) K.W. Wagner: Arch. Elektrotech., 2 (1914), 371.
31) K. Hayashi, M. Fukui and I. Uei: J. Ceram. Assoc. Jpn., 89 (1981), 165 (in Japanese).
32) K.K. Karkkainen, A.H. Sihvola and K.I. Nikoskinen: IEEE Trans. Geosci. Remote Sensing, 38 (2000), 1303.
33) J.B. Kim, T.W. Kim and C.G. Kim: J. Appl. Polym. Sci., 100 (2006), 2189.
34) H. Looyenga, Physica, 31 (1965), 401.

Some aspects of foaming slag

Johan Martinsson, Björn Glaser, Du Sichen
KTH Royal Institute of Technology, Stockholm, Sweden

Keywords: Slag foaming, viscosity, lime dissolution in foaming slag, droplet movement

Abstract: Foaming slag has been a topic of research for decades because of its crucial role in BOF-converters and electric arc furnaces (EAF). However, due to the great difficulties in the study under extreme conditions in these processes, the understanding of the formation of foam and its behavior is still very limited. The present work aims at experimental studies on some aspects of foaming slag using both cold model and foaming converter slag at steelmaking temperature, namely the apparent viscosity of slag foam, the residence time of metal droplets in foam and the dissolution of lime in foam.

1. Introduction

Foaming slag plays crucial role in both BOF-converters and electric arc furnaces (EAF). For example, slag starts foaming in BOF only a couple of minutes after blowing has initiated and slag foaming continues almost throughout the whole period of decarburization [1]. Unfortunately, the understanding of foaming and the mechanism related to this phenomenon are still far from satisfaction. Discussions regarding whether the reactions in the BOF processes take place at the interface between the steel droplets and the foaming slag or at the interface between the steel bath and the slag are still going on, though many studies have been carried out for decarburization and dephosphorization processes [2-10].

Foaming slag consists of gas, liquid and even solid phases [7, 10, 11]. The knowledge regarding (1) the impact of foaming on the movement of the slag phase, (2) the movement of droplets in the foam, and (3) the dissolution of lime in a foaming slag is still lacking. The focus of the present work is to carry out both cold model study and experiments at steelmaking temperature to improve the understanding of the above-mentioned aspects.

2. Experimental

2.1 Cold model study.

Figure 1 shows schematically the setup of the cold model. It consisted a transparent Plexiglas cylinder (inner diameter: 93 mm and height: 280 mm). A silica filter with pore size 10-16 µm was used to separate the gas compartment (100 mm above the bottom of the vessel) from the silicon oil. This arrangement ensured a uniform distribution of gas flow through the horizontal section. Argon gas was used to generate the foam. Silicon oils with different dynamic viscosities were studied. A Bronkhorst mass flow meter (model F-201CV-1K0-AAD-33-V, calibrated for 1 ln/min^{-1} Ar, 2 bar (g)/0 bar (g) at 293 K) and a Bronkhorst High-Tech B.V.E -7000 flow-buss controller were used.

Since different gas flow rates created foams with different relative foaming heights ($\Delta h/h_0$), different amounts of silicone oil were used to keep a constant foam height, 180 mm for all experiments.

For the viscosity measurements a viscometer Brookfield LVDV-II+Pro using the Rotating Spindle Technique was mounted above the vessel. As measurement spindle a Brookfield standard spindle of model LV2 was used with a cylindrical bob diameter of 18.6 mm and a height of 6.7 mm. All parameters needed for the viscosity measurements with this type of spindle are given by standard controlling software of the viscometer provided by the company Brookfield. Viscosity measurements were started when the foam of silicone oil had become stable.
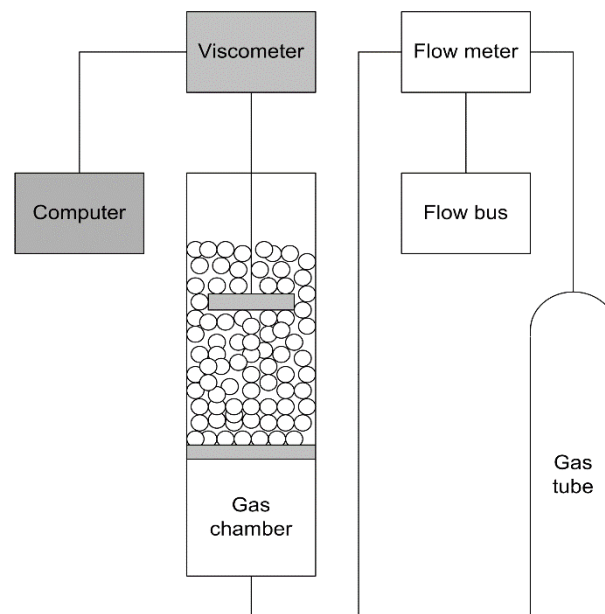

Figure 1. Cold model experimental setup.

Particle movement

In order to record the movement and path of particles and droplets, a high speed camera and a regular camera were mounted close to the vessel. The particles and droplets were dropped from 20 mm above into the stabilized foam. The falling time were measured with a stop watch and the resulting average velocity was calculated. Different materials and particle sizes were used. At least, ten tests with each of the particles and droplets were conducted in order to confirm the reproducibility of the results.

2.2   Experiments at steelmaking temperature

Setup

The high temperature experiments were carried out in an open air setup using an induction furnace with a water cooled copper coil. The setup is schematically shown in Figure 2. For temperature measurement and experimental control, an infrared temperature sensor (model thermometer CTM-1SF75-C3) was used, instead of thermocouples that would be affected by the magnetic field [12]. The IR-sensor was calibrated with a pyrometer of model Raytek Thermoalert ET.

To prepare the slag, FeO was produced first by mixing Fe_2O_3 and iron powder. The mixture was heated to 1123 K and kept there for approximately 70 hours in a closed Fe crucible under argon atmosphere. After taking out from the Fe crucible, the FeO was crushed into smaller pieces and mixed with CaO (calcined for 10 hours at 1173 K) and an already pre-melted slag consisting of 54 mass% CaO and 46 mass% SiO_2 for the final slag composition.
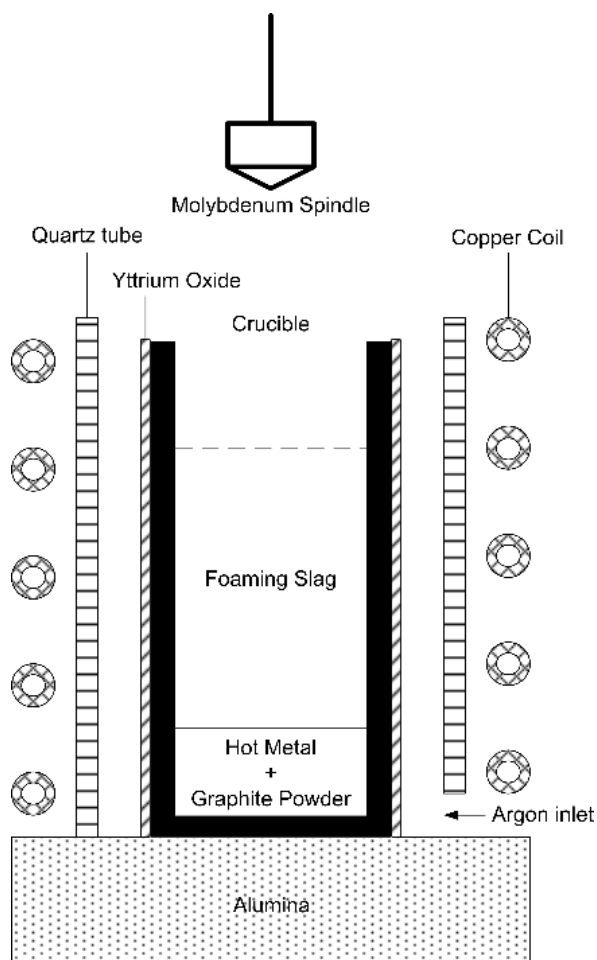

Figure 2. High temperature experimental setup.

Graphite crucibles (with an inner diameter of 30 mm, wall and bottom thickness of 10 mm and a total height of 140 mm) were employed. All crucibles were painted on the outside with yttrium oxide paint to reduce oxidation during experiment. In order to generate foaming slag, 7 g of hot metal (3.9 mass% carbon), 1 g of graphite powder and 67 g slag was put into the crucible.

Viscosity measurement

Preliminary experiment indicated that the foaming slag had very high viscosity. Hence, a viscometer of model Brookfield RVDV-II+Pro that was suitable for the range of viscosities of the foam was used for the measurements. A nonstandard spindle made of molybdenum was

used. The spindle was designed as a cylinder with a conical tip to be able to introduce the spindle easily into the slag. The cylindrical part of the spindle was 15 mm in diameter and 7 mm in height. The conical part had a height of 4 mm. The spindle was calibrated with standard liquids before use.

When the foam was stabilized, the viscosity measurement was started by introducing the spindle into the foam. Different rotation speeds were employed for the measurements.

Lime dissolution

Lime provided by TATA Steel was cut and polished into 1.0 x 1.0 x 1.0 cm cubes. During the experiment, one cube was added when a foaming slag was observed and an appropriate temperature was reach (around 1600 °C). The furnace was turned off after 30, 60 or 120 seconds and the slag was solidified spontaneously within seconds. The degree of dissolution of each cub was evaluated by measuring the dimensions of the reacted cub.

3. Results and Discussion

3.1 Apparent viscosity

The results of viscosity measurements show that the silicone oil foam is a shear thinning non-Newtonian fluid. This finding is in accordance with literature [13]. Hence, the term of apparent viscosity is used in the later discussion. The apparent viscosity is presented in Figure 3a and 3b at different RPM for the two silicon oils, respectively.
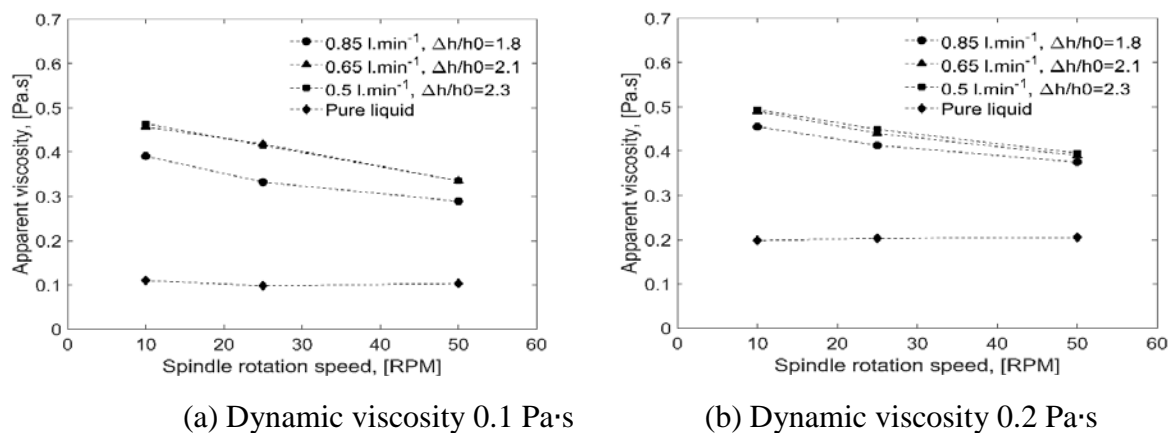

(a) Dynamic viscosity 0.1 Pa·s   (b) Dynamic viscosity 0.2 Pa·s

Figure 3. The apparent viscosity of silicon oil foam as a function of spindle rotation speed

The apparent viscosity of the foam is much higher than the dynamic viscosity of pure silicone oil. In the low rotation speed region, the apparent viscosity is up to five times higher as in pure silicon oil, as given in Figure 3(a) and 3(b). The apparent viscosity also seems to vary with gas flow rate, an increasing viscosity with decreasing gas flow rates can be observed.

Similarly, the slag foam also shows a non-Newtonian shear thinning behavior, (Figure 4). Also, the measured apparent viscosity in slag foam is much higher comparing to the pure slag.

Non-Newtonian fluids are difficult to predict, since it depends on the experimental setup and conditions. For example, the results may differ with the type of spindle as well as vessel. Despite of the nature of the non-Newtonian flow, the results shown in Figures 3 and Figure 4

still indicate evidently that the dynamic viscosity of the liquid (for both oil and slag) plays much less important role in determining the apparent viscosity of the foam and therefore the movement of the particles in the foam.
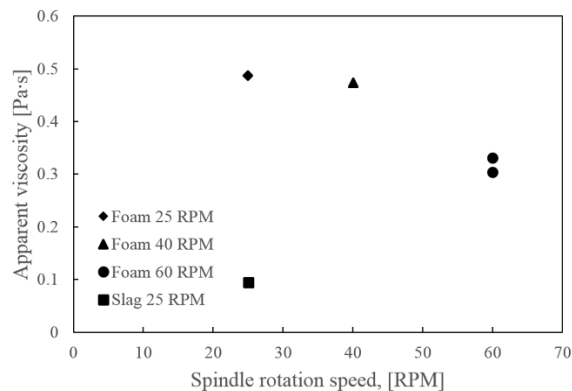

Figure 4 Apparent viscosity of foaming slag as a function of spindle rotation speed.

A comparison of the apparent viscosities of the two different silicone oils (Figure 3) reveals that the apparent viscosity of the foam using 0.2 Pa·s oil is only 10-20% higher than the foam formed by the silicone oil of 0.1 Pa·s. The fact that the apparent viscosities are not proportional to their dynamic viscosities indicates that there is a common factor affecting the viscosity of the foam. The rotation of the spindle has to not only overcome the viscous force, but also the surface tension of the bubbles. A rough calculation reveals that the change of the surface area leads to an increase of the surface area. [14, 15] The energy change due to the increase of the surface area plays more profound role than the resistance force due to the viscosity.

3.2   Residence time of particles in foaming slag

The falling times of the particles and droplets in silicon oil foam were determined. It was observed that larger particles of high density destroyed somehow the foam, making smaller bubbles collide and turn into bigger ones, and fell fast down towards the bottom of the vessel. For lighter and smaller particles and droplets, the paths were not straightly downwards. The resistance of the foam bubbles pushed the particles and droplets aside as they fell, prolonging the residence time. It can be observed that the velocity of these particles and droplets are much lower than expected. Table 1 presents the times of steel and alumina particles falling through a foam of 0.18 m in height. The average velocities of the particles and the calculated terminal velocities are also listed in the table. It is shown surprisingly that the calculated terminal velocities using the dynamic viscosity are more than 10 times higher than the experimentally determined velocity. Even the velocities calculated using the apparent viscosities of the foam are much higher than the experimental values. It is evident that the energy needed to deform the bubbles due the increase of surface area plays the dominating role in the movement of the particles. Any model using Stoke law to estimate the resistance time of the droplets in the foaming slag would greatly underestimated the time and the slag-metal reaction. It is seen in Table 1 that the difference between the values calculated using Stoke law and the experimental data is more profound in the case of alumina particles. In view that the density difference in this case is more close to that between the steel and slag, the values obtained for alumina might provide more relevant picture. Nevertheless, the movement of steel droplets in the foaming

slag could be much slower than the droplets in the foam of silicon oil, since the density difference in the former case is less.

Table 1 The falling times of different particles in foamed silicon oil

Type of particles	Steel particle		Alumina	
Particle size [mm]	2	3	3	5
Average Falling time [s]	12.4	4.3	23	8.6
Average velocity [m/s]	0.0145	0.0420	0.0077	0.021
Calc. Velocity (stokes law, liquid viscosity) [m/s]	0.148	0.33	0.098	0.272
Calc. Velocity (stokes law, foam viscosity) [m/s]	0.042	0.049	0.024	0.030
Experimental conditions: Viscosity 99.88 [cP] Surface Tension 0.05 [N/m] Foam 0.18 [m] Gas fraction 0.83 Bubble size 2-4 [mm]				

3.3   Lime dissolution.

Figure 5 presents the size of the lime cube as a function of the dissolution time. In this case, a slag containing 45mass% FeO was used. This composition would correspond the slag during the initial stage of the converter process, wherein the FeO content is high. It is interesting to mention that a comparison with the dissolution rate of lime in the pure slag without foaming reveals no appreciable difference in the dissolution rate. The reason for this similarity is a topic of ongoing project.
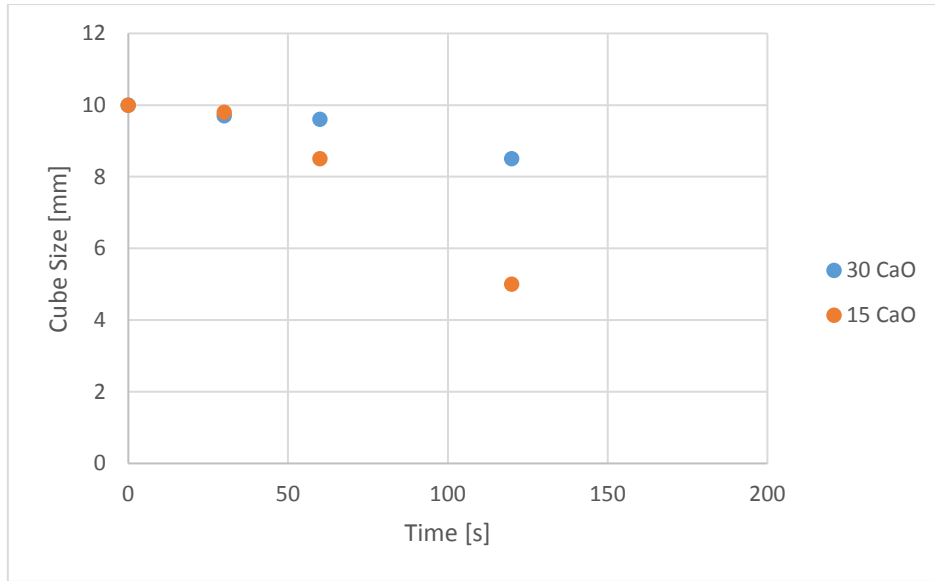
Figure 5 Size of the lime cube as a function of dissolution time in foaming slag of initial stage of blowing, Temperature: 1550-1600 ^{o}C, Slag composition: 30 CaO: 45wt%FeO-30wt%CaO-25wt%SiO$_2$ and 5 CaO: 45wt%FeO-15wt%CaO-40wt%SiO$_2$

Figure 6 presents the size of the lime cube as a function of the dissolution time in the slag after the initial stage of the blowing. Slag containing 25mass% FeO were studied.
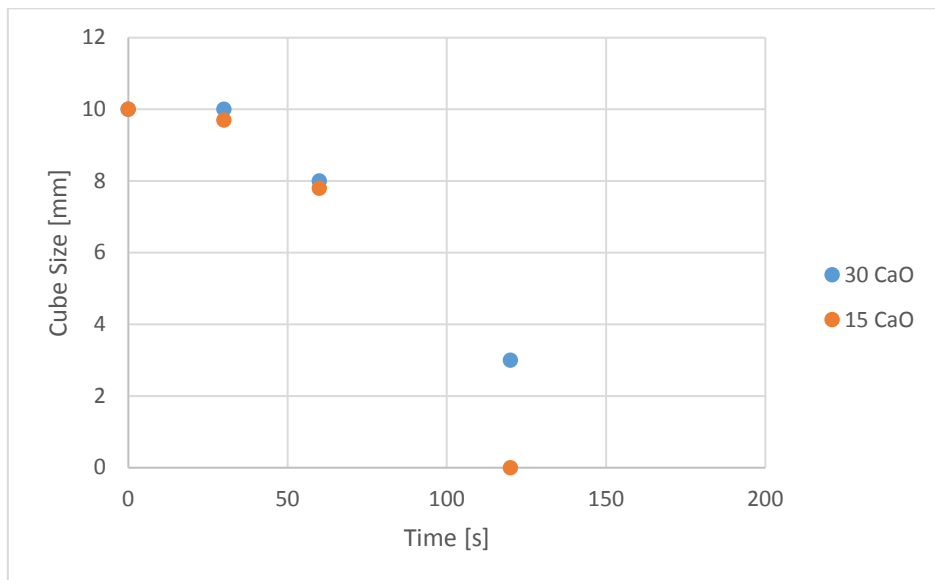

Figure 6 Size of the lime cube as a function of dissolution time in foaming slag after initial stage of blowing, Temperature: 1550-1600 degC. Slag compositions: 30 CaO: 25wt%FeO-30wt%CaO-35wt%SiO$_2$-10wt%MnO and 15 CaO: 25wt%FeO-15wt%CaO-

It should be mentioned that the slag having higher silica content dissolves lime faster. Preliminary study indicates that this is probably due to the structure of the foam. Detailed investigation is currently carried out to gain a thorough understanding.

Summary

Some aspects of slag foaming were studied in the present work. The results revealed confidently that the surface tension has much bigger impact on the apparent viscosity and therefore on the movement of particles in the foam in comparison with the dynamic viscous energy. The required surface energy change could slow down the particle movement greatly in a foaming slag, staying more than 10 times longer in the foam than evaluated by terminal velocity in pure liquid. Therefore the use of the dynamic viscosity to estimate the residence time of a particle is seriously questioned. The dissolution of lime in the foaming slag corresponding to the initial stage of oxygen blowing was found to have similar rate as in liquid slag. However, foaming slag initial having higher viscosity seemed to have faster dissolution. This behavior could be attributed to the structure of the foam.

References:

1. Heikki Jalkanen and Lauri Holappa, In *Treatise on Process Metallurgy*, ed. Seshadri Seetharaman (Elsevier: Boston, 2014), pp 223-270

2. Cicutti, C., et al., *Analysis of slag foaming during the operation of an industrial converter.* Latin American applied research, 2002. **32**(3): p. 237-240.

3. Deo, B., et al., *Characterization of slag-metal droplet-gas emulsion in oxygen steelmaking converters.* ISIJ international, 1996. **36**(6): p. 658-666.

4. Martín, M., M. Rendueles, and M. Díaz, *Emulsion Analysis in a Gas/Liquid/Liquid Reactor With Top Blowing.* The Canadian Journal of Chemical Engineering, 2004. **82**(2): p. 249-255.

5. Jung, S.-M. and R.J. Fruehan, *Foaming characteristics of BOF slags.* ISIJ international, 2000. **40**(4): p. 348-355

6. Meyer, H., et al., *Slag-metal emulsions and their importance in BOF steelmaking.* J METALS, 1968. **20**(7): p. 35-42.

7. Ito, K. and R.J. Fruehan, *Study on the foaming of CaO-SiO2-FeO slags: Part II. Dimensional analysis and foaming in iron and steelmaking processes.* Metallurgical Transactions B, 1989. **20**(4): p. 515-521.

8. Luomala, M.J., et al., *Splashing and Spitting Behaviour in the Combined Blown Steelmaking Converter.* ISIJ International, 2002. **42**(9): p. 944-949.

9. Ek, M., *A study of some aspects of gas-slag-metal interactions: Towards dynamic process model and control.* 2012.

10. Brämming, M., *An Operational View on Foaming and Slopping Control in Top-blown BOS Vessels.* 2015.

11. Ito, K. and R.J. Fruehan, *Study on the foaming of CaO-SiO2-FeO slags: Part I. Foaming parameters and experimental results.* Metallurgical Transactions B, 1989. **20**(4): p. 509-514.

12. Smalcerz, A. and R. Przylucki, *Impact of Electromagnetic Field upon Temperature Measurement of Induction Heated Charges.* International Journal of Thermophysics, 2013. **34**(4): p. 667-679.

13. Cohen-Addad, S., R. Höhler, and O. Pitois, *Flow in foams and flowing foams.* Annual Review of Fluid Mechanics, 2013. **45**(1): p. 241.

14. C. A. Miller, P. Neogi, *Interfacial Phenomena: Equilibrium and Dynamic Effects*, 2nd ed., Surfactant Science Series, Vol. 139, CRC Press, Taylor & Francis Group, Boca Raton, Florida, USA 2008.

15. R. G. Mortimer, *Physical Chemistry*, 2nd ed., Academic Press, Burlington, MA, USA 2000.

New Lime Based Slag Conditioners
to Improve the Dephosphorization
in the BOF Process of Dillinger

H. Lachmund[*], Y. Xie
AG der Dillinger Hüttenwerke, Dillingen, Germany

M. Nispel, T. Chopin, J. Noldin
Lhoist S.A., Nivelles, Belgium

Abstract:

A new and fully compatible lime based slag enhancer – named Booster[™] – was developed by Lhoist to improve BOF steelmaking by boosting the metallurgical properties of lime. Initial pilot trials have demonstrated the higher dephosphorization efficiency of the new product and extensive in-blow sampling allowed a close follow-up of the slag path. Later, industrial trials carried out in close cooperation with Dillinger have confirmed these initial findings. This paper discusses the development and results of both pilot and industrial trials.

1. Introduction

In BOF steelmaking the slag forming process has a major impact on the metallurgical results as well as on the refractory wear. The aimed chemistry of BOF slags is mainly controlled by the addition of lime to guarantee a suitable chemical composition of the final slag formed with the oxides SiO_2, FeO_n, MnO and P_2O_5 developed during the oxygen blow. Due to the short blowing time of about 15 minutes the kinetics of the lime dissolution influences the refining character of the slags. In the past different fluxes like fluorspar have been used to accelerate the lime dissolution with negative effects on refractory wear and environmental pollution. Therefore a new environmental friendly slag conditioner was developed.

2. Metallurgical fundamentals

The slag path in the ternary system $CaO\text{-}FeO_n\text{-}SiO_2$ during the oxygen blowing process and its influence on the dephosphorization and refractory wear were often investigated in the past (Figure 1) [1-4].
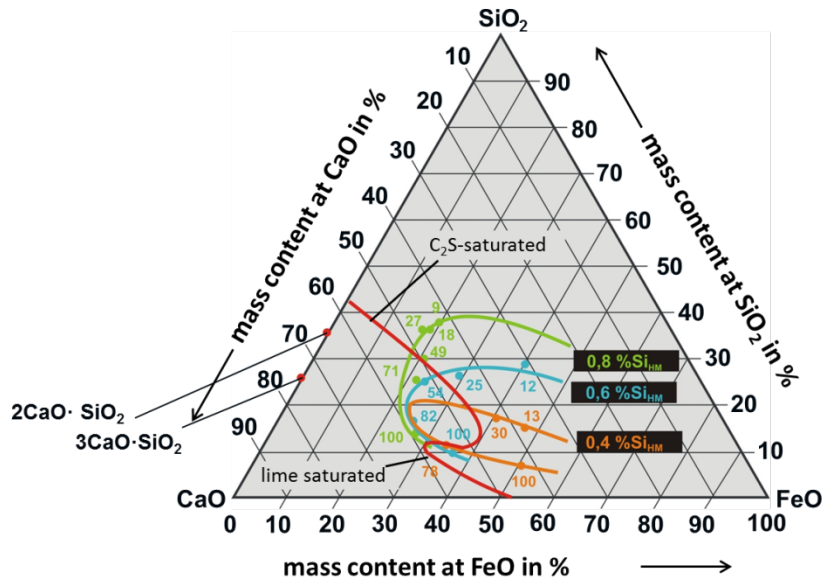
Figure 1. Slag path in the FeO'-CaO'-SiO$_2$' system for different Si contents in the hot metal [1]

Here the kinetics of the lime dissolution has a big impact on the slag characteristics. In the early stage of the blowing process at low temperatures the high iron oxide activity promotes the reactivity of the slags which leads to interactions of the iron oxide-rich phosphorus containing silicate slags with the solid lime [5]. The infiltration of iron oxide into the solid lime leads to the formation of calcium ferrite and calcium wüstite and thus improving the dissolution of lime. Additionally the silicon and phosphorus react to phosphorus containing calcium silicates in the solid state (Figure 2) [6]. On the other hand the continuous supply of iron oxide over the complete blowing process and the strong bath agitation ensure the progressive lime dissolution.
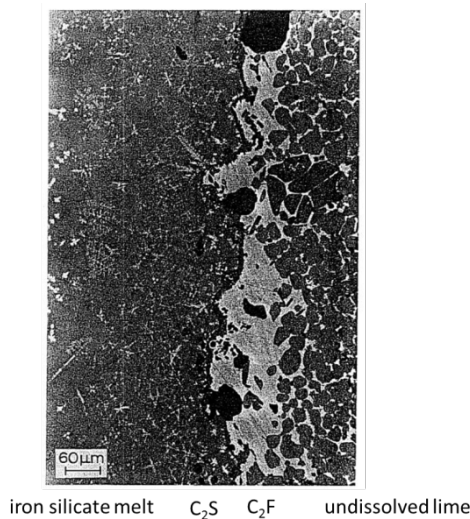

Figure 2. Reaction interface between soft burnt lime and an iron silicate melt [6]

Especially these early slags with low basicity have the highest MgO solubility and are therefore responsible for the refractory wear. More than 75% of the observed refractory wear are slagged in the first quarter of the blowing process due to the slow dissolution rate of the lime and the preferred silicon and iron oxidation in this blowing period [1].

An internal Dillinger simulation model has been developed which calculates the time dependent development of the concentrations of the elements dissolved in the liquid steel and of the respective oxides in the liquid slag phase during the whole BOF process. Furthermore the corresponding temperature of the steel bath, the temperature distribution in the scrap pieces charged into the BOF vessel, as well as the lime dissolution are calculated in each time step (Figure 3) [7].
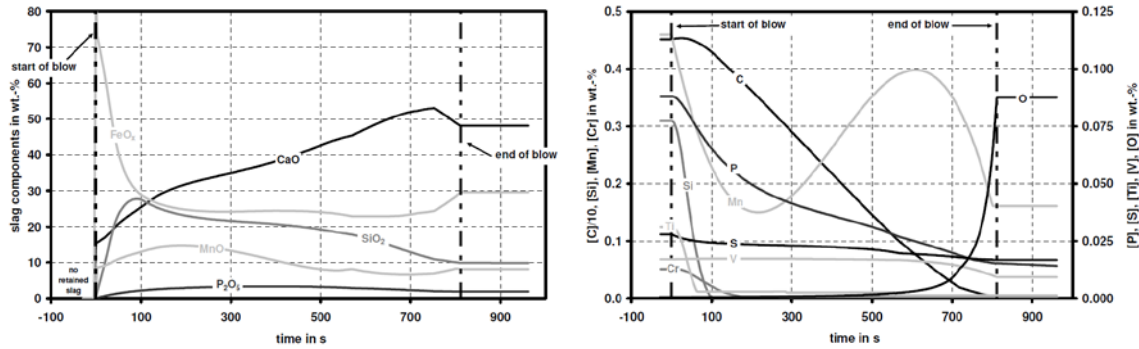

Figure 3. Theoretical concentration profiles of the oxides in the slag phase and dissolved elements in the melt [7]

During the post stirring time after the blowing period an empirical equilibrium concerning the phosphorous distribution $L_P = (\%P_2O_5)/[\%P]$ between slag and steel melt is used as a function of the current theoretical values for the bath temperature T in K and the iron content of the slag (%Fe) in wt.-%:

$$log_{10}\left(\frac{(\%P_2O_5)}{[\%P]}\right) = 8.38 + 2.5 \cdot log_{10}\big((\%Fe)\big) - 0.0476 \cdot (\%Fe) + \frac{16410}{T} \qquad (1)$$

Therefore, it is widely accepted that a new product, that enhances slag formation, might bring important benefits for the BOF process.

3. Product description

In order to provide the steelmaking industry with a cost effective and environmental friendly fluxing agent, Lhoist has developed an innovative lime based slag conditioner called Booster™, which consists of an engineered lime based compact, of which the chemistry can be tailored according to different needs and constrains. Furthermore, Booster™ is fully compatible with modern environmental and safety requirements.

Figure 4. Two different types of Booster™

Figure 4 shows a mixture of two different types of slag conditioners, produced with Lhoist's IP protected technology. This technology allows to tailor-make slag conditioners according to the customer needs. Therefore a large variety of substances, such as $CaO \cdot Al_2O_3$, $3CaO \cdot Al_2O_3$, $CaO \cdot 2Al_2O_3$, $12CaO \cdot 7Al_2O_3$, Al_2O_3, B_2O_3, NaO_3, TiO_2, Fe, FeO, Fe_2O_3, $CaO \cdot Fe_2O_3$, $2CaO \cdot Fe_2O_3$, CaF_2 and MnO in combination with $CaCO_3$, $MgCO_3$, CaO and MgO, can be used to enhance slagmaking compared to pebble lime.

The compacted product also features a strongly increased physical stability, drastically reducing the fines generation compared to pebble lime, which is a naturally friable product. After extensive product development effort, different types of lime-based slag conditioners were selected to be tested in pilot scale.

4. Pilot scale experiments

Once different product formulations were pre-selected, pilot scale trials were conducted at the pilot plant of swerea|MEFOS in Luleå, Sweden, with the aim of testing the efficiency of Booster™ in BOF™ steelmaking.
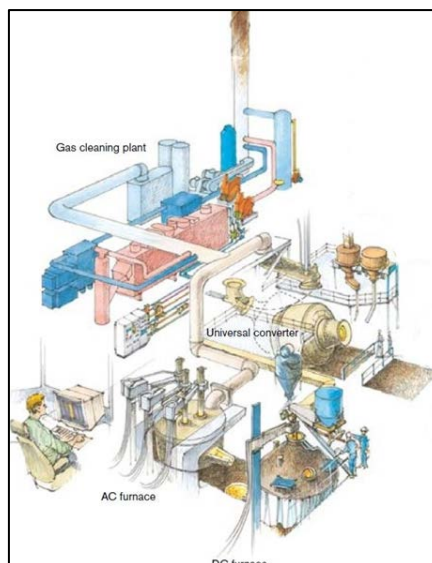

Figure 5. Layout of the swerea|MEFOS pilot installation [8]

The experimental setup used at MEFOS (Figure 5) consists of a 10 ton EAF for the hot-metal production and a 6 ton universal converter in BOF mode to carry out the metallurgical tests.

The hot-metal was prepared by using the AC-EAF to smelt a pig iron with known composition, together with the needed alloys to achieve the hot metal chemistry shown in the table below:

Table 1. Target hot-metal composition of swerea|MEFOS trials

Element	Mn	C	Si	P	S
Weight-%	0.40	4.2	0.35	0.080	0.02

The average chemical composition of the produced hot-metal is shown in the table below.

Table 2. Achieved hot-metal composition of swerea|MEFOS trials

Element	C	S	Si	Mn	P	Ni	V	Cr	Al
Wt-%	3.69	0.0166	0.341	0.427	0.0753	0.0947	0.0274	0.0595	0.147

Special attention was paid on the silicon content of the hot-metal, as it is difficult to guarantee a constant chemical composition of the hot-metal due to the spontaneous formation of SiO_2 in ambient atmosphere, reducing the silicon content of the hot-metal. The temperature of the hot-metal before charging into the converter was adjusted to be constantly in the range of 1380°C.

In parallel to the hot-metal preparation, the minerals mix was prepared. Although both pebble lime (quicklime) and Booster™ were sieved before transportation, the material needed to be re-screened, because the quicklime as well as the different types of Booster™ travelled 2400 km by truck from Belgium to the pilot plant in Luleå. The screening was performed right before charging the converter with a mesh size of 10 mm. Up to 7% of fines was generated during the transport with the quicklime, whereas <<1% of fines was generated by the slag conditioners, evidencing the superior mechanical properties of Booster™, compared with pebble lime.

Figure 6. Up to 7% of fines generated during sieving of quicklime

Figure 7. Virtually no fines generated during the long distance transportation of Booster™

As far as the charging sequence is concerned, during the temperature adjustment of the hot-metal, 110 kg/thm of scrap were loaded into the converter, followed by 33 kg/thm of CaO. Directly after this the hot-metal was loaded into the converter and the top-lance oxygen blowing process was initiated after raising the converter to the upside position. All blowing parameters including the lance pattern (height, flowrate) and bottom stirring were kept constant between reference and sample heats. The off-gas composition was monitored continuously and the blowing process was stopped according to the level of CO_2 in the off-gas. For 3 minutes a post-stirring procedure was performed, before the final sampling and tapping of the converter. The aimed tapping temperature was 1730°C, while the achieved average tapping temperature was 1739°C, which indicates the good control of the apparatus.

Before, during and after the blowing, steel- and slag-samples were taken and the metal temperature was measured simultaneously, using a special sub-lance system, developed by swerea|MEFOS. The head of the sub-lance system consists of a standard Pt/Rh-type of temperature sensor connected to a measurement system calibrated in the range of 1200°C to 1800°C and a steel cup below to take a metal sample. The cup is connected via a steel rod to the sub-lance system, which is used for sampling the slag. The final hot-metal sample (Me1) was taken right before loading the converter. One minute after starting the blow, the inblow-sampling started. Every two minutes a metal sample (Me2 to Me7) was taken simultaneously to the slag sample (Sl2 to Sl7). After end of blow, the converter was tilted and the slag and steel was sampled (Sl8 and Me8). After the sampling the converter was raised again for the post-stirring period of 3 minutes. The converter was then finally tilted again for sampling the slag and metal (Sl9 and Me9) after post-stirring and followed by emptying the converter. The sampling schedule is shown in figure 8.
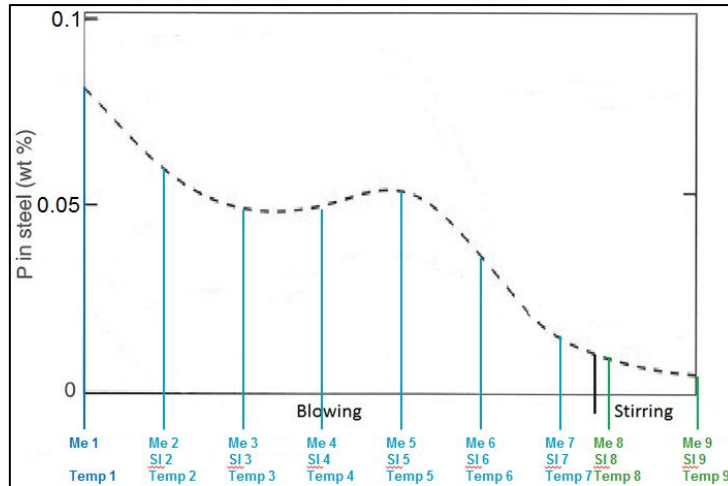
Figure 8. Schedule for metal-sampling, slag-sampling and temperature measurement

The metal and slag samples were analyzed at the process laboratory after each heat, using XRF technique after separating any magnetic parts from the slag. The lollipop-type hot-metal samples were analyzed with a LECO device (S, C) and XRF for the other elements. The steel samples were analyzed fully with XRF. All analysis were performed using the standard calibrations for hot-metal, steel and slag usually used by SSAB.

The average achieved phosphorus distribution L_P per group of mineral mix (reference and 100% replacement of quicklime by Booster™), taken after turndown and after post-stirring, are shown in table 3.

Table 3. Average phosphorus distribution after turndown and after post-stirring

Type	L_P turndown	L_P tapping
Reference	67	116
Material A	78	135
Material B	**87**	**143**
Material C	53	139
Material D	53	145
Material E	58	146
Material F	64	147

The L_P evolution of material B, which showed 30% improved L_P after turndown and 23% improved L_P after post-stirring compared to pebble lime, is shown in the graph below.

Material B features an increased L_P compared to pebble lime already in the early stage of blow (figure 9). Two minutes after starting the blowing process the phosphorus content in the hot-metal had already dropped from 0.076% to 0.062%. In case of the reference heats, the phosphorus content was reduced only from 0.078% to 0.074% in the same time.

Utilizing Booster™, the main dephosphorization started 4 minutes earlier compared to the reference. The dephosphorization kinetic during the main dephosphorization phase is similar for both types of experiment. This results in the improvement explained before due to the earlier start of the main dephosphorization phase and the offset in terms of L_P at the beginning of the process which can be measured until the end of the process.
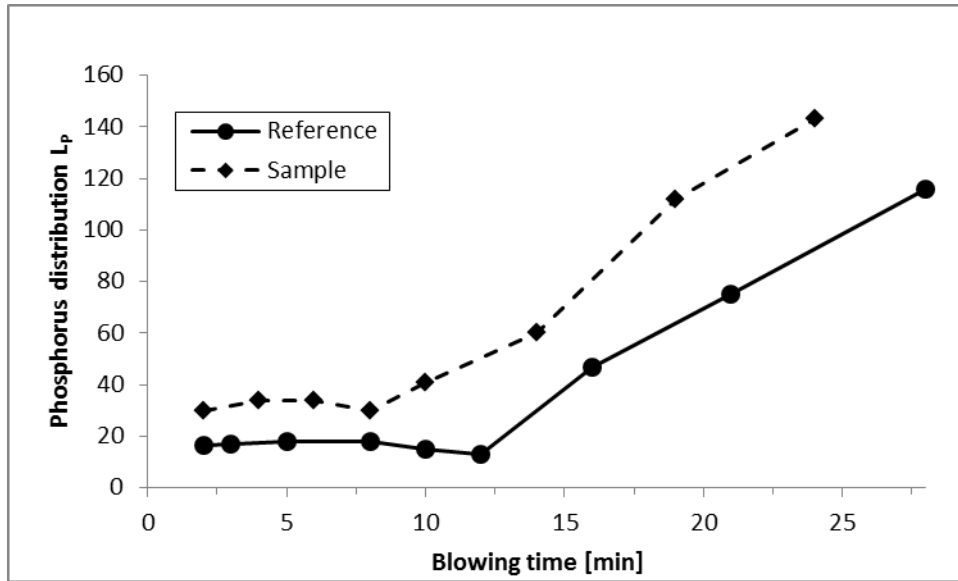
Figure 9. L_P evolution of pebble lime (Reference) and material B (Sample)

To better understand the metallurgical results, analysis of ternary diagrams were performed. Figure 10 shows the liquidus surface section of the slag system CaO-SiO_2-FeO_n-$4\%MgO$ calculated with MTDATA 6.0. The MTDATA software package is explained in detail in [9]. The slag samples Sl2 to Sl9 are plotted into the liquidus section and the according slag pathways are shown for the reference as well as material B (Sample) heats.
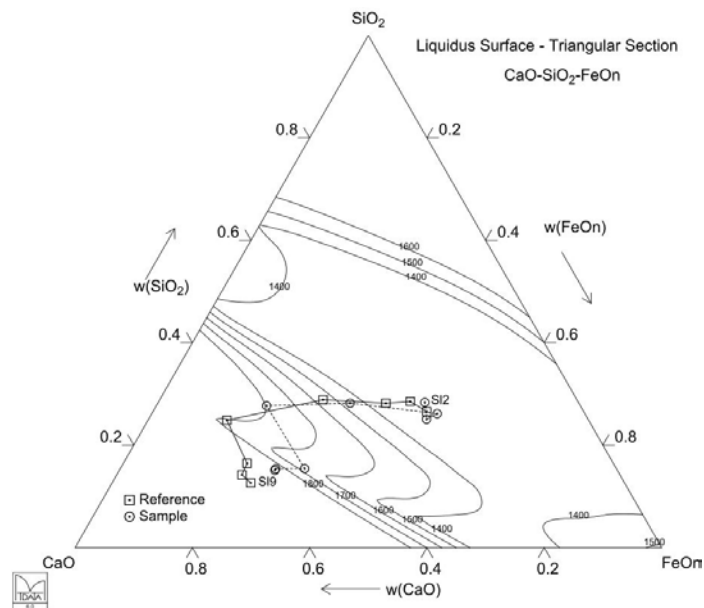

Figure 10. Liquidus surface plot and slag evolution of pebble lime (Reference) and material B (Sample)

Both slag systems are located in the olivine region of the ternary diagram during the early phase of the blowing process. Both slag systems follow a similar slag path into the dicalciumsilicate (C_2S) region of the ternary system. Nevertheless, the slag formed with Booster™ stays longer in the olivine region – being liquid at process conditions – whereas the slag formed with pebble lime evolves more quickly into the – high melting point – C_2S region, leading to an earlier formation of dry slag. The reference slag system also moves

deeper into the C$_2$S region compared to the slag system generated with Booster™, increasing the amount of solid slag being produced. The slag system formed with material B is always closer to the liquid part of the ternary system, which facilitates the early formation of a liquid slag in the second half of the blowing process, enabling an early start of the main dephosphorization phase.

5. Industrial scale experiments

The slag conditioner showing the best results in pilot scale (material B) was selected to conduct industrial scale experiments. The industrial trials have been performed at Dillinger in the 190 t BOF converter No. 1 [10]. During the trial, BOF No. 1 was operated with Booster™ and pebble lime. In contrast to the pilot scale trials, it was decided to replace 30% and 20% of pebble lime by Booster™, while the total CaO amount was kept constant between reference and trial heats. The reference heats have been produced on the same converter under standard operation conditions. Additionally three comparable BOF No. 1 operation campaigns were provided as a reference.

The standard procedure for the trial and reference heats was as follows. First, approx. 5 tons of pebble lime per heat was charged into the empty converter using lime bins above the converter. The predefined amount of Booster™ was fed from another bin into the weighing bin. Approximately 50 tons of scrap and 160 tons of desulphurised hot metal were charged into the converter. The hot metal analysis could vary slightly, but the amount of hot metal as well as scrap was kept nearly constant for all heats. After 1000 Nm³ of oxygen blown, the predefined amount of Booster™ was fed into the converter. Afterwards the remaining pebble lime (if needed) was fed into the converter using the lime bins. A minimum of 2 Nm³/min of nitrogen gas has been fed through the 6 bottom tuyeres at any time. After main decarburization was over, the gas was switched to argon (if required) and the flow rate was increased to 5 Nm³/min. After 9000 – 11000 Nm³ of oxygen (approx. 15 – 17 minutes) the blowing process was stopped by the blowing model of the converter. The conditions to stop the blow were also kept constant for all heats. The converter stayed upright for a 2 minute post stirring period with 5 Nm³/min flow rate of argon or nitrogen. Afterwards the converter was tilted to measure the tapping temperature and to take steel and slag samples. The trial observation ended after taking these samples.

Figure 11 shows the liquidus surface section of the slag system CaO-SiO$_2$-FeO$_n$-2%MgO calculated with MTDATA 6.0. The average slag compositions of the samples taken after end of blow are plotted into the liquidus section for the reference as well as material B (Sample B1 and B2) heats.
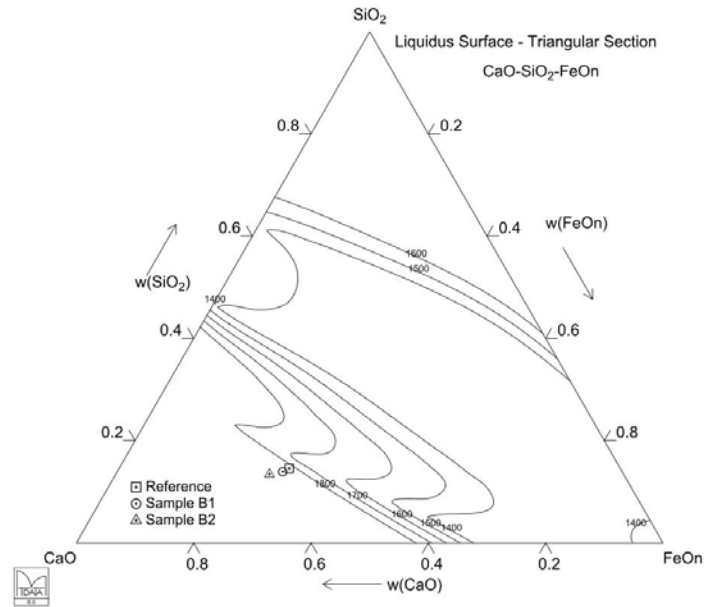
Figure 11. Liquidus surface plot and slag composition of pebble lime (Reference) and slag conditioner (Samples) produced during the second trial at Dillinger

5.1 Dephosphorization

The L_P improvement was below the maximum levels achieved in the pilot trial carried out at MEFOS with 100% Booster™, but still significant (%L_P +19%) for 30% Booster™ mixed with 70% pebble lime. Considering the high performance standards of Dillinger as far as de-P is concerned this is remarkable.
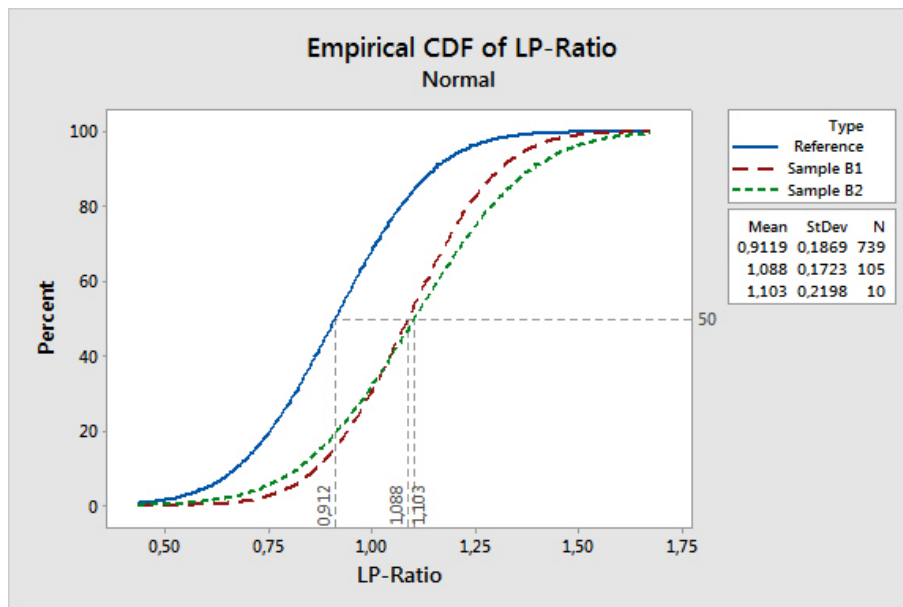

Figure 12. Cumulated density plot of L_P-ratio ($L_{P,achieved}$ / $L_{P,theoretic}$) for reference and test heats

5.2   Generation of fines:

The observation made during the unloading of the big bags and the tipping of the trucks confirmed the outstanding improvement achieved by Booster™. The amount of dust that is generated during these processes was reduced drastically. The sampling and sieving analysis performed by Dillinger showed a reduction of fines from 20% down to 1% for Booster™ at the chute ② of the converter (Figure 13).
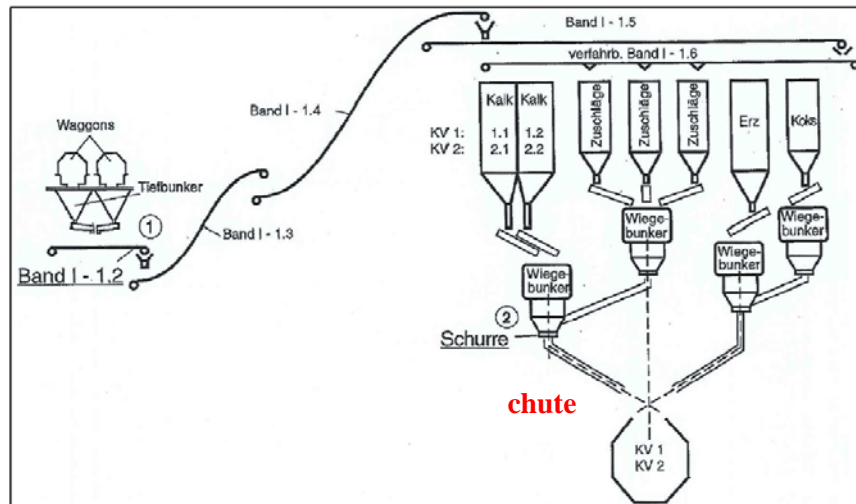

Figure 13. Schematic drawing of Dillinger's lime handling installation

Furthermore, to confirm the low amount of fines lost in the dedusting system, the evolution of the pH of the washing water was followed. The measurement of the pH value does not provide reliable quantitative results, but it clearly shows a reduction of the pH-pickup during the CaO addition of Booster™ compared to standard pebble lime during the blow (Figure 14).
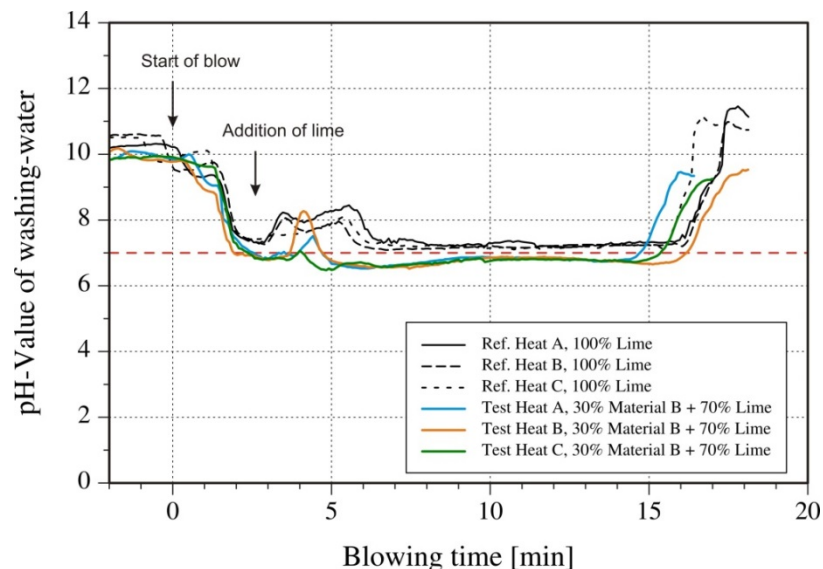

Figure 14. Comparison of the pH-value of washing water for heats with and without addition of slag conditioner

The increase in pH is caused by the basicity of $Ca(OH)_2$, which is formed during the hydration of the CaO fines in the washer after the offgas system.

6. Conclusion

A new slag enhancer called Booster™ was developed by Lhoist. This new product was tested in pilot scale trials carried out at swerea|MEFOS in Sweden, demonstrating clear improvement in dephosphorization (de-P) and drastic reduction of fines generation, when compared with quicklime. After these successful pilot trials the product was tested at the BOF melt shop in Dillinger, corroborating several positive effects of Booster™, for example, better dephosphorization and fines reduction.

Lhoist and Dillinger shall continue the cooperation to improve the use of Booster™. Additional trials shall demonstrate new benefits of the new product as well as to allow Dillinger to fine-tune the process to maximize the value creation of Booster™.

7. References

1) K.H. Obst, E. Schürmann, G. Mahn, W. Münchberg, D. Nolle: Arch. Eisenhüttenwesen 51 (1980) No. 10, p. 407/12

2) G. Trömel, W. Ullrich, J. Willems, W. Rudack: Stahl u. Eisen 83 (1963) S. 1226/34

3) G. Trömel, E. Görl: Arch. Eisenhüttenwesen 35 (1964), p. 287/98

4) H. Hiebler, W. Krieger: BHM 137 (1992), No. 7, p. 256/62

5) E. Schürmann, W. Florin, E. Höffken, W. Ullrich, H. Schicks: Stahl u. Eisen 106 (1986), No. 23, p. 1273/80

6) P. Williams, M. Sunderland, G. Briggs: Ironmaking and Steelmaking, 1982, Vol. 09, No. 4, p.150/62

7) D. Schöne, ISBN 978-3-8440-1846-2 (Dissertation RWTH Aachen University), Shaker Verlag, 2013

8) https://www.swerea.se/sites/default/files/publications/pilot_plant_equipment.pdf

9) Davies R H, Dinsdale A T, Gisby J A, Robinson J A J, Martin S M, MTDATA - Thermodynamics and Phase Equilibrium Software from the National Physical Laboratory, *CALPHAD*, 26 (2002), pp. 229-271.

10) N. Bannenberg, M. Bock, R. Bruckhaus, V. Fiedler, H. Lachmund: Conference Pre-Prints 3rd European Oxygen Steelmaking Conference, 2000, Birmingham, UK, p. 129/34

From Oil to Coal Injection – Experiences and First Development Steps

O. Mattila, K. Keski-Ruismäki, T. Paananen
SSAB Europe Oy, Raahe Steel Works, Finland

Abstract: The commissioning of PCI at Raahe steel works have been intensive project which was launched by investment decision at February 2014. Project consisted of the design work of PCI facility, extensive training plan for employees as well as wide-ranging clarification of the pulverized coal properties, manufacture and necessary measurements.

The behavior of PC in blast furnace process, process modifications and process control contained also substantial amount of work. Initial development actions targeted to reach stable blast furnace operation at the injection rate of 160 kg/thm which was achieved within one year of injection in October 2016.

This paper describes the most important development actions and some highlights during the project.

1. Introduction

Pulverized coal injection (PCI) has been discussed in Raahe steel works since the start of extra heavy bottom oil (ERP) injection and the increase of the popularity of PCI as auxiliary fuel of the Blast Furnace (BF). The development of crude oil refinery made it possible to utilize ERP fractions as vehicle fuel in a more efficient way. More valuable uses of ERP – compared to BF injection – made the PCI investment economically feasible option for Raahe steel works leading to the investment decision on February 2014.

Overall schedule for the project was:

- 02/2014 Investment decision
- 07/2014 - 09/2014 Land construction work
- 08/2014 - 12/2014 Concrete foundation work
- 12/2014 - 06/2015 Frame assembly
- 12/2014 - 06/2015 Machine and appliance installation
- 03/2015 - 06/2015 Electric and automation installation
- 07/2015 - 09/2015 Testing
- 09/2015 - 12/2015 Production

During the PCI investment decision the coal tar was also used as auxiliary injectant of BF. The overall change of injectants from oil+tar to PCI can be seen in **Figure 1**.
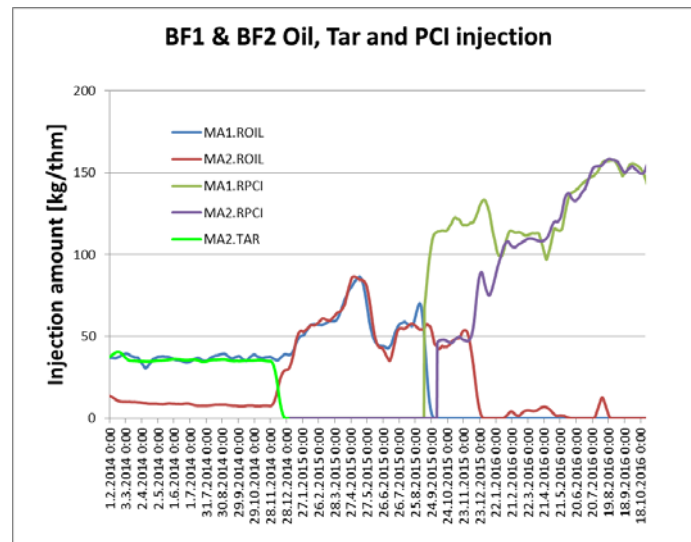
Figure 1. Injection amount of oil, tar and PCI during transition from oil to PCI.

Even though the PCI has been discussed over the years in ironmaking department in Raahe, the operational knowledge of PCI process did not existed in the steel works before the project start. The work of PCI investment project consisted of basic knowledge gathering of coals, processing & analyzing of coal, as well as creating selection criteria for coal together with the actual process design and construction.

During the project, special attention was laid to create comprehensive education and training plan for the whole ironmaking department and associated departments like IT, chemical analysis services not to forget the BOF department. Employee training consisted over 300 full working days for process operation solely. For example, two days course solely on BF operation with PCI was held by Luc Bonte, known as expert in PCI related issues in blast furnace.

1.1 Safety during the project

During the construction project regular safety rounds and safety meetings were held. Named safety coordinator operated during the project. Despite of systematic safety efforts two (2) unfortunate accidents occurred during the project for external contractors.

1. Small worker (female) was driving a big wheel loader. When she stopped the machine and descended from the cabin, the lowest step was located too high for her. She felt strong pain on her knee during descending to the ground level. One week sick leave.
2. Installation group lifted the 1000 kg blower with crane. Crane could not reach the final position horizontally. Blower was pushed by muscle strength to the final location. On the next day one mechanics felt pain on his leg. After the medical inspection (strained groin) worker could continue with lighter tasks.

2. Preparation studies and development steps at the beginning of the project

To gain necessary information for basic PCI layout, benchmark visits for technical options of PCI process were made to existing PCI facilities before the supplier and main equipment selection. Fine tuning the design was made during the construction project.

Processing issues were also benchmarked with several visits to existing PCI plants in Europe. Processing issues consisted of coal selection criteria as well as possibilities and

requirements of using multiple raw materials simultaneously in the grinding and drying (GAD) facility. Blast furnace operation, problems and control with PCI was the top priority topic.

The basic information of coal processability (grinding properties, tar compound liberation, analytical needs etc.) were studied by Pikkuaho [1]. The more detailed description of separate coal maceral behavior in PCI process chain (maceral identification and their associated properties, dielectric constants of various coal grades, effect of moisture on dielectric constant as well as optical observation of coal softening temperature with hot stage microscope) were studied by Vuorenmaa [2].

The work within the ironmaking development team consisted of:

- Coal specification analysis of more than 30 available coal grades, more detailed chemical analyses of dozen of coal grades followed by the value in use (VIU) analysis of five most promising coals to select the best coal grade for Raahe.
- Modification and testing the blast furnace level 2 information system (*Rauti*) to be able to tolerate raw coal handling and coal use in blast furnace.
- Gain information of pulverized coal manufacture, GAD process control and critical parameters and control of blast furnace operation.

2.1 Coal analytics

Based on the carried studies the following laboratory equipment (**Figure 2**) were decided to take in to use to get necessary analyses of coal:

- Moisture measurement, Eltra CW-800M
- Particle size measurement, Beckman Coulter LS13 320MW
- Chemical analyses (C,S) Eltra CS580AS
- Flow ability measurement, FreemanTechnology, FT4
- Rotary sample dividers, Retch PT-200 and Quantachrome Rotary Micro riffler

Figure 2. Analysis equipment in PCI use. From Left: PT-200, Micro Riffler, Eltra CW800M, LS13 320MW, FT4.

2.2 Construction project and basic information

The information obtained from other blast furnaces using PCI and the analysis of the needs of Raahe's ironmaking department lead to following process equipment, layout (**Figure 3**) and capability information:

- Main contractor: Claudius Peters GmbH
- Raw Coal delivery systems and crushing: Sandvik
- Mill units with classifier: Loesche x2
- Hot gas generation: Brinkman x2 (Blast furnace gas)
- Fine coal filter unit: Scheuch
- Automation: Valmet (formerly Metso DNA)
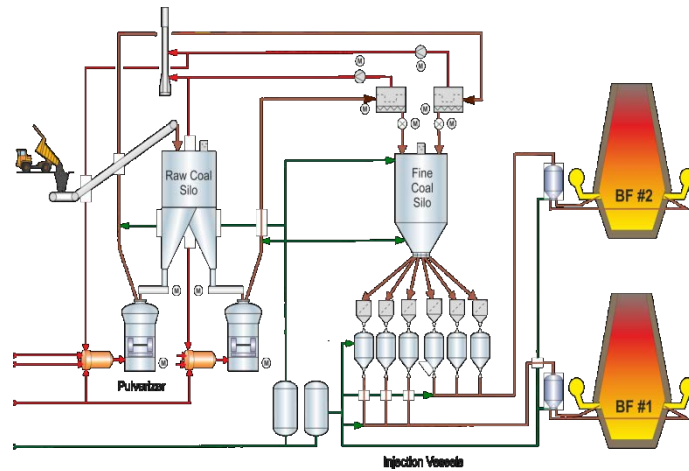- Steel constructions: Ruukki Construction

Figure 3. Layout of the PCI process.

Basic information of the PCI facility:

- Maximal grinding capacity 450000 t/a , (2x220 kg/thm, 2x32,5 t/h)
- Maximal injection rate 1660-1930 kg/h/tuyere for BF1 and BF2 respectively
- Raw coal storage capacity 950 m3 (10 h)
- Fine coal storage capacity 1050 m3 (10 h)
- Distributor capacity 55 m3 (2 h) for both BF's

2.3 Injection start-up plan

Change from oil to PCI started with the BF1. Step-by-step plan (**Figure 4**) was made to gradually proceed with the transition. Tests of basic control circuit of GAD facility and BF injection control were made simultaneously. In case of failures in mechanics or process control, the transition back to oil had to be possible if necessary. Other criteria were set by invidual tuyere coal amount in relation to tuyere C/O –ratio.

	kg/h/tuyere	kg/thm	Control group 1							Control group 2							Control group 3						
			1	2	3	4	5	6	7	8	9	10	11	12	13	14	15	16	17	18	19	20	21
Coal	864	18					1							1								1	
Oil		76		1	1	1		1	1	1	1	1	1		1	1	1	1	1	1	1		1
Coal	819	52			1		1			1		1		1			1			1		1	
Oil		40		1		1		1	1		1		1		1	1		1	1		1		1
Coal	749	104		1	1	1	1	1	1	1	1	1	1	1	1	1	1	1	1	1	1	1	1
Oil		0																					

Figure 4. Three phase plan to increase the injection amount of PC at start-up.

2.4 Injection control tuning

As the injection amount increased and the number of coal lance increased the injection amount accuracy was closely monitored. The equal distribution accuracy specification was set to +-2.5 %. Random peaks as well as periods of unsatisfied accuracy existed on the accuracy trends over the first months of injection. **Figure 5** shows the problematic accuracy behavior. Due to injection inaccuracy, automatic lance flushing sequences as well as injection line the control valve "*global opening target value*" was taken into use which improved the accuracy. Random peaks were identified to occur when coal powder was packing on the pipeline

upstream of the control valve (slide gate type). Packing of coal powder on the pipeline caused the coal flow measurement sensor (capacitive type) to drift out of the measurement range.
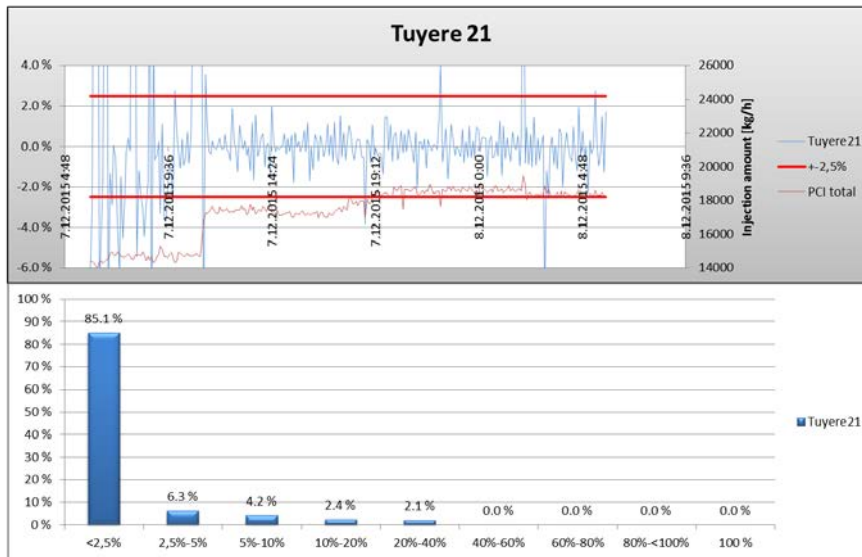

Figure 5. Injection accuracy measurement on BF1, Tuyere 21. Blue measurement value should stay within thick red lines to reach accuracy requirement.

Accuracy problems increased after short period of improvement leading to the stoppage of the BF process and opening the distributor unit to check the integrity of mechanical parts. Mechanical parts were damaged from the sudden pressure change inside the distributor. Correcting mechanical support structures were designed and installed shown in **Figure 6**. Injection accuracy improved clearly – shown in **Figure 7** – making it possible to develop injection control further on.
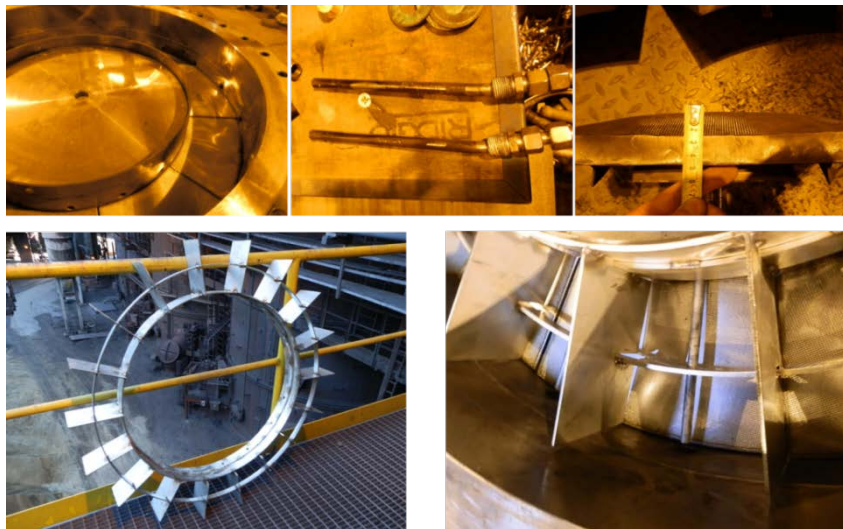

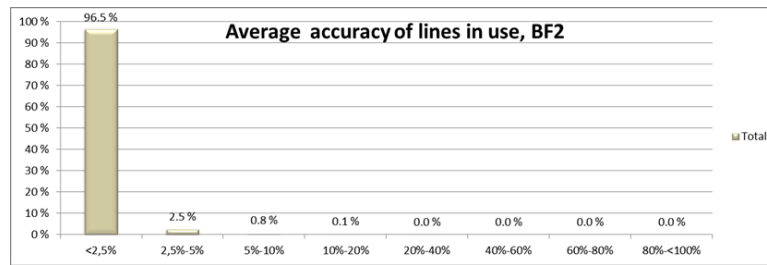**Figure 6.** Damaged distributor parts and additional support structure installation.

Figure 7. Improved injection accuracy due to design improvement.

Lance injection control circuit based on the invidual tuyere air flow measurement to reach adjusted and even carbon-to-oxygen ratio (C-O ratio) was developed. The idea of invidual lance C-O control was to improve burning characteristics of PC. **Figure 8** shows the calculated C-O ratios for BF1 having C-O control circuit turned on (left) and BF2 having only equal distribution of coal control turned on (right). Clear difference exists in tuyere carbon-to-oxygen ratio between the two controlling principles. The overall C-O control accuracy depends of course from the accuracy of the air flow measurement. To improve air flow measurement one annubar tube (Itabar flow sensor) was implemented on to the hot blast flow to check the accuracy of current air flow measurement system.
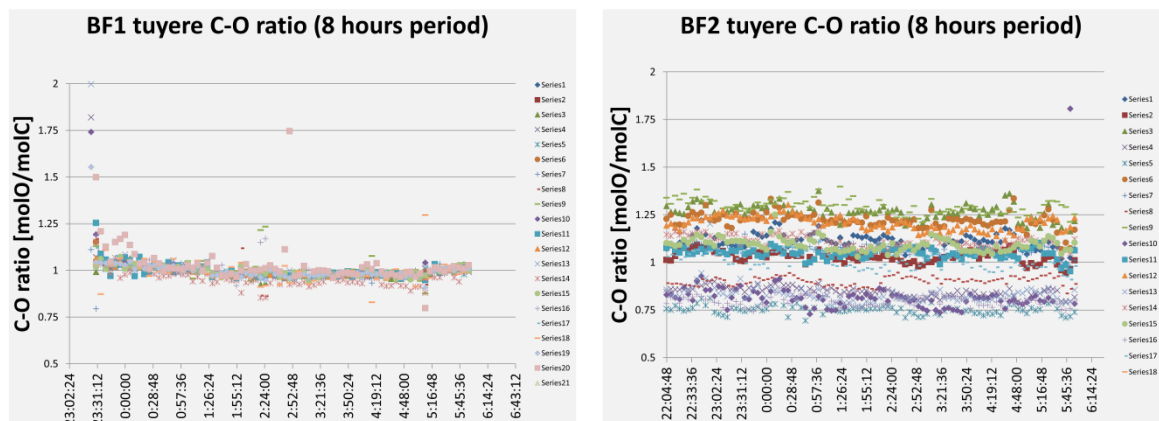

Figure 8. Tuyere C-O ratios with(left) and without(right) air measurement control.

3. Blast Furnace Process observations

3.1 Identification of dust and sludge carbon origin

During injection start at BF1, dust and sludge compositions were closely monitored. The purpose was to detect critical injection conditions when coal burning is insufficient. TGA based method [3] was fine-tuned for Raahe's BF1 dust and sludge by Niemelä [4]. Temperature program with dust and demineralized sludge sample weight loss curves are shown in **Figure 9**. Based on the measurements, small correlation was found to favor higher blast oxygen concentration at higher injection rates, although the process variation was high due to insufficient injection control (no C-O control available during that time). The limit of insufficient BF process stability could be seen at injection rate of 135kg/thm (**Figure 10**) at first months of PCI operation having root causes in ferrous burden charging pattern, charged raw material quality changes and uneven injection control.
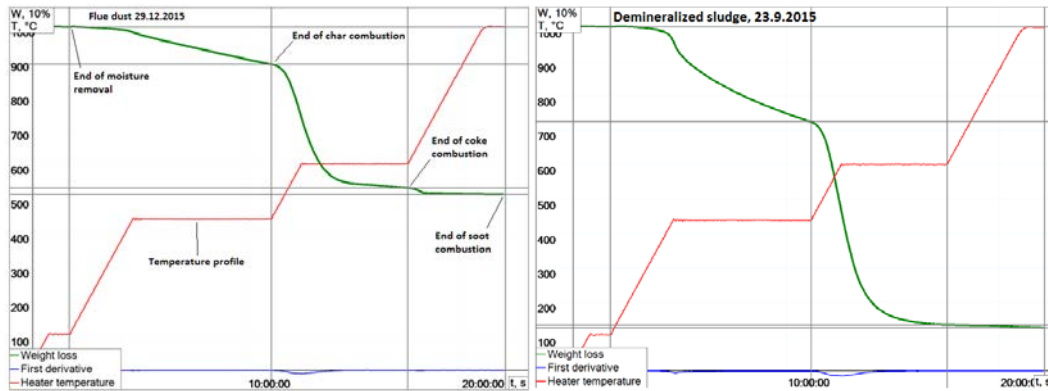
Figure 9. Applied TGA-based method to dust and demineralised sludge. (Niemelä 2015)
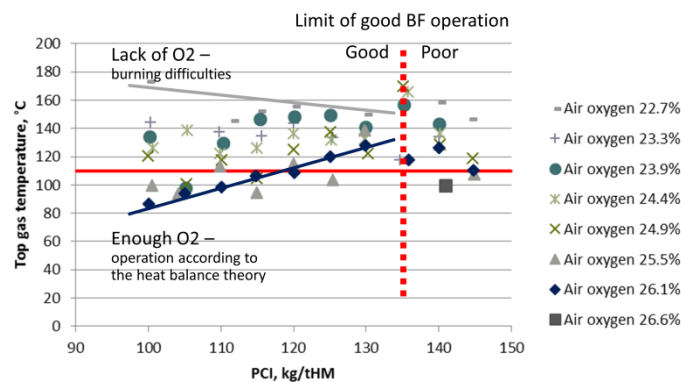

Figure 10. Limit of good BF operation at the PCI rate of 135 kg/thm.

3.2   BF gas cleaning observations

The beginning of coal injection was also monitored by the means of BF gas cleaning water quality. Clear positive changes are observable in the water Chemical Oxygen Demand (COD), and Potassium (K) having descending trend as PCI rate increases and coke rate decreases shown in **Figure 11**. Sulphate (SO_4^{2-}) was found to correlate with oil injection indicating gaseous sulphur bearing compounds formed during sulphur-rich oil combustion in BF raceway. The reasons for the water quality changes can be traced to overall BF performance, difference of chemical composition of injectants, change in the circulating element behavior inside the BF and to the coke dust particle escape during charging.
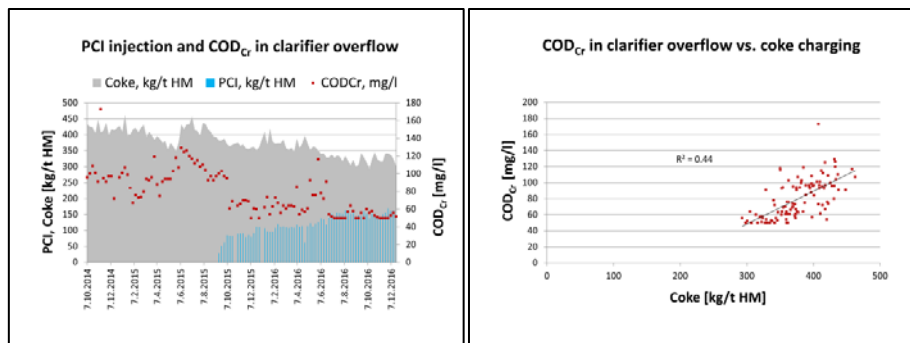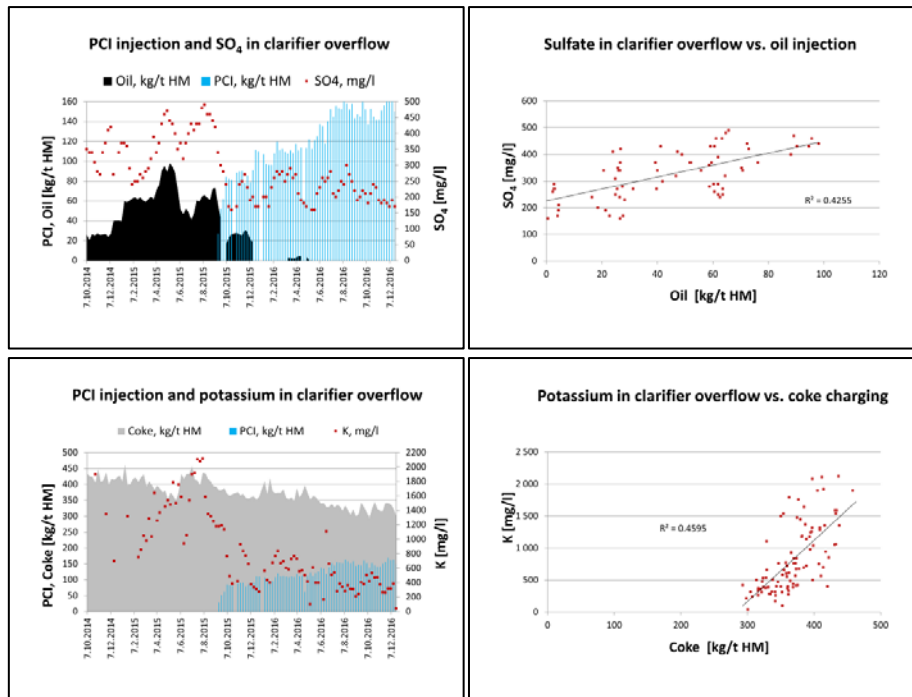
Figure 11. BF gas cleaning water quality indicators (from top) Chemical Oxygen Demand (COD), Sulphate (SO_4^{2-}) and Potassium (K) having clear trend during injectant transition.

3.3 Monitoring coal flow and tuyere phenomena

Tuyere camera system by Paul Wurth was installed on each tuyere. Overall image illumination value is connected to the injection safety logic of to suppress the coal flow in case of tuyere blockage by scuffolds inside the BF. Images from each tuyere are stored in the database where they can be accessed and analyzed for further information.

Images clearly showed the excessive build-up of material on the tuyere surface which was analyzed to consist mainly of porous PCI ash. Based on the observations, sample analyses and mathematical modelling results on the flow fields the lance length and lance type were changed to minimize material build-up (**Figure 12**). In consequence of taken actions, coal plume was centered better to the tuyere, turbulence decreased a little on the lance tip and build-up rate of coal ash decreased.
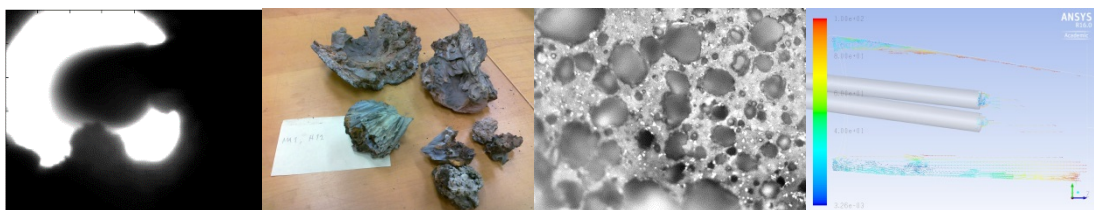

Figure 12. From left to right: Material build-up on the tuyere surface, samples of build-up material, microscope image of material and mathematical modelling of flow vectors on the tuyere surface.

Basic image analysis program was developed with Matlab to extract coal plume size and location, coal plume transmittance and temperature distribution [5]. As an example the coal flow angle in respect to coal lance is clearly correlated with the periodical changes in blast temperature which can be seen in **Figure 13**. The pulsating type of coal flow can also be clearly identified by image analysis enabling the corrective action identification.
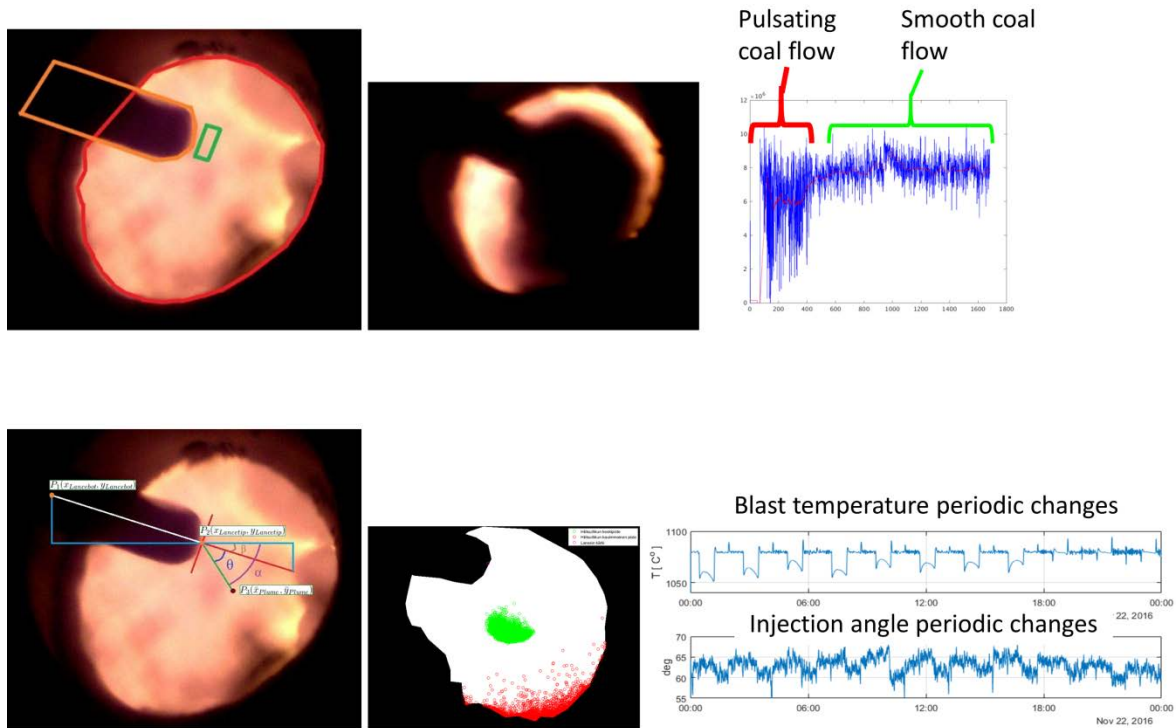
Figure 13. Tuyere image analysis shoving; period of pulsating coal flow type (upper); change in coal flow angle during blast air temperature changes (lower). [5]

4. GAD Process observations

4.1 Chemical composition and flow ability properties

GAD1 and GAD2 stations were able to produce constant quality coal powder after initial teething problem fixes in hot gas generation and basic tuning. Produced fine coal grain size distribution is shown in **Figure 14** meeting the requirements of delivery contract. More concern had to be set to the flow properties of raw coal in raw coal silo. Raw coal showed highly deviating flow properties compared to the material after grinding and drying measured by the FT4 flow ability tester. Raw coal is very sensitive to process vibrations making the flow energy rise dramatically which can be seen in **Figure 15**. Multiple nitrogen guns in raw coal silo decreased the raw coal delivery problems to the GAD units.
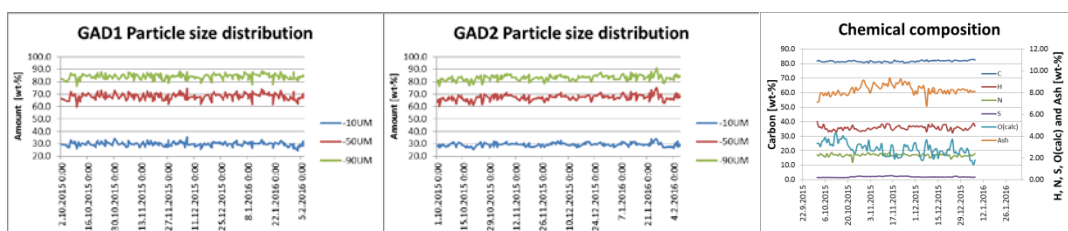

Figure 14. Measured particle size distributions and chemical composition of fine coal powder.
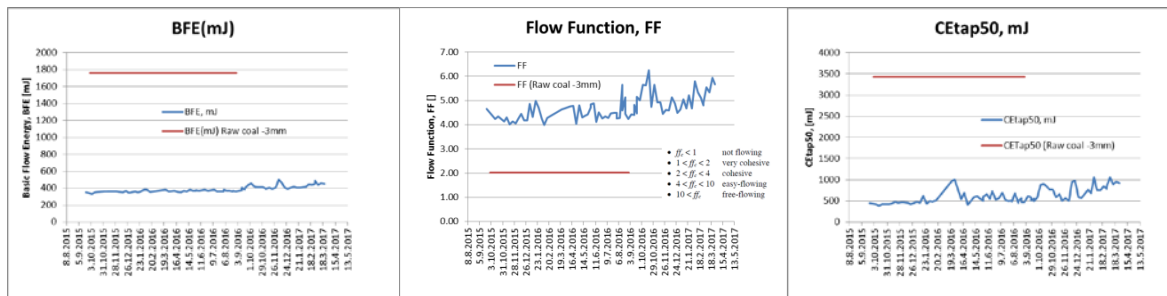
Figure 15. Measured flow ability properties of raw coal and fine coal powder (from left to right) Basic flow energy (BFE), Flow Function (FF) and flow energy after vibration (CEtap50). Raw coal red line, fine coal powder blue line.

4.2 Moisture issue of dried coal powder

Major issue in GAD plant was related to moisture behavior in fine coal silo. Sieve units downstream of fine coal silo had severe moisture condensation problem on the inner surfaces (above and below sieve elements) creating hard and wet accumulations of coal particles shown in **Figure 16**. Hard and moist (up to 37 wt-%) particles ending up to the injection pipeline will cause problems in injection accuracy. The injection control circuit, based on the capacitive flow sensor, suffers also from rapid moisture fluctuations.

Root cause was identified to be the moisture condensation from the drying air remaining between the particles on the fine coal silo. Samples taken from the BF injection line showed 0.2 wt-% higher moisture values compared to normal process samples taken upstream of fine coal silo. By adjusting the drying air composition and renewal rate, moisture pick-up was decreased to 0.1 wt-% helping the condensation problem. Produced fine coal moisture content is found to follow ambient air moisture creating the need to develop more detailed control model for GAD units to completely avoid moisture problems.
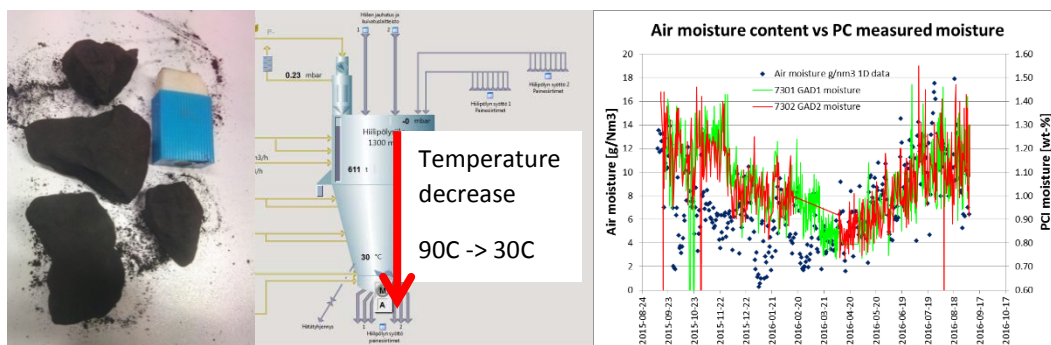

Figure 16. Hard and wet particle formation inside sieve units, temperature decrease and relation of ambient moisture and coal powder moisture.

4.3 GAD main driveshaft failure

After half a year of operation GAD2 main driveshaft broke down suddenly due to shaft manufacture defect. Driveshaft failure caused GAD2 unit to stand still until replacement part was manufactured (14.2.2016-6.4.2016). After replacing one driveshaft the GAD1 was stopped for inspection requiring immediate chance of the shaft. GAD1 was out of operation 11.4.2016-29.4.2016 thus delaying the further development and the increase of PCI amount in blast furnaces. Broken shaft can be seen in **Figure 17**.

Figure 17. Broken driveshaft of GAD2.

5. Blast furnace charging

In Raahe blast furnace charge consist of iron burden (pellets, briquettes, limestone, BOF slag, scrap) and coke. The round shape and small size of pellets compared to coke makes it possible for pellets to percolate into the coke layer. The philosophy in PCI increase was to maintain coke layer thickness constant and increase the thickness of iron burden layer. Due to skip charging system in use there is a limit in iron burden weight after which the skip volume is the limiting factor. Above 140 kg/thm PCI rate 2Coke + 2Pellet skip charging practice have to be changed to 2Coke + 3Pellet skip charging practice.

To be able to compensate the lack of burden surface profile scanner research co-operation has been made to develop burden layer calculation model (**Figure 18**) based on pilot scale tests and DEM modelling [6]. Layer calculation model has been used for testing different charging patterns.
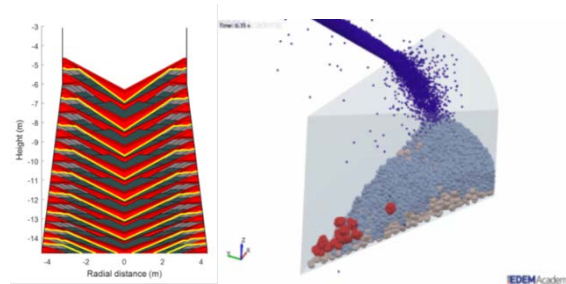

Figure 18. Burden layer calculation model developed to factory use(left) and DEM modeling of layer formation(right). [6]

6. Overall results of development actions

The overall effect of process development actions as well as "learning curve" to implement completely new main raw material in use can be summarized to elemental carbon consumption of Blast furnace shown in **Figure 19** (left). In the period plotted to the figure overall injection amount is increased from 100 kg/thm to 160 kg/thm. Due to chemical composition of the used coal grade the replacement ratio of PCI to coke has been in good level of almost 0.9 during the injection start. The relation of PCI rate to coke rate is shown in **Figure 19** (right).
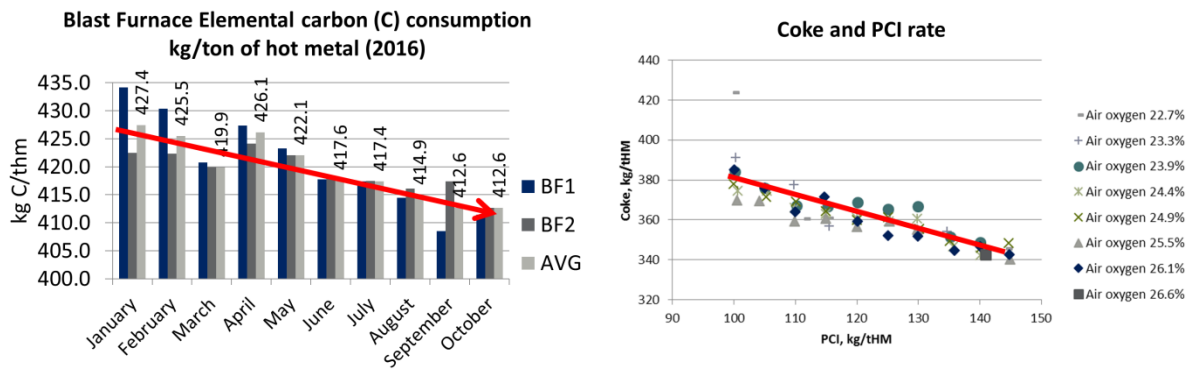
Figure 19. (left) Blast furnace elemental carbon use during increase of injection from 100 to 160 kg/thm. (right) coke and PCI replacement curve.

7. Conclusions

The start-up of PCI as a completely new main raw material have proceeded quite well despite of minor drawbacks. Special thanks have to be addressed to the production employees having positive and forward looking attitude in the early steps in PCI use. Common target, well done preparations, flexibility and co-operation between different departments have been crucial to reach the initial PCI target of 160 kg/thm.

References:

1) Pikkuaho, J. *The effect of coal properties on coal powder processability and coal powder injectability.* MSc thesis. University of Oulu, Oulu 2015. 90 p.

2) Vuorenmaa, V. *Coal macerals and their behavior in PCI process.* MSc thesis. University of Oulu, Oulu 2015. 107 p.

3) Ng, K. W., Giroux, L., MacPhee, T., Todochuck, T., Taggart, L., Scott, G. Development of a TGA Technique for Carbon Differentiation in BF Dust and Sludge. METEC and 2nd ESTAD 2015, 15-19 June 2015, Düsseldorf, Germany.

4) Niemelä, J. *Monitoring of blast furnace 1 operation with various PCI and oxygen enrichment rates.* MSc thesis. University of Oulu, Oulu 2016. 119 p.

5) Vares, S. *BF Tuyere phenomena imaging and measurement.* MSc thesis. University of Oulu. Oulu 2017. 91 p.

6) Mitra, T and Saxén, H. (2016) Discrete element simulation of charging and mixed layer formation in the ironmaking blast furnace. *Comp. Part. Mech.* (2016) 3:541–555.

GEORG STECHAUNER[1]

IMPACT OF VARIOUS REFRACTORY MATERIALS ON THE WEAR OF STOPPER RODS ON CONTINUOUS CASTING

G. Stechauner[1,*], M. Brombauer[1], S. Ilie[1], R. Fuchs[1], C. Fürst[1]
[1]voestalpine Stahl GmbH, voestalpine-Strasse 3, 4020 Linz
*Corresponding author: georg.stechauner@voestalpine.com

Abstract

Steel cleanliness is a complex topic, which is influenced at almost every step in the production line. It starts on the liquid side in the converter and ends in the solidified slab, and is further topic to modification by heat-treatments or rolling. To produce and provide high quality steel, the steelmaker has to be able to control the inclusions in the as cast slab, where they can range from the nano- to micro scale. In this work, the authors studied the influence of alumina, magnesia and MA-spinel refractories as a stopper rod material in a Ca-treated low carbon, high manganese steel. The stopper rods were recovered after a full casting sequence and are compared to virgin stopper rods. The experimental work consists of optical light microscopy, scanning electron microscopy, and computer aided surface analysis. While the alumina stopper rod shows a chemical reaction to the Ca-treatment, with the formation of various calcium-aluminates, the MA-spinel and magnesia stopper rods show only a minor chemical reaction zone.

Keywords:

Stopper rod, flow control, clogging, MA-spinel, calcium-aluminates, magnesia

1. Introduction

The production of high-quality steel for the application in automotive or security relevant components of petroleum industry requires a deep knowledge of the involved processes during casting. The investigated process of this work is the reaction and wear of stopper rod material with the liquid steel. Particles of refractory material separating from the stopper rod tip inevitably flow into the mould, with the last chance of separation through floatation to the mould slag. Any particle, that fails to rise, will become permanently entrapped within the slab and is likely to reduce the quality of the final product and can lead to expensive repairing steps or even the need to scrap the slab.

In Al-killed steel, a strong tendency to clogging is inhibited by that addition of Ca, which leads to a modification of alumina Al_2O_3 particles to calciumaluminates $CaO*Al_2O_3$ (CA) [1]. These CA particles, if treated correctly, exhibit a lower melting point, and thus greatly decrease the tendency to clogging. One side effect of the Ca treatment however is the reaction of Ca with stopper rod refractory material [2]. These effects on the modification of functional material were also reported in MgO-C systems after Ca-treatment [3]. The authors observe that the penetration of Ca is carried by the grain boundaries of MgO, moving through the fine grain region and disaggregating the sintered MgO grains.

Another mechanism that has to be considered is the formation of MA-spinel ($MgAl_2O_4$). The Al_2O_3 from deoxidizing the steel reacts with the MgO refractories [4,5]. The authors show clear evidence of a spinel layer formation on the liquid/refractory interface.

Rembold et al. [6] performed investigations of stopper rod tip wear in a thin-slab caster considering magnesia and spinel refractories without a gas nozzle. The actual stopper rod positions from level one records were compared to the computer assisted wear analysis. A centrepiece of the performed work was the delicate sample preparation, in order to obtain comparable specimens. However, the remaining spread in results for comparable boundary conditions shows the intricate nature of this topic.

In this work, we focus on the chemical modifications occurring during the casting of a Ca-treated low carbon high manganese steel sequence on alumina, magnesia and MA-spinel stopper rods.

2. Experimental

The investigated stopper rods were recovered after a casting sequence of four to ten ladles of Ca-treated low carbon steel with a chemical composition according to **Table 1**.

Table 1 – Chemical composition of low carbon steel

	C	Mn	Al	Si	Ca	Cr,Mo,V,Nb
wt.-%	0.04	1.5	0.03	0.3	0.0015	0.4

The composition of the three refractories investigated is given in **Table 2.** The nozzle system applied in the alumina and magnesia stopper rods is a purging tube with a central outlet of about 1mm, while the outlet of the MA-spinel nozzle has a circular shape.

Table 2 – Composition, geometry and nozzle system of stopper rods

Stopper Rod	Typical value, %				
	MgO	SiO₂	Al₂O₃	CaO	others
MgO	88	2	6	1	3
MA-Spinel	21	4	72	0	3
Al₂O₃	<1	<1	94	<1	3

After cutting the recovered rod tips in half they were scanned and a computer assisted area analysis was performed, which will be explained in detail next. In a first step, the graphic software Paint.NET [7] was used to remove all pixels that could be identified as remainders of slag. The benefit of this software tool lies in the high magnification that allows a manipulation of individual pixels, as well as the use of layers to obtain consistent results throughout all the stopper rods. Exactly these layers were used to place the scanned images on top of each other and align them by using internal features such as the nozzle system or the inner diameter. Next the contour was traced using pixel graphics at high magnification to obtain the 2D area of the stopper rod. The results from the mechanical wear analysis are given in section 3.1.

The reaction between liquid steel and functional refractories was investigated in detail. A sample was taken from the front of the stopper rod and hot embedded in SnBi to provide conduction necessary for SEM investigations (**Figure 1**).

Figure 1 – MgO stopper rod tip after recovery and cutting. The central purging outlet is in the centre of the tip. Black box marks SEM-sample location.

SEM investigations of the interface regions between liquid steel and refractories were performed on a ZEISS Ultra 55. EDX spectra and mappings were using an Oxford X-Max 50 Plus SDD-EDX detector together with Oxford AZtek software. Microprobe analysis of the alumina sample was performed on a Cameca SX-100 microprobe analyser equipped with five WDX-detectors.

3. Results and Discussion

3.1. Computer assisted mechanical wear analysis

The result of computer assisted wear analysis is shown in **Figure 2**, with the black area being the eroded material. The erosion of magnesia tips appears to be concentrated around the tip and central section, while there seems to be a maximum in wear for the other refractories around the sides, where the distance to the tundish nozzle is minimal, thus the flow rate is maximal. The values for eroded area and volume, respectively, are given in **Table 3**. Considering the density and the operation time of the stopper rods, the rate of mass loss can be calculated. The calculated data is further compared to recorded stopper rod positions from level one measurement.

Table 3 – Calculation of wear rates from image analysis and the movement of stopper rod from level one records

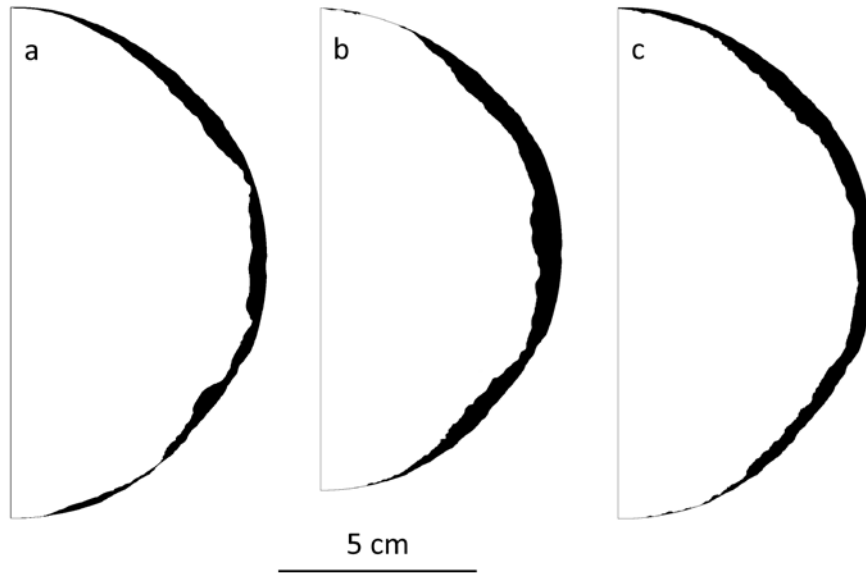|	r [cm]	A [cm^2]	V [cm^3]	ρ [g/cm^3]	m_{wear} [g]	Cast time [h]	Wear rate [g/h]	Level one [mm]
MgO	12.9	59.6	516.0	2.51	115.5	9.2	12.6	8.4
MA	12.3	51.0	431.5	2.60	144.8	8.8	16.5	14.2
Al2O3	12.9	58.6	507.5	2.83	154.3	6.8	22.7	7.0

Figure 2 – Digitalized 2D wear of a) MgO, b) MA-spinel, and c) Al2O3 stopper rod tips.

Comparing the calculated wear to the measured stopper rod positions (Table 3) delivers no concise correlation. This is in agreement with the findings of Rembold et al. [6] who reported erosion to be inconsistent with stopper rod position. In the case of the MA-spinel stopper rod, it should be noted, that the radius was considerably smaller, thus the greater wear according to the stopper rod position had less impact on the total mass of lost tip material.

Calculating wear rates based upon image analysis as performed here is a delicate topic, and some of the encountered problems shall be highlighted next. To begin with, there is no option of comparing the stopper rod after operation to the exactly same one in a virgin state. Small manufacturing discrepancies can lead to considerable variations in calculated wear. This problem was approached by considering every stopper rod in the calculation to have a perfect semi-circle in its virgin state, as the error introduced by this simplification should even out between the different rods.

Another, and more impactful difficulty, was the alignment of the individual rods. There exists no inner feature that is identical in all stopper rods and could be used as a clear starting point of analysis. In our work, features such as the inner and outer diameter, the shape of the rod tip, as well as remainders of the nozzle system were used to align the images.

Lastly, the recorded stopper rod level cannot be used as a direct wear indicator, as the counterpart within the tundish will also face wear. A recovery of this tundish nozzle was however not possible, as a recovery can only be performed after the tundish is cooled down to room temperature, and it will then be submerged under the solidified steel rests. Recovering the tundish nozzle from the mould side did not succeed, as the bonding between the solidified steel to the refractory was to strong and the tundish nozzle was damaged in the recovery process.

Considering all these problems, the results obtained are still in line with literature and appear to be consistent. The wear rates for the high quality materials, MgO and MA-spinel, are considerably lower than the one for the alumina stopper rod. In the following section the higher stability of the former materials to the latter one will be highlighted.

3.2. Chemical interactions of liquid steel and refractory

Additionally to the wear analysis, the chemical interaction with the surrounding liquid steel and modification of the refractory materials during continuous casting were analysed by scanning electron microscopy (MgO, MA-spinel) and microprobe (Al_2O_3), respectively. All samples show a slag coating/glassy phase from the recovery process when lifting the stopper rod through the tundish slag. This glazing is not in the scope of this work, as it had no impact on the chemical interactions during the casting process whatsoever. Bright areas in the SEM figures are voids, filled with the hot embedding material SnBi. We assume prior direct contact of the liquid metal with these areas through open porosity in the interface region. Dark grey areas are remainders of steel that were trapped during stopper rod recovery and solidified. Within the unmodified core material carbon fibres are detected, that are added to the functional product to improve the wetting properties.

The refractories show an unmodified base material, which is identical throughout the core and starts in shallow depths of less than 1 mm. The area between the unmodified core and the slag coating is the reaction zone where the modification on the refractory occurs. The interactions of the individual zones will be shown next.

3.2.1. Magnesia – MgO

The overview of the MgO stopper rod consisted of a thick slag glazing with some steel droplet remainders and shows a reaction zone with a width of approximately 700 microns. The core material was not affected by the casting process and EDX mapping in **Figure 3** shows the unmodified MgO grain. Close to the hot side in the interaction zone, the MgO grains exhibit a modification of the fine grain boundaries which is shown in **Figure 4**.
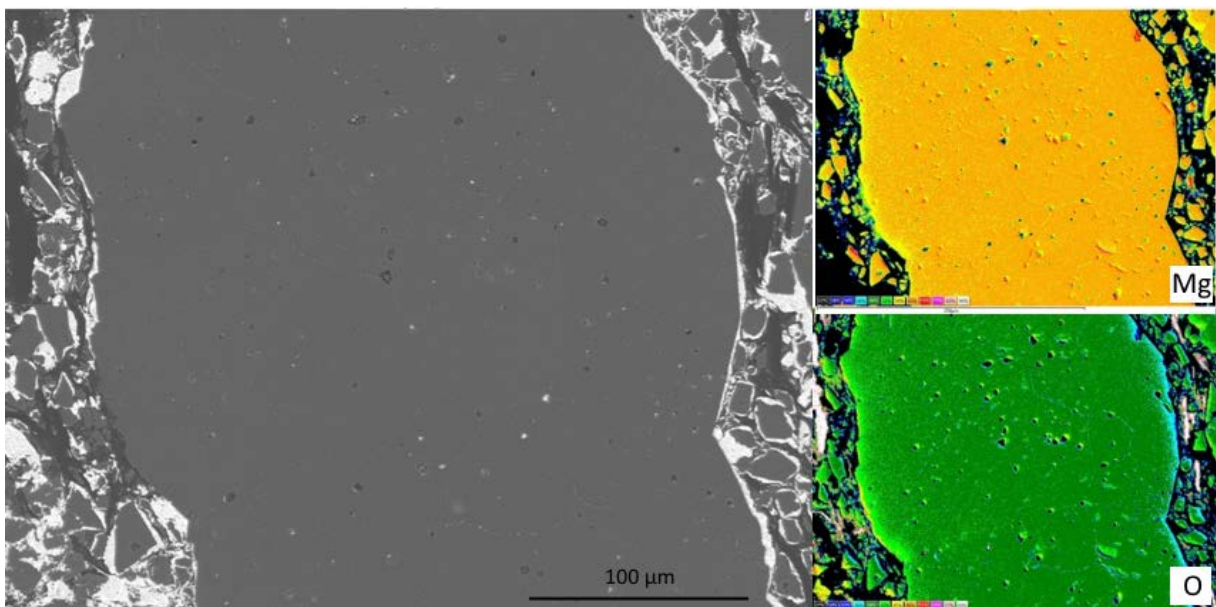

Figure 3 – Unmodified base material showing pure MgO grain. Grain boundaries are barely visible and a sparse contamination of Fe and Mn particles along these fine grain boundaries is detected.

From Figure 3 we can see that the initial MgO grain is densely packed, basically free of voids and has a well-defined composition. The fine grain boundaries are barely visible and have little contamination of Fe and Mn particles. No other impurity elements are detected along the grain boundaries or within the individual MgO grains.
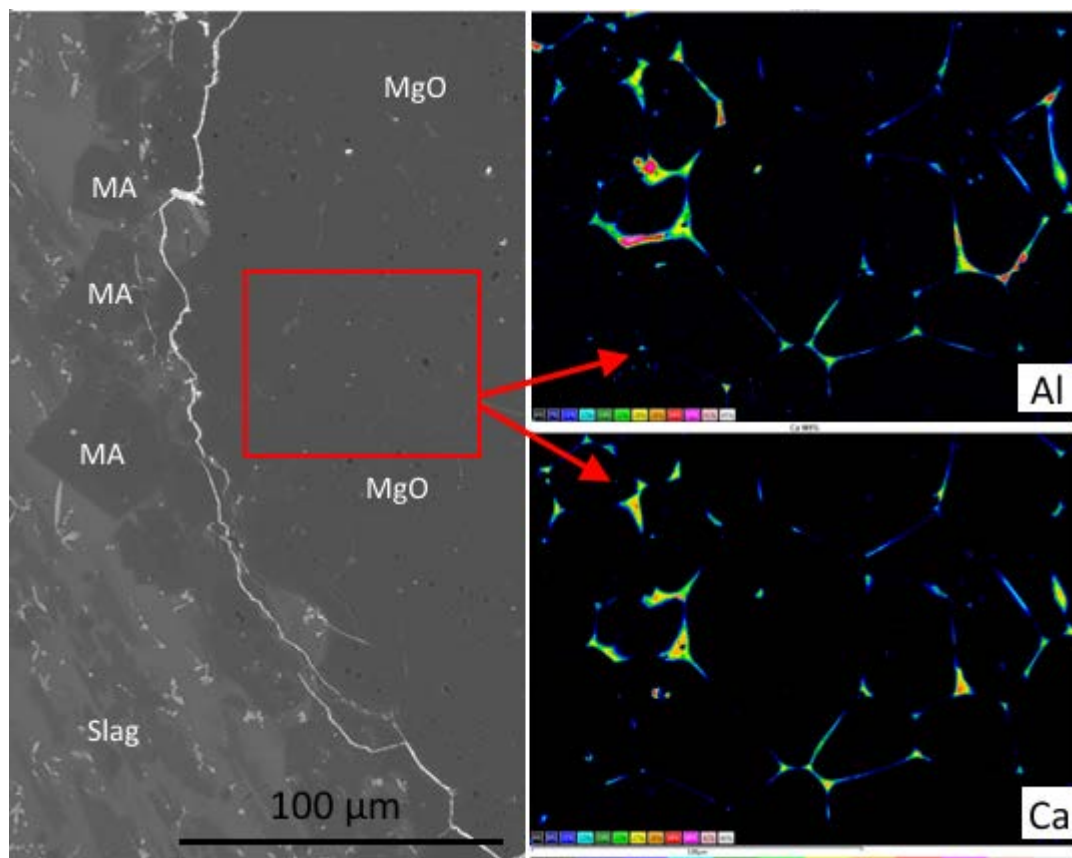
Figure 4 – Mapping on the hot side shows an MgO grain next to former hot side shows clear intrusion of impurity phases into grain boundaries and formation of MA-spinel on the front.

After being in contact with liquid steel, thus experiencing high temperatures and chemical attack, the grain boundaries become exposed. From EDX measurements we learn that the concentration of Ca, Si and Zr on the grain boundaries increases, while the internal composition of the fine grains stays pure MgO. On the interface to the former liquid steel, cubic MA-spinel particles are observed. These findings coincide well with the findings of Bavand-Vandchali et al. [5].

3.2.2. Magnesium-Aluminate spinel – MA spinel

A comparable picture is drawn upon investigating the MA-spinel stopper rod. The overview in SEM shows an unmodified base material, and a thin reaction zone of about 300 microns. Two detailed EDX mappings, from the unmodified base material and the modified MA-spinel in the reaction zone, respectively, were measured and are shown in **Figure 5 and 6**.

Figure 5 shows a densely packed and homogeneous core material of MA-spinel, with no further contamination elements. In contrast to the MgO stopper rod, no fine grain boundaries are visible in the unmodified state. Like before, the elements contaminating the grain boundaries and thus leading to a degradation of the refractory are supplied by the liquid steel.
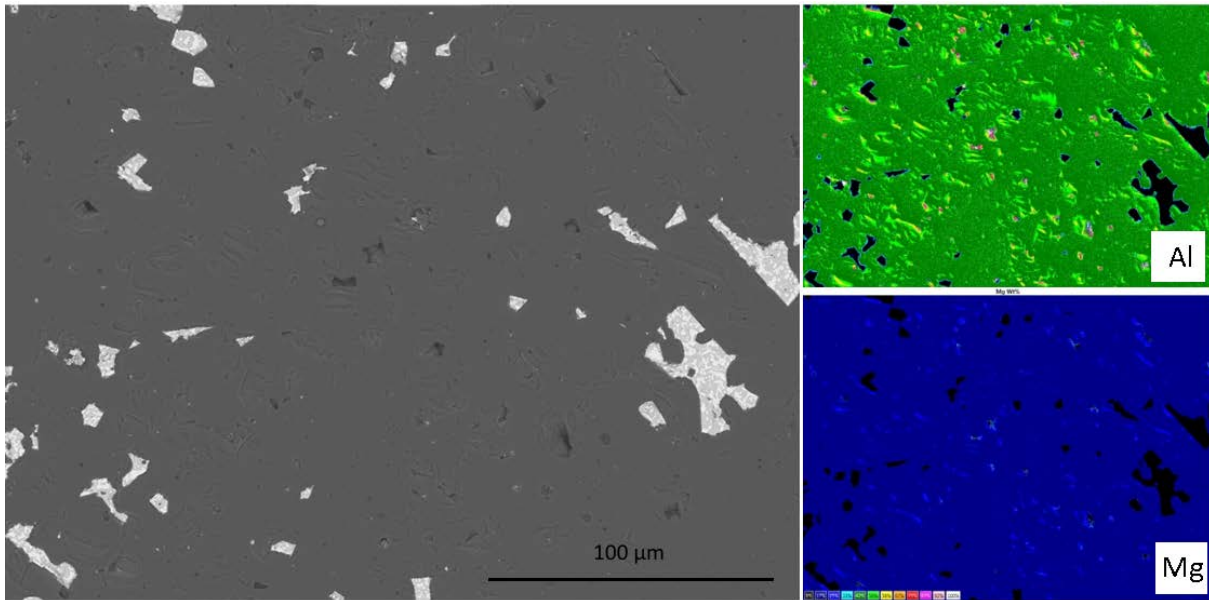
Figure 5 – Unmodified core material of the MA-spinel with no visible grain boundaries and no detected contamination.
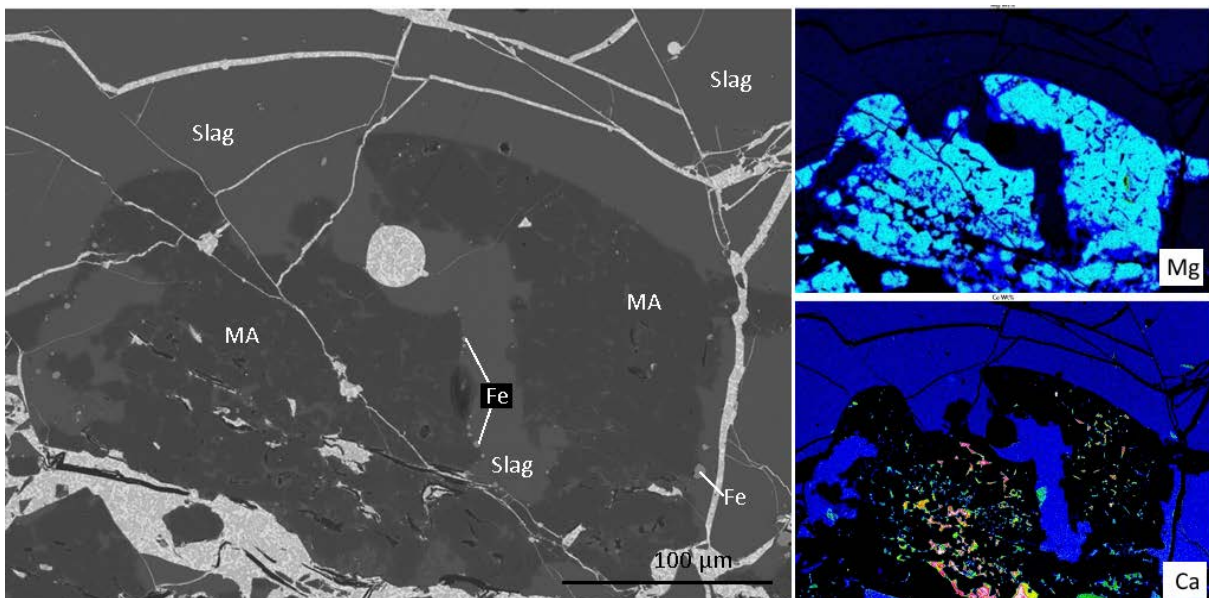

Figure 6 – Interaction of a MA-spinel grain with the liquid steel leads to an impurity phase on grain boundaries.

The interaction with the liquid steel can be seen from Figure 6. Distinct grain boundaries consisting of impurity phase are detected. Next to the refractory, some grey spots can be identified as residual steel. None of these droplets are detected within the grains. The modification of the fine grain boundaries thus appears to be driven by a diffusive or chemical process. It is also clear from Figure 6 that the impurity element Ca is concentrated mainly on the boundaries within the grain, while no concentration peaks were detected on the hot side. We thus assume that the Ca modification leads to low melting phases that are continuously removed during the casting process. A similar explanation was given by Verma et al. [2] who investigated the impact of Ca treatment on the modification of MA-spinel inclusions.

3.2.3. Alumina – Al₂O₃

The extensive modification of alumina by Ca is well reported [1,8]. To obtain a clear image on the chemical interaction and the developing phases, we apply microprobe investigations. **Figure 7** is taken from the tip of the stopper rod. The blue base material is original alumina, with a sequence of CA_x modifications towards the hot side.
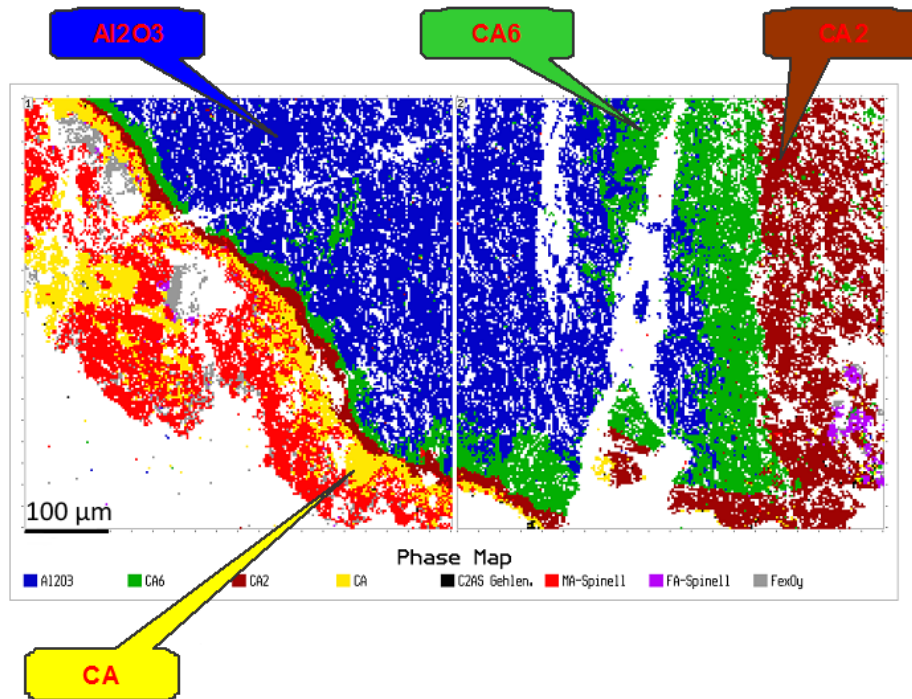

Figure 7 – Microprobe analysis of alumina stopper rod after casting sequence in Ca-treated steel.

The modification sequence is discussed in detail in ref. [1] and follows

$$Al_2O_3 \rightarrow CA_6 \rightarrow CA_2 \rightarrow CA \rightarrow CA_{x(liq).}$$

This easy modification sequence ultimately leading to liquid phases appears to be a dominant factor in the high wear rates determined in section 3.1. Further investigations of EDX mappings for the alumina stopper rod in Ca treated low carbon steel are planned.

4. Conclusion

This study comprises analyses of three refractory materials used in stopper rods in continuous casting steel production. These stopper rods are faced with mechanical wear as a result of high flow rates between the rod tip and the tundish, as well as chemical degradation as a consequence of the interaction between liquid steel and the refractories themselves. In the scope of this work, both effects were investigated and are summarized as follows:

1. From the area analysis as well as the stopper rod position, the sequence of durability decreases from MgO over MA-spinel to Al_2O_3. The wear at the MgO stopper rods is

concentrated around the tip, while the other two materials experience higher erosion on the sides where flow rates are maximal.

2. No direct correlation exists between the recorded stopper rod positions and the calculated wear rates.

3. The analysis of chemical interaction shows a residual slag glazing on all stopper rods which is not considered in this work, as it is a remnant of the recovery process.

4. The chemical modification at the MgO and MA-spinel appears to be focused on the grain boundaries, which can lead to a loss of coherency between the fine grains of the sintered material and thus lead to separation. The alumina stopper rod exhibits a wide reaction zone of various CA-modifications. The liquefaction of these CA can explain the high wear rates.

References

[1] G. Ye, P. Jönsson, T. Lund, „Thermodynamics and Kinetics of the Modification of Al_2O_3 Inclusions", *ISIJ Int.*, 36 (1996) p.105-108.

[2] N. Verma, P.C. Pistorius, R.J. Fruehan, M.S. Potter, H.G. Oltmann, E.B. Pretorius, "Calcium Modification of Spinel Inclusions in Aluminum-killed Steel: Reaction Steps", *Metall. Mater. Trans. B*, 43 (2012) p.830-840.

[3] E. Benavidez, E. Brandaleze, L. Musante, P. Galliano, "Corrosion Study of MgO-C Bricks in Contact with a Steelmaking Slag", *Proc. Mat. Sci.*, 8 (2015) p.228-235.

[4] M. Guo, S. Parada, P.T. Jones, E. Boydens, J.V. Dyck, B. Blanpain, P. Wollants, "Interaction of Al2O3-rich slag with MgO-C refractories during VOD refining - MgO and spinel layer formation at the slag/refractory interface", *J. Europe Cer. Soc.*, 29 (2009) p.1053-1060.

[5] M. Bavand-Vandchali, F. Golestani-Fard, H. Sarpoolaky, H.R. Rezaie, C.G. Aneziris, "The influence of in situ spinel formation on microstructure and phase evolution of MgO-C refractories", *J. Europe Cer. Soc.*, 28 (2008) p.563-569.

[6] M. Rembold, O. Chahin, N. Ross, B. Williams, R.J. O'Malley, "Investigation of Stopper Rod Tip Wear on a Thin-Slab Caster", *AIST Iron & Steel Techn.*, 7 (2015) p.43-51.

[7] www.getpaint.net, v.4.0.13, Free version.

[8] L. Zhang, B.G. Thomas, "State of the Art in Evaluation and Control of Steel Cleanliness", *ISIJ Int.*, 43 (2003) p.271-291.

Influence of Soft Reduction on the Liquid Flow Velocity and Pore Formation in the Mushy Zone

Bo Rogberg

Dep. of Materials Science and Engineering, KTH

Keywords: Centre segregation, Soft reduction, Continuous casting, Liquid fluid flow

Abstract:

Today Mechanical Soft Reduction, MSR, is an established technique to reduce center segregation and center porosity in continuous casting of blooms. To compensate for the downward liquid flow in the mushy zone, due to solidification shrinkage, the bloom is squeezed between pinch rollers at a distance where the center region is in a mushy state of liquid and solid. The downward liquid flow velocity will decrease and by that decrease the center segregation.

An analytical mathematical model of MSR was developed to calculate the liquid flow velocity along the strand taking into account the effect of height reduction at each pinch roller. The model considers how much of the height reduction will penetrate into the center and affect the liquid flow. The model is easy to apply and brings deeper understanding of the effect of MSR. Calculated results from different scenarios show that the area reduction should increase closer to the crater end.

MSR trials on a high carbon steel grade show that the center segregation decreases in proportion to the amount of reduction and clarifies the importance of applying a reduction step as close as possible to the crater end. The center porosity was also significantly reduced.

1. Introduction

In continuous casting of blooms heavy macro segregation and porosity arises along the center axis. To improve the center quality, modern blooms mashines[1-3] are equipped with a reduction zone for Mechanical Soft Reduction, MSR, consisting of 4-10 pinch rollers. The main aim is to reduce the height of the strand at each pinch roller in small steps and by that reduce the mushy zone area in order to compensate for solidification shrinkage. This reduces the liquid flow velocity relative to the solid phase in the casting direction.

It is shown[4], that during stationary conditions, at a fully developed mushy zone along the strand, the average downward liquid flow velocity relative to the solid, v_l^{rel}, for an arbitrary strand cross-section is proportional to the casting speed, v_{cast}, and solidification shrinkage, β:

$$v_l^{rel} = v_{cast} \cdot \beta \tag{1}$$

The high casting speed in continuous casting (when compared to ingot casting), results in high v_l^{rel} according to Eq. (1) and an extended mushy zone in the center. This is the main cause for the formation of center segregations and porosity in blooms.

Figure 1a shows a schematic drawing of a strand with liquid, mushy zone and solid as well as the liquid flow, v_l^{rel}, indicated by arrows. At the end a pore is marked out. The pore is growing in the casting direction with the same speed as the casting speed. Figure 1b shows schematically the pressure in the liquid. At the end of solidification the pressure decreases sharply due to the increased resistance to fluid flow. When the pressure decreases below the equilibrium pressure for gas precipitation center porosity will form.
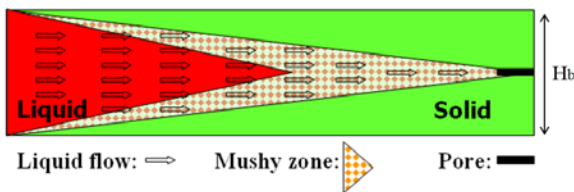

Figure 1a. Schematic view of a solidifying strand. Arrows indicate the downward liquid flow, v_l^{rel}, due to solidification shrinkage.
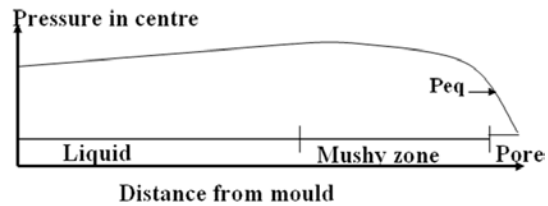
Figure 1b. Schematic diagram showing the pressure in the liquid vs distance from meniscus for a curved caster.

Miyazawa and Schwerdtfeger[5] calculated already in the early 1980s the liquid flow velocity in relation to the solid phase in the mushy zone in slabs due to solidification shrinkage. It was shown that the melt velocity component in the casting direction is about 100 times larger than the velocity component in the horizontal direction against the outer surface, see Figure 2a
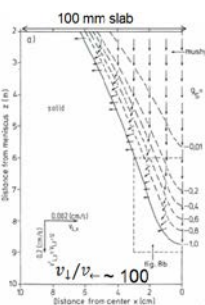

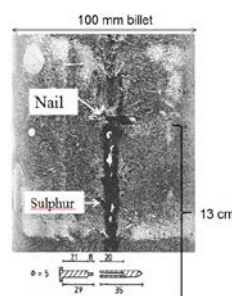**Figure 2a**. Calculated liquid flow vectors in a slab, Ref 5

Figure 2b. Sulpur print with S-doped nail shot into a billet

For a strand cross section the downward velocity vector, $v_\downarrow$, has its highest value in the center. This is due to the lowest resistance in the mushy zone prevailing along the centerline. Evaluation of velocity ratios in Figure 2a gives $v_\downarrow / v_l^{rel} {\sim} 1.3$ at the centre. Closer to the surface the ratio decreases.

The sulphur print in Figure 2b shows experiments with a FeS doped nail shot into a billet[6]. In this case the ratio $v_\downarrow / v_l^{rel} {\sim} 2$, i.e. substantially higher value than for the slab. The higher fluid flow velocity is due to the 2D solidification and is the main reason to the more severe macro segregation in blooms and billets compared to slabs.

2. Deformation behaviour of the strand due to height reduction

The height reduction of the strand by a pinch roller is illustrated in Figure 3a, which shows velocity vectors, v, for the solid and liquid before and after reduction for a longitudinal section. It is the relative velocity ratio between liquid and solid that will change by the reduction. Figure 3b and c shows the solid and liquid cross sections A_s and A_l before and after height reduction. The height, h, decreases but the width, w, increases due to the spread.
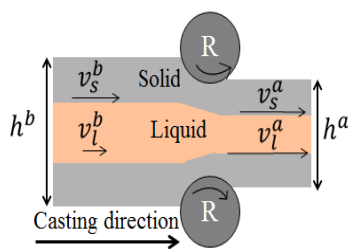

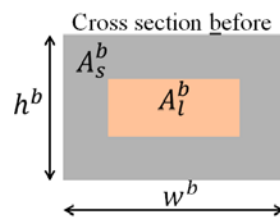**Figure 3a.** Height reduction of the strand by pinch rollers.

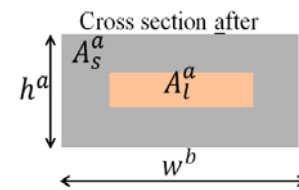**Figure 3b.** Cross section before height reduction

Figure 3c. Crosse section after height reduction

As mentioned in the introduction, it is the velocity difference between liquid and solid phase, expressed as, v_l^{rel}, that causes segregations and pores. A special case of interest to study is 'homogeneous deformation'. This case is illustrated in Figure 4a and b with the shape of a longitudinal volume element before and after height reduction. The liquid in the center is deformed in proportion to the solid phase deformation. This will not affect v_l^{rel} and hence not the center segregation and porosity. In Figure 4c the liquid area has deformed more relative to the solid area and a part of the liquid area, ΔA_l^{Push} is pushed backward and will decrease the downward flow velocity
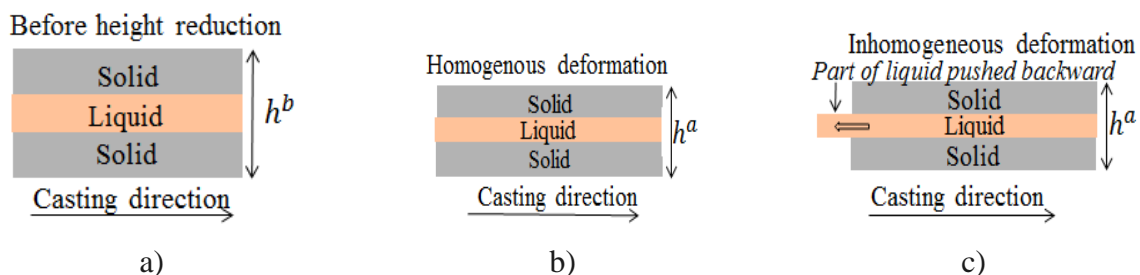

Figure 4. Shape of strand including liquid and solid phases. a) Before a height reduction. b) After homogenous deformation. c) After an inhomogeneous deformation

To be able to calculate the influence of MSR on the liquid flow it is necessary to know how much of the area reduction will contribute to the push back of liquid. This can be estimated by comparing the deformation of the liquid core with a void closure during plastic deformation. Such data can be found in the literature for rolling and forging cases. The void closure, equivalent to the decrease of the liquid area ratio, A_l^a/A_l^b, can be expressed as $\ln(A_l^a/A_l^b) = C \cdot \ln(A^a/A^b)$ where C is a closure constant dependent on different deformation conditions, such as temperature gradients and roller contact area. During MSR the height reduction is small and the expression can be simplified to a linear relationship:

$$\frac{A_l^a}{A_l^b} = 1 - C\left(1 - \frac{A^a}{A^b}\right) \qquad (2)$$

Where A^a and A^b are the areas of the strand cross section after and before reduction and the term $(1 - A^a/A^b)$ defines the area reduction. In the case $C = 1$, Eq.(2) is equal to $A_l^a/A_l^b = A^a/A^b$ which corresponds to 'homogenous deformation'. The void will never close and no push back of liquid occurs. The push back of liquid area ratio, $\Delta A_l^{Push}/A_l^b$, that contributes to the decrease of the liquid flow velocity, can now be estimated by the difference between the cases with $C>1$ and $C=1$ in Eq.(2):

$$\frac{\Delta A_l^{Push}}{A_l^b} = P \cdot (1 - A^a/A^b) \qquad (3)$$

Where, $P = C - 1$, is the push constant.

In the early work by Leduce et.al[7] it is reported that complete dense material by rolling slabs with voids is obtained with elongations between 2-5 corresponding to area reduction ratios of 0.5 to 0.8. This gives $C= 1.25-2$. Wallerö[8] measured the void closure by Filia-wax experiments giving $C=1.4-2.6$.

Figure 5a shows results from Leduce et. al. and in Figure 5b the liquid area ratio is plotted against area reduction ratios for C=1,2 and 3 and the push back liquid area ratios for P=1 and 2. In this presentation the value of C=2 is chosen in the analysis.
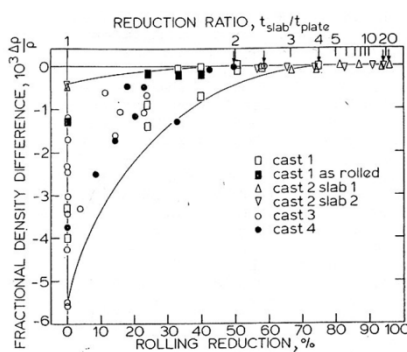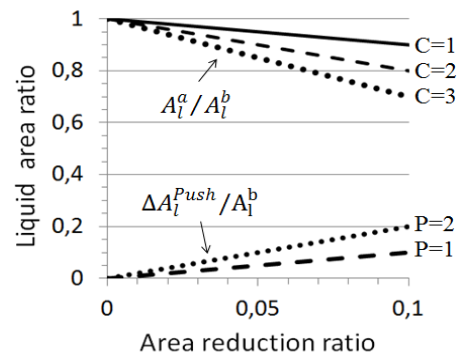

Figure 5a. Void closure results from[7]

Figure 5b. Liquid area ratio versus the area reduction ratio for different values of C in Eq. (2) and P in Eq. (3)

3. Model of liquid flow velocity due to deformation and solidification shrinkage

The influence of MSR on the relative liquid fluid flow velocity, v_l^{rel}, along the strand can be estimated according to the model proposed by Rogberg[4].

$$v_l^{rel}(x) = -v_{cast} \cdot \left[1 - \frac{\rho_s}{\rho_l} + \frac{(A(x)-A(ML))}{(A(x) - A_s(x))} \cdot \frac{\rho_s}{\rho_l} \right] \qquad (4)$$

Where x is distance from meniscus, $A_s(x)$ is solid area, $A(x)$ is strand area and $A(ML)$ is the strand area at the position of the metallurgical length, ML. This analytical equation is easy to use and can be implemented to monitor the flow velocities for on line control systems.

4. **Soft reduction trials on a high carbon steel grade and results**

Experiments with MSR were carried out on a bloom caster, size 365x265 mm. Main machine data is given in Table 1 and especially distances from meniscus to the pinch rollers. The layout of the straightening and withdrawal unit is displayed in Figure 6. A gauge device was installed at each pinch roller to measure the height.

Table 1. Basic data for the bloom caster

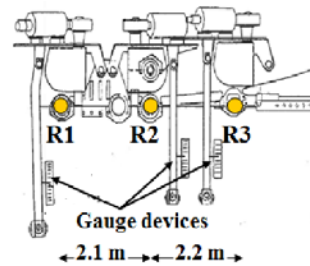| - 3 strand curved machine. - Bloom size365x265 mm, 265x265 mm - Radius: 12 m - Casting speed 0.6 to 1.2 m/min	- Withdrawal unit: 3 pinch and unbending rollers located at R1=17.7 m, R2=19.8 m, and R3=22 m from meniscus

Figure 6. Straightening and withdrawal unit with pinch rollers. R1, R2 and R3 and gauge devices for measurement of strand height reduction.

Soft reduction[9] was carried out on high carbon steels for hot strip. The composition of the tested steel grade in weight% was ~ 0.76 % C, 0.010%S and 0.28% Si. Trials with different combinations of height reduction were performed with details listed in Table 2 as well as results. The carbon concentrations along the center were evaluated by analyzing chips from drilling ~ 15 holes, Ø=5 mm. Thus it was possible to determine the maximum segregation ratio, Cmax/Co as well as the calculate the average segregation ratio Cav/Co, where Co is the heat analysis.

Table 2. Soft reduction trials on high carbon steel grade. Bloom size 365x265 mm.

Trial	Height reduction, mm				Segregation ratio		Visual porosity
	R1	R2	R3	Tot	C_{av}/C_0	C_{max}/C_0	
1, ref	0	0	0	0	1.30	1.60	Yes
2	7	3.5	5.5	16	1.11	1.18	No
3	7	0	0	7	-	-	Yes
4	7	3.5	0	10.5	1.17	1.39	No
5	3.5	1.5	5.5	10.5	1.16	1.30	Small

Sulphur prints were taken from longitudinal sections and the visual porosity along the bloom center axis was noted. It should here be mentioned that the dendrite structure was 100% columnar for all the trials.

The sulphur print in Figure 7a is the reference trial 1 without MSR. The centre is heavily segregated with single V-segregates appearing at certain intervals. The porosity is clearly

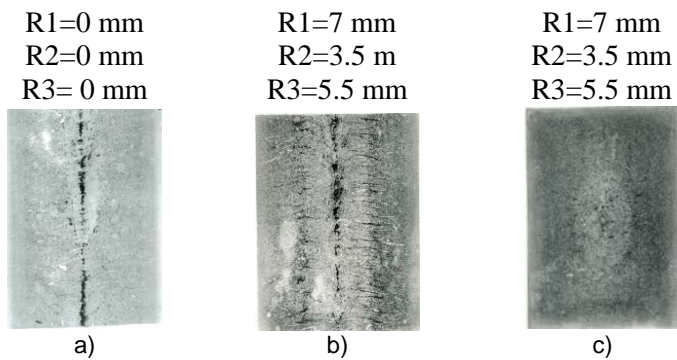visible and the maximum segregation ratio is as high as 1.6.

R1=0 mm   R1=7 mm   R1=7 mm
R2=0 mm   R2=3.5 m   R2=3.5 mm
R3= 0 mm R3=5.5 mm R3=5.5 mm

a)   b)   c)

Figure. 7. Sulphur prints from longitudinal and cross section. a)
Reference Trial 1 b) Trial 2. c) Trial 2 cross section

Trial 2 shows the effect from a total height reduction of 16 mm. The sulphur print in Figure
7b reveals severe half way cracks at distances between 28-60 mm from the centre. The
orientation of the crack plane is perpendicular to the centre axis and is created by the
elongation of the strand. The sulphur print from the cross section, Figure 7c, shows just small
signs of cracks, probably with the same origin as in Figure 7b. Consequently no cracks could
be detected with a plane oriented parallel to the central axis. The maximum centre
segregation ratio decreased to 1.18.

In trial 3, MSR was only performed at R1 and it can be seen in Figure 8a that cracks appear at
the same position as in Figure 7b. The conclusion is that 7 mm height reduction at R1 is too
large and will give cracks due to too long elongation of the strand.

In trial 4 the amount of height reduction at R1 and R2 was the same as in trial 2 but no
reduction was carried out at R3. In comparison with trial 2 the maximum segregation ratio
increased to 1.39. The sulphur print in Figure 8b shows cracks but no visual porosity could be
seen on the ground sample. The conclusion is that MSR at R3, closer to the crater end, has
about the same effect to reduce segregations as MSR at only R1+R2.

In the last trial 5, height reduction was reduced to 3.5 mm at R1 with the intension to avoid
cracks. The sulphur print in Figure 8c shows almost no half way cracks with just small visual
centre porosity. The maximum segregation ratio obtained was 1.30, quite lower than the
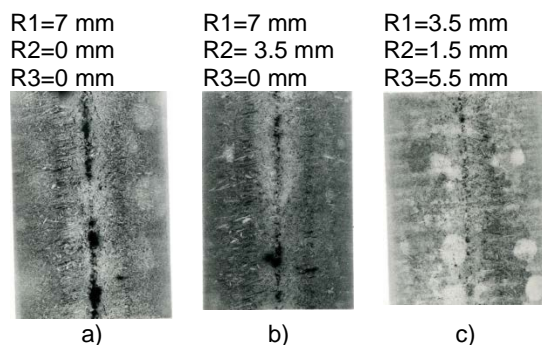reference value of 1.60.

R1=7 mm   R1=7 mm   R1=3.5 mm
R2=0 mm   R2= 3.5 mm R2=1.5 mm
R3=0 mm   R3=0 mm   R3=5.5 mm

a)   b)   c)

Figure 8. Longitudinal Sulphur prints. a) Trial 3. b)
Trial 4. c) Trial 5

Results from measurements of height and width on bloom samples are presented in figure 9a. No bulging of the parallel sides could be noticed. In Figure 9b the elongation $=\ln(\frac{h^b \cdot w^b}{h^a \cdot w^a})$ and the spread $= \ln(\frac{w^a}{w^b})$ is plotted. The ratio between elongation and spread is ~ 2.5.

The data in figure 9b can be utilized to explain the development of cracks due to MSR. A height reduction of 7 mm at R1 corresponds to an elongation of ~ 2% and spread of 0.8%. This elongation caused transversal cracks shown in Figure 7b but no longitudinal cracks in Figure 7c due to the spread. By reducing the height reduction at R1 to 3.5 mm, corresponding to 1% elongation, almost no cracks were visible. It seems that at R1 the reduction should be below 1% to avoid cracks. A reduction of 5 mm at R3, corresponding to 1.1% elongation gave no cracks. At R3 the liquid pool is smaller in the centre compared to the position at R1 and that seems to have had a positive effect on the crack propensity. The conclusion is that the steel grade can sustain higher elongation without cracking when the liquid fraction is smaller. Regarding the influence of spread no experimental value exceeded 1% and that could explain the absence of longitudinal cracks.
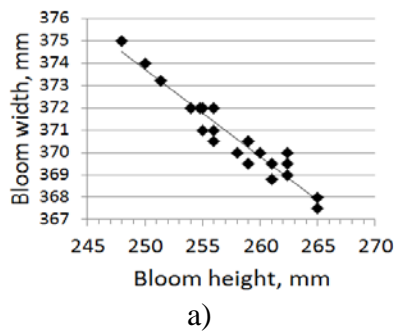

a)	b)

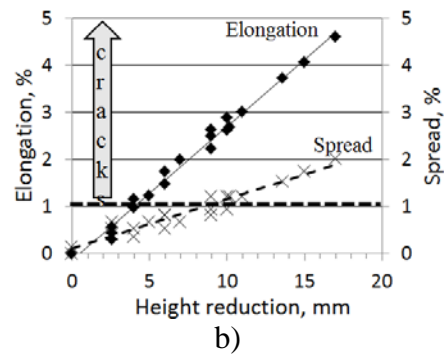**Figure 9a**. Measurements of height and width after MSR.

Figure 9b. Calculated elongation and spread vs height reduction

5. Analysis of the liquid flow velocities

In Figure 10a the influence of different height reductions are plotted at a roller position, $p=19.8$ m from the meniscus by aid of Eq.(4). The continuous curve shows the case with no MSR. The downward liquid flow velocity is constant, 2.4 cm/min throughout the metallurgical length. The dashed line, corresponding to $\Delta h=5$ mm and $C=2$, shows an instant decrease of the flow velocity to 1.2 cm/min. Closer to the meniscus the flow velocity increases to just below 2.4 cm/min which is to be expected. The reason is that the inflow of liquid to the mold will decrease by $\Delta A_l^{Push} \cdot v_{cast}$. For $\Delta h=10$ mm the liquid flow velocity has gone down to almost zero and at that point compensate for the flow caused by the solidification shrinkage. The results in Figure 10a indicate that both the instant decrease of flow velocity and duration effect, defined as the length corresponding to velocities smaller than 2 cm/min (~85% of 2.4 cm/min), is approximately proportional to the amount of height reduction.

The individual effect of MSR at positions, 17.8 m, 19.8 m and 22 m, can be seen in Figure 10b for the case of $\Delta h=5$ and $C=2$. The results have been plotted in the same diagram for comparison. The maximum velocity decrease is about the same at each position but the effect of MSR differs. The upturn in flow velocity is slower for positions closer to the meniscus. The reason is that the liquid area is larger and hence ΔA_l^{Push} will be larger. The duration effect is 5.7 m, 1.9 m and 1.1 m respectively. If the target of MSR is to obtain the

same duration length at each pinch roller the height reduction has to increase successively closer to the crater end, *ML*.

The effect of applying MSR at the same time for the 3 positions with $\Delta h=5$ and $C=2$ can be seen in Figure 10c. The first 2 pinch rollers have a clear effect but the last, at $p=22$ m, has a somewhat smaller effect, especially regarding the duration length. The dotted line shows how $A(x')/A(ML)$ varies along the strand. As earlier pointed out the push back effect is much larger at $p=17.7$ m than at $p=22$ m.
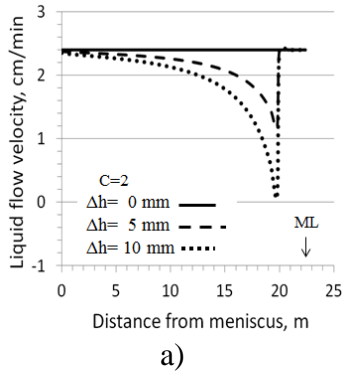

a)

Figure 10a. Liquid flow velocities, $v_l^{rel}(x')$, for the case of C=2, MSR at position p=19.8 m from meniscus and different height reductions, Δh
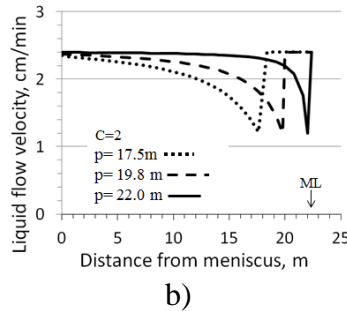
b)

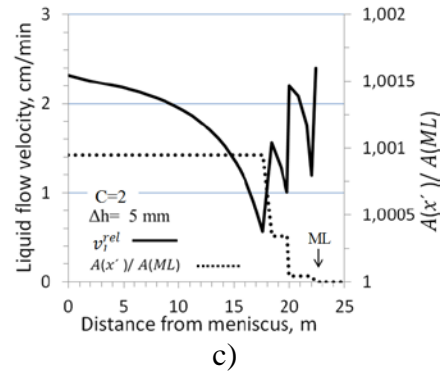**Figure 10b**.Individual effect of MSR at each pinch roller

c)

Figure 10c. MSR applied at the same time. Dotted line shows of $A(x')/A(ML)$.

A relevant question is how long the mushy zone has to be in the centre to create the necessary downward liquid flow velocities that in its turn creates the centre segregation? To check that 6 longitudinal samples were taken from the front end of a bloom with size 265x265 mm. Figure 9 shows sulphur prints from a high carbon steel grade cast at 0.6 m/min. At the bottom the dummy bar head as well as pieces of the cooling scrap is visible. Regular bridging starts to occur at a distance of about 1.2 m cast length corresponding to ~4 times the thickness of the bloom. The conclusion is that the last pair of pinch roller should be located at a distance no longer than 4 times the bloom height from the crater end to avoid bridging. It should be mentioned that measured distance 1.2 m is independent of normal casting speed upper and lower machine limits.
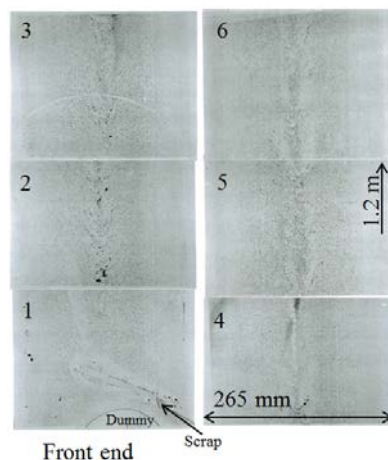

Figure 11. Sulphur prints from front end of bloom at casting speed of 0.6 m/min. Regular bridging starts after ~1.2 m cast length

6. Conclusions

- By the developed analytical mathematical model it is possible to estimate the influence of MSR on the downward liquid flow velocity behaviour in the mushy zone
- Calculated results show that the distances between the pinch rollers should decrease closer to crater end and at the same time the amount of reduction should increase to reduce the downward flow velocity in a more efficient way to reduce centre segregation and porosity
- Practical results indicate that the centre segregation in continuously cast high carbon steels develop and gradually increases in the mushy zone over a longer distance
- The necessary length of the mushy zone, to obtain bridging in the centre, is about 4 times the height of the bloom
- Elongation of the bloom due to MSR should be kept below 1% to avoid internal cracks for high carbon steels

References:

1. Y. Shen, G. Li, S. Yang, M. Zhu, *Dynamic soft reduction for continuously cast rail bloom*, J. Iron and Steel Research, Int. 14 (2007), 13-17
2. C. Moon, K. Oh, J. Lee, S. L, Y. Lee, *Effect of the rolling surface profile on centreline segregation in soft reduction process*, ISIJ Int., 52 (2012), 1266
3. C. Ji, S. Luo, m.Zhu, *Analysis and application of soft reduction amount for bloom continuous casting process*, ISIJ International, 54 (2014), 504-510
4. B. Rogberg, Ph.D. Thesis: *High temperature properties of steels and their influence on the formation of defects in continuous casting*, KTH, (1982)
5. . K. Miyazawa, K. Schwerdtfeger, *Macrosegregation in continuously cast steel slabs: preliminary theoretical investigation on the effect of steady state bulging*, Arch. Eisenhüttenwes. 52 (1981), 415-422
6. G. Engström, H. Fredriksson and B. Rogberg: *On the Mechanism of Macrosegregation Formation in Continuously Cast Steels*,. Scandinavian J of Metallurgy, 12 (1983), p. 3
7. Leduce et. al., *Density changes during hot rolling of cast steel slabs*, J. Metals Technology, 1980, July: 269~273
8. Wallerö A, *Closing of a central longitudinal pore in hot rolling*, Journal of Mechanical Working Technology, 12 (1985) 233-242
9. B. Rogberg, A. Lagerstedt, *Challenges linked to soft reduction on slabs and blooms to improve centre quality*, Scanmet 5, (2016)

Estimation of KR Stirring Energy
Using Numerical Analytical Approach

Teppei Tamura(1), Masaki Miyata(1), Shin-ichi Shimasaki(2) and Yoshihiko Higuchi(3)

(1)Process Research Laboratories, Nippon Steel & Sumitomo Metal Corporation, Kamisu, Japan

(2)Department of Electro-Mechanical Systems Engineering, National Institute of Technology, Kagawa College, Takamatsu, Japan

(3)Mechanical Engineering, College of Industrial Technology, Amagasaki, Japan

Abstract: In the present study, the numerical analytical approach for KR process was investigated. The vortex shape, the relative position between the impeller and the vortex and the stirring power of the impeller were successfully simulated by CFD approach. The calculated results were almost same as the observed ones in the cold model. The estimation of stirring energy using numerical analytical approach was effective especially for the case when the intersection of the vortex surface with the impeller blades occurs.

1. Introduction

The KR(Kanbara Reactor) process[1] has been used for mainly hot metal desulfurization. In the KR process, an impeller is dipped in molten iron and rotated at the rotation speed over 100 rpm to disperse the desulfurization flux into the molten iron. In order to control and improve the desulfurization behavior, prior evaluations of flow of molten iron and flux, surface shape of molten iron in a ladle, and stirring energy of impeller are necessary. In this work, the numerical analytical approach was investigated. The vortex surface shape and the stirring energy of impeller estimated by CFD were evaluated by the comparison with the experimental results of the water cold model.

2. Experimental procedure

Figure 1 shows the schematic diagram of the water model equipment used in this work. It consisted of the vessel and impeller both made of acrylic resin, the motor and the torque transducer. The vessel was filled with water to the 350 mm level from the bottom after the impeller was set up at submergence depth. Torques to rotate the impeller at the constant rotation speeds were measured by the torque transducer at the various conditions shown on Table 1.
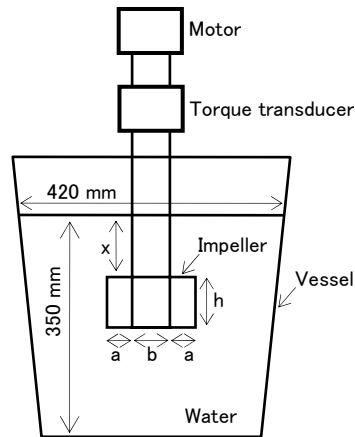
Figure 1. Water model experimental apparatus.

Table 1 Experimental conditions.

Water vessel	Depth of water bath		350 mm
	Surface diameter of water bath		420 mm
	Bottom diameter of water bath		347 mm
Impeller	Number of the blades		4
	Length of the blade	'a' in Fig. 1	40 mm
	Thickness of the blade	'b' in Fig. 1	60 mm
	Width of the blade	'h' in Fig. 1	80 mm
	Submergence depth	'x' in Fig. 1	100 mm
	Maximum rotation speed		550 rpm

3. CFD simulation method

CFD simulation in this work was performed by ANSYS Fluent. The sliding mesh function in transient model was used to describe impeller rotations in the water bath and the VOF method was employed to represent interface between water and air. The computational domain was only 1/4 of the KR water model with four-blade impeller in order to compress the computation time as shown in Fig. 2. The sliding zone was set to involve the impeller and the near-field water region as shown in Fig. 2. In this research, Reynolds Stress model (RSM) was used as a turbulence model.
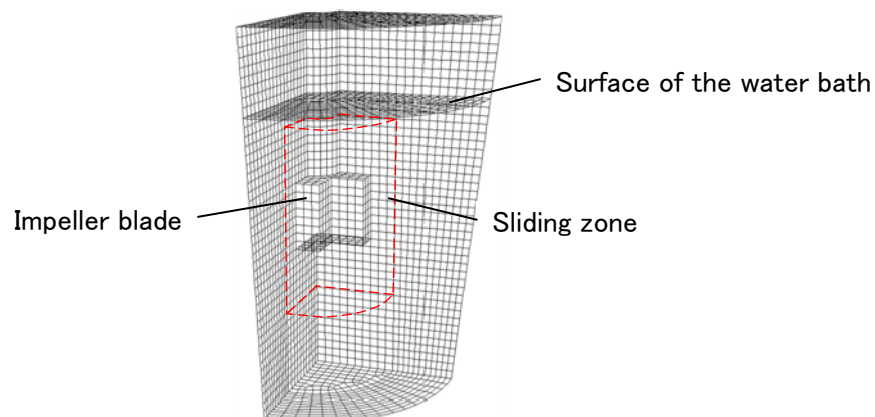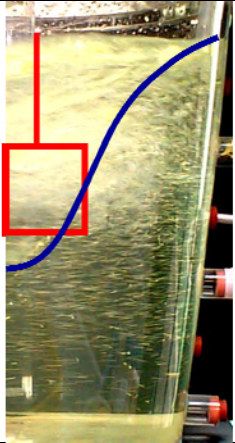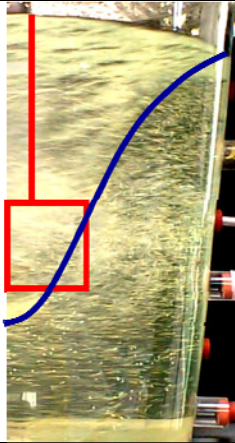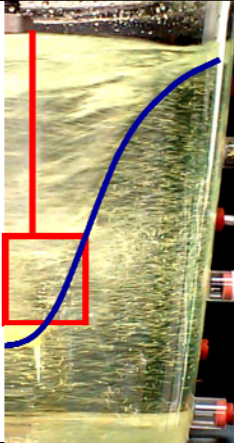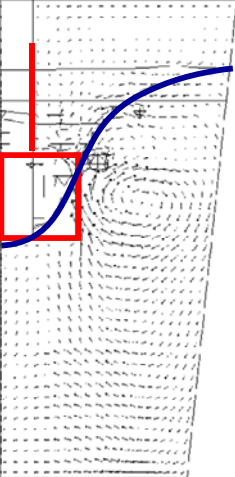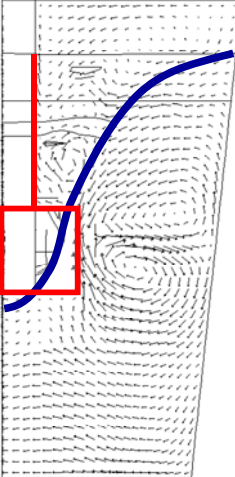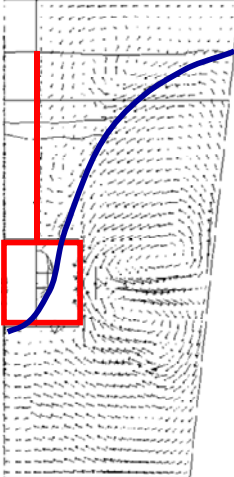

Figure 2. Water model experimental apparatus.

4. Results and Discussion

4.1 Vortex shape

Table 2 shows the comparison between observed and calculated vortex shape of water surface at the impeller immersion depth of 50 mm to 150 mm and the rotation speed of 300 rpm. Those are almost same shape. Therefore, CFD method could be effective to estimate vortex shape in order to figure out the relative position between the impeller and the vortex and avoid hot metal over flow from the ladle in the cases when new shape impeller is tested and impeller rotation speed is changed.

Table 2 Comparison between observed and calculated vortex shape of water surface at the rotation speed of 300 rpm.

	impeller immersion depth		
	50 mm	100 mm	130 mm
Cold model			
CFD			

4.2 Stirring energy

In this work, the stirring power was calculated by substituting the measured torque into Eq. (1).

$$P = 2\pi nT \tag{1}$$

Where P is the stirring power (W), n is the rotation speed of the impeller (rps) and T is the torque (N·m).

The stirring power was also calculated by empirical formulas expressed in Eqs. (2)–(8)[2]. These formulas are based on the assumption of the submergence of the impeller blades.

$$N_P = \frac{P}{\rho\, n^3 d^5} = \frac{A}{\mathrm{Re}} + B \left(\frac{10^3 + 1.2\,\mathrm{Re}^{0.66}}{10^3 + 3.2\,\mathrm{Re}^{0.66}} \right)^p \left(\frac{H}{D} \right)^{\left(0.35 + \frac{2h'}{D} \right)} (\sin\theta)^{1.2} \tag{2}$$

$$A = 14 + \left(\frac{2h'}{D} \right) \left\{ 670 \times \left(\frac{d}{D} - 0.6 \right)^2 + 185 \right\} \tag{3}$$

$$B = 10^{\left\{ 1.3 - 4 \times \left(\frac{2h'}{D} - 0.5 \right)^2 - 1.14 \times \left(\frac{d}{D} \right) \right\}} \tag{4}$$

$$p = 1.1 + 4 \times \left(\frac{2h'}{D} \right) - 2.5 \times \left(\frac{d}{D} - 0.5 \right)^2 - 7 \times \left(\frac{2h'}{D} \right)^4 \tag{5}$$

$$l_c = \left(\frac{10^3 + 0.6\,\mathrm{Re}}{10^3 + 1.6\,\mathrm{Re}} \right) \left(\frac{d}{2} \right) \tag{6}$$

$$h' = h \quad (h \le 2l_c) \tag{7}$$

$$h' = 2l_c \quad (h > 2l_c) \tag{8}$$

Where N_p is the power number (-), ρ is the liquid density (kg/m^3), d is the impeller diameter (m), Re is the Reynolds number (-) $= d^2 n \rho / \mu$, μ is the liquid viscosity (kg/(m·s)), H is the depth of the liquid bath (m), D is the inner diameter of the liquid bath (m), h is the blade width (m), $2h'$ is the effective blade width (m) and θ is the blade angle to the rotation plane (rad).

Comparison between observed and calculated stirring energy is shown in Fig. 3. Both values of those stirring energy were increased with increasing of the impeller rotation speed. The observed stirring energy was changed by the submergence depth and either equal to, or smaller than, that calculated by those empirical formulas[2]. For example, at the rotation speed of 400 rpm, the observed stirring energy was increased with increase of submergence depth and smaller than the stirring energy calculated by Eqs. (2)–(8)[2], which are based on the assumption of the submergence of the impeller blades. That is because the depth of vortex become larger at higher rotation speed of the impeller and when the vortex surface intersect with the blade of the impeller, a part of the blade idles away above the vortex surface.
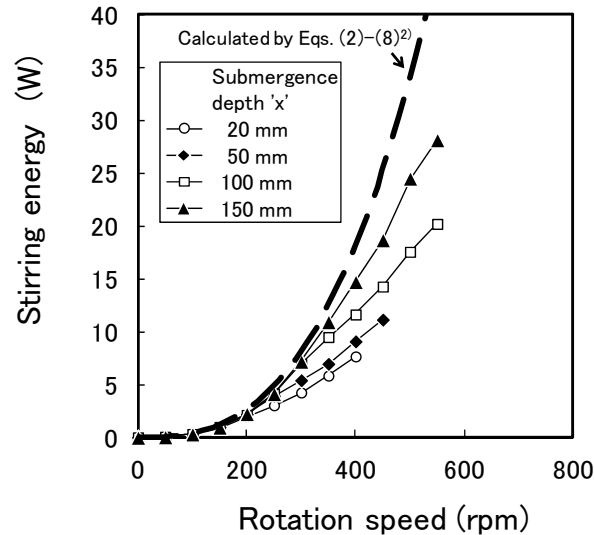
Figure 3. Comparison between the observed and calculated stirring energy.

The stirring energy estimated by CFD was also increased with increase of submergence depth and smaller than the stirring energy calculated by Eqs. (2)–(8)[2] and had the same trend as the observed stirring energy as shown in Fig. 4. Therefore, the estimation of stirring energy using numerical analytical approach is effective especially for the case when the intersection of the vortex surface with the impeller blades occurs.
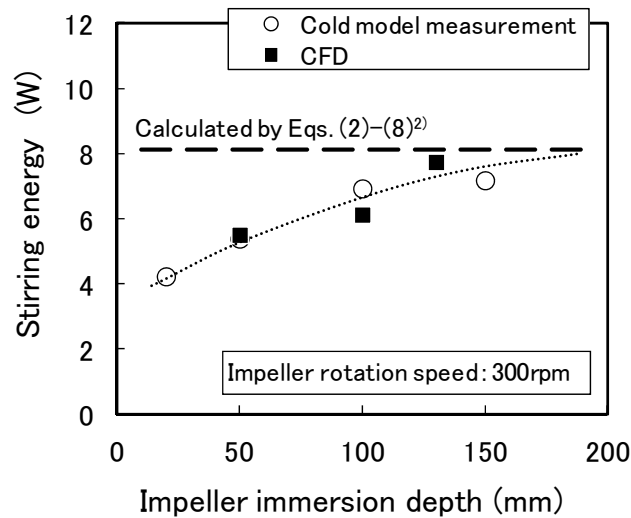
Figure 4. Comparison among the observed stirring energy, the stirring energy calculated by empirical formulas and the stirring energy estimated by CFD stirring energy at the rotation speed of 300 rpm.

5. Conclusions

The numerical analytical approach for KR process was investigated. The vortex shape, the relative position between the impeller and the vortex and the stirring power of the impeller were successfully simulated by the CFD approach. The calculated results were almost same as the observed ones in the cold model. The estimation of stirring energy using numerical analytical approach was effective especially for the case when the intersection of the vortex surface with the impeller blades occurs.

References:

1) K. Kanbara, T. Nisugi, O. Shiraishi and T. Hatakeyama, The mechanical stirring method, *Tetsu-to-Hagane*, 58 (1972), s. 34.

2) Shinji Nagata, *Power of the stirring machine*, Tokyo, 1957.

Development of Electric Arc Furnaces for Uniform Melting

Yoshikazu Tanaka[1], Takashi Yamauchi[1], Masato Ogawa[2]
(1. Chita Plant, Daido Steel Co., Ltd.; 2. Machinery Division, Daido Steel Co., Ltd.)

Abstract: The electric arc furnaces in the steelmaking process uses large amounts of energy, and so it has high needs of the energy reduction. Many of electric arc furnaces in Japan, including Daido Steel Co., Ltd. have been using the three-phase AC electric arc furnaces. The three-phase AC electric arc furnace has a cylindrical furnace wall and three electrodes which are respectively positioned at the apices of the triangle, so it has difference of distance between the electrodes and the furnace wall. This difference has caused the scrap melts ununiform (the scrap that is located in front of the electrode can be easily melted, but the scrap that is distant from electrodes is difficult to be melted), so at furnace wall in the front of electrodes (hot spot) a large amount of energy have lost. This time, to solve this problem, we have developed an electric arc furnace that has the apparatus for rotating the furnace shell under the furnace shell, and introduced in November 2013. The furnace with rotating apparatus can replace the positional relationship between the electrodes and the furnace wall, so can resolve ununiform melting and reduces the energy loss in the hot spot. As a result, we have succeeded in reducing the amount of energy in the electric arc furnace.

1. Introduction

The Japan Iron and Steel Federation has been promoting the reduction of CO2 by the transfer and dissemination of state-of-the-art energy-saving technology to the introduction and developing countries by around 2020 as Commitment to a Low Carbon Society[1]. To solve these problems, it is a very important development of efficient melting technology in an electric arc furnace that can be large energy reduction in the steel manufacturing process.

2. Problem of AC Electric Arc Furnace; Ununiform Melting

Many of electric arc furnaces in Japan, including Daido Steel Co., Ltd. (hereafter called "our company") have been using the three-phase AC electric arc furnaces. This three-phase AC electric arc furnace has a cylindrical furnace wall and three electrodes which are respectively positioned at the apices of the triangle, so it has difference of distance between the electrodes and the furnace wall. The ununiform melting of scrap caused by this difference has been a long-standing problem[2,3].

The situation in our conventional furnace (B-furnace) at just before the scrap is melted is shown in Figure1 The scrap that located in front of the electrodes (hot spot) has already melted, and the furnace wall at hot spot is exposed. On the other hand, the scrap that located far from electrodes (cold spot) has not melted yet. When we melt scrap in this situation, a large amount of energy is loses to the furnace wall in the hot spot. The heat loss amount at water-cooled panel fixed at furnace wall of B-furnace is shown in Figure2 In the near part to the electrodes of the B-phase, large amount of energy is lost. As a result, energy loss due to ununiform melting in this furnace was 30MJ/t.
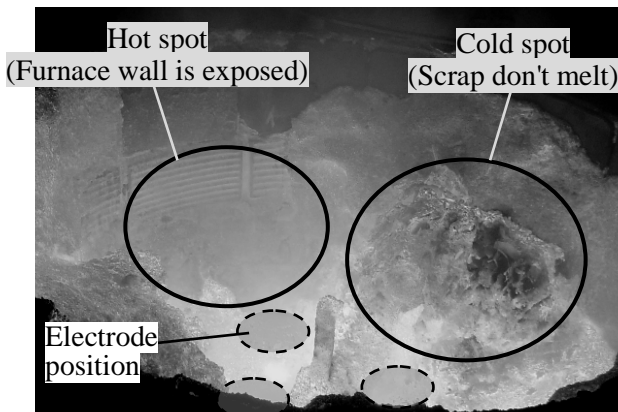
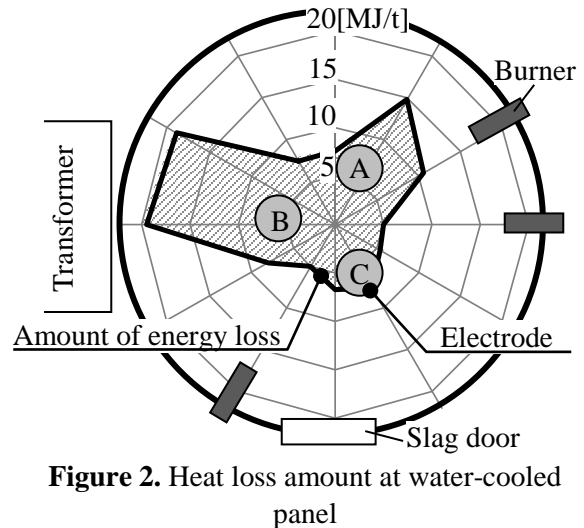**Figure 1.** Situation of just before the scrap is melted

Figure 2. Heat loss amount at water-cooled panel

Main solutions to the ununiform melting was burners on the furnace wall[4]. We also have been utilizing the burners as a solution to the ununiform melting, these has been effective in terms of reducing electric power consumption and improving productivity. However the following problem also has occurred.

- Because the energy by the combustion has bad thermal efficiency in comparison with the electric power, the energy consumption increases by using burner.
- The melting cost at night increases by using burner, when the fuel such as the LNG is expensive in comparison with the electric power at night .
- By the rebound by the flame of the burner, the water-cooled panel fixed at the furnace wall and refractory at the furnace wall is damaged.

In this study, we have developed an electric arc furnace that has the apparatus for rotating the furnace shell, and introduced in November 2013, to reduce the energy for melting scrap. This furnace is able to reduce the energy loss in the hot spot by replacing the positional relationship between the electrodes and the furnace wall (hot spot and cold spot) and solve ununiform melting in three-phase AC electric arc furnace drastically.

3. Equipment Specifications

The specifications and diagrammatic representation of electric arc furnace that we have introduced in November 2013 is shown Table1 and Figure3 respectively. Graphite electrodes are inserted downwards into the furnace shell through the furnace roof as with the conventional electric arc furnace, and connected to the power supply equipment via conductors. Rotating the furnace shell is achieved by a bearing and motor that is installed under the furnace shell. Rotating angle of furnace shell has been designed 0-50° from the original position because of the interference of the furnace shell and peripheral equipment.

Table 1. Specifications of electric arc furnace with furnace rotating

Furnace type	AC - Furnace rotating
Tapping method	EBT
Capacity	150t
Inner diameter	7000mm
Transformer	120MVA
Maximum voltage	1300V
Maximum current	70kA
Burner	Coherent type $\times$ 4
Rotating angle	0 - 50°

Electrode

Furnace roof

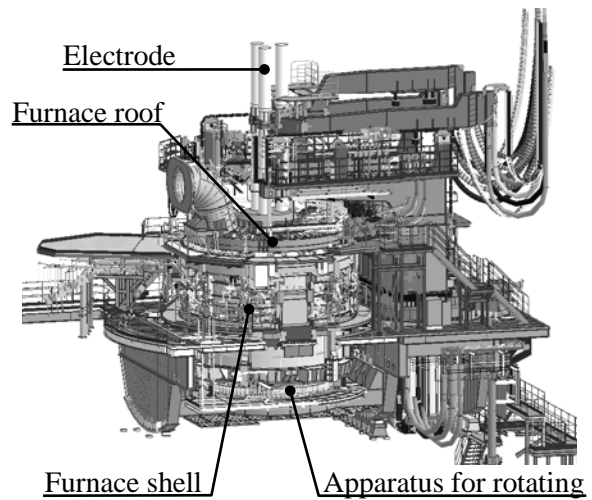Furnace shell   Apparatus for rotating

Figure 3. Diagrammatic representation of electric arc furnace

4. Rotating Operation Result

First, we made a comparison of operating with or without rotating furnace shell in order to confirm the effect of the rotating. In the operation without rotating, the melting of the scrap is performed at an angle of furnace 0° at all time, as in the conventional electric arc furnace. The operation with rotating is shown in Figure4. After the first charging, the melting of the scrap is performed at an angle of furnace 0°. Then after second charging, the furnace shell was rotated by 50° from the original position in the counter-clockwise direction and the melting of the scrap is performed in this state. Then, after the completion of the melting scrap in the vicinity of electrode, the furnace shell was rotated to 0° and the melting of the scrap is performed in this state until tapping.

1st charging (110t)   2nd charging (50t)   Melt down   Tapping

[Phase]   1st melting phase   2nd melting phase   Oxidation phase

[Rotating Angle]   [0°]   [50°]   [0°]

[State in furnace]
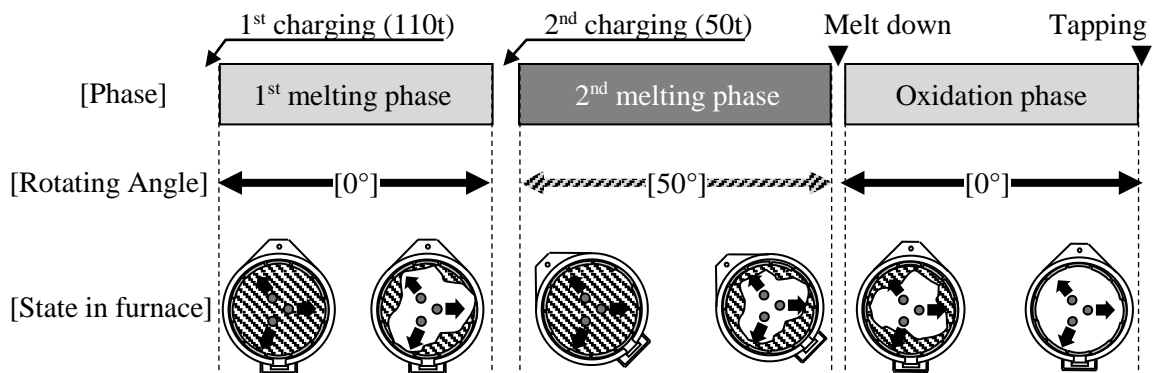
Figure 4. Operation with furnace rotating

We appreciated the result by the following methods. Water-cooled panels are fixed inside the furnace shall and are equally divided into 16 in the circumferential direction. We watch and record the water temperature of each panel. When the scrap melting proceed in the vicinity of the water-cooled panel, the water temperature rises since the heat of the arc and molten steel is transmitted directly. Therefore, if the melting of the scrap proceed in front of the water-cooled panels, the water temperature is rising. Conversely, if the melting of the scrap don't proceed in front of the water-cooled panels, the water temperature is not rising.

That is, it can be evaluated that the smaller the water temperature difference between the panels is, the more uniformly the melting scrap in the furnace is proceeding. Amount of energy loss on the water-cooled panels with or without rotating furnace shell is shown in Figure5. Amount of energy loss is the Q_n of the following equation.

$$Q_n=\{ \Sigma (T_n-T_{In})\}\cdot t\cdot V\cdot g\cdot C / M \qquad\qquad ....(1)$$

T_n : De-water temperature of water-cooled panel (K)

T_{In} : Feed-water temperature of water-cooled panel (K)

t : Operation time (min)

V : Flow rate of cooling water (m^3/min)

g : Density of water:1 (t/m^3)

C : Specific heat of water : 4.18 (MJ/K$\cdot$t)

M : Amount of molten steel (t)

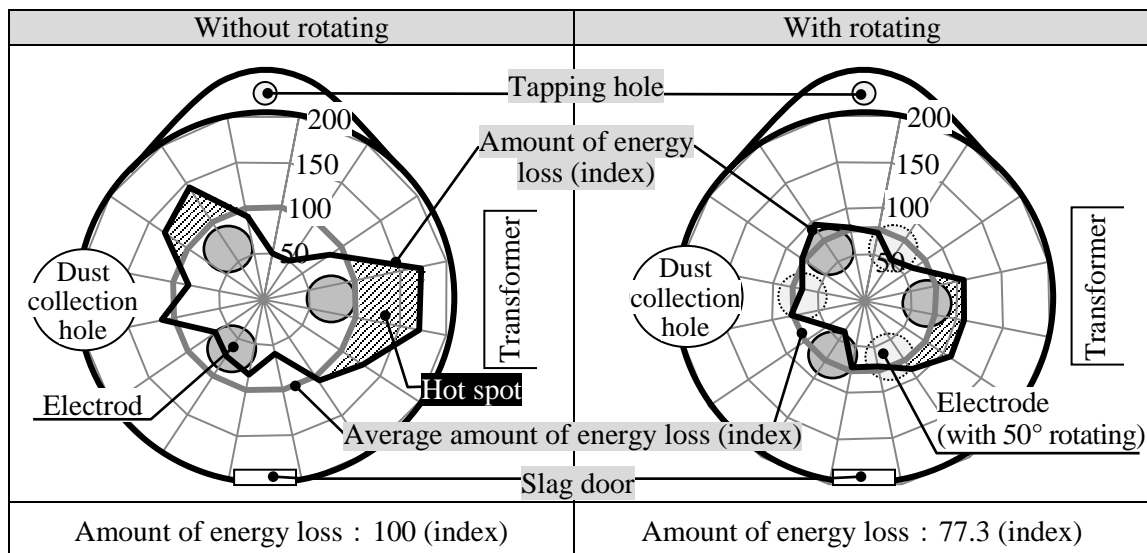| Without rotating	With rotating
Amount of energy loss : 100 (index)	Amount of energy loss : 77.3 (index)

Figure 5. Amount of energy loss on the water-cooled panels

Without rotating, a large amount of energy lost in the vicinity of electrode (hot spot), therefore it was declared that scrap melted ununiformly in the furnace. On the other hand, with rotating, by the effect of the replacement of the hot spot and the cold spot, difference of energy loss between the each panel is small, therefore scrap melted uniformly in the furnace. This uniform melting led to the energy loss reduction of 22.7% on the water-cooled panels. The relationship between the energy loss rate on the furnace shell and electric power consumption rate is shown in Figure6. The energy loss rate on the furnace shell (R_Q) is defined as an index expressed by the following equation. The energy loss on each panel(Q'_n) was defined Q_n-Q_{Ave} in the case of $Q_n>Q_{Ave}$ or 0 in the case of $Q_n<Q_{Ave}$.

$$R_Q=\{\Sigma (Q'_n-Q_{Ave})\} / Q_{Total} \qquad\qquad .... (2)$$

$Q_{Ave}=\{\Sigma Q_n\}/16$
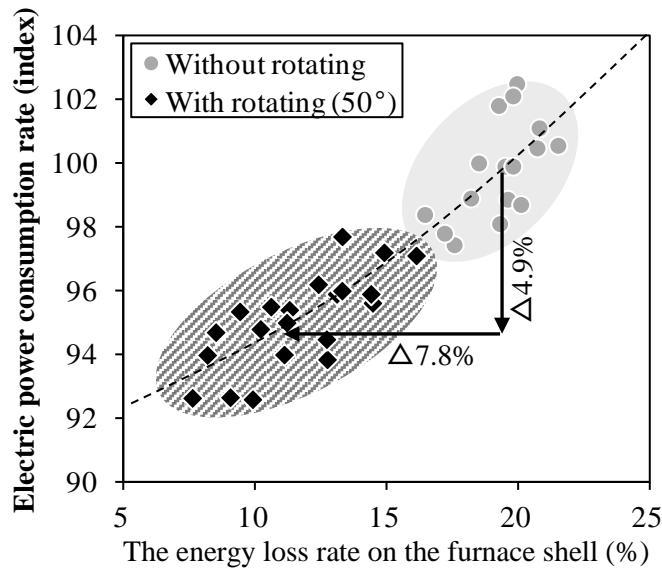
$Q_{Total}=\Sigma Q_n$

Figure 6. Relationship between the energy loss rate on the furnace shell

The energy loss rate on the furnace shell(R_Q) represents the rate of the hatched portion in Figure5. This rate on the operation without rotating accounts for approximately 20% of the total. As this rate becomes large, it can be represent that the scrap melt ununiformly, and it lead to the increase of the electric power consumption rate by the supply of extra energy. Further, as shown in Figure6, by uniform melting effect of the rotating operation the energy loss rate on the furnace shell was reduced 7.8% on average, and the power-on time was shorten 5.2%, electric power consumption rate was reduced 4.9%.

5. Examination of Optimal Rotating Angle

In the above section, it was described that effect of uniform melting in the case of replacing hot spot and cold spot in the state that the furnace shell was rotated 50° from the original position (maximum angle). In this section, in order to investigate influence of rotating angle, we operated that furnace by changing the angle at the phase that we operated at 50° in the operation method in Figure4. Figure7 show the relationship between rotating angle at that time and total energy consumption rate(index) of the furnace including the electric power and burner, other combustion heat. This time, combustion heat of the carbon was calculated as 100% secondary combustion. As a result, it was proved that the energy is the lowest at rotating angle 35°. This is because a problem has occurred that scrap in the vicinity of tap hole is difficult to melt in EBT(Eccentric Bottom Tapping)-type electric arc furnace. The diagrammatic representation of EBT-type electric arc furnace is shown in Figure8. Because the tapping hole is arranged at a position protruding from the circumference of the furnace shell and scrap charged in the vicinity of tapping hole is far from the electrode, scrap in the vicinity of tapping hole had not been able to be effectively heated and the furnace had been operated only in order to melt this scrap in the end of the operation. Currently, we are in operation at furnace rotating angle 35°.
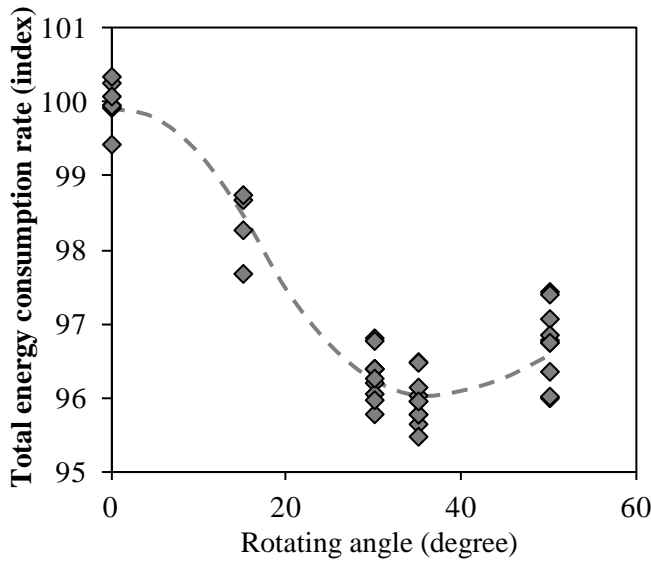
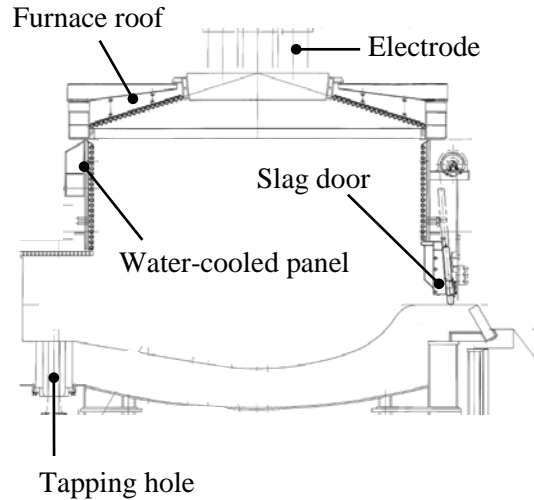**Figure 7.** Relationship between rotating angle and total energy consumption rate

Figure 8. Diagrammatic representation of EBT-type electric arc furnace

6. Application to Scrap Charging

As a further method of applying the furnace rotating, we investigated the proper position of furnace shell when scrap charged, and report on its effect. In our furnace, scrap is charged by the clamshell bucket shown in Figure9. The bucket has a structure to charge scrap to the furnace by opening the blades in the bottom of the bucket by pulling the wire connected to the blade by a crane. By the relationship of the placement of the bucket and the crane, bucket open direction is perpendicular to the line connecting the slag door and tapping hole in all of our electric arc furnaces. Due to this positional relationship, fine scrap fall through the initial open gap of the blade of the bucket and easily thrown concentrated in vicinity of the slag door and tapping hole. This fine scrap became a big lump by welding in the melting process and is often remain unmelted in the furnace wall. In our furnace, the slag door is used as slag-off and the insertion opening for molten steel temperature-measuring probe, therefore it is necessary to melt the big lump in the vicinity of slag door by oxygen blow (hereafter cutting). It is preferable to reduce the cutting time and a amount of oxygen because extension of the cutting time is a cause of increase of the workload and deterioration of safety, furnace cooling. In addition, long cutting time lower the yield of the iron. So, we tried to shift the positional relationship of the opening direction of the bucket and the slag door/ tapping hole by rotating the furnace shell to 50° before scrap charging. If we change the angle of the furnace at the time of the scrap charging, productivity losses do not occur, because it is possible to rotate the furnace and open the furnace roof at the same time. Relationship between the composition ratio of fine scrap and the amount of cutting oxygen is shown in Figure10. Because it was able to avoid charging the scrap that is difficult to melt in vicinity of slag door by rotating furnace shell before charging, the amount of cutting oxygen was reduced by approximately 31% and cutting time was shortened by approximately 30%.
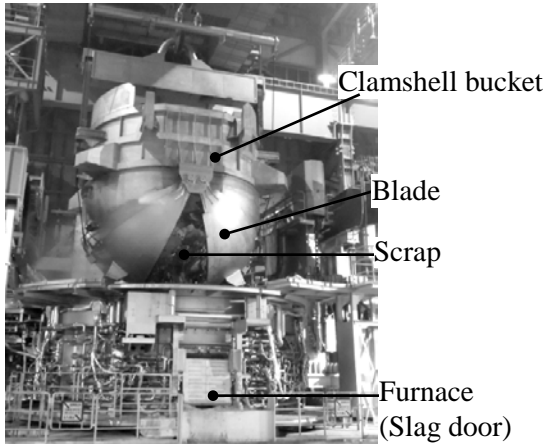
Figure 9. Picture of scrap charging
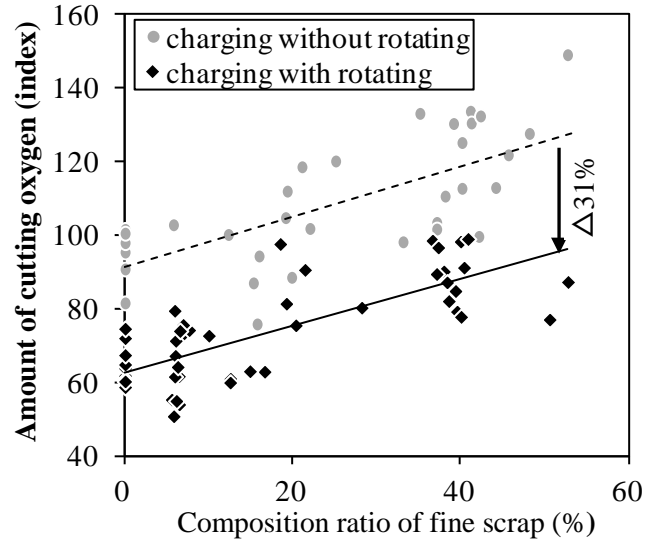
Figure 10. Relationship between composition ratio of fine scrap and amount of cutting oxygen

7. Summary of the Furnace Rotating Effect

The optimum operation method utilizing the furnace rotating is shown in Figure11. The heat balance of the electric arc furnace in the case of operated as shown in Figure11 is shown in Figure12. By the introduction of the electric arc furnace which can rotate the furnace shell, scrap in the furnace was melted more uniformly than before and the energy loss in the furnace shell is reduced, the following effects are obtained, thermal efficiency was improved by 2.6%, the total energy consumption was reduced by 4.1%, operating time was shortened 6.1%. As just described, we had been able to achieve a fundamentally solve ununiform melting in the three-phase AC electric arc furnace and achieved a large energy-saving effect.

Figure 11. Optimum operation with furnace

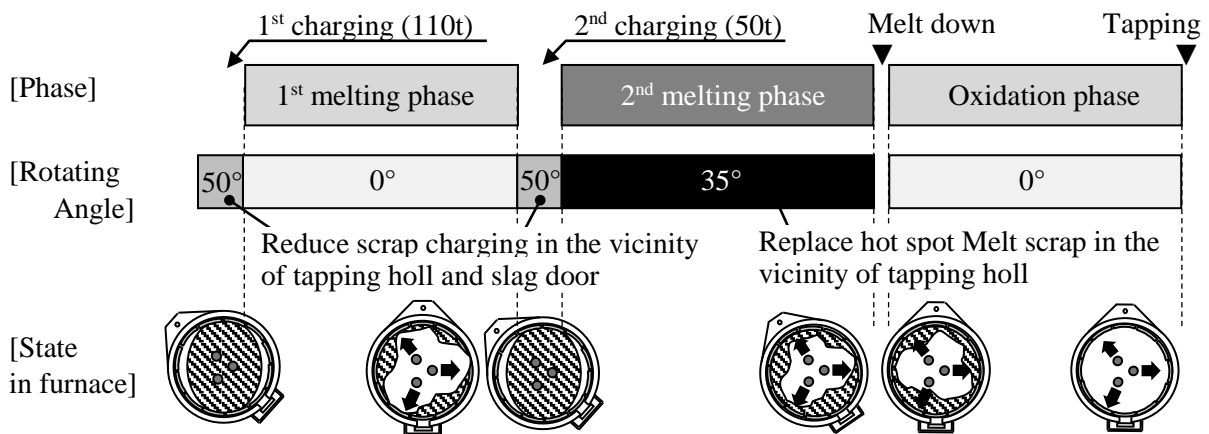|	Without rotating	With rotating (operation as Figureure 11)
Heat balance (index)	Metal oxidation 12.5 / Combustion 23.9 / Electric power 63.6 (Input) — Other 23.2 / Cooling water 11.8 / Slag 3.5 / Molten steel 61.5 (Output) — total 100	Metal oxidation 12.2 / Combustion 24.1 / Electric power 59.6 (Input) — Other 21.0 / Cooling water 9.9 / Slag 3.5 / Molten steel 61.5 (Output) — total 95.9
Thermal efficiency	61.5%	64.1%
Operating time (index)	100	93.9

Figure 12. Heat balance of the electric arc furnace

8. Conclusions

In Chita plant, we drastically resolved ununiform melting in the three-phase AC electric arc furnace by the development and introduction of the furnace rotating, and achieved a significant energy saving effect.

In addition, by combining the uniform melting technology by electric power using the furnace rotating and utilization of combustion energy by burner, it is found that the electric arc furnace with furnace rotating have a flexibility that is capable of pursuing the operating at the minimum cost point always against fluctuations in the unstable energy unit price and against operating time zone while maintaining productivity. Therefore, it has been proven that the electric arc furnace with furnace rotating jumps on the bandwagon.

References:

1) Japan Business Federation, Action plan for low-carbon society, 17 Jan. 2013, <http://www.keidanren.or.jp/policy/2013/003.html>.

2) Kiyoshi Morii, *Steelmaking by Electric Arc Furnace*, Japan, The Japan Iron and Steel Federation, 2000

3) Tosio Nanjyo, Jyunichi Kawabata, Arc Furnace(1), *Industrial Heating*, Vol.35, No.2 (1998), 73-89.

4) Tosio Nanjyo, Jyunichi Kawabata,et al., Effective Utilization of Electric Power and Productivity Improvement of Arc Furnace (3), *Industrial Heating*, Vol.34, No.4(1997), 23-36.

Application of Electrolytic Extraction to Determine Inclusion Characteristics in Steel

Andrey KARASEV, Hongying DU and Pär JÖNSSON
KTH Royal Institute of Technology, 10044 Stockholm, Sweden

Keywords: steel, deformation, non-metallic inclusions, electrolytic extraction.

Abstract: It is well known that non-metallic inclusions in steel can have a harmful effect on the quality of final steel product. This is especially apparent, when the inclusions such as sulfides and oxy-sulfides are elongated during a deformation of steels. In this case, the anisotropy of mechanical properties of the deformed steels can be increased significantly. Therefore, it is very important to precisely evaluate the characteristics of deformed inclusions when assessing the final quality of steels.

During last 20 years, the electrolytic extraction (EE) technique has successfully been applied for three-dimensional (3D) investigations of different inclusions and clusters in various steel grades. In this study, the electrolytic extraction technique was used for the 3D investigations of non-metallic inclusions in different steel grades (containing 0.003-0.042% of S) in samples taken before and after deformation. Based on the obtained results, the harmful effect of deformed oxy-sulfides and sulfides was discussed with respect to the quality and mechanical properties of the final steel products.

1. Introduction

It is well known that non-metallic inclusions can significantly decrease the quality and mechanical properties of the final steel product and that the effect is influenced by their size, number, composition and morphology. This is especially apparent if the inclusions in steels were elongated during a deformation. In this case, the anisotropy of the mechanical properties in steel in both the longitudinal and transverse directions can increase dramatically. Therefore, a detailed determination of the characteristics of deformed inclusions is very important to evaluate the final properties of steel.

According to results obtained in previous studies [1-6], the use of conventional two-dimensional (2D) investigations of non-metallic inclusions (NMI) and clusters on polished cross sections of metal samples have some significant shortcomings and disadvantages. This is especially clear in investigations of clusters and NMI having complex morphologies or for inclusions that have been elongated due to a deformation of the steel. Since only sections of inclusions can be measured on a polished surface of metal sample, it leads to significant errors and a large scattering of the results obtained by using this 2D method.

During the last 20 years, more and more publications have appeared, in which the electrolytic extraction (EE) technique has been applied for three-dimensional (3D) investigations of different inclusions and clusters in various steel grades [1-9]. In this technique, electrolytic extraction is used to separate inclusions from the steel specimens and thereafter the solution is filtrated to collect the extracted inclusions on film filters. Thereafter, the reliable characteristics (real size, morphology, number and composition) of NMI and clusters can be accurately investigated these film filters by using scanning electron microscopy (EE+SEM method). In some previous studies [4-7, 9] it was reported that this 3D method have major advantageous in comparison to the traditional 2D method for

investigations of complex and deformed inclusions and clusters. Moreover, it was reported [4, 7-9] that the EE method was successfully applied for investigations of deformed MnS inclusions in different steels.

In this study, the electrolytic extraction technique was used for 3D investigations of non-metallic inclusions in different steel grades and in samples taken before and after deformation. Samples of rolled or forged industrial steels having sulfur contents between 0.003 to 0.042% were used for the assessment of the inclusion characteristics (such as the size, volume fraction, aspect ratio, surface area of inclusions, etc.). Based on the obtained results, the harmful effect of deformed oxy-sulfides and sulfides was discussed with respect to the overall quality and some mechanical properties of the final steel products.

2. Experimental procedures

Steel samples for 3D investigations of non-metallic inclusions (NMI) were taken before and after deformation of industrial steels having different sulfur contents. Thereafter, the metal samples were cut in a longitudinal direction to enable a determination of the reliable characteristics of deformed inclusions.

The non-metallic inclusions were electrolyticaly extracted from steel samples by using a 10%AA electrolyte (10v/v% acetylacetone-1w/v% tetramethylammonium chloride-methanol) or a 2% TEA electrolyte (2 v/v% triethanol amine - 1 w/v% tetramethylammonium chloride - methanol). The steel matrix was dissolved during electrolytic extraction. However, the non-metallic inclusions, which are more stable, did not dissolve during the extraction. The inclusions from electrolyte, were collected after extraction on a surface of a membrane polycarbonate film filter with an open pore size of 0.05 or 0.4 µm. Thereafter, the inclusions were investigated by using a scanning electron microscope (SEM) equipped with an EPMA. A schematic illustration of the electrolytic extraction process of steel sample and the filtration of the electrolyte containing inclusions after an extraction is shown in Figure 1.
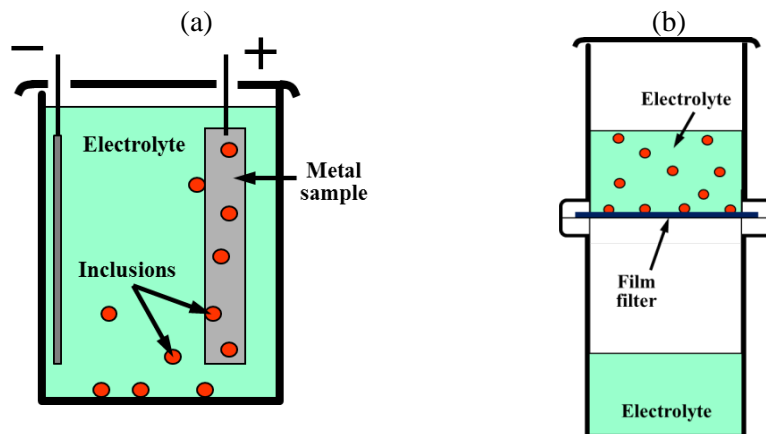
Figure 1. Schematic illustration of electrolytic extraction of steel sample (a) and filtration of electrolyte containing inclusions after a completed extraction (b).

On average, 0.01-0.3 g of metal was dissolved during the electrolytic extraction trials. In these EE trials, the depth of a dissolved metal layer on a surface of the investigated steel sample varied from 0.08 to 0.25 mm. The characteristics of the NMI as size, number, composition and morphology were investigated on a surface of film filters by using SEM with EPMA. Figure 2 shows typical SEM images of different non-metallic inclusions observed on filter surfaces including the measurement length (L) and width (W) of the deformed inclusions determined by SEM investigations. The number of investigated

inclusions varied from 200 to 3000 inclusions per steel sample. The EE+SEM method was applied for investigations of NMI in the size range from 0.05 to 500 microns. The equivalent size of inclusions (d_{eq}) in steel samples taken before and after deformation was calculated as the product $\sqrt{L \cdot W}$.
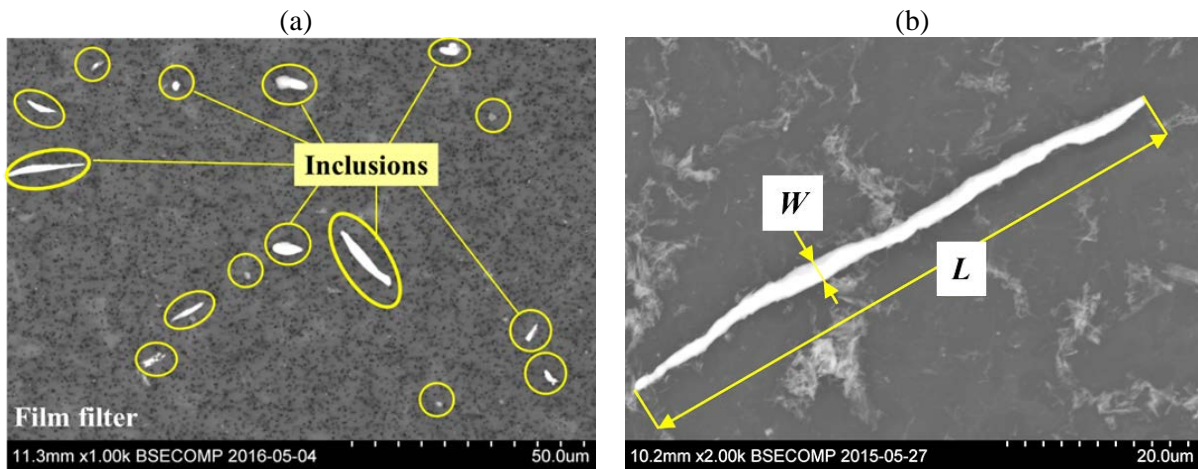
Figure 2. Typical SEM image of non-metallic inclusions observed on filter surface (a) and size measurement of deformed inclusions by SEM investigations (b).

3. Results
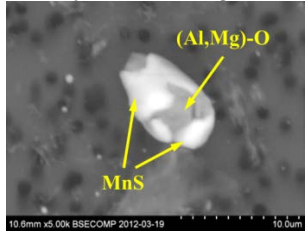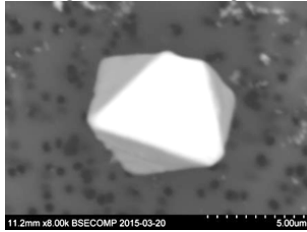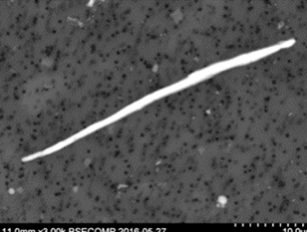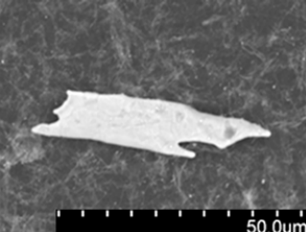
3.1. Non-metallic inclusions before and after deformation.

The electrolytic extraction method can successfully be applied for 3D investigations of different non-metallic inclusions in steel samples taken before and after deformation [4, 6, 7, 9]. For instance, the sulfides that have precipitated during solidification of the melt have various shapes, which easily can be elongated during the deformation of steel. Some typical oxy-sulfides and sulfides in steel samples collected before and after deformation of steels are shown in Table 1. The results show that the frequencies of different types of deformed sulfides can vary in a wide range depending on the steel grade, S content, condition of steel deformation, compositions, and locations of these inclusions, etc.

It is apparent that the reliable characteristics (morphology, size and number) of these inclusions could be determined correctly by using 3D investigations by using the EE+SEM method. If the deviation of the polishing section from the rolling direction is only 1-3º, the error for 2D measured length of elongated sulfides on polished cross section of steel sample (CS+SEM method) can reach 20-60% from the real 3D measured length (EE+SEM method) of these inclusions [4, 6].

Overall, 3D investigations of sulfides and oxy-sulfides, which have complicated shapes before and after deformation, are preferable to use compared to the 2D method. For instance, Figure 3 shows the typical relationships between the length (*L*) and width (*W*) for different oxy-sulfides and sulfides, given in Table 1, in rolled steel samples with various S contents [7]. Also, the characteristics of different deformed inclusions obtained by 3D investigations by using the EE+SEM method can be discussed with respect to their effect on the final properties of different steel grades.

Table 1. Some typical oxy-sulfides and sulfides found in samples taken before and after deformation of steels.

NMI before deformation	(a) Oxy-sulfide (ingot)	(b) regular MnS (ingot)	(c) eutectic MnS (ingot)
	$L \sim 3\text{-}14$ µm	$L \sim 4\text{-}15$ µm	$L \sim 10\text{-}55$ µm
NMI after deformation	(d) Deformed oxy-sulfide	(e) Rod-like sulfide	(f) Plate-like sulfide
	$L \sim 3\text{~}30$ µm	$L \sim 10\text{-}500$ µm	$L \sim 5\text{-}70$ µm
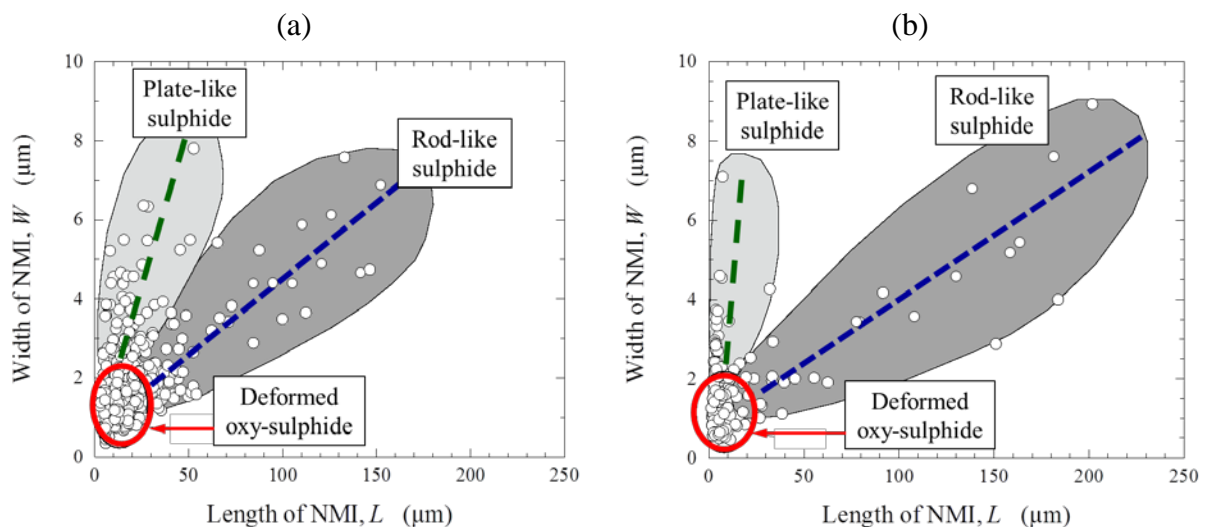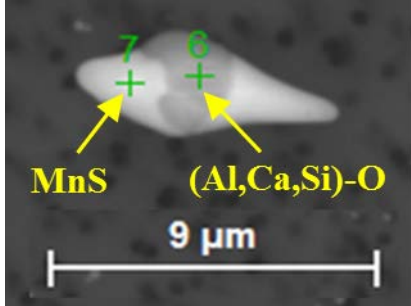
Figure 3. Relationships between length (*L*) and width (*W*) in different deformed non-metallic inclusions in steels having: (a) 0.042% S and (b) 0.003% S [7].

3.2. Deformation of inclusions in different zones of steel bar.

The deformation of sulfides and oxy-sulfides in different zones was investigated in samples taken from different zones (surface, middle and central) of a bar (Ø120 mm) from a 316L stainless steel grade containing 0.009% S. Typical inclusions observed on a film filter after electrolytic extraction of steel samples are shown in Table 2. The frequencies of the deformed MnS (Type I, $\%n_{(I)} = 9\text{-}21\%$) and oxy-sulfides (Type II, $\%n_{(II)} = 73\text{-}86\%$) depend on the investigated steel zone. The other inclusions (4-6%) having sizes in the range from 2 to 10 µm correspond to undeformed oxides. Therefore, these inclusions have an insignificant effect on the anisotropy of the mechanical properties of steel and they are not discussed in this study.

Table 2. Some typical non-metallic inclusions detected in a deformed 316L stainless steel.

Type I (MnS sulfide)	Type II (oxy-sulfide)
MnS ~ 90-100 %, (Al,Ca)O < 10 %; L = 7-132 µm; AR = 7-25; $\%n$ = 9-21%	MnS ~ 30-90 %, (Al,Ca,Si)O ~ 10-70%; L = 2-39 µm; AR = 1-7; $\%n$ = 73-86%

A schematic illustration of the investigated zones in a 316L steel bar and the particle size distributions for each type of inclusions observed in different zones are shown in Figure 4. As follows from Fig. 4 (b) and 6(c), the number of small size sulfides and oxy-sulfides decreases significantly from the surface to the central zone of the bar. On the other hand, the central zone of the bar has largest number of large size inclusions (30-130 µm). Based on the obtained results, the deformation of the steel matrix and the content of non-metallic inclusions in different zones of the steel bar can be discussed. Moreover, the effect of different types of deformed inclusions on the mechanical properties in different zones of the 316L steel bar can be determined.

(a)	(b)	(c)
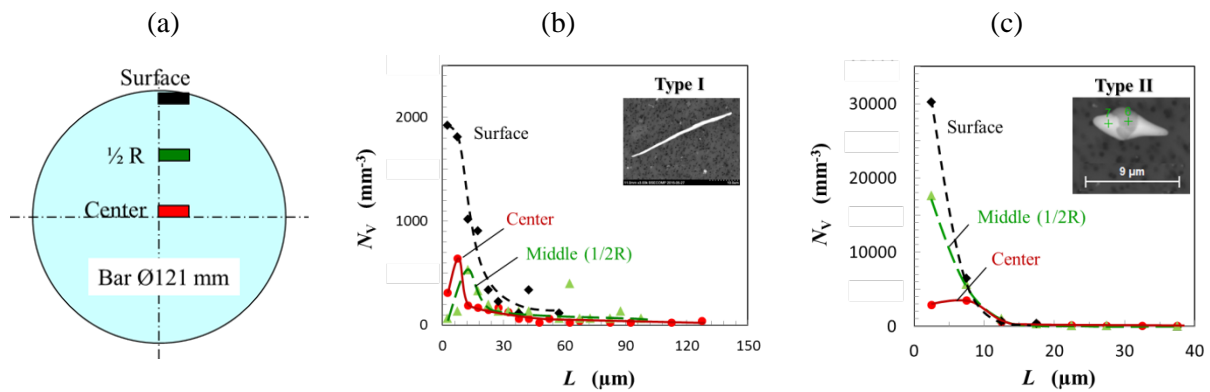
Figure 4. Schematic illustration of steel samples from different zones of a bar (a) and the particle size distributions of different types of inclusions in different zones of a 316L steel bar (b) Type I and (c) Type II.

3.3. Effect of deformed inclusions on some mechanical properties.

The influence of some steel characteristics on the mechanical properties such as the fatigue limit can be determined as follows:

$$MP = K_{me} \cdot K_{con} \cdot K_{NMI} \tag{1}$$

where MP is the evaluated mechanical property of the final steel. K_{me} is the parameter, which depends on the characteristics of metal matrix (hardness, residual stress, etc.). K_{con} is the parameter corresponding to the other technological conditions, which can influence the evaluated mechanical property (test method, temperature, etc.). K_{NMI} is the parameter, which depends on the characteristics of non-metallic inclusions in steel (such as the size, number,

volume fraction, aspect ratio, etc.). In this case, the change of mechanical property (ΔMP) which depends on the NMI characteristics in the steel is proportional to the change of the K_{NMI} value (ΔK_{NMI}).

The McClintock's model [10, 11] was used in this study for the evaluation of the harmful effects of deformed inclusions in different size ranges on the mechanical properties. This model describes the formation of shear bands between NMI and the metal matrix in steel, depending on the K_{NMI} value. This, in turn, can be determined by the volume fraction and aspect ratio of inclusions. The results obtained from the 3D investigations of the NMI characteristics can be used for an evaluation of the critical size of deformed inclusions, which promotes a shearing between the metal matrix and NMI and causes ductile fractures. For instance, it was found that a possibility for shearing in the metal matrix and ductile fracture in stainless steel with a 0.003% S content increases drastically for sulfides with lengths larger than 70 µm [7].

4. Conclusions

The successful application of the electrolytic extraction technique for 3D investigations of non-metallic inclusions in different steel grades at KTH during last eight years can be summarized as follows:

- The electrolytic extraction technique can successfully be applied as a precise analytical method for 3D investigations of the inclusion characteristics in samples of various industrial steel grades taken before and after deformation (rolling, forging, etc.).
- Non-metallic inclusions (such as oxy-sulfides and sulfides) in investigated steel grades after deformation can be classified depending on their morphology for deformed oxy-sulfides, rod-like sulfides and plate-like sulfides. The fractions of these inclusions in different steels depend on such parameters as the S content, the degree of steel deformation, etc.
- Based on the precise 3D determinations of the characteristics of different deformed inclusions, the harmful effect of these inclusions on some mechanical properties can be evaluated in various steel grades.

References:

1) A.V. Karasev and H. Suito, Analysis of Size Distributions of Primary Oxide Inclusions in Fe-10 mass pct Ni-*M* (*M* = Si, Ti, Al, Zr, and Ce) Alloy, *Metall. Mater. Trans. B*, 30B (1999), 259-270.

2) H. Ohta and H. Suito, Characteristics of Particle Size Distribution of Deoxidation Products with Mg, Zr, Al, Ca, Si/Mn and Mg/Al in Fe-10mass% Ni Alloy, *ISIJ Int.*, 46 (2006), 14-21.

3) H. Doostmohammadi, A. Karasev, P.G. Jönsson. A Comparison of a Two-Dimensional and a Three-Dimensional Method for Inclusion Determinations in Tool Steel. Steel Res. Int., 81 (2010), 398-406.

4) Y. Kanbe, A. Karasev, H. Todoroki and P.G. Jönsson, Analysis of Largest Sulfide Inclusions in Low Carbon Steel by Using Statistics of Extreme Values, *Steel Res. Int.*, 82 (2011), 313-322.

5) Y. Kanbe, A. Karasev, H. Todoroki and P.G. Jönsson, Application of Extreme Value Analysis for Two- and Three-Dimensional Determinations of the Largest Inclusion in Metal Samples, *ISIJ Int.*, 51 (2011), 593-602.

6) A. Karasev, Y. Bi and P.G. Jönsson, Three-Dimensional Investigation of Large-Size Inclusions and Clusters in Steels by Using the Electrolytic Extraction Technique, Proc. of the Iron and Steel Technology Conference (AISTech-2013), 6-9.05.2013, Pittsburgh, Pa., USA, (PR-364-109 – 2013), 1-7.

7) A. Karasev, K. Jafari and P.G. Jönsson, Assessment of Sulphide Inclusions in Deformed Steels and Their Effect on Steel Quality, The 9th Inter. Conf. on CLEAN STEEL, Budapest, Hungary, 8-10 September (2015), No. f07-05, 1-8.

8) X. Zhang, L. Zhang, W. Yang and Y. Dong, Characterization of MnS Particles in Heavy Rail Steels Using Different Methods, *Steel Res. Int.*, 88 (2017), 1600080, 1-16.

9) A. Karasev and P.G. Jönsson, Assessment of Non-Metallic Inclusions in Different Industrial Steel Grades by Using the Electrolytic Extraction Method, 5th Int. Conf. on Process Development in Iron and Steelmaking SCANMET-V, Luleå, Sweden, 12-15 June (2016), 7 p.

10) F. A. McClintock, Ductility [M]. Metals Park: American Society for Metals, 1968.

11) G. Xiao, H. Dong, M. Wang, W. Hui, Effect of Sulfur Content and Sulfide Shape on Fracture Ductility in Case Hardening Steel, *Journal of Iron and Steel Research International*, 18 (2011), 58-64.

Scrap Meltdown Progress in an AC Electric Arc Furnace Based on Current Harmonic Distortion

Christoffer N. Schmidt[1,2], Nils Å.I. Andersson[1], Anders Tilliander[1], Pär G. Jönsson[1], Pär Ljungqvist[2]

1. KTH Royal Institute of Technology, Sweden
2. Outokumpu Stainless AB, Avesta

Abstract: To decrease furnace wear and improve energy efficiency the meltdown progress of the scrap inside the furnace must be known. This work use electrical disturbances, specifically current harmonic distortions to show new tools that can be used for meltdown control in the electric arc furnace. By comparing the disturbances over time and between three scrap levels it is shown that the disturbances decrease to lower levels when the scrap level is lower. Specifically, the 2nd and 3rd harmonic decrease while the 5th harmonic is stable during the course of the meltdown. Hence, the intersection when the 2nd and 3rd harmonics decrease to a value lower than the 5th harmonic can be used as an indication of the scrap meltdown progress.

1. Introduction

The electric arc furnace (EAF) is a very important key technology to support a sustainable society as well as to promote a circular economy, due to that different recycled metallic scrap and oxidic rest products can be melted and make the base for the production of new steel grades. A substantial amount of energy is needed to operate an EAF, so it is of vital importance to improve the process control of the furnace in order to decrease the energy consumption.

During an operation of the EAF, the electric arcs inside the furnace are very unstable, which results in the introduction of disturbing loads in the power system [1]. In addition, the lengths of the arcs are constantly disturbed by falling scrap and the change in the arc length affects both the current and voltage waveforms [2]. One of the created disturbances is harmonic distortions, which introduces currents and voltages on frequencies that are integer multiples of the fundamental frequency [3]. These harmonic distortions can cause severe damage to the electric equipment to an extent that their presence in power systems have been limited in the IEEE standard 519 [4].

The electric arc furnace is one of the main identified power units that cause harmonic distortions [3, 5-7]. Hence, a lot of research has been conducted on studying the electric arc furnace, focused on harmonic distortions. The common way to approach the electric arc furnace and its harmonic distortions is to try to mitigate its effect on the utility system. Some studies have been focused on the modelling of the current and voltage waveforms, but this is generally looking at only a few waveform cycles and not the entire process [8-10]. Researchers have often enlightened the difference between different process states, but the focus is seldom to model the meltdown period of the scrap in the EAF.

Today, when several mitigation techniques exists [7] and the influence on the power system is reduced, the research can be directed on studying the metallurgical process. Some attempts have been made to further enhance the knowledge of the molten state by using variables connected to the power system. More specifically, one way that has been reported is to study the noise of the current signal where clear differences could be seen between different areas of meltdown [11]. Today, one of the more successful implementations is the use of harmonic

distortions to identify the presence of cold scrap at the base of the electrodes, where it was used in combination with the structure born sound to estimate the presence of free burning arcs [12].

When trying to identify the meltdown procedure using any variables in the electric arc furnace, the main problem is often to measure the reference scrap level. Thus, this work compares the harmonics distortions both over time and with different scrap levels. The scrap level data is taken from a work that utilises a process control camera to take snap shots of the scrap inside the furnace to make an estimation of the scrap level [13].

2. Harmonic distortions

The fundamental frequency of the current in an electric arc furnace is 50 Hz (60 Hz in countries with 60 Hz mains supply). The 2nd harmonic would then be 100 Hz as it is 2*50 Hz. Hence, the harmonic number for an electric arc furnace follows the following equation

$$F = k * 50 \ Hz \tag{1}$$

where k is the harmonic number and F is the frequency of the kth harmonic in Hz.

Commonly used to express the severity of harmonic distortions is the total harmonic distortion (THD). The THD value is calculated as the root square sum of the individual harmonics, divided by the fundamental current according to the following equation [1]:

$$THD(\%) = \frac{\sqrt{\sum_{i}^{n} I_i^2}}{I_f} * 100 \tag{2}$$

where n is the total number of harmonics being considered, I_i is the current of harmonic i and I_f is the fundamental current.

3. Method

3.1 Furnace operation

The electric arc furnace had a tapping mass of roughly 90 tonnes of liquid steel. In general the electric arc process cycle contains the 6 steps shown in figure 1. Some difference occur between each individual furnace, especially regarding the step down period. In particular, some furnaces does not use a step down. The refining period is used for oxidation or reduction and super heating. The numbers of scrap baskets may differ, depending on the relationship between the loading equipment, furnace volume and ladle sizes. Hence, step 1, 2, 3 and 4 are repeated until the sought steel volume is reached. All heats that are considered for this work consist of two basket operation. As the first basket is loaded before power on, the operational procedure is very much like the one shown in figure 1.
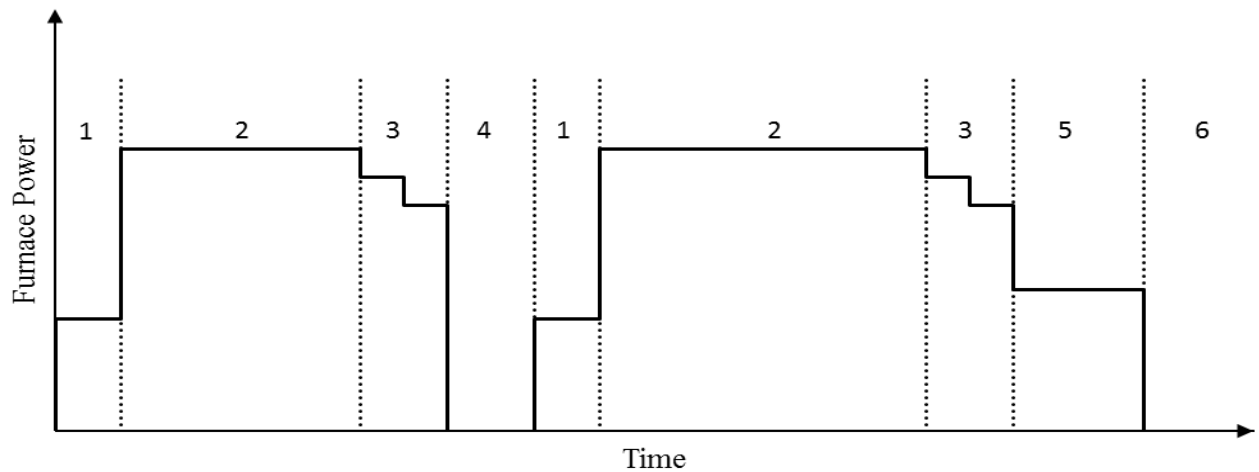
Figure 1. The different steps of an EAF cycle. 1. Boredown 2. Main melting period 3. Step down 4. Scrap insertion 5. Refining 6. Tapping, preparation and maintenance.

3.2   Data set

In total, 139 heats were considered. Later, 11 heats were removed due to that the operators turned off the electrode protection system. Hence, this indicated that the electrodes were too short to operate the furnace in an optimal manner. Moreover, 9 heats were removed due to that the video recordings contained too much smoke, so that it was impossible to estimate the scrap level. After a variable control, 2 heats were removed because the THD values were unreasonably high as well as very unstable. This, indicating that the process was not operating optimally. So, after the data treatment, 117 charges were used in the final comparison.

3.3   Scrap level estimations

During a previous work [13] the 117 heats were classified according to the observed amount of scrap remaining in the furnace when the furnace was opened for the insertion of the second basket. Three levels were defined from one to three where one corresponded to the lowest amount of scrap remaining in the furnace and three the highest. The criteria for scrap level one was that there had to be a visible steel bath. For scrap level two, the remaining scrap in the furnace had to be hot and partially melted. Heats classified as scrap level three had a large amount of cold unmelted scrap remaining in the furnace. An example of the observed levels can be seen in figure 2. The distribution among the three scrap levels are specified in table 1.

Figure 2. Examples of the three scrap levels. From left to right, scrap level one, scrap level two and scrap level three. Before the insertion of the second scrap basket.

Table 1. Number of heats for each scrap level classification [13]

Scrap level	One	Two	Three
Heats	20	60	37

3.4 Electrical data

The electrode control system continuously logged the electrical parameters of the furnace including the harmonic distortions. The individual harmonic values up to the 15th harmonic along with the THD value of the current were logged for each second for each individual phase together with a mean value for all three phases.

4. Results

Figure 3 shows the average of the total harmonic distortion during the meltdown of the first basket as an average of all the heats. The average THD is decreasing slightly during the main melting period, where the tap position is highest. More precisely, it changes from a value of around 6.6 % at 280 seconds of melting to a value of 6.1 % after 670 seconds of melting. However, this decrease is very close to the variation within this period. As it is seen that there is a peak of 6.8 % at 590 seconds of melting.
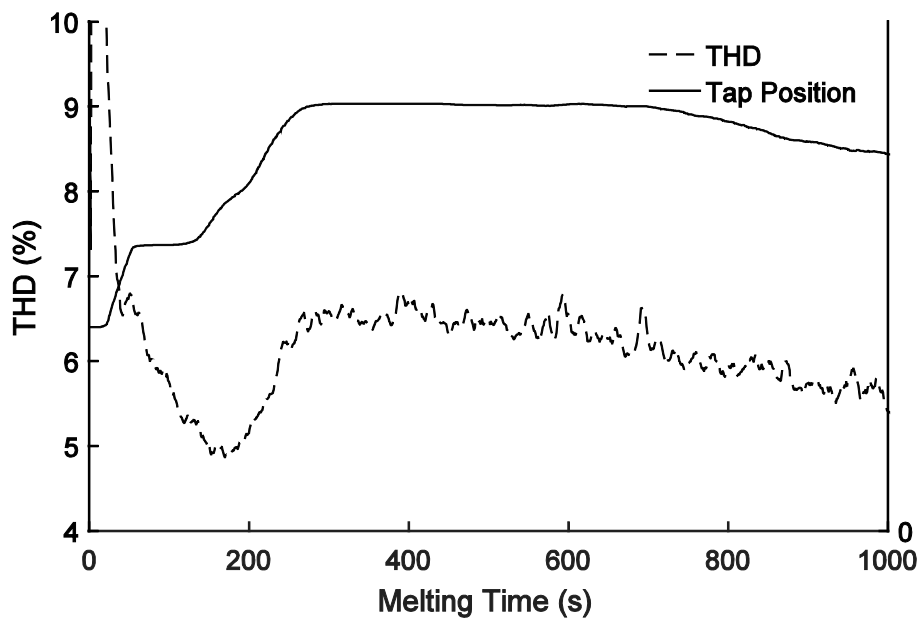
Figure 3. THD over time for the meltdown of the first scrap basket. An average of the 10 seconds back tracking average of all heats.
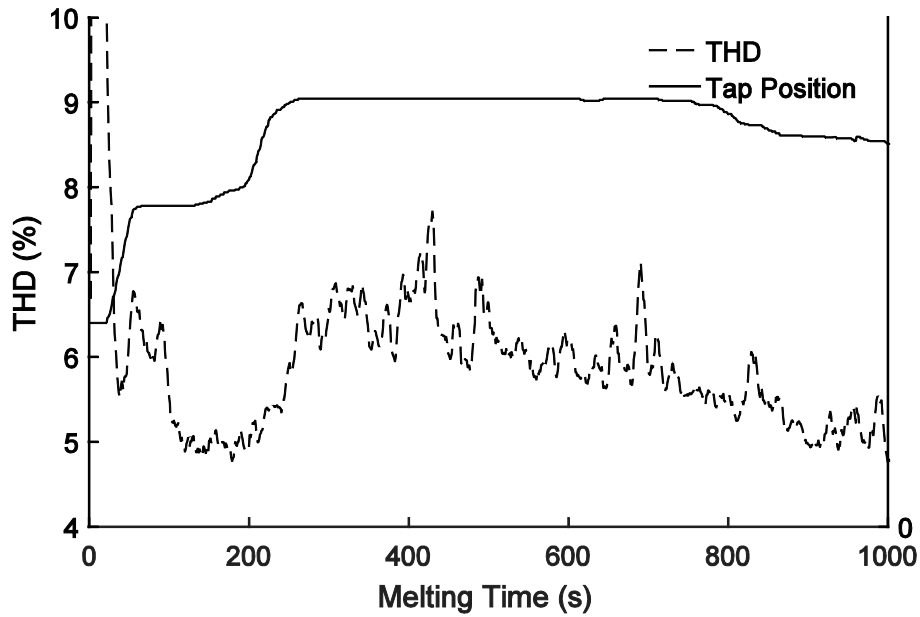
Figure 4. THD over time for the meltdown of the first scrap basket. An average of the 10 seconds back tracking average of all heats classified as scrap level one.

As there is a general decrease when looking at all heats, it is interesting to look at the average THD meltdown when looking at only the lowest scrap level. In figure 4 the decrease of the THD level over the main melting period is larger than in figure 3: More precisely, the THD decreases from a level of 6.8 % at 310 seconds to a value of 5.5 after 750 seconds. Additionally, it can be seen that the variation is higher. The maximum average THD value is 7.7 % and the lowest 5.5 % during the main meltdown period.

As the THD value consists of several individual harmonics, it is vital to look into the separate harmonics as well. There is a clear difference in how the individual harmonics develop over time, from the main meltdown period to a flat bath period. When comparing the individual harmonics during the course of a meltdown it was shown that the 2nd and 3rd harmonic have high variation due to disturbances while the 5th harmonic was more stable [14]. In figure 5 the individual development of these three harmonics are shown during the meltdown in the EAF.

Figure 5. Individual harmonic distortion for the 2nd, 3rd and 5th harmonics over time for the meltdown of the first scrap basket. 10 seconds backtracking average.

During the main meltdown period between 300 and 700 seconds it is seen that the 2nd harmonic decrease around 0.2 %. Additionally, the 3rd harmonic decrease roughly 0.3 %. Meanwhile, the 5th harmonic does not decrease. Furthermore, during the latter part of the meltdown, after 850 seconds the 2nd and 3rd harmonic has a lower value than the 5th harmonic. Note that he only time that the 5th harmonic changes is during the boredown. Hence, it seems like it changes when the furnace power changes. Contradictory, it does not decrease during the step down. However, the changes in power during the step down is not as large as during the boredown. Building on the observations in figure 5 and the difference observed earlier when comparing the THD progression for scrap level one with the average THD progression it is interesting to compare the scrap levels. Hence, the development of these harmonics for the different scrap levels and the intersection of the 2nd and 3rd harmonic with the 5th harmonic is shown in figure 6, 7 and 8.
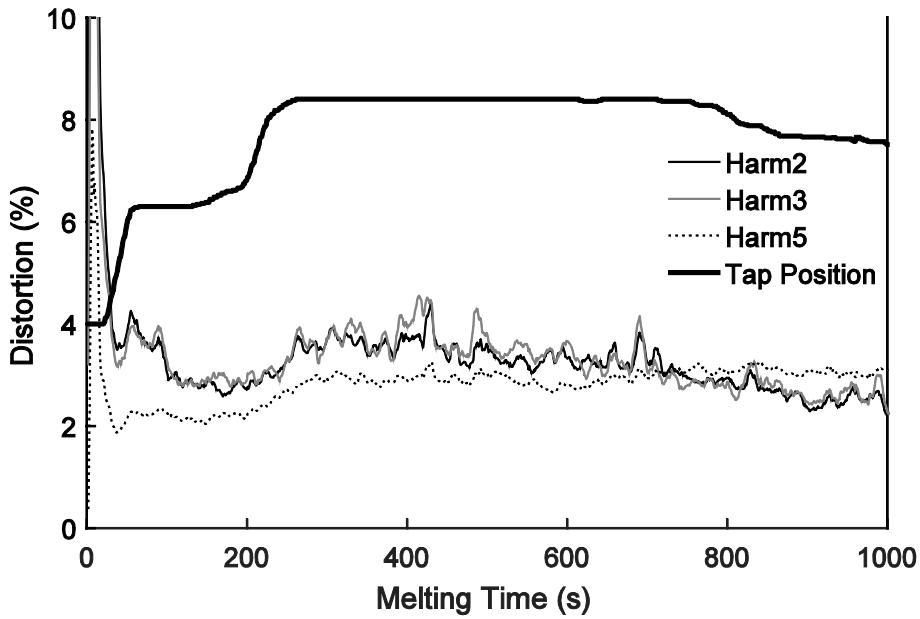
Figure 6. Individual harmonic distortion for the 2nd, 3rd and 5th harmonics over time for the meltdown of the first scrap basket as an average for all heats classified as scrap level one. 10 seconds backtracking average.

In figure 6 the three harmonics are shown for scrap level one. Here, the decrease of the 2nd and 3rd harmonic is 0.6 % and 1 % and the intersection between the 2nd and 3rd harmonic and the 5th harmonic occurs after 750 seconds. Additionally, compared to the average for all heats, the intersection occur before the stepdown process has started.
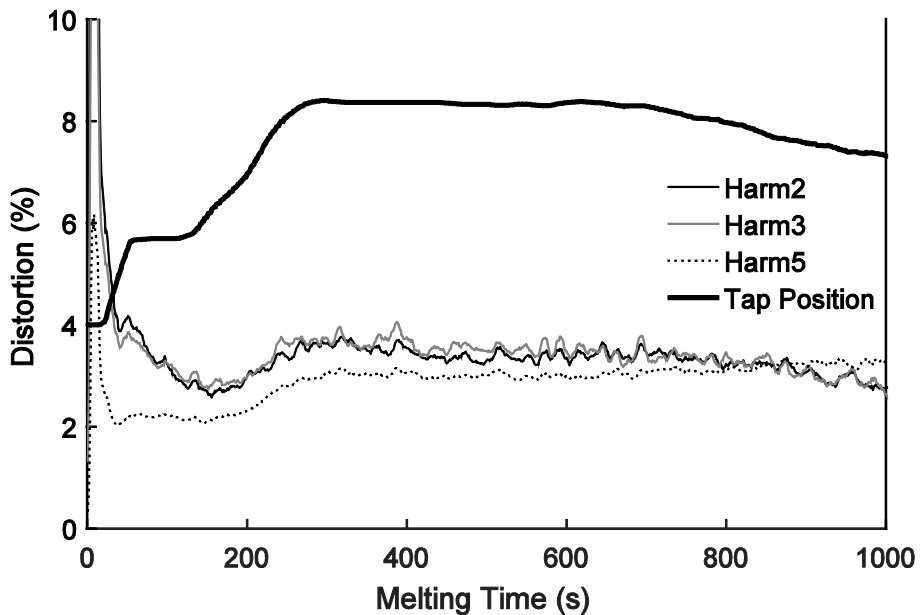
Figure 7. Individual harmonic distortion for the 2nd, 3rd and 5th harmonics over time for the meltdown of the first scrap basket as an average for all heats classified as scrap level two. 10 seconds backtracking average.

Figure 7 shows the same graph but for scrap level two. Here, the decrease is 0.3 % for the 2nd harmonic, 0.6 % for the 3rd harmonic and the intersection between the harmonics are at 860 seconds. Additionally, the intersection occurs after the step down process has begun. Figure 8 shows the highest scrap level, scrap level three.

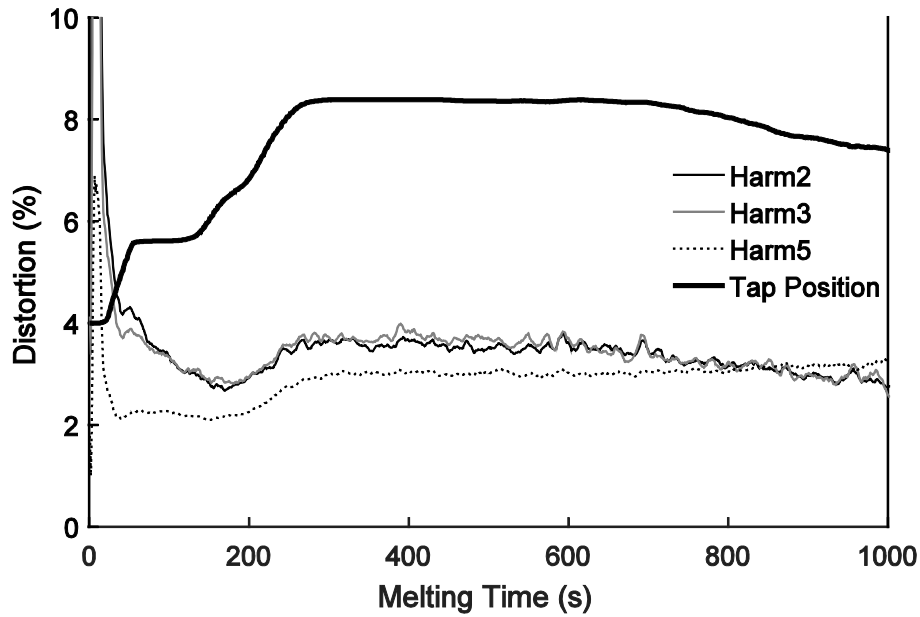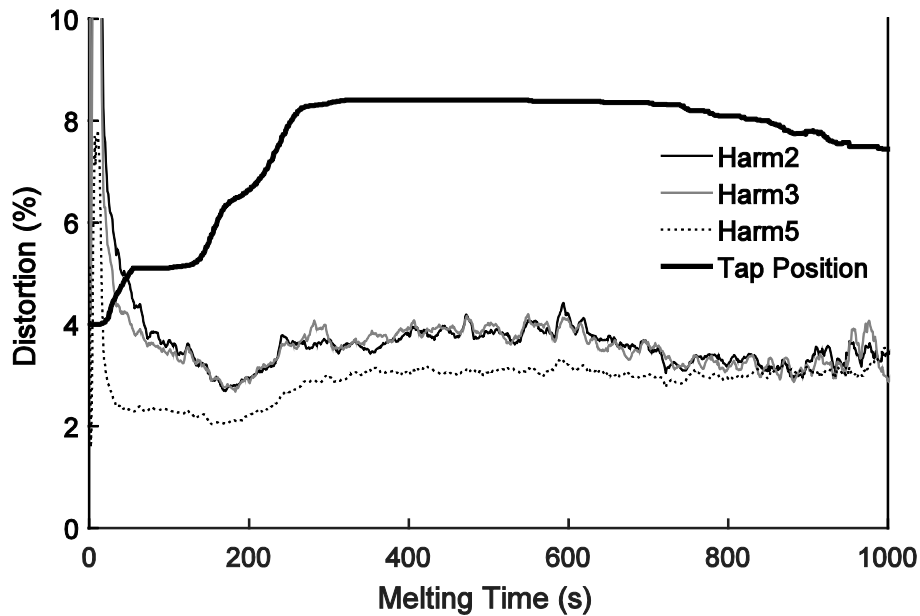**Figure 8.** Individual harmonic distortion for the 2nd, 3rd and 5th harmonics over time for the meltdown of the first scrap basket as an average for all heats classified as scrap level three. 10 seconds backtracking average.

Here, there is no distinct decrease for the 2nd and 3rd harmonic during the main meltdown period and the intersection between the three harmonics does not occur during main meltdown period. Actually, as the 2nd and 3rd harmonic increases after the initial intersection at 860 seconds of melting, it is not clear that it occurs at all. The results for the different scrap levels is summarised in table 2.

Table 2. The decrease of the 2nd and 3rd harmonic over the cause of the main meltdown period for all scrap levels. The intersection of the 2nd and 3rd harmonic with the 5th harmonic.

	Decrease 2nd	Decrease 3rd	Intersection
Scrap level one	0.6 %	1 %	750 s
Scrap level two	0.3 %	0.6 %	860 s (Stepdown)
Scrap level three	0.1 %	0.1 %	880 s (Stepdown)

5. Discussion

In figure 3, there is a hint that the total harmonic distortion decreases when considering all heats independent of the tap position. However, when looking only at the lowest scrap level the decrease was larger. For scrap level one, there was a decrease of 1 % of the THD between the start of the meltdown period and the start of the step down period, while the average

decrease was 0.5 % when considering all scrap classes. Additionally, it decreased to a lower absolute value. This shows that the THD is lower when the scrap level is lower. Additionally, this shows that a higher decrease can be connected to a lower scrap level inside the furnace.

That the THD decrease with increasing melting time and lower scrap level can be used for process control. Though, the decrease is close to the range of which the THD vary over the cause of a meltdown. Hence, as a deciding tool it will cause a lot of false alarms. As the individual harmonics show to decrease differently over the cause of the meltdown they can instead be used as decision tools. It is shown that the 2nd and 3rd harmonics decrease over the cause of the meltdown while the 5th harmonic stays stable and only change during the initial boredown period. Table 2 summarises the differences between the three scrap levels, and it is clear that the decrease for the 2nd and 3rd harmonic is largest for the lowest scrap level. Furthermore, for the highest scrap level, scrap level three, there is almost no decrease at all. Along with that, the intersection between the 2nd and 3rd with the 5th harmonic happens earlier in the meltdown process for scrap level one.

If the 5th harmonic value is referred to as an outcome of the power setting and the furnaces general conditions the 2nd and 3rd can be used as a progress of the meltdown in the individual heat. Then, the intersection of the 2nd and 3rd harmonic with the 5th harmonic can be used as an indication of the meltdown progress. Hence, knowing the point of the intersection gives vital information of the time needed for further melting operations. As the meltdown time after this point before power-off is longer for scrap level one, the perceived scrap level is consequently lower.

The meltdown procedure and harmonic distortion development is not the same for all furnace environments. Hence, when designing a decision system it might not be that the intersection between the individual harmonics might not always occur, or it might occur to early or to late depending on the furnace volume and scrap basket burden. A set value could be used instead of the 5th harmonic value. However, such a value would not be dynamic or related to the furnace power. However, it could be a function of furnace power. Nonetheless, such value would require careful design. While, the 5th harmonic value is instantly available and in relation to the other harmonics.

6. Conclusions

In this work, the harmonic distortion progress have been evaluated over the cause of the first basket meltdown in a 90 tonnes EAF. Both the overall THD and the progress of individual harmonics have been compared between three levels of scrap meltdown. In general the harmonic distortion decreases with increasing meltdown time.

These specific observations were made during the work:

- The harmonic distortion decrease was larger and reached lower levels when the observed scrap level after power-off was lower.

- The 2nd and 3rd harmonics decrease over the cause of the meltdown while the 5th harmonic is stable.

- The intersection of the 2nd and 3rd harmonics with the 5th harmonic can be used as an indication of the scrap meltdown progress.

- This intersection occurred earlier in the meltdown process in the cases where the scrap level was lower after power-off.

Overall it is believed that the decrease of the 2nd and 3rd harmonic can be used as an indication of the scrap meltdown progress. If not compared to the 5th harmonic a set level can be used.

Acknowledgement

References

1) A. I. Toma, G. N. Popa, A. Iag, and S. I. Deaconu, "Experimental analysis of electric parameters of a 100 t UHP electric arc furnace," in *Industrial Technology (ICIT), 2010 IEEE International Conference on*, (2010), pp. 919-924.

2) I. Vervenne, K. Van Reusel, and R. Belmans, "Electric arc furnace modelling from a "power quality" point of view," in *2007 9th International Conference on Electrical Power Quality and Utilisation*, (2007), pp. 1-6.

3) L. Cividino, "Power factor, harmonic distortion; causes, effects and considerations," in *Telecommunications Energy Conference, 1992. INTELEC'92., 14th International*, (1992), pp. 506-513.

4) I. F II, "IEEE recommended practices and requirements for harmonic control in electrical power systems," (1993).

5) Y. Hase, "Waveform Distortion and Lower Order Harmonic Resonance," in *Handbook of Power Systems Engineering with Power Electronics Applications*, ed: John Wiley & Sons, Ltd, (2012), pp. 531-540.

6) R. G. Ellis and P. Eng, "Power system harmonics–a reference guide to causes, effects and corrective measures," *An Allen-Brandley Series of Issues and Answers-Rockwell Automation*, (2001), p. 3.

7) D. Sajeesh and S. Jadhav, "Research on Power Quality Issues in Electric Arc Furnace and Its Mitigation Techniques," in *International Journal of Engineering Research and Technology*, (2014).

8) Y.-J. Liu, G. W. Chang, and R.-C. Hong, "Curve-fitting-based method for modeling voltage–current characteristic of an ac electric arc furnace," *Electric Power Systems Research,* 80 (2010), pp. 572-581.

9) G. Chang, Y. Liu, and C. Chen, "Modeling voltage-current characteristics of an electric arc furnace based on actual recorded data: A comparison of classic and advanced models," in *Power and Energy Society General Meeting-Conversion and Delivery of Electrical Energy in the 21st Century, 2008 IEEE*, (2008), pp. 1-6.

10) G. W. Chang, C.-I. Chen, and Y.-J. Liu, "A neural-network-based method of modeling electric arc furnace load for power engineering study," *IEEE Transactions on Power Systems,* 25 (2010) , pp. 138-146.

11) M. Blachnik, T. Wieczorek, K. Mączka, and G. Kopeć, "Identification of liquid state of scrap in electric arc furnace by the use of computational intelligence methods," in *International Conference on Neural Information Processing*, (2010), pp. 700-707.

12) B. Dittmer, K. Krüger, D. Rieger, S. Leadbetter, T. Matschullat, and A. Doebbeler, "Process state detection of electric arc furnaces by structure-borne sound evaluation," *Stahl und eisen,* 129 (2009) , pp. 33-41.

13) C. N. Schmidt, N. Å. I. Andersson, P. Jönsson, A. Tilliander, and P. Ljungqvist, "Measurement techniques for meltdown control in a stainless steel AC electric arc furnace," in *ESSC & DUPLEX 2017*, Bergamo, (2017).

14)   S. Mendis and D. Gonzalez, "Harmonic and transient overvoltage analyses in arc furnace power systems," *IEEE Transactions on Industry Applications,* 28 (1992) , pp. 336-342.

Direct Alloying Steel with Chromium by Carbothermic Reduction of Chromite Ore and FeO$_x$

Xianfeng Hu[1], Lena Sundqvist Ökvist[1,2], Johan Eriksson[1], Qixing Yang[2] and Bo Björkman[2]

[1] Process Metallurgy Department, Swerea MEFOS AB, PO Box 812, SE-971 25, Luleå, Sweden

[2] Department of Civil, Environmental and Natural Resources Engineering, Luleå University of Technology, SE-971 87, Luleå, Sweden

Keywords: carbothermic reduction, chromite ore, direct alloying

Abstract: Direct chromium alloying by chromite ore is promising technology for producing Cr-containing steels. This paper presents a series of stepwise studies, in which the effect of FeO$_x$ addition on the carbothermic reduction of chromite ore was investigated. The results from the thermogravimetric experiments show that iron powder and mill scale significantly enhance the carbothermic reduction of synthetic chromite (FeCr$_2$O$_4$) and chromite ore, respectively. The enhancing effect can be attributed to the dissolution of the reduced chromium into the added iron or the formed iron, which decreases the activity of chromium. The effect of using the designed alloying briquettes made from 'chromite ore + mill scale + petroleum coke' has been tested in the induction furnace trials. The results show that the yield of chromium from chromite ore is higher when the amount of mill scale addition in the designed alloying briquettes is higher. The obtained results have led to the proposal of using chromite ore, FeO$_x$ and carbonaceous material as an alloying mixture to directly alloy steel with chromium. The use of the designed alloying mixture to directly alloy steel with chromium can potentially improve the raw material efficiency and energy efficiency.

1. Introduction

Chromium is an important alloying element, which is used in many types of steels with chromium contents ranging from 0.1 wt.% to 30 wt.%. If the entire value chains are considered, the production of Cr-containing steels can be in general considered as two sequential steps: i) ferrochrome production by smelting reduction of chromite ore in the submerged arc furnace (SAF); ii) steel alloying with chromium by charging steel scrap and ferrochrome into the melting furnace, such as the electric arc furnace (EAF). Ferrochrome production *via* step i) is an energy-intensive process with specific energy consumption being 3.5-4.0 MWh/tonne of ferrochrome[1] and the chromium yield from such a process is typically 80-85%.[2] To improve the overall energy/cost-efficiency it would be promising if the ferrochrome production process and the alloying process can be integrated into a single step. This idea, known as direct chromium alloying by smelting reduction of chromite ore in the converter, has been tested since 1990s by directly charging chromite ore powder or pellets into the hot metal together with coke/coal and oxygen injection, during which chromite ore can be reduced into chromium substantially by smelting reduction and the steel can be directly alloyed with chromium.[3]–[6] The pilot trials carried out by different researchers showed that the Cr yield can reach 70-100 wt.%,[3, 5] which is comparable or even higher than that from the ferrochrome production process in the SAF. The integration of the step i) and step ii) indicates energy-saving, as the energy that would otherwise be required to melt ferrochrome can be potentially saved; further the high chromium yield also indicates improved raw materials efficiency. This proposed direct chromium alloying process is

preferably to be connected to the pig iron melt production process as high carbon content in the hot metal is a prerequisite for the reduction of chromite ore with high chromium yield; further the high carbon content in the produced crude steel melt inevitably becomes a burden for the downstream decarburization process.

The purpose of this paper is to present the results from a series of stepwise studies on the carbothermic reduction of chromite ore and FeOx (iron powder, mill scale and magnetite) and to explore the potential of using a mixture of 'chromite ore + FeOx + carbonaceous material' to directly alloy steel with chromium. The newly proposed direct alloying process can potentially be applied to produce Cr-containing steels and it may work as a supplement of the earlier proposed direct chromium alloying process.

2. The effect of iron on the carbothermic reduction of chromite

2.1 The effect of iron in the chromite ore on the carbothermic reduction of chromite

Chromite ore is an oxide mineral with spinel structure and in general it can be expressed as $[Mg^{2+},Fe^{2+}](Cr^{2+},Al^{3+},Fe^{3+})_2O_4$. The chromium to iron ratio is an important index to characterize the chromite ore and the ratio varies from one type of the ore to another. For metallurgical applications the Cr/Fe ratio is approximately in the range 1.5-3.0.

When chromite ore is subjected to solid-state carbothermic reduction, iron in the chromite is reduced first then chromium being reduced due to the fact that iron is more readily reduced than chromium. The nascent iron formed during the reduction will pick up some carbon due to the *in situ* dissolution of carbon into the iron. The formed iron in the initial stage of the reduction is believed to have a significant enhancing effect on the following-up reduction of chromium, as the formed iron will dissolve the reduced chromium and thus reduce the activity of the reduced chromium; this enhancing effect is further enhanced due to the dissolution of carbon, which further decreases the activity of the reduced chromium. This principle may be well documented by the other researchers who investigated the reduction of chromite ore with different Cr/Fe ratios and found that the ore with lower Cr/Fe ratio can be reduced much easier, as shown in **Figure 1**.
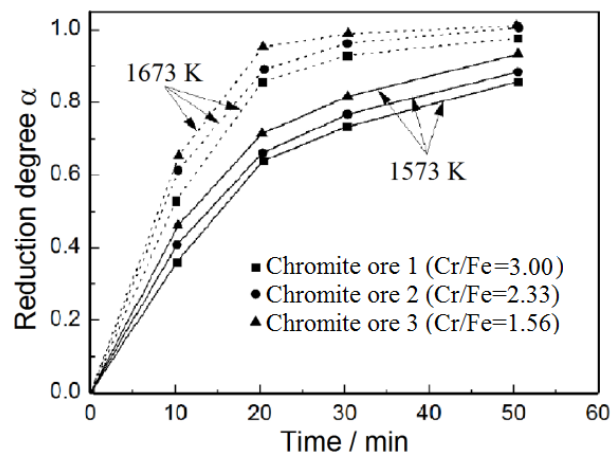
Figure 1. Carbothermic reduction of three types of chromite ore with different Cr/Fe mass ratios.[7]

2.2 The effect of iron addition on the carbothermic reduction of chromite

Figure 2 shows the effect of iron powder addition on the carbothermic reduction of chromite ore. [8] It is seen that the added iron powder significantly enhance the carbothermic reduction of chromite ore and this enhancing effect is improved with increasing amount of iron powder addition. The results may confirm that the externally added iron can work as the

same of the iron from the chromite ore regarding to enhancing the carbothermic reduction of chromite by decreasing the activity of the reduced chromium.
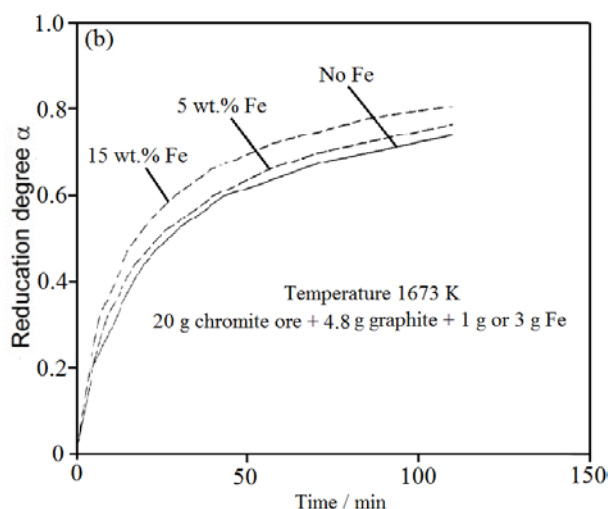
Figure 2. The effect of iron powder addition on the carbothermic reduction of chromite ore.[8]

3. Stepwise studies

3.1 Carbothermic reduction of synthetic $FeCr_2O_4$ with various amount of iron powder addition[9]

As described in the foregoing section the effect of iron on the carbothermic reduction of chromite ore can be attributed to the dissolution of the reduced chromium into the iron and thus decreasing the activity of chromium. To confirm this and clarify the reduction mechanism thermogravimetric experiments on the reduction of synthetic $FeCr_2O_4$ by graphite with various amounts of iron powder addition were carried out. The results, as shown in **Figure 3**, clearly indicate that the iron in the $FeCr_2O_4$-graphite mixture enhances the reduction of $FeCr_2O_4$ and the enhancing effect increases when increased amounts of iron powder (up to 80 wt.%) are added. The XRD analysis of the samples with different amounts of iron powder addition and with various reduction degrees are shown in **Figure 4**. The results show that the carbothermic reduction of $FeCr_2O_4$ without iron powder addition proceeds *via* two steps, *i.e.*, the reduction of FeO species followed by the reduction of Cr_2O_3 species in the $FeCr_2O_4$, as Cr_2O_3 appears as an intermediate phase during the reduction. However, it seems that the carbothermic reduction of $FeCr_2O_4$ with 80 wt.% proceeds only *via* one step and the reduction product is Fe-Cr-C alloy. **Figure 5** shows the selected diffraction peaks for graphite, Fe-Cr-C ally and mixed carbide, $(Cr,Fe)_7C_3$. For Fe-Cr-C alloy it is seen that the diffraction peaks shift slightly towards a low (2θ) diffraction angle as the reduction proceeds. This is due to the interstitial dissolution of carbon and substitutional dissolution of chromium in the iron, both of which increase the lattice parameter of the alloy phases. For the mixed carbide, $(Cr,Fe)_7C_3$, it is seen that the diffraction peaks also shift towards a low (2θ) diffraction angle as the reduction proceeds. This is due to the substitutional dissolution of chromium into $(Cr,Fe)_7C_3$.

In summary, the experimental results from this study shows that: (i) the iron can enhance the carbothermic reduction of $FeCr_2O_4$; (ii) the iron addition has changed the carbothermic reduction mechanism of $FeCr_2O_4$ and the reduction of $FeCr_2O_4$ with up to 80 wt.% iron powder addition is likely to be a one-step process; (iii) during the reduction the chromium directly dissolved in the formed iron (or Fe-C) ally and/or formed mixed carbide, $(Cr,Fe)_7C_3$, which thus decrease the activity of the chromium and enhance the reduction process.
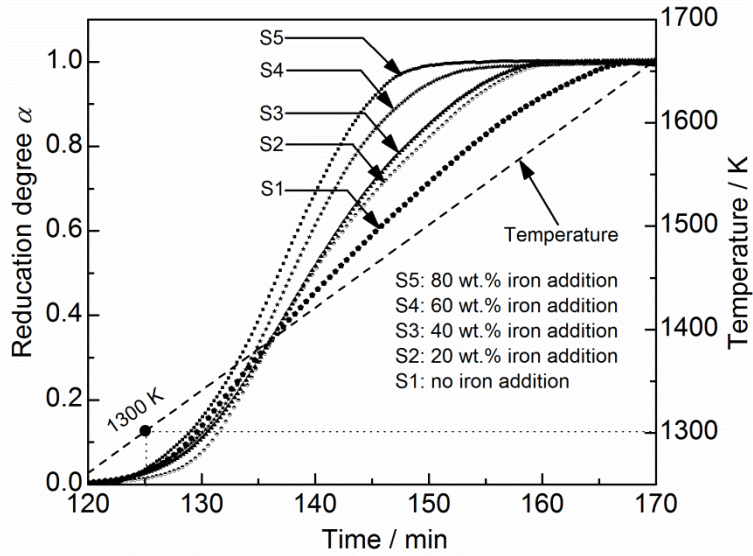
Figure 3. Non-isothermal reduction of synthetic $FeCr_2O_4$ by graphite with various amounts of iron powder addition.
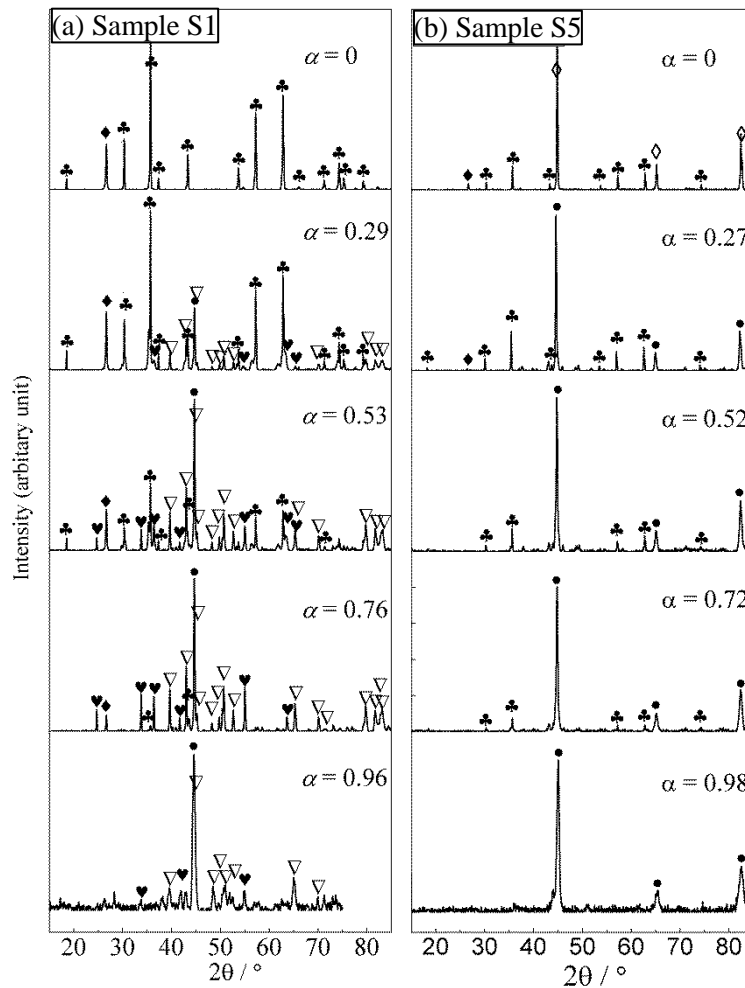
Figure 4. XRD patterns of the samples with different amounts of iron powder addition and with various reduction degrees α: (a) sample S1 (no iron addition) and (b) sample S5 (80 wt.% iron addition) [♣-$FeCr_2O_4$; ♦-graphite; ♥-Cr_2O_3; ◊-Fe; ●-Fe-Cr-C alloy; ∇-$(Cr,Fe)_7C_3$].
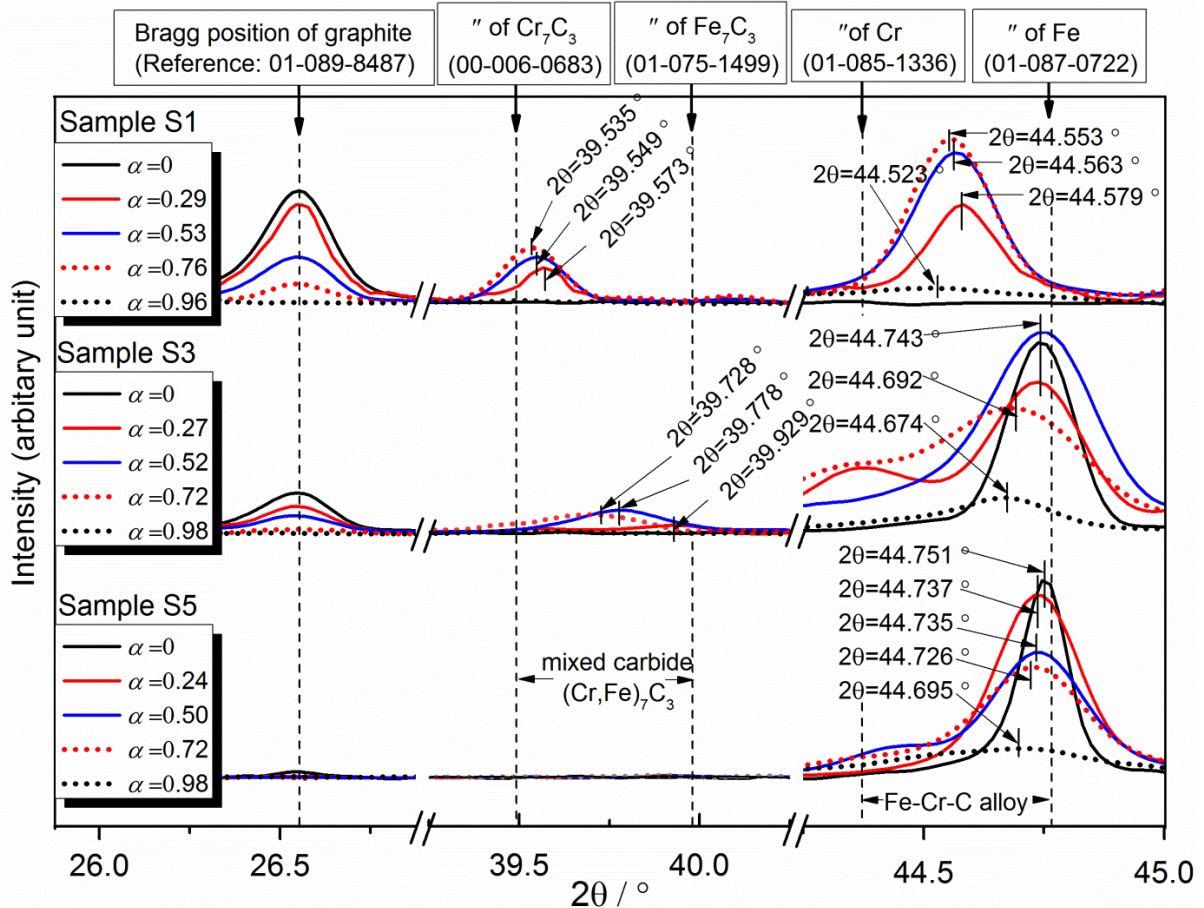
Figure 5. Selected diffraction peaks of graphite, $(Cr,Fe)_7C_3$ and Fe-Cr-C alloy for sample S1 (no iron addition), sample S3 (40 wt.% iron addition) and sample S5 (80 wt.% iron addition) at different reduction degree α.

3.2 Carbothermic reduction of a mixture of chromite ore and mill scale[10]

According to the above findings it is believed that a mixture of chromite ore, iron-containing species and carbonaceous material can be potentially used as a direct alloying mixture. It is well aware that it is expensive to use iron powder in the industrial process, therefore mill scale (a by-product from the hot metalworking processes, containing mainly FeO_x) is selected. To confirm that mill scale has the same effect as the added iron powder regarding to enhancing the carbothermic reduction of chromite, thermogravimetric experiments on the reduction of chromite ore by petroleum coke with various amounts of mill scale addition were carried out. **Figure 6** shows the effect of mill scale addition on the reduction of chromite ore. It is seen that the reduction of chromite ore with higher amount of mill scale addition leads to larger reduction degree at lower temperatures and in shorter time. **Figure 7** shows the XRD analysis of the samples with different amounts of mill scale addition and at different reduction temperatures. The results show that mill scale is reduced to iron first and then chromite ore being reduced. Therefore the enhancing effect of mill scale addition on the carbothermic reduction of chromite ore can be attributed to the presence of reduced iron, which dissolves the reduced chromium and thus decrease the activity of the chromium. This is consistent to the results shown earlier.

The experimental results from this study lead to the proposal of using 'chromite ore + mill scale + petroleum coke' as an alloying precursor to directly alloy steel with chromium. To

confirm the effectiveness of the designed alloying precursor, induction furnace trials in various scales have been carried out in the following studies.
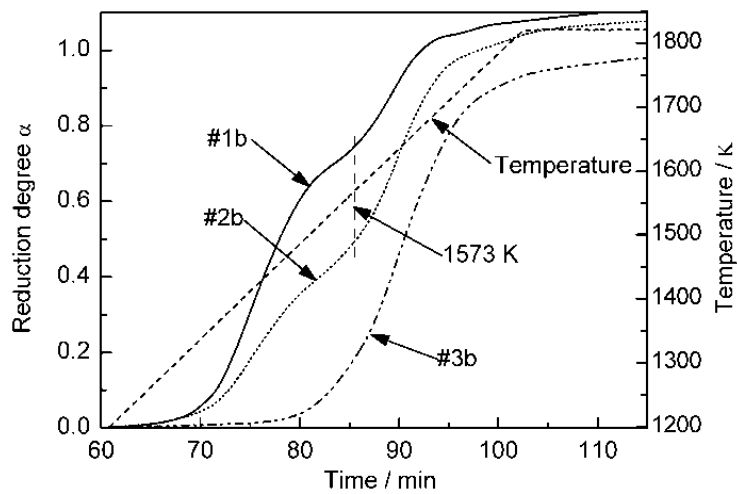
Figure 6. Non-isothermal reduction of chromite ore by petroleum coke with various amounts of mill scale addition.
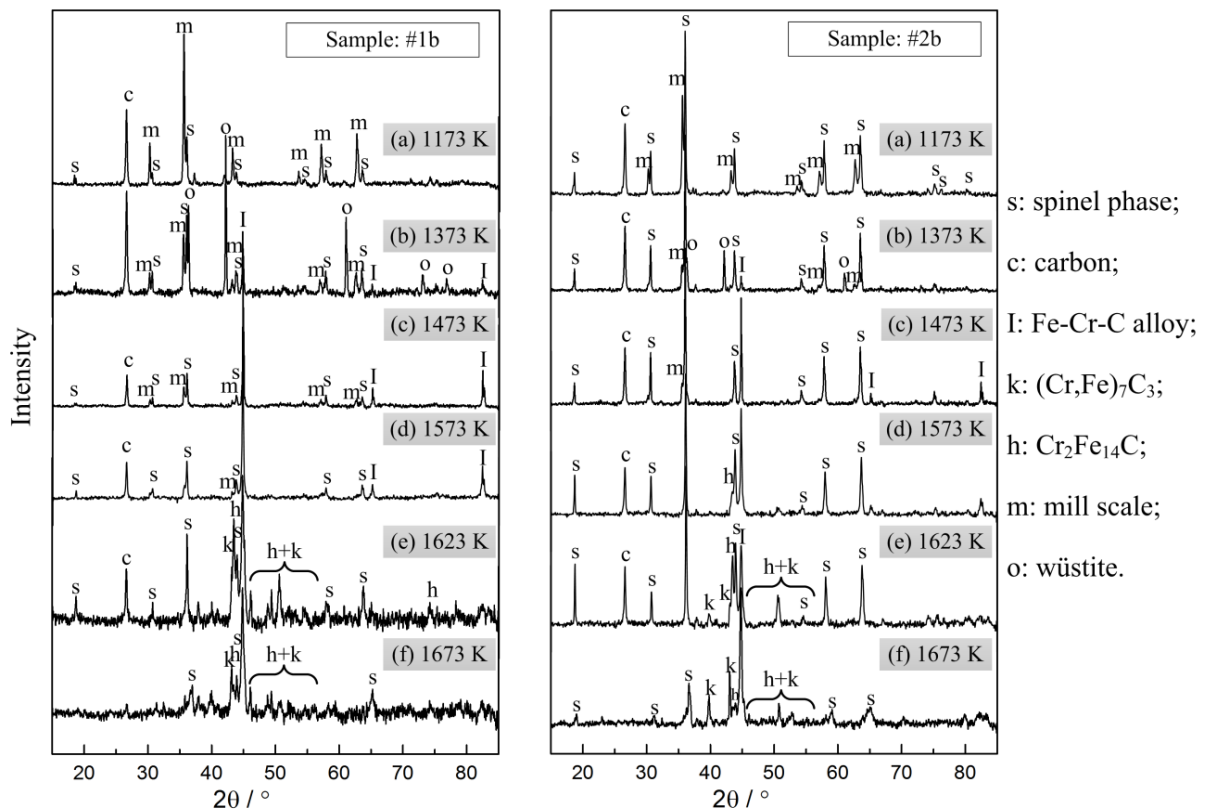
Figure 7. XRD analyses of the fractional reduced samples (#1b and #2b) cooled down from (a) 1173 K, (b) 1373 K, (c) 1473 K, (d) 1573 K, (e) 1623 K and (f) 1673 K.

3.3   Induction furnace trials[11]

The induction furnace trials were carried out in three scales, namely, single-piece-briquette trials (around 200 grams), 7 kg-scale trials and 80 kg-scale trials. The chromite ore, mill scale and petroleum coke were milled into powders and made into different briquettes with Cr to

233

Fe mass ratios being 0.05, 0.10 and 0.20 in the C1 briquette, C2 briquettes and C3 briquettes, respectively. During the trials, certain amount of the briquettes and steel scrap were charged into the induction furnace together with slag-formation materials, as shown in **Table 1**. The materials in the induction furnace were heated to1823-1873 K and then the final metal samples and slag samples were obtained and chemically analyzed. By considering the mass balance of chromium in the metal samples and in the slag samples, the Cr yield as a function of Cr/(Cr + Fe) mass ratio can be plotted, as shown in **Figure 8**. It is seen that the Cr yield from the briquettes increases with the decrease in Cr/(Cr+Fe) in the briquettes. In other words, the more mill scale added to the briquettes, the higher the Cr yield. The Cr yield can be up to 99.9% when the ratio of Cr to (Cr+Fe) in the briquettes is 0.05, and up to 93.0% when the ratio is 0.10. However, when the ratio of Cr to (Cr+Fe) in the briquettes reaches 0.20, the Cr yield can only be 67.1%.

Table 1. The materials used in various types of induction furnace trials (the mass ratios of Cr to Fe in the C1 briquettes, C2 briquettes and C3 briquettes are 0.05, 0.10 and 0.2, respectively).

Trial type	Briquettes		Steel scrap /kg	Slag-forming materials /kg		
	ID	Mass /kg		Calcium aluminate	Lime	Silversand
Single-piece-briquette trials	C1	0.17	-	-	-	-
	C2	0.22	-	-	-	-
	C3	0.18	-	-	-	-
7-kg-scale trials	C1	2.30	4.60	0.06	0.03	-
	C2	2.31	4.60	0.12	0.36	0.24
	C3	2.30	4.60	0.04	0.15	0.08
80-kg-scale trials	C2	20.2	60.0	0.39	1.27	0.72
	C3	20.2	60.0	1.00	3.14	2.11
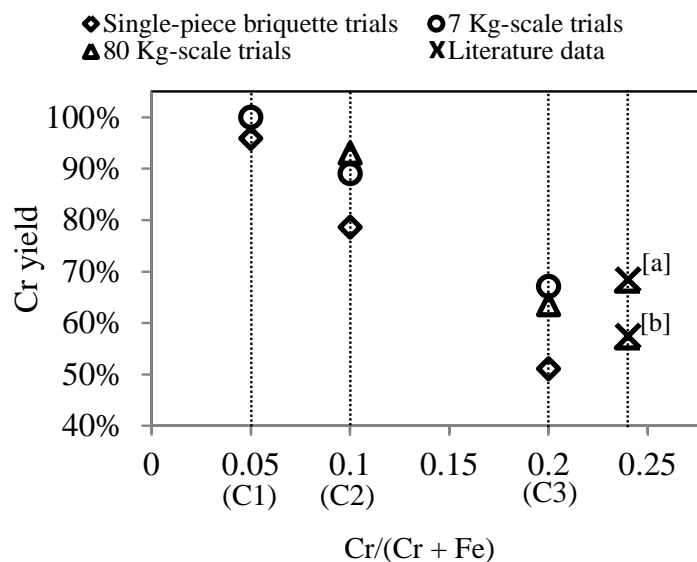
Figure 8. The dependence of Cr yield as a function of Cr/(Cr + Fe) mass ratio in the alloying briquettes. (The derived literature data are based on smelting reduction of a mixture of mill scale, low-grade chromite ore and 1.1 times stoichiometric amount of carbon (point [a] for coke and point [b] for graphite) in a 5-kg-scale SAF[12]).

During the direct alloying process by using the designed alloying briquettes chromium is reduced from the chromite ore in the briquettes, the unreduced chromium is left in the slag in the form of oxide. The high yield of chromium from carbothermic reduction of chromite ore

in the direct alloying process can be attributed to the enhancing effect of mill scale, or the reduced iron from mill scale, which decreases the activity of the reduced chromium. These results and explanation may be well documented by the experimental results shown in foregoing studies.

4. Outlook

According to the experimental findings it is believed that the designed alloying mixture 'chromite ore + mill scale + carbonaceous material (such as petroleum coke and coal)' can be potentially used to produce Cr low-alloyed or micro-alloyed steels (Cr <1 wt.%) by directly charging the alloying precursor into the EAF in the form of mixture or briquettes/pellets. In this case the ratio of the charged alloying precursor to the charged steel scrap should be controlled to an acceptable value, which will not disturb a normal EAF operation. Further, it is believed that the designed alloying precursor can also be feasible to alloy steels with 1-10 wt.% Cr. However, in this case an external pre-heating and pre-reduction process are favorable to be applied in connection with the EAF process. The application of this designed alloying precursor has the potential to improve the raw material efficiency and energy efficiency, as high chromium yield from chromite ore can be expected and the new proposed process has high integration.

5. Conclusions

This paper presents the results from a series of stepwise studies, which have led to the proposal of using chromite ore, FeO_x and carbonaceous material as an alloying mixture to directly alloy steel with chromium. The conclusions can be drawn as follows:

(i) Iron powder can enhance the carbothermic reduction of $FeCr_2O_4$ and the enhancing effect increases when increased amounts of iron powder (up to 80 wt.%) are added; during the reduction the chromium directly dissolves in the formed iron (or Fe-C) alloy and/or formed mixed carbide, $(Cr,Fe)_7C_3$.

(ii) When mill scale is reduced together with chromite ore by petroleum coke, mill scale is reduced first and then chromite ore being reduced. The mill scale can enhance the carbothermic reduction of chromite ore.

(iii) The enhancing effect from (i) and (ii) can be attributed to the dissolution of the reduced chromium into the added iron or the formed iron, which decreases the activity of chromium.

(iv) According to the results from the induction furnace trials the yield of chromium from chromite ore increases with the decrease in Cr/(Cr+Fe) mass ratio, or, in other words, increases with the increase in the amount of mill scale addition in the designed direct alloying briquettes.

References:

1) M. J. Niayesh and G. W. Fletcher, An assessment of smelting reduction processes in the production of Fe–Cr–C alloys, in *INFACON 4*, 1986, pp. 115–123.

2) C. N. Harman and N. S. S. R. Rao, A process for the recovery of chromium and iron oxide in high carbon ferro chrome slag to obtain chromium and iron in the form of saleable metal, in *INFACON 13*, 2013, pp. 103–108.

3) S. Takeuchi, H. Nakamura, T. Sakuraya, T. Fujii, and T. Nozaki, Pilot Plant Experiment of Smelting Reduction Using Fine Chromium Ore," *J. Iron Steel Inst. Japan*, vol. 76 (1990), pp. 1847–1854.

4) T. Takaoka, Y. Kikuchi and Y. Kawai, Fundamental Study on Rapid Reduction of Chromium Ore in Basic Oxygen Furnace, *J. Iron Steel Inst. Japan*, vol. 76 (1990), pp. 1839–1846.

5) C. Treadgold, *The production of stainless steel through smelting reduction of chrome ores using coal and oxygen*, British Steel, Teesside Technology Centre, 1990.

6) J. P. Hoffman, Oxygen-coal in-bath smelting reduction-a future process for the production of iron and stainless steel? *J. S. Afr. Inst. Min. Metall.*, vol. 92 (1992), pp. 253-273.

7) H.G. Vazarlis and A. Lekatou, Pelletising-Sintering, prereduction, and smelting of Greek chromite ores and concentrates, *Ironmak. Steelmak.*, vol. 20 (1993),pp. 42–53.

8) J. VAN Deventer, The Effect of Additives on the Reduction of Chromite by Graphite: an Isothermal Kinetic Study, *Thermochim. Acta*, vol. 127 (1988), pp. 25–35.

9) X. Hu, L. Teng, H. Wang, L. Sundqvist Ökvist, Q. Yang, B. Björkman and S. Seetharaman, Carbothermic Reduction of Synthetic Chromite with/without the addition of Iron Powder, *Isij Int.*, vol. 56 (2016), pp. 2147-2155.

10) X. Hu, Q. Yang, L. Sundqvist Ökvist and B. Björkman, Thermal Analysis Study on the Carbothermic Reduction of Chromite Ore with the Addition of Mill Scale, *Steel Res. Int.*, vol. 87 (2016), pp. 562–570.

11) X. Hu, L. Sundqvist Ökvist, J. Eriksson, Q. Yang and B. Björkman, Direct alloying steel with chromium by briquettes made from chromite ore, mill scale and petroleum coke, *Steel Res. Int.*, vol. 87 (2016).

12) A. Ahmed, M. K. El-Fawakhry, M. Eissa and S. Shahein, Direct chromium alloying by smelting reduction of mill scale and low grade chromite ore, *Ironmak. Steelmak.*, vol. 42 (2015), pp. 648–655.

Experimental and numerical modelling of multiphase flows in continuous casting reactors

Antje Rückert, Tim Haas and Herbert Pfeifer
Department for Industrial Furnaces and Heat Engineering, RWTH Aachen University,
Aachen Germany

Multiphase flows play a major role in metallurgical reactors, e.g. non-metallic inclusions in tundish and mold as well as the gas plume in a ladle and the spray cooling of the strand. Inclusions hinder the metal forming process and lead often to fatigue. The cleanliness of steel is important to fulfill the customer's requirements. The gas plume in the ladle is responsible for the crucial mixing process, homogenizing the melt in terms of concentration and heat. However, the complex multiphase interaction is not completely understood so far. An unbalanced cooling of the strand causes thermal induced stresses. Hence, a deeper understanding of these flow phenomena lead to improved products.

An Euler-Lagrange approach has been chosen to simulate these multiphase flows. The corresponding model is called discrete phase model (DPM) in ANSYS FLUENT. Thereby, the trajectories of the gas bubbles in a ladle as well as the droplets in spray cooling are computed by balancing all impacting forces. These forces and their influence on the resulting particle paths and flow patterns are investigated.

In this paper, two examples for the use of DPM models to simulate multiphase flows in metallurgy are presented. The shape and velocity of the gas plume in a ladle and the resulting mixing efficiency and the spray characteristics and the cooling film is simulated. To validate the calculations and improve the chosen DPM model, water model studies are conducted.

1. Introduction

Multiphase flows play a major role in metallurgy, e.g. non-metallic inclusions in tundish and mold as well as the gas plume in a ladle and the spray cooling of the strand. In the steel ladle, the melt is homogenized in composition and temperature and adjusted to defined values. In addition, non-metallic particles are separated. The spray cooling of the strand needs to be homogenous, otherwise thermal induced stresses can lead to the failure of the product. Increasing demands of the industry for high performance steels of highest purity and homogeneous optimal technological properties for components to increase the product life cycle require a comprehensive understanding of the processes in secondary metallurgy as well as during the cooling. This provides opportunities to improve the plant productivity and the product quality.

Due to the high costs and difficulties regarding investigations on the real process, numerical modelling in combination with water model experiments for validation is a competitive alternative. A detailed knowledge of the multiphase flow in the water model of a ladle enhances the basic understanding of the process and generates a data basis for the validation of the numerical simulations.

There are basically two main approaches for the numerical simulation of the movement of gas bubbles or droplets and their interaction with the surrounding melt. In Euler-Euler models a complete set of transport equations is solved for each additional phase. The high-density

differences between gas and melt, especially in cases of very high momentum input into the system, result in stability problems during the calculation. Furthermore, the computational cost for each additional phase is considerable, as an additional set of transport equations must be solved. The second approach is the so-called Euler-Lagrange model. In this model, discrete volume elements (bubbles/droplets) are introduced into the surrounding fluid and their trajectories are determined by force equilibrium. Drag and dynamic lift forces specify the interaction between the primary phase and the particles.

There are many publications that deal with the study of flow structure in a steel ladle [1-7]. Both water models and numerical simulations are utilized. According to the literature, Euler-Lagrange approaches are mostly used to simulate heterogeneous lift free jets in the ladle. Subject of the investigations is usually the mixing behavior in the ladle as a function of various process parameters such as ladle geometry, position of the plug and rinsing intensity.

Spray cooling research has been conducted for decades but was mainly experimental in nature [8-16]. A numerical approach was derived by Issa [17] for a pneumatic atomiser. Thereby, the Euler-Lagrange approach was utilised to model dispersed coolant droplets in an airstream. Yamasaki et al. [18] modelled spray cooling in a secondary cooling zone of a continuous casting machine by employing the Moving Particle Simulation method. In this study the effects of the droplet diameter, contact angle between water and rolls and the spray angle were investigated. The numeric works mentioned above focused on a specific issue of spray cooling. A numerical model which is able to depict the droplet flow between a hydraulic atomiser's orifice and the wall correctly has not been derived so far, though.

2. Bubble driven flow in a ladle

2.1 Experimental Setup

Figure 1 shows the experimental setup of the water model. The according geometrical data is given in table 1. The model is a 1:5 scale model of a 185 t ladle furnace. This model allows analyzing porous plugs, perforated plates as well as individual nozzles with different positions in the bottom. For the shown investigations, a porous plug has been used. To adjust various gas flow rates a mass flow controller is installed.
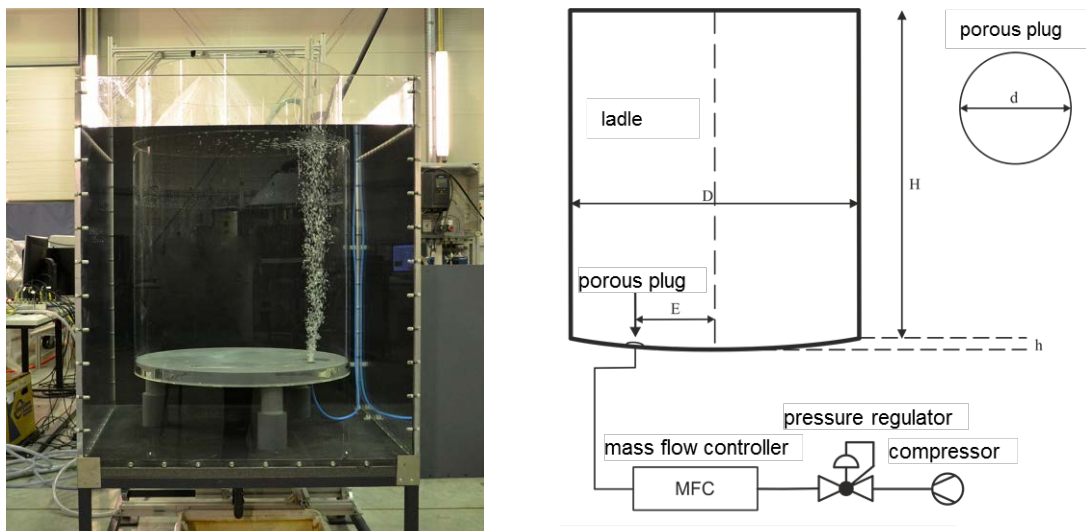
Figure 1. Water model of the ladle, picture (left) and scheme (right)

Table 1. Geometric data of the water model

ladle diameter	0.64	m
water level	0.646	m
diameter of the porous plug	20	mm
eccentricity of the porous plug	0.21	m
gas addition above the bottom	4	mm

To determine the bubble sizes and shapes images of heterogeneous lift free jets are recorded by means of a digital SLR camera (figure 2, left). The resulting bubble size distributions are used as boundary conditions for the numerical simulations (figure 2, right).
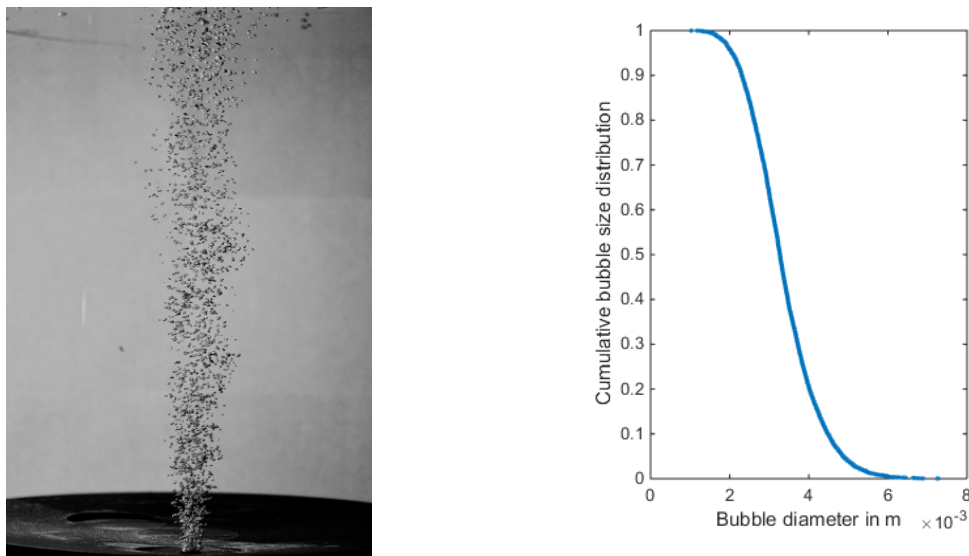
Figure 2. Heterogeneous lift jet (left) and cumulative bubble size distribution (right)

The particle image velocimetry (PIV) is used for measuring the flow fields. The model is placed in an outer tank with flat acrylic glass walls (figure 3). This minimises the effects of image distortion caused by the curved model walls and stabilise the ladle model mechanically. A porous plug is set in eccentric in the ladle's bottom. The measurement technique comprises a CCD double frame camera with a resolution of 2048x2048 pixel. The delay time between the double frames is 10,000 µs. A Nd:YAG double pulse laser (λ=532 nm) is used to expose the images. An optical device fans out the laser beam into a thin light sheet. The light sheet is placed at the symmetry plane of the ladle model to ensure the exposed particles are on the main flow plane.
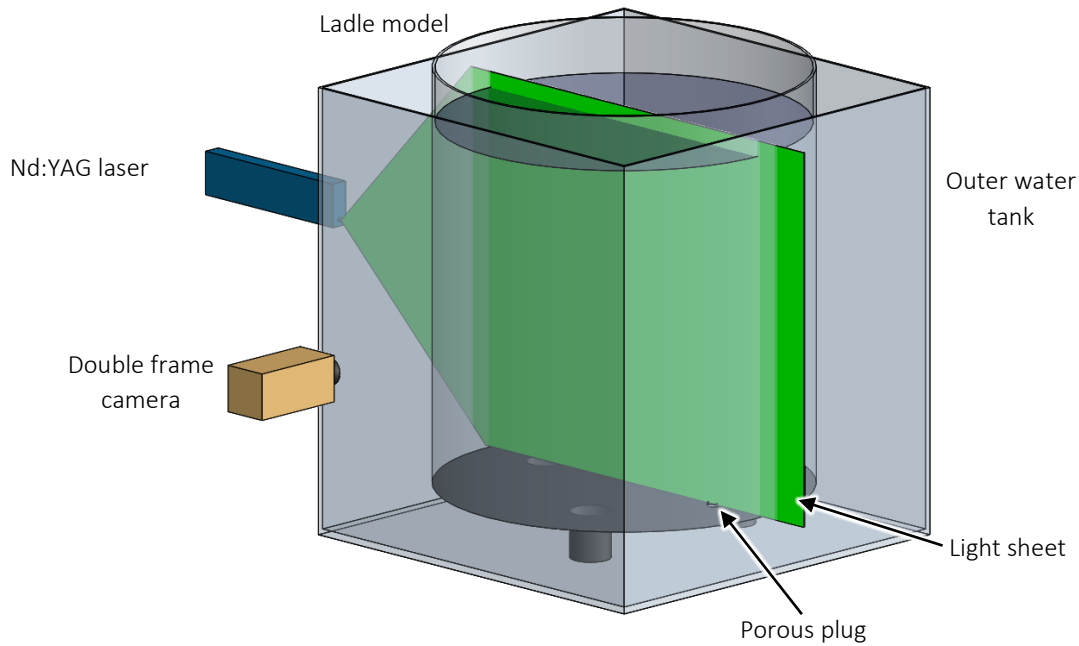
Figure 3. Setup of the PIV measurements

2.2 Numerical model

In case of the water model, the investigated setup consists of three independent phases, a continuous water phase, air above the water which is taken into account to depict the movement of the free surface and dispersed pressured air bubbles. The model of the real ladle consists of three continuous phases, steel, slag and air as well as dispersed argon bubbles. The interfaces between the two or three continuous phases (water/air respectively steel/slag/air) are tracked by the Eulerian volume of fluid (VOF) model. For the dispersed bubbles, the Lagrangian discrete phase model (DPM) is utilized. In the Lagrangian approach, the bubble trajectories are modelled independent of the mesh by balancing all impacting forces. Owing to that, bubbles smaller than the mesh size can be modelled and the mesh requirements are lower.

The ladle's dimensions and phase distribution are in accordance with currently operated process units. However, the slight bottom curvature, applied in some ladles is not considered. The water model is in downscales geometrically by the factor 5. Moreover, the sidewalls are not slightly tapered but flat. For the calculation, a structured mesh of 1,427,712 hexahedral cells is applied on the geometry. To improve the quality of the mesh, it contains an O-grid located around the symmetry axis as shown in Figure 4. On all boundaries, a no-slip boundary condition is applied, except for the wall above the air, at which a zero-shear condition is used. The zero-shear condition proofed to support the numerical stability of the phase boundary modelling.
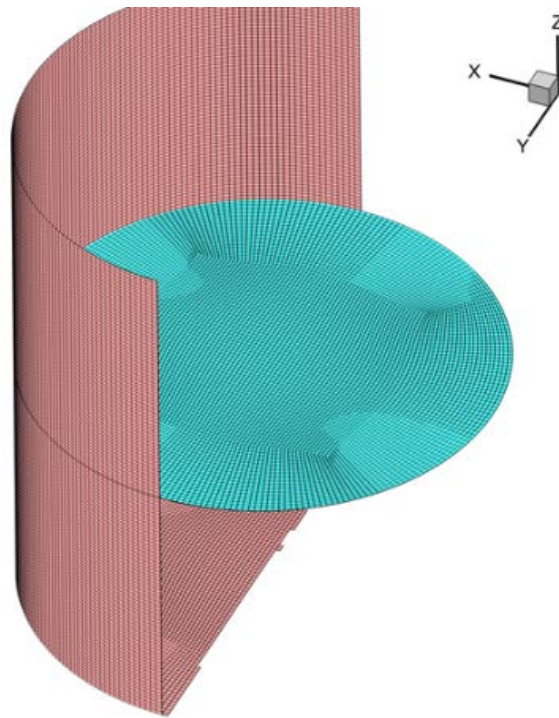
Figure 4. Computational mesh comprising an O-grid

2.3 Results

The velocity profiles in the exposed y=0 plane measured by PIV is compared to the calculated numerical solution in Figure 5. The plot shows the calculated fluid velocity averaged over a calculation time of 11 to 22 seconds. For a higher visibility of the free surface the air phase above the water was blanked out. For the computation of turbulences, the large eddy turbulence model was used. The general flow structure is in close agreement, though the 'eye' of the circulating flow is slightly shifted towards the ladle axis and the free surface in the numerical result. The velocity is slightly understated in the region outside the gas plume and strongly understated in the gas plume. However, this can be explained by the accumulation of tracer particles at the fluid-bubble phase boundary. Because of the accumulation, the measured flow velocity is the bubbles rise velocity rather than the velocity of accelerated fluid. The rise velocity of the gas bubbles is in close agreement with the velocities measured in the gas plume region.
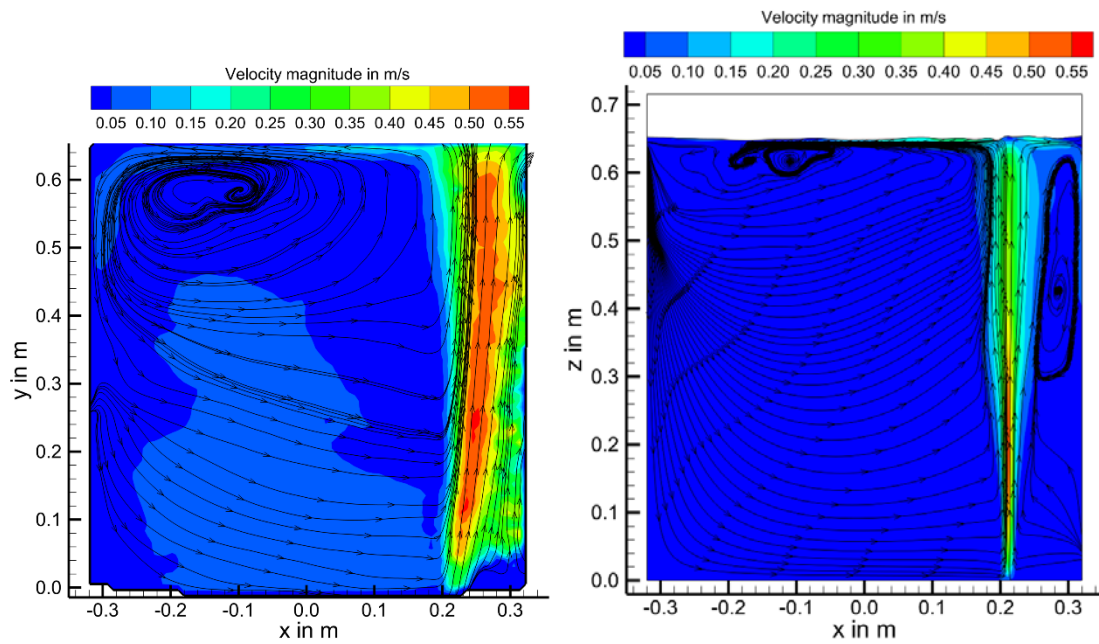
Figure 5. Velocity profile within the water model measured by PIV (left) and computed by CFD (right)

The physical properties and the geometry of the introduced CFD model was modified so that it depicts the fluid flow in the actual cell. The results are shown in Figure 6. Alike in the water model the gas plume induces a circulating flow, which's center is located close to the phase boundary between metal and slag. Entering the slag phase, the argon bubbles are slowed down significantly. This can be explained by decline of the density gradient driven buoyancy force and the increased viscosity of the slag phase. Consequently, the phase boundary between slag and air (free surface) is only slightly disturbed while the phase boundary between slag and metal is elevated it the region of the gas plume.
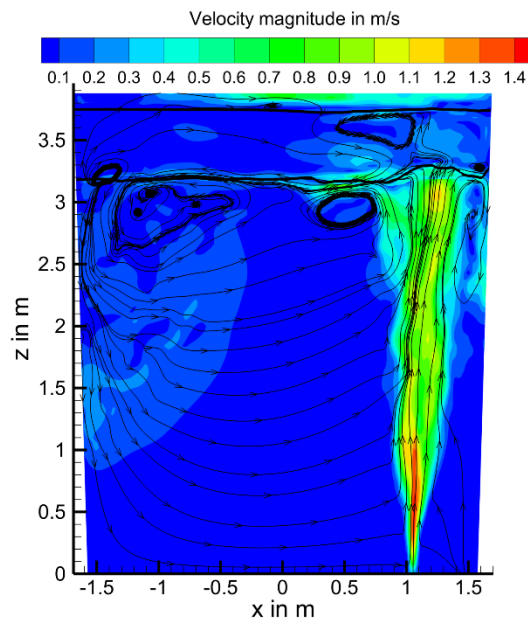
Figure 6. Velocity profile within the steel ladle

3. Spray cooling

3.1 Experimental Setup

The setup is depicted in figure 7. The investigated nozzle is connected to the water supply line via a pressure regulator. The impingement density is measured with a mechanical three-dimensional patternator.
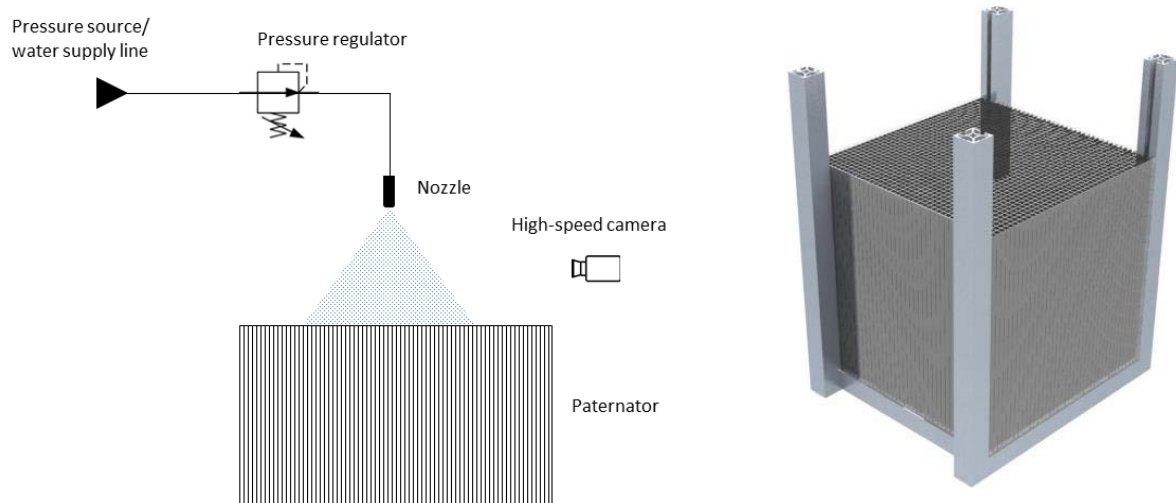
Figure 7. Experimental setup (left) and utilised mechanical patternator (right)

The properties of the nozzle are listed in table 2. According to the supplier, the inner geometry ensures a homogenous outflow, that is to say a homogenous impingement density. The coolant is considered to have the properties of water because it is most commonly used in industrial applications.

Table 2. Properties of the investigated nozzle

Parameter	Value
Orifice diameter	1.25 mm
Spray angle	45° degree
Pressure	1-4 bar
Nozzle to patternator distance	20-40 cm

The patternator consists of 37x38 tubes with a rectangular 10 mm x 10.8 mm opening area. The impingement density in each tube is determined. To measure the mass of water in each tube, plastic float markers are used to mark the filling height. In addition, the droplet velocity is measured with a high speed camera with a recording rate of 20000 frames per second. The resulting flow field is calculated by cross correlation.
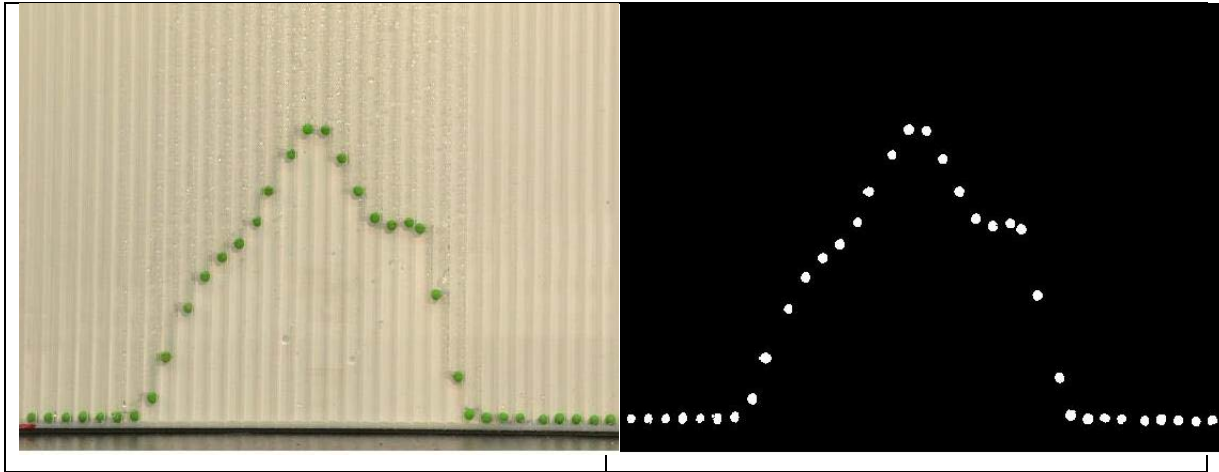
Figure 8. Photograph of a patternator row before (left) and after image processing (right)

3.2 Numerical Model

The numerical spray model is derived for the nozzle used in the experiment. The modelled spray consists of a large number of small droplets, which are finely dispersed in the surrounding air. Owing to the small droplet size and the possible occurrence of droplet-droplet interactions, the Euler-Lagrange approach is chosen to model the multiphase flow. The droplets are released by a Langrangian injection boundary condition. Amongst the atomiser's properties listed in table 2, an initial droplet diameter, respectively a diameter distribution and an initial droplet velocity need to be specified.

Beyond the solid-cone injection boundary condition pre-implemented in Fluent, a novel boundary condition is developed which promise to be in better accordance with the homogenous nozzle outflow. For that, a number of concentric circles that contain injection points are defined within the nozzle's orifice. To ensure a homogenous droplet outflow, the distance between the circles has to be equal to the distance of the injection points on one circle.

For the modelling of the water film, a coupling between the Lagrangian DPM model and the Eulerian VOF model was implemented. Before reaching the wall, the coolant is present as finely dispersed droplets that are modelled by the DPM. Then the droplets reaches the wall, respectively the water film on the wall, they are transferred into a continuous phase. The transfer between the two states is considered by mass and momentum source terms in the VOF model.

3.3 Results

The impingement densities using the solid-cone injection boundary condition are characterised by a pronounced maximum that is located at the spray axis. This, however, is not in accordance with the supplier's information that the impingement is homogenously distributed over the whole impact area. Owing to that, a different injection boundary condition is implemented in which the nozzle outflow is assumed homogenous over the orifice. The resulting impingement densities with an initial droplet diameter of 100 μm are compared in figure 9. The newly implemented injection boundary condition results in an almost homogenous impingement density.
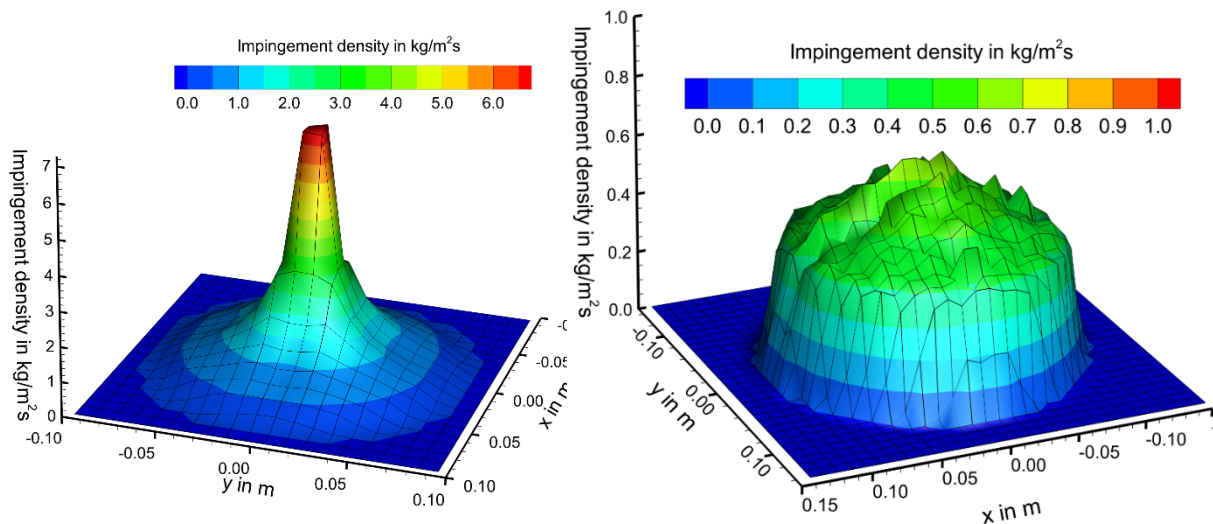
Figure 9. Calculated impingement density with pre-implemented (left) and new (right) injection boundary condition

The numerical results are validated by experimental data. Figure 10 (left) shows the measured impingement density in 20 cm distance from the nozzle orifice for a nozzle pressure setting of 2 bar. The values are recorded by a mechanical patternator. It can be seen that the impingement density is almost homogenously distributed over the whole impact area but shows a narrow maximum at the spray axis. Furthermore, two less pro-nounced local maximums can be found at the outer impingement area. In addition, the droplet velocity is recorded by a high speed camera and cross correlation. The result is shown in figure 10 (right). The maximum velocity is about 15 m/s at the nozzle orifice and declines slightly to a value of about 10 m/s at an orifice distance of 180 mm. These results indicate that a velocity estimation by the Bernoulli approach, as proposed by Wozniak [19], is inappropriate. The neglect of the surface energy in an atomisation process results in a significant error, which is in the order of 300% for the considered nozzle.
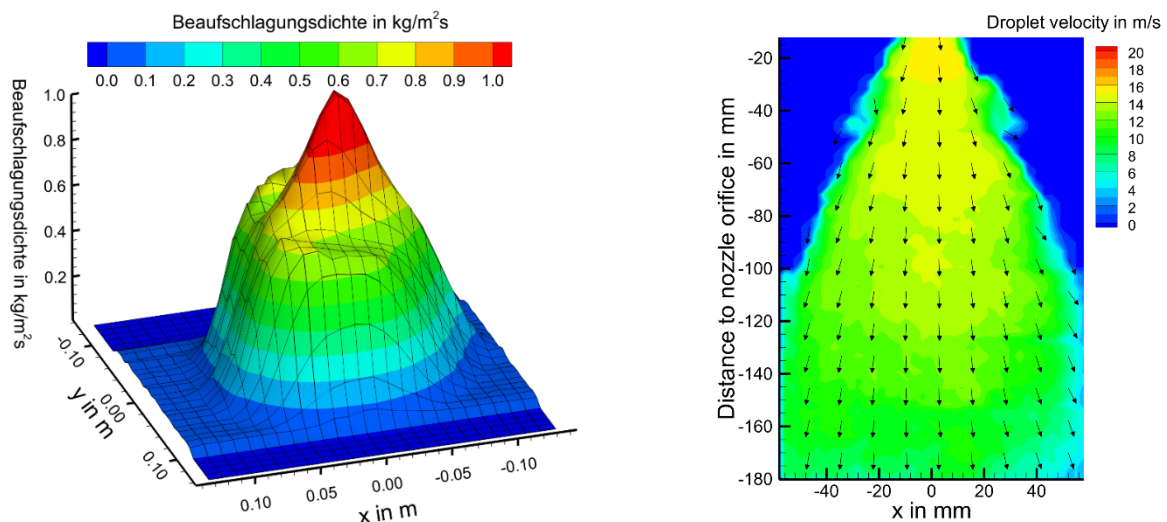
Figure 10. Experimentally measured impingement density (left) and velocity profile (right) with 2 bar nozzle pressure and 200 mm nozzle to paternator distance

The pre-implemented as well as the new implemented injection boundary condition show a deviation from the experimental data. The pre-implemented injection boundary does not match the experimental measurements at all. The maximum is far too high while the impact area is too small. The new implemented injection boundary condition is in much better accordance. The highest deviation is located at the spray axis where the experimental data shows a maximum that is more pronounced than in the numerical model. Furthermore, the two peaks at the outer impact area are not depicted in the model.

The modelling of the water film is shown in figure 11. The film is colored by the film thickness. A comparison with experimental results indicates that the numerical model is in fine qualitative agreement with the actual spray process.
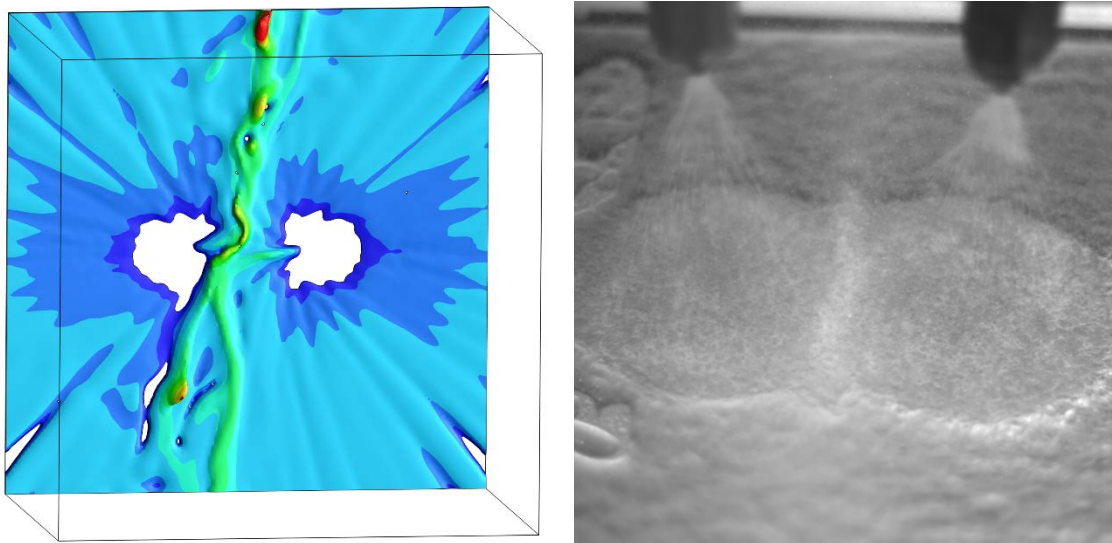
Figure 11. Numerical model (left) and experimental validation (right) of the resulting water film generated by two nozzles

4. Conclusion

The numerical model of the steel ladle is in close agreement with the PIV measurements conducted in a 1:5 water model of a 185 t ladle. The major difference is the position of the 'eye', which is slightly shifted. The results of the real ladle seems to understate the spout. Further investigations and a comparison to plant data are necessary for a closer examination of the spout phenomenon.

For the spray cooling process it was found, that the injection boundary condition is most decisive for the accuracy of the model. The solid-cone model, which is implemented in Fluent, utilizes a probability function to distribute the droplet's injection points. A comparison with physically measured data indicated though, that this is inappropriate to model the investigated atomizer's spray patterns. In order to overcome this drawback, a new injection type was developed. Thereby, the injection points are homogenously distributed over the whole atomizer's orifices area. The initial spray direction is calculated as a function of the injection point's distance to the spray axis. The spray patterns obtained with the novel injection type showed good quantitative and qualitative accordance with the physically measured data. A

comparison between the measured and the calculated data also showed a strong deviation between the droplet velocities. In this work, the initial droplet velocity was calculated by the pressure applied to the atomizer. This neglects the atomization process though, in which energy is transformed into surface energy. The strong deviation indicates that the initial droplet velocity requires further investigation.

References:

1) Alexiadis, A., Bubble dispersion patterns in bubbly-flow released from a porous plug into a gas-stirred ladle. *Applied Mathematical Modeling*, Volume 31 (2006) pages 1534-1547.

2) Chen, Y., Pang, Y. and Zhang, X., Numerical Study on effects of Molten Steel Flow about different Blowing Argon Position in Ladle Furnace. *Advanced Materials Research*, Volume 146-147 (2011) page. 1031-1037.

3) Ganguly, S. and Chakraborty, S., Numerical modelling studies of flow and mixing phenomena in gas stirred steel ladles. *Ironmaking and Steelmaking*, Volume 35(7) (2008) pages 524-530.

4) Guo, D.C., Gu, L. and Irons, G.A., Developments in modelling of gas injection and slag foaming. *Applied Mathematical Modelling*, Volume 26 (2002) pages 263-280.

5) Jauhiainen, A., Jonsson, L. and Sheng, D., Modelling of Alloy mixing into steel; The influence of porous plug placement in the ladle botton on the mixing of alloys into steel in a gas-stirred ladle. A comparison made by numerical simulation. *Scandinavian Journal of Metallurgy*, Volume 30 (2000) pages 242-253.

6) Kwon, Y.-J., Zhang, J. and Lee, H.-G., A CFD-based Nucleation-growth-removal Model for Inclusion Behavior in a Gas-agitated Ladle during Molten Steel Deoxidation. *ISIJ International*, Volume 48(7) (2008) pages 891-900.

7) Liu, H., Qi, Z. and Mianguang, X., Numerical Simulation of Fluid Flow and Interfacial Behavior in Three-phase Argon-Stirred Ladles with One Plug and Dual Plugs. *Steel Research International*, Volume 82(4) (2011) pages 440-458.

8) Jacobi, H., Kaestle, G., Wünneberg, K.: Heat Transfer in Cyclic Secondary Cooling during Solidification of Steel. *Ironmaking and Steelmaking* Volume 11 (1984), pages 132-145.

9) Müller, H., Jeschar, R.: Wärmeübergang bei der Spritzwasserkühlung von Nichteisenmetallen. *Fortschrittberichte der VDI Zeitschriften* Volume 77 (1983), pages 1-131.

10) Klinzing, W., Rozzi, J., Mudawar, I.: Film and Transition Boiling Correlations for Quenching of Hot Surfaces with Water Sprays. *Journal of Heat Treating* Volume 9 (1992), pages 91-103.

11) Puschmann, F., Specht, E.: Transient measurement of heat transfer in metal quenching with atomized sprays. *Experimental Thermal and Fluid Science* Volume 28(6) (2004), pages 607-615.

12) Mudawar, I., Estes, K.: Optimizing and Predicting CHF in Spray Cooling of a Square Surface. *Journal of heat Transfer* Volume 118 (1996), pages 672-679.

13) Abdalrahman, K.: *Influence of Water Quality and Kind of Metal in the Secondary Cooling Zone of Casting Process*. Dissertation, Otto-von-Guericke-Universität, Fakultät für Verfahrens- und Systemtechnik, 2012.

14) Alam, U.: *Experimental Study of Local Heat Transfer during Quenching of Metals by Spray and Multiple Jets.* Dissertation, Otto-von-Guericke-Universität, Fakultät für Verfahrens- und Systemtechnik, 2011.

15) Baumeister, K., Simon, F.: Leidenfrost Temperature - Its Correlation for Liquid Metals, Cryogens, Hydrocarbons and Water. *Journal of Heat Transfer* Volume 95 (1973), pages 166-173.

16) Raudensky, M., Horsky, J.: Secondary cooling in continuous casting and Leidenfrost temperature effects. *Ironmaking and Steelmaking* Volume 32(2) (2005), pages 159-164.

17) Issa, R., Yao, S.: Numerical Model for Spray-Wall Impaction and Heat Transfer at Atmospheric Conditions. *Journal of Thermophysics and Heat Transfer* Volume 19(4) (2005), pages 441-447.

18) Yamasaki, N., Shima, S., Tsunenari, K., Hayashi, S., Doki, M.: Particle-based Numerical Analysis of Spray Water Flow in Secondary Cooling of Continuous Casting Machines, *ISIJ International* Volume 55(5) (2015), pages 976-983.

19) Wozniak, G.: *Zerstäubungstechnik*. Springer, 2003.

Effect of Ca-Mg Substitution on Transport Properties of Aluminosilicate Glasses and Melts

Sohei SUKENAGA*, Kyung-HO KIM*, Koji KANEHASHI** and Hiroyuki SHIBATA*

*Institute of Multidisciplinary Research for Advanced Materials,
Tohoku University, Sendai Japan
**Nippon Steel & Sumitomo Metal Corporation, Chiba, Japan

Abstract: Aluminosilicate melt is one of the important oxide system in the high temperature materials processing. Knowledge of properties (e.g. thermal conductivity, viscosity) of the melt is essential for understanding phenomena at high temperatures. In the present study, the effect of Ca-Mg substitution on thermal conductivity and viscosity was investigated in Al_2O_3-SiO_2-CaO-MgO system. The laser flash method was used to measure the thermal conductivity of the silicate glasses. The viscosity of the melts was measured using the rotating crucible method under air atmosphere. By substituting Ca by Mg in aluminosilicate, the values of thermal conductivity increased and viscosity decreased. Structure of the quenched samples was investigated by Raman spectroscopy and ^{27}Al MAS NMR. Polymarization degree was not changed considerably in all samples. On the other hand, the fraction of aluminum atom in five-fold coordination increased with substituting Ca by Mg in aluminosilicate glass.

1. Introduction

Transport properties of molten silicate, such as thermal conductivity and viscosity, play very important role to understand metallurgical phenomena at high temperature. These properties are strongly related with microstructure of the molten silicate. The measured values have been summarized from the view point of the measure of polymerization of SiO_4 tetrahedra since the SiO_4 tetrahedra is a basic unit of the silicate glass and melts [1]. It has been, however, noticed that the measure of depolymerization could not have examined all the measured results [2, 3]. In this study, the effect of substituting Ca by Mg in aluminosilicate on the thermal conductivity and viscosity was investigated. Structure of the quenched samples was investigated by Raman spectroscopy and ^{27}Al MAS NMR.

2. Experiments

Chemical composition of the samples, density (ρ) and heat capacity (Cp) were listed in the table 1. The samples were melted in a platinum crucible and quenched in the copper mold. The quenched samples were glassy, and heated again for one hour at 15 K below glass transition temperature to reduce the residual stress for manufacturing the disk shape sample. The disk shape sample, 5 mm in diameter and 0.5 – 1 mm in thickness was used for thermal diffuvity measurement using a laser flash method. The density was measured by Archimedes method. The heat capacity was estimated from chemical composition of the sample using partial molar heat capacity of each oxide [4].

The thermal diffusivity, α, was measured using a laser flash method [5]. The thermal conductivity was estimated by equation (1).

$$\lambda = \alpha \, \rho \, Cp \qquad (1)$$

The viscosities of the sample melts were measured using the rotating crucible method at between 1823-1673 K. The measurement process has been described in detail previously [3].

Table 1 Chemical composition (mol%), density and heat capacity of the samples.

Chemical composition (mol%)				Density, ρ (g/cm^3)	Heat Capasity, C_P (J K^{-1} g^{-1})
Al$_2$O$_3$	SiO$_2$	CaO	MgO		
15	55	30	-	2.702	0.747
15	55	-	30	2.646	0.794

3. Results and discussion

The effect of molar ratio of MgO to CaO+MgO on the measured thermal conductivity at room temperature and viscosity at 1837 K were shown **Figure 1 (a) and (b).** The value of thermal conductivity increased with ratio of MgO, which substituted CaO. On the other hand, the viscosity was decreased.

It has been known that the thermal conductivity and viscosity are affected by a local structure of silicates. In Raman spectroscopy asymmetric stretching of Si-O$^-$ (non-bridgeng oxygen) and Si-O^0 (bridging oxygen) would be obsereved in btween 850 -1200 cm^{-1}, and the Raman spectra would be shifted to low wavenumber with increasing a number of non-bridging oxygen around silicon atom. The measured Raman spectra of Al$_2$O$_3$-SiO$_2$-(CaO or MgO) glass was shown in **Figure 2**. The obtained Raman spectra were almost same comapering two Raman spectra. This result indicates that the difrerence of the thermal conductivity and viscosity could not be affected by degree of polymarization of silicates.
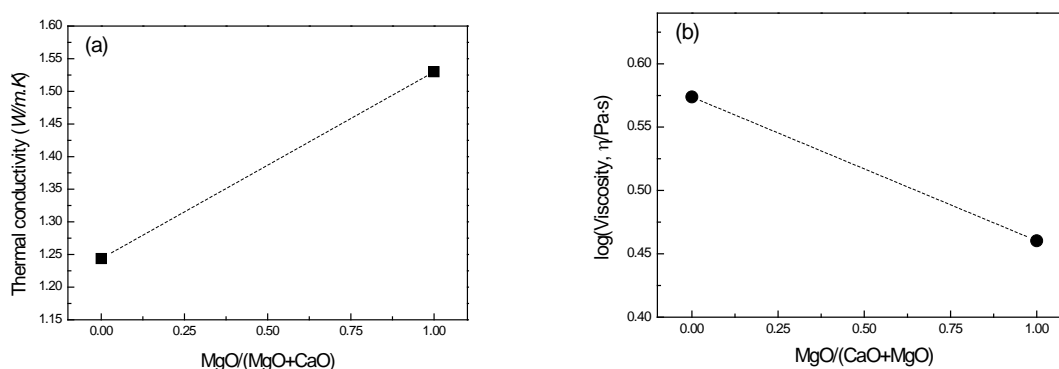
Figure 1 Thermal conductivity at room temperature (a) and viscosity at 1837K (b) with substitution Ca by Mg.

^{27}Al MAS NMR spectra of the samples were shown in Figure 3. The peak at 60 ppm is assigned to aluminum ion in four-fold coordination (AlO$_4$), and the shoulder at around 30 ppm is assigned to aluminum ion (AlO$_5$) in five-fold coordination. It is found that the amount of AlO$_5$ in Al$_2$O$_3$-SiO$_2$-MgO glass is larger than that in Al$_2$O$_3$-SiO$_2$-CaO. It has been suggested that bond between cation and oxygen is weaker with increasing a coordination number of cation. From this consideration, it is estimated that average strength of bonds in the aluminosilicate network structure with MgO is weaker.
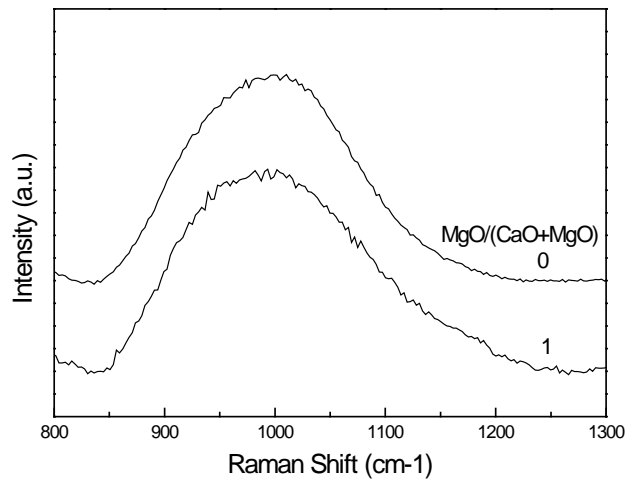
Figure 2 RAMAN spectra of quenched samples with substitution Ca by Mg.
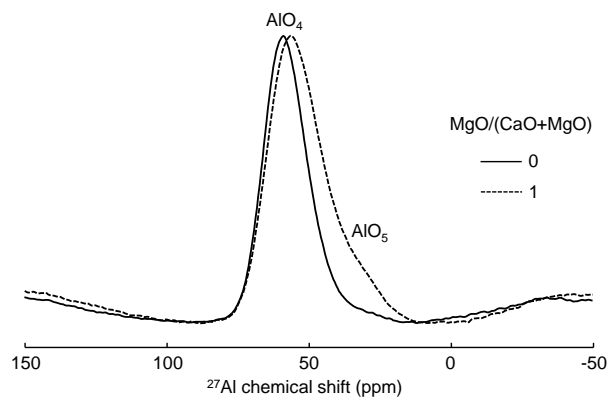
Figure 3 ^{27}Al MAS NMR spectra of Al_2O_3-SiO_2-(CaO or MgO) glasses, obtained at 18.8 T.

It has been reported that the average strength of bonds in the aluminosilicate network structure increases with a decrease in the cationic potential, Z/r, of the charge compensator cations; here, Z is the valence number and r is the cationic radius [6]. The obtained results of ^{27}Al MAS NMR spectra could be consistent with the reported idea. Then, it is likely that the viscosity is lower in the aluminosilicate melt contained MgO due to the decrease of the average strength of bonds. On the other, the tendency of the thermal conductivity could not be explained in the same way. The difference of thermal conductivity is likely to be related to a coordination number of aluminum ion because the increase of the number may increase thermal transport path.

4. Summary

By substituting Ca by Mg in aluminosilicate, the values of thermal conductivity increased and viscosity decreased. It is likely that the main factor of the local structure of aluminosilicate to control thermal conductivity and viscosity is different each other.

The content of the paper was presented in the 37th Japan Symposium on Thermophysical Properties in 2016 in Okayama Japan.

References:

1) K.C. Mills, The Influence of Structure on the Physico-chemical Properties of Slags, *ISIJ Int.*, **33**(1993), 148-155.

2) W. H. Kim, I. Sohn, and D. J. Min, A Study on the Viscous Behaviour with K_2O Additions in the CaO–SiO_2–Al_2O_3–MgO–K_2O Quinary Slag System, *Steel Research Int.*, **81**(2010), 735-741.

3) T. Higo, S. Sukenaga, K. kanehashi, H. Shibata, T. Osugi, N. Saito and K. Nakashima, Effect of Potassium Oxide Addition on Viscosity of Calcium Aluminosilicate Melts at 1 673–1 873 K, *ISIJ Int.*, **54**(2014), 2039-2044.

4) R.G. Berman and T.H. Brown, **Heat capacity of minerals in the system Na_2O-K_2O-CaO-MgO-FeO-Fe_2O_3-Al_2O_3-SiO_2-TiO_2-H_2O-CO_2: representation, estimation, and high temperature extrapolation**, *Contrib. Mineral Petrol.*, **89**(1985), 168-183.

5) H. Shibata, H. Ohta, A. Suzuki and Y. Waseda, Applicability of Platinum and Molybdenum Coatings for Measuring Thermal Diffusivity of Transparent Glass Specimens by the Laser Flash Method at High Temperatures, *Materials Trans. JIM*, **41**(2000), 1616-1620.

6) B.N.Roy and A. Navtrosky, Thermochemistry of Charge-Coupled Substitutions in Silicate Glasses: The System $M_{1/n}^{n+}$ AlO_2-SiO_2 (M=Li, Na, K, Rb, Cs, Mg, Ca, Sr, Ba, Pb), *J. Am. Ceram. Soc.*, **67**(1984), 606-610.

Reaction Behaviors of Metallic Iron and Lower Oxides of Iron in the Sintering Bed

Kazuya Fujino[1]*, Taichi Murakami[2]* and Eiki Kasai[2]*
1) Faculty of Science and Engineering, Chuo University, Tokyo, Japan
2) Graduate School of Environmental Studies, Tohoku University, Sendai, Japan

Abstract: Iron ore sintering process plays important roles not only in the preparation of agglomerated burden for a blast furnace but also to in the utilization of recycle materials such as metallurgical dusts and sludge. Some of them contain certain amount of metallic iron and/or lower oxides of iron such as wustite and magnetite, which have potentials to supply oxidation heats during sintering. Further, increasing use of magnetite ore concentrates in the sintering process is expected in future. If the oxidation heat of the iron-bearing materials are efficiently utilized, it will make possible to reduce the used amount of coke, which is the main heat source of the process, and therefore CO_2 emissions from the process will decrease. However, the oxidation reactions compete with the combustion reaction of coke particles. Therefore, it is necessary to examine in detail their reduction/oxidation behaviors in the sintering bed.

In this study, oxidation experiments of metallic iron and wustite particles were carried out using a sintering simulator. Effects of their mixing ratios, particles sizes, and coexisting CaO component were examined. Coke combustion preceded the oxidation reactions of the iron bearing materials in the most of the case. The oxidation rates were strongly dependent on their particle sizes. They were retarded by the formation of a dense oxide layer at the surface, but the melt-formation promoted by the addition of CaO component shows the possibility to reactivate the reactions.

1. Introduction

Iron ore sintering process accounts for about 3% of the total anthropogenic CO_2 emissions in Japan. To reduce the emissions, it is essential to decrease the amount of coke used in the process and alternative heat sources are necessary to be considered. For example, use of biomass char will be a possible solution, since it is regarded as a carbon neutral fuel. It also showed a significant decrease in the sintering time as well as in the formed amount of NOx and SOx[1]. However, it tended to leads to significant decreases in the yield and strength of the sinter products[2]. On the other hand, utilizations of partial reduced iron ore[3] and used steel can chip[4] were tried but they led to lowering productivities due to significant decreases in the permeability of the sintering bed.

Hematite and goethite have been major iron forms of the iron ore resources used in the sintering process. Recently, however, development of new iron resources have been progressing. In this situation, increasing use of fine magnetite ores is expected in future[5]. Other iron source containing Fe^{2+} is, for example, mill scales produced in the milling process. It contains lower oxidation state of iron oxides such as wustite and magnetite as well as metallic iron. However, utilization of a large amount of mill scale also caused a decrease in the productivity[6].

The main reason of such decreases of the productivity is lowering the permeability of the sintering bed, since the oxidations of iron-bearing materials did not give voids like coke combustion. Formed iron oxides remained with even increased volume after sintering. This study was performed to clarify the oxidation behaviors of iron bearing materials in the sintering bed and a way of efficient utilization of such materials was discussed.

2. Experimental

Hematite and calcium carbonate powder reagents were mixed and granulated around alumina balls of 2.0 mm in diameter using a disc-pelletizer to prepare mini-pellets with size between 2.38 and 2.8 mm (called ACP). Chemical composition of the adhering layer of ACP can be regarded as CaO–Fe_2O_3 binary system after the calcination of calcium carbonate as shown in Table 1.

Table 1 Mixing ratios of Fe_2O_3 and CaO for preparation of adhering layer of ACP

Pellet name	Fe_2O_3 (%)	CaO (%)
ACP-10	90.0	10.0
ACP-15	85.4	14.6
ACP-20	79.8	20.2
ACP-25	73.9	26.1
ACP-30	67.7	32.3
ACP-35	61.2	38.8

Metallic iron and metallurgical coke (fixed carbon: 87 mass%) particles with size between 1.0 and 2.0 mm and wustite particles with size between 1.0 and 2.4 mm were used to the experiment. Wustite sample was prepared by the reduction of hematite reagent under the atmosphere of $CO:CO_2 = 1:1$ at 1000°C for 144 ks. Its oxidation state was identified as by XRD $FeO_{1.094}$. In order to examine the effect of existing state of CaO component, calcium oxide particles with size between 1.0 and 2.0 mm (called LP) were prepared by crushing the sintered tablet prepared using $CaCO_3$ reagent.

Generated heats were calculated based on the assumption that both of metallic iron and wustite would be completely oxidized to Fe_2O_3. The mixing ratios of the iron bearing materials to ACP were set based on the heat equivalent to the standard case of 1.3 g-coke to the total sample. When coke was completely replaced by metallic iron and wustite particles, their amount of additions were 6.1 and 21.2 g, respectively.

Figure 1 shows a schematic diagram of the sintering simulator. Inside diameter of alumina tube is 35 mm and a standard height of the sample bed was set at 20 mm. Packed beds of the alumina balls with the heights of 50 and 20 mm were placed above and below the sample bed, in order to preheat introduced gas and to preventing dropping of formed melt, respectively.
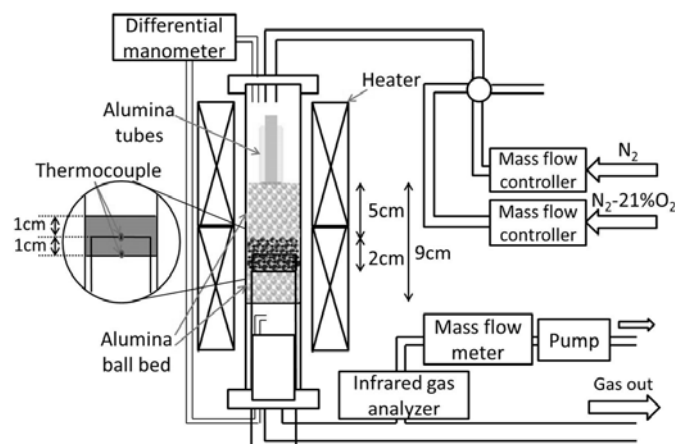
Fig. 1 Schematic diagram of sintering simulator

Sample bed was first heated up to 900°C under N_2 stream to prevent the oxidation of agglomeration agent. Then the gas flow rate was increased to be 0.45 Nm/s. When sample bed

temperature became stable, gas was changed to N_2-21 vol%O_2 so that heat profile was given to the sample bed by the combustion/oxidation heats. Bed temperatures at the center and the bottom of sample bed, total pressure drop of the sample and alumina ball beds and CO, CO_2 and O_2 concentrations of the outlet gas were measured continuously.

When wustite particles are mixed with ACP, the height of sample bed exceeded 20 mm because energy density of wustite was not large as other materials. In the case using CaO particles, they were mixed with 21.1 g of wustite particles. Base CaO concentration of the sample bed was set as 10 mass%CaO and it was changed to examine the effects of existing state and CaO concentration on the structural change and pressure drop of the sintering bed.

Experimental conditions were summarized in Table 2.

Table 2 Experimental conditions

	CaO source	Coke (g)	Metal. Iron particle (g)	Wustite particle (g)	Total CaO in sample bed (mass%)	Diameter of Heat source (mm)	Sample bed height (mm)
Coke	ACP-10	1.31	0.0	0.0	10.0	1.0 – 2.0	20
Fe	ACP-25	0.0	6.06	0.0	10.0	1.0 – 2.0	20
W	ACP-35	0.0	0.0	21.1	9.5	1.0 – 2.4	30
W	ACP-15	0.0	0.0	21.1	4.3	1.0 – 2.4	30
W	LP-15	0.0	0.0	21.1	15.0	1.0 – 2.4	20
W	LP-10	0.0	0.0	21.1	10.0	1.0 – 2.4	20
W	LP-5	0.0	0.0	21.1	5.0	1.0 – 2.4	20

3. Results and discussion

Bed temperature profiles at the center and bottom of sample bed are shown in Fig. 2. Higher bed temperatures were observed in the cases using coke and metallic iron. The case using metallic iron (Fe ACP-25) shows discontinuous and fluctuated changes. This seems to be caused by short-circuit of thermocouples due to formation of conductive oxide melt. Low bed temperatures of the cases using wustite (W ACP-15 and W ACP-35) may be due to their slow and incomplete oxidations.
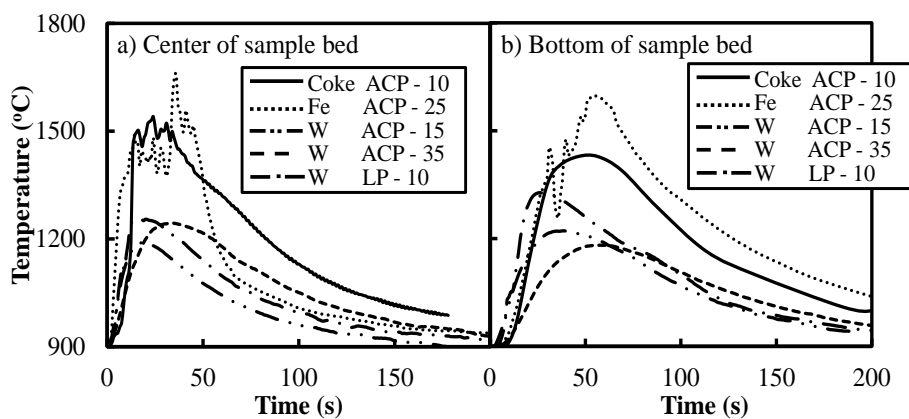
Fig. 2 Changes in sample bed temperatures, a) center and b) bottom, observed for different cases

Changes in O_2 concentration of outlet gas in the cases using coke (Coke ACP-10), metallic iron (Fe ACP-25) and wustite (W ACP-15, W ACP-35 and W LP-10) are shown in Fig. 3 compared to that of a blank case. The blank curve was obtained by changing gas from N_2 to N_2-21vol%O_2 with the gas flow of 0.45 Nm/s through a packed bed of the alumina balls. Oxidation rates of different cases were calculated considering the differences of the O_2 concentration of the outlet gases between the case of each experimental condition and the blank case (see Fig. 4). "Reaction ratio" of unity indicates that both of fixed carbon and iron components were completely oxidized to CO_2 and Fe_2O_3, respectively. Reaction ratio of coke reached to about 0.8 but that of metallic iron was as low as about 0.58. The cases using wustite showed even lower values like 0.46, 0.49 and 0.51. These seems to be caused by the suppression of gas diffusion through dense magnetite layers formed on the surface of wustite particles and therefore bed temperature did not sufficiently increased.

Changes in the pressure drop of the sintering bed observed for the different cases are compared in Fig. 5. The case using coke (Coke ACP-10) shows a decrease in the pressure drop after an initial rapid increase. This behavior can be explained as follows: the initial increase was led by a rapid increase in bed temperature due to starting of coke combustion and the succeeding decrease was caused by increasing void fraction caused by disappearance of coke particles and rearrangement of the bed structure[7]. In the case using

Fig. 3 Changes in O_2 gas concentration in the outlet gas for different cases and a blank test

Fig. 4 Changes in reaction ratios of materials observed for different cases

Fig. 5 Changes in pressure drop of sample and alumina beds observed for different cases

metallic iron (Fe ACP-25), pressure drop first decreases and starts to increase after showing a peak at 50 s. The initial decrease in pressure drop may be caused by the formation of melt and rearrangement of bed structure and succeeding increase in pressure drop seems to be caused by drop-down of formed melt and blocking the voids for gas flow[8].
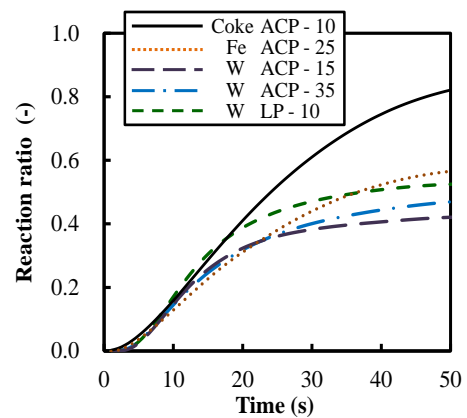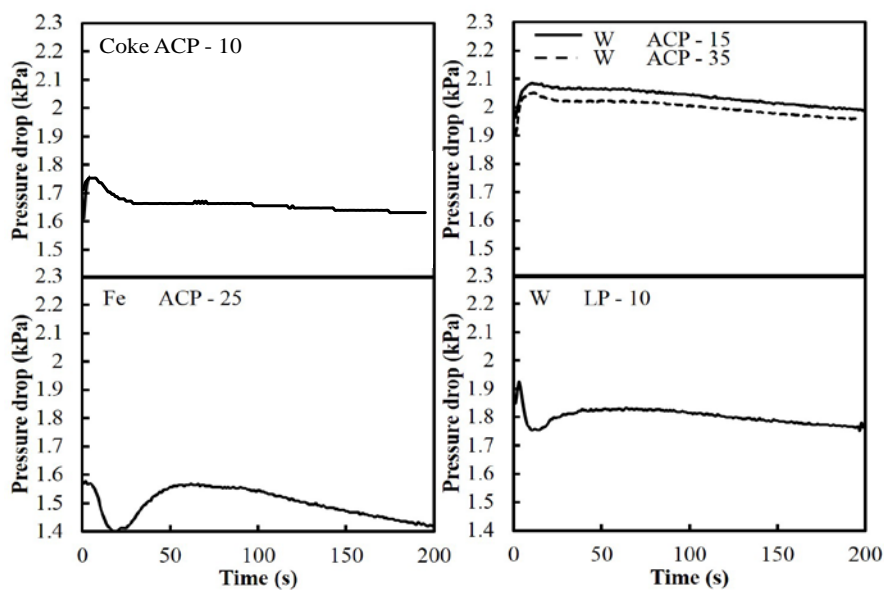
In the cases using wustite mixed with model pellets (W ACP-15) and (W ACP-35), pressure drops initially increases similar to the case using coke. After that, however, they only show gradual decrease instead of rapid decrease. Further, CaO concentration of the model pellets did not affect the pressure drop of the bed. On the contrary, the case of wustite mixed with CaO particles (W LP-10) gave a sharp decrease in pressure drop. In order to discuss the effect of the existing state of CaO component on the pressure drop, photos of the vertical cross sections of (W ACP-35) and (W LP-10) after sintering are shown in Fig. 6. In the case of (W ACP-35), white balls and black particles outlined by white dotted circles are mainly observed. These are alumina balls and wustite particles, respectively. Wustite particles are remained as their initial shapes and the adhering layers of ACP does not seem to be deformed. On the other hand, wustite particles of (W LP-10) were melted and residual CaO particles are hardly observed. Further, large blocks formed at bottom of sample bed, which were originated from the melt of wustite and CaO. It suggests that a certain size of CaO particles, in other words, segregation of CaO component in the order of its particle size promotes the melt formation and rearrangement of bed structure during sintering.
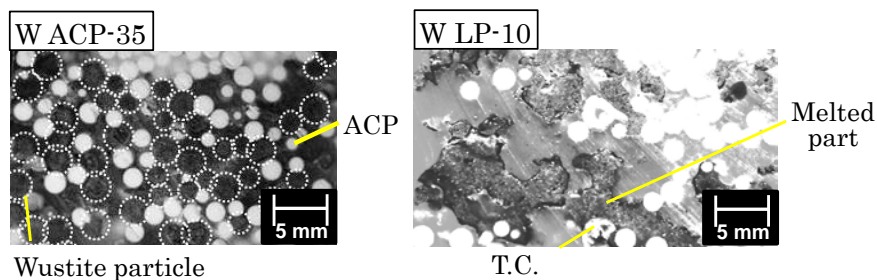
Fig. 6 Cross sectional photos of sample bed after reaction in the cases using Wustite (W ACP-35 and LP-10)

Large differences in pressure drop profiles shown in Fig. 5 seems to be attributed to differences among the sample bed structures. In the case of (W ACP-35), bed structure did not significantly change and therefore the pressure drop mainly depended on the bed temperature. While, in the case of (W LP-10), melt formation and its flow led to a remarkable structural change of the bed like the case using metallic iron particles[8]. This seems to be the reason of its significant decrease in the pressure drop. Succeeding increase in the pressure drop may be
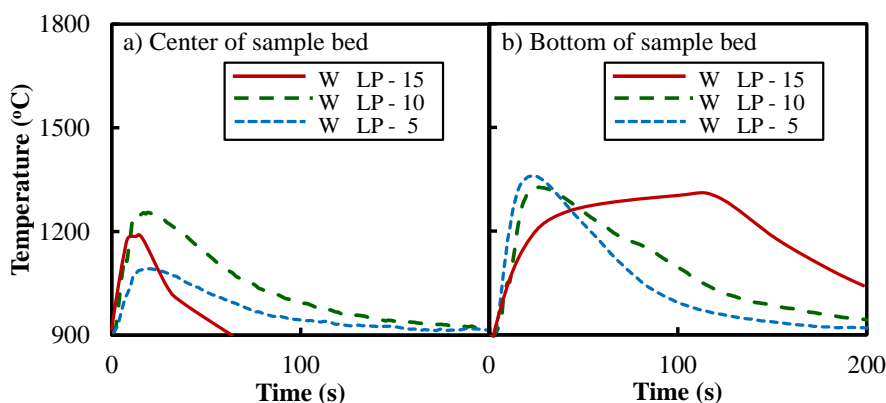
Fig. 7 Changes in the sample bed temperature, a)center and b)bottom, for the cases using Wustite (W LP-15, W LP-10 and W LP-5)

caused by the blocking of the gas flow path by the large blocks formed at the bottom of the bed. An excess amount of melt formation will bring about similar phenomenon in the sintering bed.

The results shows the possibility to utilize wustite component as an effective heat source in the sintering bed by controlling the existing state of CaO component. Figure 7 shows temperature profiles of sample bed at center and bottom in the cases using wustite mixed with CaO particles when varying average CaO concentration in three levels. In the case of 10 mass%-CaO (W LP-10), the center and bottom temperatures reached to 1250 and 1320°C, respectively, and then both decreased gradually. When CaO concentration decreased to 5 mass% (W LP-5), maximum temperature at the bed

Fig. 8 Changes in the reaction ratio of wustite for the cases of "W LP-15", "W LP-10" and "W LP-5"

center decreased to 1100°C, while in the case of (W LP-15), the bottom bed temperature shows a unique shape showing longer holding time at high temperature. Estimated reaction ratios of wustite for these cases are shown in Fig. 8. It increased with an increase in the amount of CaO particle addition. Their vertical cross section images of the sample bed after experiment are shown in Fig. 9. In the case of (W LP-5), many particles were remained un-melted, while a

Fig. 9 Cross sectional photos of sample bed after reaction in the cases using wustite and CaO particles, "W LP-5", "W LP-10" and "W LP-15"

certain amount of melt was generated to form agglomerates in the case of (W LP-10). Large melted blocks were also observed at the bottom part of sample bed in the case of (W LP-15). It shows that a large amount of melt flowed down to the bed bottom. Changes in pressure drop of the sample bed observed for the above mentioned cases are shown in Fig. 10. In all the cases, pressure drop once decreased after the initial increases and then increased again. The second increase is larger in higher CaO compositions. Such a phenomenon was also observed in the case using metallic iron particles (see Fe ACP-25 in Fig. 5) and it can be
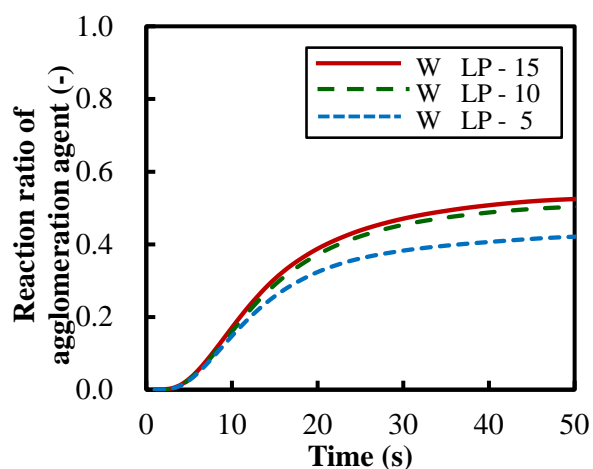
Fig. 10 Changes in pressure drop of sample and alumina beds observed for the cases using wustite and CaO particles, "W LP-5", "W LP-10" and "W LP-15"

explained as that the gas flow paths were blocked by the bulk melt flown down to the bed bottom[8].

When wustie particles were used, it is necessary to first consider CaO–FeO–Fe_2O_3 diagram. It is because a part of Fe^{2+} of wustite particles is oxidized to Fe^{3+} component during the process. Figure 11 is a diagram calculated by using FactSage. In the course of the oxidation of wustite particles, magnetite may first form on their surfaces. When it contacts with CaO component, melt forms in the region of around 20 mass%CaO at the temperature as low as 1200°C. In addition, even if the oxidation of iron oxide further proceeds, CaO concentration corresponding to the low temperature melting region does not change significantly. Therefore, melt can stably exists during the oxidation process to hematite. The maximum bed temperature of the case (W ACP-15) did not reach to 1350°C and that of the case (W ACP-35) at the bottom bed did not reach to 1200°C. Therefore, structural change of the bed hardly occurred in both cases. The addition of CaO particles, however, can provide local composition of about 20 mass%-CaO and surrounding CaO and iron oxide components will fuse into the formed melt by keeping the composition. It may be a reason a large melt formation occurred in the case (W LP-15).
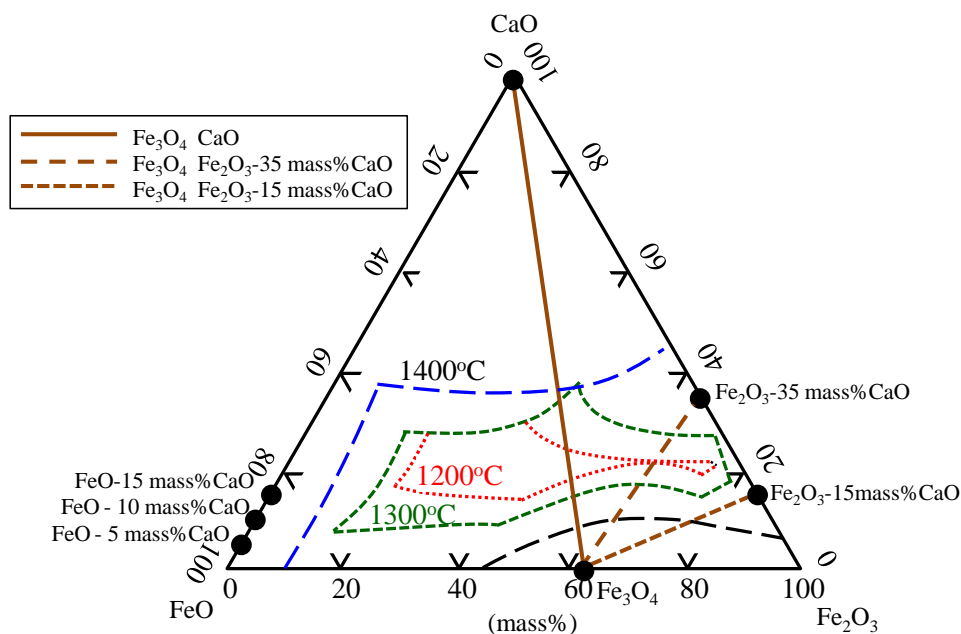
Fig. 11 Ternary diagram of CaO - FeO - Fe_2O_3 system

Melt formation promotes both the structural change of bed and the oxidation reaction of iron oxides. Therefore, it is necessary to properly control the local CaO composition in the vicinity of wustite particles. Controls of size distribution and existing state of CaO components will be principal keys for it.

References:

1) R. Lovel, K. Vining and K. Dell'Amico: *Sect. C: Miner. Process. Extr. Metall.*, 2(2009), 618

2) C. O. Tze, A. Eric, C. R. E. Burce, T. Dennis, R. A. David, F. Ray, F. Trevor and T. Donna: *Miner. Eng.*, 8 (2008), 167

3) M. Nakano, T. Yamanaka, N. Hayakawa and M. Nagabuchi: *ISIJ Int.*, 38 (1998), 16

4) M. Fujimoto, T. Inazumi and Y. Okuno: *CAMP-ISIJ*, 7 (1994), 143

5) K. Nakayama: *Kinzokusigen Rep.*, 42 (2012), 595

6) K. Takihira, N. Fujii and Y. Konishi: *CAMP-ISIJ*, 8 (1995), 913

7) E. Kasai, J. Yagi and Y. Omori: *Tetsu-to-Hagané*, 70 (1984), 1567

8) K. Fujino, T. Murakami and E. Kasai: *ISIJ Int.*, 53 (2013), 1617

Interfacial Properties Related to Iron & Steelmaking

Masashi Nakamoto[1] and Toshihiro Tanaka[2]
1 Low Temperature center, Osaka University
2 Graduate School of Engineering, Osaka University

Abstract: In high temperature iron and steelmaking processes where liquid Fe, molten slag/flux and solid oxides exist, many kinds of phenomena resulting from the existence of the interface between these substances, i.e. the interfacial tension between these substances, are founded. Then, in general, it has been known that the efficiency of processes and the quality of steel products are influenced by the interfacial phenomena and the accompanying events. Therefore, considerable effort to figure out the interfacial phenomena occurred in ironmaking and steelmaking processes and clarify the true value of interfacial tension itself have been devoted by many researchers so far in order to realize the sophistication of ironmaking and steelmaking processes. Here, we introduce the outcome of our recent researches related to the interfacial tension between liquid Fe alloy, molten slag/flux and solid oxide, and those interfacial phenomena. Thus, we report the topic on the engulfment behavior of liquid iron by molten slag/flux for the measurement of those interfacial tension by the oscillating droplet technique with their core-shell droplet in international space station, and effect of interfacial properties on neck growth of alumina particles at sintering in molten iron etc.

1. Introduction

In iron & steelmaking processes, liquid iron (hot metal and liquid steel) coexist with molten slag & flux or solid oxide[1,2]. The phenomena like reactions and emulsification between them have a huge effect on the processes. Recently, the optimization of operation technologies including environmental aspects is expected, which enhances a demand for understanding unclarified interfacial phenomena. Contrary to its importance, the interfacial properties like interfacial tension have not been investigated very much in comparison with the surface tension for liquid Fe-based alloy and molten slag & flux because of a difficulty on measurement. In addition, the large differences in available results have prevented the comprehension of interfacial phenomena between liquid iron and molten slag & flux or solid oxide.

To solve this issue, we plan to measure the interfacial tension between molten iron and molten slag & flux by oscillating droplet technique with iron/slag & flux core-shell droplet sample in international space station (ISS). One of the essential experimental conditions is the perfect engulfment of liquid iron by molten slag & flux. Therefore, we have evaluated the engulfment of liquid iron by molten slag & flux. In addition, the interfacial phenomena between liquid iron and solid oxide such as inclusions, i.e. adhesion, agglomeration and coalescence of inclusions on the immersion nozzle in a continuous casting process, have been discussed from the viewpoints of how the interfacial tension and wettability as statistic properties affect dynamic phenomena such as agglomeration. Hence, we have investigated the neck growth of alumina particles at sintering in liquid iron to clarify the effects of their interfacial properties, viz. interfacial tension and wettability, on the adhesion, agglomeration and coalescence of inclusions.

2. Engulfment of liquid iron by molten slag & flux[3]

Electrolytic iron powder was used as metal sample. Blast furnace slag (BF slag) and commercially available welding ilmenite type flux (IL flux) were used as slag & flux sample. BF slag is mainly SiO_2-CaO-MgO-Al_2O_3 system. IL flux consists of $FeTiO_3$, $KAlSi_3O_8$, Fe-Mn alloy, SiO_2, Talc, lime stone, MnO_2 and starch etc. as shown in **Table 1**. Iron powder and the powdered slag & flux are mixed and pressed to make a compact with 10 mmϕ and 7mm height (**Figure 1**). The compact was melted in arc furnace for 30 s in each side of compact (upper and lower).

Table 1. An example of constituents of ilmenite type flux (mass%). IL flux: ilmenite type coating flux. Ilmenite: $FeTiO_3$, orthoclase: $KAlSi_3O_8$, quartz: SiO_2, talc: $Mg_3Si_4O_{10}(OH)_2$, lime stone: $CaCO_3$, starch: $(C_6H_{10}O_5)_n$.

	Ilmenite	Orthoclase	Fe-Mn	Quartz
IL flux	35	16	15	10
	Talc	Lime stone	MnO_2	Starch
	8	6	5	5
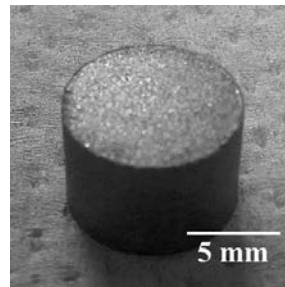
Figure 1. Appearance of compact prepared by pressing the mixture of electrolytic Fe powder and BF slag powder.

Figure 2 shows the appearance of samples with a) BF slag and b) IL flux after arc melting. In BF slag sample, iron is partly covered with slag. On the other hand, iron is totally engulfed by flux to create a metal/flux core-shell droplet in IL flux sample. This means that IL flux is suitable for the measurement of interfacial tension between liquid iron and molten slag & flux by oscillating droplet technique in ISS. Elemental analysis of slag and flux after arc melting by energy dispersive X-ray spectroscopy was conducted. The result of analysis is shown in **Table 2**. IL flux contains Fe oxide, Ti oxide and Mn oxide, which can lead to the good wettability of molten flux to liquid iron and the decrease of interfacial tension between liquid iron and molten slag[1].

Then, we conducted the calculation of morphologies of a double droplet of liquid Fe and molten slag by focusing on spreading coefficient, S_{Slag}[4,5].

$$S_{Slag} = \gamma_{Metal} - (\gamma_{Slag} + \gamma_{Metal/Slag}) \qquad (1)$$

where γ_{Metal}, γ_{Slag}, $\gamma_{Metal/Slag}$ are surface tension for liquid metal, surface tension for molten slag and interfacial tension between liquid metal and molten slag. Figure 3 shows the calculated morphologies of a double droplet of liquid Fe and molten slag at the different S_{Slag}. Liquid iron is engulfed by molten slag in case of $S_{Slag} > 0$ while liquid iron is partly covered with molten

slag in case of $S_{Slag} < 0$. From this result, we found that the engulfment behavior of liquid iron by molten slag is roughly evaluated based on spreading coefficient, S_{Slag}.
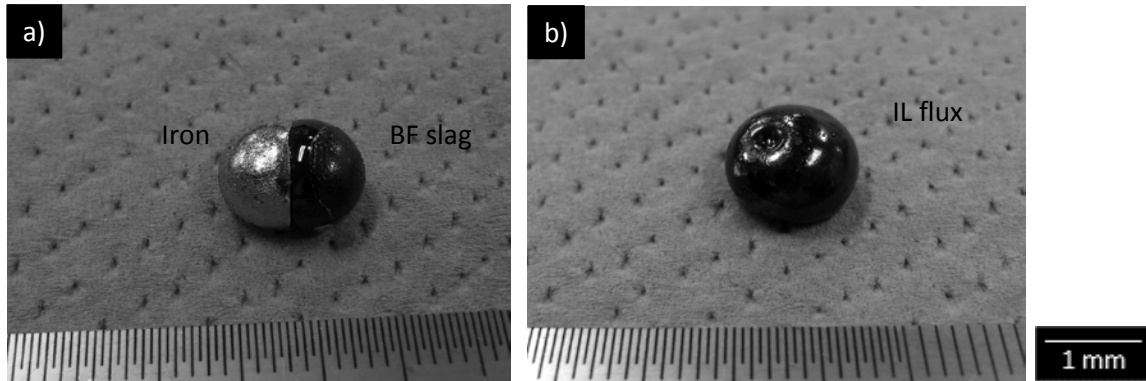
Figure 2. Appearance of samples after arc melting. a) BF slag sample and b) IL flux sample.

Table 2 Elemental analysis of slag and fluxes after arc melting by energy dispersive X-ray spectroscopy (mass%).

	O	F	Ca	Si	Al	Mg	Na	K	Ti	Mn	Fe
BF slag	33.6		25.0	13.8	7.1	4.0			1.3	1.4	13.8
IL flux	27.9		6.2	11.4	2.3	2.1	1.0	1.0	18.3	13.0	16.8
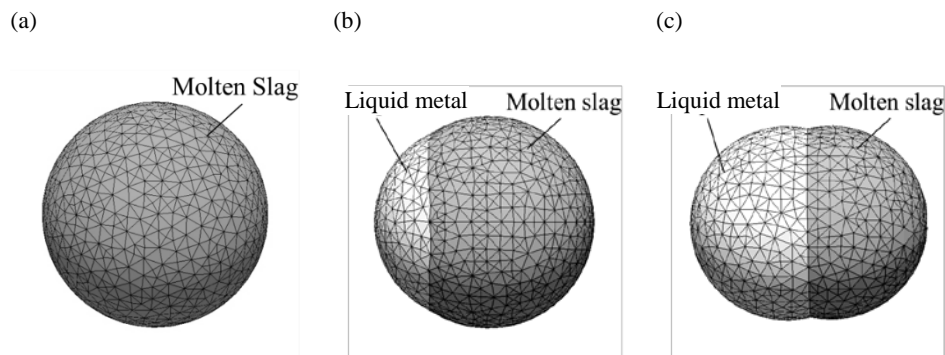
Figure 3. Calculated morphologies of a double droplet of liquid metal and molten slag at the different S_{Slag}. S_{Slag} are (a) 110, (b) -7 and (c) -69. The snapshots are from the numerical surface energy minimization performed with a free software "Surface Evolver" [6, 7].

3. Effect of Interfacial Properties on Neck Growth of Alumina Particles at Sintering in Liquid Iron[8]

The appearances of the alumina balls kept a) under Ar gas atmosphere for 24 h holding time and b) in liquid iron for 10 h holding time are shown in **Figure 4** as examples. Two alumina balls are stuck together in both case, which means that sintering of the alumina balls occurs. The neck diameter of all the samples plotted against holding time are shown in **Figure 5**. The neck diameter of the sample kept under conditions of temperature 1773 K under an Ar gas atmosphere increases with increasing time, *i.e.*, sintering of the alumina balls proceeds with time. The neck growth in liquid iron at 1773 K is much faster than that in an Ar gas atmosphere at 1773 K. These results show that neck growth between alumina balls, *i.e.*, sintering between alumina balls, in liquid iron is faster than in an Ar gas atmosphere.
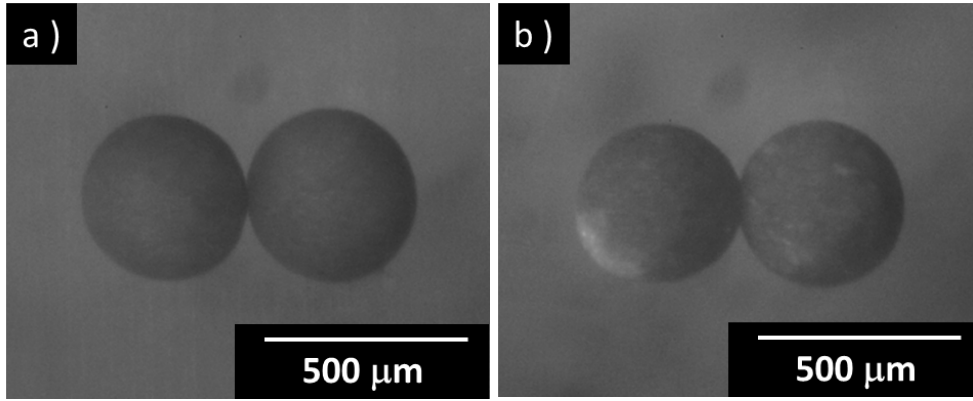
Figure 4. Appearances of alumina balls after sintering. a) Under Ar gas atmosphere for 24 h holding time and b) in liquid iron for 10 h holding time.

The sintering mechanism of alumina balls in this study was regarded as volume diffusion based on the value of m, which is botained by plotting the logarithm of neck radius against the logarithm of holding time and determining the slope $1/m = 0.228$, assuming that a and $A(T)$ are constant[9-11]. A temperature-dependent constant $A(T)$ is given as Eq. (2).

$$A(T) = \frac{K\gamma_s V_0 D}{RT} \quad (2)$$

where K is a constant depending on the geometry of the sample and on the diffusion path, γ_s is the surface tension of the material, V_0 is the molar volume, D is the self-diffusion coefficient of the material, R is the gas constant, and T is the temperature. The relationship between the neck radius and time is expressed as

$$x = \left(\frac{a^n K\gamma_s V_0 D}{RT}\right)^{0.228} \cdot t^{0.228} \quad (3)$$

where a is the radius of the paticle and n is the constant for sintering mechanism. When fitting Eq. (3) to the time dependence of the neck radius under an Ar gas atmosphere at 1773 K,

$$\left(\frac{a^n K\gamma_s V_0 D_{1773}}{RT}\right)^{0.228}\bigg|_{Ar,1773K} = 15.6 \quad (4)$$

was obtained. The fitting curve is in good agreement with the experimental data in **Fig. 5**.
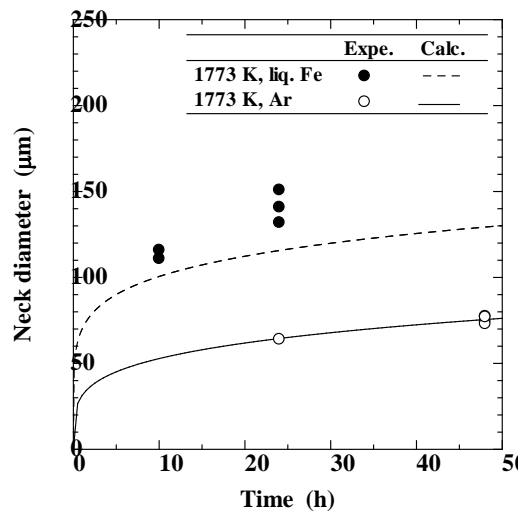
Figure 5. Relationship between neck diameter and time. Comparison of neck radius changes in experiments and neck diameter changes calculated by considering the wettability of liquid iron/alumina.
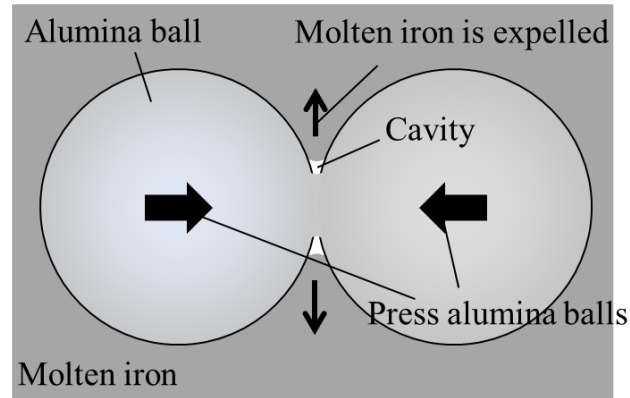
Figure 6. Illustration of sintering promotion mechanism for alumina balls in liquid iron.

We tried to formulate the equation for neck growth of particles in a liquid that includes the effect of wettability between a particle and a liquid on the interactive force acting on the particles because a liquid tends to be extracted from the gap between particles when the particles in the liquid contact each other and the liquid does not wet the particle, i.e. the relationship between liquid iron and solid alumina, as shown in **Figure 6**[12-14]. The interactive force generated by wettability was evaluated by considering that this behavior is attributable to capillary phenomena, *i.e.* capillary forces. Here, it is assumed that at the microscale, the capillary phenomena at the gap between particles are same as those between two plates. Then, the expression for the neck growth of particles at sintering under pressure was derived as Eq. (5):

$$x = \left(\frac{a^n K \gamma_S V_0 D}{RT}\right)^{0.228} \left\{1 + \left(-\frac{4 a \gamma_L \cdot \cos\theta}{x^2}\right) \cdot \frac{a}{\pi \gamma_S}\right\}^{0.228} \cdot t^{0.228} \quad (5)$$

where $(a^n K \gamma_S V_0 D/RT)^{0.228}$ is $(a^n K \gamma_S V_0 D/RT)^{0.228}|_{\text{Ar},1773\text{K}} = 15.6$. Equation (5) means that the neck growth of particles at sintering in liquid iron under the pressure of capillary phenomena can be calculated when the surface tension of the liquid, γ_L, the contact angle between the liquid and a particle, θ, the radius of the particle, a, and the surface tension of the particle material, γ_S, are known. The calculated neck growth curve based on Eq. (5) is shown in **Figure 5**. The available data for $\gamma_L(1925 \text{ mN/m})$, $\theta(130°)$ and $\gamma_S(997.5 \text{ mN/m})$ in references[15-17] are used, and the value of $a(160 \text{ μm})$ is obtained based on the observation of alumina balls in the experiment. The equation was numerically solved because the variable x is included in both sides of the equation. The calculation results obtained by considering the wettability roughly reproduced the time dependence of the neck radius of alumina particles in liquid iron without any meaningless parameters. This result concludes that the promotion of sintering of alumina ball in liquid iron attributes to the bad wetting of liquid iron on solid alumina.

References:

1) K. Ogino, *Kouon Kaimen Kagaku*, Agne Gijutsu Center Inc., Tokyo, 2008 (in Japanese).

2) Nippon Steel Corp. (Editor), *Tetsu to Tekkou ga Wakaru Hon*, Nippon Jitsugyo Publishing, Tokyo, 2004 (in Japanese).

3) M. Nakamoto, H. Goto, M. Suzuki and T. Tanaka, Evaluation of Engulfment of Molten Iron by Molten Slag/Flux for Preparation of their Core-shell Droplet, *Int. J. Microgravity Sci. Appl.* 32, (2015), 320103.

4) S. Torza and S. G. Mason, Coalescence of two immiscible liquid drops, Science, 163 (1969) 813.

5) J. Guzowski, P.M. Korczyk, S. Jakiela and P. Garstecki, Effects of unsteadiness of the rates of flow on the dynamics of formation of droplets in microfluidic systems, *Soft Matter*, 8 (2012) 7269.

6) K.A. Brakke, The surface evolver, *Experimental Mathematics*, 1 (1992) 141.

7) J. Berthier and K.A. Brakke, The Physics of Microdroplets, Scrivener Publishing, Massachusetts, 2012.

8) M. Nakamoto, T. Tanaka, M. Suzuki, K. Taguchi, Y. Tsukaguchi and T. Yamamoto, Effects of interfacial properties between molten iron and alumina on neck growth of alumina balls at sintering in molten iron, *ISIJ Int.*, 54 (2014), 1195-1203.

9) H. Ichinose and G.C. Kuczynski, Self-diffusion in sintering of metallic particles, *Acta Mater.*, 10 (1962), 209.

10) D.L. Johnson and I.B. Cutler, Diffusion Sintering: II, Initial Sintering Kinetics of Alumina, *Powder J. Am. Ceram. Soc.*, 46 (1963), 541.

11) I.I. Spivak, R.A. Andrievskii and K.L. Chevasheva, A model investigation of the sintering of zirconium, *Powder Metall. Metal Ceram.*, 7 (1968), 458.

12) S. N. Singh, Morphology of alumina deposits from aluminum-killed steel frozen in a constricted nozzle, *Metall. Trans.*, 5 (1974), 2165.

13) V. H. Knuppel, K. Brotzmann and N. W. Forster, Untersuchungen über oxydische Vereinreinigungen in aluminiumberuhigten weichen Stählen, *Stahl Eisen*, 85 (1965), 675.

14) V. V. Yaminsky, V. S. Yushchenko, E. A. Amelina and E. D. Shchukin, Cavity formation due to a contact between particles in a non-wetting liquid, *J. Coll. Int. Sci.*, 96 (1983), 301.

15) B. J. Keene, Review of data for the surface tension of pure metals, *Int. Mater. Rev.*, 38 (1993), 157.

16) B. J. Keene, Review of Data for the Surface Tension of Iron and Its Binary Alloys, *Int. Mater. Rev.*, 33 (1988), 1.

17) B. J. Keene, Slag Atlas 2nd ed., Verlag Sthleisen GmbH, Düesseldorf, (1995), 513.

Recent Iron-making Operation in NSSMC

Yoshifumi MORIZANE and Hisashi KUMAOKA
Ironmaking Division, Muroran Works, Nippon Steel & Sumitomo Metal Corporation

Abstract: Nippon Steel & Sumitomo Metal Corporation (NSSMC) and their group companies have been trying to introduce new and innovative technologies, including technologies to use low-grade raw materials, measures to prolong the service life of blast furnaces and coke ovens, etc., in the field of ironmaking. This report outlines the condition of production and technical development in ironmaking technologies in NSSMC.

1. Changes of Production Structure in Japanese Steel Making Industry

The trends of the number of operating blast furnaces in Japan and their inner volume (IV) are shown in Figure 1. The size of the Japanese blast furnace has been expanded again since 2000 on the occasions of their relining to respond to the needs for production increase: for example, Oita No.1 and No. 2 blast furnaces were enlarged from 4,884 m^3 and 5,245 m^3, respectively, to 5,775 m^3 (at present, the largest blast furnaces in Japan). The number of furnaces has been decreased from 61 in 1973 to 27 in 2016.
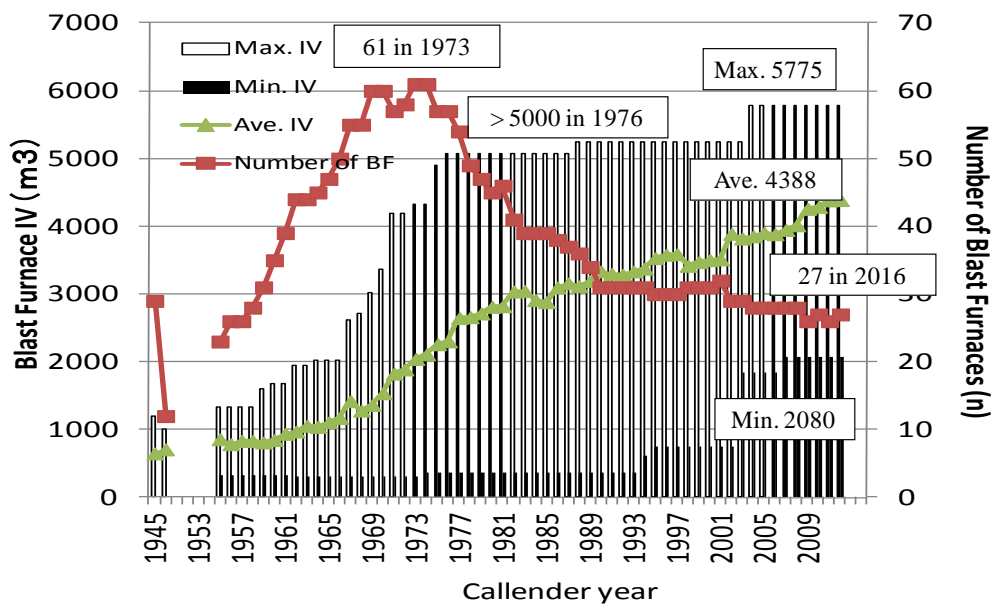
Figure 1. Trend of the number of blast furnaces in Japan and their inner volume

2. Changes of Iron-making Operation in NSSMC
2.1. Blast Furnace

Former Nippon Steel Corporation (NSC) and Sumitomo Metal Industries, Ltd. (SMI) were merged in October 2012, and Nippon Steel & Sumitomo Metal Corporation (NSSMC) was established, which is the second largest steel making company in the world. The location of 13 blast furnaces working in the steel mills of NSSMC group is shown in Figure 2. The capability of annual production is about 46 million tons. In order to promote production efficiency, Kimitsu No. 3 blast furnace was shut down in March 2016. Also, Kokura No. 2 blast furnace is scheduled to be shut down at the end of 2020 fiscal year. As the number of blast furnaces is decreased, the higher productivity of each furnace is required in NSSMC.

BF	I.V.	'12.5.28~	'12.10~	'14.4.20~	'16.3.12~
Tobata 4BF	4,250	4,250	4,250	5,000	5,000
Nagoya 1BF	5,443	5,443	5,443	5,443	5,443
Nagoya 3BF	4,300	4,300	4,300	4,300	4,300
Kimitsu 2BF	3,273	4,500	4,500	4,500	4,500
Kimitsu 3BF	4,822	4,822	4,822	4,822	Blow-off
Kimitsu 4BF	5,555	5,555	5,555	5,555	5,555
Oita 1BF	5,775	5,775	5,775	5,775	5,775
Oita 2BF	5,775	5,775	5,775	5,775	5,775
Muroran 2BF	2,902	2,902	2,902	2,902	2,902
Kokura 2BF			2,150	2,150	2,150
Kashima 1BF			5,370	5,370	5,370
Kashima 3BF			5,370	5,370	5,370
Wakayama 1BF			3,700	3,700	3,700
Wakayama 5BF			2,700	2,700	2,700
NSSMC Total	**42,095**	**43,322**	**62,612**	**63,362**	**58,540**

NSC ⎫
SMI ⎬ Merged (October 2012)
Nisshin Steel * 1

Muroran 2BF 2,902m³

Kashima 1BF 5,370m³
3BF 5,370m³

Kokura 2BF
2,150m³→Blow-off
(end of '20 fy)

Nagoya 1BF 5,443m³
3BF 4,300m³

Kimitsu 2BF 3,273m³→4,500m³ (May 2012)
3BF 4,822m³→Blow-off (March 2016)
4BF 5,555m³

Tobata 4BF
4,250m³→5,000m³ (April 2014)

Oita 1BF 5,775m³
2BF 5,775m³

Kure 1BF 2,650m³→Relining ('19)
2BF 2,080m³→Blow-off ('19)

Wakayama 1BF 3,700m³
5BF 2,700m³

*1 Procedures to make Nisshin Steel Co., Ltd. (Nisshin Steel) a subsidiary of NSSMC have been completed on March 13, 2017.

Figure 2. Blast furnaces Working in NSSMC group's Steel Works

Figures 3, 4 and 5 show the trends of productivity, coke ratio and reducing agent ratio, respectively, of NSSMC's blast furnaces after 2009 fy. And the relationship between inner volume of blast furnaces and the capability of pulverized coal injection (PCI) is shown in Figure 6. Former NSC has enlarged the capability of PCI and decreased coke ratio, so as to decrease the production cost and enhance the ability to respond to the change in raw materials quality. After NSSMC was established, the capability of PCI was enlarged in August 2016 at Kashima Works, which belonged to former SMI. And also, the enlargement of PCI capability is planned at former SMI's Wakayama Works in March 2017. After the enlargement of PCI capability, each works tries to decrease coke ratio.
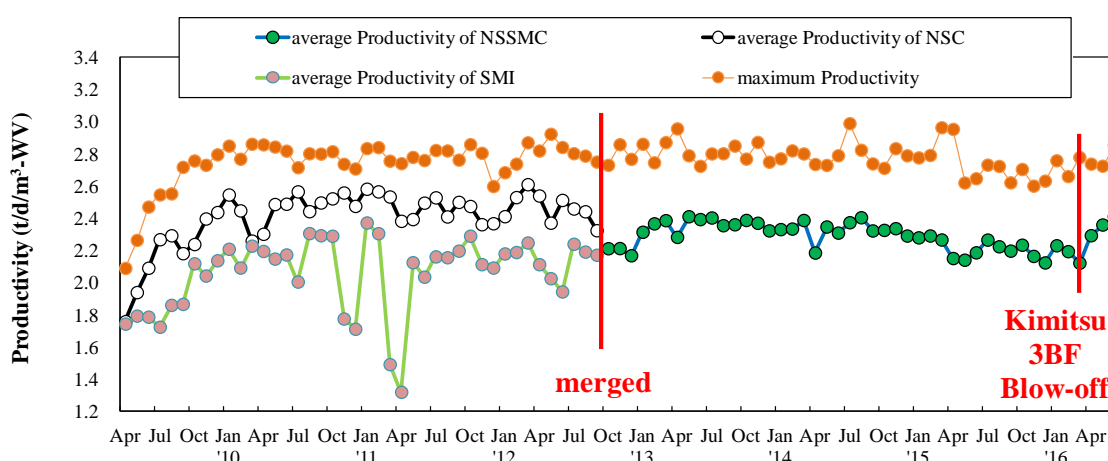
Figure 3. Trend of Blast Furnace Productivity

268
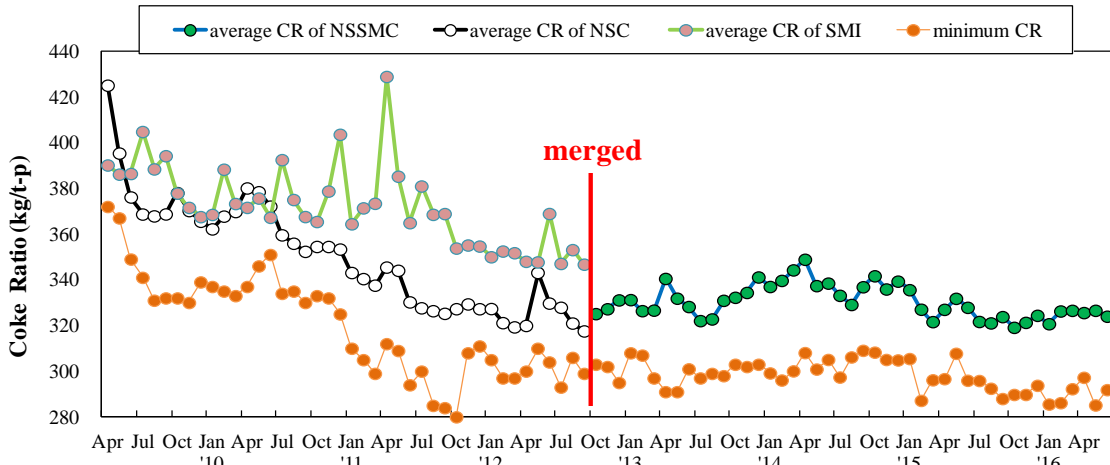
Figure 4. Trend of Blast Furnace Coke Ratio
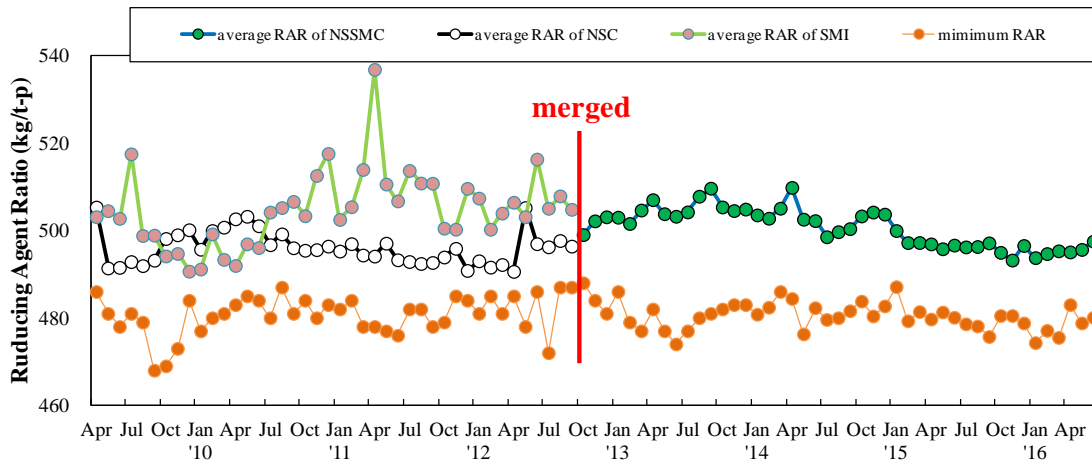
Figure 5. Trend of Blast Furnace Reducing Agent Ratio

M2: Muroran No. 2 BF
C2, C4: Kimitsu No. 2 & 4 BF
W1, W5: Wakayama No. 1 & 5 BF
T4: Tobata No. 4 BF

I1, I3: Kashima No. 1 & 3 BF
N1, N3: Nagoya No. 1 & 3 BF
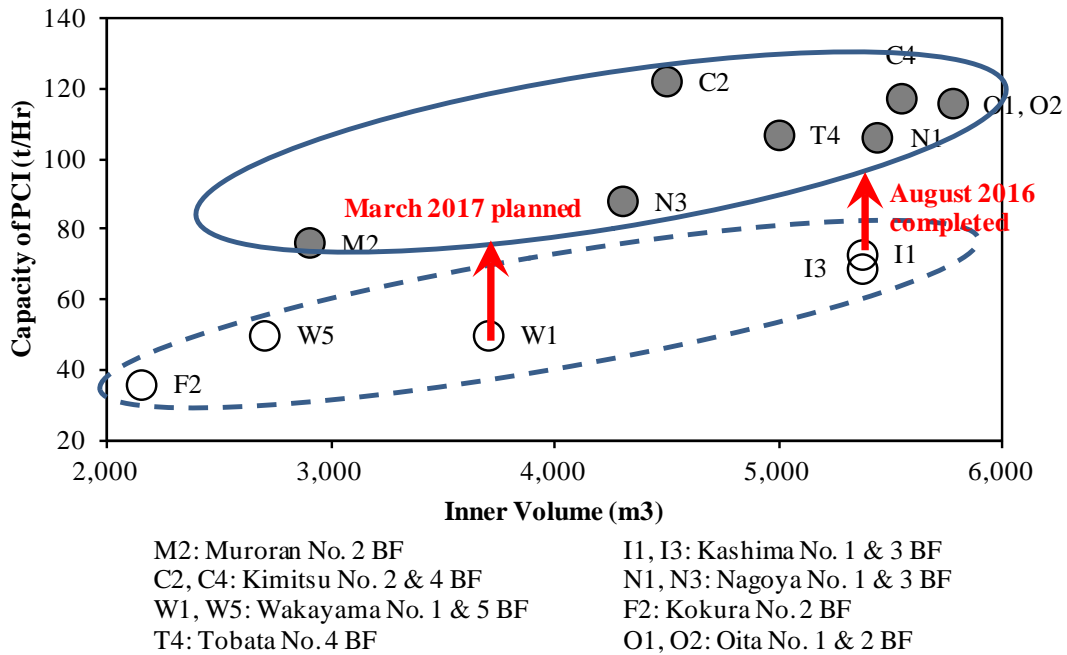F2: Kokura No. 2 BF
O1, O2: Oita No. 1 & 2 BF

Figure 6. Pulverized Coal Injection Capacity and Inner Volume of Blast Furnaces

2.2. Sintering Machine

The dimensions of operating sintering machines in NSSMC are shown in Table 1. And Figure 7 shows the trends of production, productivity, sintering area and availability of NSSMC's sintering machines. For few years, productivity has been decreased, because of the deterioration of iron ore quality. And because most plants have been working for long time, availability of sintering machines has been decreased in order to keep maintenance time. As the countermeasures for the sinter production, the sintering bed area has been expanded and production of sinter has been maintained.

Table 1. Sintering Machine Working in NSSMC

	Works	Plant No.	Width (m)	Length (m)	Area (m^2)	Productivity (t/day/m^2)	Start up
former NSC	Yawata	3	4.2	120	504	29.3	1,970
	Muroran	6	5.0	92	460	22.2	1,976
	Nagoya	1	4.0	66	265	27.2	1,964
		2	4.0	70	280	29.8	1,967
		3	4.2	100	420	30.3	1,969
	Kimitsu	1	3.5	61	211	32.1	1,968
		2	4.0	70	280	33.8	1,969
		3	5.5	127	700	31.1	1,971
	Oita	1	5.5	101	555	32.6	1,972
		2	5.5	120	660	30.0	1,976
Subtotal					4,335	29.8	
former SMI	Kashima	2	5.4	100	540	25.2	1,973
		3	5.0	120	600	24.7	1,977
	Wakayama	4	3.7	71	260	29.5	1,968
		5-1	2.5	49	122	33.5	1,969
		5-2	3.7	50	185		2,009
Subtotal					1,707	112.9	
NSSMC Total					6,042	53.3	

* Kokura No. 3 sintering machine of former SMI was shut down in November 2016.
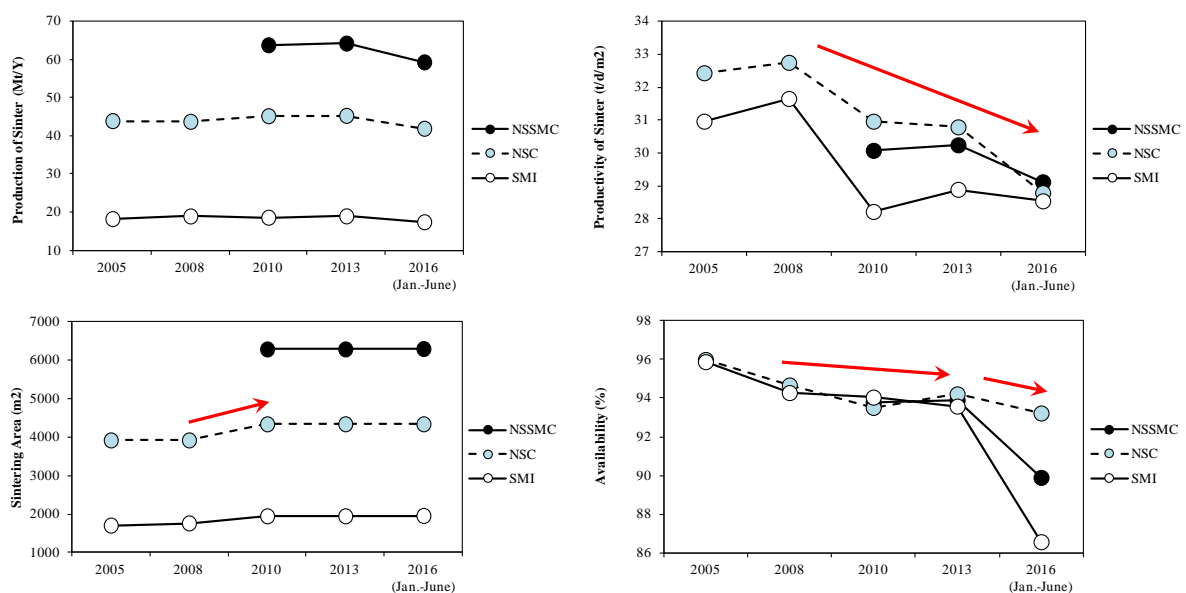

Figure 7. Trends of Sinter Production, Productivity, Sintering Area and Availability

2.3. Coke Oven

The dimensions of operating coke ovens in NSSMC are shown in Table 2. Twenty three batteries and 2,240 ovens have been working. Many batteries in NSSMC were constructed during the era of rapid economic growth in the 1970's, and some batteries have been already working for more than 40 years. As the result, as shown in Figure 8, the coke production has been decreased gradually in recent few years. In order to balance coke demand and supply in NSSMC, construction and repair plans of coke onens have been running at Kashima and Kimitsu Works, and the needs of coke ratio reduction has been increased.

Table 2. Coke Oven Plant Working in NSSMC

|	Works	Plant No.		number of Ovens	Types	Width (m)	Length (m)	Hight (m)	Charge Volume (m³)	Start up
former NSC	Yawata	4		90	NSC	0.400	13.40	4.00	18.1	1,965
		5		110	NSC M	0.450	15.70	6.00	37.6	1,970
	Muroran	5		100	NSC	0.430	14.20	5.00	27.1	1,969
		6		42	NSC	0.430	15.80	6.50	39.1	1,979
	Nagoya	1		100	DKH	0.450	13.59	5.00	27.1	1,964
		2		110	DKH	0.450	13.59	5.00	27.1	1,967
		4		100	NSC S	0.435	15.69	5.92	36.2	1,969
		5		64	SCOPE	0.450	16.60	6.70	43.7	2,013
	Kimitsu	1		90	NSC M	0.450	15.70	5.50	34.3	1,968
		2		95	NSC M	0.450	15.70	5.50	34.3	1,969
		3		100	NSC M	0.450	15.70	5.50	34.3	1,969
		4		92	NSC M	0.430	15.70	6.50	39.1	1,971
		5		92	NSC M	0.430	15.70	6.50	39.1	1,973
	Oita	1		78	NSC S	0.440	15.80	5.93	37.0	1,972
		2		78	NSC S	0.440	15.80	5.93	37.0	1,972
		3		82	NSC S	0.440	15.80	6.09	37.8	1,976
		4		82	NSC S	0.440	15.80	6.09	37.8	1,976
		5		64	SCOPE	0.450	16.60	6.70	43.7	2,008
	Subtotal	18		1,569					630.4	
former SMI	Kashima	1	ABCD	154	Sumitomo-Coppers	0.460	16.50	7.13	48.7	1,971
			E	40	Paul Wurth					2,011
		2	ABC	138	Sumitomo-Coppers	0.460	16.50	7.13	48.7	1,973
			D	41	Sumitomo-Coppers					1,981
	Wakayama	4		76	Sumitomo-Coppers	0.450	14.62	5.00	29.3	1,967
		5		92	Sumitomo-Coppers	0.450	14.62	5.00	29.3	1,967
		new 1		130	ACRE JN60	0.450	15.98	6.00	38.5	2,009
	Subtotal	5		671					194.5	
NSSMC Total		23		2,240					824.9	
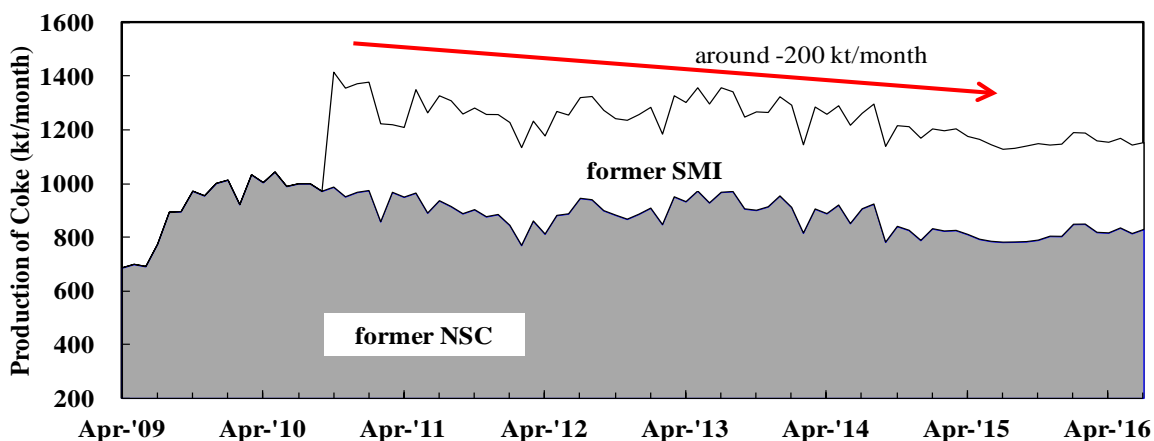
Figure 8. Trend of Coke Production

3. Topics on Blast Furnace

3.1. Relining of Tobata No. 4 Blast Furnace

The dimensions of Tobata No. 4 blast furnace before and after the relining in 2014 are shown in Figure 9. The characteristics of this relining are as follows:

(1) Enlargement of Inner Volume

Avoiding major modifications to the equipment from the standpoint of keeping the cost of relining within reasonable limits, the inner volume of the furnace was enlarged from 4250 m^3 to 5000 m^3.

(2) Change of Charging Equipment

In order to improve the controllability of burden distribution at the top of the furnace, the charging equipment was changed from bell top to bell-less top.

(3) Improvement of Shaft and Hearth Cooling System

So as to improve the cooling ability at the area, where the stave heat load is relatively high, copper staves were employed instead of ferrum casting ductile (FCD) staves. As the measure to obtain longer service life of the furnace, carbon block with titanium carbide (TiC) added was adopted.

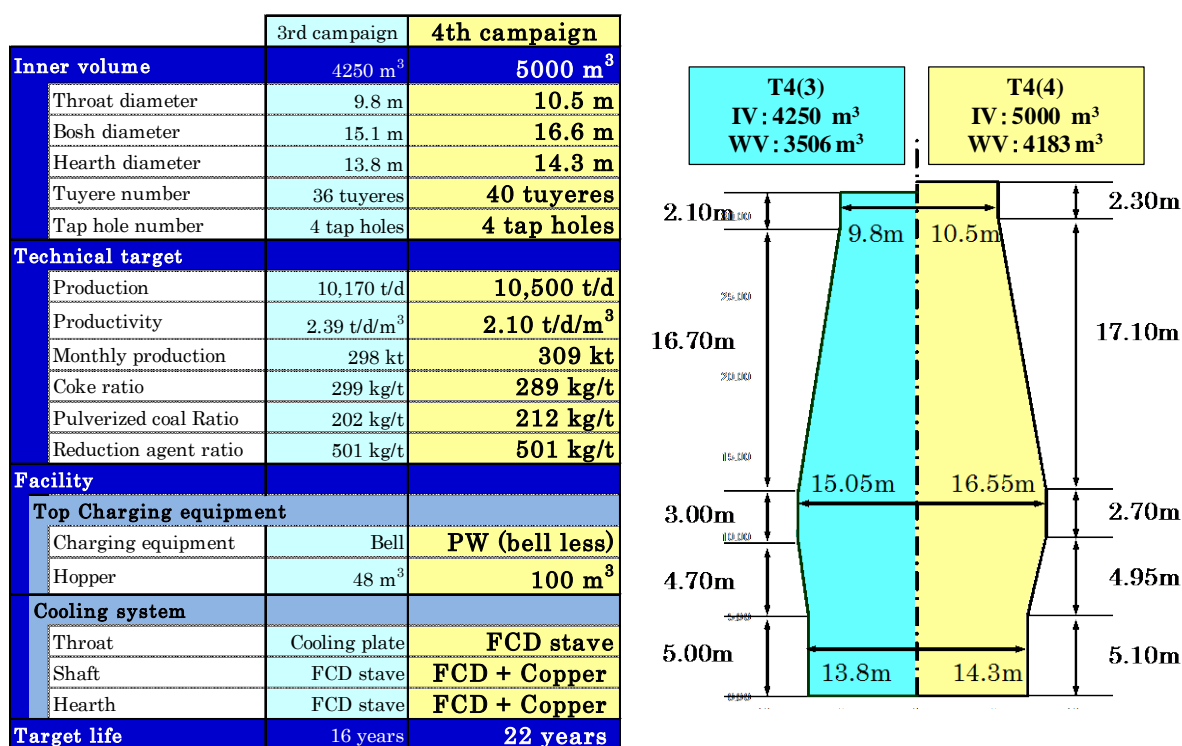The relining was completed in 85 days as scheduled.

	3rd campaign	4th campaign
Inner volume	4250 m^3	**5000 m^3**
Throat diameter	9.8 m	**10.5 m**
Bosh diameter	15.1 m	**16.6 m**
Hearth diameter	13.8 m	**14.3 m**
Tuyere number	36 tuyeres	**40 tuyeres**
Tap hole number	4 tap holes	**4 tap holes**
Technical target		
Production	10,170 t/d	**10,500 t/d**
Productivity	2.39 t/d/m^3	**2.10 t/d/m^3**
Monthly production	298 kt	**309 kt**
Coke ratio	299 kg/t	**289 kg/t**
Pulverized coal Ratio	202 kg/t	**212 kg/t**
Reduction agent ratio	501 kg/t	**501 kg/t**
Facility		
Top Charging equipment		
Charging equipment	Bell	**PW (bell less)**
Hopper	48 m^3	**100 m^3**
Cooling system		
Throat	Cooling plate	**FCD stave**
Shaft	FCD stave	**FCD + Copper**
Hearth	FCD stave	**FCD + Copper**
Target life	16 years	**22 years**

Figure 9. Dimensions of Tobata No. 4 Blast Furnace before and after the Relining in 2014

Figure 10 shows the trends of the productivity, coke ratio and reducing agent ratio of Tobata No. 4 blast furnace after the blow-in in April 2014. As the result of consideration of the burden distribution at the top of the furnace, using simulation model and 1/3 scale model, the transition from bell top operation to bell-less top operation was smoothly completed. Pulverized coal injection was started at 8th day after blow-in, and coke ratio reached below 300 kg/t-pig at 1 and half month later. Increasing blast volume gradually, the productivity successfully reached 2.1 t/d/m^3 at 20th day after blow-in.
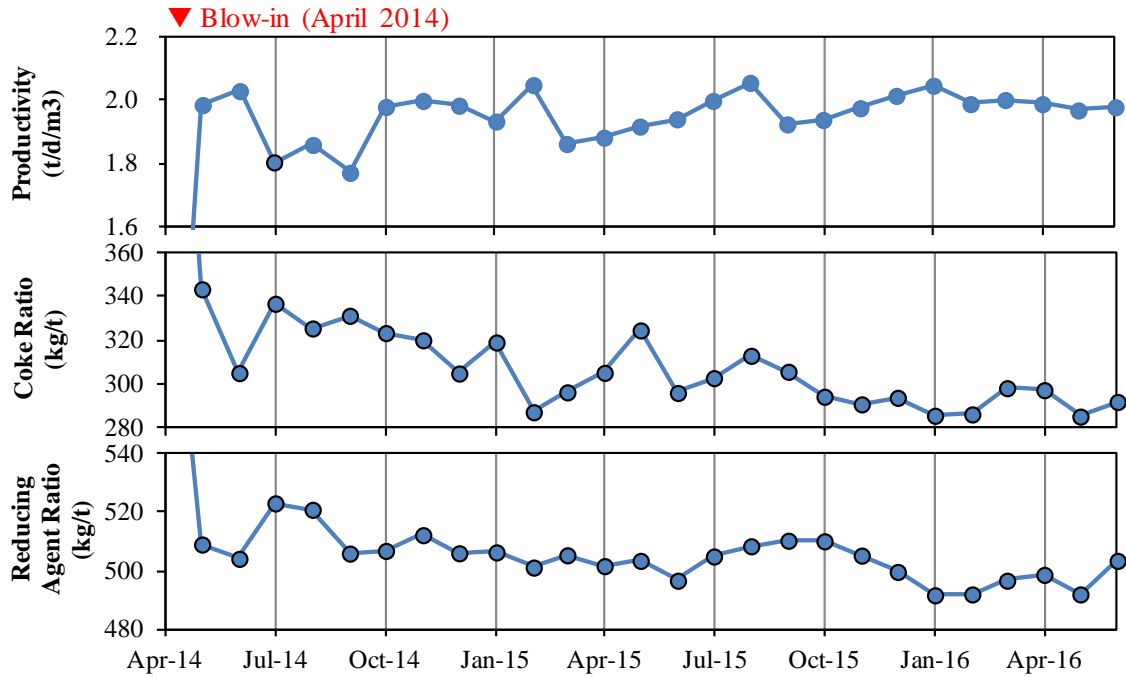
Figure 10. Trend of Tobata No. 4 Blast Furnace Operation after Blow-in in April 2014

3.2. High Productivity Operation at Kimitsu No. 2 Blast Furnace

The issues and measures against high productivity and low coke ratio operation of the blast furnace are shown in Figure 11. In high productivity operation of the blast furnace, because time for heating and reducing of materials inside the furnace is shortened, improvements of characteristics of materials, adjustment of burden distribution, and improvement of reducibility by using hydrogen as the reducer, for example, are required. Specific contents required in high productivity and low coke ratio operation of blast furnaces are summarized as follows:

(1) Burden distribution
- Keeping stable center gas flow
- Controllability and estimation of burden distribution
  - Accurate burden distribution model by Discrete Element Method (DEM), 1/3 scale model and highly accurate measurement
  - On-line profile meter
(2) Visualization technology
- Tuyere camera
- Blast furnace monitoring
(3) Automatic operation control system
(4) Permeability control
- Increasing O_2 enrichment ratio as a function of pulverized coal ratio (PCR)
- Coke quality; for example, minimizing standard deviation of Drum Index (DI)
(5) Reducibility
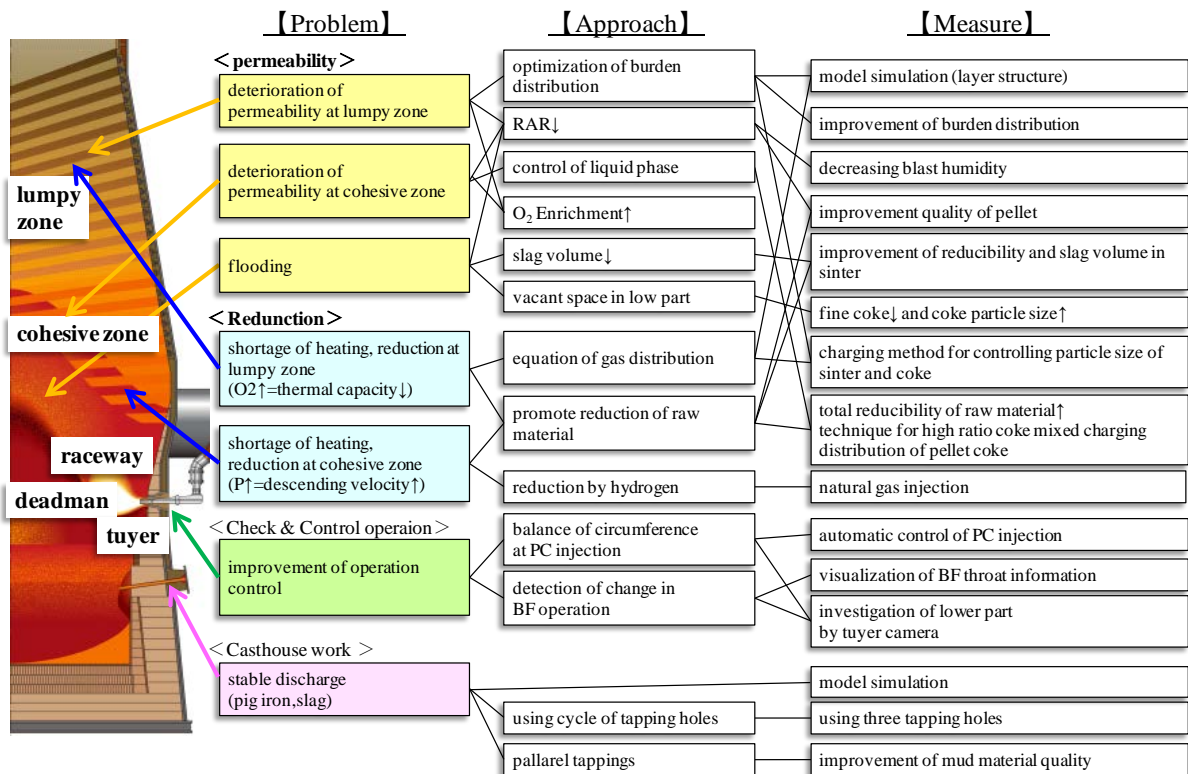- Reducibility property of iron-ore (sinter ore, pellet)
- Hydrogen reduction

Figure 11. Issues and Measures against High Productivity and Low Coke Ratio Operation

After the shut-down of Kimitsu No. 3 blast furnace in March 2016, trial to increase the productivity of Kimitsu No. 2 blast furnace up to 2.7 t/d/m^3 has been performed. This trial includes improvement of permeability and reducibility inside the furnace by adjusting burden distribution, and stabilization of iron and slag discharge in the hearth, etc. As shown in Figure 12, the productivity of Kimitsu No. 2 blast furnace has been kept 2.7 t/d/m^3 since the end of 2016.
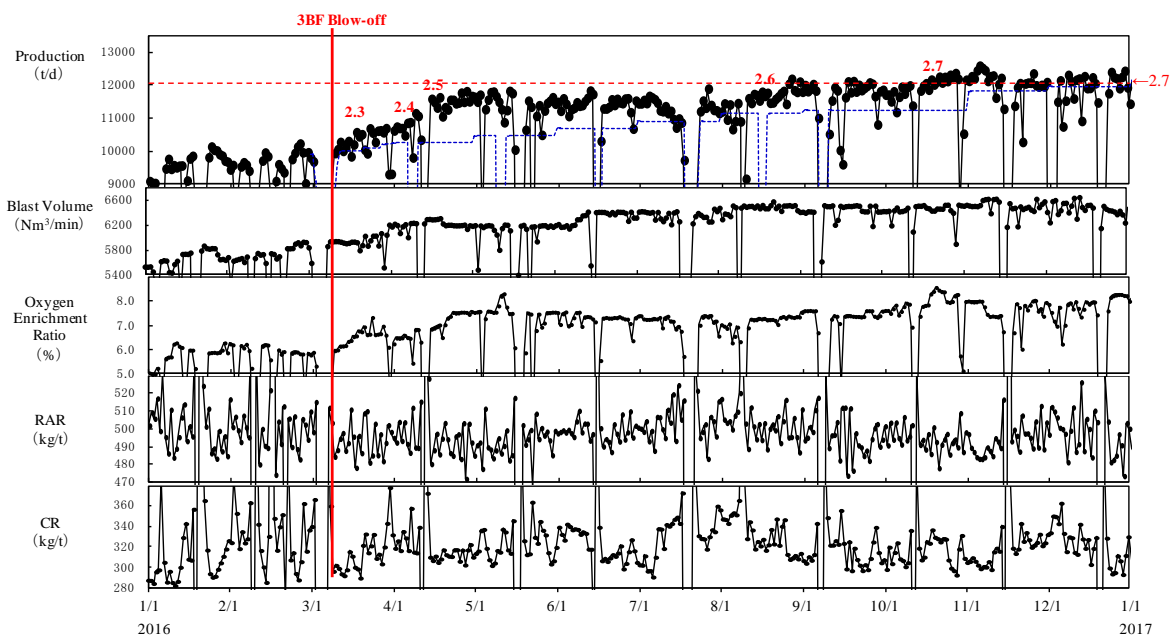

Figure 12. Trend of Kimitsu No. 2 Blast Furnace Operation

3.3.   Repairing the Blast Furnace Profile

At Wakayama No. 4 blast furnace (3rd generation), which was blown-in in February 1982 and whose inner volume was 2700 m^3, corruption of stave pipes was started in 1986. At that time, consideration of stave replacement technique during the campaign of the blast furnace was started. In March 1987, 4 shaft staves of Wakayama No. 4 blast furnace (3rd generation) was replaced during 69 hours and 50 minutes shut-down of the furnace for the first time in the country. Since then, stave replacement during furnace campaign has been performed at many other furnaces.

At Muroran No. 2 blast furnace, the number of corrupted stave pipes started to increase rapidly, suggesting the erosion of the furnace wall, in 2013. As the result of the change in inner wall profile of the furnace, the operation became unstable. In order to improve permeability and to stable gas flow inside the furnace, adjustment of burden distribution was tried. In spite of the trial, permeability remained unstable, and coke ratio had been over 300 kg/t, as shown in Figure 13.
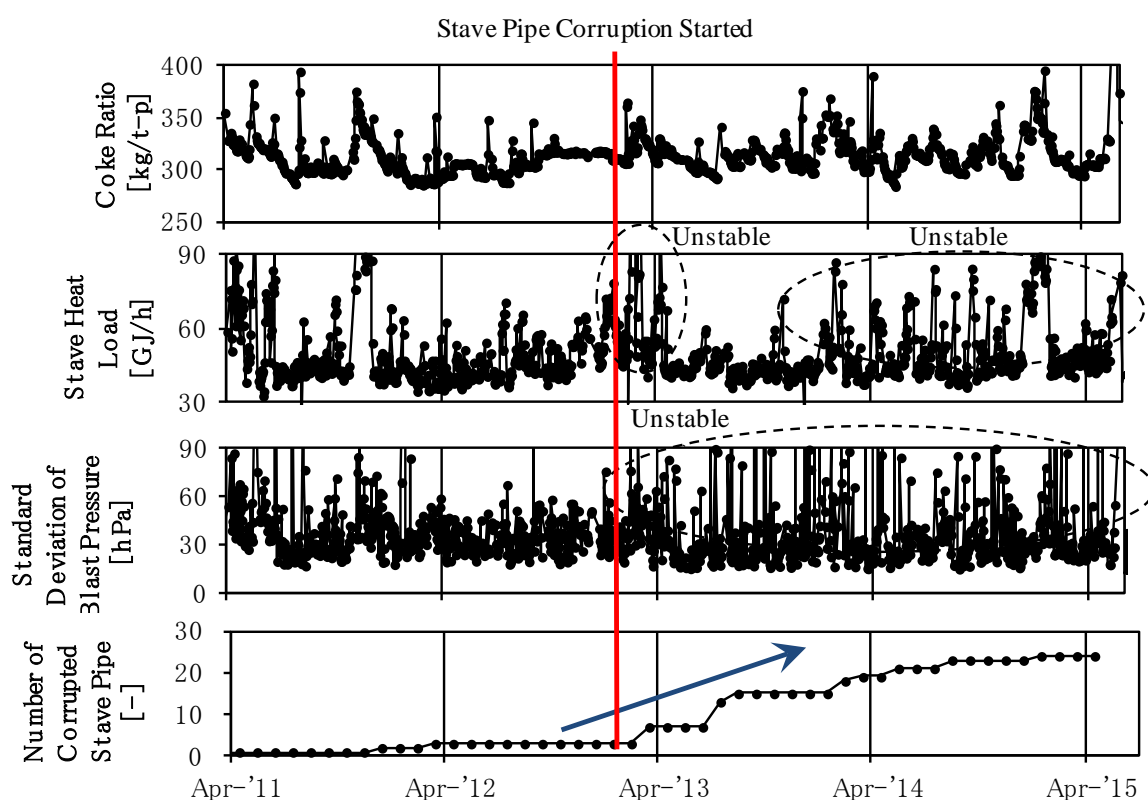

Figure 13. Trend of Muroran No. 2 Blast Furnace Operation before Stave Replacement

As the measure against unstable operation condition, it was decided to replace 41 damaged staves, at the bosh level of the furnace. The replacement was completed during 134 hours and 56 minutes shut-down in May 2015, after 14 years from the blow-in. Instead of FCD staves, copper staves were employed as new staves, so as to improve cooling ability at the bosh.

Figure 14 shows the operation result of Muroran No. 2 blast furnace during January and July 2015. After the replacement of staves in May, permeability and stave heat load became stable. Since then, coke ratio has been relatively low level, around 285 kg/t, as the result of repairing inner profile of the furnace.
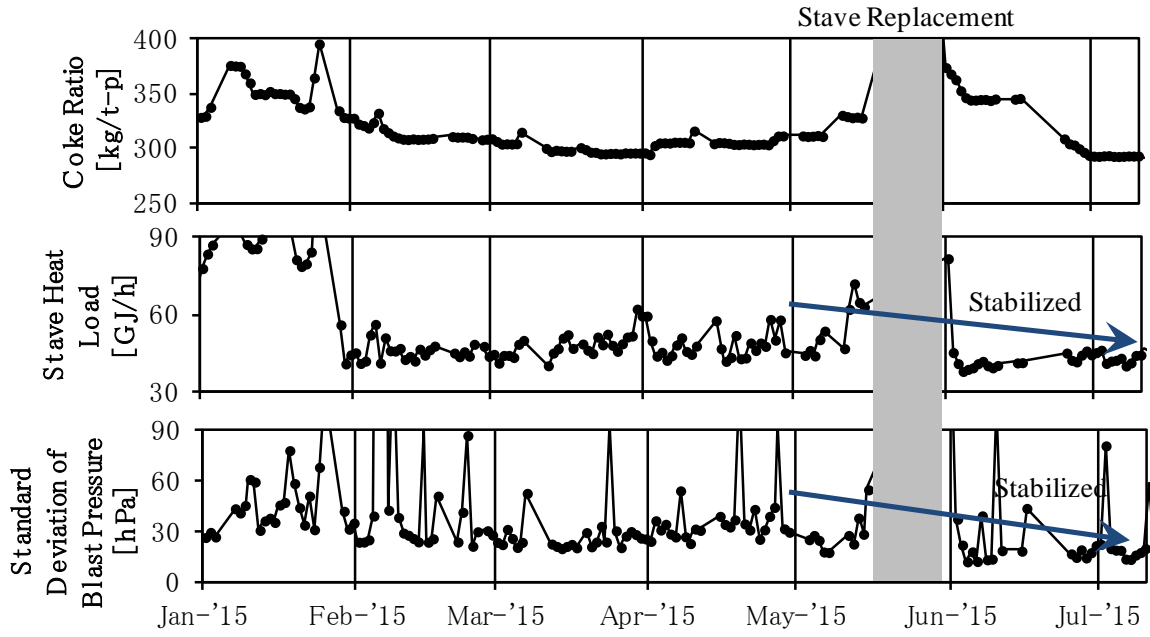
Figure 14. Trend of Muroran No. 2 Blast Furnace Operation before and after Stave Replacement

4. Conclusion

Several attempts in the field of ironmaking performed recently in NSSMC are mentioned above. Since the conditions of the natural resources and environment surrounding the ironmaking processes are supposed to be more and more difficult, NSSMC will pursue technical development to respond to the needs of the time.

New Charging Technique of Nut Coke at Blast Furnace with Center Feed Type Bell-less Top

Y. Kashihara[1], Y. Iwai[1], K. Fukada[1], H. Matsuno[1], H. Horikoshi[2] and K. Yamamoto[2]

1: Steel Research Laboratory, JFE Steel Corporation
2: East Japan Works (Keihin), JFE Steel Corporation

Abstract: Improved permeability and increased gas utilization have been desired in order to achieve low coke rate operation of blast furnaces. Coke mixed charging in the ore layer is one measure for realizing these improvements. A new charging technique for mixing nut coke in the ore layer at a blast furnace with a center feed type bell-less top was developed and investigated in an experiment with a 1/18.8 scale model of an actual blast furnace at JFE Steel. The discharge pattern of the mixed nut coke discharged from the bell-less top was improved, and the radial distribution of the mixed nut coke ratio at the furnace top after the mixed materials were charged in the blast furnace was also improved by the new charging technique in which nut coke was charged in the determined port of the upper bunker before ore was charged in the upper bunker. The new charging technique was applied to an actual blast furnace at JFE Steel, and improvement of gas permeability and a decrease in coke rate were confirmed.

1. Introduction

Reduction of CO_2 emission from the steel industry has become an important issue in recent years. In the steel works, the ironmaking process accounts for 70% of total energy consumption[1]. Therefore, research on low reducing agent rate and low coke rate operation of the blast furnace has been carried out with the aim of reducing energy consumption in the ironmaking process. Improvement of reducibility and permeability is important for achieving these operational conditions, and one measure for realizing this is coke mixed charging in the ore layer[2 - 6].

In mixing coke in the ore layer at the blast furnace, a measure in which the ore and coke were discharged from the ore bin at stockhouse was applied[6], but differences in the diameter and density of the ore and coke caused segregation during transport from the stockhouse to the top bunker[7]. When the ore and coke separated after charging of these materials in the furnace top, the effect of this technique in improving reducibility and permeability decreased. Thus, to prevent segregation during transport, mixing of the ore and coke near the point of discharge in the furnace top is necessary. At a blast furnace with a bell-less top of the 3 parallel bunker type, coke and ore mixed charging was carried out by simultaneous discharge of the ore and coke using 2 top bunkers[3,4] to prevent segregation of the coke.

Coke and ore mixed charging was also investigated at a blast furnace with a center feed type bell-less top. The author et al.[6] showed that the mixed coke ratio in the initial stage of discharge from the top bunker could be controlled by changing the discharge pattern of the mixed coke from the ore bin at the stockhouse. However, the mixed coke ratio in the middle and final stages of discharge from the top bunker could not be controlled by this method. At the blast furnace with the center feed type bell-less top, the method of simultaneous discharge

of ore and coke by using 2 top bunkers to prevent coke segregation could not be applied because only one line is used for transport from the stockhouse to the furnace. Thus, to improve the discharge pattern of the mixed coke from the top bunker by controlling the mixed coke ratio in the later stage of discharge at the blast furnace with the center feed type bell-less top, it was necessary to apply a new charging method in which the ore and coke are mixed during discharge from the top bunker, like the simultaneous discharge method which prevents coke segregation in the top bunker, and not the conventional method in which the coke and ore are mixed at the stockhouse.

In this study, a scale model experiment was carried out to develop a new charging technique for controlling the discharge pattern of the mixed coke from the top bunker at the blast furnace with the center feed type bell-less top. Next, the effect of the charging method on the mixed coke ratio distribution of the materials charged in the furnace top was investigated by a scale model experiment. Finally, an operating test in which the new charging method was applied was carried out at JFE Steel's East Japan Works (Keihin District) No. 2 blast furnace.

2. Experimental Procedure

Figure 1 shows the concept of the new charging method. In the conventional charging method in which nut coke and ore were mixed before the materials were charged in the top bunker, the mixed nut coke segregated in the top bunker, and the mixed coke ratio in the final stage of discharge from the top bunker decreased[6]. Therefore, a new charging method in which the nut coke was charged in the top bunker before the ore was charged in the top bunker was investigated by a scale model experiment.
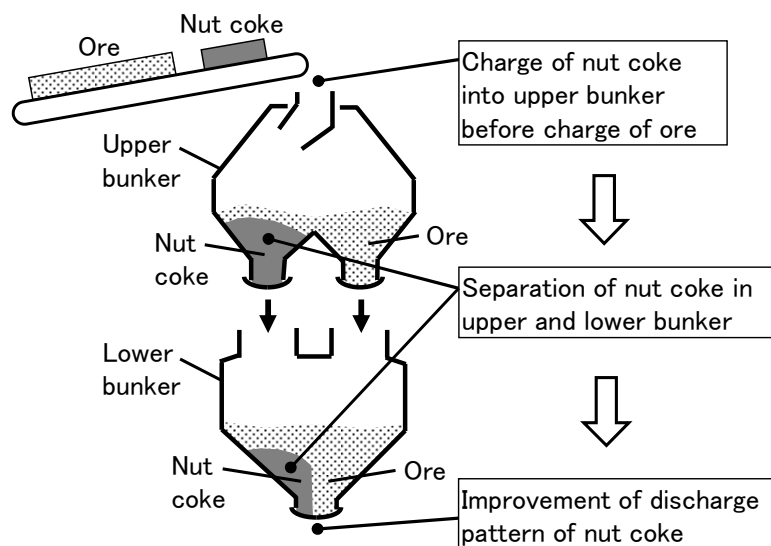

Figure 1. Concept of new charging method of nut coke.

Figure 2 shows a schematic illustration of the experimental apparatus. The experimental apparatus is a 1/18.8 scale model of JFE Steel's Keihin No. 2 blast furnace, which has a bell-less type charging system with a center feed type bell-less top. The scale model consists of an ore bin, a coke bin, a surge hopper, belt conveyers, a bell-less top and a model furnace to simulate the charging system of the actual blast furnace. In this experiment, the Froude number, which is the ratio of inertia to gravity, was matched with that of the actual blast

the tuyere), and we think that it is effective to prevent the decrease of pulverizing ability of the simultaneous pulverization of converter slag and coal, after pulverization and magnetic selection.

2-3. Prevention of excessive pulverization or coarse pulverization due to simultaneous pulverization of converter slag and coal

Figure 2 shows the distribution of particle size before and after simultaneous mixed pulverization of converter slag and coal. Slight lowering of average particle size and expansion of standard deviation were recognized by addition of 20 kg/t of converter slag. However, they were within the range of normal operation, and we prevented excessive pulverization or coarse pulverization due to simultaneous pulverization of converter slag and coal.
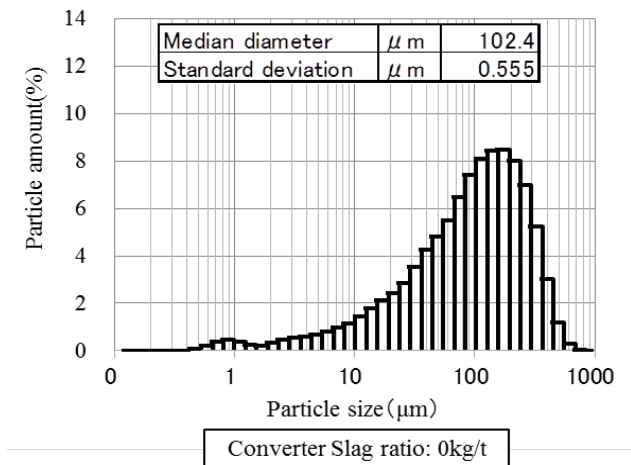

Figure 1: HGI of Coal and Original Converter Slag, before and after Magnetic Separation

Figure 2: Distribution of Particle Size before and after Simultaneous Mixed Pulverization of Converter Slag and Coal

3. Results

Figure 4 shows the relationship among the converter slag injection ratio and the pressure loss at lower part of the blast furnace, with daily data. We corrected the blast pressure change due to the difference of PC ratio and coal types. Together with the increase of converter slag injection ratio, the pressure loss at the lower part of the blast furnace decreases, however, there was a decreasing tendency of reduction effect of pressure loss at the lower part of the blast furnace with 10 kg/t or more of injection ratio. It is estimated that the converter slag injection may improve the fluidity of slag staying in the bird's nest area at the raceway, while the increase of converter slag injection amount has decrease the reduction of the pressure loss amount by the increase of slag flow-in amount[4], [5]. After this trial, we continue converter slag injection of 20 kg/t under the PC ratio 200 kg/t operation. With the composition of raw materials and coal types of this time at Kobe Works, the changed amount of coke ratio is assumed to be -5kg/t. Finally, we achieved the recycling of converter slag under the total amount molten iron pretreatment system.

Figure 4: Relationship between Converter Slag Ratio and Pressure Loss at the Lower Part of Blast Furnace

REFERENCE
1) J Ma : ISIJ int 39(1999),7,p697
2) L Okvis et al : ISIJ int. 41(2001),12,p1429
3) L Okvist et al : ISIJ int. 44(2004),9,p1501
4) T Kato et al : CAMP-ISIJ Vol.28 (2015)-99
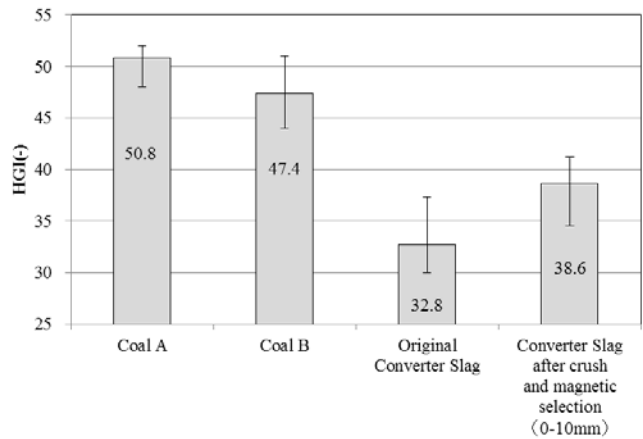5) N Mitsuoka et al : CAMP-ISIJ Vol.28 (2015)-100

investigation. The materials were charged by the same charging method as that at Keihin No. 2 blast furnace (C, O1, O2), and the surface profile and radial distribution of the mixed coke ratio at the furnace top of the model furnace were measured. The surface profile was measured with a laser profile meter, and the charged materials were collected by inserting cylinders 30 mm in diameter vertically into the burden surface from the upper direction to measure the radial distribution of the mixed coke ratio at the furnace top.

Table 1. Experimental conditions.

	Charging method of nut coke into upper bunker	Number of nut coke ports (-)	Discharge time lag of nut coke (s)
Base	mixing with ore before charge into upper bunker	4	0
Case1	charging separately before charge of ore	1	0
Case2	charging separately before charge of ore	1	0.3

3. Experimental Result and Discussion

3.1 Effect of Nut Coke Charging Method on Discharge Behavior of Nut Coke

Figure 3 shows the effect of the charging method of the nut coke in the upper bunker and in the lower bunker on the discharged weight ratio of the mixed coke ratio discharged from the top bunker. The mixed coke ratio is the ratio of the coke weight to the weight of the coke and ore, and the discharged weight ratio is the ratio of the integrated weight of the collected materials to the total collected weight. In Case1, the mixed coke ratio discharged from the lower bunker in the final stage was higher than that in Base. Thus, the charging method in which the nut coke was charged in a port of the upper bunker before the ore was charged in the upper bunker is effective for increasing the mixed coke ratio in the final stage of the materials discharged from the lower bunker.

Then, in Case2, the mixed coke ratio discharged from the lower bunker in the initial stage was lower than that in Case 1. Thus, the charging method in which the discharge of the materials in the port where the nut coke was charged was started after the discharge of the materials in the ports other than the port where the nut coke was charged was started was effective for decreasing the mixed coke ratio in the initial stage of the materials discharged from the lower bunker.

At Keihin No. 2 blast furnace, the ore is charging by reverse tilting[9], which is the method of charging from the central part to the peripheral part. This means the initial materials discharged from the lower bunker are charged in the central part of the furnace top. When the mixed coke ratio in the initial stage of discharge was high, a large amount of nut coke descended to the deadman because the deadman coke was replaced by the coke charged in the central part of the furnace top. When the voidage of the deadman coke decreased as a result of mixing of nut coke in the deadman, the pressure drop in the blast furnace increased[10] and the residual amount of slag and metal in the blast furnace increased[11]. Thus, the most suitable charging method of the nut coke is Case 2 because the mixed coke ratio in the final stage of discharge from the top bunker is high and the mixed coke ratio in the initial stage of discharge from the top bunker is low.
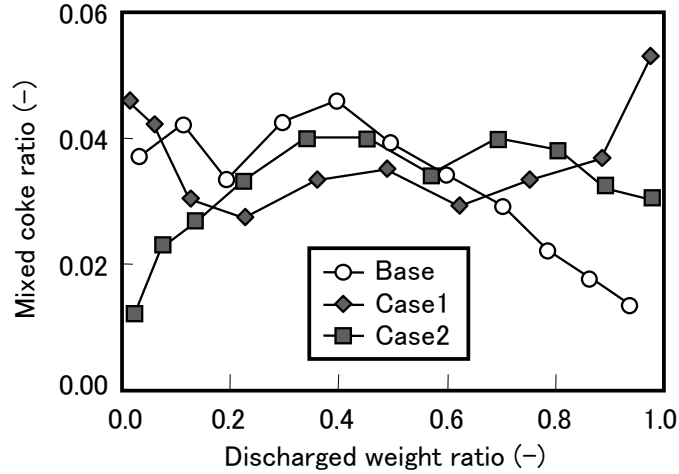
Figure 3. Change in mixed coke ratio discharged from top bunker.

3.2 Effect of Nut Coke Charging Method on Mixed Coke Ratio Distribution at Furnace Top

Figure 4 shows the results of measurements of the surface profiles after charging. In Base and Case 2, the new charging method which was estimated to be the most suitable in section 3.1, the measurement results were compared. Both results showed similar surface profiles.
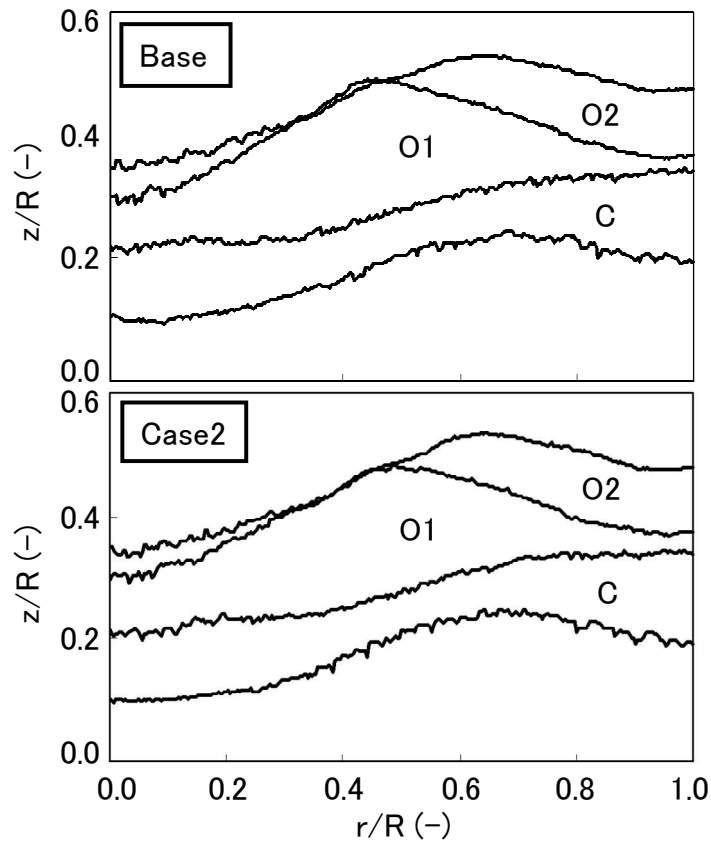

Figure 4. Comparison of surface profiles after charging.

Figure 5 shows the effect of the mixed coke charging method on the radial distribution of the mixed coke ratio. In Base, the mixed coke ratio at the central part was high because the mixed nut coke ratio in the initial stage of discharge from the top bunker was high, as shown in Fig. 3, and the materials discharged in the initial stage were charged in the central part of the furnace top by reverse tilting. In Case 2, the mixed coke ratio at the central part was low because the mixed nut coke ratio in the initial stage of discharge from the top bunker was low, as shown in Fig. 3, and the materials discharged in the initial stage were charged in the central part of the furnace top by reverse tilting. The mixed coke ratio was high at r/R = 0.5－0.8, which was near the top of the heap charged in the last rotation of the chute, because the mixed nut coke ratio in the final stage of discharge from the top bunker was high, as shown in Fig. 3. Thus, the new charging technique in which the nut coke charging method was changed made it possible to controll the radial distribution of the mixed coke ratio at the furnace top while maintaining the surface profile.

As a result, when using the new charging technique, in which the nut coke was charged in one port of the upper bunker and the discharge of the materials in the port where the nut coke was charged was started 0.3 sec after starting the discharge of the materials at the ports other than the port where the nut coke was charged, increase in the mixed coke yield in the ore layer was expected by the decrease in segregated mixed coke to the central part at the furnace top[12] and improvement of the permeability in the cohesive zone was expected.
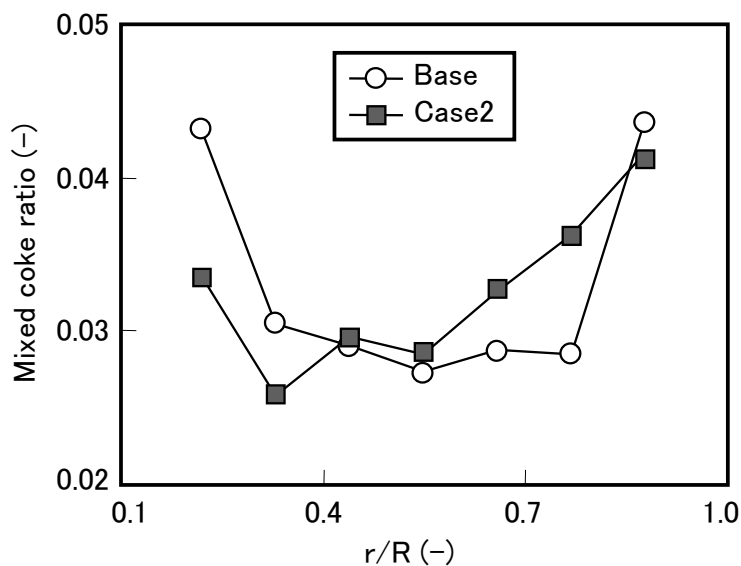

Figure 5. Effect of mixed coke charging method on radial distribution of mixed coke ratio.

4. Operational Test for Examination of Change in Nut Coke Charging Method

To estimate the effect of the new charging technique on the operation of the actual blast furnace, an operational test was carried out at Keihin No. 2 blast furnace. At Keihin No. 2 blast furnace, coke is charged in one batch (C) and ore is charged in two batches (O1, O2). Before the test operation, the nut coke was charged by the conventional method, which correspond to Base in the scale model experiment. The new charging technique, i.e., Case 2 in the scale mode experiment, was applied during test operation. The discharge time lag in this test was decided to be 1 sec, which is the estimated value when the Froude number of the actual condition was near that of the experimental condition. The nut coke charging method was changed in both ore batches, and the discharge time lag was 1 sec in both ore batches.

Figure 6 shows the typical permeability index before and after the change in the nut coke charging method. The permeability index increased due to the decrease in coke rate, generally. However, at the same coke rate, the permeability index after the change in the nut coke charging method was lower than that before the change in the nut coke charging method. Especially, after the change in the nut coke charging method, the pressure drops in the lower shaft decreased. It is thought that the pressure drop in the cohesive zone decreased by the increase in the mixed coke yield in the ore layer.

As a result, the new charging technique in which the nut coke charging method was changed is an effective control measure for reducing the permeability resistance of the blast furnace by improving the mixed coke ratio at the blast furnace with the center feed type bell-less top.
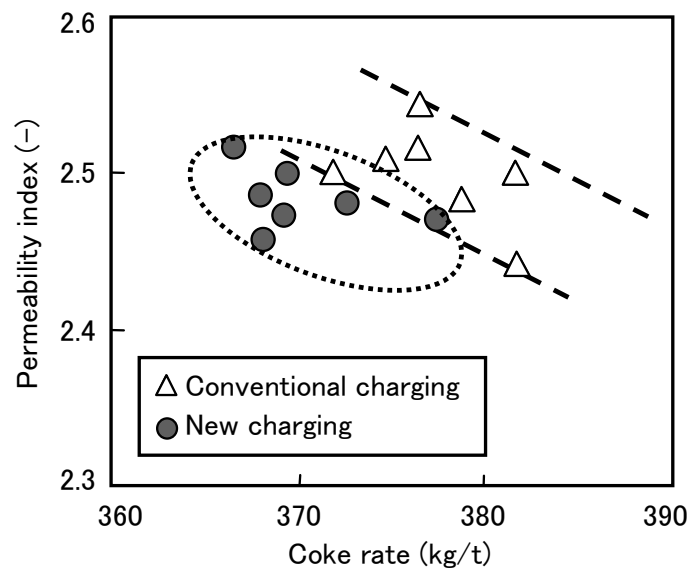

Figure 6. Comparison of permeability index before and after change in charging method of nut coke.

5. Conclusions

A charging technique to improve permeability of blast furnace by controlling the mixed coke ratio distribution in the ore layer was investigated at a blast furnace with a center feed type bell-less top. First, a new charging technique for controlling the discharge pattern of the mixed coke discharged from the top bunker was investigated in a scale model experiment. Then, the effect of the new charging technique on the mixed coke ratio distribution in the ore layer stacked in the furnace top was investigated in a scale model experiment. Finally, the effect of the new charging technique on the operation of the actual blast furnace was investigated. The following conclusions were obtained.

(1) The charging method in which nut coke was charged in one determined port of the upper bunker before ore was charged in the upper bunker prevented segregation of the nut coke in the top bunker, and the mixed coke ratio of the materials in the final stage of discharge from the lower bunker increased. The charging method in which the materials of the port where the nut coke was charged were discharged in the lower bunker after the discharge of the materials of ports other than the port where the nut coke was charged reduced the mixed coke ratio of the materials in the initial stage of discharge from the lower bunker.

(2) The charging method in which discharge into the lower bunker of the materials in the port where the nut coke was charged was started after discharge into the lower bunker of the

materials in the ports other than the port where the nut coke was charged improved the radial distribution of the mixed coke ratio.

(3) An operational test of the new charging technique, in which the nut coke charging method was changed, was carried out at Keihin No. 2 blast furnace. The permeability index was decreased by application of the new charging technique.

References:

1) T. Ariyama, R. Murai, J. Ishii and M. Sato, Reduction of CO_2 Emissions from Integrated Steel Works and Its Subjects for a Future Study, *ISIJ International*, 45 (2005), 1371.

2) S. L. Yaroshevskii, V. A. Nozdrachev, A. P. Chebotarev, V. A. Rudenko, S. A. Feshchenko, A. M. Kuznetsov, V. P. Padalka, N. S. Khlaponin and A. V. Kuzin, Efficiency of Using Coke Fractions Smaller than 40mm in Blast Furnace, *Metallurgist*, 44 (2000), 598.

3) S. Watakabe, K. Takeda, H. Nishimura, S. Goto, N. Nishimura, T. Uchida and M. Kiguchi, Development of High Ratio Coke Mixed Charging Technique to the Blast Furnace, *ISIJ International*, 46 (2006), 513.

4) A. Murao, Y. Kashihara, S. Watakabe and M. Sato, Development of FCG Dynamic Control Technique at Mixed Charging of Massive Coke into Ore Layer, *ISIJ International*, 51 (2011), 1360.

5) Y. Kashihara, Y. Sawa and M. Sato, Effect of Hydrogen Addition on Reduction Behavior of Ore Layer Mixed with Coke, *ISIJ International*, 51 (2012), 1979.

6) A. Murao, Y. Kashihara, N. Oyama, M. Sato, S. Watakabe, K. Yamamoto and Y. Fukumoto, Development of Control Techniques for Mixing Small Coke at Bell-less Top Blast Furnace, *ISIJ International*, 55 (2015), 1172.

7) K. Sunahara, C. Kamijo and T. Inada, Investigation on Mechanism of Size and Density Segregations of Burden Particle in the Blast Furnace, *55th Ironmaking Conf. Proc.*, ISS, Warrendale, PA, (1996), 3.

8) M. Hattori, B. Iino, A. Shimomura, H. Tsukiji and T. Ariyama, Development of Burden Distribution Simulation Model for Bell-less Top in a Large Blast Furnace and Its Application, *ISIJ International*, 33 (1993), 1070.

9) T. Sato, T. Nouchi, K. Takeda and H. Kamano, Development of Burden Distribution Control with an Advanced Bell-less Top at Chiba No.6 Blast Frunace, *Tetsu-to-Hagané*, 86 (2000), 648.

10) T. Sato, M. Sato, K. Takeda and T. Ariyama, Control of Peripheral Gas Flow and Design of Burden Quality for Low Reducing Agent Operation of Blast Furnace, *Tetsu-to-Hagané*, 92 (2006), 1006.

11) T. Nouchi, M. Sato, K. Takeda and T. Ariyama, Effect of Operation Condition and Casting Strategy on Drainage Efficiency of the Blast Furnace Hearth, *ISIJ International*, 45 (2005), 1515.

12) Y. Kashihara, Y. Iwai, N. Ishiwata, N. Oyama, H. Matsuno, H. Horikoshi, K. Yamamoto and M. Kuwabara, Development of New Charging Technique for Mixing Coke in Ore Layer at Blast Furnace with Center Feed Type Bell-less Top, *ISIJ International*, 57 (2017), 665.

Converter Slag Recycling by Tuyere Injection in High PC rate operation at Kobe No.3 blast furnace

Nayuta Mitsuoka[*], Kota Tanaka[*], Tomonori Maeda[*], Hitoshi Toyota[*], Atsushi Sato[*], Tadasu Matsuo[*],

[*] Ironmaking Department, Kobe Works, Kobe Steel Ltd

1. Introduction

Generation amount of converter slag at Kobe Works is 57kg/t, and it's P concentration is as low as 0.8% when compared with 1.9%, that of the slag generated in pretreatment furnace, therefore, there is a possibility to be recycled as an alternative lime-based material for the iron-making process. Kobe No.3 blast furnace continues the all-pellet operation and the low sinter ratio operation, therefore, lumpy lime stone charge from the blast furnace top is large. So, coarse grains (10 mm or more) of converter slag was promoted to recycle as charging from the furnace top, as to decrease endothermic amount of decomposition by lime stone charging from the blast furnace top. On the other hand, fine grains (0 - 10 mm) could not be charged to the blast furnace top from the viewpoint of pressure loss. For this reason, in-house recycle amount (for sintering) of fine grains remained at 59%, and we had to sell 41% to the outside. We expected big cost reduction, if fine grains of converter slag were able to be effectively used in the Works, and a recycle system of converter slag under the total molten iron pretreatment system was able to be established.

Kobe No.3 blast furnace (4th: inner volume of 2,112 m^3, blowing-in date: December 17, 2007) has continued the high pulverized coal (PC) ratio and low coke ratio operation under the all-pellet operation (September 2001).
To pursue further cost reduction under the high PC ratio and low coke ratio operation in the future, improvement of the permeability in the bird's nest at the lower part of the blast furnace and prevention of amount of lime stone charged, is needed, and the tuyere injection of converter slag is considered to be an effective means.

This is reported that we achieved the recycling of converter slag under the total molten iron pretreatment system, and in the process, obtained knowledge on the reduction of pressure loss at the lower part of the blast furnace[1-3] by injection of converter slag.

2. Pretreatment technology toward the converter slag injection
2-1. Technical issue of pretreatment toward the blast furnace tuyere injection of converter slag

Table 1 shows the properties of converter slag, lime stone and dolomite. Comparing with lime stone and dolomite considered as flux injection material into the tuyere, converter slag contains FeO, and is low melting point and low endothermic amount of resolution, because it's pre-melt. Therefore, we found that converter slag was excellent in heating and fusibility, assimilability and slag forming property, and dropping property, and it had the improvement effect of permeability when it was injected to the tuyere of the blast furnace, from the laboratory examination[4].

Table 1: Properties of Converter Slag, Lime Stone and Dolomite

	FeO (mass%)	SiO_2 (mass%)	CaO (mass%)	Al_2O_3 (mass%)	MgO (mass%)	CaO /SiO_2 (-)	Melting point (℃)	Heat of fusion (J/g)	Heat of decomposition (J/g)
Converter slag	10.0	46.9	18.6	4.5	6.4	0.40	1352	63.4	-
Lime stone	0.0	54.8	0.6	0.0	0.6	0.01	2572(CaO)	-	1782.3(CaO)
Dolomite	0.0	30.2	1.1	0.3	20.5	0.04	2800(MgO)	-	1560.6(MgO)

In order to use fine converter slag in the blast furnace, we assumed the shared use of existing coal pulverization facility to avoid new investment in facility, and identified the following two technical issues:
①Lowering of coal pulverization ability due to the simultaneous pulverization of converter slag and coal.
②Excessive pulverization or coarse pulverization of coal due to simultaneous pulverization of converter slag and coal.

2-2. Prevention of lowering in coal pulverizing ability in the simultaneous pulverization of converter slag and coal.

Figure 1 shows Hard Grove Index (HGI) of coal and converter slag, before and after the magnetic separation. When HGI indicates high, it means that pulverizing ability is good. As original converter slag contains approximately 10 % Fe, HGI decreases remarkably, but pulverizing ability was able to be significantly improved by avoiding coarse Fe grains with crush and magnetic selection. The injection of converter slag is set to approximately 20kg/t of the amount of injected PC approximately 200kg/t (approximately 10 % of the total amount of injected pulverized fine materials into

the tuyere), and we think that it is effective to prevent the decrease of pulverizing ability of the simultaneous pulverization of converter slag and coal, after pulverization and magnetic selection.

2-3. Prevention of excessive pulverization or coarse pulverization due to simultaneous pulverization of converter slag and coal

Figure 2 shows the distribution of particle size before and after simultaneous mixed pulverization of converter slag and coal. Slight lowering of average particle size and expansion of standard deviation were recognized by addition of 20 kg/t of converter slag. However, they were within the range of normal operation, and we prevented excessive pulverization or coarse pulverization due to simultaneous pulverization of converter slag and coal.
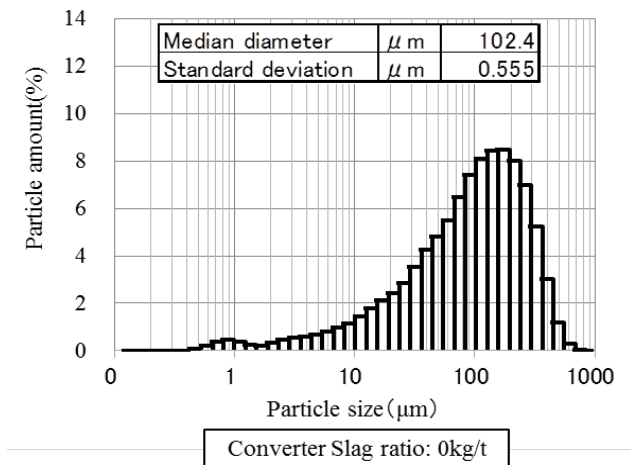

Figure 1: HGI of Coal and Original Converter Slag, before and after Magnetic Separation

Figure 2: Distribution of Particle Size before and after Simultaneous Mixed Pulverization of Converter Slag and Coal

3. Results

Figure 4 shows the relationship among the converter slag injection ratio and the pressure loss at lower part of the blast furnace, with daily data. We corrected the blast pressure change due to the difference of PC ratio and coal types. Together with the increase of converter slag injection ratio, the pressure loss at the lower part of the blast furnace decreases, however, there was a decreasing tendency of reduction effect of pressure loss at the lower part of the blast furnace with 10 kg/t or more of injection ratio.It is estimated that the converter slag injection may improve the fluidity of slag staying in the bird's nest area at the raceway, while the increase of converter slag injection amount has decrease the reduction of the pressure loss amount by the increase of slag flow-in amount[4], [5]. After this trial, we continue converter slag injection of 20 kg/t under the PC ratio 200 kg/t operation. With the composition of raw materials and coal types of this time at Kobe Works, the changed amount of coke ratio is assumed to be -5kg/t. Finally, we achieved the recycling of converter slag under the total amount molten iron pretreatment system.

Figure 4: Relationship between Converter Slag Ratio and Pressure Loss at the Lower Part of Blast Furnace

REFERENCE
1) J Ma : ISIJ int 39(1999),7,p697
2) L Okvis et al : ISIJ int. 41(2001),12,p1429
3) L Okvist et al : ISIJ int. 44(2004),9,p1501
4) T Kato et al : CAMP-ISIJ Vol.28 (2015)-99
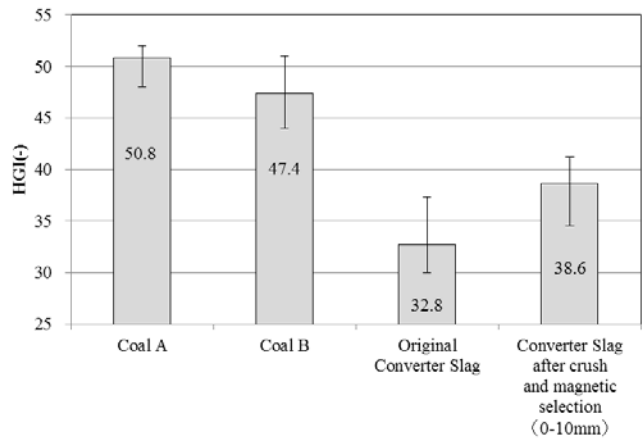5) N Mitsuoka et al : CAMP-ISIJ Vol.28 (2015)-100

Upgrading and Recycling of Blast Furnace Sludge

Andersson A.[1], Morcel A.[2], Gullberg A.[2] and Ahmed H.[1,3]

[1]Luleå University of Technology, [2]Swerea MEFOS, [3]Central Metallurgical Research and Development Institute, Helwan, Egypt

Contact: Anton Andersson, anton.andersson@ltu.se, +46920493409

Conclusion

i.   Fine-grained, low zinc-containing blast furnace (BF) sludge could be upgraded – removing zinc.
ii. The low-zinc fraction of the upgraded sludge could be recycled to the BF via cement-bonded briquettes.

Introduction

Recycling of both BF dust and sludge to the BF is desirable as both have a chemistry dominated by iron and carbon. Depending on the operation of the BF, the dominating output of zinc can be via the top gas. In order to recycle both the BF dust and sludge, a bleed of Zn need to be introduced to avoid accumulation of Zn in the furnace. Figure 1.
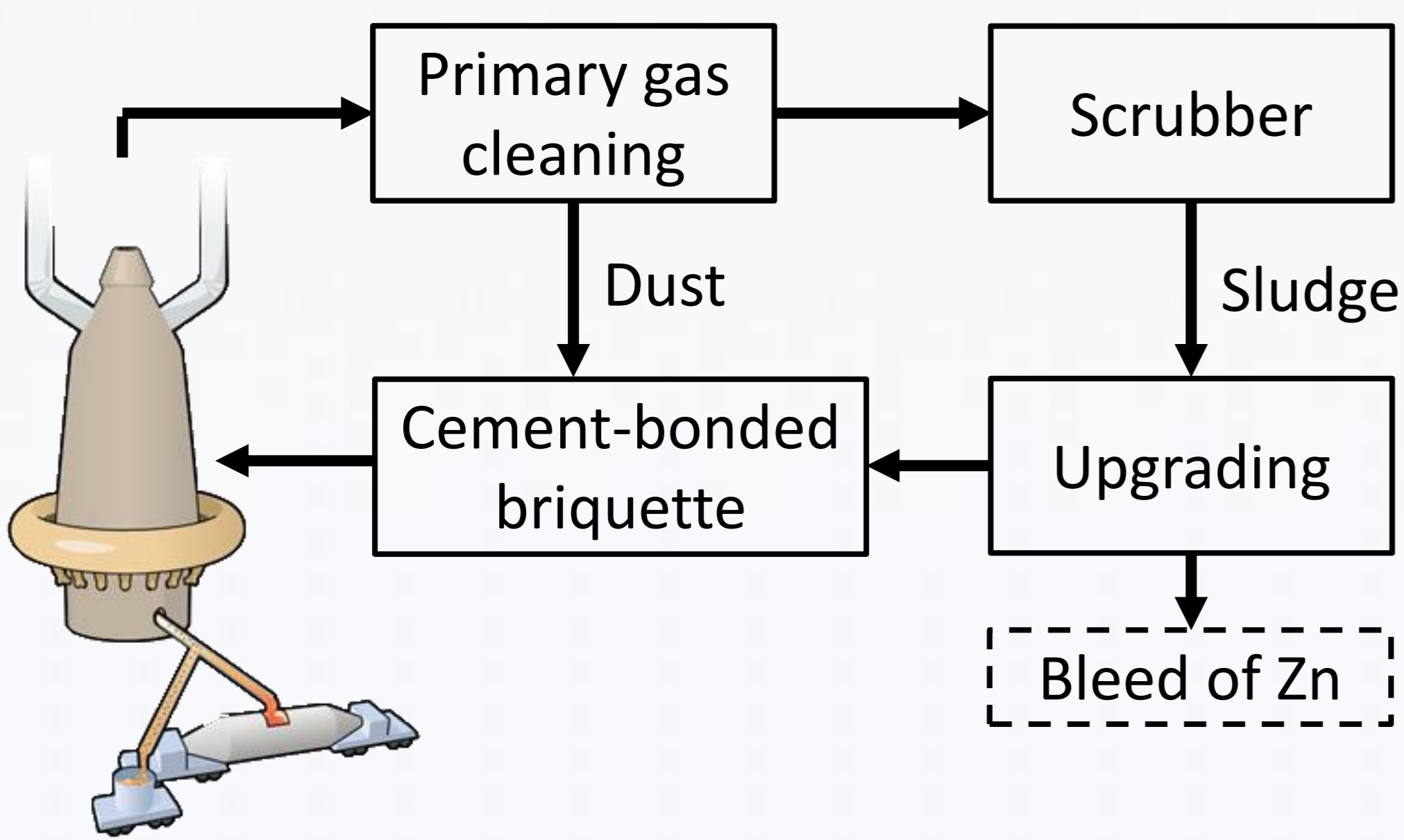

Figure 1: Bleed of Zn. [BF illustration from SSAB Europe]

Aim

The aim of the study was to investigate if a low-zinc, fine-grained BF sludge could be upgraded – by removing zinc – and recycled in the BF using cement-bonded briquettes.

Upgrading and Briquetting

A low-zinc containing, fine-grained BF sludge was upgraded using different methods including hydrocycloning, sulfuric acid leaching and the tornado process. The efficiency of the separation of zinc from iron and carbon is presented in the table below. The low-zinc fraction from the tornado process was included in a cement-bonded briquette for recycling in the BF.

Distribution of total amount to low-zinc fraction (%)				
Method	Zn	Fe	C	Solids
Hydrocyclone	26	66	37	59
Leaching, pH 1	5	91	100	86
Leaching, pH 3	20	96	100	93
Tornado	19	37	39	31

Laboratory Scale BF Experiment

A laboratory scale BF experiment developed by LKAB was utilized to study three different briquette recipes:

i.   One reference recipe representing the industrial briquette currently recycled.
ii. One with 10 wt% added upgraded BF sludge.
iii. One with 20 wt% added upgraded BF sludge.

The addition of upgraded BF sludge did not have any negative effect on the reducibility of the briquette. Furthermore, the added BF sludge improved the integrity of the briquettes after reduction.
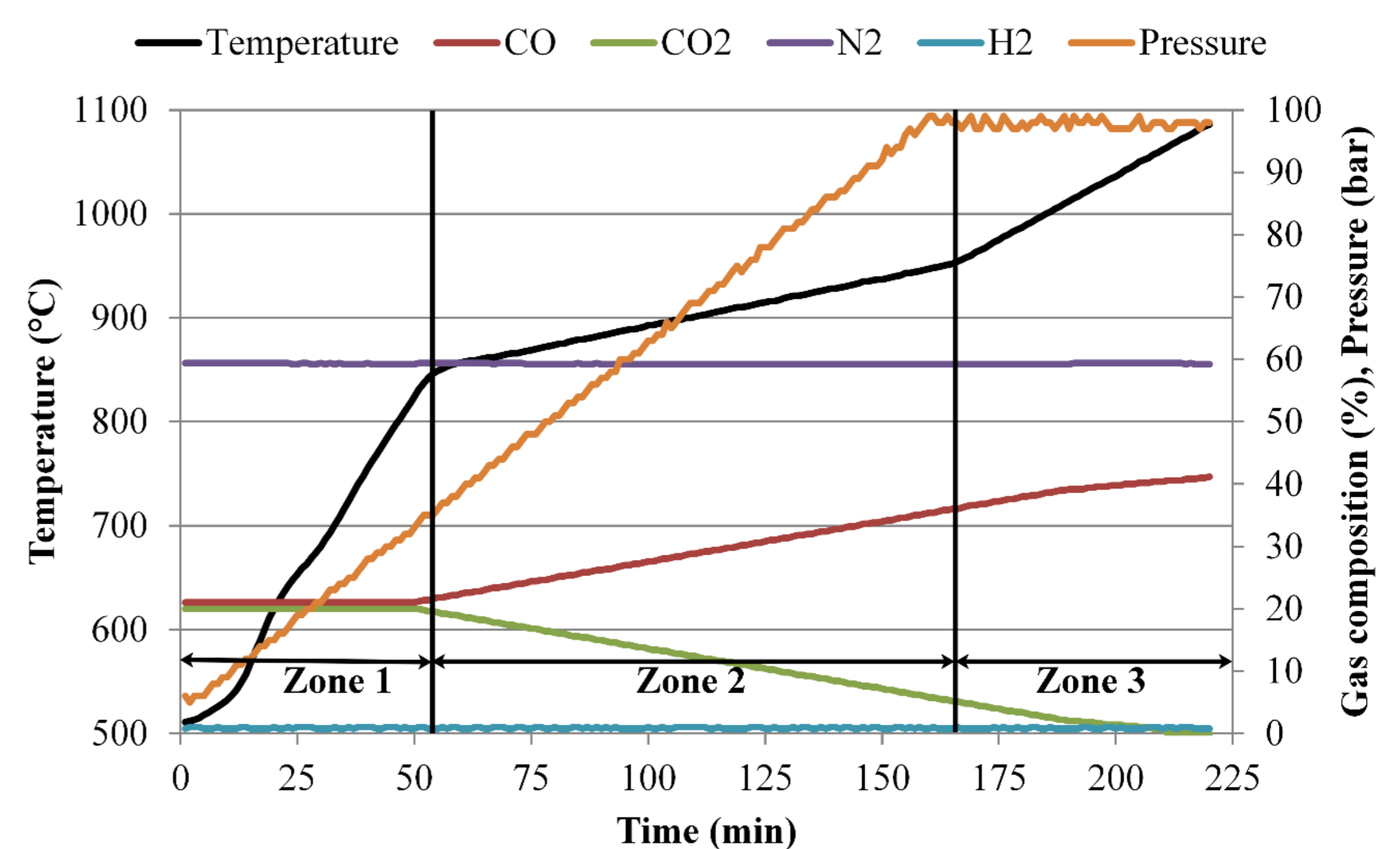

Figure 2: Laboratory scale BF experiment.

LKAB Experimental BF

The three briquette recipes were charged as basket samples in the LKAB EBF during campaign K32 in 2016. The addition of upgraded BF sludge did not affect the reducibility or the strength of the briquettes negatively.
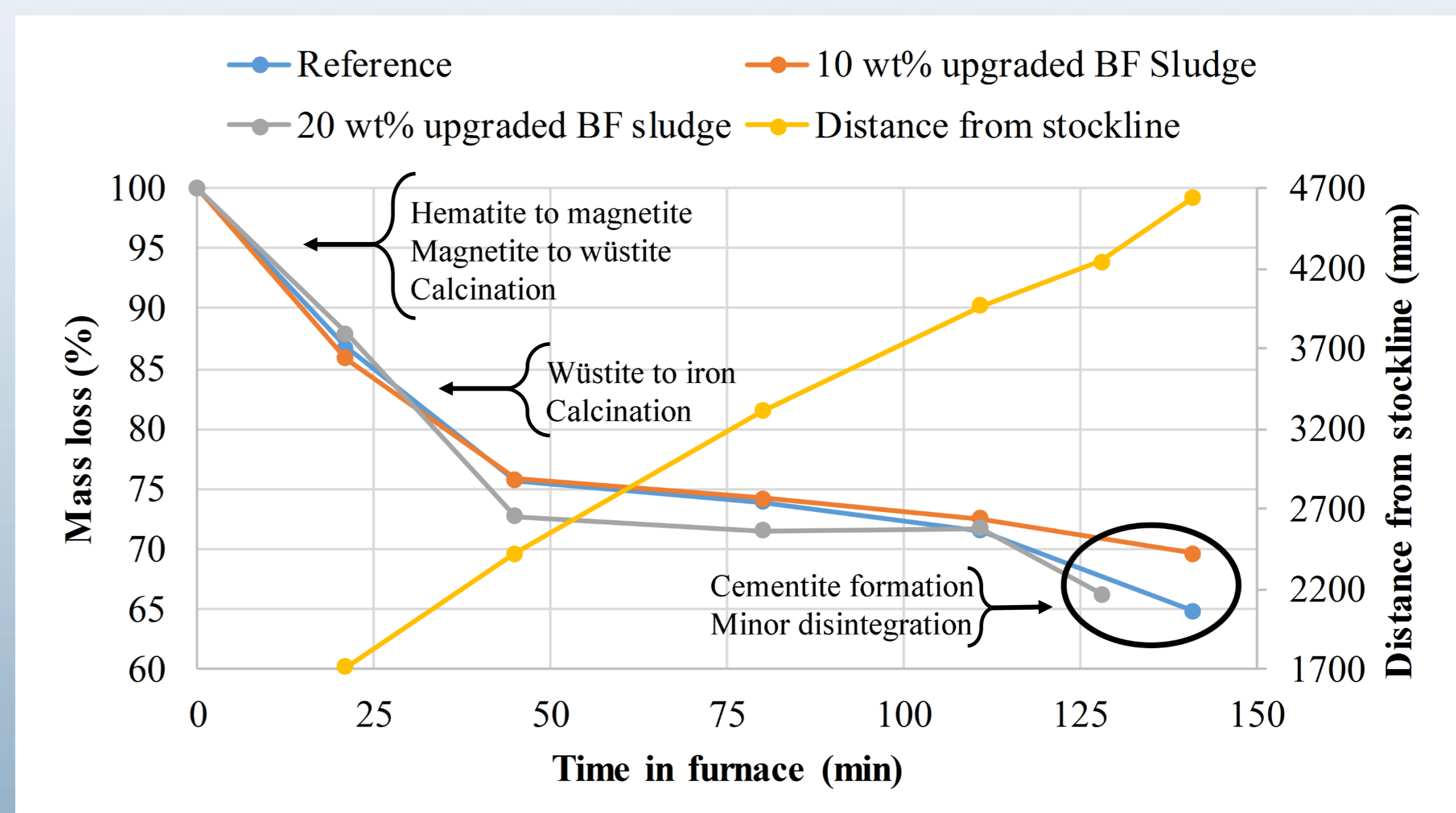

Figure 3: Mass loss and reactions in the LKAB EBF.

LULEÅ
UNIVERSITY
OF TECHNOLOGY

Jernkontoret, the Swedish Steel Producers' Association,
is pleased to announce the international conference:

3rd Ingot Casting, Rolling and Forging Conference, ICRF 2018
16–19 October 2018

Follow the event on www.icrf2018.com

Jernkontoret

The Swedish Steel Producers' Association

Since its foundation back in 1747, Jernkontoret has been owned jointly by the Swedish steel companies. Jernkontoret represents Sweden's steel industry on issues that relate to trade policy, research and education, standardisation, energy, the environment and sustainability as well as transportation issues. Jernkontoret also manages the joint Nordic research in the steel industry. In addition, Jernkontoret draws up statistical information relating to the industry and carries on research into the history of mining and metallurgy.